frontiers | Research Topics

Differences in shale oil and gas reservoirs across various sedimentary environments: theories and applications

Edited by
Hu Li and Ahmed E. Radwan

Published in
Frontiers in Earth Science
Frontiers in Environmental Science

ISSN 1664-8714
ISBN 978-2-8325-5699-3
DOI 10.3389/978-2-8325-5699-3

About Frontiers

Frontiers is more than just an open access publisher of scholarly articles: it is a pioneering approach to the world of academia, radically improving the way scholarly research is managed. The grand vision of Frontiers is a world where all people have an equal opportunity to seek, share and generate knowledge. Frontiers provides immediate and permanent online open access to all its publications, but this alone is not enough to realize our grand goals.

Frontiers journal series

The Frontiers journal series is a multi-tier and interdisciplinary set of open-access, online journals, promising a paradigm shift from the current review, selection and dissemination processes in academic publishing. All Frontiers journals are driven by researchers for researchers; therefore, they constitute a service to the scholarly community. At the same time, the *Frontiers journal series* operates on a revolutionary invention, the tiered publishing system, initially addressing specific communities of scholars, and gradually climbing up to broader public understanding, thus serving the interests of the lay society, too.

Dedication to quality

Each Frontiers article is a landmark of the highest quality, thanks to genuinely collaborative interactions between authors and review editors, who include some of the world's best academicians. Research must be certified by peers before entering a stream of knowledge that may eventually reach the public - and shape society; therefore, Frontiers only applies the most rigorous and unbiased reviews. Frontiers revolutionizes research publishing by freely delivering the most outstanding research, evaluated with no bias from both the academic and social point of view. By applying the most advanced information technologies, Frontiers is catapulting scholarly publishing into a new generation.

What are Frontiers Research Topics?

Frontiers Research Topics are very popular trademarks of the *Frontiers journals series*: they are collections of at least ten articles, all centered on a particular subject. With their unique mix of varied contributions from Original Research to Review Articles, Frontiers Research Topics unify the most influential researchers, the latest key findings and historical advances in a hot research area.

Find out more on how to host your own Frontiers Research Topic or contribute to one as an author by contacting the Frontiers editorial office: frontiersin.org/about/contact

Differences in shale oil and gas reservoirs across various sedimentary environments: theories and applications

Topic editors
Hu Li — Sichuan University of Science and Engineering, China
Ahmed E. Radwan — Jagiellonian University, Poland

Citation
Li, H., Radwan, A. E., eds. (2024). *Differences in shale oil and gas reservoirs across various sedimentary environments: theories and applications*. Lausanne: Frontiers Media SA. doi: 10.3389/978-2-8325-5699-3

Table of contents

Frontiers in Earth Science

TYPE Editorial
PUBLISHED 05 November 2024
DOI 10.3389/feart.2024.1514734

OPEN ACCESS

EDITED AND REVIEWED BY
Alexander Kokhanovsky,
German Research Centre for
Geosciences, Germany

*CORRESPONDENCE
Hu Li,
lihu860628@126.com,
lihu@suse.edu.cn
Pengju Li,
378737466@qq.com

RECEIVED 21 October 2024
ACCEPTED 22 October 2024
PUBLISHED 05 November 2024

CITATION
Li H, Li P, Luo J, Radwan AE, Wang H and Li H (2024) Editorial: Differences in shale oil and gas reservoirs across various sedimentary environments: theories and applications. *Front. Earth Sci.* 12:1514734.
doi: 10.3389/feart.2024.1514734

Editorial: Differences in shale oil and gas reservoirs across various sedimentary environments: theories and applications

Hu Li[1,2,3,4]*, Pengju Li[1,2,3]*, Ji Luo[1,2], Ahmed E. Radwan[5],
Haijun Wang[1,2] and Hongying Li[1,2,3]

[1]School of Economics, Sichuan University of Science and Engineering, Zigong, China, [2]Research Center of Industrial Transformation and Innovation, Sichuan University of Science and Engineering, Zigong, China, [3]Sichuan Key Provincial Research Base of Intelligent Tourism, Sichuan University of Science and Engineering, Zigong, China, [4]National Key Laboratory of Oil and Gas Reservoir Geology and Exploitation (Southwest Petroleum University), Chengdu, China, [5]Faculty of Geography and Geology, Institute of Geological Sciences, Jagiellonian University, Kraków, Poland

KEYWORDS

shale oil and gas, reservoir characteristics, pore structure, geological theories, experimental geological technology, sedimentary environment

Editorial on the Research Topic
Differences in shale oil and gas reservoirs across various sedimentary environments: theories and applications

1 Introduction

The United States Geological Survey (USGS) classifies shale oil and gas plays as "continuous petroleum accumulations." These reservoirs are not discrete, conventional traps formed by hydrocarbon migration and accumulation but rather represent widespread, pervasive hydrocarbon resources, typically found within rocks characterized by relatively low matrix permeability (McMahon et al., 2024). Shale oil and gas, hydrocarbons stored within shale formations, constitute a significant unconventional resource crucial for optimizing the global energy mix and achieving carbon peaking and neutrality goals.

The United States pioneered shale oil and gas development, completing its first commercial natural gas well in 1825, drawing from Upper Devonian shales near Fredonia, New York (McMahon et al., 2024). The United States possesses abundant shale oil and gas resources, with estimated geological resources exceeding 0.246×10^{12} t of shale oil and 290×10^{12} m^3 of shale gas. Two decades of exploration, development, and technological advancement have resulted in sophisticated extraction techniques, including three-dimensional (3D) development strategies, refracturing technologies, enhanced oil recovery (EOR) methods, and extended-reach ("U"-shaped) well designs. From 2007 to 2023, the United States shale oil and gas production surged from approximately 11.2×10^4 t/d to over 300.0×10^4 t/d, surpassing conventional oil and gas production in 2017. By 2023, shale oil and gas accounted for over 60% of total oil and gas production and are projected to remain a major contributor to energy production for the foreseeable future.

Inspired by the successful North American experiences in shale gas plays such as the Barnett, Marcellus, Haynesville, Fayetteville, Woodford, and Eagle Ford, China's shale gas exploration has accelerated significantly since 2005 (Li, 2023a; Li J. et al., 2024). Unconventional resources, particularly shale gas, are expected to extend the productive life of China's oil and gas industry. Over a decade of dedicated research, development, and field trials has yielded significant breakthroughs in shale oil and gas exploration and development in China, achieving commercial-scale production from marine shale gas formations in the south and continental shale oil resources nationwide (Chen et al., 2019; Dang et al., 2022). National-level demonstration zones, such as Fuling for marine shale gas and Daqing Gulong for continental shale oil, along with the Ordos Basin shale oil development pilot area, have been established, marking the beginning of a shale revolution in China (Jia et al., 2024). In 2022, global natural gas production reached 4.03 × 10^{12} m^3, with unconventional gas contributing 28.62%. Shale gas production increased by 704.34 × 10^8 m^3. According to data released by China's National Energy Administration, technically recoverable shale gas resources in China are estimated at 21.80 × 10^{12} m^3, establishing shale gas as a key driver of future natural gas production growth (He et al., 2024). China holds substantial shale oil resources, with 16 prospective shale formations identified across more than ten sedimentary basins. These predominantly lacustrine shale oil reservoirs are characterized by strong heterogeneity, significant cumulative thickness, limited areal extent, relatively low thermal maturity, and diverse organic matter types. The latest resource assessment by the Ministry of Natural Resources estimates China's geological shale oil resource potential at 397.46 × 10^8 t, with technically recoverable resources estimated at 34.98 × 10^8t. Onshore medium-to high-maturity shale oil resources, approximated at 283 × 10^8t, represent a strategically vital area for securing China's long-term oil supply.

Exploring unconventional resources has demonstrably proven that the successful development of shale oil and gas hinges on innovative geological theories and advancements in engineering technologies. Geological innovations, spurred by breakthroughs in laboratory analytical techniques, have laid a crucial foundation for this success (Fan et al., 2020; Abolghasemi and Andersen, 2021). Experimental analyses focusing on shale source rock evaluation, pore structure characterization, gas content analysis, physical property measurements, brittleness evaluation, fluid flow mechanisms, and geomechanical properties provide critical scientific data supporting geological assessments, target selection, reserve estimation, development planning, and policy formulation (Li et al., 2023c; Peng et al., 2024). Globally, exploration and development efforts targeting shale oil and gas in marine-continental transitional and terrestrial formations have yielded significant breakthroughs, driving the development of numerous geological theories and technologies for shale oil and gas extraction (Li J. et al., 2022).

To systematically summarize these global advancements in shale oil and gas exploration and development, comprehensively document practical achievements, further delineate exploration directions and resource prospects, and inform policy and decision-making, we organized this research topic entitled "Differences in Shale Oil and Gas Reservoirs across Various Sedimentary Environments: Theories and Applications," soliciting high-quality contributions from researchers worldwide. We received 30 submissions. Following a rigorous peer-review process, evaluation by guest associate editors, and final review by the editor-in-chief, eleven papers were accepted for publication, representing an acceptance rate of 36.7%. These papers comprehensively reflect theoretical and technological innovations in shale oil and gas exploration and development, with a focus on shale pore structure (three papers), hydraulic fracturing (four papers), and depositional environments (three papers). This Research Topic provides valuable guidance for global shale oil and gas exploration and development, particularly in China.

2 Shale pore structure

Quantitative characterization of shale pore structure is crucial for efficient shale gas exploration and development. In recent years, a suite of qualitative and quantitative characterization methods has been developed, including scanning electron microscopy (SEM), mercury intrusion porosimetry (MIP), low-temperature gas adsorption (LTGA), computed tomography (CT) scanning, and nuclear magnetic resonance (NMR) analysis (Guo et al., 2019; Shan et al., 2022; Wang et al., 2022). SEM provides direct, qualitative visualization of pore morphology and geometry. Other methods offer quantitative insights into critical parameters such as porosity, pore size distribution, pore volume, and specific surface area, but often lack the resolution to differentiate these parameters by specific pore types. Three papers on this research topic systematically investigate pore structure, quantitatively characterizing the complexity of shale pore networks (Figure 1A) (Li H. et al., 2024).

Leveraging organic geochemistry, mineralogy, nitrogen adsorption, physical property analyses, and SEM, Wang et al. (Manuscript ID: 1368326) investigated the pore structure characteristics of Lower Cambrian shales in the southeastern Upper Yangtze Platform. Their study reveals a strong correlation between total organic carbon (TOC) content and the abundance of quartz and clay minerals, underscoring the critical role of TOC in controlling pore structure development. TOC exhibited positive correlations with pore volume, specific surface area, and porosity, and negative correlations with average pore diameter. Furthermore, they observed significant variations in shale pore structures under different gas content and preservation conditions. Employing fractal theory to characterize pore structure complexity, they concluded that the Lower Cambrian shales exhibit complex pore networks, with fractal dimensions D1 and D2 negatively correlated with average pore diameter and positively correlated with TOC, specific surface area, and total pore volume. This methodological framework applies to other shale plays. An et al. (Manuscript ID: 1365516) utilized low-temperature carbon dioxide and nitrogen adsorption, coupled with high-pressure mercury injection, to investigate the complexity and controlling factors of pore structure in the Shuijingtuo Formation shale, employing a fractal dimension approach. Using the V-S, FHH, and Menger sponge models to calculate fractal dimensions, they determined distinct values for micropores, mesopores, and macropores. Their results indicate positive TOC and vitrinite reflectance (Ro) correlations with D1 and D2 and negative correlations with D3. Similarly, pore volume and specific surface area showed positive correlations with D1 and D2, and negative correlations with D3.

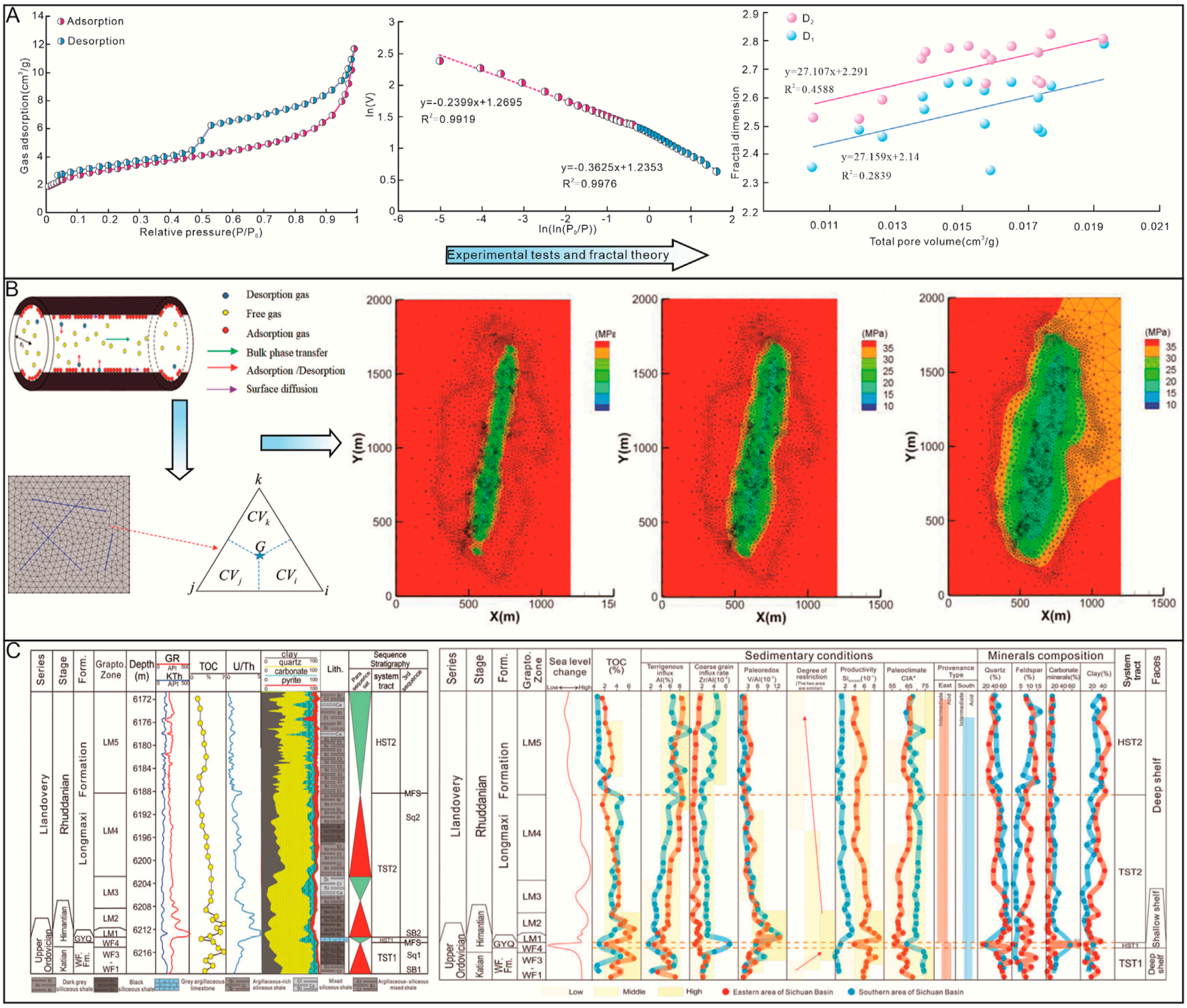

FIGURE 1
The main research methods involved in the research topic. **(A)** Shale pore structure characterization based on fractal theory (Li H. et al., 2024); **(B)** Production simulation of fractured horizontal well based on an unstructured grid Xiao et al.; **(C)** Evaluation of shale sedimentary environment based on elemental analysis Yang et al.

It is important to note that fractal theory is not the sole method for characterizing the complexity of pore structures (Li H. et al., 2022). Alternative techniques offer complementary approaches, such as moment estimation, machine learning, and deep learning algorithms. An integrated approach leveraging multiple experimental techniques and mathematical methods represents the future for comprehensively characterizing shale pore structure. Recognizing the multifaceted factors influencing shale pore characteristics, Sun et al. (Manuscript ID: 1375241) focused on typical overpressured shale gas wells in the Yongchuan, Luzhou, and Dazu areas. Through an integrated analysis of well logs, fluid inclusion data, and numerical simulations, they identified the dominant mechanisms responsible for the development of significant overpressure and characterized the history of the evolution of pressure from early burial to late uplift. They concluded that hydrocarbon generation and associated expansion are the primary drivers of overpressure development and that variations in organic matter pore morphology, structure, and connectivity exist within the deep Wufeng-Longmaxi shale (Chen et al., 2022; Dang et al., 2022). Moreover, their findings suggest that higher overpressure conditions are conducive to preserving larger organic-matter-hosted pores and enhanced overall reservoir porosity.

3 Shale hydraulic fracturing

Shale, a thinly laminated, brittle, and ultra-low permeability rock, necessitates large-scale hydraulic fracturing to achieve commercial gas flow rates due to the unique mechanisms governing natural gas adsorption and storage within its complex pore network (Shan et al., 2021; Wang and Wang, 2021; Fan et al., 2022; Li, 2022; 2023b). The fundamental principle of hydraulic fracturing lies in injecting high-pressure fluids to create fractures within the target formation, establishing conductive pathways for gas migration to the wellbore. Zhang et al. (Manuscript ID: 1326861), leveraging mineral composition and pore structure analyses, developed a multi-mineral equivalent model applicable to complex lithologies, enabling the accurate calculation of compressional wave velocity (Vp) and shear wave velocity (Vs.). These velocities serve as the foundation for pre-stack seismic inversion and the prediction of elastic parameters, including Poisson's ratio and Young's modulus. This research demonstrated successful application in the fine-grained, heterogeneous lithologies of the Lucaogou Formation within the Jimsar Sag, Junggar Basin, providing essential data for optimizing hydraulic fracture design. Recognizing the multi-faceted factors influencing hydraulic fracture effectiveness, Wang et al. (Manuscript ID: 1334175) simplified a layered reservoir system into a transversely isotropic medium and developed a model to estimate borehole deformation precisely. Based on this estimated deformation, they constructed a predictive model for fracture initiation pressure. Their results reveal that circular boreholes in layered reservoirs deform into elliptical shapes under the influence of *in-situ* stresses, with the ellipse's major axis deviating from the principal stress direction. This underscores the significant influence of rock anisotropy on borehole deformation and subsequent fracture propagation. Xiao et al. (Manuscript ID: 1257219) characterized fracture geometry and complex boundary conditions using microseismic data integrated within a discrete fracture model (Figure 1B). Subsequently, they established a comprehensive seepage flow model for fractured wells with complex fracture networks, based on a dual-porosity-discrete fracture conceptualization (Yin et al., 2018; Li J. J. et al., 2022). Numerical solutions were obtained by combining unstructured grids and the control volume finite element method. Furthermore, it acknowledges the critical importance of *in-situ* stress and formation pressure in shale gas development, parameters that directly influence wellbore stability, horizontal well trajectory planning, and hydraulic fracturing effectiveness. Zhang et al. (Manuscript ID: 1225920) developed a sophisticated finite element simulation model for the Longmaxi Formation shale in the Nanchuan area. This model, informed by a comprehensive dataset of seismic, logging, and experimental rock mechanics data, elucidates the coupled relationships between *in-situ* stress, formation strain, and formation pressure, enabling the prediction of the spatial distribution of formation pressure and pore pressure coefficients. This integrated approach provides valuable insights for optimizing well design and completion strategies in challenging shale gas reservoirs.

4 Sedimentary environment of organic-rich shale

Shale deposition is inextricably linked to its depositional environment, which is, in turn, governed by a complex interplay of factors, including basin tectonics, sediment supply, paleoclimate, water salinity, and redox conditions (Liu and Xie, 2017; Zhai et al., 2019). Shale deposition is particularly sensitive to fluctuations in these environmental parameters, often preserving a record of high-frequency variations. Yang et al. (Manuscript ID: 1391445) investigated the Wufeng-Longmaxi Formation shales of the eastern and southern Sichuan basin to elucidate the influence of the depositional environment and its evolution on organic matter content and mineral composition. Using key elemental geochemical proxies, they reconstructed the marine depositional environment of these shales, revealing the impact of paleoenvironmental evolution on reservoir heterogeneity (Figure 1C). Zhang et al. contributed two important studies to this research topic (Manuscript ID: 1403575 and 1277359), focusing on shale depositional environments. In their first study, based on major and trace element geochemistry, they characterized the depositional setting of the Dawuba Formation in Well CY1 within the Middle and Upper Yangtze areas. An index of compositional variability (ICV) value below 1, coupled with elevated chemical index of alteration (CIA) and Th/U values, points to deposition under warm, humid climatic conditions characterized by intense chemical weathering. Furthermore, V/(V+Ni), Cu/Zn, and Ce/La ratios suggest that the organic-rich intervals of the Dawuba Formation accumulated under predominantly dysoxic bottom-water conditions. This warm, humid paleoclimate likely supported high biological productivity, while the dysoxic conditions facilitated the preservation of organic matter within the accumulating sediments. In their second contribution, focusing on the Permian Capitanian-Changhsingian black shales of the Nanpanjiang intra-platform basin, they integrated geochemical data, encompassing TOC, major, trace, and rare earth element (REE) concentrations from 62 outcrop samples, to decipher the depositional conditions and organic matter accumulation characteristics. The integrated approach, combining paleontological analyses, major and trace element geochemistry, and stable carbon and oxygen isotope data, provides a robust framework for reconstructing paleo-depositional environments and understanding the controls on organic matter enrichment in shales.

In addition to these contributions focused on shale, this research topic also features a study investigating the relationship between structural characteristic and tight gas accumulation in sandstones. Yang et al. (Manuscript ID: 1296459), integrating core and outcrop observations, seismic interpretations, and burial history reconstructions, analyzed the hydrocarbon source rocks, sedimentary characteristics, reservoir properties, and structural framework of the Qiulin structure. Their work explores the influence of the Yanshan-Himalayan tectonic events on tight gas accumulation within the Shaximiao Formation.

5 Summary

Shale oil and gas reservoirs exhibit diverse characteristics due to their depositional environment variations. Effective development of these resources requires a thorough understanding of how these environments influence reservoir quality. This research topic focuses on the variability of shale oil and gas reservoirs across diverse depositional settings and its implications for both fundamental geological understanding and practical applications. From marine to lacustrine and terrestrial environments, the depositional setting exerts a primary control on key reservoir parameters, including organic matter type and abundance, thermal maturity, mineralogical composition, pore structure, and geomechanical properties, especially brittleness (Fan et al., 2024). For example, marine shales typically exhibit higher organic content and well-developed lamination, whereas lacustrine shales often display more complex lithofacies variations and a wider range of organic matter types. These inherent differences ultimately dictate reservoir fracability, permeability, and consequently, hydrocarbon production potential.

Accurate identification and characterization of depositional environments are paramount for successfully evaluating and developing shale oil and gas resources. Conventional reservoir characterization techniques often prove inadequate for capturing the complexities arising from variable depositional settings. Therefore, an integrated, multidisciplinary approach incorporating sedimentology, geochemistry, and geophysics is essential. High-resolution sedimentological facies analysis enables more accurate prediction of favorable reservoir distribution, while rock physics investigations can illuminate the pore structure and mechanical properties of shales deposited in different environments. Integrating these diverse datasets facilitates the optimization of horizontal well trajectories, hydraulic fracturing designs, and other production enhancement strategies, ultimately leading to improved hydrocarbon recovery factors and reduced development costs.

The eleven papers comprising this research topic focus on three key areas: characterization of shale pore structure, hydraulic fracturing in shales, and the influence of depositional environments on shale properties. However, these represent only a subset of the broader research landscape necessary to comprehensively understand shale oil and gas reservoir variability across diverse depositional settings. Future research should prioritize the detailed characterization of depositional environments, quantifying the impact of these environments on reservoir properties, and exploring how this knowledge can inform and optimize shale gas exploration strategies. Advanced experimental techniques coupled with sophisticated mathematical and numerical modeling approaches are crucial for advancing our understanding and maximizing the efficient development of shale oil and gas and other unconventional hydrocarbon resources to meet the ever-increasing global energy demand. To further advance this critical area of research, we are pleased to announce a second volume of this research topic and encourage wider participation from the scientific community, especially contributions from international researchers.

Author contributions

HuL: Conceptualization, Data curation, Formal Analysis, Funding acquisition, Methodology, Project administration, Supervision, Writing–original draft, Writing–review and editing. PL: Data curation, Formal Analysis, Methodology, Supervision, Writing–review and editing. JL: Conceptualization, Resources, Supervision, Validation, Writing–review and editing, Funding acquisition, Project administration, Visualization. AR: Formal Analysis, Methodology, Resources, Writing–review and editing, Conceptualization, Data curation, Supervision, Validation. HW: Formal Analysis, Software, Writing–review and editing, Investigation, Methodology, Project administration, Resources. HoL: Conceptualization, Data curation, Formal Analysis, Software, Writing–review and editing.

Funding

The author(s) declare that financial support was received for the research, authorship, and/or publication of this article. This study was financially supported by the Key Research Base for Social Sciences of Zigong Social Science Federation, Research Center of Industrial Transformation and Innovation (No. CZ24B01), the Open Fund of Sichuan Key Provincial Research Base of Intelligent Tourism (No. ZHYR24-05), the Open Fund of the National Key Laboratory of Oil and Gas Reservoir Geology and Exploitation (Southwest Petroleum University) (No. PLN 2023-31), the Open Fund of the Shale Gas Evaluation and Exploitation Key Laboratory of Sichuan Province (No. YSK2023001).

Conflict of interest

The authors declare that the research was conducted without any commercial or financial relationships that could be construed as a potential conflict of interest.

Publisher's note

References

Abolghasemi, E., and Andersen, P. Ø. (2021). The influence of adsorption layer thickness and pore geometry on gas production from tight compressible shales. *Adv. Geo-Energy Res.* 6 (1), 4–22. doi:10.46690/ager.2022.01.02

Chen, Y. H., Zhu, Z. W., and Zhang, L. (2019). Control actions of sedimentary environments and sedimentation rates on lacustrine oil shale distribution, an example of the oil shale in the Upper Triassic Yanchang Formation, southeastern Ordos Basin (NW China). *Mar. Petrol. Geol.* 102, 508–520. doi:10.1016/j.marpetgeo.2019.01.006

Chen, Z. P., Liao, Y., Li, L., Chen, L., Wang, P., Zuo, Y., et al. (2022). Implication of alkane carbon and hydrogen isotopes for genesis and accumulation of over-mature shale gas: a case study of Longmaxi Formation shale gas in Upper Yangtze area. *Front. Earth Sci.* 10, 901989. doi:10.3389/feart.2022.901989

Dang, W., Nie, H. K., Zhang, J. C., Tang, X., Jiang, S., Wei, X., et al. (2022). Pore-scale mechanisms and characterization of light oil storage in shale nanopores: New method and insights. *Geosci. Front.* 13 (5), 101424. doi:10.1016/j.gsf.2022.101424

Fan, C. H., Li, H., Qin, Q. R., He, S., and Zhong, C. (2020). Geological conditions and exploration potential of shale gas reservoir in Wufeng and Longmaxi Formation of southeastern Sichuan Basin, China. *J. Petrol. Sci. Eng.* 191, 107138. doi:10.1016/j.petrol.2020.107138

Fan, C. H., Nie, S., Li, H., Radwan, A. E.*., Pan, Q. C., Shi, X. C., et al. (2024). Quantitative prediction and spatial analysis of structural fractures in deep shale gas reservoirs within complex structural zones: a case study of the Longmaxi Formation in the Liuzhou area, southern Sichuan Basin, China. *J. Asian Earth Sci.* 263, 106025. doi:10.1016/j.jseaes.2024.106025

Fan, C. H., Xie, H. B., Li, H., Zhao, S. X., Shi, X. C., Liu, J. F., et al. (2022). Complicated fault characterization and its influence on shale gas preservation in the southern margin of the Sichuan basin, China. *Lithosphere* 2022, 8035106. doi:10.2113/2022/8035106

Guo, X. B., Huang, Z. L., Zhao, L. B., Han, W., Ding, C., Sun, X., et al. (2019). Pore structure and multi-fractal analysis of tight sandstone using MIP, NMR and NMRC methods: a case study from the Kuqa depression, China. *J. Petrol. Sci. Eng.* 178, 544–558. doi:10.1016/j.petrol.2019.03.069

He, X. P., Cai, X., Gao, Y. Q., Ding, A. X., Jiang, Z. G., He, G. S., et al. (2024). Experimental technologies of shale gas exploration and development:Research progress and development direction. *Nat. Gas. Ind.* 44 (7), 12–26. doi:10.3787/j.issn.1000-0976.2024.07.002

Jia, C. Z., Wang, Z. G., Jiang, L., and Zhao, W. (2024). Progress and key scientific and technological problems of shale oil exploration and development in China. *World Petrol. Ind.* 31, 1–11. doi:10.20114/j.issn.1006-0030.20240530001

Li, H. (2022). Research progress on evaluation methods and factors influencing shale brittleness: a review. *Energy Rep.* 8, 4344–4358. doi:10.1016/j.egyr.2022.03.120

Li, H. (2023a). Coordinated development of shale gas benefit exploitation and ecological environmental conservation in China: a mini review. *Front. Ecol. Evol.* 11, 1232395. doi:10.3389/fevo.2023.1232395

Li, H. (2023b). Deciphering the formation period and geological implications of shale tectonic fractures: a mini review and forward-looking perspectives. *Front. Energy Res.* 11, 1320366. doi:10.3389/fenrg.2023.1320366

Li, H., He, S., Radwand, A. E., Xie, J. T., and Qin, Q. R. (2024b). Quantitative analysis of pore complexity in lacustrine organic-rich shale and comparison to marine shale: insights from experimental tests and fractal theory. *Energy Fuel* 38 (17), 16171–16188. doi:10.1021/acs.energyfuels.4c03095

Li, H., Zhou, J. L., Mou, X. Y., Guo, H. X., Wang, X. X., An, H. Y., et al. (2022b). Pore structure and fractal characteristics of the marine shale of the Longmaxi Formation in the Changning area, southern Sichuan basin, China. *Front. Earth Sci.* 10, 1018274. doi:10.3389/feart.2022.1018274

Li, J., Li, H., Jiang, W., Cai, M. L., He, J., Wang, Q., et al. (2024a). Shale pore characteristics and their impact on the gas-bearing properties of the Longmaxi Formation in the Liuzhou area. *Sci. Rep.* 14, 16896. doi:10.1038/s41598-024-66759-7

Li, J., Li, H., Yang, C., Ren, X. H., and Li, Y. D. (2023c). Geological characteristics of deep shale gas and their Effects on shale fracability in the Wufeng-Longmaxi formations of the southern Sichuan basin, China. *China. Lithosphere* 2023 (1), 4936993. doi:10.2113/2023/4936993

Li, J., Li, H., Yang, C., Wu, Y. J., Gao, Z., and Jiang, S. L. (2022a). Geological characteristics and controlling factors of deep shale gas enrichment of the Wufeng-Longmaxi Formation in the southern Sichuan basin, China. *Lithosphere* 2022, 4737801. doi:10.2113/2022/4737801

Li, J. J., Qin, Q. R., Li, H., and Wan, Y. F. (2022c). Numerical simulation of the stress field and fault sealing of complex fault combinations in Changning area, Southern Sichuan Basin, China. *Energy Sci. Eng.* 10 (2), 278–291. doi:10.1002/ese3.1044

Liu, C., and Xie, Q. B. (2017). Depositional, sedimentary, and diagenetic controls on reservoir quality in carbonate successions: a case study from the carbonate gas reservoirs of the Lower Triassic Feixianguan Formation, eastern Sichuan Basin, China. *J. Petrol. Sci. Eng.* 163, 484–500. doi:10.1016/j.petrol.2017.12.063

Mcmahon, T. P., Larson, T. E., Zhang, T., and Shuster, M. (2024). Geologic characteristics, exploration and production progress of shale oil and gas in the United States: an overview. *Petrol. expl. Dev.* 51 (4), 925–948. doi:10.1016/s1876-3804(24)60516-1

Peng, Y. Y., Li, Y. F., Yu, H., Han, P. R., Zhu, C., and He, M. C. (2024). Mechanical properties of coal and rock with different dip angles based on true triaxial unloading test. *J. Min. Strata Control Eng.* 6 (2), 023037. doi:10.13532/j.jmsce.cn10-1638/td.20231222.001

Shan, C., Ye, C., Zhang, Z., Zou, C., He, F., Zhang, H., et al. (2022). Reservoir characteristics and resource potential analysis of transitional shale gas in Southern Sichuan Basin. *Front. Earth Sci.* 10, 909469. doi:10.3389/feart.2022.909469

Shan, S. C., Wu, Y. Z., Fu, Y. K., and Zhou, P. H. (2021). Shear mechanical properties of anchored rock mass under impact load. *J. Min. Strata Control Eng.* 3 (4), 043034. doi:10.13532/j.jmsce.cn10-1638/td.20211014.001

Wang, J., and Wang, X. L. (2021). Seepage characteristic and fracture development of protected seam caused by mining protecting strata. *J. Min. Strata Control Eng.* 3 (3), 033511. doi:10.13532/j.jmsce.cn10-1638/td.20201215.001

Wang, X., Li, J., Jiang, W., Zhang, H., Feng, Y., and Yang, Z. (2022). Characteristics, current exploration practices, and prospects of continental shale oil in China. *Adv. Geo-Energy Res.* 6 (6), 454–459. doi:10.46690/ager.2022.06.02

Yin, S., Jia, Q., and Ding, W. L. (2018). 3D paleotectonic stress field simulations and fracture prediction for marine-continental transitional facies forming a tight-sandstone reservoir in a highly deformed area. *J. Geophys. Eng.* 15 (4), 1214–1230. doi:10.1088/1742-2140/aaad97

Zhai, G. Y., Li, J., Jiao, Y., Wang, Y., Liu, G., Xu, Q., et al. (2019). Applications of chemostratigraphy in a characterization of shale gas sedimentary microfacies and predictions of sweet spots -taking the Cambrian black shales in Western Hubei as an example. *Mar. Petrol. Geol.* 109, 547–560. doi:10.1016/j.marpetgeo.2019.06.045

frontiers | Frontiers in Earth Science

TYPE Original Research
PUBLISHED 01 September 2023
DOI 10.3389/feart.2023.1257219

EDITED BY
Hu Li,
Southwest Petroleum University, China

REVIEWED BY
Hong-Bin Liang,
Chongqing University of Science and Technology, China
Lingfu Liu,
University of Wyoming, United States

*CORRESPONDENCE
Keren Wang,
✉ wangkeren@petrochina.com.cn

RECEIVED 12 July 2023
ACCEPTED 21 August 2023
PUBLISHED 01 September 2023

CITATION
Xiao H, Chen M, Jing C, Zhao H and Wang K (2023), Production simulation and prediction of fractured horizontal well with complex fracture network in shale gas reservoir based on unstructured grid.
Front. Earth Sci. 11:1257219.
doi: 10.3389/feart.2023.1257219

Production simulation and prediction of fractured horizontal well with complex fracture network in shale gas reservoir based on unstructured grid

Hongsha Xiao[1], Man Chen[1], Cui Jing[1], Huiyan Zhao[1] and Keren Wang[2]*

[1]Sichuan Changning Natural Gas Development Co., Ltd., Chengdu, Sichuan, China, [2]Development Division of Southwest Oil & Gas Field Company, Chengdu, Sichuan, China

In order to accurately simulate the productivity variation characteristics of fractured wells with complex fracture network in shale gas reservoir, based on the multiple migration mechanism of shale gas, the micro-seismic data and discrete fracture model were used to characterize the fracture geometry and complex boundary characteristics, and the comprehensive seepage mathematical model of fractured wells with complex fracture network was established based on the dual porosity-discrete fracture model, and the numerical solution was carried out by combining the unstructured grid and the control volume finite element method. The sensitivity analysis of the influence of key parameters such as fracture conductivity, physical property difference in composite area and Langmuir volume on the production performance of fractured horizontal wells is carried out. This study provides theoretical methods and calculation tools for accurate prediction of productivity change and optimization of production system of fractured horizontal wells with complex fracture network in shale gas reservoirs.

KEYWORDS

shale gas reservoir, complex fracture network, fractured horizontal well, production prediction, numerical simulation

1 Introduction

Shale gas reservoir is an important exploration field proposed in China's energy development plan to vigorously enhance exploration and development, and continuously and efficiently promote the development and utilization of shale gas resources, which has important strategic significance for optimizing China's clean energy production capacity layout and reducing natural gas dependence on foreign countries (Zou et al., 2020). China is generally rich in shale gas resources. It is estimated that the technically recoverable reserves of shale gas in China are 21.8 trillion cubic meters, and the proven reserves exceed 1 trillion cubic meters (Li, 2023). At present, three national shale gas demonstration zones have been built in Fuling, Changning-Weiyuan and Zhaotong, and China's shale gas production is planned to reach 80 to 100 billion cubic meters by 2030 (Yang et al., 2020).

By referring to the key technologies of the shale gas revolution in North America, the multi-cluster fracturing technology of horizontal wells has become a key method to efficiently develop and utilize shale gas resources (Wu et al., 2022; Sun, 2023). Through the implementation of the "close cutting and large displacement and temporary plugging and diversion" technology, the tight reservoir is "broken" to form the SRV (stimulated reservoir volume) region, the natural fracture groups around the near well are opened and communicated, the seepage field around the horizontal wellbore is improved, and the final recoverable reserves of a single well are increased (Xie, 2018; Liu et al., 2019). However, the characterization of complex fracture network geometry and mathematical expression of flow exchange between different systems have been the key problems, affecting prediction accuracy of production after fracturing. Brown et al. (2011), Yuan et al. (2015) divided the fractured horizontal well and shale gas reservoir into stimulated and initial regions, adopting multi-linear and dual porosity models to obtain the solution. Xu et al. (2015), Fan et al. (2015), Zhang et al. (2015) respectively used the circular or rectangular composite region model to simplify the complex fracture geometry, and the flow characterization was carried out by combining the continuum model. In order to more accurately predict the effect of fracture properties on flow mechanism and production, Karimi-Fard et al. (2004), Altwaijri et al. (2018) established the discrete fracture model to display and characterize the length, angle and width of each fracture, and then carried out the production impact analysis. Jiang and Rami (2015) further combined the respective advantages of continuous medium model and discrete fracture model, the discrete fracture model is adopted for large-scale hydraulic fracturing fractures, and continuous medium model is used for small-scale natural fracture system, which ensures the efficiency and accuracy of production prediction of fractured horizontal wells with complex fractures. However, the above models did not take into account the gas-water two-phase flow in the SRV region and gas-water co production characteristics caused by fracturing fluid retention.

In addition, researchers (Ozkan et al., 2011; Stalgorova and Mattar, 2013; Wang, 2014; Li et al., 2015; Zhao et al., 2018) established analytical and semi-analytical models respectively to predict the production of horizontal wells after fracturing in shale gas reservoirs. However, the analytical and semi-analytical model mainly uses the symmetric main fracture model, the whole or local regular rectangular or circular SRV region to simplify the hydraulic fracture network, and for gas-water two-phase flow, an approximate solution is obtained by defining a pseudo pressure function to transform it into single-phase seepage. The above processing will significantly affect the accuracy of production performance and productivity prediction for fractured horizontal wells. The numerical model is more suitable to deal with the geometry characteristics of the complex fracture network, and can accurately characterize the complex boundary characteristics of the fracture network through the spatial mesh dispersion, and is convenient for coupling the multi-scale and multi-phase seepage mechanism of shale gas reservoirs (Wu and Pruess, 1988; Geiger et al., 2004; Lv et al., 2012; Moinfar et al., 2013; Wu, 2014; Zhang et al., 2017; Wang et al., 2020; Zhang et al., 2023).

To sum up, this study combined with micro-seismic data and discrete fracture model to characterize fracture geometry and complex boundary characteristics on the basis of comprehensive consideration of multiple flow mechanisms in shale gas reservoir, and established a dual continuum-discrete fracture coupling seepage model. A fully implicit numerical solution model is established by using unstructured triangular mesh and controlled volume finite element method. Combined with the field data, the productivity change characteristics of horizontal wells after fracturing were simulated and predicted, and the key factors affecting the production and EUR of single well were analyzed.

2 Physical model and basic assumptions

Natural fractures and bedding are developed in shale reservoirs, the brittle mineral content of favorable development series of strata is high (Cai, 2020; Zhu et al., 2022; Li et al., 2023), and the fracture network stimulation area is formed near the well after fracturing (Zhao et al., 2018). The field monitoring of micro-seismic results of shale fractured horizontal wells shows (as shown in Figure 1) that there are dense signal response points around the wellbore during the fracturing process, and complex reformations are formed during the fracturing process. Therefore, micro-seismic monitoring data and discrete fracture model were applied to characterize the fracture geometry and complex boundary characteristics of the reconstruction area, and the flow characteristics of the composite area of the original reservoir and the stimulation area were described based on the dual medium model (Moinfar et al., 2013; Cheng et al., 2020).

The assumptions of the physical model are as follows: 1) Considering the retention of fracturing fluid in the formation, gas-water two-phase flow occurs in hydraulic fracturing fractures and fractures in the reconstruction area, while single-phase gas isothermal seepage occurs in the shale matrix and the original reservoir area. 2) Ignoring the vertical heterogeneity of physical properties of shale reservoirs, two-dimensional grid is used to describe them approximately; 3) There is a quasi steady state channeling between the matrix system and the fracture system, and the fluid enters the fracture system from the matrix system under the action of pressure difference, and flows into the horizontal wellbore through the fracture and produces.

3 Mathematical model

3.1 Micro-nano scale flow model of shale gas reservoir

Shale reservoir has a complex pore structure, and gas seepage in the reservoir has multiple flow mechanisms such as Knudsen diffusion, surface adsorption diffusion, slip flow and viscous flow (Geng et al., 2016; Wu et al., 2016; Zhang et al., 2018) (as shown in Figure 2).

In the process of shale gas development, the thickness of adsorption layer decreases, and the effective flow pore size increases further. The effective pore radius of removing the adsorption layer can be expressed as:

$$r_{abs} = r - d_M\theta = r - d_M\frac{p/Z}{p/Z + p_L} \tag{1}$$

Where, d_M is the molecular diameter of the gas, m; r is the actual radius of the matrix pores, m; θ is the true gas coverage, dimensionless; p is the current pore pressure, Pa; p_L is Langmuir pressure, Pa; Z is the true gas compression factor, dimensionless.

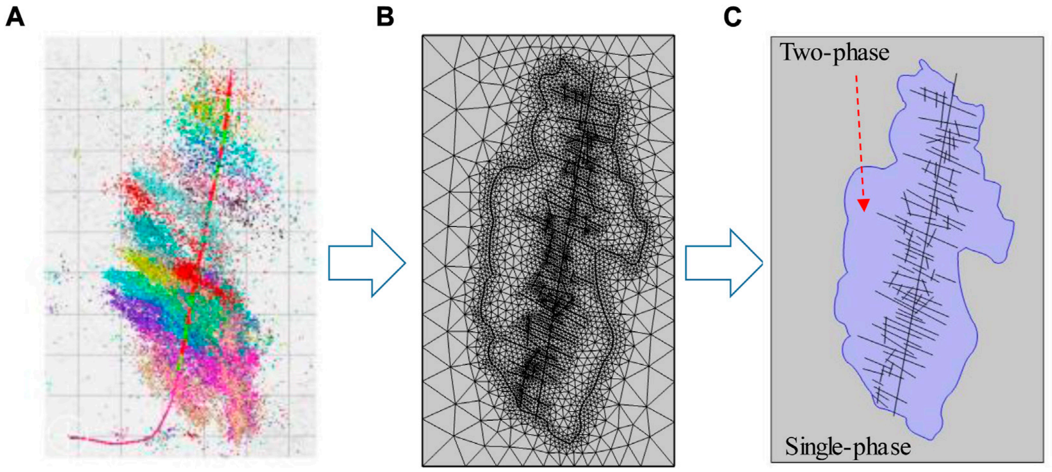

FIGURE 1
Diagram of physical model. **(A)** Model of fractured horizontal well with complex fracture network in shale gas reservoir based on micro-seismic data (Cheng et al., 2020). **(B)** Schematic diagram of grid division (6,857 triangles). **(C)** Assumptions of seepage models in different regions.

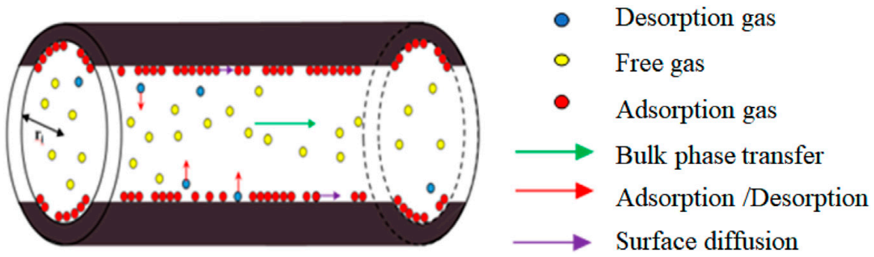

FIGURE 2
Gas transport mechanism in micro and nano pores of shale matrix (Javadpour, 2009; Guo et al., 2022).

Considering the stress-sensitive effect, the porosity and permeability of shale matrix related to pore pressure can be expressed as:

$$\begin{aligned} \varphi(p) &= \varphi_r + (\varphi_i - \varphi_r)e^{-\eta(p_i-p)} \\ k(p) &= k_i e^{-\Psi(p_i-p)} \end{aligned} \tag{2}$$

Where, $\varphi(p)$ is the porosity of the matrix considering stress sensitivity; φ_i is the initial porosity, dimensionless; φ_r is the porosity under maximum stress, dimensionless. $k(p)$ is the matrix permeability after considering stress sensitivity, nD; k_i is the original permeability of matrix, nD; η is the stress sensitivity coefficient of porosity, Pa^{-1}; ψ is the stress-sensitive coefficient of permeability, Pa^{-1}; p_i is the original gas reservoir pressure, Pa.

The effective pore radius of the matrix considering the thickness of the adsorption layer and the stress-sensitive effect is as follows:

$$r_e = \sqrt{8\tau \frac{k_{on,abs} e^{-\Psi(p_i-p)}}{\varphi_r + (\varphi_i - \varphi_r)e^{-\eta(p_i-p)}}} \tag{3}$$

Where, τ is the tortuosity, which is the ratio of the actual length of the flow path to the represented length.

In the circular organic nanopores, the apparent permeability contributed by the bulk phase gas based on the Beskok model can be expressed as:

$$k_{\text{on,bulk}} = -\frac{r_e^2 \varphi(p)}{8\tau}(1 + \alpha Kn)\left(1 + \frac{4Kn}{1 + Kn}\right) \tag{4}$$

Where, Kn is Knudsen diffusion constant, dimensionless; α is the rarefied gas effect coefficient, dimensionless, which can be calculated by the following equation:

$$\alpha = \alpha_0 \frac{2}{\pi} \tan^{-1}\left(\alpha_1 Kn^{\beta}\right) \tag{5}$$

Where, α_0 is the rarefied gas coefficient under $K_n \to \infty$ condition; α_1 and β are fitting constants.

The apparent permeability considering the real gas effect can be expressed as:

$$k_{\text{on,surface}} = D_s \frac{\mu_{gr} R T C_{sc} \varphi(p)}{M_g p^2 \tau} \tag{6}$$

Where, D_s is the surface diffusion coefficient, m^2/s; μ_{gr} is the gas viscosity after considering the real gas effect, mPa·s; R is the universal gas constant, Pa/(mol•K); T is the absolute temperature, K; M_g is the molecular weight of gas, g/mol; C_{sc} is the concentration of adsorbed gas in Langmuir monolayer on the pore surface, kg/m^3. The calculation equation is as follows:

$$C_{sc} = \frac{4\theta M_g}{\pi d_M^3 N_A} \tag{7}$$

Where, N_A is Avogadro's constant, $6.022\times10^{23}\mathrm{mol}^{-1}$.

The surface diffusion coefficient can be calculated as follows:

$$D_s = D_s^0 \frac{(1-\theta) + \frac{\kappa}{2}\theta(2-\theta) + [H(1-\kappa)](1-\kappa)\frac{\kappa}{2}\theta^2}{\left(1-\theta+\frac{\kappa}{2}\theta\right)^2} \tag{8}$$

$$H(1-\kappa) = \begin{cases} 0, \kappa \geq 1 \\ 1, 0 \leq \kappa \leq 1 \end{cases}, \kappa = \frac{\kappa_b}{\kappa_m} \tag{9}$$

Where, $H(1-\kappa)$ is Heaviside function; κ_b is the plugging rate, m/s; κ_m is migration rate, m/s; D_s^0 represents the surface diffusion coefficient when the gas coverage is 0, m^2/s, which is calculated by the following equation:

$$D_S^0 = 8.29 \times 10^{-7} T^{0.5} e^{-\frac{\Delta H^{0.8}}{RT}} \tag{10}$$

Where, ΔH is the isothermal adsorption heat of gas, J/mol.

The total gas transport flux includes free gas phase transport and surface diffusion of adsorbed gas in circular tube pores. After taking into account the cross-sectional area of the circular tube, the apparent permeability of the matrix pore is as follows:

$$\begin{aligned} k_{\mathrm{app}} &= \varsigma_{\mathrm{bulk}} k_{\mathrm{on,bulk}} + \varsigma_{\mathrm{surface}} k_{\mathrm{on,surface}} \\ &= \frac{r_e^2}{\left(r_e^2 + \theta d_M\right)} k_{\mathrm{on,bulk}} + \left[1 - \frac{r_e^2}{\left(r_e^2 + \theta d_M\right)}\right] k_{\mathrm{on,surface}} \end{aligned} \tag{11}$$

Where $\varsigma_{\mathrm{bulk}}$ is body phase gas weight coefficient, its value is equal to the ratio of the cross-sectional area occupied by the body phase gas and the total cross-sectional area, dimensionless; $\varsigma_{\mathrm{surface}}$ is surface diffusion weight coefficient, its value is equal to the ratio of the cross-sectional area occupied by the surface diffusion gas to the total cross-sectional area, dimensionless.

3.2 Comprehensive seepage model of multi-scale flow mechanisms

Further, based on the dual media-discrete fracture model, the comprehensive seepage model of fractured horizontal well is established as follows:

①Seepage control equations of matrix system:

$$\nabla \cdot \left(\frac{k_{\mathrm{app}}}{\mu_g B_g} \nabla p_{\mathrm{g}ml}\right) - \alpha_l \frac{k_{\mathrm{app}}}{\mu_g B_g}\left(p_{\mathrm{g}ml} - p_{\mathrm{gf}l}\right) + q_{\mathrm{des}} = \frac{\partial\left(\phi_{\mathrm{m}l}/B_g\right)}{\partial t} \tag{12}$$

Where,

$$q_{\mathrm{des}} = -\rho_s\left(1 - \phi_{\mathrm{m}l} - \phi_{\mathrm{f}l}\right)\frac{\partial V_E}{\partial t} \tag{13}$$

Where, B_g is the volume coefficient of gas, dimensionless; p_{gm} is the matrix system gas pressure, MPa; p_{gf} is the fracture system gas pressure, MPa; q_{des} is the desorption production of matrix, m^3/s; φ_{m} is the matrix system porosity, dimensionless; φ_{f} is the porosity of fracture system, dimensionless; α is the shape factor, dimensionless; ρ_s is the density of shale rock, g/cm^3; The subscripts l=1, 2, 1 denotes the inner zone, 2 denotes the outer zone.

②Seepage control equations of fracture system:

For inner zone:

$$\nabla \cdot \left(\frac{k_{\mathrm{f}} k_{ru1}}{\mu_u B_u}\nabla p_{\mathrm{f}u1}\right) + \alpha_1 \frac{k_{\mathrm{app}} k_{ru1}}{\mu_u B_u}\left(p_{\mathrm{m}u1} - p_{\mathrm{f}u1}\right) = \frac{\partial}{\partial t}\left(\frac{S_{\mathrm{f}u1}\phi_{\mathrm{f}1}}{B_u}\right) \tag{14}$$

For outer zone:

$$\nabla \cdot \left(\frac{k_{\mathrm{f}}}{\mu_g B_g}\nabla p_{\mathrm{fg2}}\right) + \alpha_2 \frac{k_{\mathrm{app}}}{\mu_g B_g}\left(p_{\mathrm{mg2}} - p_{\mathrm{fg2}}\right) = \frac{\partial}{\partial t}\left(\frac{\phi_{\mathrm{f2}}}{B_g}\right) \tag{15}$$

Where, p_{f} is the pressure of the natural fracture system, MPa; k_{f} is the permeability of natural fractures in shale reservoirs, mD; k_r is the relative permeability, dimensionless; Subscript u=g, w, where g represents the gas phase and w represents the water phase.

③Control equations of hydraulic fracture seepage:

$$\nabla \cdot \left(\frac{k_{\mathrm{F}} k_{rul}}{\mu_u B_u}\nabla p_{\mathrm{F}u}\right) + q_{u\mathrm{sct}} = \frac{\partial}{\partial t}\left(\frac{\phi_{\mathrm{F}} S_{\mathrm{F}u}}{B_u}\right) \tag{16}$$

Where, k_{F} is hydraulic fracture permeability, mD; φ_{F} is the hydraulic fracture porosity, dimensionless; q_{gsct} is horizontal well production, m^3/s; p_{F} is the hydraulic fracture pressure, MPa.

4 Model solving

4.1 Element characteristic matrix

First, the element characteristic matrix of Eq. (12) is constructed based on triangular mesh and control volume finite element method (as shown in Figure 3), and the average mesh pressure p_{gm} and average saturation $S_{\mathrm{f}u}$ of the matrix system are approximated by triangle vertex interpolation:

$$\begin{aligned} &p_{\mathrm{gm}}(x,y) = \sum_{v=\mathrm{i}}^{\mathrm{k}} N_v(x,y) p_{\mathrm{gm}v}, \; p_{\mathrm{f}ul}(x,y) = \sum_{v=\mathrm{i}}^{\mathrm{k}} N_v(x,y) p_{\mathrm{f}ulv} \\ &S_{\mathrm{f}ul}(x,y) = \sum_{v=\mathrm{i}}^{\mathrm{k}} N_v(x,y) S_{\mathrm{f}ulv} \end{aligned} \tag{17}$$

Where N_v is the interpolation function.

For the convection term in the matrix system seepage equations, Galerkin's weighted margin method and Gauss's law are used to obtain:

$$\iint_{\Omega_{\mathrm{i}}} \nabla \cdot \left(\bar{\bar{\lambda}} \cdot \nabla p_{\mathrm{g}ml}\right) \mathrm{d}V = \sum_{v=\mathrm{j,k}} T_{\mathrm{i}v}\left(p_{\mathrm{ig}ml} - p_{v\mathrm{g}ml}\right) \tag{18}$$

Where $T_{\mathrm{i}v}$ represents the conductivity matrix given by the following equation:

$$\begin{aligned} T_{\mathrm{i}v} &= A\left(\lambda_x \frac{\partial N_{\mathrm{i}}}{\partial x}\frac{\partial N_v}{\partial x} + \lambda_y \frac{\partial N_{\mathrm{i}}}{\partial y}\frac{\partial N_v}{\partial y}\right) \\ &= \frac{1}{4A}\left(\lambda_x a_{\mathrm{i}} a_l + \lambda_y b_{\mathrm{i}} b_l\right) \end{aligned} \tag{19}$$

The above equations establish the net flow of the control volume of the inflow node i of triangle ijk. Similarly, the net inflow flow equation of nodes j and k can be established. Then the flow matrix of the virtual finite control volume unit can be obtained as:

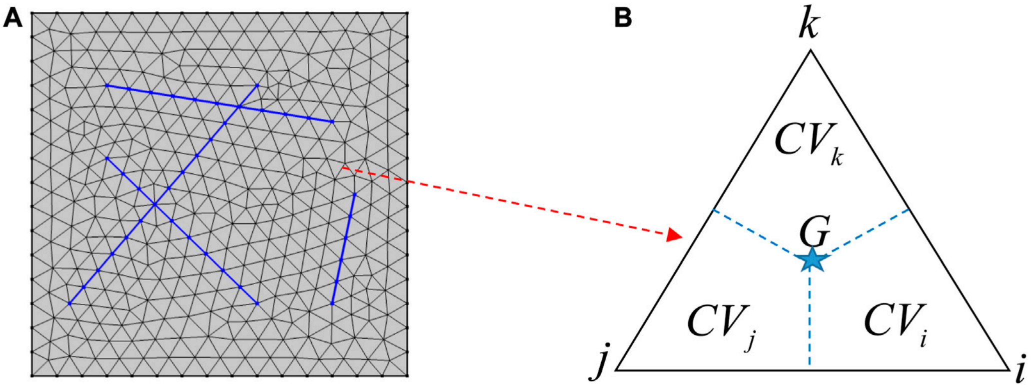

FIGURE 3
Schematic diagram of unstructured mesh generation. **(A)** Triangular mesh generation for large-scale discrete fractures. **(B)** Virtual finite control volume mesh in triangular mesh, which is formed by connecting the center of gravity of a triangle to the midpoint of each side.

$$\begin{pmatrix} T_{\mathrm{ij}}+T_{\mathrm{ik}} & -T_{\mathrm{ij}} & -T_{\mathrm{ik}} \\ -T_{\mathrm{ji}} & T_{\mathrm{ji}}+T_{\mathrm{jk}} & -T_{\mathrm{jk}} \\ -T_{\mathrm{ki}} & -T_{\mathrm{kj}} & T_{\mathrm{ki}}+T_{\mathrm{kj}} \end{pmatrix}\begin{pmatrix} p_{\mathrm{igm}l} \\ p_{\mathrm{jgm}l} \\ p_{\mathrm{kgm}l} \end{pmatrix}=\begin{pmatrix} f_{\mathrm{gmi}} \\ f_{\mathrm{gmj}} \\ f_{\mathrm{gmk}} \end{pmatrix} \tag{20}$$

Eq. (20) is the processing format of the convection term of the controlled volume finite element method based on triangular mesh. In Eq. (12), the cross-flow term between matrix system and fracture system, as well as the adsorption and desorption term and the time derivative term of matrix system are numerically calculated using the traditional finite element method.

Taking gas phase as an example, the finite element integral numerical calculation format for constructing the cross-flow term is as follows:

$$\begin{aligned}\iint_{\Omega_{\mathrm{m}}} N_\nu \alpha \frac{k_{\mathrm{app}}}{\mu_{\mathrm{g}}B_{\mathrm{g}}}(p_{\mathrm{m}}-p_{\mathrm{f}})d\Omega_{\mathrm{m}} &= \iint_{\Omega_{\mathrm{m}}} N_\nu \alpha \frac{k_{\mathrm{app}}}{\mu_{\mathrm{g}}B_{\mathrm{g}}}\left(\sum_{\nu=\mathrm{i}}^{\mathrm{k}} N_\nu p_{\mathrm{m}\nu}-\sum_{\nu=\mathrm{i}}^{\mathrm{k}} N_\nu p_{\mathrm{f}\nu}\right)d\Omega_{\mathrm{m}} \\ &= \begin{pmatrix} \left(\alpha\frac{\mathrm{A}k_{\mathrm{app}}}{3\mu_{\mathrm{g}}B_{\mathrm{g}}}\right)_{\mathrm{i}} & 0 & 0 \\ 0 & \left(\alpha\frac{\mathrm{A}k_{\mathrm{app}}}{3\mu_{\mathrm{g}}B_{\mathrm{g}}}\right)_{\mathrm{j}} & 0 \\ 0 & 0 & \left(\alpha\frac{\mathrm{A}k_{\mathrm{app}}}{3\mu_{\mathrm{g}}B_{\mathrm{g}}}\right)_{\mathrm{k}} \end{pmatrix}\begin{pmatrix} p_{\mathrm{m}i}-p_{\mathrm{f}i} \\ p_{\mathrm{m}j}-p_{\mathrm{f}j} \\ p_{\mathrm{m}k}-p_{\mathrm{f}k} \end{pmatrix}\end{aligned} \tag{21}$$

For the adsorption and desorption term and the time derivative term, the finite element integral numerical calculation format is constructed by combining Euler backward difference as follows:

$$\begin{aligned}&\frac{A}{3\Delta t}\begin{pmatrix} \left(\frac{\phi_{\mathrm{m}}}{B_{\mathrm{g}}}\right)_i^{n+1}-\left(\frac{\phi_{\mathrm{m}}}{B_{\mathrm{g}}}\right)_i^{n} \\ \left(\frac{\phi_{\mathrm{m}}}{B_{\mathrm{g}}}\right)_j^{n+1}-\left(\frac{\phi_{\mathrm{m}}}{B_{\mathrm{g}}}\right)_j^{n} \\ \left(\frac{\phi_{\mathrm{m}}}{B_{\mathrm{g}}}\right)_k^{n+1}-\left(\frac{\phi_{\mathrm{m}}}{B_{\mathrm{g}}}\right)_k^{n} \end{pmatrix} \\ &+\frac{A}{3\Delta t}\begin{pmatrix} \left[(1-\phi_{\mathrm{m}}-\phi_{\mathrm{f}})V_{\mathrm{E}}\right]_i^{n+1}-\left[(1-\phi_{\mathrm{m}}-\phi_{\mathrm{f}})V_{\mathrm{E}}\right]_i^{n} \\ \left[(1-\phi_{\mathrm{m}}-\phi_{\mathrm{f}})V_{\mathrm{E}}\right]_j^{n+1}-\left[(1-\phi_{\mathrm{m}}-\phi_{\mathrm{f}})V_{\mathrm{E}}\right]_j^{n} \\ \left[(1-\phi_{\mathrm{m}}-\phi_{\mathrm{f}})V_{\mathrm{E}}\right]_k^{n+1}-\left[(1-\phi_{\mathrm{m}}-\phi_{\mathrm{f}})V_{\mathrm{E}}\right]_k^{n} \end{pmatrix}\end{aligned} \tag{22}$$

Eqs 17–22 construct the element characteristic matrix of shale matrix gas phase seepage equation based on triangular mesh and controlled volume finite element method. Similarly, the element characteristic matrix of shale fracture system seepage equation can be constructed.

For hydraulic fracturing fractures, the discrete fracture model is used to reduce their dimensionality to a one-dimensional line segment with a certain width. The interpolation function of the gas phase equation can be expressed as:

$$\begin{aligned} p_{\mathrm{gF}} &= \frac{x_{\mathrm{j}}-x}{\Delta l}p_{\mathrm{gFi}}+\frac{x-x_{\mathrm{i}}}{\Delta l}p_{\mathrm{gFj}} \\ &= N_{\mathrm{i}}p_{\mathrm{gFi}}+N_{\mathrm{j}}p_{\mathrm{gFj}} \\ &= \left[N_{\mathrm{i}}\ N_{\mathrm{j}}\right]\begin{bmatrix} p_{\mathrm{gFi}} \\ p_{\mathrm{gFj}} \end{bmatrix} \end{aligned} \tag{23}$$

Combined with the interpolation function, Eq. (16) of the hydraulic fracture seepage control equation is constructed in the following numerical calculation format:

$$\begin{aligned} &\iint_{\Omega_{\mathrm{F}}} N_\nu \frac{\partial}{\partial l_{\mathrm{F}}}\left(\lambda_{\mathrm{gF}}\frac{\partial p_{\mathrm{gF}}}{\partial l_{\mathrm{F}}}\right)d\Omega_{\mathrm{F}} \\ &= w_{\mathrm{F}}\times\Delta l_{\mathrm{F}}\times\lambda_{\mathrm{gF}}\times\frac{\partial N_\nu}{\partial l_{\mathrm{F}}}\begin{bmatrix}\frac{\partial N_{\mathrm{i}}}{\partial l_{\mathrm{F}}} & \frac{\partial N_{\mathrm{j}}}{\partial l_{\mathrm{F}}}\end{bmatrix}\begin{bmatrix} p_{\mathrm{gFi}} \\ p_{\mathrm{gFj}} \end{bmatrix} \\ &= w_{\mathrm{F}}\times\lambda_{\mathrm{gF}}\times\begin{bmatrix} \frac{1}{\Delta l_{\mathrm{F}}} & -\frac{1}{\Delta l_{\mathrm{F}}} \\ -\frac{1}{\Delta l_{\mathrm{F}}} & \frac{1}{\Delta l_{\mathrm{F}}} \end{bmatrix}\begin{bmatrix} p_{\mathrm{gFi}} \\ p_{\mathrm{gFj}} \end{bmatrix} \end{aligned} \tag{24}$$

For the time term:

$$\iint_{\Omega_{\mathrm{F}}} N_l \frac{\partial\left(S_{\mathrm{gF}}\phi_{\mathrm{F}}/B_{\mathrm{gF}}\right)}{\partial t}d\Omega_{\mathrm{F}} = w_{\mathrm{F}}\times\frac{\Delta l_{\mathrm{F}}}{2\Delta t}\times\begin{pmatrix} \left(\frac{S_{\mathrm{gF}}\phi_{\mathrm{F}}}{B_{\mathrm{gF}}}\right)_{\mathrm{i}}^{n+1}-\left(\frac{S_{\mathrm{gF}}\phi_{\mathrm{F}}}{B_{\mathrm{gF}}}\right)_{\mathrm{i}}^{n} \\ \left(\frac{S_{\mathrm{gF}}\phi_{\mathrm{F}}}{B_{\mathrm{gF}}}\right)_{\mathrm{j}}^{n+1}-\left(\frac{S_{\mathrm{gF}}\phi_{\mathrm{F}}}{B_{\mathrm{gF}}}\right)_{\mathrm{j}}^{n} \end{pmatrix} \tag{25}$$

Similarly, the characteristic matrix of water phase unit in fracturing fracture system can be further constructed.

4.2 The whole region iteratively solves the matrix

The pressure value of each system in the next time step is characterized by the fully implicit calculation format. The "dimensionality reduction" treatment of fractured fractures is carried out and embedded into the reservoir flow model. By assembling the characteristic matrix of each unit, the fully implicit iterative solution matrix for the whole region is constructed as follows:

$$\left\{\begin{matrix} \mathbf{T}_{\mathrm{gf}}^{k}+\delta\mathbf{T}_{\mathrm{gf}}^{k}\mathbf{P}_{\mathrm{gf}}^{k}-\mathbf{W}_{\mathrm{gmf}}^{k}-\dfrac{\delta\mathbf{N}_{\mathrm{gf}}^{k}}{\Delta t} & \delta\mathbf{W}_{\mathrm{gmf}}^{k}\left(\mathbf{P}_{\mathrm{gm}}^{k}-\mathbf{P}_{\mathrm{gf}}^{k}\right)+\mathbf{W}_{\mathrm{gmf}}^{k} & \delta\mathbf{T}_{\mathrm{gf}}^{k}\mathbf{P}_{\mathrm{gf}}^{k}+\dfrac{\delta\mathbf{N}_{\mathrm{gf}-S_{\mathrm{wf}}}^{k}}{\Delta t} \\ \mathbf{W}_{\mathrm{gmf}}^{k} & \mathbf{T}_{\mathrm{gm}}^{k}+\delta\mathbf{T}_{\mathrm{gm}}^{k}-\delta\mathbf{W}_{\mathrm{gmf}}^{k}\left(\mathbf{P}_{\mathrm{gm}}^{k}-\mathbf{P}_{\mathrm{gf}}^{k}\right) & \\ & -\mathbf{W}_{\mathrm{gmf}}^{k}-\dfrac{\delta\mathbf{N}_{\mathrm{gm}}^{k}}{\Delta t}-\dfrac{\delta\mathbf{V}^{k}}{\Delta t} & \\ \mathbf{T}_{\mathrm{wf}}^{k} & & \delta\mathbf{T}_{\mathrm{gf}}^{k}\mathbf{P}_{\mathrm{gf}}^{k}+\dfrac{\delta\mathbf{N}_{\mathrm{wf}}^{k}}{\Delta t} \end{matrix}\right\} \times \begin{bmatrix} \delta\mathbf{P}_{\mathrm{gf}}^{k} \\ \delta\mathbf{P}_{\mathrm{gm}}^{k} \\ \delta\mathbf{S}_{\mathrm{wf}}^{k} \end{bmatrix} = \begin{bmatrix} \mathbf{R}_{\mathrm{gf}}^{k} \\ \mathbf{R}_{\mathrm{gm}}^{k} \\ \mathbf{R}_{\mathrm{wf}}^{k} \end{bmatrix} \tag{26}$$

Finally, the numerical well model of fractured horizontal well is established and put into Eq. (26):

$$q_{\mathrm{usct}}^{n+1}=\sum_{i=1}^{N_F}\mathrm{PI}_{ui}^{n+1}\left(p_{\mathrm{bh}}-p_{\mathrm{avei}}\right)^{n+1} \tag{27}$$

Where, q_{usct} is the daily gas and water production ground conditions, m^3/d; p_{bh} is bottom-hole flow pressure, MPa; p_{avei} is the average pressure of the grid block where the well source and junction are located, MPa; N_F is the total number of intersection points between fractured fractures and horizontal wellbore. PI_{ui} is the production index, $m^3/d/MPa$. Through iterative computations, when the accuracy requirements of δP and δS_w are met, the stable value under current time step is obtained and the calculation of the next time step is started.

5 Results and discussion

5.1 Pressure distribution prediction and analysis

For a fractured horizontal well with a complex fracture network (Figure 1) in the south Sichuan shale gas reservoir block, the triangular grid was used to discrete the spatial grid of the whole area, and a fully implicit numerical simulation program was developed to simulate and predict the production dynamic characteristics of fractured horizontal wells. The basic parameters of the model are shown in Table 1. The calculation equation of the fracture relative permeability curve is: $k_{\mathrm{rgf}}=1-S_{\mathrm{wf}}$, $k_{\mathrm{rwf}}=S_{\mathrm{wf}}$.

Figure 4 shows the change of gas well pressure of fractured horizontal wells with complex fracture networks of shale gas for 100 days, 1 year and 10 years, respectively. As can be seen from the figure, the pressure propagation presents the characteristics of non-uniform distribution in the complex fracture network area, and the pressure propagation is faster in the well section with high reconstruction degree. At the same time, the gas well pressure propagation gradually expands outward with time, and the pressure at the boundary of the inner and outer regions is also non-uniform due to the influence of the complex fracture network boundary shape. When the pressure propagates to the original reservoir area, its pressure propagation speed is significantly slower than that of the reconstruction area, indicating that the reconstruction area of complex fracture network is the main contribution area to the pressure drop and production of shale gas wells.

In addition, Figure 5 shows the production decline curves of fractured horizontal wells with and without SRV region. By comparison, it can be seen that the SRV region formed by complex fracture networks will significantly increase the daily and cumulative gas production of fractured wells, indicating that compared to traditional double wing hydraulic fracturing method, fracture network fracturing is more conducive to achieving higher single well EUR and production efficiency for horizontal wells in shale gas reservoirs.

5.2 Effect of fracture water saturation on productivity

Figure 6 shows the influence of different fracture water saturation on gas well productivity. Due to the low flowback rate of fracturing fluid in shale reservoirs, a large amount of fracturing fluid remains in the reservoir, resulting in gas-water two-phase flow characteristics in fractured wells and near wellbores. The simulation results show that the higher the fracture water saturation, the lower the daily gas production. When the fracture water saturation is 0.2, 0.3, and 0.4, the cumulative gas production after 10 years of depletion production is 194 million m^3, 170 million $m^3$and 145 million m^3, respectively. Therefore, the retained fracturing fluid has a significant impact on gas well productivity.

5.3 Effect of fracture conductivity on productivity

Figure 7 shows the influence of different hydraulic fracture conductivity on gas well productivity. As can be seen from the figure, the higher the diversion capacity, the higher the early daily gas output, but the difference degree gradually decreases with the increase of production time. When the diversion capacity CFD is 0.25D cm, 0.5D cm and 1.0D cm, the cumulative gas production after 10 years of depletion is 133 million m^3, 180 million m^3 and 194 million m^3, respectively. Therefore, in the hydraulic fracturing process of shale gas reservoir, it is necessary to improve the conductivity of fracturing fractures as much as possible to increase the production.

5.4 Effect of permeability of stimulation area on productivity

Figure 8 shows the influence of permeability in the stimulation area on gas well productivity. It can be seen that the higher the permeability of the stimulation area, the larger the daily gas

TABLE 1 Basic parameters of the model.

Original reservoir pressure, p_i, MPa	46	Matrix nanopore radius, r_e, nm	2
Reservoir thickness, h, m	80	Stress sensitivity factor, d_f, MPa^{-1}	0.05
Horizontal well length, L, m	1700	Reservoir temperature, T, K	323
Bottom hole flow pressure, p_{bh}, MPa	14	gas specific gravity, r_g	0.6
Langmuir pressure, p_L, MPa	15	Langmuir volume, V_L, m^3/kg	0.01
Stimulated inner zone		**Outer zone**	
Fracture permeability, k_{f1}, mD	0.001	Fracture permeability, k_{f2}, mD	0.0005
Fracture porosity, φ_{f1}	0.15	Fracture porosity, φ_{f2}	0.05
Matrix permeability, k_{m1}, mD	0.0001	Matrix permeability, k_{m2}, mD	0.0001
Matrix porosity, φ_{m1}	0.02	Matrix porosity, φ_{m2}	0.02
Fracture water saturation, S_{wf1}	0.2	Fracture water saturation, S_{wf2}	0

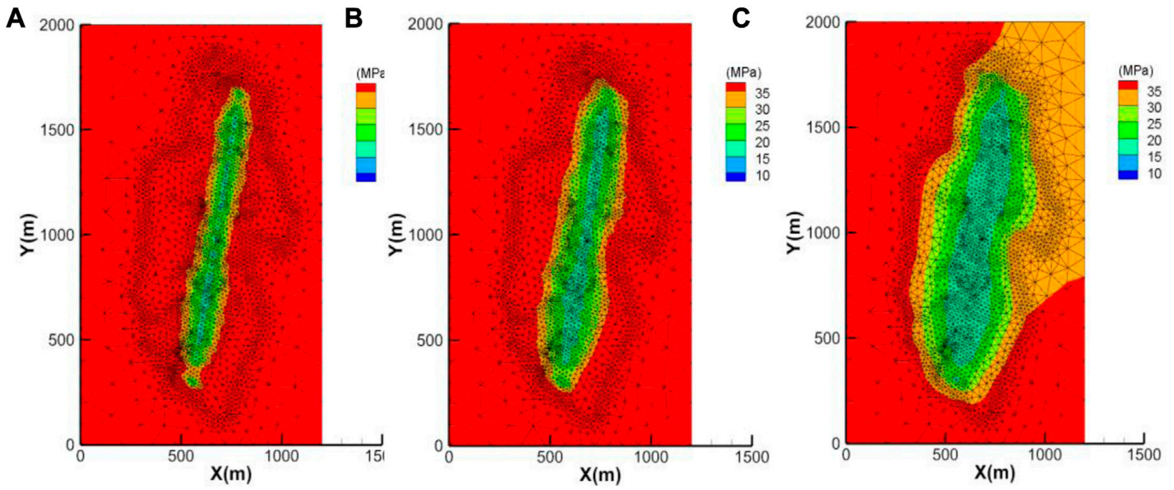

FIGURE 4
Pressure distribution of fractured wells with complex fracture network under different production time. **(A)** After 100 days' production. **(B)** After 1 year' production. **(C)** After 10 years' production.

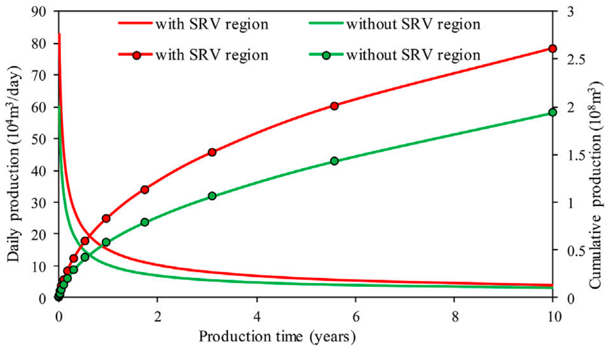

FIGURE 5
Production of fractured horizontal well with and without SRV region.

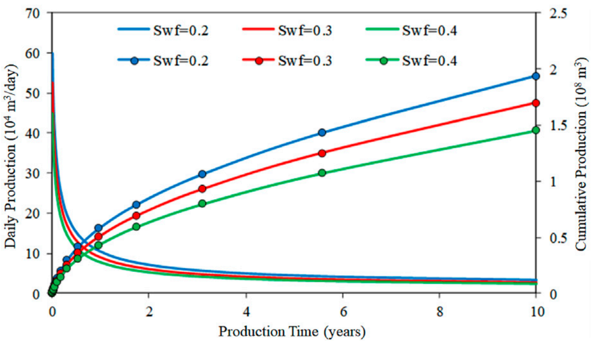

FIGURE 6
Effect of different fracture water saturation on gas well production.

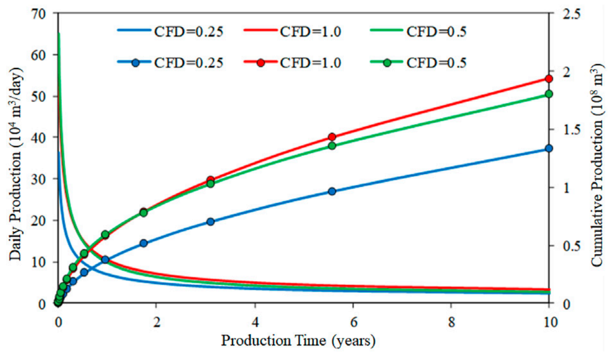

FIGURE 7
Effect of different fracture conductivity on gas well production.

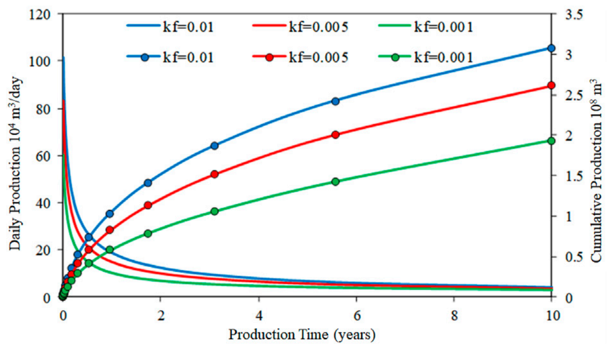

FIGURE 8
Effect of different permeability in SRV region on gas well production.

production of the gas well in the early stage, and the larger the cumulative production of the gas well, indicating that the fracturing stimulation area around the horizontal well is more fully stimulated. When the fracture permeability in the stimulation area is 0.001mD, 0.005mD and 0.01mD, the cumulative gas production after 10 years of depletion production is 194 million m^3, 261 million m^3 and 308 million m^3, respectively. It is the key to improve the production of shale gas wells by optimizing the construction parameters, increasing the stimulation degree of the stimulation area and improving the seepage capacity of shale reservoir.

5.5 Effect of Langmuir volume on productivity

Figure 9 shows the influence of different Langmuir volume V_L on gas well production curves. As can be seen from the figure, the larger the V_L value, the larger the daily gas production and cumulative gas production of the gas well, and the slower the decline rate of gas well production. With the progress of gas well production, the free gas in fracture and matrix system is preferentially produced. The continuous reduction of reservoir pressure makes the gas adsorbed on the surface of organic matter begin to desorption, and enter the fracture system as a reservoir supplementary gas source, delaying the decline of gas well production. When Langmuir volume V_L is 0.01 m^3/kg, 0.02 m^3/kg and 0.03 m^3/kg, the cumulative gas production after 10 years of depletion production is 193 million m^3, 260 million m^3 and 313 million m^3, respectively. Adsorption and desorption is a unique seepage mechanism of shale gas reservoir, which is different from conventional gas reservoir. With the progress of production, the reservoir pressure decreases and the adsorption gas is desorbed in large quantities, which will contribute to the production replenishment and stable production of fractured horizontal wells in shale gas reservoir in the middle and later stages.

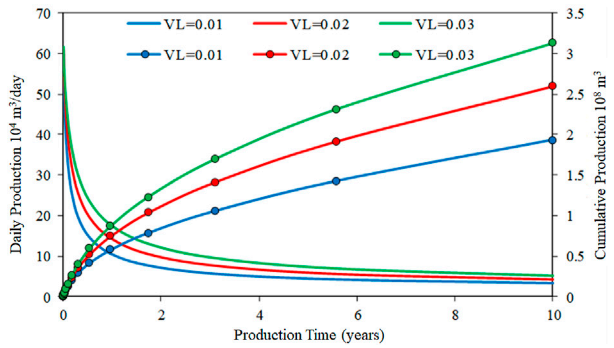

FIGURE 9
Effect of different Langmuir volume on gas well production.

6 Conclusion

(1) Simulation studies show that the micro-seismic data and discrete fracture model can be used to reasonably characterize fracture geometry and complex boundary characteristics, and the influence of fracture network on production dynamics can be accurately simulated.
(2) Parameter sensitivity analysis shows that the higher the fracture water saturation, the lower the gas well production; The hydraulic fracture conductivity has obvious influence on the early production of shale gas fractured horizontal wells. Complex fracture network stimulation area is the main contribution area of shale gas well output, the better the stimulation effect, the higher the permeability of the stimulation area, the higher the output of shale gas well. Therefore, the fracturing reconstruction of shale gas wells is mainly to improve the reconstruction degree and increase the reconstruction volume.
(3) For fractured horizontal wells in shale gas reservoirs, with a large amount of free gas produced in fractures and matrix systems, the early high production stage ends, and the adsorbed gas adsorbed on the surface of shale matrix is desorbed due to the reduction of reservoir pressure, which becomes the key to the production replenishment and stable production in the middle and late period. The more desorption gas, the greater the cumulative gas production.

Data availability statement

The raw data supporting the conclusion of this article will be made available by the authors, without undue reservation.

Author contributions

HX: Methodology, Software, Writing–original draft, Investigation. MC: Data curation, Investigation, Resources, Writing–review and editing. CJ: Formal Analysis, Investigation, Writing–review and editing. HZ: Investigation, Resources, Writing–original draft. KW: Conceptualization, Supervision, Validation, Writing–review and editing.

Funding

The authors declare financial support was received for the research, authorship, and/or publication of this article. This study was financially supported by the China Postdoctoral Science Foundation (Grant No. 2022M722638), and the Science and Technology Cooperation Project of the CNPC-SWPU Innovation Alliance (Grant No. 2020CX020202).

Conflict of interest

HX, MC, CJ, and HZ were employed by the company Sichuan Changning Natural Gas Development Co., Ltd. KW was employed by the Development Division of Southwest Oil & Gas Field Company.

Publisher's note

References

Altwaijri, M., Xia, Z. H., Yu, W., Qu, L. C., Hu, Y. P., Xu, Y. F., et al. (2018). Numerical study of complex fracture geometry effect on two-phase performance of shale-gas wells using the fast EDFM method. *J. Petroleum Sci. Eng.* 164, 603–622. doi:10.1016/j.petrol.2017.12.086

Brown, M., Ozkan, E., Ragahavan, R., and Kazemi, H. (2011). Practical solutions for pressure-transient responses of fractured horizontal wells in unconventional shale reservoirs. *SPE Reserv. Eval. Eng.* 14 (6), 663–676. doi:10.2118/125043-PA

Cai, M. F. (2020). Key theories and technologies for surrounding rock stability and ground control in deep mining. *J. Min. Strata Control Eng.* 2 (3), 033037. doi:10.13532/j.jmsce.cn10-1638/td.20200506.001

Cheng, L. S., Wu, Y. H., Huang, S. J., Fang, S. D., Ma, M., Xue, Y. C., et al. (2020). A comprehensive model for simulating gas flow in shale formation with complex fracture networks and multiple nonlinearities. *J. Petroleum Sci. Eng.* 187, 106817. doi:10.1016/j.petrol.2019.106817

Fan, D., Yao, J., Sun, H., Zeng, H., and Wang, W. (2015). A composite model of hydraulic fractured horizontal well with stimulated reservoir volume in tight oil & gas reservoir. *J. Nat. Gas Sci. Eng.* 24, 115–123. doi:10.1016/j.jngse.2015.03.002

Geiger, S., Roberts, S., Matthai, S. K., Zoppou, C., and Burri, A. (2004). Combining finite element and finite volume methods for efficient multiphase flow simulations in highly heterogeneous and structurally complex geologic media. *Geofluids* 4, 284–299. doi:10.1111/j.1468-8123.2004.00093.x

Geng, L. D., Li, G. S., Tian, S. C., Sheng, M., Ren, W. X., and Zitha, P. (2016). A fractal model for real gas transport in porous shale. *AIChE J.* 63, 1430–1440. doi:10.1002/aic.15516

Guo, W., Zhang, X. W., Yu, R. Z., Kang, L. X., Gao, J. L., and Liu, Y. Y. (2022). A model for the apparent gas permeability of shale matrix organic nanopore considering multiple physical phenomena. *Front. Earth Sci.* 9, 2296–6463. doi:10.3389/feart.2021.813585

Javadpour, F. (2009). Nanopores and apparent permeability of gas flow in mudrocks (shales and siltstone). *J. gas Can. Petroleum Technol.* 48, 16–21. doi:10.2118/09-08-16-DA

Jiang, J. M., and Rami, M. Y. (2015). A multimechanistic multicontinuum model for simulating shale gas reservoir with complex fractured system. *Fuel* 161, 333–344. doi:10.1016/j.fuel.2015.08.069

Karimi-Fard, M., Durlofsky, L. J., and Aziz, K. (2004). An efficient discrete-fracture model applicable for general-purpose reservoir simulators. *SPE J.* 9, 227–236. doi:10.2118/88812-PA

Li, H. (2023). Coordinated development of shale gas benefit exploitation and ecological environmental conservation in China: A mini review. *Front. Ecol. Evol.* 11, 1232395. doi:10.3389/fevo.2023.1232395

Li, H. T., Wang, J. C., Li, Y., and Luo, W. (2015). Deliverability evaluation method based on volume source for horizontal wells by staged fracturing. *Nat. Gas. Ind.* 35, 55–63. doi:10.3787/j.issn.1000-0976.2015.09.008

Li, J., Li, H., Yang, C., Ren, X. H., and Li, Y. D. (2023). Geological characteristics of deep shale gas and their effects on shale fracability in the Wufeng–Longmaxi Formations of the southern Sichuan Basin, China. *Lithosphere* 2023 (1), 4936993. doi:10.2113/2023/4936993

Liu, Y. W., Gao, D. P., Li, Q., Wan, Y. Z., Duan, W. J., Zeng, X. G., et al. (2019). Mechanical frontiers in shale-gas development. *Adv. Mech.* 49 (1), 201901. doi:10.6052/1000-0992-17-020

Lv, X. R., Yao, J., Huang, Z. Q., and Zhao, J. (2012). Study on discrete fracture model two-phase flow simulation based on finite volume method. *J. Southwest Petroleum University:Science Technol. Ed.* 34, 123–130. doi:10.3863/j.issn.1674-5086.2012.06.018

Moinfar, A., Varavei, A., Sepehrnoori, K., and Johns, R. T. (2013). *Development of a coupled dual continuum and discrete fracture model for the simulation of unconventional reservoirs*. The Woodlands, TX, USA: Study SPE 163647 presented at the SPE Reservoir Simulation Symposium.

Ozkan, E., Brown, M., Raghavan, R., and Kazemi, H. (2011). Comparison of fractured-horizontal-well performance in tight sand and shale reservoirs. *SPE Reserv. Eval. &Engineering* 14 (02), 248–259. doi:10.2118/121290-PA

Stalgorova, E., and Mattar, L. (2013). Analytical model for unconventional multifractured composite systems. *SPE Reserv. Eval. Eng.* 16, 246–256. doi:10.2118/162516-PA

Sun, Z. M. (2023). Superimposed hydrocarbon accumulation through multi-source and multi-stage evolution in the cambrian xixiangchi group of eastern sichuan basin: A case study of the pingqiao gas-bearing anticline. *Energy Geosci.* 4 (1), 131–142. doi:10.1016/j.engeos.2022.09.001

Wang, H. T. (2014). Performance of multiple fractured horizontal wells in shale gas reservoirs with consideration of multiple mechanisms. *J. Hydrology* 510, 299–312. doi:10.1016/j.jhydrol.2013.12.019

Wang, X. C., Rasouli, V., Damjanac, B., Yu, W., Xie, H. B., Li, N., et al. (2020). Coupling of fracture model with reservoir simulation to simulate shale gas production with complex fractures and nanopores. *J. Petroleum Sci. Eng.* 193, 107422. doi:10.1016/j.petrol.2020.107422107422

Wu, K. L., Li, X. F., and Chen, Z. X. (2016). Micro-scale effects of gas transport in organic nanopores of shale gas reservoirs. *Nat. Gas. Ind.* 36, 51–64. doi:10.3787/j.issn.1000-0976.2016.11.007

Wu, K. (2014). *Numerical modeling of complex hydraulic fracture development in unconventional reservoirs*. Austin, TX, USA: The University of Texas at Austin.

Wu, Y. S., and Pruess, K. A. (1988). A multiple-porosity method for simulation of naturally fractured Petroleum reservoirs. *SPE Reserv. Eval. Eng.* 3, 327–336. doi:10.2118/15129-PA

Wu, Z. W., Cui, C. Z., Jia, P. F., Wang, Z., and Sui, Y. F. (2022). Advances and challenges in hydraulic fracturing of tight reservoirs: A critical review. *Energy Geosci.* 3 (4), 427–435. doi:10.1016/j.engeos.2021.08.002

Xie, J. (2018). Practices and achievements of the Changning-Weiyuan shale gas national demonstration project construction. *Nat. Gas. Ind.* 38, 1–7. doi:10.3787/j.issn.1000-0976.2018.02.001

Xu, J. C., Guo, C. H., Wei, M. Z., and Jiang, R. Z. (2015). Production performance analysis for composite shale gas reservoir considering multiple transport mechanisms. *J. Nat. Gas Sci. Eng.* 26, 382–395. doi:10.1016/j.jngse.2015.05.033

Yang, Z. H., Hu, Z. Q., Xiong, L., Ding, J. H., Shen, B. J., Shi, H. L., et al. (2020). Gas storage characteristics and coupling characteristics of deep shale gas: A case study of well-X in southern sichuan basin, China. *Reserv. Eval. Dev.* 10, 20–27. doi:10.13809/j.cnki.cn32-1825/te.2020.05.003

Yuan, B., Su, Y. L., Moghanloo, R. G., Rui, Z. H., Wang, W. D., and Shang, Y. Y. (2015). A new analytical multi-linear solution for gas flow toward fractured horizontal wells with different fracture intensity. *J. Nat. Gas Sci. Eng.* 23, 227–238. doi:10.1016/j.jngse.2015.01.045

Zhu, Q. Y., Dai, J., Yun, F. F., Zhai, H. H., Zhang, M., and Feng, L. R. (2022). Dynamic response and fracture characteristics of granite under microwave irradiation. *J. Min. Strata Control. Eng.* 4 (1). doi:10.13532/j.jmsce.cn10-1638/td.20210926.001019921

Zhang, D. L., Zhang, L. H., Zhao, Y. L., and Guo, J. J. (2015). A composite model to analyze the decline performance of a multiple fractured horizontal well in shale reservoirs. *J. Nat. Gas Sci. Eng.* 26, 999–1010. doi:10.1016/j.jngse.2015.07.034

Zhang, L. H., Jia, M., Zhang, R. H., and Guo, J. J. (2017). Discrete fracture network modeling and numerical simulation of fractured reservoirs. *J. Southwest Petroleum University:Science Technol. Ed.* 39, 121–127. doi:10.11885/j.issn.1674-5086.2016.03.31.03

Zhang, R. H., Chen, M., Tang, H. Y., Xiao, H. S., and Zhang, D. L. (2023). Production performance simulation of a horizontal well in a shale gas reservoir considering the propagation of hydraulic fractures. *Geoenergy Sci. Eng.* 221, 111272doi:10.1016/j.petrol.2022.111272

Zhang, T., Li, X. F., Wang, X. Z., Li, J., Sun, Z., Feng, D., et al. (2018). A discrete model for apparent gas permeability in nanoporous shale coupling initial water distribution. *J. Nat. Gas Sci. Eng.* 59, 80–96. doi:10.1016/j.jngse.2018.08.024

Zhao, J. Z., Ren, L., Shen, C., and Li, Y. M. (2018a). Latest research progresses in network fracturing theories and technologies for shale gas reservoirs. *Nat. Gas. Ind.* 38, 533–546. doi:10.1016/j.ngib.2018.03.007

Zhao, Y. L., Zhang, L. H., and Shan, B. C. (2018b). Mathematical model of fractured horizontal well in shale gas reservoir with rectangular stimulated reservoir volume. *J. Nat. Gas Sci. Eng.* 59, 67–79. doi:10.1016/j.jngse.2018.08.018

Zou, C. N., Guo, J. L., Jia, A. L., Wei, Y. S., Yan, H. J., Jia, C. Y., et al. (2020). Connotation of scientific development for giant gas fields in China. *Nat. Gas. Ind.* 40, 1–12. doi:10.3787/j.issn.1000-0976.2020.03.001

Frontiers | Frontiers in Earth Science

TYPE Original Research
PUBLISHED 28 September 2023
DOI 10.3389/feart.2023.1225920

OPEN ACCESS

EDITED BY
Hu Li,
Southwest Petroleum University, China

REVIEWED BY
Guanxiong Ren,
Southwest Petroleum University, China
Shuai Yin,
Xi'an Shiyou University, China

*CORRESPONDENCE
Douzhong Zhang,
✉ zdz1357@163.com

RECEIVED 20 May 2023
ACCEPTED 11 September 2023
PUBLISHED 28 September 2023

CITATION
Zhang D, Chen K, Tang J, Liu M, Zhang P, He G, Cai J and Tuo X (2023), Prediction of formation pressure based on numerical simulation of *in-situ* stress field: a case study of the Longmaxi formation shale in the Nanchuan area, eastern Chongqing, China.
Front. Earth Sci. 11:1225920.
doi: 10.3389/feart.2023.1225920

Prediction of formation pressure based on numerical simulation of *in-situ* stress field: a case study of the Longmaxi formation shale in the Nanchuan area, eastern Chongqing, China

Douzhong Zhang[1,2]*, Kongquan Chen[2], Jiguang Tang[1], Ming Liu[3], Peixian Zhang[3], Guisong He[3], Jun Cai[1] and Xiusong Tuo[1,2]

[1]School of Geosciences, Yangtze University, Wuhan, China, [2]Cooperative Innovation Center of Unconventional Oil and Gas, Yangtze University, Wuhan, China, [3]Sinopec East China Oil and Gas Company, Nanjing, China

The *in-situ* stress and formation pressure are important parameters in shale gas development. They directly affect the well wall stability, the direction of horizontal well drilling, and the fracturing effect during the shale gas development process. There are abundant shale gas resources in the southeastern Chongqing-Sichuan area, but the structure in the area is complex, and it is difficult to predict the *in-situ* stress and formation pressure. Therefore, in this paper, a finite element simulation model was established based on a large number of seismic, logging, and experimental rock mechanics data and the prediction accuracy of the stress field simulation was effectively improved. The construction of the stress field was based on the combined spring model, as well as the data related to the measured *in-situ* stress and the formation pressure obtained during drilling. The coupling relationship between the *in-situ* stress, the formation strain, and the formation pressure were derived to carry out the prediction of the distributions of the formation pressure and the formation pressure coefficient. The prediction results showed that the present-day maximum principal stress direction in the study area was about NE65°–110°, and the present-day maximum principal stress was 56.12–93.79 MPa. The present-day minimum principal stress direction was about NE335°–20°, and the present-day minimum principal stress was 48.06–71.67 MPa. The formation pressure was 2.8–88.25 MPa, and the formation pressure coefficient was 0.74–1.55. The formation pressure distribution was greatly affected by fault, tectonic location, *in-situ* stress and rock petrophysical properties, and the overpressure areas of the formation were distributed in the synclines and the deeply buried areas. This study shows that the finite element based formation pressure prediction method is effective.

KEYWORDS

shale gas, numerical simulation, in-situ stress field, formation pressure, coupling relationship, complex tectonic transition area. 1

1 Introduction

Formation pressure is the reflection of the environmental stress of formation pore fluids, in which vertical load plays a leading role. For shale gas reservoirs, the variation of formation pressure is very large, often manifested as abnormal pressure (Chen et al., 2020; Sun et al., 2023). Abnormal pressure includes abnormal high pressure and abnormal low pressure. The measured formation pressure results are discrete, but the prediction of shale gas sweet spots requires a continuous formation pressure distribution. At this time, the conventional methods based on logging data, such as the Eaton method and the equivalent depth method, make the forecasting strategy of formation pressure further developed (Zhang, 2013). It is obvious that conventional logging method is an indirect method to predict formation pressure. Generally, the response of abnormal high pressure on logging curve is high porosity, low density, low wave velocity and low resistivity; while the abnormal low pressure shows the increase of density and resistivity, and the decrease of acoustic time difference (Sun et al., 2023). However, there are many factors that affect the change of rock porosity, density and acoustic wave time difference, such as undercompaction, temperature, diagenesis and structure (Xiong et al., 2016; Ma et al., 2020). Therefore, the formation pressure obtained by conventional methods often fails in complex structural areas. From the formation mechanism of formation pressure, it is affected by the superposition of overlying load and difference of horizontal tectonic stresses. Therefore, the finite element method based on geomechanics is a more direct method to predict formation pressure.

The Sichuan Basin and its surrounding areas contain rich reserves of shale gas resources, and the proven reserves exceed 2×10^{12} m^3 (Guo et al., 2014; Nie et al., 2021). As the main horizontal section for shale gas exploration and development in southern China, the Silurian Longmaxi Formation has entered a stage of commercial shale gas development (Guo et al., 2014). The Nanchuan Area is another shale gas production area in the Sichuan Basin except for the Jiaoshiba Area (He et al., 2021). The Wufeng-Longmaxi Formation shale gas reserves have reached 1700 × 10^8 m^3, and the Pingqiao Anticline has a shale gas production capacity of 6.5×10^8 m^3. The testing production of a single well was 7.1×10^4 to 29.1×10^4 m^3/d, and the production varies greatly (He et al., 2021). Since the Mesozoic and Cenozoic, the Sichuan Basin has experienced multiple periods of tectonic movement, resulting in a complex distribution of the magnitude and direction of the *in-situ* stresses in the Longmaxi Formation (Chen et al., 2020; Ma et al., 2020; Wang, 2020; Luan et al., 2022). The Nanchuan Area is located at the edge of the Sichuan Basin and is a high-pressure–normal-pressure transition zone for shale gas. The pressure coefficient is distributed between 0.8 and 1.5. Therefore, the research on the prediction of the distributions of the *in-situ* stress and formation pressure plays an important role in the exploration and development of shale gas in this area.

Because of the low porosity and low permeability properties of shale gas reservoirs, horizontal well drilling and hydraulic fracturing technology have been widely adopted worldwide in recent decades to improve shale gas recovery. However, the selection of borehole direction of horizontal wells and the fracture propagation of hydraulic fracturing, are inseparable from the *in-situ* stress. Numerous previous studies have been conducted on how to predict the *in-situ* stress field, and relatively mature research methods have gradually been developed, such as the logging interpretation method and the core testing method (Kingdon and Fellgett, 2016; Xing et al., 2018; Zhang et al., 2023). These methods can accurately obtain the *in-situ* stress data of single wells, but it is impossible to predict the *in-situ* stress field of an area with no wells. With the continuous progress of research, some researchers have conducted numerical simulation studies on *in-situ* stress based on finite element principles combining logging calculation and core testing method (Chatterjee and Pal, 2010; Wang et al., 2017; Chen et al., 2018). The reservoir pressure while drilling tester can directly measure the formation pressure of the target zone. The Schlumberger's Pressure Xpress and Pressure XPresS-HT instruments have also used the Quartzdyne quartz pressure sensors to measure formation pressure (Xue et al., 2023). The core component of these instruments is the quartz pressure sensor, which calculates the real pressure and temperature values through the solution algorithm, and then gets the accurate measurement results of the dynamic response of the formation pressure. In addition, the formation pressure prediction based on logging algorithm depends on the high resolution of logging data. The common interpretation models include effective stress method, Bowers method, empirical statistical model method, equivalent depth method, Eaton method, etc., which determine formation pressure through the compaction characteristics of rocks in the depth domain (Shi et al., 2020). The mechanical modeling method used by most researchers in the process of numerical modeling is to simulate the stress field of the formation outside the fault as an isotropic body (Higgins et al., 2008; Huang et al., 2019; Li et al., 2020). In a complex tectonic zone, the distributions of the mechanical parameters of the rocks within a layer vary considerably (Li et al., 2023; Peng et al., 2023). If the stress field simulation is carried out using an isotropic mechanical model, the accuracy of the simulation results will be greatly affected. Therefore, in this study, we divided the mechanical parameters into different regions based on the distributions of mechanical parameters of rocks, which could effectively improve the accuracy of the simulation results (Yang et al., 2021; Si et al., 2023).

The formation pressure, also known as the formation pore fluid pressure, is one of the important indicators in the evaluation of shale gas preservation. It is an indispensable parameter for determining the safety of drilling operations during the development of shale gas. Its ratio to the hydrostatic pressure, being called the formation pressure coefficient, is also one of the important parameters in the evaluation of shale gas reservoirs. Currently, the method of predicting the formation pressure in a well and the surrounding areas still includes the use of resistivity and sonic logging data (Mouchet and Mitchell, 1989; Sun, 2017; Chen et al., 2021; Li et al., 2021). For the prediction of the formation pressure in an area, the relationship between the acoustic wave time difference of the effective stress equation and the pore pressure can be used (i.e., the Eaton method) (Eaton, 1972; Fillippone, 1979; Carpenter, 2015). The Eaton method can also be used to establish different calculation models for different regions. Therefore, many researchers have used the Eaton method as the basis and have combined the actual geological conditions of each

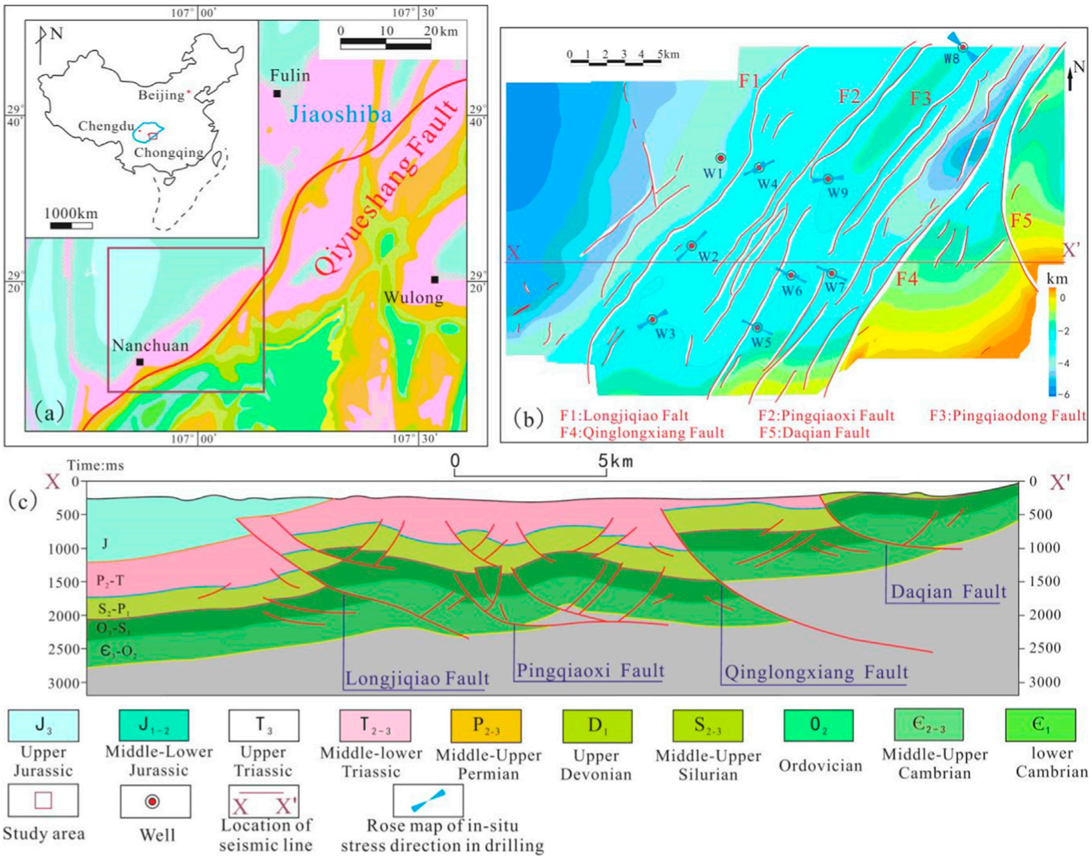

FIGURE 1
(A) Location of the study area; **(B)** basal boundary tectonic map of the Silurian Longmaxi Formation in the Nanchuan Area; and **(C)** structural profile of a survey line XX′.

study area to modify the model parameters, which can effectively improve the prediction accuracy of the formation pressure. The application of these methods, however, is inseparable from the development of the layer velocity field model. With continuous research progress, the sampling accuracy of the layer velocity data points must be greater than 12 ms, in order to obtain formation pressure prediction results that meet the accuracy requirements (Xu et al., 2015; Huo et al., 2021). The accuracy of the layer velocity modeling in complex tectonic zones cannot meet the requirement for formation pressure prediction. The method of predicting the formation pressure is mainly to use logging data to predict the values in the wells and surrounding areas. It is difficult to predict the formation pressure in areas between wells.

Using the principle of finite element numerical simulation, in this study, we used the seismic data and logging data and the ANSYS Software to predict the *in-situ* stress field of the Longmaxi Formation in the Nanchuan Area. Additionally, considering the characteristics of the lateral isotropy and longitudinal anisotropy of the shale reservoirs, the formation pressure and formation pressure coefficient were predicted based on the combined spring model. The prediction results of the formation pressure distribution obtained in this study can provide a reference for the deployment, exploration, and development of a shale gas well networks in similar areas.

2 Geological background

The study area is located in the southeast part of the Sichuan Basin (southwest of the Jiaoshiba Area) (Figure 1). The Silurian Longmaxi Formation in this area was deposited in a deep-water shelf sedimentary environment (He et al., 2021). The shale of the Longmaxi Formation have three main lithofacies: siliceous shale, mixed shale and clay shale (Ju et al., 2019). The deposition environment was characterized by a high paleo-productivity and an anoxic environment (Wang et al., 2017), resulting in the enrichment of organic matter and providing the area with a rich source material (Figure 2). In terms of the tectonic location, the area is located in the tectogene on the southeastern margin of the Sichuan Basin. The surface undulates greatly in this area. The Jurassic strata are exposed in the northwest, and the Silurian strata are exposed in the southeast. Overall, the burial depth of the target layer gradually decreases from northwest to southeast, and the burial depths are 500–5,800 m. Most of the faults in the Nanchuan Area have a strike of the north-east direction. The causal mechanism in these faults was the long-distance conduction of the intracontinental orogeny in the Jiangnan Uplift. In the Mid-Yanshanian, the study area was subjected to a thrusting stress from the south-east, causing the faults to be mainly north-east trending. In the Late Yanshanian, a small number of nearly south-north trending faults were formed

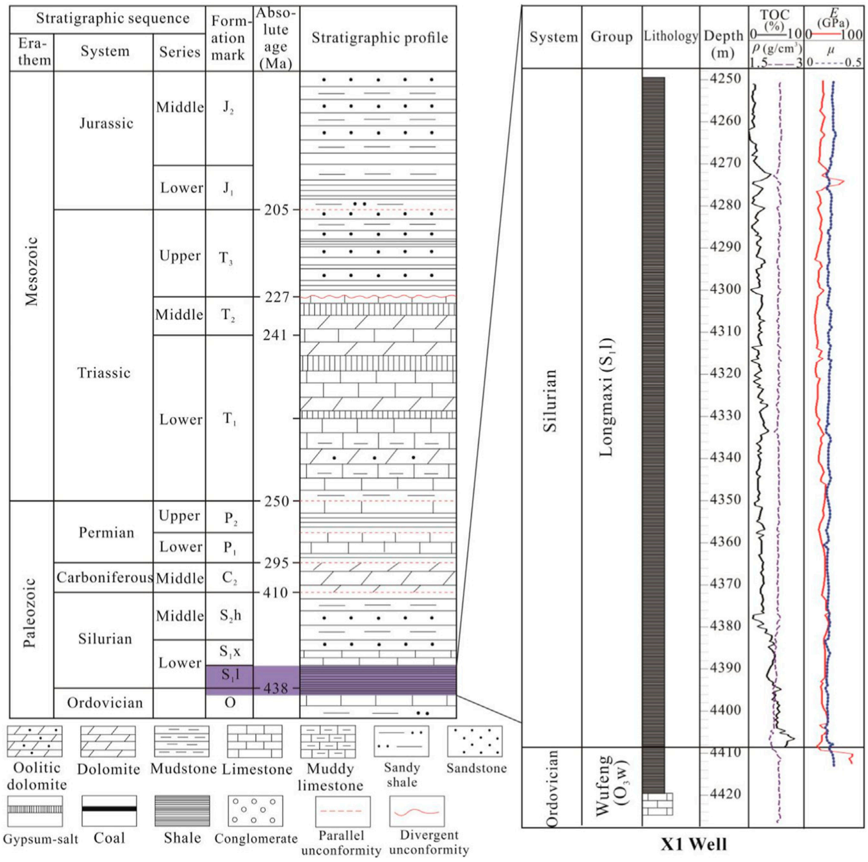

FIGURE 2
Comprehensive stratigraphic units of the Nanchuan area, eastern Sichuan Basin.

under a east-west trending stress (Wang et al., 2017). Currently, because of the influence of the compression of the Indian and Eurasian Plates, the main body of the Qinghai-Tibet Plateau has moved eastward, producing an eastward compressive stress. After transmission, a southwest-northeast compressive stress field was formed in this area (Wang and Shen, 2020).

The tectonic deformation on the boundary of the study area is mainly controlled by the Qinglongxiang Fault, and the internal tectonic deformation is controlled by the Pingqiaoxi, Longjiqiao, and Yangchungou Faults (Figure 1). The Qinglongxiang Fault is a basement thrust fault that thrusts upward to the surface. The fault runs through the entire study area from north to south and has a large fault dips to the northeast. The Permian upper-plate is exposed and a Cambrian detachment has developed, causing the Daqian Fault to slip along the Middle Cambrian strata. The development of a fault-propagation fold resulted in the formation of the Baima Syncline. In addition, the southern section of the Daqian Fault changes from northeast to north-northwest because of the change in the direction of tectonic stress. Affected by the Daqian Fault and the Qinglongxiang Fault, the northward dipping Shiqiao Nasal Shape Structure was formed. The Precambrian detachment at the bottom is strong. The basement fault extends farther, crossing the Qinglongxiang Fault, and the upper Silurian strata contains almost no detachment. The tectonic deformation to the west of the Qinglongxiang Fault and the east of the Longjiqiao Fault is relatively strong. The Precambrian basement fault detachment gradually weakens and eventually disappears at the bottom of the Longjiqiao Fault. The upper cap rocks are mainly controlled by the Cambrian detachment and the development of the fault-related folds, such as the Dongsheng Anticline and the Pingqiao Anticline. They all plunge to the northeast and disappear. To the west of the Longjiqiao Fault, the deformation progressively weakens. Therefore, there is no strong faulting and folding in the forward belt of the thrust nappe structure, and only detachment occurs. For the tectonic deformation in eastern Sichuan, the Cambrian is the main detachment surface of the along-bedding detachment. The stratigraphic angle of the lower plate of the fault is relatively small, and the overall low-angle slope transitions to an open syncline in the basin. In some areas, the north-northwest trending fault cuts the early small northeast-trending fault because of the later transformation. In the southern areas, a nearly south-north trending fault-propagation fold has formed because of the nearly east-west compression in the late period.

3 Methods

3.1 Numerical simulation of *in-situ* stress

The present-day stress field is the *in-situ* stress field caused by the present-day tectonic stress. This stress directly affects the core technologies used in shale gas development, including the horizontal well drilling and hydraulic fracturing technology. Carrying out research on the present-day stress field in complex tectonic transform areas is conducive to finding favorable areas for shale gas production. The factors that affect the distribution of *in-situ* stress field mainly include the characteristics of structural development, rock mechanical properties, fault distribution characteristics, boundary stress environment (the direction and size of tectonic stress), etc. In this study, the simulation study of *in-situ* stress field in the Nanchuan area of the Eastern Chongqing is carried out based on the finite element method.

In-situ stress field simulation mainly includes the following steps: 1) Geological model; 2) Mechanical model; 3) Determination of boundary conditions; 4) Numerical simulation results; 5) Computer calculations and analyses of the simulation results.

3.1.1 Geological model

The geological model is the basic model of the numerical simulation of the *in-situ* stress field, which directly affects the mechanical model, mathematical model, the division of boundary elements, and the gap of finite elements (Kaiser et al., 2005; Barba et al., 2010; Ju and Wang, 2018; Wu et al., 2021). On the basis of seismic data and the basal boundary tectonic map of the present-day Longmaxi Formation in the Nanchuan area, a basic geological model was established. To establish a geological model that fully reflects the main geological characteristics of the study area, the model considered all the faults that control the tectonics (Jiu et al., 2013; Ju et al., 2017; Liu et al., 2022). The geological data revealed that for the major faults in the area (i.e., the Longjiqiao Fault, Pingqiaoxi Fault, Pingqiaodong No. 1 Fault, Qinglongxiang Fault, and Daqian Fault), the cutting horizon is generally the Cambrian-Permian, which extends upward to the surface and downward to the Precambrian basement.

3.1.2 Mechanical model

The simulation scheme used in this study adopted the finite element analysis method to treat the research area as an ideal elastic body, and the simulation was carried out under this state. The strain was produced on the plane as a result of the action of the stress, and the stress and strain in each finite element were assumed to be uniform.

The reasonable selection of the mechanical parameters of the rocks directly affects the accuracy of the numerical simulation. Therefore, in this study, the overall characteristics of the rock series were considered when selecting the regional mechanical parameters of the rocks. The geological model used in this study was mainly divided into two units: the fault unit and the surrounding rock unit. The values of the physical parameters of these two units were different, but each was regarded as an isotropic elastic body. According to the compressional wave time difference, shear wave time difference, and density data for the Longmaxi Formation in the study area, the following equations were used to calculate the elastic modulus and Poisson's ratio of the formation (Xu, 2014):

$$E_{\mathrm{d}} = \frac{\rho}{\Delta t_s^2} \cdot \frac{3\Delta t_s^2 - 4\Delta t_p^2}{\Delta t_s^2 - \Delta t_p^2} \tag{1}$$

$$\mu_{\mathrm{d}} = \frac{\Delta t_s^2 - 2\Delta t_p^2}{2\left(\Delta t_s^2 - \Delta t_p^2\right)^2} \tag{2}$$

Where E_{d} is dynamic Young's modulus (GPa); μ_{d} is dynamic Poisson's ratio; ρ is rock density (kg/m^3); $\triangle t_{\mathrm{p}}$ is compressional wave time difference (μs/m); and $\triangle t_{\mathrm{s}}$ is shear wave time difference (μs/m).

The dynamic-static conversion equation for the mechanical parameters of the rocks was used for the mechanical property interpretation (Xiong et al., 2016). The conversion equations for the mechanical parameters of the rocks in the study area are as follows (Eqs 3, 4):

$$E_{\mathrm{s}} = 0.2928E_{\mathrm{d}} + 17.82 \tag{3}$$

$$\mu_{\mathrm{s}} = 3.968\mu_{\mathrm{d}} - 0.7551 \tag{4}$$

Where E_{d} and E_{s} are dynamic and static Young's modulus (GPa); μ_{d} and μ_{s} are dynamic and static Poisson's ratio.

3.1.3 Determination of boundary conditions

Affected by the compression of the Indian Plate and the Eurasian Plate, a southwest-northeast compressive stress field has formed in the southeastern margin of the Sichuan Basin. The direction of the drilling-induced fractures in the Nanchuan Area was statistically analyzed, and the results showed that the present-day maximum principal stress direction is NE65°–150° (Figure 1). It represents the range of a clockwise rotation from NE65° to 150°. The range of angles covered by this result is 85°. For complex structural zones, deflection in the direction of principal stress exceeding 90° is common (Higgins et al., 2008; Ju et al., 2019). The large deflection in the direction of the principal stress is due to a well-developed faults in the study area (Figure 1). Therefore, fault is the factor that cause the disturbance of local stress and its direction deflection. There are many methods for obtaining *in-situ* stress, such as the triaxial rock mechanics experiments, the logging data calculation method, the hydraulic fracturing method, and the borehole stress relief method. In this study, we mainly use the logging data to calculate the *in-situ* stress data for the drilled wells in the area. The calculation results revealed that the maximum principal stress in the study area is 63.3–78.39 MPa, and the minimum principal stress is 54–68.16 MPa. The simulation experiment was repeated to obtain the most suitable loading data.

Because the *in-situ* stress situation is relatively complex and it is not clear how the stress acts on the boundary, in this study, we assumed the stress on the boundary to be uniform. A geological model was established using the ANSYS Software, and the corresponding mechanical parameters were assigned to the geological units. In the model developed in this study, a three-node triangular element was used for the grid division. According to the principle of finite element division, the grid units of the fault and its surrounding area were small, with a high grid density; and the grids in the other areas were large, with a small density. After the division, the grid of the model contained 59,363 nodes and 29,632 elements in total. After several simulations, the optimal simulation results were obtained when the maximum principal stress (75 MPa) and the minimum principal stress (65 MPa) were applied at 45° northeast and 135° northwest from the boundary, respectively (Figure 3).

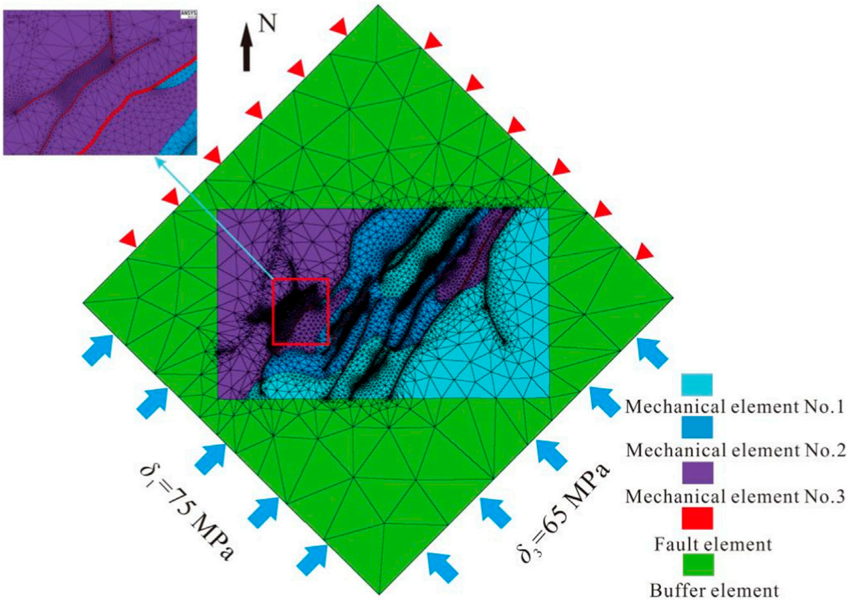

FIGURE 3
Model grid division using ANSYS. δ_1 and δ_3 represent the horizontal maximum and minimum principal stresses respectively.

In the finite element method, the geological body is regarded as a finite continuous element connected by nodes. By endowing the geological body with mechanical parameters and imposing boundary stress conditions, the changes of stress, strain and displacement of each node in the region under the stress environment are calculated, which never reflects the change characteristics of the stress field of the geological body.

The displacement of any node (x, y) in the model can be expressed as:

$$\begin{cases} w = \mu(x, y) \\ v = v(x, y) \end{cases} \tag{5}$$

Where w and v are the displacement in the X and Y direction, respectively.

Based on geometric equations, the relationship between strain and displacement is presented.

$$\begin{cases} \varepsilon_x = \dfrac{\delta w}{\delta x} \\ \varepsilon_y = \dfrac{\delta v}{\delta y} \\ \varepsilon_{xy} = \dfrac{\delta w}{\delta x} + \dfrac{\delta v}{\delta y} \end{cases} \tag{6}$$

Strain matrix is expressed as:

$$[\varepsilon] = [B][\delta]^e \tag{7}$$

Where [b] is geometric matrix, $[\delta]$ is nodal displacement matrix.

According to the principle of virtual displacement, The derived node load matrix is:

$$[P] = [K][\delta] \tag{8}$$

Where $[P]$ is integral nodal load matrix, $[K]$ is integral stiffness matrix, $[\delta]$ is node displacement matrix.

Based on the elastic mechanics equation, the relationship between stress and strain is:

$$[\sigma] = [D][\varepsilon] \tag{9}$$

Where $[D]$ is elasticity matrix.

3.2 Method of predicting formation pressure

Formation pressure is the pressure of fluids in the pores of an underground rock mass on the rock's skeleton, and it interacts with the *in-situ* stress. In particular, in strongly deformed tectonic zone, the deformation of the underground formation is complex, and the relationship between the *in-situ* stress and the formation pressure also becomes more complex. Therefore, the shale formation in the study area is considered to be a transversely isotropic medium and a longitudinally anisotropic medium based on the linear isotropic combined spring model (Thiercelin and Plumb, 1994). According to the theory of solid mechanics, we derived the relationship between the formation pressure and the *in-situ* stress under formation deformation. Logging data can accurately reflect the downhole formation pressure. Because of the complexity of the underground formation and the impacts of multiple factors, such as the tectonics and burial depth (Wang et al., 2010; Brooke-Barnett et al., 2015; Rajabi et al., 2017; Zeng et al., 2019), it can be difficult to predict the planar distribution characteristics of the formation pressure from the drilling data. Accurate prediction of the formation pressure distribution can effectively guide the deployment of the well networks for shale gas development. The technical process of this study is shown in Figure 4.

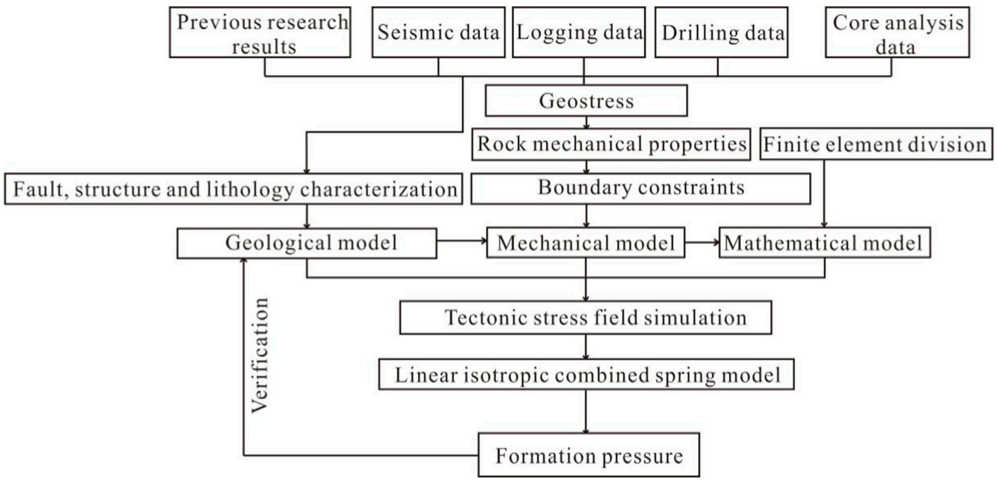

FIGURE 4
Technical process of this study (modified after Ding et al., 2016).

3.2.1 Linear isotropic combined spring model

Based on the generalized Hooke's law, the linear isotropic combined spring model of various systems comprehensively considers the influences of various factors, such as the formation's elasticity, the tectonic pressure, and the tectonic deformation. In addition, this law has been applied widely in the prediction of the *in-situ* stress in shale formations (Thiercelin and Plumb, 1994; Ostadhassan et al., 2012; Najibi et al., 2017).

$$\sigma_{\mathrm{h}} - \alpha P_{\mathrm{p}} = \frac{\mu}{1-\mu}\cdot\left(\sigma_{\mathrm{v}} - \alpha P_{\mathrm{p}}\right) + \frac{E}{1-\mu^2}\varepsilon_{\mathrm{h}} + \frac{E_\mu}{1-\mu^2}\varepsilon_{\mathrm{H}} \tag{10}$$

$$\sigma_{\mathrm{H}} - \alpha P_{\mathrm{p}} = \frac{\mu}{1-\mu}\cdot\left(\sigma_{\mathrm{v}} - \alpha P_{\mathrm{p}}\right) + \frac{E}{1-\mu^2}\varepsilon_{\mathrm{H}} + \frac{E_\mu}{1-\mu^2}\varepsilon_{\mathrm{h}} \tag{11}$$

Therefore, various factors, such as the horizontal stress, the tectonic deformation of the formation, and the overlying formation pressure, are used as the basic information to determine the coupling relationship between the stress, strain, and formation pressure based on the linear isotropic combined spring model (Eqs 10, 11) and the geological characteristics in the Nanchuan Area. Then, a formation pressure prediction equation suitable for the strong tectonic deformation (Eq. 12 in the study area is established. The equation is as follows:

$$\alpha P_{\mathrm{p}} = \frac{\mu}{2\mu-1}\cdot\sigma_{\mathrm{v}} + \frac{1-\mu}{2-4\mu}\left(\sigma_{\mathrm{H}} + \sigma_{\mathrm{h}}\right) + \frac{E}{4\mu-2}\left(\varepsilon_{\mathrm{H}} + \varepsilon_{\mathrm{h}}\right) \tag{12}$$

Where α is Biot coefficient; P_{p} is formation pore pressure (MPa); μ is Poisson's ratio; σ_{v} is overlying formation pressure (MPa); σ_{H} is horizontal maximum principal stress (MPa); σ_{h} is horizontal minimum principal stress (MPa); E is Young's modulus (MPa); ε_{H} is maximum principal strain in the horizontal direction; and ε_{h} is minimum principal strain in the horizontal direction.

In this study, the Biot coefficient was obtained according to the differential equivalent medium model (Zou and Chen, 2018; Zhou et al., 2022). There is a positive correlation between Biot coefficient and porosity. The calculated results show that the average Biot coefficient of the Longmaxi shale is 0.76.

3.2.2 Formation strain

The formation strain (i.e., the formation's linear strain) is the ratio of the length increment caused by the deformation of a small line segment of the formation in a certain direction to the original length. The formation strain directly affects the correlation between the horizontal stress and the vertical stress (Lv et al., 2022). In the horizontal area of the formation, the interaction between the horizontal stress and the vertical stress was almost nonexistent (Lv et al., 2022). As the degree of formation deformation increased, the mutual influence of the horizontal stress and the vertical stress also increased. The Petrol Software was used to extract the maximum and minimum curvature values (K_{H} and K_{h}, respectively) of the strata in the Longmaxi Formation tectonic map (Figure 5). Using the thin plate theoretical Eqs 13, 14 (Sun, 2017), the horizontal maximum and minimum structural strains ε_{H} and ε_{h} in the horizontal direction are calculated:

$$\varepsilon_{\mathrm{H}} = h\cdot K_{\mathrm{H}} \tag{13}$$

$$\varepsilon_{\mathrm{h}} = h\cdot K_{\mathrm{h}} \tag{14}$$

Where ε_{H} is horizontal maximum strain; ε_{h} is horizontal minimum strain; h is burial depth of tectonic curved surface (m); K_{H} is maximum curvature in horizontal direction; and K_{h} is minimum curvature in horizontal direction.

3.2.3 Overburden pressure

The overburden pressure is the gravity of the overlying formation, and it was calculated according to the basic gravity calculation equation:

$$\sigma_{\mathrm{v}} = \int_0^h \rho(h)g\,dh \tag{15}$$

where σ_{v} is pressure of overlying formation (MPa); h is buried depth (m); $\rho(h)$ is the function of change in formation density with increasing depth (g/cm^3); and g is acceleration of gravity (m/s^2).

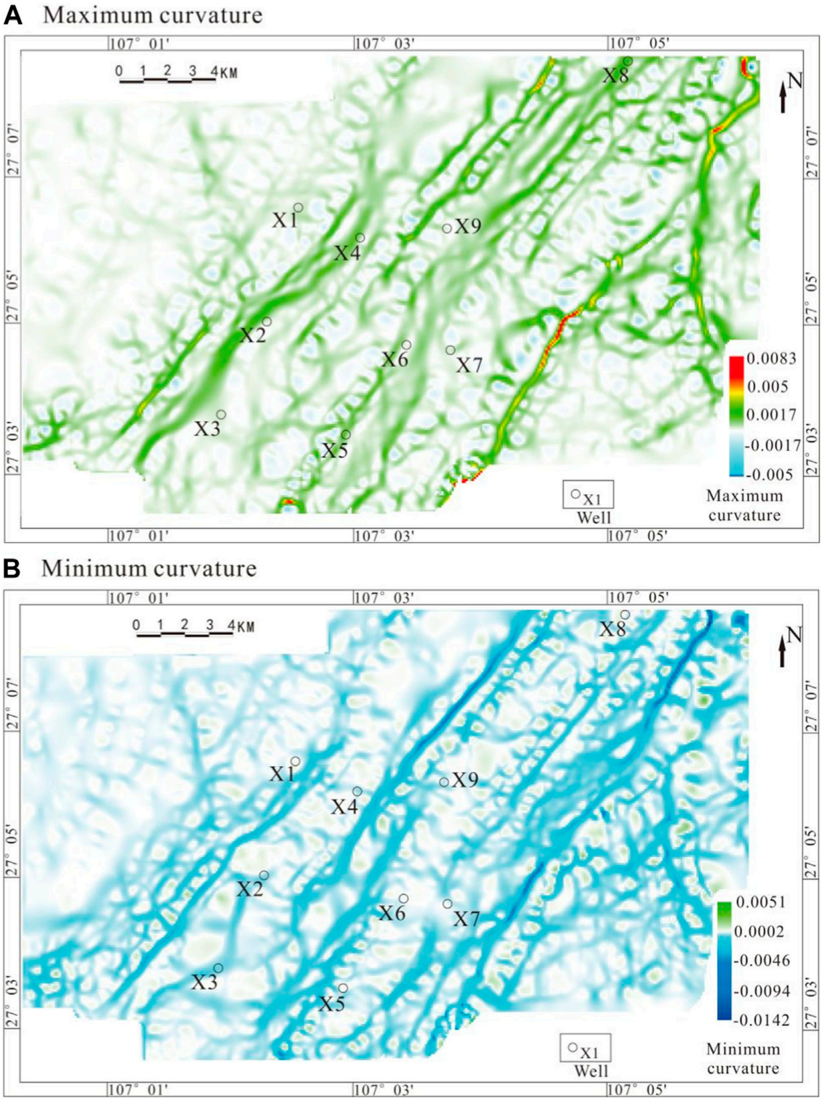

FIGURE 5
Curvature distribution of Silurian Longmaxi Formation in the Nanchuan area: **(A)** Maximum curvature; and **(B)** Minimum curvature.

Because of the density of the overlying formation, it is not an isotropic body and is greatly affected by the burial depth of the formation. According to the density logging data for wells X1, X2, and X4 in the Nanchuan Area, the relationship between the density of the overlying formation and the depth was fitted as follows (Figure 6; Eq. 16):

$$\rho(h) = 0.0177 \cdot \ln(h) + 2.5438 \tag{16}$$

The fitted equation for the density of the overlying formation (Eq. 16) was substituted into the equivalent overlying formation pressure equation (Eq. 12), and the overlying formation pressure for the wells with drilling data in the area was calculated. The fitting results are given in Table 1. The deviations of the calculation results were all less than 1%, which was within the allowable deviation range. These results show that the calculation results of this equivalent equation can effectively reflect the pressure distribution of the formation overlying the Longmaxi Formation in the Nanchuan Area.

4 Results

4.1 Interpretation results of rock mechanics parameters

To verify the accuracy of the calculation results of the mechanical parameters, rock samples were collected from wells X1 and X2 in the Longmaxi Formation in the study area.

The data from the triaxial stress tests were fitted with the seismic calculation data (Table 2; Figure 7). The rock mechanics parameters shown in Figure 2 include Young's modulus and Poisson's ratio. These values are obtained from the linear elastic section in the middle segment of the curve in Figure 7, which represents the stable mechanical state of the rock underground (Yin et al., 2018). The fitting results showed that the deviation of the Young's modulus was less than 1%, and the deviation of the Poisson's ratio was less than 8%. These deviations were within the acceptable range, so the calculation results were reliable.

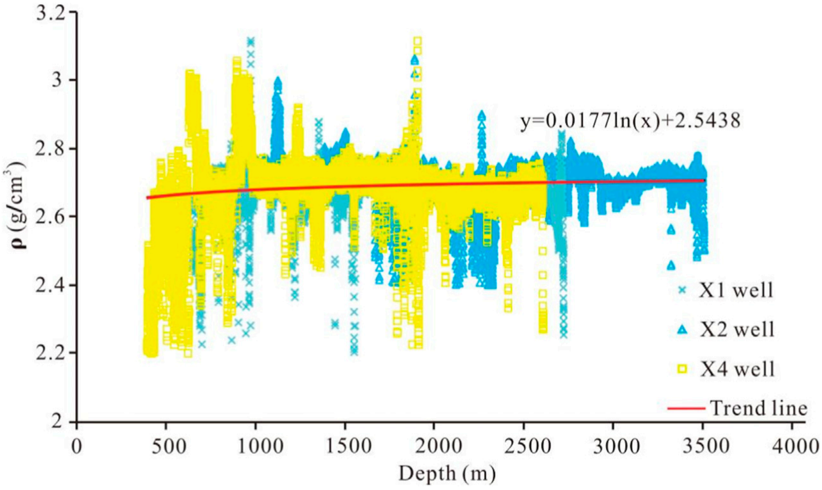

FIGURE 6
Fitting of density logging data from wells in the Nanchuan Area.

TABLE 1 Fitting of overlying formation pressure.

Well	Measured log data (MPa)	Fitting formula calculation (MPa)	Error (%)
X1	106.779	107.066	0.270
X2	70.429	69.998	−0.610
X3	45.850	46.183	0.725
X8	70.749	72.559	−0.269

TABLE 2 Fitting of the mechanical parameters of the Silurian Longmaxi Formation in the Nanchuan Area.

Well	Depth (m)	Triaxial stress test data		Seismic data calculation	
		E (GPa)	*μ*	*E* (GPa)	*μ*
X1	4395.7–4396.0	32.99	0.195	32.86	0.203
X2	3439.2–3439.5	31.50	0.236	31.37	0.220

Therefore, distribution of the Young's modulus and Poisson's ratio of the Longmaxi Formation in the Nanchuan Area were calculated using Eqs 1–4 (Figure 8).

According to the differences in the distributions of the Young's modulus and Poisson's ratio, different mechanical units were defined, and the average values of the Young's modulus and the equivalent Poisson's ratio of the rock in the different regions were calculated (Table 3). The mechanical parameters of faults were generally selected to be 50%–70% of the Young's modulus of the surrounding rock. In contrast, the Poisson's ratio of the fault was larger than that of the normal sedimentary strata, and the difference between the two was usually between 0.02 and 0.1. The values for the buffer area were generally selected as the average Young's modulus and Poisson's ratio values of the simulated area (except for the fault area).

4.2 Numerical simulation of *in-situ* stress

The comparison results of the measured values of the *in-situ* stress obtained by drilling in the study area show that the deviations between the simulated horizontal maximum principal stress and the actual measured *in-situ* stress were all less than 3 MPa, and the stress deviation rate was less than 2% (Table 4). The deviations between the simulated minimum horizontal principal stress and the measured *in-situ* stress were all less than 4 MPa, and the deviation rate was mostly less than 5%. The deviation rate of the horizontal differential stress (the difference between the horizontal maximum principal stress and the horizontal minimum principal stress) was slightly higher, but most of the values were less than 15%, and the deviations were less than 2 MPa. After comprehensive analysis, we concluded that the deviation of the simulation results was within a reasonable range and that they generally conformed to the actual geological law.

(1) Present-day maximum principal stress

The simulation results revealed that the study area is in a compressive stress field environment, and the present-day

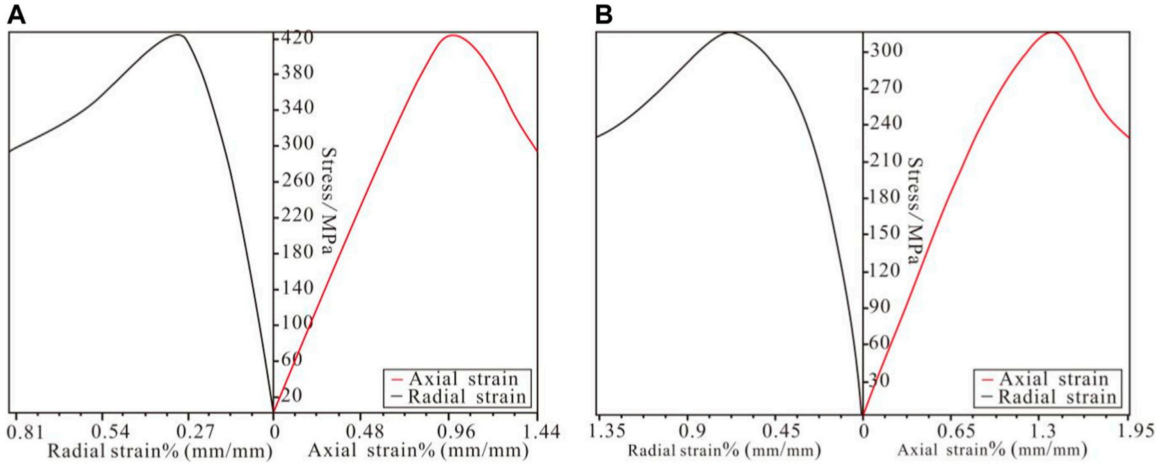

FIGURE 7
Stress-strain curves for the Longmaxi Formation shale in the Nanchuan Area: **(A)** sample from Well X1; and **(B)** sample from Well X2.

maximum principal stress direction is NE65°–110°, which is consistent with the direction of the drilling-induced fractures. Because of the impact of the pre-existing faults, when the *in-situ* stress acts on the fault, component forces will be generated along the fault direction, causing the direction of the maximum horizontal principal stress to deflect to the east (Figure 9A).

The difference between the directions of the maximum horizontal principal stress on the east and west sides was approximately 45°. The range of the maximum principal stress was 56.12–93.79 MPa. The maximum principal stress values in the anticline and the fault zone were the smallest (52.32–68.5 MPa), and they were in the low-stress area. However, the stress values at the tip of the extension of the fault zone and the bend area of the fault were relatively large, and stress concentration occurred in these areas. The region can be regarded as being in a critical state, in which the fracture has been about to penetrate and form a fault, but this penetration has not yet occurred.

The high- and low-stress areas of the faults with different strikes and the nearby areas also were different. The stress values of the southwest-northeast trending faults in the study area were slightly smaller than those of the southeast-northwest trending faults. For example, for the faults in the west, when the tectonic stress was transmitted in the areas containing faults with different strikes, the difference in the strike of the fault caused a change in the equivalent physical parameters of the rocks near the fault, resulting in a change in the fault stress and also a change in the stress value in the surrounding areas. The present-day maximum principal stress in the area to the left of the Longjiqiao Fault (F1) in the study area was relatively large. The burial depth of the stratum in this area was greater than 4500 m, and the confining pressure was relatively large, which affected the mechanical parameters of the rock to a certain extent. The burial depth in the area on the right of the Longjiqiao Fault (F1) was relatively shallow, and the present-day maximum principal stress value was relatively small. The stress value in the syncline area in this zone was higher than that in the nearby flat area. Excluding the influence of the faults, the core area of the anticline was significantly larger than its wing area. However, the situation was the opposite in the anticline area, and the stress value in this area was relatively low. The compressive stress in the core area of the anticline was the smallest, and it has gradually increased toward the two wings.

(2) Present-day minimum principal stress

The present-day minimum principal stress of the Longmaxi Formation in the Nanchuan Area, Eastern Chongqing, is also compressive stress, and the direction of the stress is NE335°–20°, which is consistent with the direction of the well wall collapse during drilling. The present-day minimum principal stress value is in the range of 48.06–71.67 MPa (Figure 9B).

The distribution of the minimum principal stress throughout the entire area was uneven. The distribution of the low-value area was obviously controlled by the faults and depth. The fault zone area was a low-value area with values of 48–55 MPa. Similarly, with the Longjiqiao Fault (F1) as the boundary, the minimum horizontal principal stress values to the west of the fault were relatively large (69.3–71.3 MPa), and the values to the east of the fault were relatively small (50.6–68.1 MPa). They also were affected mainly by the distribution of the mechanical parameters of the rocks.

5 Discussion

5.1 Distribution law of formation pressure

The formation pressure prediction equation (Eq. 5) is used to obtain the distribution of the formation pressure in the study area (Figure 8). The results were fitted using the measured formation pressure data (Table 5). The formation pressure of the target zone is obtained through pressure measurement while drilling, and the mud pulse signal is used to measure formation pressure in real time. The equipment used is SDC-I pressure gauge while drilling.

The predicted values were compared with the actual measured data. The results revealed that the deviations between the predicted

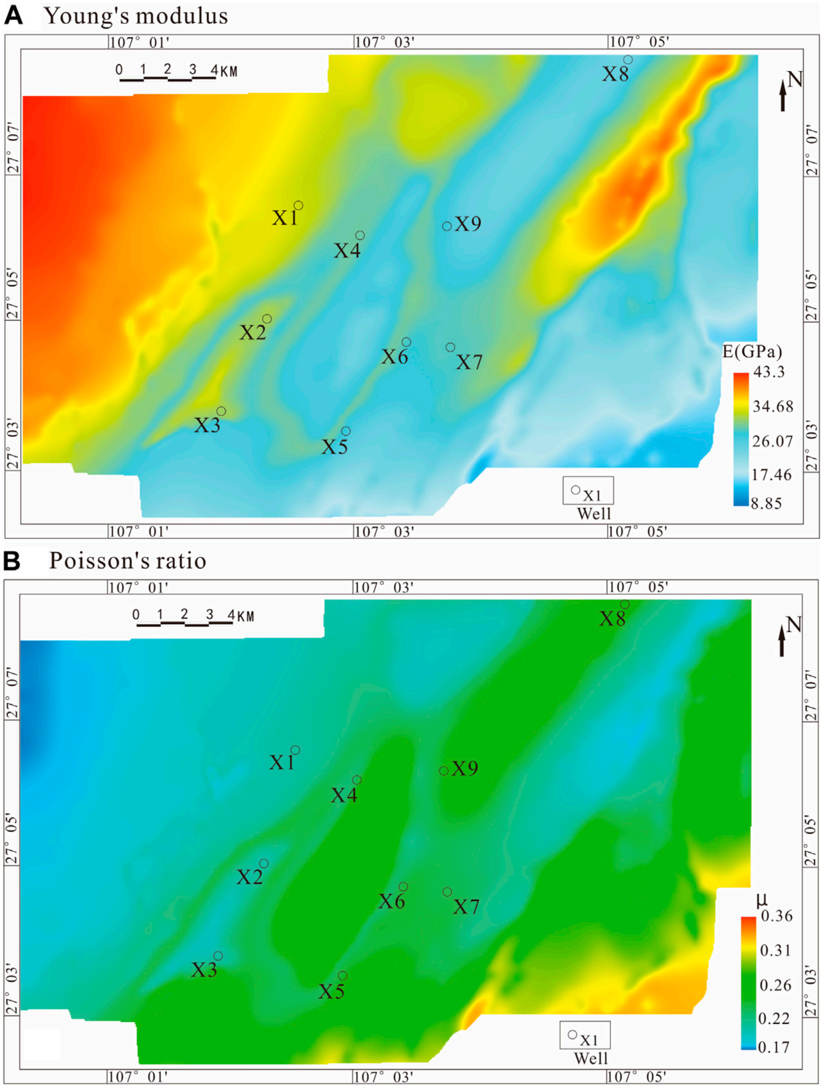

FIGURE 8
Distribution of mechanical parameters of the Silurian Longmaxi Formation in the Nanchuan Area: **(A)** Young's modulus; and **(B)** Poisson's ratio.

TABLE 3 Mechanical parameters used in the simulation of the stress field in the Nanchuan Area.

Mechanical unit	Formation mechanics unit			Fault	Buffer
	Unit 1	Unit 2	Unit 3		
E (GPa)	27.8	33.7	41.7	21.4	34.6
μ	0.237	0.223	0.218	0.276	0.227

values of the formation pressure and the measured values were less than 3 MPa, the deviation percentage was less than 4%, and the deviation of the formation pressure coefficient results was also less than 0.05 (Table 5). The deviations were within the allowable range, the results were generally consistent with the actual geological laws, and the simulation results were reliable. The results show that the coupling relationship between ground stress, formation strain and formation pressure can be well applied in complex deformation area, and the accuracy of formation pressure prediction can be improved.

Based on the formation pressure prediction results (Figure 10), the range of the formation pressure in the area was 2.8–88.25 MPa. The distribution of formation pressure is affected by many factors such as fault, *in-situ* stress, tectonic location and petrophysical parameters. The distribution of the formation pressure was greatly affected by the burial depth of the formation and the tectonic position (Chatterjee, 2008). The areas with high formation pressures were distributed mainly to the west of the Longjiqiao Fault (F1) and in the syncline area between the Pingqiao No. 1 Fault (F3) and the Qinglongxiang Fault (F4). The formation pressures are in these areas were between 55.78 MPa and 88.25 MPa. Additionally, the burial depths of the formation in these two areas were large (>3500 m). The area with a low formation pressure was distributed mainly in the southeastern part of the study area. The burial depth of formation in this area (<1,000 m) was the shallowest in the study area, and the formation pressure was less than 20 MPa.

TABLE 4 Comparison of present-day *in-situ* stress field data.

Well	Maximum principal stress			Minimum principal stress			Horizontal stress difference		
	Measured value (MPa)	Simulated value (MPa)	Error (%)	Measured value (MPa)	Simulated value (MPa)	Error (%)	Measured value (MPa)	Simulated value (MPa)	Error (%)
X1	85.7	83.96	−1.2	75.8	72.1	−4.9	9.9	11.86	19.8
X2	78.39	76.9	−1.9	68.16	65.68	−3.64	11	11.22	2
X3	66.6	67.2	0.9	60.6	60.3	−0.5	6	6.9	15
X4	66.6	67.48	1.32	59	60.45	2.46	6.6	7.03	6.52
X5	63.3	64.5	1.9	54	56.48	4.59	9.3	8.02	−13.76

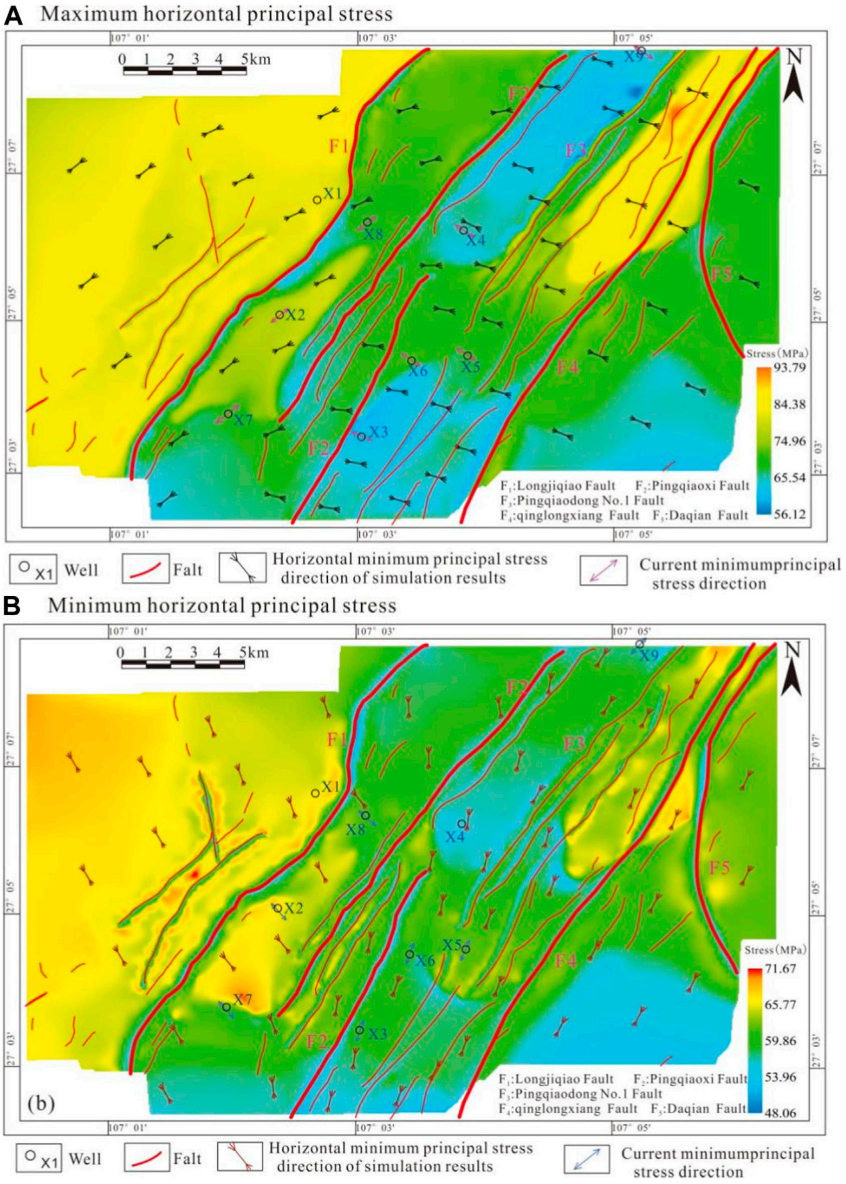

FIGURE 9
In-situ stress field of the Silurian Longmaxi Formation in the Nanchuan Area: **(A)** maximum horizontal principal stress; and **(B)** minimum horizontal principal stress.

TABLE 5 Fitting of the formation pressure and formation pressure coefficient.

Well	Formation pressure			Formation pressure coefficient		
	Measured value (MPa)	Predicted value (MPa)	Error (%)	Measured value (MPa)	Predicted value (MPa)	Error (%)
X1	60.71	60.23	−0.79	1.38	1.369	−0.79
X2	46.70	46.67	−0.74	1.35	1.349	−0.74
X3	42.48	43.08	1.42	1.34	1.359	1.42
X4	49.75	48.65	−2.27	1.32	1.29	−2.27
X6	49.63	47.82	−3.79	1.32	1.27	−3.79

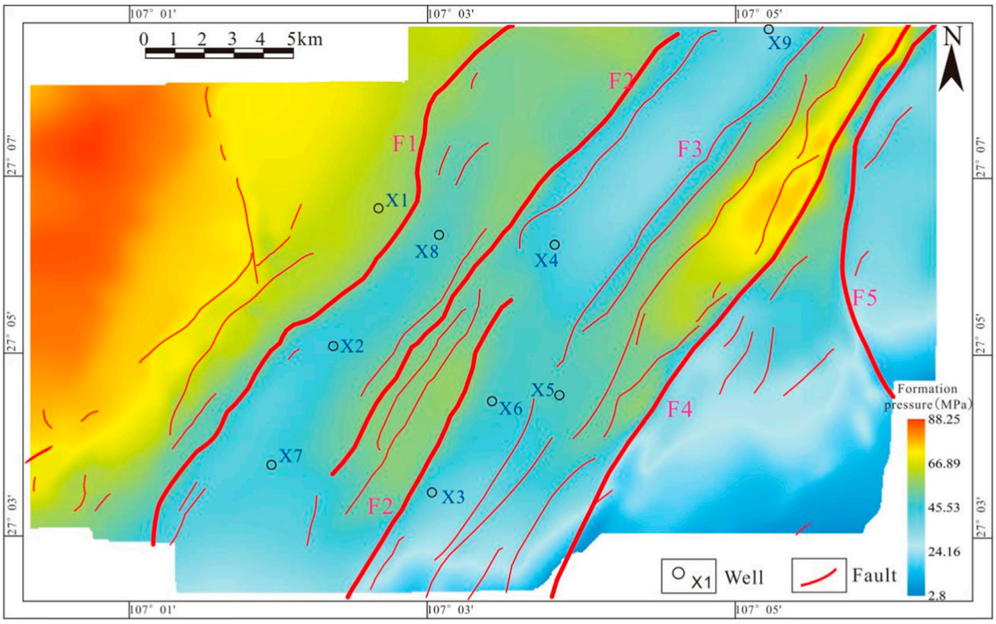

FIGURE 10
Formation pressure distribution of the Silurian Longmaxi Formation in the Nanchuan Area.

The main reason for this was that in the shallow buried area, the overlying strata pressure is low, the positive pressure on the shale bedding surface of Longmaxi Formation is reduced, the fracture is in the open state, resulting in the shale gas escape. In the area where the degree of formation deformation was large, the formation pressure gradient was relatively large, about 12 MPa/km. In the areas with a small degree of formation deformation, the formation pressure gradient was relatively small, about 3 MPa/km.

The coefficient of formation pressure is the ratio of formation pressure to hydrostatic pressure at the same depth, which can directly reflect the change of formation pressure system in the area, and plays an important role in drilling safety and well pattern layout. The Eq. 17 is used to calculate the distribution of the formation pressure coefficient (Figure 11).

$$\alpha_p = P_p / P_h \tag{17}$$

where α_p is formation pressure coefficient; P_p is formation pressure (MPa); and P_h is hydrostatic pressure (MPa).

The formation pressure coefficient ranged from 0.74 to 1.55 (Figure 11), and most of the areas exhibited formation overpressure (pressure coefficient >1.1), the formation pressure in the areas near the basin (the western part of the F1 Fault) is above 1.4. The normal-pressure zone (0.9 < pressure coefficient <1.1) was distributed around the fault. The low-pressure zone (pressure coefficient <0.9) was distributed in the fault zone area and the shallow-buried area in the southeastern part of the study area.

5.2 Factors affecting formation pressure

The results show that the formation pressure in complex tectonic deformation area is controlled by multiple factors such as formation deformation, *in-situ* stress and petrophysical parameters. Therefore, considering the influence of various factors on formation pressure, the prediction accuracy of formation pressure in complex tectonic deformation areas can be improved (Guo and Zhang, 2014; Fang et al., 2018).

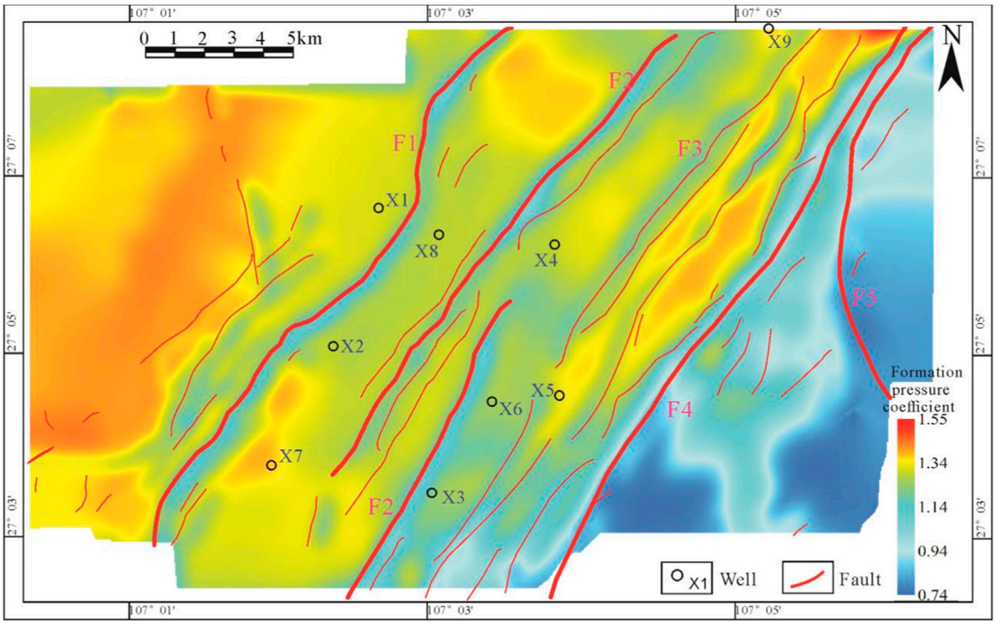

FIGURE 11
Distribution of formation pressure coefficient of the Silurian Longmaxi Formation in the Nanchuan Area.

(1) Faults

In the faults and surrounding areas, the formation pressure was low. The high formation pressure areas occurred in the regions far from the faults. This was mainly due to the development of through-going fractures in the faults and surrounding areas during the formation of the faults, leading to the escape of shale gas. As the distance from the fault increased, the stress concentration phenomenon weakened, and a set of areas where fractures developed but were unconnected gradually formed at distances far from the faults (Shen et al., 2015; Zheng et al., 2019). This area has been conducive to the accumulation and storage of shale gas, resulting in an increase in the formation pressure and the formation of a high-value area.

As shown in Figure 11, the formation pressure on the southeast side of the fault is slightly greater than that on the northwest side. This phenomenon has been confirmed by the formation pressure test results of various wells. This is because the faults in the study area have left-lateral characteristics, which will aggravate the plane heterogeneity of tectonic stress (He, 2021). It causes the southeast side of the fault to be under strong compression conditions, while the northwest side is under weak compression conditions. Thus, the southeast side of the fault has relatively low formation pressure, while the northwest side has relatively high formation pressure (Figure 11).

(2) Structural position

Generally, the more intense the structural deformation is, the higher the degree of fracture development is. The fracture development density is within the appropriate range, which is conducive to shale gas reservoir. Therefore, the formation pressure distribution in different structural locations is quite different. In addition to the fault area, the most intense deformation is in the back and syncline area. The results show that the formation pressure in the synclinal core is high (70–76.2 MPa) and gradually decreases toward the two wings, while the formation pressure in the anticlinal core is low (33.6–42 MPa) and gradually increases toward the two wings. The main reason is that with the formation deformation and bending, the inverted “V” type tensile fracture with downward opening is formed in the synclinal core area with the increase of deformation degree, which is conducive to shale gas accumulation and high formation pressure. On the other hand, the anticlinal area is easy to form the “V” tensile fracture with the opening up, which is easy to cause the shale gas escape and the formation pressure is relatively reduced.

(3) Petrophysical property

Rock physical properties mainly refer to rock mechanical parameters (Young’s modulus and Poisson’s ratio). The research results show that formation pressure in rock strata is positively correlated with Young’s modulus and negatively correlated with Poisson’s ratio. The main reason is that the larger Young’s modulus is and the smaller Poisson’s ratio is in the formation, the more difficult deformation is to occur in the region. When tectonic stress is received, the change of formation pore space can be reduced, so that these regions can maintain high formation pressure. Strata with small Young’s modulus and large Poisson’s ratio are prone to deformation under the influence of tectonic stress, forming new fractures and gradually connecting with other previous fractures, resulting in shale gas escape and formation pressure reduction.

Hydrocarbon generation can promote the formation of secondary pores, thus improving the petrophysical properties and formation pressure of shale reservoirs. In the hydrocarbon generation period, the paleooverpressure was formed under the action of hydrocarbon generation. However, whether the ancient overpressure can be preserved depends on the sealing properties of the overlying layer. If the overburden layer is destroyed, the paleooverpressure environment will change to normal pressure or even negative pressure (Ju et al., 2019). According to the formation pressure evaluation results of the Longmaxi Formation in the study area, overpressure is extremely common (Figure Figure11), and its formation is due to the expansion and pressurization mechanism of hydrocarbon generation (Tang et al., 2022).

(4) *In-situ* stress

The present geostress includes overlying strata pressure and horizontal stress. The overlying formation pressure is the gravity of the overlying formation, which depends on the depth of the formation. The influence of overlying formation pressure on formation pressure (formation pore pressure) mainly includes two aspects. First, in the area with a large burial depth, with the increase of overlying formation pressure, the confining pressure of the formation increases, so does the Young's modulus of the rock, thus affecting the formation pressure. Second, as the burial depth decreases, the overlying formation pressure gradually decreases, so does the positive pressure of the bedding surface of the Longmaxi shale. When the pore pressure of the local layer is greater than the breakthrough pressure, a large number of micro-fractures will be formed, forming new storage space and providing a channel for the shale gas to escape, resulting in the decrease of formation pressure.

The influence of horizontal geostress is mainly manifested in the squeezing effect of horizontal geostress on formation pores. The greater the horizontal *in-situ* stress is and the greater the angle between it and crack strike, the stronger the squeezing effect on formation pores and the stronger the restraint effect on gas in pores, and the better the formation pressure can be maintained. On the contrary, the smaller the horizontal stress is, the smaller the angle between it and the fracture strike is, the smaller the binding force on the gas in the pores is. When it is greater than the breakthrough pressure, the pore space of the formation will increase and the formation pressure will decrease.

Through this study, we found that four factors (fault, structural position, petrophysical property, *in-situ* stress) affect formation pressure. Since formation pressure is caused by overlying load and *in-situ* stress, therefore, *in-situ* stress is the primary factor affecting formation pressure. For faults, structural position and petrophysical property, they will play a certain role in regulating formation pressure, so they are secondary factors. On the whole, *in-situ* stress belongs to external factor, while faults, structural position and petrophysical property belong to internal factor. The external factor has a greater influence on formation pressure.

Compared with the traditional methods, the interpretation method of formation pressure adopted in this paper is based on its genetic mechanism. Therefore, it has advantages in the prediction of formation pressure compared with the traditional methods. However, this method is still a static model. In fact, the formation pressure of shale reservoirs can change continuously during the development of hydrocarbons. Therefore, how to construct a dynamic model of shale formation pressure is a scientific problem worth further exploration in the future.

6 Conclusion

On the basis of this study, the following conclusions can be drawn.

1. The direction of the present-day maximum horizontal principal stress in the Nanchuan Area is about NE65°–110°, and the magnitude is 56.12–93.79 MPa. The direction of the present-day horizontal minimum principal stress is about NE335°–20°, and the magnitude is 48.06–71.67 MPa. The *in-situ* stress direction is greatly affected by the faults, and slight deflection occurs in the fault area. The present-day distribution of the *in-situ* stress is greatly affected by the tectonic position and burial depth, and the distribution exhibits a northeast-southwest trend. The stress values in the fault area are small, and stress concentration occurs at the tip and bend of the fault.
2. The formation pressure in the Nanchuan Area is between 2.8 MPa and 88.25 MPa, and the pressure coefficient is 0.74–1.55. The burial depth and formation position have relatively large influences on the distribution of the formation pressure. The fractures in the fault zone area are dense and connected, which makes it easy for the shale gas to escape, leading to a low formation pressure. The formation pressure values in the syncline area are greater than those in the anticline area. The formation pressure gradient in the fold area is larger than that in the flat area. The *in-situ* stress in the anticline area is relatively small, the formation pressure is less than 40 MPa, and the pressure coefficient is 1.33–1.38.
3. In this study, the prediction accuracy of the *in situ* stress field was effectively improved by dividing the geological model into mechanical units. In addition, based on the linear isotropic combined spring model, the influences of the formation's deformation and the *in-situ* stress on the formation pressure were considered, and the accuracy of the formation pressure prediction was improved. A technique for predicting the formation pressure distribution of shale gas reservoirs in complex structural areas was developed, and it is not only applicable to the Nanchuan area, but also to shale gas reservoirs in other complex tectonic transformation areas worldwide.

Data availability statement

The original contributions presented in the study are included in the article/Supplementary material, further inquiries can be directed to the corresponding author.

Author contributions

DZ is responsible for the idea and writing of this paper and KC, JT, ML, PZ, GH, JC, and XT are responsible for the data interpretation. All authors contributed to the article and approved the submitted version.

Funding

This research was funded by the project “Fine Structural Analysis and Shale Gas Preservation Evaluation in Nanchuan-Wulong Area” (No. P21087-6) of the Ministry of Science and Technology of Sinopec.

Conflict of interest

Authors ML, PZ, and GH were employed by the Sinopec East China Oil and Gas Company.

The remaining authors declare that the research was conducted in the absence of any commercial or financial relationships that could be construed as a potential conflict of interest.

Publisher’s note

References

Barba, S., Carafa, M. M. C., Mariucci, M. T., Montone, P., and Pierdominici, S. (2010). Present-day stress-field modelling of southern Italy constrained by stress and GPS data. *Tectonophysics* 482, 193–204. doi:10.1016/j.tecto.2009.10.017

Brooke-Barnett, S., Flottmann, T., Paul, P. K., Busetti, S., Hennings, P., Reid, R., et al. (2015). Influence of basement structures on *in situ* stresses over the Surat Basin, southeast Queensland. *Geophys. Res. Solid Earth.* 120, 4946–4965. doi:10.1002/2015JB011964

Carpenter, C. (2015). Seismic-Frequency-vs. Seismic interval velocity based porepressure prediction. *J. Pet. Technol.* 67, 141–144. doi:10.2118/0315-0141-jpt

Chatterjee, R. (2008). Effect of normal faulting on *in-situ* stress: A case study from mandapeta field, krishna-godavari basin, India. *Earth Planet Sci. Lett.* 269, 458–467. doi:10.1016/j.epsl.2008.02.040

Chatterjee, R., and Pal, P. K. (2010). Estimation of stress magnitude and physical properties for coal seam of Rangamati area, Raniganj coalfield, India. *Raniganj Coalf. India Int. Coal Geol.* 81, 25–36. doi:10.1016/j.coal.2009.10.006

Chen, J., Gao, J., Pu, Y., Yang, D., Qi, Q., Wen, Z., et al. (2021). Machine learning method for predicting and warning of rockbursts. *J. Min. Strata Control Eng.* 3 (1), 013026. doi:10.13532/j.jmsce.cn10-1638/td.20200922.001

Chen, K., Zhang, D., and Tuo, X. (2020). Relationship between geological structure and marine shale gas preservation conditions in the western Middle Yangtze Block. *Nat. Gas. Ind. B* 7 (6), 583–593. doi:10.1016/j.ngib.2020.04.002

Chen, S., Tang, D., Tao, S., Xu, H., Li, S., Zhao, J., et al. (2018). Characteristics of *in-situ* stress distribution and its significance on the coalbed methane (CBM) development in fanzhuang zhengzhuang block, southern qinshui basin, China. *Petrol. Sci. Eng.* 161, 108–120. doi:10.1016/j.petrol.2017.11.042

Ding, W., Zeng, W., Wang, R., Jiu, K., Wang, Z., Sun, Y., et al. (2016). Method and application of tectonic stress field simulation and fracture distribution prediction in shale reservoir. *Earth Sci. Front.* 23 (2), 63–74. doi:10.13745/j.esf.2016.02.008

Eaton, B. A. (1972). The effect of overburden stress on geopressure prediction from well logs. *J. Petroleum Technol.* 24 (8), 929–934. doi:10.2118/3719-PA

Fang, H. H., Sang, S. X., Wang, J. L., and Ju, W. (2018). Pore characteristics and its significance on shale gas reservoir: A case study of the Longmaxi shale in the nanchuan region, chongqing, south China. *Int. Oil Gas. Coal Technol.* 18 (3–4), 512–536. doi:10.1504/IJOGCT.2018.093127

Fillippone, W. R. (1979). “On the prediction of abnormally pressured sedimentary rocks from seismic data,” in *49th ann. Internat mtg* (Houston, Texas: Soc. Expi. Geophys. Expanded Abstracts), 2667–2676. doi:10.4043/3662-MS

Guo, T. L., and Zhang, H. R. (2014). Formation and enrichment mode of Jiaoshiba shale gas field, Sichuan Basin. *Petrol. Explor Dev.* 41 (1), 31–40. doi:10.1016/s1876-3804(14)60003-3

Guo, X., Hu, D., Li, Y., Liu, R., and Wang, Q. (2014). Geological features and reservoiring mode of shale gas reservoirs in Longmaxi Formation of the Jiaoshiba area. *Acta Geol. Sin. Engl. Ed.* 88 (61), 1811–1821. doi:10.1111/1755-6724.12347

He, L. (2021). Study on the influence of structural deformation characteristics of wujiang fault zone on shale gas reservoirs area of fuling. Master’s thesis. Yangtze: Yangtze University, 44–48. doi:10.26981/d.cnki.gjhsc.2021.000044

He, X., He, G., and Gao, Y. (2021). Geological characteristics and enrichment laws of normal-pressure shale gas in the basin-margin transition zone of SE Chongqing. *Nat. Gas. Ind.* 41 (1), 59–71. doi:10.3787/j.issn.1000-0976.2018.12.001

Higgins, S., Goodwin, S., Donald, A., Bratton, T., and Tracy, G. (2008). Anisotropic stress models improve completion design in the Baxter shale. *SPE* 115736, 11. doi:10.2118/115736-MS

Huang, S., Liu, D., Cai, Y., and Gan, Q. (2019). *In situ* stress distribution and its impact on CBM reservoir properties in the Zhengzhuang area, southern Qinshui Basin, North China. *J. Nat. Gas Sci. Eng.* 61 (1), 83–96. doi:10.1016/j.jngse.2018.11.005

Huo, J., Shi, J., and Shen, X. (2021). Pore pressure prediction methods for new blocks and undrilled deep strata: A case study of the high pressure gas wells along the southern margin of the junggar basin. *Nat. Gas. Ind.* 41 (3), 104–111. doi:10.3787/j.issn.1000-0976.2021.03.012

Jiu, K., Ding, W. L., Huang, W. H., Zhang, Y., and Zhao, S. (2013). Fractures of lacustrine shale reservoirs, the zhanhua depression in the bohai bay basin, eastern China. *Mar. Petrol. Geol.* 48, 113–123. doi:10.1016/j.marpetgeo.2013.08.009

Ju, W., Wang, J., Fang, H., and Sun, W. (2019). Paleotectonic stress field modeling and prediction of natural fractures in the Lower Silurian Longmaxi shale reservoirs, Nanchuan region, South China. *Mar. Petroleum Geol.* 97, 20–30. doi:10.1016/j.marpetgeo.2018.10.052

Ju, W., and Wang, K. (2018). A preliminary study of the present-day *in-situ* stress state in the Ahe tight gas reservoir, Dibei Gasfield, Kuqa Depression. *Mar. Petrol. Geol.* 96, 154–165. doi:10.1016/j.marpetgeo.2018.05.036

Ju, W., Wu, C. F., Wang, K., Sun, W., and Chang, X. (2017). Prediction of tectonic fractures in low permeability sandstone reservoirs: A case study of the Es3 m reservoir in the block shishen 100 and adjacent regions, dongying depression. *Petrol. Sci. Eng.* 156, 884–895. doi:10.1016/j.petrol.2017.06.068

Kaiser, A., Reicherter, K., Hübscher, C., and Gajewski, D. (2005). Variation of the present-day stress field within the north German basin—Insights from thin shell FE modeling based on residual GPS velocities. *Tectonophysics* 397 (1-2), 55–72. doi:10.1016/j.tecto.2004.10.009

Kingdon, M. W., Fellgett, J. D. O., and Williams, J. D. (2016). Use of borehole imaging to improve understanding of the *in-situ* stress orientation of Central and Northern England and its implications for unconventional hydrocarbon resources. *Mar. Petrol. Geol.* 73, 1–20. doi:10.1016/j.marpetgeo.2016.02.012

Li, C., Guo, P., and Ren, D. (2020). The advent of precision epigenetics for medulloblastoma. *Petroleum Geol. Recovery Effic.* 19 (6), 47–48. doi:10.18632/oncoscience.507

Li, J., Zhang, P., and Zhou, Z. (2023). Quantitative characterization on dynamic methane flow in Chinese marine shales: an experimental study. *Unconv. Resour.* 3, 44–53. doi:10.1016/j.uncres.2022.11.005

Li, S., Liu, G., Jia, R., Jia, F., and Wang, K. (2021). Study on friction effect and damage evolution of end face in uniaxial compression test. *J. Min. Strata Control Eng.* 3 (3), 033014. doi:10.13532/j.jmsce.cn10-1638/td.20210325.001

Liu, Z., Shi, B., Ge, T., Sui, F., Wang, Y., Zhang, P., et al. (2022). Tight sandstone reservoir sensitivity and damage mechanism analysis: A case study from ordos basin, China and implications for reservoir damage prevention. *Energy Geosci.* 3 (4), 394–416. doi:10.1016/j.engeos.2021.05.001

Luan, He., Cao, Y., Jiang, Y., Guan, Y., Li, C., Zhang, S., et al. (2022). Implementation of tension-shear coupling failure mode of rock bolts in FLAC3D and its application. *J. Min. Strata Control Eng.* 4 (6), 063029. doi:10.13532/j.jmsce.cn10-1638/td.20220727.002

Lv, J., Yin, S., Sun, Y., Liu, L., Li, W., Tao, D., et al. (2022a). A new method for predicting injection multiples of extreme displacement in waterflood reservoirs. *Energy Geosci.* 3 (4), 465–472. doi:10.1016/j.engeos.2022.01.002

Lv, X., Fu, M., Zhang, S., Liu, Y., Ding, X., Meng, X., et al. (2022b). The effect of thermal fluid derived from mud diapir on sandstone reservoirs in the Yinggehai Basin, South China Sea. *Energy Geosci.* 3 (4), 473–484. doi:10.1016/j.engeos.2021.10.001

Ma, X., Xie, J., Yong, R., and Zhu, Y. (2020). Geological characteristics and high production control factors of shale gas reservoirs in Silurian Longmaxi Formation, southern Sichuan Basin, SW China. *Petroleum Explor. Dev. Online* 47 (5), 901–915. doi:10.1016/s1876-3804(20)60105-7

Mouchet, J. P., and Mitchell, A. (1989). *Abnormal pressure while drilling*. Paris: Editions Technip, 45–48. doi:10.1016/S0140-6701(97)83234-1

Najibi, A. R., Ghafoori, M., Lashkaripour, G. R., and Asef, M. R. (2017). Reservoir geomechanical modeling: *in-situ* stress, pore pressure, and mud design. *Petrol. Sci. Eng.* 151, 31–39. doi:10.1016/j.petrol.2017.01.045

Nie, H., Chen, Q., Zhang, G., Sun, C., Wang, P., and Lu, Z. (2021). An overview of the characteristic of typical Wufeng–Longmaxi shale gas fields in the Sichuan Basin, China. *Nat. Gas. Ind. B* 8 (3), 217–230. doi:10.1016/j.ngib.2021.04.001

Ostadhassan, M., Zeng, Z., and Zamiran, S. (2012). "Geomechanical modeling of an anisotropic formation-bakken case study," in *46th US rock mechanics/geomechanics symposium* (American Rock Mechanics Association), 1–6. doi:10.1016/j.petrol.2018.02.059

Peng, J., Liu, X., Zhuang, X., Ma, Z., Pan, W., Fan, Z., et al. (2023). Geochemical characteristics and sedimentary environment of source rocks in the qiangtang basin: new discoveries from the upper triassic xiaochaka formation in the woruoshan mountain. *Unconv. Resour.* 3, 103–110. doi:10.1016/j.uncres.2022.12.001

Rajabi, M., Tingay, M., King, R., and Heidbach, O. (2017). Present-day stress orientation in the clarence moreton basin of new south wales, Australia: A new high density dataset reveals local stress rotations. *Basin Res.* 29, 622–640. doi:10.1111/bre.12175

Shen, G., Clemmons, C., and Shen, X. (2015). "Integrated 1-D workflow for pore-pressure prediction and mud-weight window calculation for subsalt well sections," in *The 49th US rock mechanics/geomechanics symposium* (SanFrancisco, California, USA: ARMA).

Shi, M., Liu, Z., Yang, X., Yang, J., Chen, X., Liu, H., et al. (2020). Review and prospect prediction technology for formation pore pressure by geophysical well logging. *Well Logging Technol.* 35 (5), 1845–1853. doi:10.6038/pg2020DD0435

Si, S., He, J., Zhao, Y., Chuang, E., Bai, Y., and Wu, W. (2023). Diagenesis of tight sandstone and its influence on reservoir properties: A case study of fuyu reservoirs in songliao basin, China. *Unconv. Resour.* 3, 84–92. doi:10.1016/j.uncres.2022.12.002

Sun, J. (2017). Mechanics criterion and factors affecting overburden stability in solid dense filling mining. *Int. J. Min. Sci. Technol.* 27 (3), 407–413. doi:10.1016/j.ijmst.2017.03.010

Sun, J., Zhang, Y., Wang, Y., Wu, Y., and Chen, H. (2023). Research progress in Formation Pressure prediction methods based on logging data. *Well Logging Technol.* 47 (2), 119–126. doi:10.16489/j.issn.1004-1338.2023.02.001

Tang, L., Song, Y., Zhao, Z., Jiang, Z., Jiang, S., Chen, X., et al. (2022). Origin and evolution of overpressure in shale gas reservoirs of the upper ordovician wufeng formation–lower silurian Longmaxi Formation in the Sichuan Basin. *Nat. Gas. Ind.* 42 (10), 37–53. doi:10.3787/j.issn.1000-0976.2022.10.004

Thiercelin, M. J., and Plumb, R. A. (1994). Core-based prediction of lithologic stress contrasts in east Texas formations. *SPE Form. Eval.* 9 (4), 251–258. doi:10.2118/21847-pa

Wang, H. (2020). Formation pressure prediction technology of infill point in low permeability oil field. *J. Phys. Conf. Ser.* 1549, 042014. doi:10.1088/1742-6596/1549/4/042014

Wang, K., Zhang, H., and Zhang, R. (2017). Analysis and numerical simulation of tectonic stress field in the dabei gas field, tarim basin. *Aata Geolofica Sin.* 91 (11), 2557–2572. doi:10.13278/j.cnki.jjuese.20210002

Wang, M., Shen, Z., Wan, L. H., Mo, M. M., Wu, Z., Li, L. L., et al. (2020). Effects of a comprehensive reminder system based on the health belief model for patients who have had a stroke on health behaviors, blood pressure, disability, and recurrence from baseline to 6 Months: A randomized controlled trial. *J. Geophys. Res. Solid Earth* 125 (2), 156–164. doi:10.1097/JCN.0000000000000631

Wang, X., Liu, Y. H., and Zhang, M. (2010). Conditions of formation and accumulation for shale gas. *Nat. Gas. Geosci.* 21 (2), 350–356. doi:10.1016/S1876-3804(11)60008-6

Wu, Z., Tang, M., Zuo, Y., Lou, Y., Wang, W., Liu, H., et al. (2021). Acoustic emission-based numerical simulation of tectonic stress field for tectoclase prediction in shale reservoirs of the northern Guizhou area, China. *Energy Geosci.* 3 (4), 436–443. doi:10.1016/j.engeos.2021.10.005

Xing, R., Liu, Y., and Wang, C. (2018). Geostress prediction and comprehensive evaluation based on logging information in coalbed methane block. *Coal Sci. Technol.* 46 (10), 216–221. doi:10.13199/j.cnki.cst.2018.10.034

Xiong, L., Wang, S., and Xu, F. (2016). An approach to locate optic disc in retinal images with pathological changes. *Pet. Drill. Techques* 44 (5), 40–50. doi:10.1016/j.compmedimag.2015.10.003

Xu, J., Chang, X., and Wang, Y. (2015). Sensitivity analysis of the residual depth about the residual velocity in the angle domain. *Chin. J. Geophys.* 58 (8), 2927–2934. doi:10.6038/cjg20150825

Xu, R. (2014). *The analysis of tectonic stress field of lishu fault depression in northeast China*. Xian: Xi'an Shiyou University, 1–6. doi:10.7666/d.Y2619727

Xue, Y., Zhi, H., Zhang, C., Yu, Q., Gao, T., and Zhang, H. (2023). Accurate measurement of dynamic response of Formation Pressure. *Well Logging Technol.* 47 (2), 224–229. doi:10.16489/j.issn.1004-1338.2023.02.015

Yang, J., Luo, M., Zhang, X., Huang, N., and Hou, S. (2021). Mechanical properties and fatigue damage evolution of granite under cyclic loading and unloading conditions. *J. Min. Strata Control Eng.* 3 (3), 033016. doi:10.13532/j.jmsce.cn10-1638/td.20210510.001

Yin, S., Lv, D., and Ding, W. (2018). New method for assessing microfracture stress sensitivity in tight sandstone reservoirs based on acoustic experiments. *Based Acoust. Exp.* 18 (4), 1–10. doi:10.1061/(ASCE)GM.1943-5622.0001100

Zeng, L. B., Lyu, W. Y., Li, J., Guo, Y., Yang, Y., Dong, S., et al. (2019). Variation in the orientation of the maximum horizontal stress in thick channel-fill sandstones with low-permeability: A case of the bonan oilfield in the bohai bay basin, eastern China. *Mar. Petrol. Geol.* 107, 32–40. doi:10.1016/j.marpetgeo.2019.04.041

Zhang, J. C. (2013). Effective stress, porosity, velocity and abnormal pore pressure prediction accounting for compaction disequilibrium and unloading. *Mar. Petroleum Geol.* 45, 2–11. doi:10.1016/j.marpetgeo.2013.04.007

Zhang, S., Wang, L., Yang, H., and Lu, L. (2023). Construction and numerical simulation research of functional supporting in deep roadways. *J. Min. Strata Control Eng.* 5 (1), 013012. doi:10.13532/j.jmsce.cn10-1638/td.20230201.001

Zheng, W., Zhang, P., and Yuan, D. (2019). Basic Characteristics of active tectonics and associated geodynamic processes in continental China. *J. Geomechanics* 25 (5), 699–721. doi:10.12090/j.issn.1006-6616.2019.25.05.062

Zhou, L., Zhang, D., Sun, J., Gu, Y., Zhang, C., and Zhang, C. (2022). Status-quo of proved oil/gas initially-in-place in China as of 2020 and its variation trend in the past decade. *Energy Geosci.* 3 (4), 343–348. doi:10.1016/j.engeos.2022.05.001

Zou, X., and Chen, Y. (2018). Geostress logging evaluation method of Longmaxi Formation shale in Fuling area based on transversely isotropic model, Sichuan Basin. *Nat. Gas. Geosci.* 29 (12), 1775–1780. doi:10.11764/j.issn.1672-1926.2018.10.017

frontiers | Frontiers in Earth Science

TYPE Original Research
PUBLISHED 16 October 2023
DOI 10.3389/feart.2023.1277359

Geochemical characteristics and sedimentary environment of black mudstone in the early Carboniferous Dawuba Formation in the Middle and Upper Yangtze region

Haiquan Zhang[1,2], Qian Zhang[1,2]*, Yexin Zhou[1,2], Baofeng Lan[3], Xintao Feng[1,2], Yi Chen[4], Qian Yu[1,2], Jinxiang Cheng[1,2], Yupeng Men[1,2] and Ankun Zhao[1,2]

[1]Chengdu Center of China Geological Survey (Geosciences Innovation Center of Southwest China), Chengdu, China, [2]Key Laboratory of Sedimentary Basin and Oil and Gas Resources, Ministry of Natural Resources, Chengdu, China, [3]Guizhou Energy Industry Research Institute Co., Ltd., Guiyang, China, [4]Guizhou Research Institute of Petroleum Exploration and Development, Guiyang, China

OPEN ACCESS

EDITED BY
Hu Li,
Southwest Petroleum University, China

REVIEWED BY
Yifan Gu,
Southwest Petroleum University, China
Meng Wang,
Chongqing University of Science and Technology, China

*CORRESPONDENCE
Qian Zhang,
✉ amazing20222022@126.com

RECEIVED 14 August 2023
ACCEPTED 02 October 2023
PUBLISHED 16 October 2023

CITATION
Zhang H, Zhang Q, Zhou Y, Lan B, Feng X, Chen Y, Yu Q, Cheng J, Men Y and Zhao A (2023), Geochemical characteristics and sedimentary environment of black mudstone in the early Carboniferous Dawuba Formation in the Middle and Upper Yangtze region.
Front. Earth Sci. 11:1277359.
doi: 10.3389/feart.2023.1277359

To further study the sedimentary environment of the black mudstone in the early Carboniferous Dawuba Formation in the Middle and Upper Yangtze regions and support regional shale gas exploration and related research, the major and trace elements of the Dawuba Formation in Well CY1, located in deep water shelf facies, were tested and analyzed. The results show that the study area contains mainly continental margin deposits affected by hydrothermal deposition, and they are rich in organic matter and have high primary productivity. The parent rocks are mainly acidic rocks, such as felsic igneous rocks, granites and some sedimentary rocks. And the provenance is mainly provided by acidic igneous rocks of the Jiangnan Paleouplift. An ICV<1 and high CIA and Th/U values indicate a warm and humid climate and under stong chemical weathering conditions. The values of V/(V+Ni), Cu/Zn and Ce/La suggest that organic-rich intervals of the Dawuba Formation accumulated under predominantly dysoxic conditions. The warm and humid climate is conducive to the flourishing of micropaleontology, and the high primary paleoproductivity and weakly reducing environment are conducive to the formation of organic-rich shale, forming high-quality reservoir source rock in the Dawuba Formation.

KEYWORDS

Dawuba Formation, element geochemistry, provenance, tectonic setting, sedimentary environment

Introduction

Natural gas resources account for a relatively large proportion of the energy structure of China, affecting the development and security of the country in key areas of economy, politics, security, etc (Guo et al., 2023; Zhang J. et al., 2023). With the vigorous development of unconventional petroleum in China, the exploration and development of shale gas in lower Paleozoic state in the Sichuan Basin has achieved remarkable results (Zhang et al., 2022; Zou et al., 2023). To further expand the resource potential, it is imperative to evaluate the shale gas resource potential of new strata in the new area of the Middle and Upper Yangtze region (Gu et al., 2022a; Gu et al., 2022b; Qiu et al., 2022; Zhang Q. et al., 2023). A set of organic-rich black shales that developed in the lower Carboniferous Dawuba Formation in southern Guizhou Province is a shelf–platform basin facies deposit with a large thickness and wide distribution (Zhang et al., 2016; Liang et al., 2022; Feng et al., 2023). Previous studies have been conducted on the reservoir characteristics of black shale in the Dawuba Formation, but the detailed geochemical characteristics and depositional environment of this black shale are relatively unknown (Qie et al., 2015; Yang et al., 2022). Therefore, in order to gain a deeper understanding of the sedimentary environment and tectonic pattern of the early Carboniferous Epoch and to select the favorable area of shale gas, this paper selects the mudstone core of Well CY1 in Changshun Sag, which is relatively developed in the deepwater facies area, for systematic petrological, mineralogical and geochemical analysis, and studies the sedimentary environment of black mudstone formation of Dawuba Formation in detail, which is of great significance for further understanding and evaluating the shale gas exploration potential in this area.

Geological setting

The Carboniferous Dawuba Formation is mainly distributed in the Liupanshui–Ziyun–Luodian area of the southern Guizhou Depression, and in the study area, the Changshun Sag is located in the northeasteran of Ziyun area, which is mainly controlled by the Anshun–Guiyang fault and the Ziyun–Liupanshui fault (Ding et al., 2019; Liang et al., 2022) (Figure 1A). The main tectonic location is the southwest Yangtze passive continental margin, which has experienced multiple tectonic movements (Qie et al., 2015). Due to the continuous uplift of the central Guizhou uplift and Jiangnan uplift in the end of the Caledonian, the whole study area was a

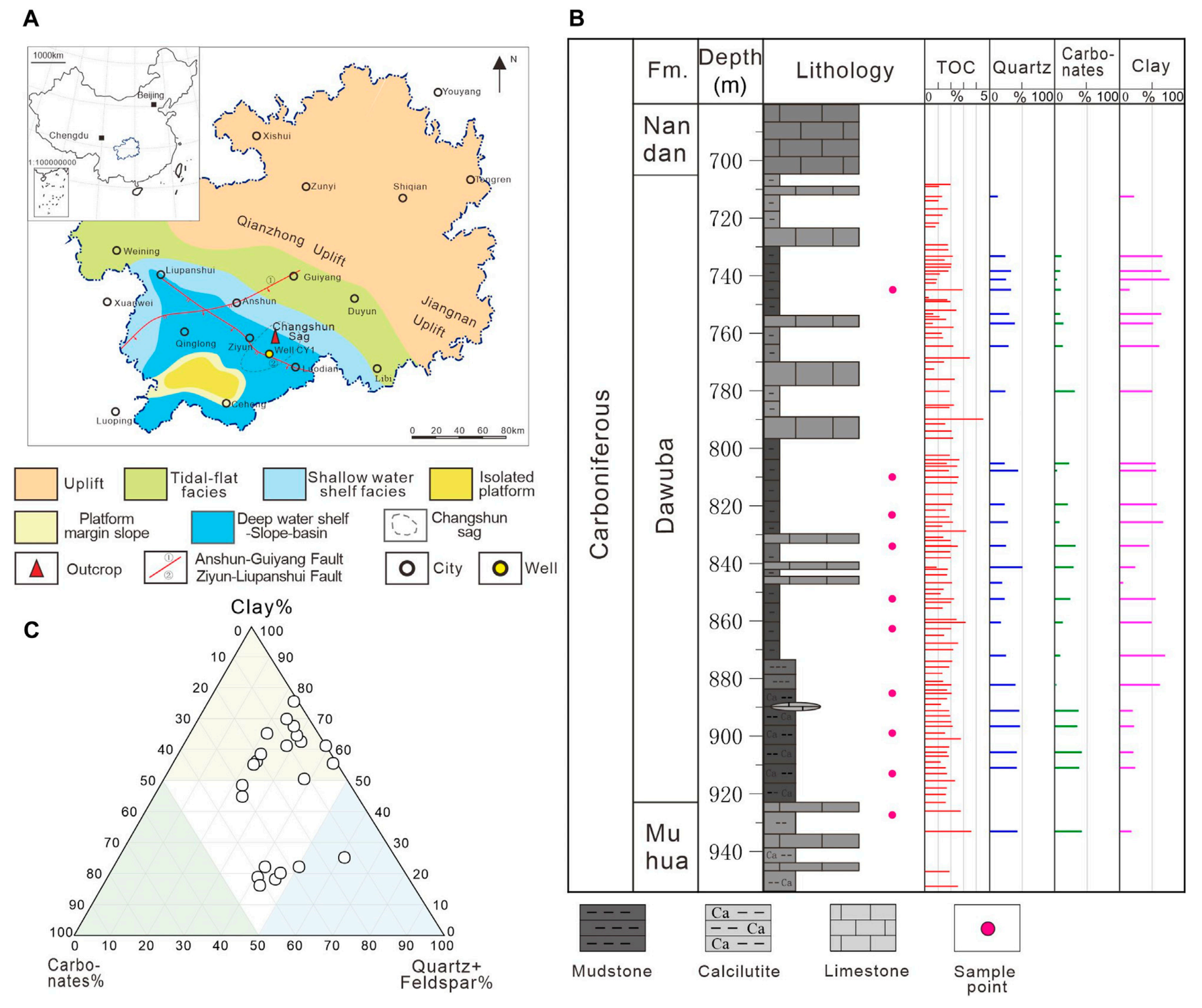

FIGURE 1
(A) Diagram of the sedimentary facies of the Dawuba Formation in Guizhou Province. (B) Stratigraphic column of the Well CY1 and the sampling location. (C) Ternary diagram of the mineral composition of the Dawuba Formation black mudstone.

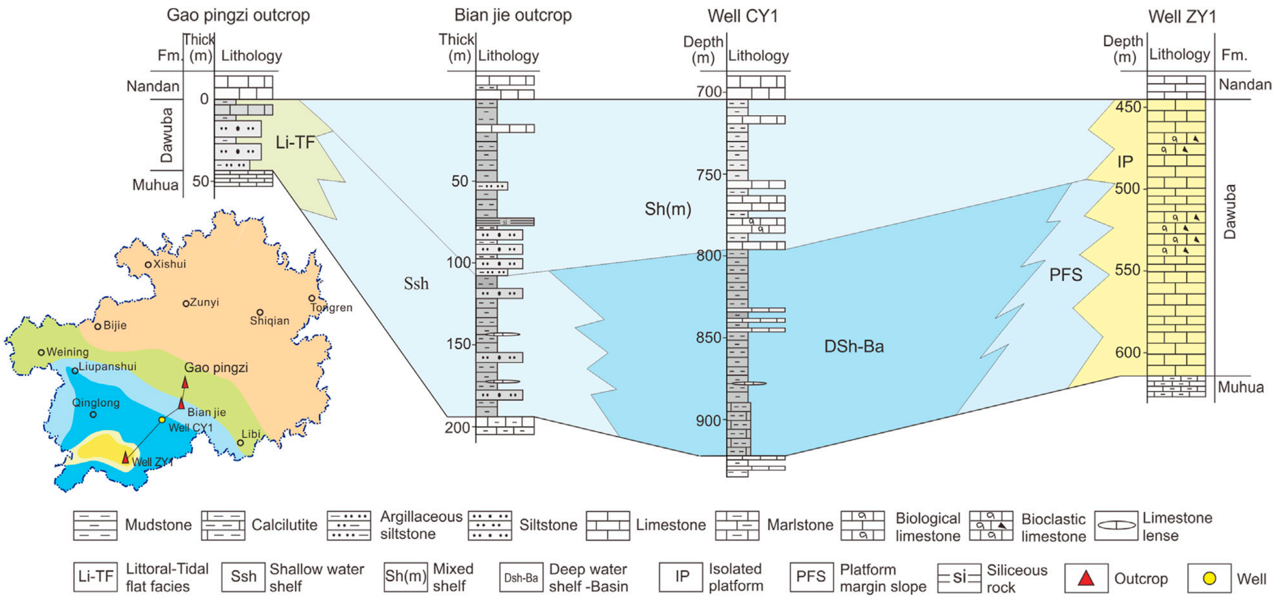

FIGURE 2
Stratigraphic correlation map of Dawuba Formation in Guizhou Province.

shallow sea environment (Fuquan, 1989; Chen et al., 2019; Yuan et al., 2019). During the Hercynian stage, the continuous expansion of the paleo-uplift and strong tectonic movement resulted in the formation of a NW-trending fault trough on the west side of the Ziyun–Liupanshui syndepositional fault through the action of strong tensile stress (Fuquan, 1989). The Late Devonian marine regression event made a carbonate platform deposition in the study area. In the Early Carboniferous period, sea transgression from the southeast direction, and the study area was transformed into shelf deposition, and gradually developed into carbonate platform facies in the late Carboniferous. Therefore, the Dawuba Formation was deposited in the inner depression of the platform and was controlled by a series of isolated carbonate platforms (Chen et al., 2018; Chen et al., 2019) (Figure 1A). The whole distribution was along the Ziyun–Liupanshui rifting trough, and the water gradually deepened from both sides of the rifting trough to the interior. From the tide flat to shelf facies (platform basin) transition, in the Zhenfeng area to the south of the Ziyun–Liupanshui fault, isolated platform deposition is developed, which makes the Dawuba Formation have a “platform-basin” facies sedimentary feature (Chen et al., 2019; Mei et al., 2021) (Figure 2). During the depositional period of the Dawuba Formation in the Changshun Sag, the water was deep and the resulting sedimentary rocks consisted of mainly mudstone initially, later incorporating limestone, indicating a gradually shallowing sedimentary sequence (Zhang et al., 2017).

In this study, the mudstone of the Well CY1, located in the favorable shale gas formation facies–deep water shelf facies area, was selected to explore the sedimentary environment of the source rock formation. Well CY1 is located in the northern part of the Changshun Sag, far from the terrigenous detrital source area, and it is part of the seaward slope zone of the carbonate platform (Figure 1A). The true thickness of the well’s Dawuba Formation is 209.03 m, and it is in conforma-ble contact with the underlying Carboniferous Muhua Formation and the overlying Carboniferous Nandan Formation (Figures 1B, C). The lower part mainly consists of black carbonaceous mudstone and carbonaceous silty mudstone (Figure 3). These are part of the deepwater shelf-slope facies (Figure 2) and contain a few visible fossils (Figure 3B). The rocks are rich in organic matter with developed cracks (Figures 3C, D). The upper part is mainly gray argillaceous limestone with black mudstone (Figure 2), featuring fossils and bio-turbation structures (Figure 3E); it is a shallowing-upward sedimentary sequence, whose sedimentary environment changed from a deepwater shelf environment to a shallow-water shelf–platform slope (Figure 2). The black mudstone in the lower part of the Dawuba Formation is rich in organic matter, has a high total organic carbon content (the TOC mean value is 1.81%) (Figure 3C), has clay minerals and microfracture development (Figure 3D), and has great hydrocarbon generation potential, making it a favorable gas source rock and reservoir for shale gas exploration (Zhang et al., 2017).

Samples and methods

A total of 106 samples from the Well CY1 were selected for TOC analysis, 25 samples were selected for mineral composition testing, and 10 samples were collected from bottom to top for major and trace element analysis. The specific sampling locations and numbering are shown in Figure 1B. All tests were completed in the laboratory of the Chengdu Geological Survey Center. Prior to the analysis and test, fresh samples were ground to particle sizes of less than 0.2 mm under pollution-free conditions for TOC content analysis. The samples were ground to 200 mesh for major and trace element analysis. The major elements were detected by a Panaco Axios mAx PW4400/40 X-ray fluorescence spectrometer (Netherlands), and the analytical error was less than 1%. The

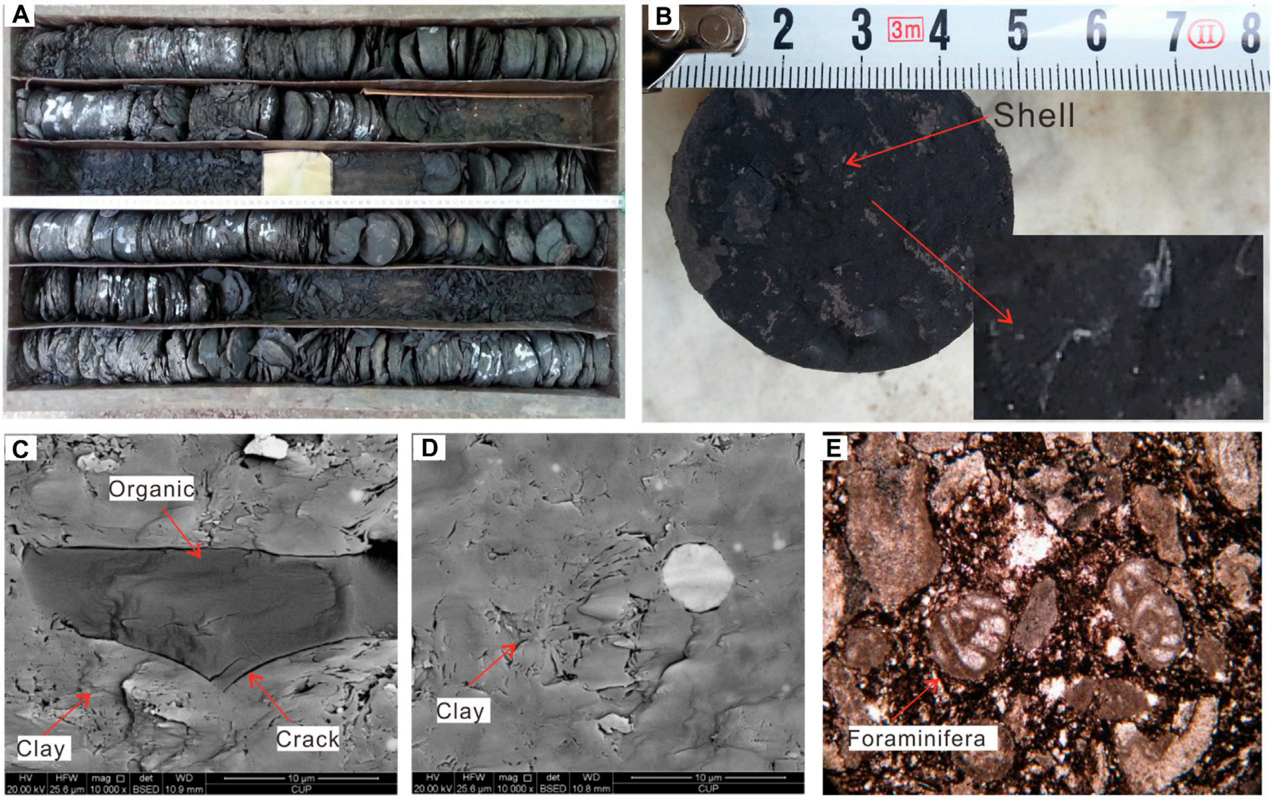

FIGURE 3
Lithologic characteristics of the Well CY1. **(A)** Black mudstone core in the lower part of the Dawuba Formation. **(B)** shell in the lower part of the Dawuba Formation. **(C)** organic matter and fracture in mudstone in the Dawuba Formation (SEM). **(D)** fractures of clay minerals in mudstone in the Dawuba Formation (SEM). **(E)** Foraminifera in the argillaceous limestone of the upper part of the Dawuba Formation.

analytical error of trace and rare earth elements was less than 5% according to the X-series II inductively coupled plasma mass spectrometer (ICP–MS; ThermoFisher, United States). A ZJ207 Bruker D8 Advance X-ray diffractometer was used for X-ray diffraction analysis. Ni-filtering Cu target radiation was adopted. The working voltage was 40 kV, the working current was 40 mA, the emission slit and scattering slit were both 1°, and the receiving slit was 0.3 mm. The measurement criteria followed SY/T5163-2010, and High Score software was used for data analysis.

Analytical results

Petrological characteristics

Analysis of 106 black mudstone samples revealed a high total organic carbon (TOC) content in the Dawuba Formation, ranging from 0.78% to 4.51%, with an average of 1.81%. There are 98 organic-rich shale samples (TOC>1%), representing 92.45% of all samples (Figure 1B). A higher TOC content indicates higher paleoproductivity in the study area. The quantitative analytical results of X-ray diffraction show that the rocks are mainly composed of clay minerals, quartz and carbonate minerals, and clay minerals contents of 3%–76% and an average content of 43.44% (Table 1; Figure 1B). The quartz contents are 15%–45%, with an average of 26.08%. Carbonate minerals have low calcite content ranging from 1% to 74% with an average of 19.08%, and low dolomite content ranging from 1% to 37% with an average of 4.92%. The content of feldspar is low, and the feldspars are mainly plagioclase, with an average content of 3.28%. The pyrite content averages 2.2% and can be observed in most rocks. The clay minerals are mainly illite/smectite (average 80.79%) with small amounts of illite (average 11.63%), chlorite (average 4.91%) and kaolinite (average 4.11%) (Table 1; Figures 3C, D). According to the shale lithofacies division (Figure 1C), most of the sample points of Well CY1 plot in the clay lithofacies area and mixed shale facies. A high content of clay minerals is conducive to the adsorption of organic matter and the formation of organic-rich shale (Figures 3C, D). At the same time, it is conducive to the formation of micropores, thereby improving the adsorption capacity of shale gas and forming high-quality reservoirs (Zhang et al., 2022; Nie et al., 2023; Zhao et al., 2023).

Major and trace element characteristics

The results of the major elements and related parameters in the Dawuba For-mation of Well CY1 are shown in Table 2 and Table 3. Compared with the Upper Continental Crust (UCC) values (Taylor and Mclennan, 1985), Al_2O_3, Fe_2O_3 and TiO_2 are slightly enriched,

TABLE 1 Mineral composition (%) and clay mineral composition (%) of the Well CY1 well.

Sample	Mineral composition (%)							Clay mineral composition (%)			
	Clay	Quartz	Plagioclase	Calcite	Dolomite	Quartz + feldspar	Carbonate< minerals	K	C	I	I/S
C1	20	5	5	33	37	10	70		14	22	64
C2	65	22	0	7	1	22	8		4	14	82
C3	63	29	0	6	0	31	6		6	12	82
C4	76	23	0	1	0	23	1	4	6	13	77
C5	13	24	7	0	7	31	7		10	15	75
C6	63	18	10	6	0	28	6		8	14	78
C7	50	32	5	8	3	37	11	3	9	11	77
C8	60	11	16	10	0	27	10		8	12	80
C9	49	19	3	20	9	22	29	1	6	14	79
C10	54	21	0	9	11	21	20		6	16	78
C11	55	42	0	1	0	42	1	3	2	12	83
C12	56	21	0	8	10	21	18	7	3	12	78
C13	66	25	0	2	3	26	5	1	1	10	88
C14	44	23	0	15	15	23	30	4	2	8	86
C15	22	13	36	27	0	49	27	2	1	10	87
C16	3	17	0	74	5	17	79	2	1	10	87
C17	54	21	0	19	3	21	22	4		10	86
C18	48	15	0	5	5	15	10	2		9	89
C19	69	23	0	3	3	23	6	2	1	9	88
C20	61	38	0	0	0	38	0	7	5	9	79
C21	18	44	0	34	1	44	35	9	7	12	72
C22	20	45	0	28	5	45	33	7	7	11	75
C23	19	40	0	39	1	40	40	7	6	10	77
C24	22	40	0	35	1	40	36	5	5	12	78
C25	16	41	0	37	3	41	40	4	4	14	78
Average	43.4	26.1	3.3	17.1	4.9	29.5	22.0	4.1	5.3	12.0	80.1

K-Kaolinite, C-Chlorite, I-Illite, I/S-llite/smectite formation.

and the other major ele-ments are slightly depleted. The enrichment of Al_2O_3 and TiO_2 indicates that there was a continuous and stable input of terrigenous debris in the Dawuba Formation during the depositional period (Zhang J. et al., 2023). The loss on ignition (LOI) was high, with a mean value of 10.77%, which was related to the abundance of organic matter in the sample (Zhang Q. et al., 2023).

The element enrichment factor (EF) = [(i/Al) sample/(i/Al) UCC] (Taylor and Mclennan, 1985; Condie, 1993; Mclennan, 2013), which is used to describe the enrichment of various trace elements in black shale, is defined as the ratio of the molar concentration of elements in the sample to the average molar concentration of the elements in the corresponding UCC (Taylor and Mclennan, 1985). Compared with the UCC, the trace elements of the Dawuba Formation in the study area are weakly enriched or not depleted except for Rb, Zr and Mo (Table 3). The enrichment of U, V, Ni, Cr, Cu, Zn may be related to hydrothermal activities or reductive sedimentary environment (Condie, 1993; Mclennan, 2013). Cu, Zn and Ni are all nutrient elements, and their enrichment indicates high paleoproductivity in this area (Steiner et al., 2001). The enrichment of Cr may be related to the influence of mantle material, it is suggested that mantle material may be involved in the diagenetic process of black rock series (Eker et al., 2012; Zhang et al., 2022). The lower abundance of redox-sensitive metals, such as Ni, V, and U,

TABLE 2 TOC and major element (10^{-2}) abundances and some associated parameters of mudstone from Well CY1.

Sample	TOC	SiO_2	Al_2O_3	Fe_2O_3	CaO	MgO	K_2O	Na_2O	TiO_2	P_2O_5	MnO	LOI	FeO	F1	F2	ICV	CIA
Y1	2.73	49.68	18.36	5.79	6.42	0.82	2.60	1.05	0.76	0.04	0.01	13.39	0.07	−1.69	1.53	0.71	75
Y2	1.65	51.64	18.71	6.06	5.67	1.57	2.36	0.79	0.86	0.06	0.03	12.44	1.47	−1.37	1.19	0.70	78
Y3	1.49	57.62	20.70	5.55	1.29	1.06	2.23	0.58	0.99	0.09	0.03	10.10	1.85	−2.26	1.80	0.51	83
Y4	2.01	55.45	23.76	4.68	0.46	1.07	3.07	0.74	1.02	0.12	0.01	9.65	0.73	−2.31	2.08	0.49	82
Y5	1.98	56.03	23.06	4.79	0.57	1.16	2.82	0.68	1.02	0.14	0.01	9.73	0.96	−2.11	2.52	0.50	83
Y6	2.20	66.04	15.07	4.37	2.10	0.80	2.12	0.69	0.73	0.08	0.02	8.70	0.14	−2.86	2.12	0.68	77
Y7	2.50	56.88	17.51	4.51	3.44	1.14	2.32	1.00	0.80	0.06	0.01	11.70	0.29	−2.08	3.09	0.71	75
Y8	3.16	56.51	18.11	7.30	1.62	1.03	2.05	0.83	0.89	0.11	0.03	11.05	0.99	−2.65	3.40	0.70	79
Y9	2.55	46.20	18.99	11.01	2.02	0.82	2.07	0.82	0.78	1.04	0.02	13.41	0.26	3.62	11.87	0.78	80
Y10	2.87	55.61	22.43	7.26	0.36	2.40	3.30	0.79	1.06	0.11	0.01	7.51	2.79	−1.89	0.08	0.69	81
average	2.31	55.17	19.67	6.13	2.40	1.19	2.49	0.80	0.89	0.19	0.02	10.768	0.95	−1.56	2.97	0.65	79
PAAS		62.80	18.90	7.18	2.19	1.29	1.19	3.68	0.99	0.16	0.11						
average/ PAAS		0.88	1.04	0.85	1.09	0.92	2.10	0.22	0.90	1.16	0.15						

TOC, total organic carbon content; F1 and F2 are discriminant functions. ICV: The index of compositional variation. CIA: The chemical alteration index. PAAS values from (Taylor and Mclennan, 1985).

TABLE 3 Trace element (10^{-6}) abundances and some associated parameters of mudstone from Well CY1.

Sample	Cu	Pb	Zn	Cr	Ni	Co	Rb	Mo	Sr	V	Nb	Zr	U	Th	V/(V+Ni)	Cu/Zn	Th/U
Y1	27.6	32.4	115	117	43.7	13.9	84.9	1.2	594	151.0	22.4	124	4.4	22.9	0.78	0.24	5.23
Y2	30.4	31.0	120	102	53.1	14.9	73.3	0.5	489	118.0	24.3	124	4.5	23.9	0.69	0.25	5.34
Y3	33.9	32.1	134	110	67.8	18.4	69.4	0.6	310	113.2	27.4	133	5.6	29.4	0.63	0.25	5.25
Y4	30.5	39.6	111	128	57.8	24.2	96.9	0.4	418	136.9	28.8	112	4.7	30.4	0.70	0.28	6.48
Y5	34.3	26.5	122	122	50.0	16.0	92.0	0.5	390	124.0	28.0	118	5.0	31.8	0.71	0.28	6.42
Y6	22.4	27.8	70	83	34.0	12.3	68.1	0.4	351	127.7	20.0	106	3.9	21.8	0.79	0.32	5.58
Y7	24.9	26.4	89	97	44.5	13.8	80.5	1.7	473	108.7	22.6	92	4.6	24.7	0.71	0.28	5.32
Y8	25.0	31.6	72	97	44.0	17.1	73.2	0.4	386	95.9	25.1	106	3.7	26.2	0.69	0.35	7.05
Y9	35.9	47.6	91	115	86.1	27.3	75.3	1.1	462	131.8	23.2	108	5.1	26.2	0.60	0.39	5.16
Y10	22.1	37.5	144	133	54.5	17.0	99.8	0.6	497	145.1	28.7	118	4.9	30.3	0.73	0.15	6.14
Average	28.7	33.3	107	110	53.6	17.5	81.3	0.7	437	125.2	25.0	114	4.6	26.8	0.70	0.28	5.80
UCC	25.0	20.0	71.0	35	20.0	10.0	112.0	1.5	350	60.0	19.0	190	2.8	10.7			
EF average	0.9	1.3	1.2	2.4	2.1	1.3	0.6	0.4	1.0	1.6	1.3	0.5	1.3	1.9			

UCC values from (Taylor and Mclennan, 1985).

suggests that the sedimentary water during the Longmaxi Stage had low reducing conditions (Zhang et al., 2022).

Rare earth element characteristics

The total amount of rare earth elements (ΣREEs) in the black mud of the Well CY1 well ranging from 213.08×10^{-6} to 308.1×10^{-6}, with an average value of 255.6×10^{-6} (Table 4), and the ratio of light to heavy rare earth elements (ΣLREE/ΣHREE) ranges from 4.63 to 12.90, with an average value of 10.05. The light REEs are considerably enriched relative to the heavy REEs. Moreover, the weak negative Eu anomaly (δEu ranging from 0.75 to 0.97 with average 0.84) and negligible δCe=0.72–1.11), negative Ce anomaly (δCes fluctuates from 0.72 to 1.11 with average 0.92), indicating a dysoxic or weak oxidation continental margin environment (Murray, 1994). The La_N/Yb_N values range from 0.91 to 1.62, with an average of 1.31 (Table 4). Most of the samlpes

TABLE 4 Rare earth element (10^{-6}) abundances and some associated parameters of Well CY1 black mudstone.

Sample	La	Ce	Pr	Nd	Sm	Eu	Gd	Tb	Dy	Ho	Er	Tm	Yb	Lu	ΣREE	LREE/HREE	La_N/Yb_N	$δEu_N$	$δCe_N$	$δEu_S$	$δCe_S$	Ce/La
Y1	51.0	93.7	10.8	36.6	5.46	0.87	4.70	0.54	3.25	0.66	2.48	0.37	2.97	0.41	214	12.9	1.62	0.51	0.93	0.80	0.92	1.84
Y2	55.0	107.0	11.6	39.3	6.20	1.08	5.47	0.70	4.41	0.87	3.09	0.45	3.62	0.50	239	11.5	1.43	0.55	0.99	0.86	0.97	1.94
Y3	62.1	119.6	13.9	48.8	8.67	1.52	7.24	0.93	5.55	1.03	3.51	0.50	4.08	0.56	278	10.9	1.43	0.57	0.96	0.89	0.94	1.93
Y4	54.5	117.9	12.4	42.7	7.21	1.33	6.10	0.78	5.05	0.98	3.53	0.52	4.23	0.59	258	10.8	1.21	0.60	1.07	0.94	1.04	2.16
Y5	64.0	113.0	14.0	48.2	8.22	1.49	7.14	0.92	5.74	1.08	3.72	0.54	4.32	0.60	273	10.3	1.40	0.58	0.88	0.91	0.87	1.77
Y6	46.5	95.1	10.4	36.1	6.29	1.03	5.31	0.68	4.19	0.79	2.72	0.39	3.13	0.43	213	11.1	1.40	0.53	1.02	0.83	0.99	2.05
Y7	51.8	105.6	11.6	40.2	6.88	1.15	5.86	0.78	4.98	0.96	3.22	0.47	3.68	0.50	238	10.6	1.33	0.54	1.01	0.84	0.99	2.04
Y8	52.5	110.6	11.6	39.5	6.71	1.26	6.05	0.80	4.80	0.90	3.11	0.46	3.74	0.53	242	10.9	1.32	0.59	1.05	0.92	1.03	2.11
Y9	56.6	99.4	15.8	62.8	15.40	3.45	15.93	2.99	18.30	2.78	7.21	0.83	5.89	0.75	308	4.6	0.91	0.67	0.80	1.02	0.76	1.75
Y10	49.6	120.4	11.4	38.3	6.56	1.13	6.05	0.87	5.97	1.15	3.88	0.58	4.57	0.63	251	9.6	1.02	0.54	1.20	0.84	1.17	2.43
Average	54.4	108.2	12.3	43.3	7.76	1.43	6.99	1.00	6.22	1.12	3.65	0.51	4.02	0.55	251	10.3	1.31	0.57	0.99	0.84	0.92	2.00

LREE/HREE = (La + Ce + Pr + Nd + Sm + Eu)/(Gd + Tb + Dy + Ho + Er + Tm + Yb + Lu), δCe = CeN/(LaN × PrN)1/2, δEu (δEu = EuN/) SmN × GdN)1/2), N is chondrite standardization(Taylor and Mclennan, 1985). S is North American shale standardization (Taylor and Mclennan, 1985).

distributed in the continental margin (La_N/Yb_N ranging from 1.49 to 1.74) (Bhatia, 1985), while a few plot between the continental margin and the deep-sea basin (La_N/Yb_N values were 0.70) (Bhatia, 1985; Liang et al., 2022), indicating that the sedimentary period may have been influenced by pelagic and deep-sea sediments (Liang et al., 2022). The standard curve of chondrite of REE is L-shaped with right-leaning (Figure 4A), reveals a deficit of light rare earth enriched the heavy one, which is basically consistent with the REEs composition characteristics of the average UCC and PAAS and consistent with the deposition characteristics of crust source material (Gromet et al., 1984; Taylor and Mclennan, 1985). In the NASC-normalized diagram (Figure 4B), most samples are distributed almost horizontally, and the composition characteristics of REEs are similar to NASC, indicating that most sediment source rocks in the study area are mainly from the continental upper crust. The REE distribution model in the study area is not quite consistent (Figure 4) (Gromet et al., 1984), which indicates an unstable sedimentary basin with intense tectonic movement during the Dawuba period.

Discussion

Rock source and origin

In marine sediments, the formation of black shale is a complex process, which is the result of the combined effects of terrigenous debris, hydrothermal sedimentation, biochemical processes, and other factors. The elements in rocks generally come from terrigenous detritus and the authigenic part of minerals, and the input of terrigenous detritus is a key factors affecting the mineral composition of black shale (Guo et al., 2023). Because the contents of $A1_2O_3$ and TiO_2 are mainly related to the input of terrigenous materials, they are relatively stable and rarely affected by diagenesis and later geological processes (Roser and Korsch, 1986). Therefore, the positive correlation between Al_2O_3 and TiO_2, while the negative correlation between $SiO_2/A1_2O_3$ and $A1_2O_3$ are indicate continuous input of terrigenous materials in the deposition process of the source region (Roser and Korsch, 1986). The black mudstone of Well CY1 shows this positive correlation (Figures 5A, B), which indicates that there is a high proportion of terrigenous material continuously input during the deposition of the Dawuba Formation. Meanwhile, Th, Nb, Ta, Zr, Rb and other incompatible elements are commonly from terrestrial sources (Cox et al., 1995). Figures 5C, D shows that Th, Nb and Al_2O_3 have a good positive correlation, indicating that the terrestrial source area of Nb and Th is relatively uniform, indicating that the terrestrial input background in the study area is relatively simple.

Black shale formation is influenced by various factors. It is usually accompanied by oceanic anoxic events and the enrichment and mass extinction, and most of it is closely related to hydrothermal sediments (Qiu et al., 2022; Zhang et al., 2022; Zou et al., 2023). Hydrothermal activities will affect the content of some elements in sediments, especially trace elements. In general, submarine hydrothermal fluids are characterized by high contents of Cu, Pb, Zn, Ni, V, Cr and other elements (Li et al., 2017; Wang et al., 2018). The studied samples show slightly enriched elements, suggesting deep source material additions. Nagarajan et al. (2014) based on

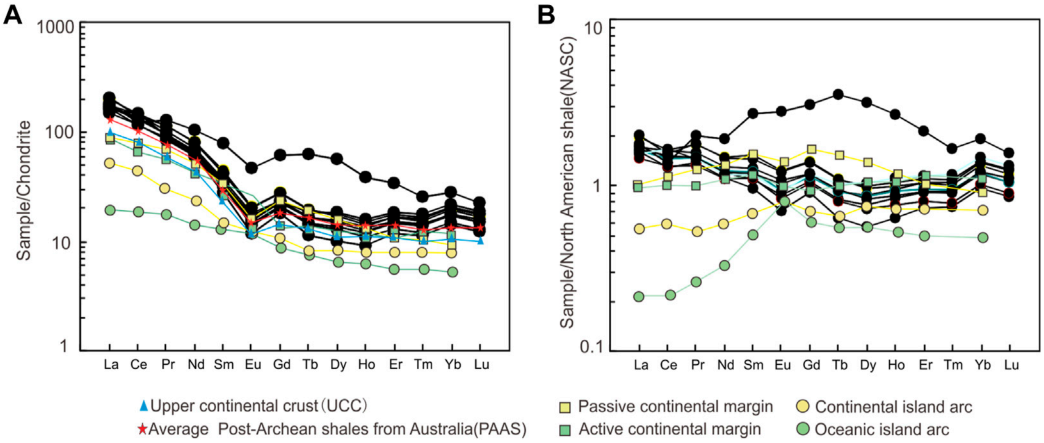

FIGURE 4
Chondrite-normalized **(A)** and NASC-normalized **(B)** REE patterns of black mudstone Well CY1. Map data from (Bhatia, 1985; Taylor and Mclennan, 1985).

geochemistry of manganese deposits in the northeastern waters of Hokkaido, Japan believe that Co deposition is mainly related to hydrogenesis, while Ni and Zn are hydrothermal. Therefore, the discrimination diagram of these elements can be used to successfully distinguish hydrothermal deposition from non-hydrothermal deposition. It can be seen from the (Cu+Co+Ni)–Fe–Mn triangle diagram and Zn–Ni–Co triangle discrimination diagram (Rona, 1978; Rona et al., 1983; Adachi et al., 1986) (Figure 6) that most of the samples fall in the hydrothermal deposition area, indicating strong submarine hydrothermal deposition. Based on the above findings, it is suggested that hydrothermal deposition partly influenced the black shale of the Dawuba Formation in the study area during the tension environment of that period. Intense pressure created a faulted basin, where hydrothermal upwelling delivered nutrient-rich matter and formed the Dawuba Formation's organic mudstone. However, relatively low concentrations of probably hydrothermal components in the studied rocks reflect that hydrothermal activity in the basin was not very high.

Provenance attribute and depositional tectonic background

The geochemical characteristics of detrital rocks in sedimentary rocks can effectively reflect the provenance characteristics. The relevant diagrams and ratios of major elements such as SiO_2, TiO_2, K_2O, and Al_2O_3 and REEs such as La, Yb and REEs with low migration ability can be used as indicators determining provenance attribute of fine clastic rocks (Roser and Korsch, 1986; Cox et al., 1995). In the SiO_2–TiO_2 diagram (Figure 7A) (Roser and Korsch, 1986), most of the samples are mainly distributed in the igneous rock area, and one plot into the sedimentary rock area, indicating that the source rock has both igneous rock and sedimentary rock contributions. In the ΣREE–La/Yb diagram (Figure 7B) (Bhatia, 1985), the samples all plot in the intersection area of sedimentary rocks and granite. Combined with Figure 4A, the source rocks are mainly acidic rocks, such as felsic igneous rocks, granites and some sedimentary rocks. This is consistent with the intermediate-felsic rocks (e.g., the Caledonian and Hercynian diorite, granodiorite, plagiogranite) from the Jiangnan uplift in the northeastern margin of the study area.

Previous studies indicate that sedimentary rock geochemistry can differentiate various tectonic settings. Roser and Korsch, (1988) established two discriminant functions, F1 and F2, according to the properties and characteristics of the main element oxides in sediments. The F1–F2 diagram can effectively distinguish the tectonic setting of the ancient sedimentary basin. The formulas are:

$$\begin{aligned} F1 = {} & -0.044 \times SiO_2 - 0.0972 \times TiO_2 + 0.008 \times Al_2\,O_3 \\ & - 0.267 \times Fe_2\,O_3 + 0.208 \times FeO - 3.082 \times MnO \\ & + 0.14 \times MgO + 0.195 \times CaO + 0.719 \times Na_2\,O \\ & - 0.032 \times K_2\,O + 7.51 \times P_2\,O_5 + 0.303; \end{aligned}$$

$$\begin{aligned} F2 = {} & -0.421 \times SiO_2 + 1.988 \times TiO_2 - 0.526 \times Al_2\,O_3 \\ & - 0.551 \times Fe_2\,O_3 - 1.61 \times FeO + 2.72 \times MnO \\ & + 0.881 \times MgO - 0.907 \times CaO - 0.177 \times Na_2\,O \\ & - 1.84 \times k_2\,O + 7.244 \times P_2\,O_5 + 43.57 \end{aligned}$$

In the F1–F2 diagrams (Figure 8), the sample points in the study area mainly fall in the passive continental margin area, indicating that the sedimentary tectonic background of the study area is passive continental margin.

The distribution patterns of REEs are widely applied to identify modern and ancient sediments from different tectonic settings (Bhatia, 1985; Eker et al., 2012). In general, sediments at passive continental margins are characterized by light REE enrichment and negative Eu anomalies. In contrast, the parent rocks of the sediments on the active continental margin are mainly volcanic rocks with low differentiation, which are characterized by heavy REE enrichment and no negative Eu anomaly (Zhang et al., 2018). The light REEs are considerably enriched in shale samples in this area, and the ratio of light to heavy REEs (ΣLREE/ΣHREE) is 10.05. It show a weak

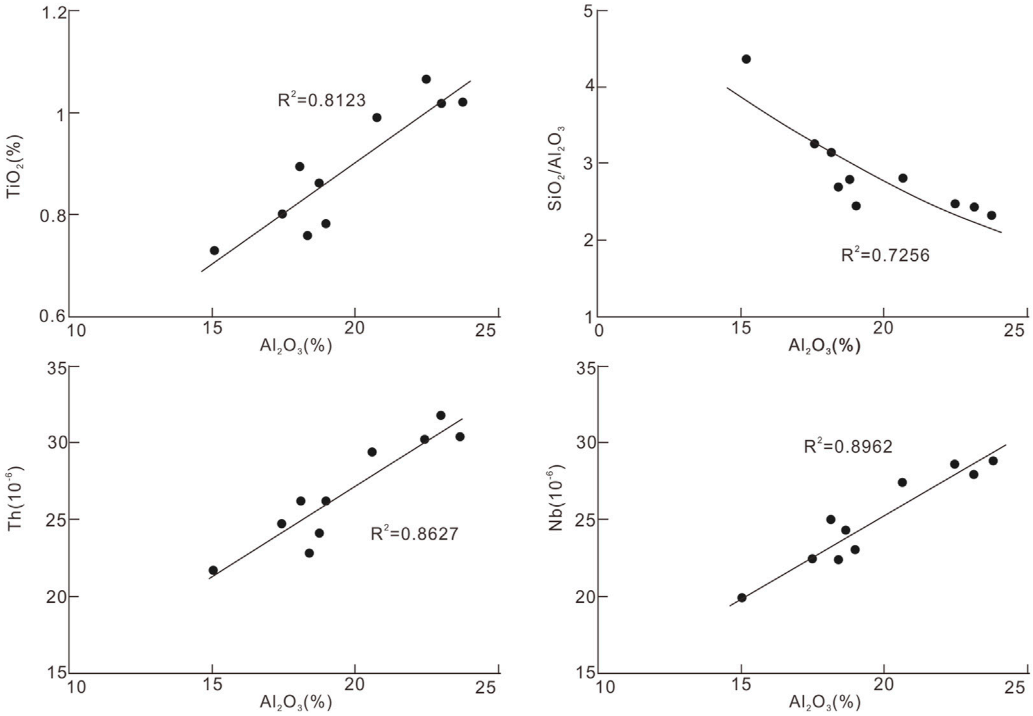

FIGURE 5
Correlation diagram of terrigenous clastic input of black mudstone in Well CY1.

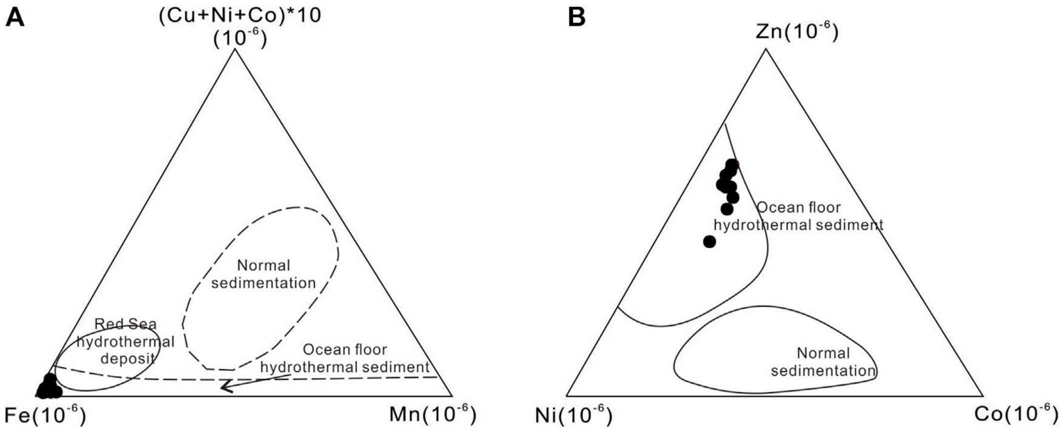

FIGURE 6
Identification diagram of hydrothermal influence on deposition of the studied mudstones. **(A)** based on Rona, 1978. **(B)** based on Adachi et al., 1986.

negative Eu anomaly (mean 0.84) (Table 4; Figure 3), which is similar to sediments in the passive continental margin. Meanwhile, Bhatia (1985) summarized REE partitioning curves of miscellaneous sandstones under different tectonic settings. Most of the REE chondrite-normalized distribution patterns and NASC-normalized distribution patterns of the Dawuba Formation black mudstone exhibit characteristics similar to the REE partition curve of passive continental margins clastic rocks (Figure 4). This is in line with the results of main and microelement discrimination, suggesting that the tectonic background of the provenance area is mainly passive continental margin.

Provenance weathering and paleoclimatology

The index of compositional variation (ICV) can determine whether a clastic sedimentary rock was first deposited or

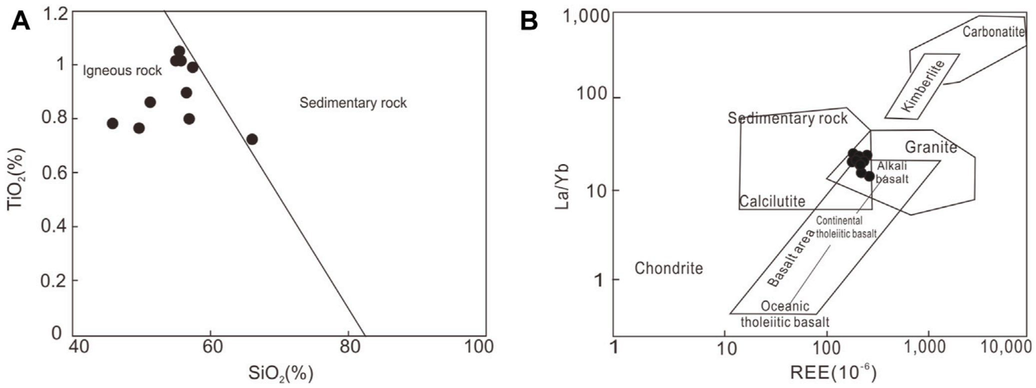

FIGURE 7
The source rock discrimination diagrams for mudstones of Well CY1. **(A)** base map from Roser and Korsch, 1986. **(B)** base map from Bhatia, 1985.

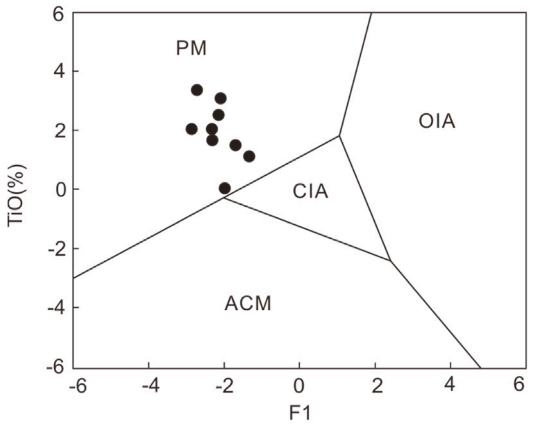

FIGURE 8
Tectonic setting discrimination diagrams of Well CY1. PM-passive continental margin; ACM-active continental margin; CIA-continental island arc; OIA-oceanic island arc. Base map is from (Roser and Korsch, 1988).

recirculated (Cox et al., 1995; Zhang J. et al., 2023). The formula is as follows:

$$ICV = mol\,(Fe_2O_3 + K_2O^* + Na_2O + CaO^* + MgO + MnO + TiO_2/mol\,(Al_2O_3)$$

All of which are molar masses, and CaO* represents the CaO abundance derived from silicate minerals. To date, no direct methods have been used to quantify and distinguish the CaO contents in silicate portions and nonsilicate portions (apatite and carbonates). K_2O^* is the corrected K_2O to eliminate the effect of potassium metasomatism on the results. The CaO* and K_2O^* contents studied here refer to the method described by McLennan and Taylor (1988) and Cox et al. (1995). It has been shown that the ICV value decreases because the primary sediments under strong weathering remain in the clay for a long time and are subjected to further weathering. Therefore, the clastic sedimentary rocks with low ICV values are considered to be from sedimentary sources containing large amounts of clay minerals, indicating the recirculation of sediments under active tectonic environments or the primary deposition of sediments under strong weathering conditions (Gaschnig et al., 2016; Zhang Q. et al., 2023). In contrast, clastic sedimentary rocks with high ICV values indicate primary deposition in an active tectonic environment (Moradi et al., 2016). Black mudstone in Well CY1 has an ICV value ranging from 0.49 to 0.71, averagely 0.65 (Figure 8A; Table 1), indicating high rock maturity. This suggests a provenance of sediment recirculation in an active tectonic environment or initial deposition under strong weathering conditions. Considering the geological history, it is probable that the Dawuba Formation was initially formed due to intensified rock weathering.

The chemical alteration index (CIA) is an important index used to judge the degree of chemical weathering in source areas (Gaschnig et al., 2016; Moradi et al., 2016). In the process of chemical weathering, Ca^{2+}, Na^+, and K^+ of unstable minerals (e.g., feldspar, dark minerals) are lost in the form of ions along with surface fluids, while Si^{4+}, Al^{3+}, and Ti^{4+} of relatively stable minerals remain. Therefore, the CIA value increases with the strengthening of weathering. Generally, CIA values of 50–65 represent primary weathering in cold and dry environments, CIA values of 65–85 represent moderate weathering in warm and humid environments, and CIA values of 85–100 represent intense weathering in hot and humid environments (Gaschnig et al., 2016; Zhang J. et al., 2023). At the same time, since metasomatism makes Ca^{2+}, Na^+ and K^+ unstable and affects CIA values, the effect of metasomatism should also be excluded when determining chemical weathering using CIA values. Under ideal conditions, if not metasomatized, the weathering proceeds along the direction of A–CN or A–K in the Al_2O_3–CaO* + Na_2O–K_2O (A–CN–K) diagram (Moradi et al., 2016). In the A–CN–K diagram, most samples in the study area are distributed along the A–CN direction, and the actual weathering line is basically parallel to the natural weathering line, indicating that the metasomatism of samples after deposition is weak, and the CIA value can be used to determine chemical weathering. The CIA value ranges from 75 to 83 (Table 1; Figure 8A), with an average of 79, indicating high chemical weathering due to intense weathering in warm and humid environments. Generally, climatic factors control sediment chemical weathering, while tectonic factors control source rock denudation and supply (Fedo et al., 1995). If the composition of major chemical elements in the sediment changes greatly and the samples in the A–CN–K triangle diagram are scattered and not compact, it indicates that the climate and tectonic environment are unstable in the provenance. In contrast, the compact distribution of plots in the A-CN-K diagram reflects the relatively stable chemical weathering and denudation in the source area (Fedo et al., 1995; Moradi et al., 2016). The distribution of studied sample is relatively compact (Figure 9B), indicating that the provenance was under relatively stable climatic and tectonic conditions during the depositional process. Moreover, the trend line of chemical weathering falls into the felsic igneous rock area (Figure 8B), indicating that the provenance consisted of mainly felsic igneous rock.

In the weathering process, U is more active than Th, and the ratio of Th/U increases as a result of weathering (Taylor and Mclennan, 1985). Therefore, the trace element Th/U is also one of the indicators used to characterize the degree of chemical weathering. The values of Th/U in the samples also ranged from 5.23 to 7.05 (Table 2), with an average value of 5.8, which was significantly higher than that of UCC (3.89) and PAAS (4.71), indicating strong chemical weathering in the provenance area, which was consistent with the results discussed above.

Paleo-oxygenation facies

The paleo-oxygen phase refers to the synthesis of various rock, biological and geochemical features caused by the characteristics of dissolved oxygen in the water body and its related changes (Li et al., 2017; Wang et al., 2018). The paleo-oxygen phase is closely related to the generation, enrichment, deposition, burial and source rock formation of organic matter, which is the focus of shale gas geology (Qiu et al., 2022). Oxygenated water is essential for thriving plants, microorganisms, and animals. This boosts initial productivity and provides ample organic matter for later stages. Second, the reducing environment of water is related to whether it is conducive to the preservation of organic matter produced after the death of organisms, which is one of the main controlling factors for the formation of organic-rich sedimentary rocks (Nie et al., 2023).

Element V is highly reactive to redox conditions and concentrated in sediments affected by low-oxygen water. Both V and Ni belong to the iron group, but V is more likely to be enriched in the reducing environment than Ni (Zhou et al., 2015). Therefore, the value of V/(V+Ni) can reflect the oxidation–reduction state of the sedimentary water body, and the value of V/(V+Ni) greater than 0.84, indicates an anoxic environment with the water sulfide and stratification. In a suboxic environment with a medium value (0.54–0.83) and no significant stratification, in a low value (0.46–0.53) show a dysoxic environment, the value less than 0.46 show a strong oxidizing environment (Zhao et al., 2016). The V/(V + Ni) values were 0.60–0.78, indicating a dysoxic–suboxic environment (Table 3; Figure 10). In addition, the Cu/Zn value can better reflect the degree of redox in the environment. If less than 0.21, it is an anoxic environment, and between 0.21 and 0.35 show a dysoxic environments. While ranging from 0.35 to 0.50 indicate a weak oxidation environments (Zhou et al., 2015; Zhao et al., 2016). The Cu/Zn values in the Well CY1 mudsone range from 0.15 to 0.39, with an average value of 0.28, which corresponds to a weak reduction environment. At the same time, the Ce/La ratio can also be used as a criterion for the oxidation reduction of sedimentary water (Zhang et al., 2017). A Ce/La ratio less than 1.5 indicates an oxygen-rich environment in the high-energy cycle, and a value between 1.5 and 1.8 indicates a dysoxic environment, while a value greater than 2 indicates a considerably anoxic environment (Zhou et al., 2015; Zhang et al., 2017). The Ce/La values in this study ranged from 1.75 to 2.43, with a mean of 2, also indicating a reducing environment. The δCe=0.72–1.11, with an average value of 0.92, shows a weak negative Ce anomaly, which also indicates a dysoxic environment in the depositional period of Dawuba Formation.

Sedimentary model and petroleum geological significance

The tectonic evolution of the Middle and Upper Yangtze region can be roughly summarized as follows: the Jinning Movement formed the basement at the end of the Neoproterozoic, the Craton basin evolution stage of plate movement in Southern China, the Proto–Tethis–Tethyan ocean evolution from the Early Paleozoic to the Middle Triassic, and then the intercontinental orogeny and foreland basin evolution in the Mesozoic and Cenozoic (Yuan et al., 2019; Liang et al., 2022). During the late Paleozoic, the southern Guizhou region was in the extensional conditionsforming as the Luipanshui–Ziyun–Luodian rifting trough that was subjected to marine transgression. The latter reached its maximum in the early Carboniferous, when the Carboniferous Dawuba Formation organic-rich mudstone was deposited (Liang et al., 2022; Yang et al., 2022). The lithofacies paleogeographic pattern of southern Guizhou is strictly controlled by regional fault expansion and tectonic compression, which is a sedimentary differentiation pattern between platforms and basins (Figure 11). Although the regional tectonic movement was intense, it still belonged to the passive continental margin sedimentary environment as a whole, which is consistent with the conclusion of the geochemical characteristics in this work (Yuan et al., 2019; Liang et al., 2022). The central Guizhou uplift and Jiangnan uplift are denudation areas of the early and Middle Caledonian uplift, and the uplift areas of the Carboniferous sedimentary period continue to uplift and expand and finally merge together (Yuan et al., 2019). The central Guizhou uplift is mainly exposed to Cambrian and Ordovician carbonate cap rocks, and the Jiangnan Paleouplift is mainly exposed to Precambrian felsic igneous rocks and metamorphic rock series (Liang et al., 2022; Yang et al., 2022). The petrological, mineralogical and geochemical characteristics reported in this work indicate that the parent rocks in the study area are mainly acidic rocks, such as felsic igneous rocks, granites and some sedimentary rocks, which is consistent with the lithology of the Jiangnan Paleouplift in the eastern part of the study area. Therefore, it is inferred that the provenance is mainly provided by acidic igneous rocks of the Jiangnan Paleouplift.

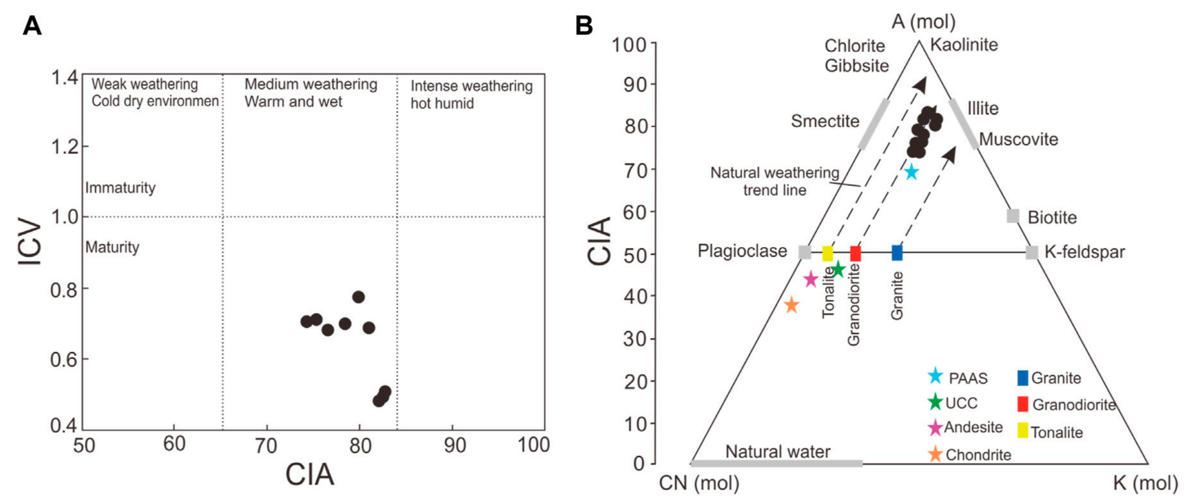

FIGURE 9
Palaeoclimate discrimination diagram of mudstones from the Well CY1. **(A)** The CIA–ICV diagram (Sensarma et al., 2008). **(B)** A–CN–K diagram of the studied rocks based on (Moradi et al., 2016).

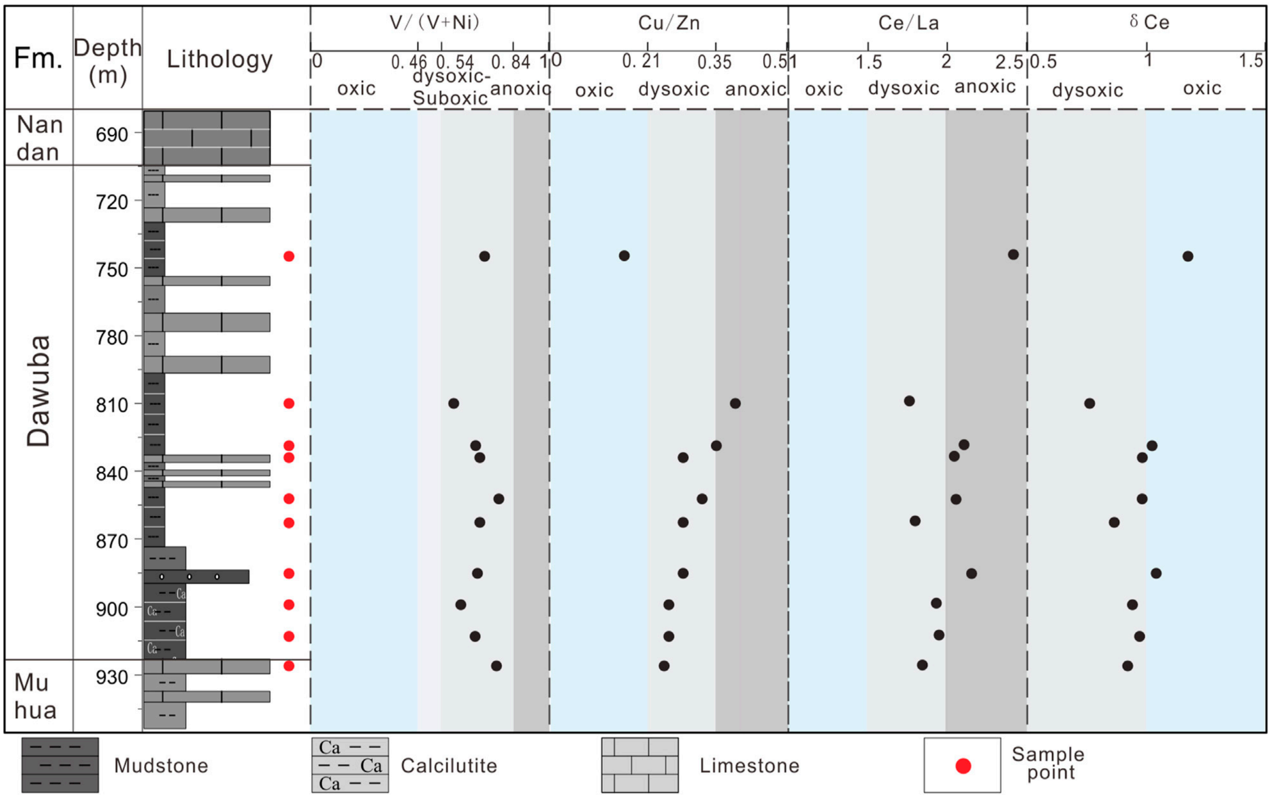

FIGURE 10
Column diagram of paleooxygen phase of Dawuba Formation (the threshold value is from Zhou et al., 2015; Zhao et al., 2016).

The tectonic stretching and extensive transgression created a low-oxygen environment that conducive to organic matter preservation. Frequent hydrothermal activities brought rich nutrients. In addition, the warm and humid climate, strong chemical weathering, and more terrigenous detritus input brought nutrients to organic matter, promoted the flourishing of organisms and produced higher paleoproductivity, and formed the organic-rich mudstone of Dawuba Formation. This mudstone layer has large thickness, wide regional distribution, high clay minerals content, and micro-fractures. It is a favorable source rock and reservoir for shale gas exploration and development.

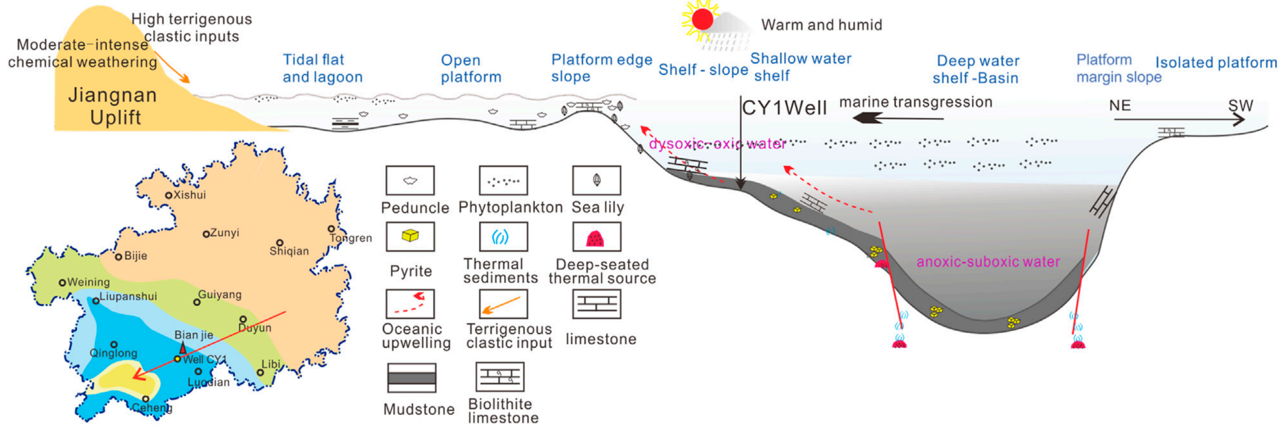

FIGURE 11
Depositional model of Dawuba Formation in the study area.

Conclusion

A systematic study on the mineralogical, petrological and geochemical characteristics of the black mudstone of the early Carboniferous Dawuba Formation in Well CY1 shows the following:

The black mudstone in Well CY1 is characterized by high clay mineral and organic matter content. The high contents of Al2O3 and TiO2 indicate that terrigenous detritus had a great influence on the depositional process. The enrichment of U, V, Ni, Cr, Cu, Zn, loss of Sr and Zn–Ni–Co ternary discrimination diagram all indicate that the depositional period of the Dawuba Formation was affected by hydrothermal deposition.

According to the characteristics of major and trace elements, the high LREE/HREE values and the weak negative δEu anomalies indicate that the study area was on a passive continental margin, and the source rocks were mainly acidic rocks and the provenance is mainly provided by Jiangnan ancient land.

The ICV value of the Dawuba Formation black mud shale in the study area is less than 1. The average CIA value is 79, and the average Th/U value is 5.8, suggesting strong chemical weathering during the sedimentary period. The sedimentary climate was warm and moist, which was conducive to the flourishing of organisms and the generation of high ancient productivity.

According to the characteristics of V/(V+Ni), Cu/Zn and Ce/La, the mudstone deposits in the Dawuba Formation formed in a weakly reducing environment, which was conducive to the preservation of organic matter and the formation of favorable source rocks and reservoirs.

Data availability statement

The original contributions presented in the study are included in the article/Supplementary Material, further inquiries can be directed to the corresponding author.

Author contributions

HZ: Writing–original draft. QZ: Writing–original draft. YZ: Conceptualization, Formal Analysis, Writing–review and editing. BL: Conceptualization, Project administration, Formal Analysis, Writing–review and editing. XF: Methodology, Project administration, Writing–review and editing. YC: Methodology, Project administration, Writing–review and editing. QY: Data curation, Writing–review and editing. JC: Data curation, Writing–original draft. YM: Data curation, Formal Analysis, Writing–review and editing. AZ: Formal Analysis, Investigation, Writing–review and editing.

Funding

The authors declare financial support was received for the research, authorship, and/or publication of this article. The research was supported by the Guizhou Provincial Fund Project [Grant No. (2022) ZD005] and Guizhou Provincial Fund Project [Grant No. (2023)-344].

Conflict of interest

Author BL was employed by the Company Guizhou Energy Industry Research Institute Co., Ltd.

The remaining authors declare that the research was conducted in the absence of any commercial or financial relationships that could be construed as a potential conflict of interest.

Publisher's note

References

Adachi, M., Yamamoto, K., and Sugisaki, R. (1986). Hydrothermal chert and associated siliceous rocks from the northern Pacific their geological significance as indication od ocean ridge activity. *Sediment. Geol.* 47 (1-2), 125–148. doi:10.1016/0037-0738(86)90075-8

Bhatia, M. R. (1985). Rare earth element geochemistry of Australian Paleozoic graywackes and mudrocks: provenance and tectonic control. *Sediment. Geol.* 45 (1-2), 97–113. doi:10.1016/0037-0738(85)90025-9

Chen, J., Yi, T., Jin, J., Wang, M., Liu, N., and Li, D. (2018). Regioselectivity of oxidation by a polysaccharide monooxygenase from *Chaetomium thermophilum*. *Coal Sci. Technol.* 46 (8), 155–163. doi:10.1186/s13068-018-1156-2

Chen, R., Yuan, K., Zhang, Z., Xu, Q., Lu, S., and He, J. (2019). Geochemical characteristics of organic-rich shale in the Dawuba Formation, western Guizhou Province. *Petroleum Geol. Exp.* 41 (1), 10–15. doi:10.11781/sysydz201901010

Condie, K. C. (1993). Chemical composition and evolution of the upper continental crust: contrasting results from surface samples and shales. *Chem. Geol.* 104 (1-4), 1–37. doi:10.1016/0009-2541(93)90140-E

Cox, R., Lowe, D. R., and Cullers, R. L. (1995). The influence of sediment recycling and basement composition on evolution of mudrock chemistry in the southwestern United States. *Geochimica Cosmochimica Acta* 59 (14), 2919–2940. doi:10.1016/0016-7037(95)00185-9

Ding, J., Zhang, J., Li, X., Lang, Y., Zheng, Y., and Xu, L. (2019). Characteristics and controlling factors of organic matter enrichment of Lower Carboniferous black rock series deposited in inter-platform region, Southern Guizhou Depression. *Lithol. Reserv.* 31 (2), 83–95. doi:10.12108/yxyqc.20190210

Eker, C. S., Sipahi, F., and Kaygusuz, A. (2012). Trace and rare earth elements as indicators of provenance and depositional environments of Lias cherts in Gumushane, NE Turkey. *Chem. Erde Geochem.* 72 (2), 167–177. doi:10.1016/j.chemer.2011.11.004

Fedo, C. M., Nesbitt, H. W., and Young, G. M. (1995). Unraveling the effects of potassium metasomatism in sedimentary rocks and paleosols, with implications for paleoweathering conditions and provenance. *Geology* 23 (10), 921–924. doi:10.1130/0091-7613(1995)023<0921:uteopm>2.3.co;2

Feng, W., Li, R., Zhao, Z., Yu, Q., Liu, W., and Cao, J. (2023). Geological characterization and exploration potential of shale gas in the Carboniferous Jiusi Formation, northern Guizhou and Yunnan provinces, SW China. *Energy Geosci.* 4 (3), 100177. doi:10.1016/j.engeos.2023.100177

Fuquan, J. (1989). Carboniferous paleogeography and paleoenvironment between the North and South China blocks in eastern China. *J. Southeast Asian Earth Sci.* 3 (1), 219–222. doi:10.1016/0743-9547(89)90025-1

Gaschnig, R. M., Rudnick, R. L., Mcdonough, W. F., Kaufman, A. J., Valley, J. W., Hu, Z., et al. (2016). Compositional evolution of the upper continental crust through time, as constrained by ancient glacial diamictites. *Geochim. Cosmochim. Acta* 186, 316–343. doi:10.1016/j.gca.2016.03.020

Gromet, L. P., Haskin, L. A., Korotev, R. L., and Dymek, R. F. (1984). The "North American shale composite": its compilation, major and trace element characteristics. *Geochim. Cosmochim. Acta* 48 (12), 2469–2482. doi:10.1016/0016-7037(84)90298-9

Gu, Y., Cai, G., Hu, D., Wei, Z., Liu, R., Han, J., et al. (2022b). Geochemical and geological characterization of upper permian linghao formation shale in nanpanjiang basin, SW China. *Front. Earth Sci.* 10, 883146. doi:10.3389/feart.2022.883146

Gu, Y., Hu, D., Wei, Z., Liu, R., Hao, J., Han, J., et al. (2022a). Sedimentology and geochemistry of the upper permian linghao formation marine shale, central nanpanjiang basin, SW China. *Front. Earth Sci.* 10, 914426. doi:10.3389/feart.2022.914426

Guo, X., Hu, D., Shu, Z., Li, Y., Zheng, A., Wei, X., et al. (2023). Exploration, development, and construction in the Fuling national shale gas demonstration area in Chongqing: progress and prospects. *Nat. Gas. Ind. B* 10 (1), 62–72. doi:10.1016/j.ngib.2023.01.009

Li, Y., Zhang, T., Ellis, G. S., and Shao, D. (2017). Depositional environment and organic matter accumulation of upper ordovician lower silurian marine shale in the upper Yangtze platform, south China. *Palaeogeogr. Palaeoclimatol. Palaeoecol.* 466, 252–264. doi:10.1016/j.palaeo.2016.11.037

Liang, Y., Tang, X., Zhang, J., Liu, Y., Zhang, Y., Yuan, K., et al. (2022). Origin of lower carboniferous cherts in southern Guizhou, south China. *Palaeogeogr. Palaeoclimatol. Palaeoecol. Int. J. Geol. Sci.* 590, 110863. doi:10.1016/j.palaeo.2022.110863

Mclennan, S. M. (2013). Relationships between the trace element composition of sedimentary rocks and upper continental crust. *Geochem. Geophys. Geosyst.* 2 (4), 203–236. doi:10.1029/2000GC000109

McLennan, S. M., and Taylor, S. R. (1988). Crustal evolution: comments on "The Archean-Proterozoic transition: evidence from the geochemistry of metasedimentary rocks from Guyana and Montana" by A. K. Gibbs, C. W. Montgomery, P. A. O'day and E. A. Erslev. *Geochimica Cosmochimica Acta* 52 (1988), 785–787. doi:10.1016/0016-7037(88)90339-0

Mei, Y., Ji, Y., Ren, J., Zhang, H., and Zhou, Y. (2021). Shale gas accumulation conditions in the lower carboniferous jiusi formation of dianqianbei depression. *J. Nat. Gas. Ind.* 41 (S1), 51–59. doi:10.3787/j.issn.1000-0976.2021.S1.007

Moradi, A. V., Sari, A., and Akkaya, P. (2016). Geochemistry of the Miocene oil shale (Hançili Formation) in the Çankırı-Çorum Basin, Central Turkey: implications for Paleoclimate conditions, source–area weathering, provenance and tectonic setting. *Sediment. Geol.* 341 (15), 289–303. doi:10.1016/j.sedgeo.2016.05.002

Murray, R. W. (1994). Chemical criteria to identify the depositional environment of chert: general principles and applications. *Sediment. Geol.* 90 (3), 213–232. doi:10.1016/0037-0738(94)90039-6

Nie, H., Jin, Z., Li, P., Jay Katz, B., Dang, W., Liu, Q., et al. (2023). Deep shale gas in the Ordovician-Silurian Wufeng–Longmaxi formations of the Sichuan Basin, SW China: insights from reservoir characteristics, preservation conditions and development strategies. *J. Asian Earth Sci.* 244, 105521. doi:10.1016/j.jseaes.2022.105521

Nagarajan, R., Roy, P. D., Jonathan, M. P., Lozano, R., Kessler, F. L., and Prasanna, M. V. (2014). Geochemistry of Neogene sedimentary rocks from Borneo Basin, East Malaysia: paleo-weathering, provenance and tectonic setting. *Chem. Erde Geochem.* 74 (1), 139–146. doi:10.1016/j.chemer.2013.04.003

Qie, W., Liu, J., Chen, J., Wang, X., Mii, H., Zhang, X., et al. (2015). Local overprints on the global carbonate δ13C signal in Devonian–Carboniferous boundary successions of South China. *Palaeogeogr. Palaeoclimatol. Palaeoecol.* 418, 290–303. doi:10.1016/j.palaeo.2014.11.022

Qiu, Z., Liu, B., Lu, B., Shi, Z., and Li, Z. (2022). Mineralogical and petrographic characteristics of the Ordovician-Silurian Wufeng-Longmaxi Shale in the Sichuan Basin and implications for depositional conditions and diagenesis of black shales. *Mar. Petroleum Geol.* 135 (1), 105428. doi:10.1016/j.marpetgeo.2021.105428

Rona, P. A., Bostrom, K., Laubier, L., and Smith, K. L. (1983). *Genesis of ferromanganese deposits diagnostic criteria for recent and old deposits*. Springer US, 473–489. Chapter 20. doi:10.1007/978-1-4899-0402-7_20

Rona, P. A. (1978). Criteria for recognition of hydrothermal mineral deposits in oceanic crust. *Econ. Geol.* 73 (2), 135–160. doi:10.2113/gsecongeo.73.2.135

Roser, B. P., and Korsch, R. J. (1986). Determination of tectonic setting of sandstone-mudstone suites using SiO_2 content and K_2O/Na_2O ratio. *J. Geol.* 94 (5), 635–650. doi:10.1086/629071

Roser, B. P., and Korsch, R. J. (1988). Provenance signatures of sandstone-mudstone suites determined using discriminant function analysis of major element data. *Chem. Geol.* 67 (1–2), 119–139. doi:10.1016/0009-2541(88)90010-1

Sensarma, S., Rajamani, V., and Tripathi, J. K. (2008). Petrography and geochemical characteristics of the sediments of the small River Hemavati, Southern India: implications for provenance and weathering processes. *Sediment. Geol.* 205 (3-4), 111–125. doi:10.1016/j.sedgeo.2008.02.001

Steiner, M., Wallis, E., Erdtmann, B. D., Zhao, Y., and Yang, R. (2001). Submarine-hydrothermal exhalative ore layers in black shales from South China and associated fossils-insights into a Lower Cambrian facies and bio-evolution. *Palaeogr. Palaeoclimatol. Palaeoecol.* 169 (3-4), 165–191. doi:10.1016/S0031-0182(01)00208-5

Taylor, S. R., and Mclennan, S. M. (1985). The continental crust: its composition and evolution. *J. Geol.* 94 (4), 57–72. doi:10.1086/629067

Wang, Y., Xu, S., Hao, F., Lu, Y., Shu, Z., Lu, Y., et al. (2018). Geochemical and petrographic characteristics of Wufeng-Longmaxi shales, Jiaoshiba area, southwest China: implications for organic matter differential accumulation. *Mar. Petroleum Geol.* 102, 138–154. doi:10.1016/j.marpetgeo.2018.12.038

Yang, J., Wen, H., Guo, X., Luo, C., Yu, W., Du, S., et al. (2022). Detrital zircon U–Pb ages and trace elements indicate the provenance of Early Carboniferous Li-rich claystone from central Guizhou, South China. *Sediment. Geol.* 442 (10), 106278–78. doi:10.1016/j.sedgeo.2022.106278

Yuan, K., Chen, R., Lin, T., Fang, X., Qin, Y., Wang, C., et al. (2019). Petrological characteristics and sedimentary environmentin the southern Guizhou during the Late Carboniferous. *Petroleum Geol. Exp.* 41 (01), 38–44. doi:10.11781/sysydz201901038

Zhang, H. Q., Wang, Z. H., Wang, H., Liu, W., Miao, Y. J., Li, Q., et al. (2016). Methemoglobin-based biological dose assessment for human blood. *Sediment. Geol. Tethyan Geol.* 36 (3), 30–36. doi:10.1097/HP.0000000000000522

Zhang, J., Li, Z., Wang, D., Xu, L., Li, Z., Niu, J., et al. (2023). Shale gas accumulation patterns in China. *Nat. Gas. Ind. B* 10 (1), 14–31. doi:10.1016/j.ngib.2023.01.004

Zhang, Q., Yu, Q., Wang, J., Xiao, Y., Chen, J., Zhao, A., et al. (2018). Sign backpropagation: an on-chip learning algorithm for analog RRAM neuromorphic computing systems. *Rock Mineral analysis* 37 (2), 217–223. doi:10.1016/j.neunet.2018.08.012

Zhang, Q., Men, Y., Yu, Q., Wang, G., Xiao, Y., Zhang, H., et al. (2022). Characteristics and enrichment genesis of the platinum group elements (PGEs) in organic rich shale of the wufeng and Longmaxi formations of upper ordovician and lower silurian in the Sichuan Basin. *Minerals* 12 (11), 1363. doi:10.3390/min12111363

Zhang, Q., Wang, J., Yu, Q., Wang, X., Zhao, A., Zhang, H., et al. (2017). The effect and safety of diacerein in patients with type 2 diabetes mellitus: a systematic review and meta-analysis. *Sediment. Geol. Tethyan Geol.* 37 (1), 97–106. doi:10.3969/j.issn.1009-3850.2017.01.013

Zhang, Q., Zhang, B., Yu, Q., Men, Y., Zhang, H., Kang, J., et al. (2023). Study on the prove-nance and tectonic setting of mudstone in the lower silurian Longmaxi formation of the yanyuan basin on the western margin of the Yangtze platform. *Minerals* 13 (2), 194. doi:10.3390/min13020194

Zhao, A., Wang, D., Zhang, Q., Lei, Z., Yu, Q., Zhang, D., et al. (2023). Sedimentary environment and organic matter accumulation of wufeng-longmaxi shales, southwest Yangtze platform: insights from geochemical and petrological evidence. *China Geol.* 6, 1–15. doi:10.31035/cg2022074

Zhao, J., Jin, Z., Jin, Z., Geng, Y., Wen, X., and Yan, C. (2016). Applying sedimentary geochemical proxies for paleoenvironment interpretation of organic-rich shale deposition in the Sichuan Basin, China. *Int. J. Coal Geol.* 163, 52–71. doi:10.1016/j.coal.2016.06.015

Zhou, L., Algeo, T. J., Shen, J., Hu, Z., Gong, H., Xie, S., et al. (2015). Changes in marine productivity and redox conditions during the Late Ordovician Hirnantian glaciation. *Palaeogeogr. Palaeoclimatol. Palaeoecol.* 420, 223–234. doi:10.1016/j.palaeo.2014.12.012

Zou, C., Zhao, Q., Wang, H., Xiong, W., Dong, D., and Yu, R. (2023). Principal characteristics of marine shale gas, and the theory and technology of its exploration and development in China. *Nat. Gas. Ind. B* 10 (1), 1–13. doi:10.1016/j.ngib.2023.01.002

Frontiers in Earth Science

TYPE Original Research
PUBLISHED 27 December 2023
DOI 10.3389/feart.2023.1296459

EDITED BY
Hu Li,
Southwest Petroleum University, China

REVIEWED BY
Cunhui Fan,
Southwest Petroleum University, China
Cheng Zhong,
Nanjing Normal University, China

*CORRESPONDENCE
Yuanyu Yang,
✉ yangyuanyu@petrochina.com.cn

RECEIVED 18 September 2023
ACCEPTED 27 October 2023
PUBLISHED 27 December 2023

CITATION
Yang Y, Li X, Wang Z and Yang W (2023), Tectonic movements of the Yanshan-Himalayan period in the northern Longmenshan and their impact on tight gas accumulation of the Shaximiao formation in the Qiulin structure, China. *Front. Earth Sci.* 11:1296459.
doi: 10.3389/feart.2023.1296459

Tectonic movements of the Yanshan-Himalayan period in the northern Longmenshan and their impact on tight gas accumulation of the Shaximiao formation in the Qiulin structure, China

Yuanyu Yang[1,2]*, Xucheng Li[2], Zeqing Wang[1] and Wenbo Yang[1]

[1]College of Earth Sciences, Chengdu University of Technology, Chengdu, China, [2]PetroChina Southwest Oil & Gasfield Company, Chengdu, China

The Jurassic strata constitute a focal area for recent exploration and development of tight gas reservoirs in the western Sichuan Basin. This study investigates the Jurassic Shaximiao Formation in the northern Longmenshan in the Western Sichuan basin, focusing on tight gas reservoirs. The research integrates core and outcrop observations, seismic interpretations, and burial history analyses to understand hydrocarbon source rocks, sedimentation, reservoir characteristics, and structural characteristics. The impact of Yanshan-Himalayan tectonic movements on tight gas reservoir accumulation in the Shaximiao Formation is dissected, primarily around the Qiulin structure. The Western Sichuan Depression basin's formation is influenced by gravitational gliding tectonics, which can be classified into the 'Three Zones and One Belt,' with Longmenshan in the frontal belt. Burial history analysis reveals distinct processes in the foreland belt and the depression basin. In the Qiulin area, gas reservoirs in the Shaximiao Formation are mainly charged by source rocks from the Xujiahe Formation. Tectonic movements play a significant role in creating favorable reservoirs and conditions for hydrocarbon migration and preservation. Natural gas accumulation is primarily controlled by fault connectivity to hydrocarbon sources and effective reservoir thickness. Gravitational sliding tectonics have shaped a fluvial-lacustrine environment for the Shaximiao Formation, with fluvial sand bodies acting as favorable reservoir zones. Small-scale normal faults formed by tectonic movements serve as conduits for natural gas migration. The research findings are of significant guidance for the exploration and development of tight oil and gas resources in western Sichuan basin.

KEYWORDS

Longmenshan, tectonic movements, structural characteristics, tight gas, Shaximiao formation, gas accumulation, Qiulin structure

1 Introduction

The Longmenshan thrust belt is a vital transpressive zone in China, situated at the junction between the Pacific and Tethys-Himalayan tectonic domains. It forms part of the complex intracontinental foreland thrust system in central and western China, drawing significant attention from researchers worldwide due to its prominence in the study of thrust belt tectonic deformation (He et al., 2022a; He et al., 2022b; Li et al., 2023). Geological research on Longmenshan began in the early 20th century and has yielded significant insights into its tectonic evolution, genetic models, uplift history, crustal structure, and deformation patterns. These accomplishments have advanced the understanding of thrust belt tectonic deformation theories and guided exploring and developing numerous large and medium-sized gas fields in western Sichuan (Yang et al., 2018; Xie et al., 2022; Yang et al., 2023a; Yang et al., 2023b; Xie et al., 2023). In recent years, significant oil and gas discoveries have been made in the northern Longmenshan foreland belt, particularly in the Shuangyushi structure. High-yield gas flows have been achieved from the Permian Qixia, Maokou Formations, and the Devonian Guanwushan Formation. The testing production capacity has reached as high as 126.77 × 10^4 m^3/d, showcasing the promising prospects for tight gas exploration in the northern Longmenshan (Deng et al., 2021; Ding et al., 2022). The primary exploration zones are situated within the northern and depression basin of the Longmenshan foreland belt, encompassing structures such as the Zitong, Bajiaochang, and Qiulin. The tectonic movements significantly influence aspects such as sedimentation, reservoir formation, migration, and accumulation (Yang et al., 2022).

The Sichuan Basin evolved from a paleo-uplift, and following the Jinning and Chengjiang movements in its early period, the basement folding in the basin area underwent reversion and cooled, leading to consolidation (Li et al., 2019; Gao et al., 2020; Liu et al., 2021). Consequently, the formation of a paleo-uplift began. The development of the Sichuan Basin can be divided into three periods. From the Cambrian to the Middle Triassic in the early period, a rift-related sedimentary basin with a cratonic marine environment was formed, primarily under extensional tectonic conditions. Carbonate rocks dominated the sedimentary deposits in this period. During the middle period, the Indosinian tectonic movement primarily influenced the Sichuan Basin. The basin was subjected to extensional tectonics, developing a series of large-scale normal faults. It resulted in the formation of a rifted basin, and during this period, the basin exhibited a phase of alternating marine and terrestrial environments. From the Jurassic to the Early Cretaceous, it experienced the Yanshan tectonic movement, manifesting as a subsidence basin. Starting from the Cretaceous, the basin underwent compressional forces due to the collision between the Longmenshan thrust belt and the rigid basement of the Sichuan Basin (Jin et al., 2009; Jin et al., 2010; Deng et al., 2018; 2018). It led to the formation of a foreland basin. As a result, the Sichuan Basin is predominantly the amalgamation of three major periods of basin evolution, leading to the development of a series of intricate structural patterns within its interior.

In the earlier periods of research, geological and structural studies in the northern Longmenshan primarily focused on the Xujiahe Formation and older strata. There has been limited investigation into the tectonic movements occurring after the Indosinian period. It only suggests a history of Yanshan uplift and strong Himalayan compression during the Yanshan-Himalayan tectonic phase. However, a detailed exploration of the Yanshan-Himalayan tectonic movements and associated structural characteristics remains insufficient. To a certain extent, this limited understanding has contributed to the lack of breakthroughs in oil and gas exploration in the Jurassic and overlying strata of the northern Longmenshan. The Shaximiao Formation exhibits extensive vertical development of fluvial sand bodies and a wide distribution in planar extent. It possesses favorable reservoir properties and significant exploration potential. Based on this, this study focuses on the Qiulin structure. An analysis of the Yanshan-Himalayan tectonic characteristics in northern Longmenshan aims to establish a definitive link between these movements and the tight gas accumulation of the Shaximiao Formation. The research offers guidance for developing tight gas reservoirs in the Sichuan Basin and oil and gas exploration in foreland basins.

2 Geological background

2.1 Tectonic setting

The Longmenshan thrust belt is a northeast-trending orogenic belt on the eastern Songpan-Ganzi highland. Regarding tectonic positioning, it lies along the western margin of the Sichuan Craton of the Yangtze Block. It is a convergence zone between the Yangtze Block, the North China Block, and the Indian Plate, presenting a predominant northeast to east-northeast orientation. In planar view, Longmenshan can be divided into the northern (from the north of Anxian to Guangyuan), the middle (from Huaiyuan to Anxian), and the southern (from Huaiyuan to the south of Ya'an) parts (Jin et al., 2009; Jin et al., 2010). It is primarily characterized by three regional and deep-seated faults: the Maoxian-Wenchuan Fault, the Yingxiu-Beichuan Fault, and the Pengguan Fault. These faults exhibit orientations consistent with the overall trend of the Longmenshan thrust belt (Figure 1A). Among them, the northern part is situated in the northeastern of the western Sichuan Depression. Influenced by the Tongwan Movement and the Late Caledonian Ancient Uplift, the northern thrust belt of the Longmenshan features a nearly complete sequence of Mesozoic, Paleozoic, and Ordovician strata (Deng et al., 2021). The area exhibits intricate structural complexity, marked by pronounced folding, with some local strata being nearly upright or even overturned. Simultaneously, a well-developed fault system is concentrated within the Devonian, Carboniferous, Permian, and Triassic formations above the Silurian strata. They often extend over considerable distances and are commonly associated with fractured zones. The Qiulin structure in the northern Longmenshan thrust belt has emerged as a focal area for oil and gas exploration in the western Sichuan region in recent years (Figure 1A). Significant discoveries have been made, particularly in formations such as the Shaximiao Formation, which represents tight gas reservoirs.

2.2 Stratigraphy

In the northern Longmenshan, the exposed surface strata predominantly include Jurassic, Permian, Triassic, Carboniferous, Devonian, Silurian, and Cambrian formations. The Middle and Late Cambrian, Ordovician, and Late Carboniferous strata are absent (Lei et al., 2012; Wu et al., 2012). The Permian formations are primarily situated near the core of the Tianjingshan anticline, with a thickness of approximately 460–600 m. The lithology predominantly

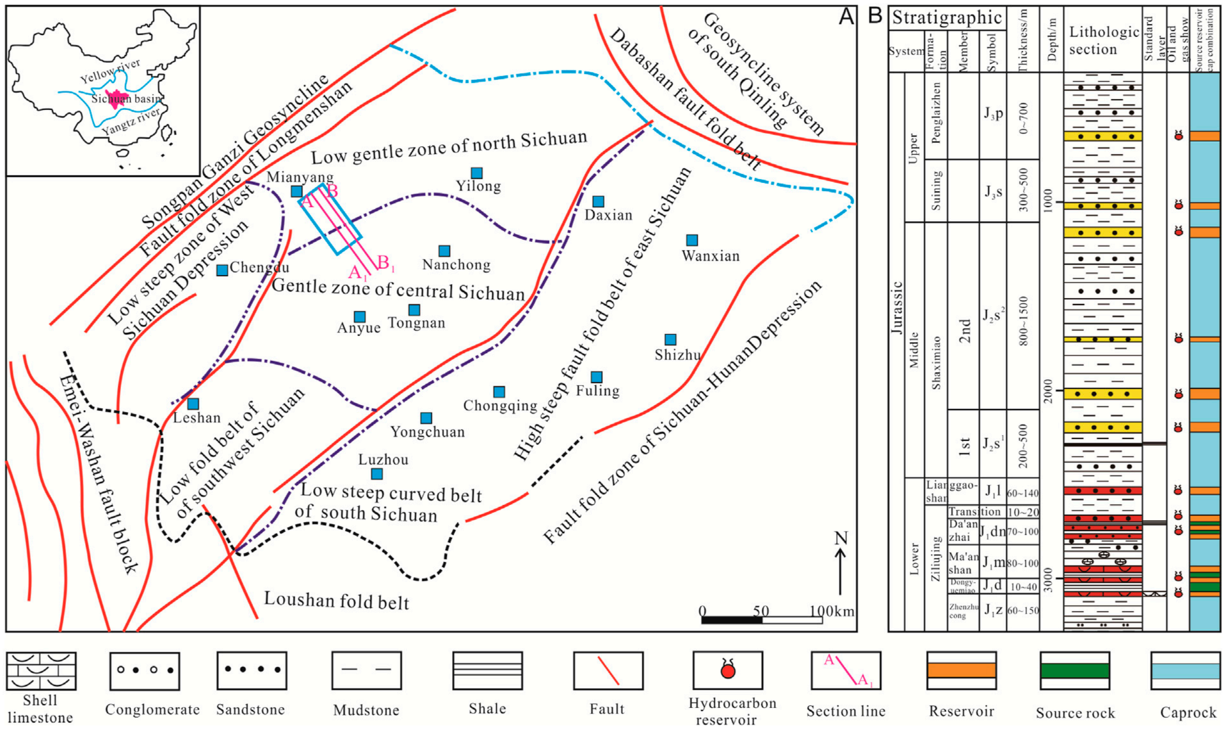

FIGURE 1
Geological setting of the study area. **(A)** The structural position of the study area; **(B)** Stratigraphic and lithological characteristics of the Shaximiao Formation (modified from Li et al., 2019a; Li et al., 2019b; Wei et al., 2021).

comprises carbonate rocks, with only the base of the Liangshan and Wujiaoping formations containing coal-bearing sand and mudstones. The Triassic formations are found on the western and northern Tianjingshan anticline, with an exposed thickness of approximately 1,000–2,500 m. The lithology is predominantly characterized by carbonate rocks, with the Feixianguan and Xujiahe formations containing predominantly terrestrial clastic rocks. The Carboniferous and Devonian formations are only exposed in the higher parts of the anticline's core and the northwest flank. The Carboniferous formation consists of approximately 70 m of carbonate rocks. The Devonian formation can be divided into upper, middle, and lower members. The lower member comprises sandstone with a thickness of around 150 m, while the middle to upper members primarily consist of marine carbonate sedimentation. The Cambrian strata are sparsely exposed in the core of the anticline, predominantly characterized by clastic rocks. The primary target reservoir of the Qiulin structure is the Jurassic Shaximiao Formation. It consists of a thick sequence of fluvial-dominated sand-mudstone sedimentation, with a thickness ranging from 800 to 2,200 m (Wei et al., 2021; Lu et al., 2022). The deposition pattern is characterized by thinning towards the southwest and thickening towards the northeast. The Shaximiao Formation is divided into two members (1st and second) based on the "Estheria shale" (Figure 1B). The 1st Member has a thickness of approximately 900–1,000 m. The Estheria shale marks its base, and the bottom of the brick-red feldspathic sandstone of the Suining Formation defines its top. This member consists of a purple-red to dark purple-red mudstone interbedded with thick layers of blocky sandstone, with sandstone thickness ranging from 10 to 20 m. It is the primary focus for exploration and development within the Qiulin structure.

3 Data and methods

3.1 Samples and data

This study focuses on the Qiulin structure as the primary analysis area, employing detailed structural interpretation and analysis of reservoir-forming processes. It aims to analyze the impacts of multiple tectonic movements during the Yanshan-Himalayan period on sedimentation, reservoir formation, oil and gas migration, and preservation of the Jurassic Shaximiao Formation in the northern of the Longmenshan and ascertain its controlling role in the accumulation of natural gas. This study's main samples and data include field investigations of 20 outcrop profiles, core observations and drilling data from 5 wells, 3D seismic data covering an area of 100 km^2, conventional and imaging logging data from 5 wells. Core observations and logging data are primarily employed to study sedimentary and reservoir characteristics. Drilling and seismic data are primarily utilized for constructing subsidence history curves. When combined with outcrop features, these data aid in analyzing periods of tectonic movement, providing a basis for structural evolution analysis. The 3D seismic data is employed for detailed structural interpretation, analyzing the tectonic movements and structural characteristics, and establishing the relationship between structures and gas accumulation. Additionally, data on the main source rocks, sedimentation, stratigraphy, and lithological characteristics of the study area have been collected.

3.2 Methods

3.2.1 Sedimentation history analysis

The sedimentary basin experiences different tectonic movements, resulting in distinct subsidence mechanisms. As a result, the subsidence magnitude and characteristics of subsidence curves also exhibit significant variations. Subsidence can typically be categorized into structural and total subsidence, with this study primarily focusing on the former.

3.2.1.1 Normal compaction model (Overburden deformation calculation)

Previous research findings have revealed that under normal pressure conditions, there exists an exponential relationship between sediment porosity and depth (Xia et al., 2018).

$$\phi(z) = \phi_0 e^{-c^* z} \tag{1}$$

Where: z represents the burial depth of sediment, $\phi(z)$ stands for the porosity of the sediment at depth z, ϕ_0 is the initial porosity of the sediment deposit, and c denotes the sediment compaction constant, reflecting the gradient of porosity change with depth.

Since a geological profile can be divided into several units, a unit could represent a geological interval characterized by sediment types such as sandstone, mudstone, limestone, dolomite, chalk, gypsum, and other lithologies. Hence, calculations based on formula (1) are performed for different lithologies separately while considering the proportions of various lithologies present within each unit.

The terrestrial strata in the study area are primarily composed of sandstone and mudstone. The calculation method for these is as follows:

$$\phi(z) = r_{sh}\phi_{osh}e^{-Csh^* z} + (1 - r_{sh})\phi_{os}e^{-Cs^* z} \tag{2}$$

Where: r_{sh} is the content of mudstone, ϕ_{osh} and ϕ_{os} are the initial porosities of mudstone and sandstone, respectively, C_{sh} and C_s are the compaction coefficients for mudstone and sandstone, respectively.

3.2.1.2 Paleothickness restoration model (backstripping calculation)

Once the porosity-depth relationship is established, the stratigraphic thickness data for different periods on current strata can be used to restore the burial paths of each layer since deposition.

3.2.1.3 Backstripping Model for continuous sedimentary profiles

For continuous sedimentary geological profiles, according to the principle of “tectonic skeleton invariance,” the burial depths of various sedimentary layers during different geological epochs can be restored using present-day stratigraphic data (Martins et al., 2023).

$$\int_{Z_1}^{Z_2} 1 - \phi(z)dz = \int_{Z_{1a}}^{Z_{2b}} (1 - \phi(z)\backslash)dz \tag{3}$$

Where: z_1 and z_2 represent the present-day burial depths of the bottom and top boundaries of the current stratum. z_{1a} and z_{2b} represent the burial depths of the bottom and top boundaries of the current stratum during a certain geological epoch.

3.2.1.4 Backstripping model for profiles with erosional surfaces

When strata undergo erosion, the porosity-depth relationship changes, and its calculation formula is as follows:

$$\phi_B = e^{-c(h+s)} \tag{4}$$

The skeletal thickness of the eroded layer before restoration is:

$$H_B = \int_{Z_1}^{Z_2} [1 - \phi(z)]dz \tag{5}$$

After erosion restoration, the skeletal thickness of the eroded layer becomes:

$$H_B = \int_{Z_1}^{Z_2} [1 - \phi_B(z)]dz \tag{6}$$

The restoration of paleo thickness for each geological period still follows the principle of tectonic skeleton invariance, thus determining the burial history of the geological stratum.

$$\int_{Z_1}^{Z_2} [1 - \phi_B(z)]dz = \int_{Z_{1a}}^{Z_2} {}^{b}[1 - \phi_B(z)]dz \tag{7}$$

For the strata below the erosional layer, the process involves calculating the skeletal thickness based on current burial depths. Then, paleo thickness during various geological periods is computed using the porosity-depth relationship restored after erosion. As for the strata above the erosional layer, the procedure is the same as that for continuous sedimentary profiles.

3.2.1.5 Basin subsidence history model

For the sake of simplicity, this study’s subsidence history model disregards the inherent strength of the lithosphere and employs a straightforward subsidence history model under the assumption of local Airy isostasy (equilibrium equation) (Zhang et al., 2009). The calculation formula is as follows:

$$Y = \frac{S^*(p_m - p_s)}{(p_m - p_w)} - \frac{\Delta SL^* p_w}{(p_m - p_w) - (W_d - \Delta SL)} \tag{8}$$

Where S is the sediment thickness adjusted for compaction, P_m, P_w, and P_s represent the mantle, water, and sediment densities, respectively, ΔSL is the amplitude of sea level change, and W_d is the paleowater depth.

3.2.2 3D seismic data processing

To thoroughly investigate the structural characteristics of the Qiulin area, delineate its structural morphology, and identify potential trap targets, a research approach was employed that transitioned from analyzing individual points to studying linear features and then further to examining broader geological patterns. This approach involved utilizing well logging and 3D seismic data as a foundation, building upon regional comprehensive research findings, and employing methods such as well-seismic correlation, integration of various cross-sections and profiles, to conduct a detailed interpretation of structural characteristics (Figure 2).

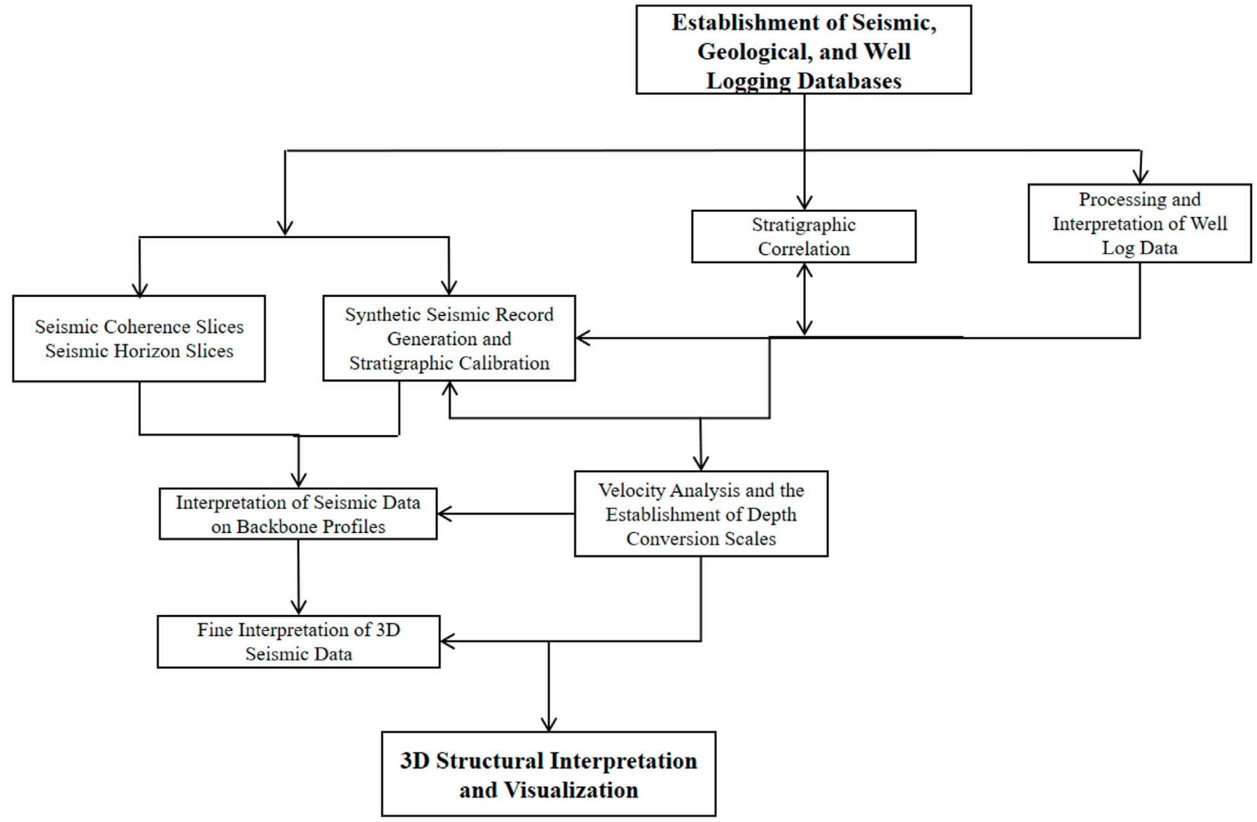

FIGURE 2
Schematic diagram of the 3D seismic structural interpretation process.

The process can be broken down into three steps: 1) Fine stratigraphic calibration and profile establishment: This involves establishing main cross-sections and analyzing seismic waveform characteristics through detailed stratigraphic calibration. 2) Interpretation of faults using coherent bodies, bed dip, and time slices combined with seismic profiles. This ensures spatial closure of faults in the study area, enabling a detailed understanding of fault profile and planar characteristics. 3) Progressive interpretation based on actual needs: Interpretation is intensified to accurately depict local structural styles and features, leading to a precise characterization. These steps culminate in a comprehensive analysis of structural characteristics, utilizing techniques such as well-seismic correlation, cross-section integration, and seismic data to create a thorough understanding of the geological formations in the Qiulin area.

4 Results

4.1 Characteristics of source rocks

The Middle to Upper Jurassic of the Sichuan Basin is primarily characterized by secondary hydrocarbon reservoirs, with the main source rocks originating from the Triassic Xujiahe Formation and Early Jurassic strata (Dai et al., 2009; Mu et al., 2019; Wu et al., 2023). Through comparative analysis of the gas source from the 1st member of the Shaximiao Formation, it is evident that the predominant gas source is mature coal-derived gas, followed by mixed sources of mature oil and coal, primarily originating from the underlying Xujiahe Formation and Jurassic source rocks (Figure 3) (Dai et al., 2009). The source rocks of the Xujiahe Formation are generally characterized by moderate to high maturity, with vitrinite reflectance ranging from approximately 0.4%–0.6% and temperatures around 500 °C. The maturity decreases gradually from the western to the eastern Sichuan Basin. The Jurassic source rocks primarily consist of organic-rich lacustrine deep-gray and black mudstones. These source rocks exhibit greater thickness in the central, northern, and eastern Sichuan basins while gradually thinning towards the western and southern Sichuan basin (Freeman et al., 1990; Wang et al., 2023). Overall, the thickness of the source rocks is generally over 50 m, with the maximum thickness reaching up to 380 m. The organic carbon content ranges from 0.03% to 32%, with an average of 0.96%. The kerogen is classified as Type II_2. Controlled by two major hydrocarbon generation centers, the Jurassic Xujiahe Formation in central Sichuan exhibits strong hydrocarbon generation (Li et al., 2022; Ma et al., 2023). Through hydrocarbon-bearing faults, the underlying natural gas can effectively charge the tight gas reservoirs of the Shaximiao Formation.

4.2 Sedimentary characteristics

In the early Jurassic, as the tectonic activity of the Longmenshan in western Sichuan gradually weakened, the Micashan-Dabashan

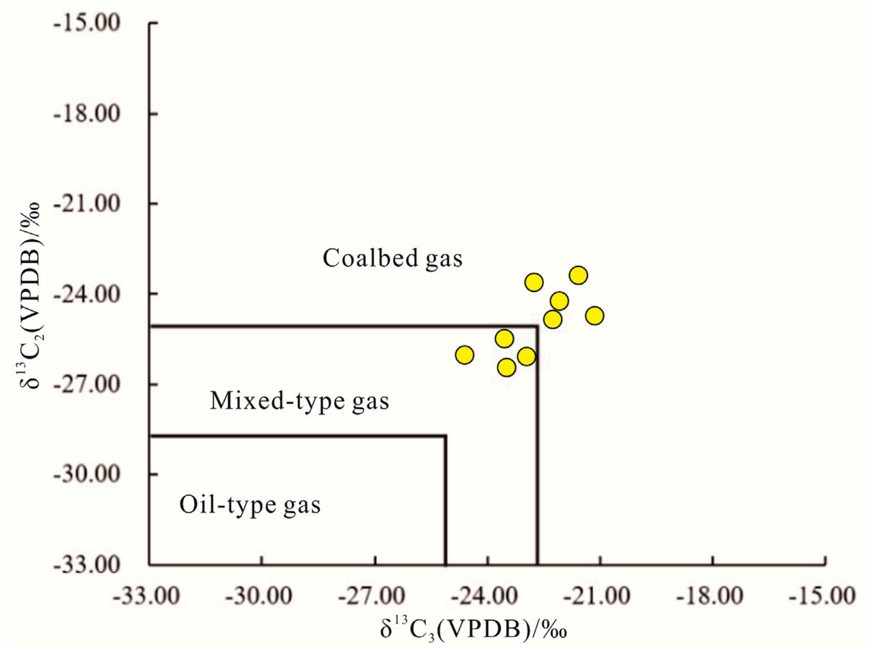

FIGURE 3
Carbon isotopes of the gas reservoir in the 1st Member of the Shaximiao Formation (see data in Dai et al., 2013; Dai et al., 2018).

tectonic zone in northern Sichuan responded to the subduction of the North China Plate and began to be active (Huang et al., 2022). As a result, the sedimentary center shifted from the western towards the northern and northeastern of the Sichuan Basin. During this period, there were two significant phases of basin expansion (Luo et al., 2013). The expansion of the basin was most extensive during the deposition of the Da'anzhai Formation, covering the areas of the eastern, northern, and central Sichuan Basin. This expansion exhibited a gradual transition from deep to shallow conditions. The deep-lake facies were present in the northeastern Sichuan Basin, particularly around the Dazhou-Wanzhou area. In contrast, in the basin regions closer to the mountain belt, sedimentation is primarily characterized by deltaic, fluvial, and alluvial fan deposits, representing a transition from the mountainous areas towards the basin.

During the Middle Jurassic Lianggaoshan Formation deposition period (referred to as the Xintiangou Formation in the Hechuan area and Qianfoya Formation in northern Sichuan basin), the sedimentary center was primarily situated in the Wangcang of the northern Sichuan to the Dazhou and Tongjiang of the northeastern Sichuan. A fan delta-lake sedimentary system existed in the northern part, while a fluvial-delta sedimentary system was prevalent in the southern and western parts (Wen et al., 2017). After the Upper Shaximiao Formation deposition, the Sichuan Basin evolved into a continental shallow-water basin. The water body was relatively shallow, and oxidation processes were prominent. The lithology consists of thick alternating layers of purplish-red and grayish-green sandstone and mudstone. During the late period of the Early Shaximiao Formation deposition, there was a significant and rapid rise in the lake level, leading to basin expansion. In the central to western Sichuan Basin, there is a widespread occurrence of black shale containing abundant leafy brachiopods at the top of the Lower Shaximiao Formation, commonly referred to as "Estheria shale." Simultaneously, during this period, the basin area gradually decreased once again. In the northwestern and northern parts of western Sichuan, the foreland areas exhibited fluvial sedimentation, while in the southern foreland of the mountain belt, there was mainly alluvial fan sedimentation transitioning to fluvial deposition (Figure 4).

Overall, during the sedimentation period of the Shaximiao Formation, tectonic activity was minimal, sedimentation was relatively gentle, and arid conditions characterized the environment. The Shaximiao Formation predominantly comprises a dark purple-red mudstone interbedded with gray-green and gray-white sandstone through the outcrop, core, logging, and seismic analysis. Based on the 'Estheria shale' as a boundary, it is divided into two members. The 1st Member has a thickness ranging from 200 to 300 m, and the second Member is 900–1,100 m. During the deposition of the 1st Member, the Qiulin structure developed a river-lake depositional system. Based on core observations from wells such as QL 16, QL 17, QL 202, and QL 205, a thick succession of blocky, extensive gray, medium-to fine-grained feldspathic sandstone beds representing channel sand bodies have been identified. These sand bodies exhibit a relatively pure sandy composition, with upward fining of grain size. The cores commonly display low-angle cross-stratification. Prominent scour surfaces are evident at the base of the sand layers, and the upper portions of these scour surfaces show sandstone beds containing mud and gravel, with gravel diameters reaching up to approximately 10 cm. This indicates deposition within a relatively high-energy fluvial channel environment. Therefore, the second Member in the study area represents meandering river deposition. The second Member can

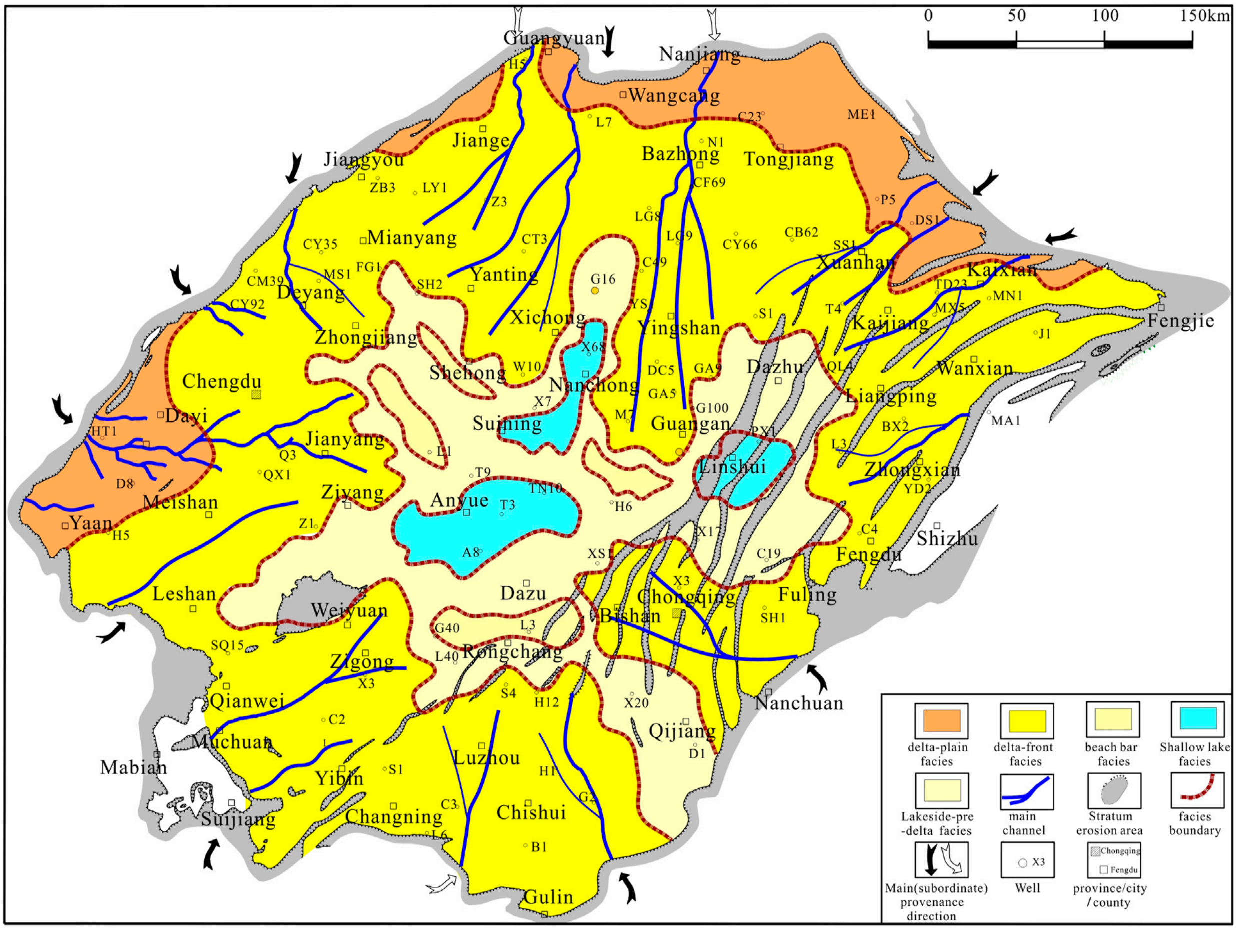

FIGURE 4
Sedimentary facies of the 1st Member of the Shaximiao Formation in the Sichuan basin.

be subdivided into four sub-members. Among these, one to three sub-members exhibit abundant sediment supply and the development of large-scale isolated sand bodies. 4 sub-member is characterized by alluvial plain sedimentary facies, which is not a favorable zone for reservoir development.

4.3 Reservoir characteristics

Tectonic movements primarily influence reservoir lithology and petrophysical properties through sediment supply. The sediment provenance in the study area is controlled by the tectonic movements of the northern Longmenshan and the Dabashan-Micangshan area, mainly originating from the northwest and northeast directions (Yu et al., 2021; Liu et al., 2023; Lyu et al., 2023). According to observations of detrital grains, cores, and thin sections, the reservoir of the second Member is predominantly composed of medium-grained lithic feldspathic sandstone (Figure 5A). The sorting is moderate to good, with subangular to subrounded grain shapes, and particle contacts are mainly point-to-line.

Based on core samples analysis from 5 wells, reservoir porosity ranges from 6% to 14%, with an average of 11.3%. Permeability is primarily distributed between 0.01 and 1 mD, with an average permeability of 0.43 mD. Sands developed during the same period exhibit similar reservoir petrophysical conditions, and porosity and permeability are positively correlated. This allows for qualitatively classifying the reservoir in this area as porous (Figure 5B). The T_2 relaxation spectrum of the second Member primarily exhibits a bimodal distribution, with an overall left-high and right-low pattern (78%) (Figure 5C), indicating a relatively higher content of small-sized pores (Gu et al., 2021; Xu et al., 2022; Yang et al., 2023c). Most samples exhibit a distinct left peak higher than the right peak, with an average T_2 cutoff value of 3.3 ms. This signifies that the reservoir samples in the study area possess small pore apertures and limited pore connectivity. Mobile fluids within the rock's pore-throat spaces are scarce, resulting in intricate pore structures forming during subsequent diagenetic processes.

4.4 Characteristics of tectonic movement

4.4.1 Tectonic characteristics during the Yanshan-Himalayan period

4.4.1.1 Analysis of depositional history

We conducted burial and subsidence history analysis on 9 wells in the study area using mud logging, logging data, and sedimentary

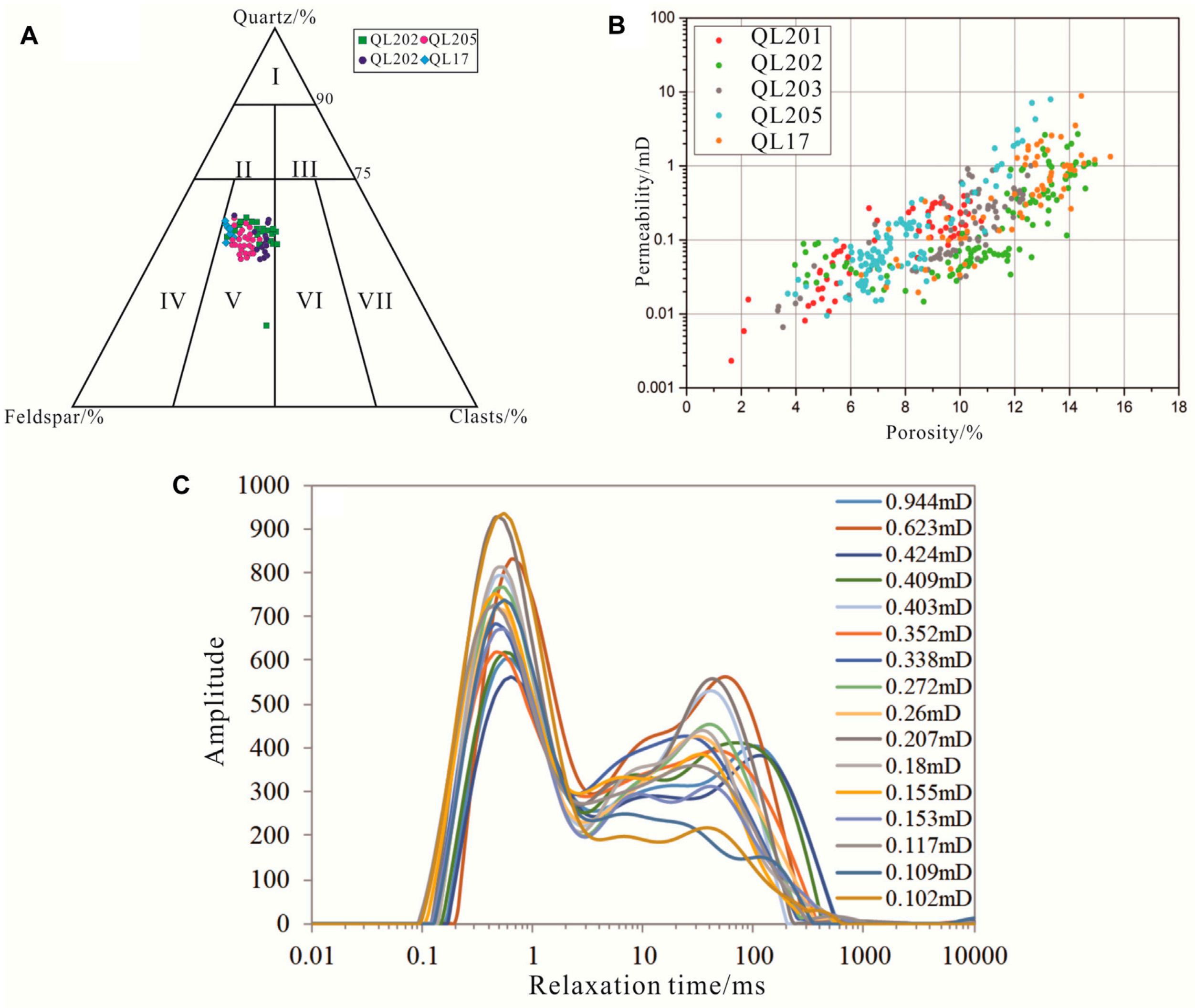

FIGURE 5
Basic reservoir characteristics of the second Member of the Shaximiao Formation. **(A)** Petrographic characteristics; **(B)** Reservoir petrophysical properties; **(C)** T_2 spectrum distribution of the core samples.

history calculation methods. Among them, 1 well (HX 1) is located in the frontal zone of the northern Longmenshan, 3 wells (Z18, Y1, and H2) are located in the frontal area, and 3 wells (W1, GJ1, SY1, and L1) are located within the basin (Figure 6A). Based on the subsidence curve analysis, it is believed that the frontal zone of the northern Longmenshan experienced a sequence of subsidence phases during the Jurassic period, which can be divided into "rapid subsidence - slow subsidence - rapid subsidence - intense uplift" phases. The sedimentary evolution of the northern frontal zone of Longmenshan and the intrabasinal area during the Jurassic is characterized by a sequence of subsidence phases: "rapid subsidence - slow subsidence - rapid subsidence - slow subsidence - rapid uplift." Compared to the frontal zone, the sedimentary history of the frontal and intrabasinal areas includes an additional Cretaceous sedimentation phase, and the influence of the Himalayan uplift during that period is relatively minor (Figure 6). The varying sedimentary history curves in different areas indicate that they were subjected to distinct tectonic settings during the same period, leading to differential subsidence and accommodating varying degrees of sedimentation (Alsalem et al., 2017; Zhu and Li, 2019; Petermann et al., 2022). The study area can be primarily categorized into frontal belt and foreland-basin sedimentary types. Despite sharing the same tectonic background, the different forms of tectonic activity have led to distinct subsidence history curves.

The subsidence history curve of the frontal belt exhibits a pattern of "rapid subsidence-slow subsidence-rapid subsidence-intense uplift," indicating that this area experienced rapid subsidence during the Early Jurassic, followed by a sustained period of slow subsidence during the Early to Middle Jurassic (Figure 6B). During the Late Jurassic to Early Cretaceous, the backside of Longmenshan experienced another rapid uplift, leading to intense subsidence in the frontal belt. This subsidence resulted in the deposition of a thick layer of conglomerates belonging to the Lianhuakou Formation. During the Late Cretaceous of the Yanshan period, the intensified tectonic activity led to rapid uplift of the entire northern Longmenshan. The frontal belt of the mountain, where Jurassic

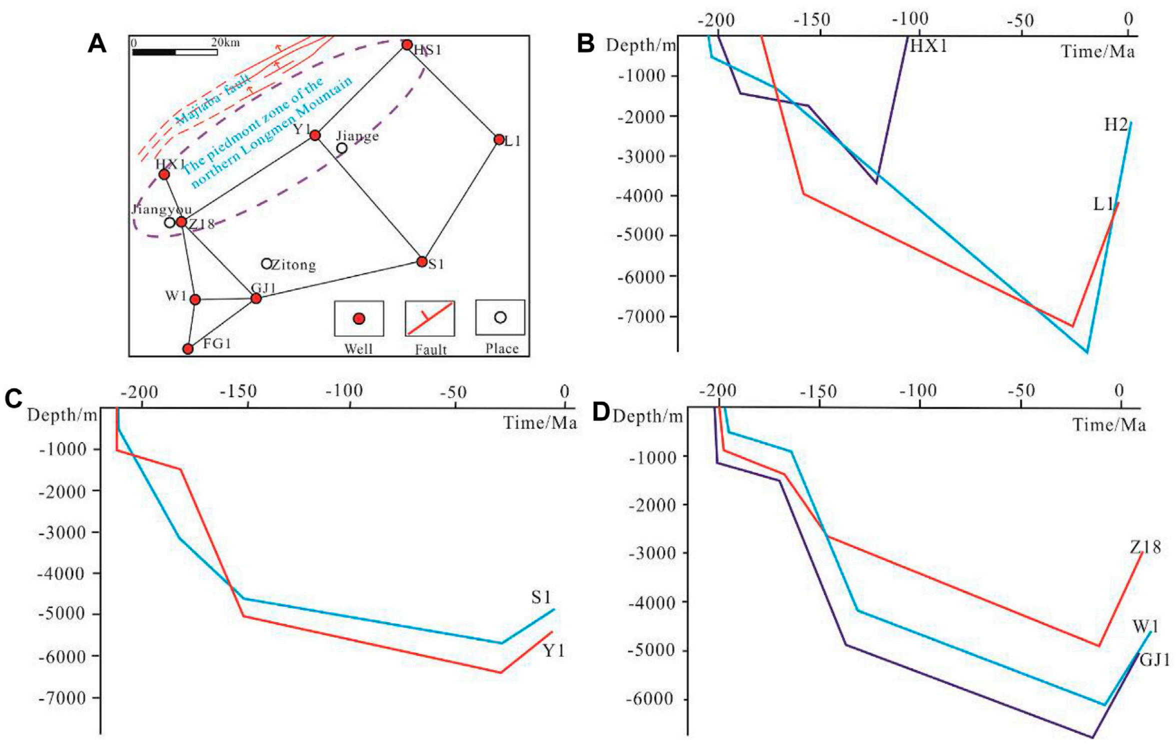

FIGURE 6
Depositional history curve of Jurassic in the foreland belt of the Longmenshan-Northwestern Sichuan Basin. **(A)** Relative position of the wells; **(B)** HX1, L1, and H2 wells; **(C)** S1 and Y1 wells; **(D)** Z18, W1, and GJ1 wells.

strata were previously exposed, was uplifted and exposed to the surface. Entering the Late Yanshan period, tectonic activity intensified, significantly uplifting the northern Longmenshan. The foreland belt of the mountain, where Jurassic strata were exposed, emerged above the water surface. The overlying Cretaceous Jianmenguan Formation was subsequently deposited atop the underlying Lianhuakou Formation. At the base of the Jianmenguan Formation, a sequence of conglomerates indicative of alluvial fan deposition was laid down. Following this phase, no new sedimentary strata were added to the foreland belt. As the Himalayan tectonic movement commenced, the foreland belt continued to experience uplift and underwent erosion.

The foreland-basin sedimentary history curve exhibits the characteristics of "rapid subsidence-slow subsidence-rapid subsidence-slow subsidence-violent uplift," indicating that the area experienced rapid subsidence during the Early Yanshan period (Figures 6B–D), followed by a sustained slow subsidence process from Early to Middle Yanshan. By the Middle-Late Yanshan period, the back ridge of Longmenshan experienced another rapid uplift, leading to intense subsidence in the foreland belt. This subsidence resulted in the deposition of a thick sequence of the conglomerates Jurassic Lianhuakou Formation and Cretaceous Jianmenguan Formation. Subsequently, the area underwent slow subsidence, leading to the deposition of the middle and upper parts of the Cretaceous strata. As the Himalayan began, the northern Longmenshan was rapidly folding and uplifting. In this area, there is an absence of Tertiary sedimentary strata. Sedimentary evidence is only present in the southern foreland basin, particularly in the Ya'an-Mingshan area.

The inflection points in the tectonic subsidence curve (indicating changes in subsidence rates) correspond closely to significant events in the geological evolution of the study area. The curve's starting point corresponds to the period of uplift of the hinterland of the northern Longmenshan and the thrust belt during the Yanshan orogeny (Figures 6B–D). The first inflection point marks the transition from intense activity to a relatively calm period. The second inflection point indicates that the curve steepens again, signifying the transition from a quiet period to intense tectonic activity during the Middle-Late Yanshan. The third inflection point shows a rapid increase, representing the intense tectonic activity and rapid uplift of the strata during the Late Yanshan in this area.

4.4.2 Structural characteristics of the foreland belt in the northern Longmenshan

4.4.2.1 Gravity sliding tectonic system

Gravity sliding deformation is typically considered a systemic structural deformation and displacement process, primarily driven by the uplift of the hinterland, causing the development of slopes (Bretas et al., 2012; Braunagel et al., 2023). Under gravity, rock layers slide downward to lower positions, forming a series of structural patterns. We divide it into four distinct zones: the uplifted zone, the slope zone, the frontal zone, and the depressed area. Gravity sliding systems exhibit mainly two thrust-style and wedge-style deformations. The most intense deformation occurs at the frontal portion of the thrust-style deformation (such as the Longmenshan thrust belt), where

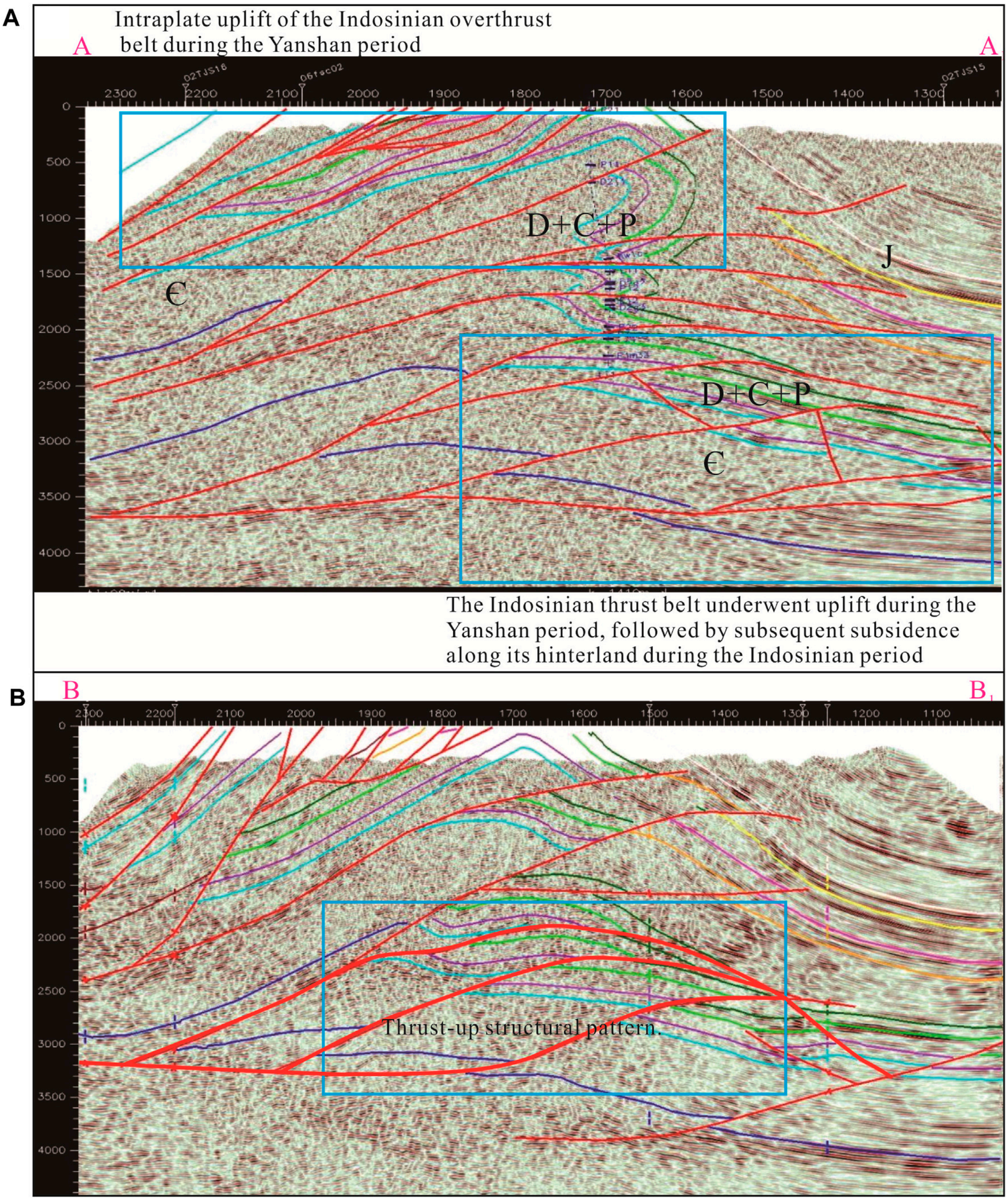

FIGURE 7
Seismic profile characteristics of gravity sliding structural system. **(A)** Structural pattern of gravity sliding foreland-style; **(B)** Thrust-up structural pattern.

deformation diminishes notably toward the rear, characterized by overall uplift (as seen in the Songpan-Ganzi highland). The central area demonstrates a large transitional slope zone (along the rear of the Longmenshan thrust belt).

In the western and central parts of the study area, the structural characteristics exhibit a typical gravity sliding foreland-style pattern. During the Indosinian-Yanshan period, these structures were influenced by gravity sliding within a compressional tectonic dynamic environment. They interacted with the rigid basement of the Sichuan Basin, resulting in intense rock deformation and the development of a series of thrust faults (Figure 7A) (Gunderson et al., 2018). In contrast, the shallow-level structures display a relatively gentle configuration, predominantly influenced by sedimentation. The intensity of tectonic deformation and displacement gradually diminishes towards the depocenter area. Due to the significant influence of the main fault on the deformation of the strata, exceeding their capacity to withstand, results in the development of disruptive faults in the rock layers, which release stress.

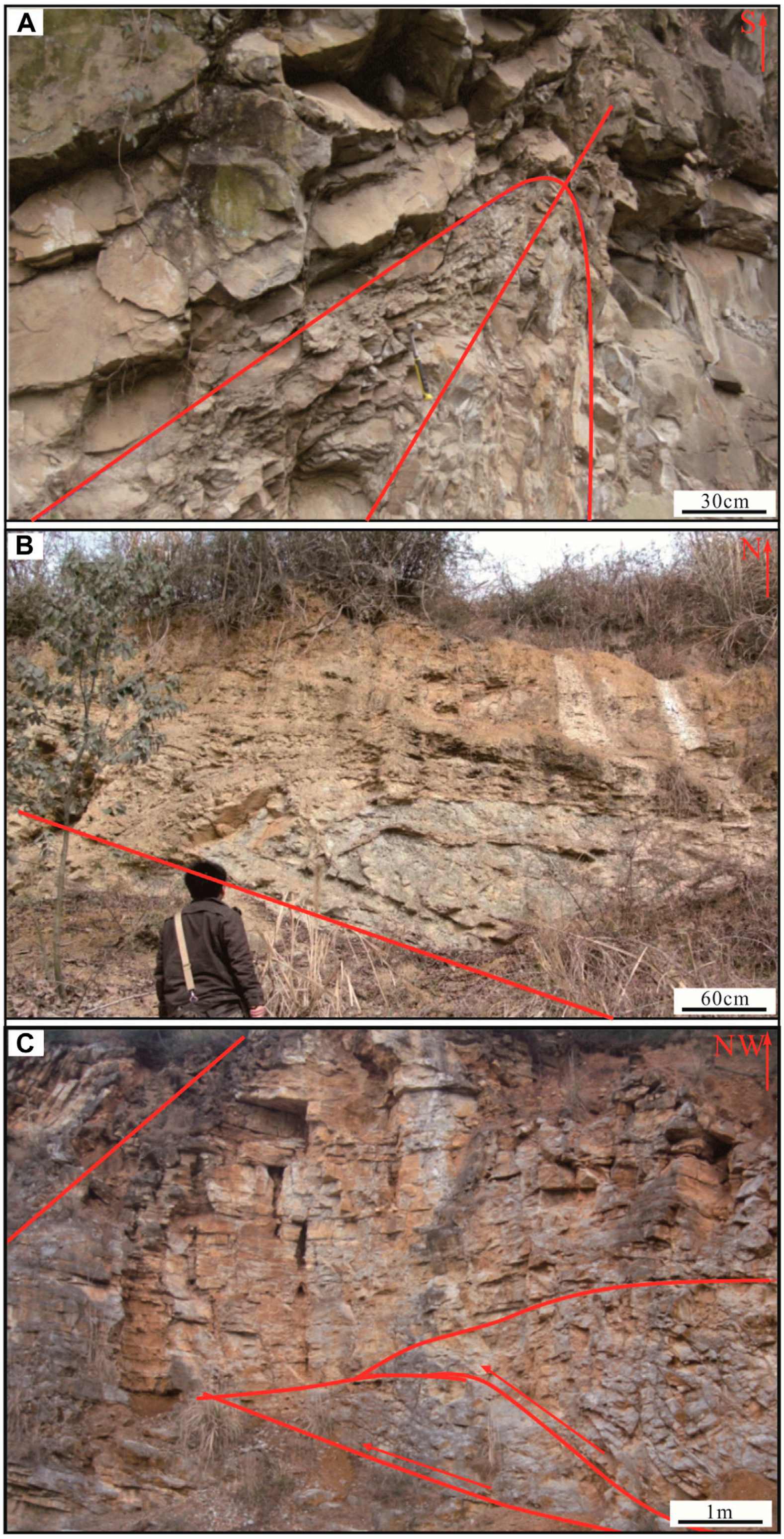

FIGURE 8
Principal structural styles of the thrust overthrust system. **(A)** Reversed syncline structural style; **(B)** Fault-bend fold structural style; **(C)** Thrust wedge structural style.

On the contrary, the subsidiary faults primarily serve a regulatory function. As a result, the trends of the main fault and subsidiary faults are generally opposite. Thrust-up structures manifest as a series of fault blocks on the plane, favoring the creation of fault block traps. Such structures often appear in clusters and are associated with duplex structures (Figure 7B).

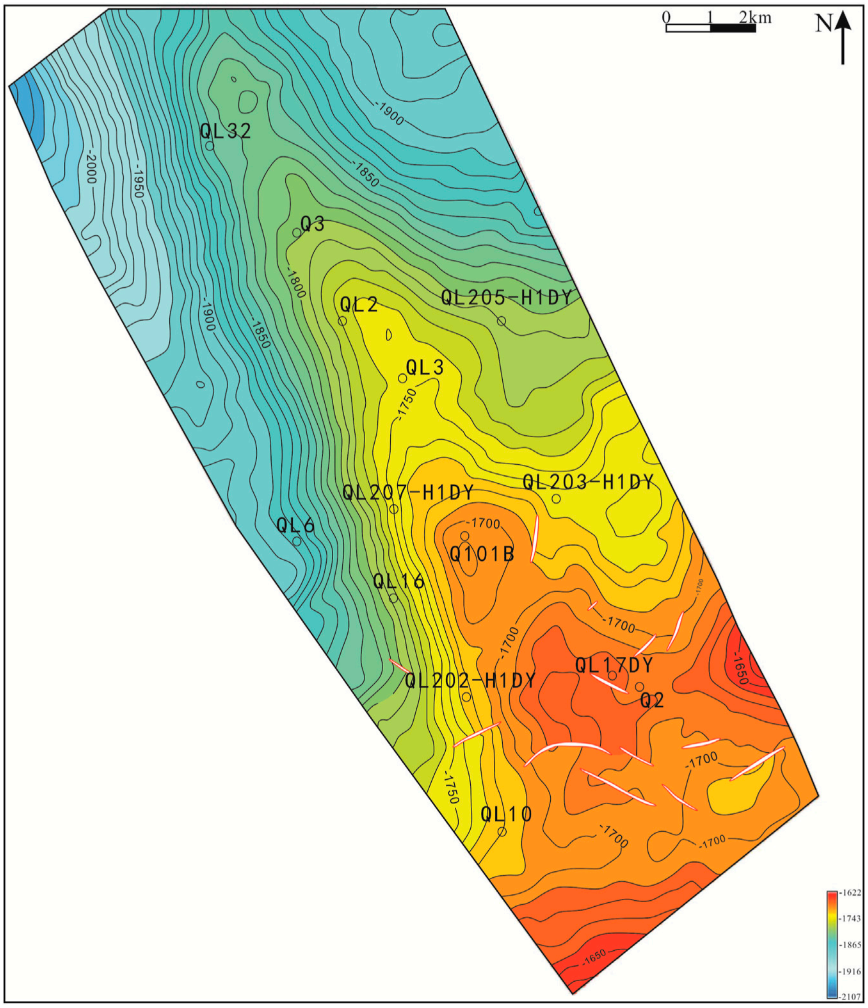

FIGURE 9
Structural map (T0) of the second Member of the Shaximiao Formation in the Qiulin structure.

4.4.2.2 Compression and over-thrusting tectonic system

During the Himalayan period, the intense collision between the Indian and Eurasian Plate led to vigorous compression in the northern Longmenshan (Thingbaijam et al., 2009). This compression profoundly reworked the extensively established structural patterns from the Indosinian-Yanshan period. Rock layers underwent renewed deformation and displacement, resulting in a more intricate network of faults and ultimately shaping the current structural configuration. In contrast, the shallow basin areas of the foreland belt mainly experienced vertical uplift effects, with relatively minor tectonic deformation. These areas largely inherited the earlier structural styles.

Duplex structures are commonly observed in the northern Longmenshan's thrust belt and hinterland areas. They are most pronounced in seismic profiles, with limited outcrop expression. These structures feature hanging-wall and footwall thrust faults. This structural pattern involves a series of imbricate thrust faults forming duplex structures. The study area predominantly inherits the thrust-up structural pattern generated by gravity sliding, modified under later compressional tectonic influences. In the northern Longmenshan hinterland, these structures are predominantly seen within the Lower Triassic and underlying formations at the front edge of the thrust zone (Figure 7B).

Reverted anticline structural style: At the Tianjingshan observation area, a surface outcrop of a reverted anticline has been identified. The exposed strata in the core of the anticline belong to the Cambrian system. The orientation of the left limb, as shown in Figures 8A 315°∠40°, while the orientation of the right limb is 292°∠87°.

Fault-bend fold structural style: A common structural style observed in orogenic and fault zones, it consists of three components: the lower fault plane, fault slope, and upper fault plane (Jiang et al., 2020). The fault-bend fold initiates above the fault slope and deforms into a folding pattern as it progresses. If the deformation continues, it may lead to the development of a thrust fault at the hinge area of the fold. In the deeper parts of the study area, the predominant structural style is the fault-bend fold. Near the Erliangmiao area, a small-scale fault-bend fold is observed in the Shaximiao Formation. The hinterland structural style appears in the core of the Tianjingshan structure. The occurrence of the fault plane,

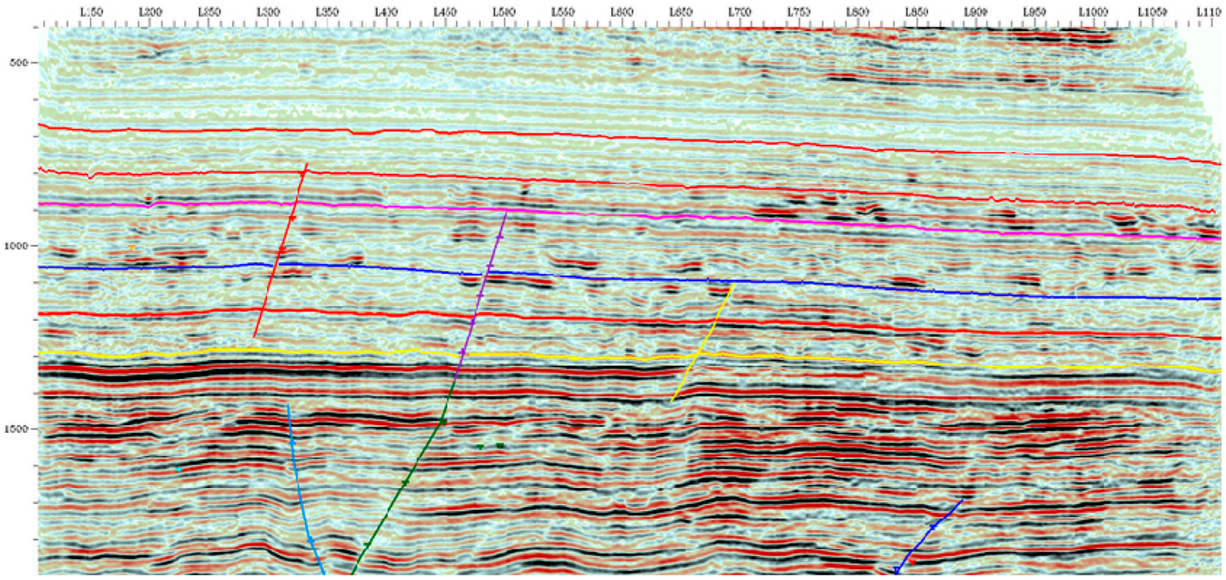

FIGURE 10
Typical fault interpretation profile of the Qiulin area.

the frontal limb, and the rear limb is 180°∠46°, 325°∠35°, and 192°∠14°, respectively (Figure 8B).

The extrusion wedge structural style: The development process of the extrusion wedge generally takes two forms (Sang et al., 2017). The first form involves the development of an extrusion wedge under early extensional stress conditions. During this period, normal faulting activity results in the deposition of syn-rift sedimentary strata within the fault basin. After the cessation of normal faulting, it experiences continuous sedimentation. As extensional stresses transition to compressional stresses, the previously active normal faults reverse and form thrust faults. This change in tectonic stress leads to the development of an extrusion wedge, altering the earlier structural pattern. The second form involves the development of an extrusion wedge through rock brittle failure under compressional stress conditions. This usually results in the formation of two conjugate reverse faults with opposite orientations. In cross-sectional view, these two conjugate reverse faults enclose a wedge-shaped block, which converges and merges at the tip of the wedge-shaped block. The sliding movement along the boundary faults propels the wedge-shaped block forward and induces folding in the overlying strata. During field geological investigations, a detachment wedge of two fault blocks was identified in the hanging wall of the northwest fault at Wenxingchang (Figure 8C).

Additionally, the study area also exhibits frontal (rear) breakout structural styles and crenulated structural styles. The frontal or rear breakout structural style occurs within a compressional environment, especially in association with fault-related folding of the frontal strata, leading to fracturing and the development of breakout structures. These structures primarily serve for stress transmission and release. Crenulated structures generally occur within the gravity-sliding foreland belt or the interior of thrust structures. They are characterized by parallel and overlapping thrust faults stacked together, with the fault planes typically oriented in parallel.

4.4.3 3D detailed structural interpretation

Based on the latest 3D seismic and logging data in the study area and previous research findings, the application of well-seismic correlation, various cross-sections, and profile integration has solidified the understanding of the structural characteristics in the Qiulin area. The Qiulin structure is primarily a single-fault structure that has undergone overall inherited development. It is situated on the down-dip slope of the northern Sichuan ancient depression. Currently, the surface expression of the structure appears as a northwest-oriented nasal-shaped uplift with some localized high points. The hinterland structure exhibits an overall northwest-oriented slope, although there are variations in the different rock layers. Northwest-oriented anticlinal structures, similar to the surface features, primarily characterize the second Member.

Additionally, the slopes on the eastern and western flanks of the structure are steeper. Multiple local structural highs have developed on the anticlinal structure and its flanks, potentially serving as favorable areas for oil and gas accumulation. The highest part is a small-scale syncline located west of well QL17. This syncline exhibits a relatively large closure area, estimated to be approximately 2.3 km^2 (Figure 9).

The folding within the Shaximiao Formation of the Qiulin Structure is not intensely pronounced, exhibiting relatively gentle structural characteristics. Local occurrences of small-scale normal faults can be observed. In the southern parts of the study area, multiple normal faults extend downward to the base of the Shaximiao Formation, primarily oriented in a northwestern direction. The length of these faults ranges from 0.8 to 2.2 km. However, in the northern parts, the development of faults is not significant (Figure 10). Therefore, the Qiulin structure is characterized by a northwestern tilting nose-shaped structure. Within the Shaximiao Formation, there is a predominant development of normal faults. This suggests that

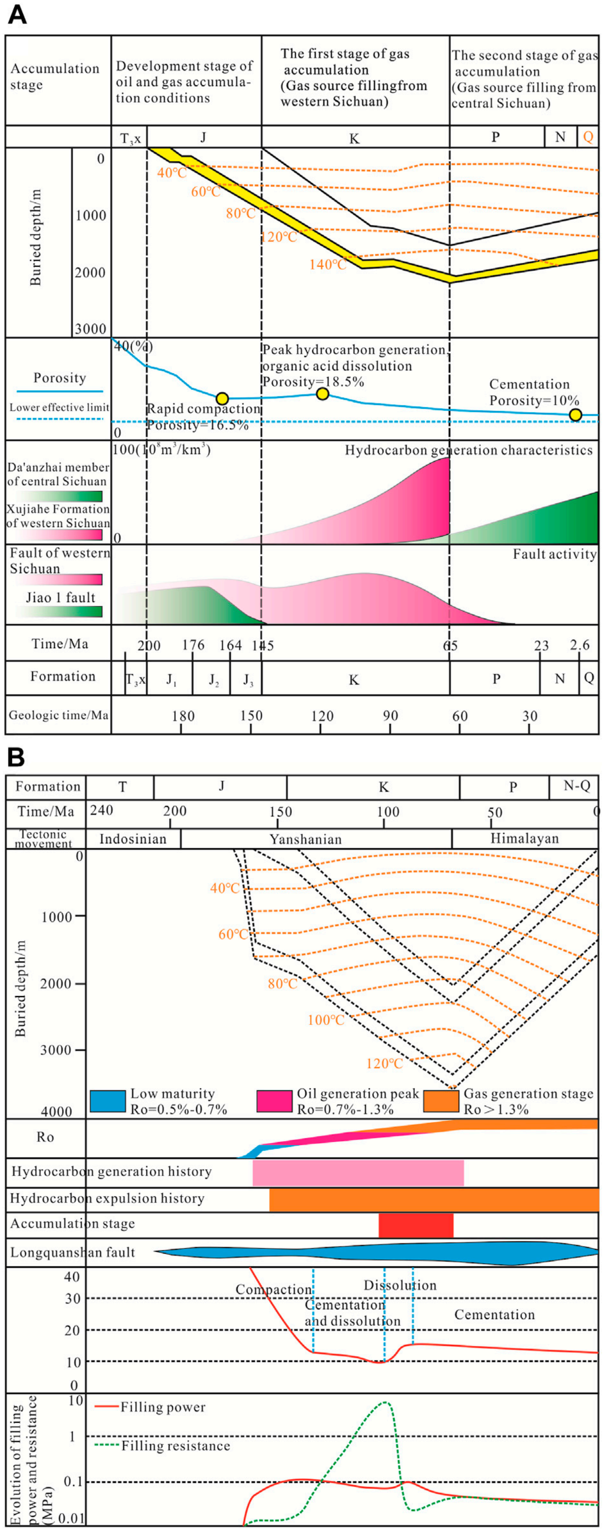

FIGURE 11
Temporal correlation of key factors in the gas reservoir formation. **(A)** The second Member of the Shaximiao Formation; **(B)** The 1st of the Shaximiao Formation.

the area was subjected to extensional tectonic forces, indicating its presence within a gravitational sliding tectonic subsidence zone during the Yanshan period. The area experienced extensional tectonic stress, resulting in a predominant uplift of the strata.

5 Discussion

5.1 Impact of tectonic movement on thermal evolution and distribution of source rocks

The Xujiahe Formation in the Early Jurassic is characterized by its multiple layers, significant sedimentary thickness, high organic matter abundance, and substantial hydrocarbon generation potential. It serves as the most crucial source rock of the Shaximiao Formation. The peak of hydrocarbon generation occurs during the Early Cretaceous to Paleogene. During the initial deposition of the Shaximiao Formation (the Middle Jurassic), hydrocarbon generation from the source rocks in the western Sichuan Basin did not reach its peak. During the Late Jurassic to Cretaceous period, abundant hydrocarbon generation occurred from the Xujiahe Formation source rocks in the western Sichuan Basin. Reservoir dissolution processes took place during this period. The frequent activity of the western Sichuan faults facilitated the migration and accumulation of hydrocarbons in deeper reservoirs, marking the first period of gas accumulation in the Shaximiao Formation. From the Cretaceous period to the present, the Da'anzhai Member of the Ziliujing Formation gradually entered the hydrocarbon generation window and began to produce a significant amount of hydrocarbons. At the same time, it was influenced by small-scale faults developed within the Jurassic strata. As the oil and gas concentration reached a certain level, there was significant intra-layer migration and regional accumulation. This led to subsequent adjustments in the gas reservoir during its later periods (Oliveira et al., 2021). Under the same sedimentary and structural background, differences in the fluid charging history can result in significant variations in the pressure evolution process of different gas reservoirs. The temporal relationship between the uplift and erosion of stratigraphic layers and the timing of oil and gas charging in the study area significantly impacts the pressure formation and evolution process of gas reservoirs (Figures 11A, B). The gas reservoirs in the Qiulin area are primarily charged by hydrocarbons from the source rock of the Xujiahe Formation. During the Late Jurassic to Cretaceous period, it generated substantial hydrocarbons. As stratigraphic layers underwent uplift and erosion, leading to a reduction in pressure, hydrocarbons migrated towards lower-potential-energy sandstone reservoirs (Li et al., 2009; Fang et al., 2011; Wu et al., 2012; Wood and Hazra, 2018). Dissolved-state natural gas began to exsolve and accumulate within the fluvial sandstone reservoirs of the Shaximiao Formation. In this process, the dynamic equilibrium between erosion-driven unloading and pressure reduction and hydrocarbon-charging-induced pressure increase, leads to the characteristic of these gas reservoirs maintaining near-normal pressure conditions.

5.2 Impact of tectonic movement on gas migration

The formation and evolution of the Sichuan Basin have undergone multiple tectonic movements, resulting in a complex system of faults and fractures, which serve as the dominant pathways

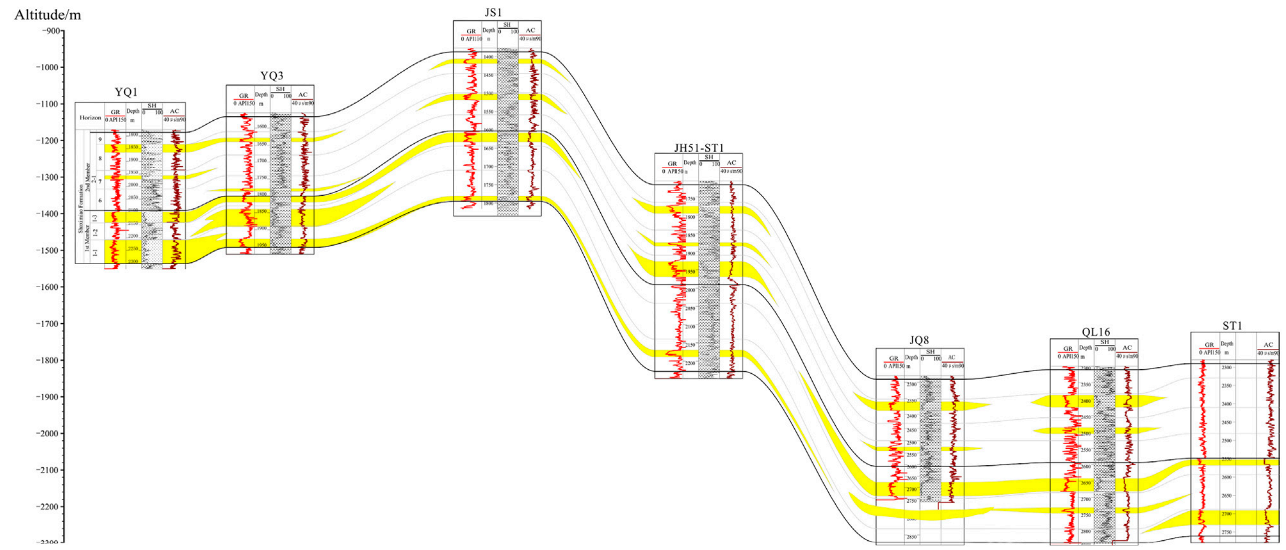

FIGURE 12
Interpreted correlations in composite cross section of 7 wells gas reservoir in the Shaximiao Formation.

for oil and gas migration (Xu and Gao, 2020; Li et al., 2021; Shan et al., 2021; Li et al., 2022). Therefore, faults and fractures are the dominant pathways for gas migration of the Shaximiao Formation reservoir in the Qiulin area. During the Yanshan period, the shallow layers (Xujiahe-Shaximiao Formations) were affected by a series of small-scale normal faults. In the peak hydrocarbon expulsion period of the Cretaceous to Paleogene, gas migrated along these minor faults and was preserved in the Shaximiao Formation reservoir.

The gas reservoirs are considered to be long-distance migrated accumulations (Zhu et al., 2013; Zhang et al., 2020; Zhang et al., 2022). The fault network plays a crucial role in migrating and accumulating gas from distant source rocks. The fault systems in the Shaximiao Formation can be classified into three types: 1) Faults that act as conduits between the Xujiahe and Shaximiao Formations; 2) Faults that facilitate communication between the Ziliujing or Lianggaoshan and other Formations; 3) Internal faults in the Shaximiao Formation. The first two categories are hydrocarbon-source faults, connecting the coal-bearing hydrocarbon source rocks of the Xujiahe Formation and the lacustrine hydrocarbon source rocks of the Lower Jurassic.

The hydrocarbon-source faults are characterized by their larger scale and longer extension distances in the western Sichuan Basin (Zhu et al., 2013; Zhang et al., 2023). These faults were generally active during the deposition of the Xujiahe to the Suining Formations. Some of these faults have remained active even in later periods. Due to the absence of Lower Jurassic hydrocarbon-source rocks in the western Sichuan area, only the gas generated from the Xujiahe Formation efficiently migrated within long-lived faults to the Shaximiao Formation. This gas preferentially filled the lower fluvial sandstones, resulting in an overall gas-rich reservoir in the 1st Member and the 1st layer of the second Member. However, varying degrees of gas enrichment in different sandstone layers within different areas indicate differences in gas migration and accumulation through the faults. The characteristics of hydrocarbon-source faults determine the overall enrichment gas features in the Shaximiao Formation. However, the small-scale faults also contribute to the localized variations in enrichment. Internal faults facilitate the connection between the upper and lower sandstone layers. The lower layer is enriched with natural gas from hydrocarbon-source faults, while the upper layer lacks such enrichment. However, gas exchange has occurred over time due to the communication effect of internal faults and the influence of later tectonic activity. In conclusion, the varying distribution of internal faults and their different roles in gas migration has led to the vertical enrichment of natural gas in multiple sandstone layers in the Shaximiao Formation (Figure 12).

5.3 Impact of tectonic movement on gas preservation

In the study area, the reservoir of the Shaximiao Formation mainly consists of distributary channel sands and river sands of the delta front. The overlying Suining Formation acts as the regional cap rock, and the Cretaceous Guankou Formation provides an extensive sealing layer distribution. This ensures the effective containment of oil and gas within the sandstone reservoirs, providing high-quality cap rock for reservoir accumulation (Wang and Shi, 2019; Cai, 2020; Fan et al., 2022; Wang et al., 2022). During the Yanshan period, the Songpan-Ganzi Plateau and the hinterland of the Longmenshan experienced a renewed uplift following the Indosinian tectonic movement. At this time, the frontal thrust zone of the Longmenshan overthrust belt exhibited a gravity-sliding structural system. During this period, the collision of the overthrust belt with the rift basin formed during the Indosinian period led to the strata’s bending and subsidence, resulting in a depression. During this time, fluvial-dominated sedimentation was predominant, with the sand bodies favoring natural gas accumulation. Furthermore, due to its extensional tectonic setting, a series of small normal faults formed, providing conduits for the migration of hydrocarbons from underlying source rocks. During the Middle-Late Yanshan and the Himalayan period, tectonic movements along these faults effectively charged the tight gas reservoirs of the Shaximiao Formation.

6 Conclusion

Based on the data from cores, outcrops, mud logging, logging, seismic interpretation, and burial history analysis, this paper takes of the tight gas reservoir in the Jurassic Shaximiao Formation in the Qiulin structure as an example. Through the study of source rocks, sedimentation, reservoir, and structural characteristics, this paper elucidates the impact of the Yanshan-Himalayan tectonic movement in the northern Longmenshan on the gas accumulation of the Shaximiao Formation. The following conclusions have been primarily drawn.

(1) Structural characteristics in the northern Longmenshan belt show variations during the Yanshan-Himalayan period. During the Yanshan period, the area was a unified unit influenced by gravity-sliding tectonics, divided into four zones: 'Uplifted Zone,' 'Slope Belt,' 'Foreland Belt,' and 'Depression Zone', known as the "Three Zones and One Belt". In the Himalayan period, vertical uplift led to complex structures, including duplex, overturned anticlines, fault-bend folds, and thrust wedges.

(2) Sedimentary history in the northern Longmenshan can be summarized as "rapid subsidence-slow subsidence-rapid uplift" phases. Early to Middle Yanshan saw rapid subsidence, followed by sustained slow subsidence. Late Yanshan witnessed increased tectonic activity and rapid uplift, continuing into the early Himalayan movement, followed by erosion.

(3) Faults and favorable reservoirs influence gas accumulation in the Qiulin area. The depocenter area favors gas accumulation in the gravitational sliding structural system. The coupling relationship between the foreland belt and the depocenter area facilitates the development of sedimentary environments, such as river-lake systems conducive to gas storage. Simultaneously, the depocenter area benefits from extensional tectonic activity that forms tensional normal faults, facilitating the migration of oil and gas. During the Himalayan period, compressional forces dominated, primarily modifying pre-existing traps or structures to varying degrees across different areas.

Data availability statement

The original contributions presented in the study are included in the article/Supplementary material, further inquiries can be directed to the corresponding author.

Author contributions

YY: Conceptualization, Data curation, Formal Analysis, Investigation, Methodology, Software, Supervision, Writing–original draft, Writing–review and editing. XL: Formal Analysis, Resources, Validation, Writing–original draft, Writing–review and editing. ZW: Software, Supervision, Writing–review and editing. WY: Conceptualization, Resources, Writing–review and editing.

Acknowledgments

YY and XL contributed to the paper's formal analysis, writing, reviewing, editing, and revising. ZW and WY contributed to the paper's editing and revising.

Conflict of interest

Authors YY and XL were employed by PetroChina Southwest Oil & Gasfield Company.

The remaining authors declare that the research was conducted in the absence of any commercial or financial relationships that could be construed as a potential conflict of interest.

Publisher's note

References

Alsalem, O. B., Fan, M. J., and Xie, X. Y. (2017). Late Paleozoic subsidence and burial history of the Fort Worth basin. *AAPG Bull.* 101 (11), 1813–1833. doi:10.1306/01251716016

Braunagel, M. J., Griffith, W. A., Biek, R. F., Hacker, D. B., Rowley, P. D., Malone, D. H., et al. (2023). Structural relationships across the sevier gravity slide of Southwest Utah and implications for catastrophic translation and emplacement processes of long runout landslides. *Geochem. Geophy. Geosy.* 24 (5), e2022GC010783. doi:10.1029/2022GC010783

Bretas, E. M., Leger, P., and Lemos, J. V. (2012). 3D stability analysis of gravity dams on sloped rock foundations using the limit equilibrium method. *Comput. Geotech.* 44, 147–156. doi:10.1016/j.compgeo.2012.04.006

Cai, M. F. (2020). Key theories and technologies for surrounding rock stability and ground control in deep mining. *J. Min. Strata Control Eng.* 2 (3), 033037. doi:10.13532/j.jmsce.cn10-1638/td.20200506.001

Dai, J., Ni, Y., Zou, C., Tao, S., Hu, G., Hu, A., et al. (2009). Stable carbon isotopes of alkane gases from the Xujiahe coal measures and implication for gas-source correlation in the Sichuan Basin, SW China. *Org. Geochem.* 40 (5), 638–646. doi:10.1016/j.orggeochem.2009.01.012

Dai, J. X., Liao, F. R., and Ni, Y. Y. (2013). Discussions on the gas source of the Triassic Xujiahe Formation tight sandstone gas reservoirs in Yuanba and Tongnanba, Sichuan Basin: an answer to Yinfeng et al. *Petrol. explor. Dev.* 40 (2), 250–256. doi:10.11698/PED.2013.02.17

Dai, J. X., Ni, Y. Y., Qin, S. F., Huang, S. P., Peng, W. L., and Han, W. X. (2018). Geochemical characteristics of ultra-deep natural gas in the Sichuan Basin, SW China. *Petrol. explor. Dev.* 45 (4), 619–628. doi:10.1016/s1876-3804(18)30067-3

Deng, B., Liu, S. G., Jiang, L., Zhao, G. P., Huang, R., Li, Z. W., et al. (2018). Tectonic uplift of the Xichang Basin (SE Tibetan Plateau) revealed by structural geology and thermochronology data. *Basin Res.* 30, 75–96. doi:10.1111/bre.12243

Deng, B., Liu, S. G., Liu, S., Jansa, L., Li, Z. W., and Zhong, Y. (2013). Progressive indosinian NS deformation of the jiaochang structure in the songpan-ganzi fold-belt, western China. *PLoS One* 8 (10), e76732. doi:10.1371/journal.pone.0076732

Deng, P., Fang, C., Deng, M. Z., and Zhao, L. (2021). New insights into structural characteristics in central-northern Longmen Mountains: implications for multiple-decollement deformation. *Petrol. Geol. Exp.* 43 (1), 45–55. doi:10.11781/sysydz202101045

Ding, X., Li, Z. Q., Li, J. N., Li, H. K., Chen, X., Liu, R., et al. (2022). Age limit of diabase dyke intrusion in Tangwangzhai-Yangtianwo compound syncline in the northern section of Longmen Mountain, western Sichuan Province. *Geol. Bull. China* 41 (8), 1409–1416. doi:10.12097/j.issn.1671-2552.2022.08.008

Fan, C. H., Xie, H. B., Li, H., Zhao, S. X., Shi, X. C., Liu, J. F., et al. (2022). Complicated fault characterization and its influence on shale gas preservation in the southern margin of the Sichuan Basin, China. *Lithosphere* 2022 (12), 8035106. doi:10.2113/2022/8035106

Fang, Y., Liao, Y., Wu, L., and Geng, A. (2011). Oil-source correlation for the paleo-reservoir in the Majiang area and remnant reservoir in the Kaili area, South China. *J. Asian Earth Sci.* 41, 147–158. doi:10.1016/j.jseaes.2011.01.012

Freeman, K. H., Hayes, J. M., Trendel, J. M., and Albrecht, P. (1990). Evidence from carbon isotope measurements from diverse origins of sedimentary hydrocarbons. *Nature* 343, 254e256. doi:10.1038/343254a0

Gao, Z., Fan, Y., Xuan, Q., and Zheng, G. (2020). A review of shale pore structure evolution characteristics with increasing thermal maturities. *Adv. Geo-Energy Res.* 4 (3), 247–259. doi:10.46690/ager.2020.03.03

Gu, M. X., Xie, R. H., and Jin, G. W. (2021). A machine-learning based quantitative evaluation of the fluid components on T-2-D spectrum. *Mar. Petrol. Geol.* 134, 105353. doi:10.1016/j.marpetgeo.2021.105353

Gunderson, K. L., Anastasio, D. J., Pazzaglia, F. J., and Kodama, K. P. (2018). Intrinsically variable blind thrust faulting. *Tectonics* 37 (5), 1454–1471. doi:10.1029/2017TC004917

He, S., Qin, Q. R., Li, H., and Zhao, S. X. (2022a). Geological characteristics of deep shale gas in the Silurian Longmaxi Formation in the southern Sichuan Basin, China. *Front. Earth Sci.* 9, 818543. doi:10.3389/feart.2021.818155

He, S., Qin, Q. R., Li, H., and Wang, S. L. (2022b). Deformation differences in complex structural areas in the southern Sichuan Basin and its influence on shale gas preservation: a case study of Changning and Luzhou area. *Front. Earth Sci.* 9, 818155. doi:10.3389/feart.2021.818534

Huang, C., Zhou, X. J., Shen, Y. W., Wen, X., Zhai, M. L., and Tan, X. C. (2022). Stratigraphic age distribution and sedimentary filling of the Guanwushan Formation in the northern segment of Longmenshan Mountains, and its palaeogeographic significance. *Acta Geol. Sin.* 96 (7), 2255–2271. doi:10.19762/j.cnki.dizhixuebao.2022056

Jiang, D. Q., Wang, M. M., Song, G. H., Yan, B., and Feng, W. (2020). Transition from fault-propagation folds to fault-bend folds determined by along-strike variations of structural styles and fault displacement-distance relationships: the Sumatou anticline, Sichuan Basin, China. *J. Struct. Geol.* 131, 103951. doi:10.1016/j.jsg.2019.103951

Jin, W. Z., Tang, L. J., Yang, K. M., Wan, G. M., Lu, Z. Z., and Yu, Y. X. (2009). Transfer zones within the Longmen Mountains thrust belt, SW China. *Geosci. J.* 13 (1), 1–14. doi:10.1007/s12303-009-0001-9

Jin, W. Z., Tang, L. J., Yang, K. M., Wan, G. M., Lu, Z. Z., and Yu, Y. X. (2010). Structural styles of longmen mountain thrust belt, SW China. *J. Earth Sci.* 21 (1), 19–31. doi:10.1007/s12583-010-0010-7

Lan, S. R., Song, D. Z., and Li, Z. L. (2021). Experimental study on acoustic emission characteristics of fault slip process based on damage factor. *J. Min. Strata Control Eng.* 3 (3), 033024. doi:10.13532/j.jmsce.cn10-1638/td.20210510.002

Lei, Y. L., Jia, C. Z., Li, B. L., Wei, G. Q., Chen, Z. X., and Shi, X. (2012). Meso-Cenozoic tectonic events recorded by apatite fission track in the northern Longmen-Micang Mountains region. *Acta Geol. sin.-eng. Ed.* 81 (1), 153–165. doi:10.1111/j.1755-6724.2012.00618.x

Li, D., Hong, F. L., Shao, Y. J., Jia, Y. P., Yong, Q. C., Yuan, F. C., et al. (2009). New carbon isotope stratigraphy of the Ediacaran-Cambrian boundary interval from SW China: implications for global correlation. *Geol. Mag.* 146, 465e484. doi:10.1017/S0016756809006268

Li, H., Tang, H. M., Qin, Q. R., Zhou, J. L., Qin, Z. J., Fan, C. H., et al. (2019a). Characteristics, formation periods and genetic mechanisms of tectonic fractures in the tight gas sandstones reservoir: a case study of Xujiahe Formation in YB area, Sichuan Basin, China. *J. Petrol. Sci. Eng.* 178, 723–735. doi:10.1016/j.petrol.2019.04.007

Li, H., Tang, H. M., Qin, Q. R., Wang, Q., and Zhong, C. (2019b). Effectiveness evaluation of natural fractures in Xujiahe Formation of Yuanba area, Sichuan basin, China. *Arab. J. Geosci.* 12 (6), 194. doi:10.1007/s12517-019-4292-5

Li, H., Wang, Q., Qin, Q. R., and Ge, X. Y. (2021). Characteristics of natural fractures in an ultradeep marine carbonate gas reservoir and their impact on the reservoir: a case study of the Maokou Formation of the JLS Structure in the Sichuan Basin, China. *Energy Fuel* 35 (16), 13098–13108. doi:10.1021/acs.energyfuels.1c01581

Li, J., Li, H., Yang, C., Ren, X. H., and Li, Y. D. (2023). Geological characteristics of deep shale gas and their effects on shale fracability in the Wufeng–Longmaxi Formations of the southern Sichuan Basin, China. *Lithosphere* 2023 (1), 4936993. doi:10.2113/2023/4936993

Li, J., Li, H., Yang, C., Wu, Y. J., Gao, Z., and Jiang, S. L. (2022). Geological characteristics and controlling factors of deep shale gas enrichment of the Wufeng-Longmaxi Formation in the southern Sichuan Basin, China. *Lithosphere* 2022 (12), 4737801. doi:10.2113/2022/4737801

Liu, K. X., Chen, J. F., Fu, R., Wang, H., Luo, B., Chen, Z. Y., et al. (2023). Distribution characteristics and controlling factors of helium-rich gas reservoirs. *Gas. Sci. Eng.* 110, 204885. doi:10.1016/j.jgsce.2023.204885

Liu, S. G., Yang, Y., Deng, B., Zhong, Y., Wen, L., Sun, W., et al. (2021). Tectonic evolution of the Sichuan Basin, southwest China. *Earth Sci. Rev.* 213, 103470. doi:10.1016/j.earscirev.2020.103470

Lu, X. L., Li, M. J., Wei, T. Q., Wu, C. J., Tang, Y. J., Wang, X. J., et al. (2022). Composition of light hydrocarbons in Jurassic tight oils in the central Sichuan Basin, China: origin and source rock correlation. *J. Petrol. Geol.* 45 (2), 163–177. doi:10.1111/jpg.12811

Luo, L., Jia, D., Qi, J. F., Wei, G. Q., and Deng, F. (2013). Tectono-sedimentary evolution of the late triassic Xujiahe Formation in the Sichuan Basin. *Acta Geol. Sin-Eng. Ed.* 87 (6), 1554–1568. doi:10.1111/1755-6724.12159

Lyu, Q., Wang, W. M., Jiang, Q. C., Yang, H. F., Deng, H., Zhu, J., et al. (2023). Basement reservoirs in China: distribution and factors controlling hydrocarbon accumulation. *Minerals* 13 (8), 1052. doi:10.3390/min13081052

Ma, D., Zhang, Z. J., Zhou, C. M., Cheng, D. W., Hong, H. T., Meng, H., et al. (2023). Element geochemical characteristics and geological significance of mudstones from the middle jurassic Shaximiao Formation in Sichuan Basin, southwest China. *ACS Omega* 8 (33), 29979–30000. doi:10.1021/acsomega.3c01496

Martins, G., Ettensohn, F. R., and Knutsen, S. M. (2023). Use of backstripping in the Triassic-Middle Jurassic, south-central Barents Sea shelf succession to understand regional tectonic mechanisms and structural responses. *Tectonophysics* 853, 229797. doi:10.1016/j.tecto.2023.229797

Mu, H., Yan, D. P., Qiu, L., Yang, W.-X., Kong, R.-Y., Gong, L.-X., et al. (2019). Formation of the late triassic Western sichuan foreland basin of the qinling orogenic belt, SW China: sedimentary and geochronological constraints from the Xujiahe Formation. *J. Asian Earth Sci.* 183, 103938. doi:10.1016/j.jseaes.2019.103938

Oliveira, G. P., Rodrigues, T. N. E., and Lie, K. A. (2021). GAWPS: a MRST-based module for wellbore profiling and graphical analysis of flow units. *Adv. Geo-Energy Res.* 6 (1), 38–53. doi:10.46690/ager.2022.01.04

Petermann, H., Lyson, T. R., Miller, I. M., and Hagadorn, J. W. (2022). Crushed turtle shells: proxies for lithification and burial-depth histories. *Geosphere* 18 (5), 1524–1537. doi:10.1130/GES02513.1

Sang, M., Xiao, W. J., Bakirov, A., Orozbaev, R., Sakiev, K., and Zhou, K. F. (2017). Oblique wedge extrusion of UHP/HP complexes in the Late Triassic: structural analysis and zircon ages of the Atbashi Complex, South Tianshan, Kyrgyzstan. *Int. Geol. Rev.* 59 (10), 1369–1389. doi:10.1080/00206814.2016.1241163

Shan, S. C., Wu, Y. Z., Fu, Y. K., and Zhou, P. H. (2021). Shear mechanical properties of anchored rock mass under impact load. *J. Min. Strata Control Eng.* 3 (4), 043034. doi:10.13532/j.jmsce.cn10-1638/td.20211014.001

Thingbaijam, K. K. S., Chingtham, P., and Nath, S. K. (2009). Seismicity in the North-west frontier province at the Indian-Eurasian Plate convergence. *Seismol. Res. Lett.* 80 (4), 599–608. doi:10.1785/gssrl.80.4.599

Wang, C., and Shi, G. (2019). Redox condition and organic carbon accumulation mechanism in the Cryogenian Nanhua Basin, South China: insights from iron chemistry and sulfur, carbon, oxygen isotopes of the Datangpo Formation. *Adv. Geo-Energy Res.* 3 (1), 67–75. doi:10.26804/ager.2019.01.05

Wang, Z., Hao, C., Jin, H., Cui, J., Wu, X., Bo, D., et al. (2023). Geochemical characteristics and hydrocarbon generation potential of main source rocks in the Upper Triassic Xujiahe Formation, Sichuan Basin, China. *Front. Earth Sci.* 11, 1233959. doi:10.3389/feart.2023.1233959

Wang, S. L., Li, H., Lin, L. F., and Yin, S. (2022). Development characteristics and finite element simulation of fractures in tight oil sandstone reservoirs of Yanchang Formation in western Ordos Basin. *Front. Earth Sci.* 9, 823855. doi:10.3389/feart.2021.823855

Wei, T. Q., Zhang, B. J., and Wang, X. J. (2021). Sedimentary characteristics of fluvial facies and analysis of reservoir differences in the second member of Jurassic Shaximiao Formation in Qiulin Area, Sichuan Basin. *Sci. Technol. Eng.* 21 (29), 12438–12446.

Wen, L., Wang, W. Z., Zhang, J., and Luo, B. (2017). Classification of sinian dengying Formation and sedimentary evolution mechanism of gaoshiti-moxi area in central Sichuan Basin. *Acta Petrol. Sin.* 33 (4), 1285–1294.

Wood, D. A., and Hazra, B. (2018). Pyrolysis S2-peak characteristics of Raniganj shales (India) reflect complex combinations of kerogen kinetics and other processes related to different levels of thermal maturity. *Adv. Geo-Energy Res.* 2 (4), 343–368. doi:10.26804/ager.2018.04.01

Wu, L. L., Liao, Y. H., Fang, Y. X., and Geng, A. S. (2012). The study on the source of the oil seeps and bitumens in the Tianjingshan structure of the northern Longmen Mountain structure of Sichuan Basin, China. *Mar. Petrol. Geol.* 37 (1), 147–161. doi:10.1016/j.marpetgeo.2012.05.011

Wu, Z. J., Li, T. F., Ji, S., Zhou, Q., and Tian, H. (2023). Gas generation from coal and coal-measure mudstone source rocks of the Xujiahe Formation in the western sichuan depression, Sichuan Basin. *J. Earth Sci.* 34 (4), 1012–1025. doi:10.1007/s12583-022-1627-z

Xia, L., Liu, Z., Li, W. L., Lu, C. J., Yang, X. G., and Liu, M. J. (2018). Ternary analytic porosity-reduction model of sandstone compaction trend and its significance in petroleum geology: a case study of tight sandstones in Permian Lower Shihezi Formation of Shilijiahan area, Ordos Basin, China. *Petrol. explor. Dev.* 45 (2), 290–301. doi:10.1016/S1876-3804(18)30032-6

Xie, G. Y., Hu, X., Wang, X. L., Yang, T., Tian, Y. Y., Xin, R. Y., et al. (2023). Structural analysis and exploration prospects of nappe-piedmont structural belt in northern Longmenshan area, Sichuan Basin. *Nat. Gas. Explor. Dev.* 46 (1), 11–17. doi:10.12055/gaskk.issn.1673-3177.2023.01.002

Xie, G. Y., Tian, Y. Y., Liu, B., Fan, S. H., Ma, Y. H., and Zhang, Y. L. (2022). Formation conditions and controlling factors of high-quality reservoirs in the middle jurassic Shaximiao Formation of the southwestern Sichuan Basin. *Nat. Gas. Ind.* 42 (7), 45–54. doi:10.3787/j.issn.1000-0976.2022.07.005

Xu, L., Li, Q., Myers, M., and Tan, Y. S. (2022). Effects of bedding direction on brine imbibition in Lower Shaximiao tight sandstone: an NMR analysis. *J. Petrol. Sci. Eng.* 210, 110006. doi:10.1016/j.petrol.2021.110006

Xu, N. Z., and Gao, C. (2020). Study on the special rules of surface subsidence affected by normal faults. *J. Min. Strata. Control Eng.* 2 (1), 011007. doi:10.13532/j.jmjsce.cn10-1638/td.2020

Yang, M. Y., Sun, W., Gong, T. T., Zhao, H., Lu, N. Z., Zhao, D. J., et al. (2023b). Characteristics and significance of the "mung bean rock" of the middle triassic leikoupo formation at majiaoba, northern section of longmen mountains, sichuan. *Min. Petrol.* 43 (2), 121–131. doi:10.19719/j.cnki.1001-6872.2023.02.12

Yang, W. W., Zhang, C., Shi, X. L., Cui, Y. J., and Zhang, Z. S. (2023c). Reconstruction of LWD-NMR T2 water spectrum and fluid recognition based on microscopic pore structure constraints. *Gas. Sci. Eng.* 221, 211386. doi:10.1016/j.geoen.2022.211386

Yang, Y., Li, Z. Q., and Long, W. (2022). New exploration field of piedmont complex fault-fold belt in the northern Longmen Mountain, Sichuan, China. *J. Chengdu Univ. Technol.* 49 (4), 414–423. doi:10.3969/j.issn.1671-9727.2022.04.02

Yang, Y. M., Bai, X. L., Yi, H. Y., Liu, R., Ma, H. L., Han, S., et al. (2023a). Progress and potential of natural gas exploration in the complex tectonic belt of Longmen Mountain: learning from drilling achievements of Well Hongxing 1. *Nat. Gas. Ind.* 43 (2), 1–14. doi:10.3787/j.issn.1000-0976.2023.02.001

Yang, Y. M., Chen, C., Wen, L., Chen, X., Liang, H., Liu, R., et al. (2018). Characteristics of buried structures in the northern Longmenshan mountains and its significance to oil and gas exploration in the Sichuan Basin. *Nat. Gas. Ind.* 38 (8), 8–15. doi:10.3787/j.issn.1000-0976.2018.08.002

Yu, G., Liu, C., Zhang, L., and Fang, L. (2021). Parameter sensitivity and economic analyses of an interchange-fracture enhanced geothermal system. *Adv. Geo-Energy Res.* 5 (2), 166–180. doi:10.46690/ager.2021.02.06

Zhang, D. D., Li, S. J., and Zhang, X. (2020). Experimental study on mining fault activation characteristics by a distributed optical fiber system. *J. Min. Strata Control Eng.* 2 (1), 013018. doi:10.13532/j.jmsce.cn10-1638/td.2020.01.010

Zhang, P. S., Xu, D. Q., and Fu, X. (2022). Evaluation of hydraulic conductivity based on fault confinement studies. *J. Min. Strata Control Eng.* 4 (2), 023033. doi:10.13532/j.jmsce.cn10-1638/td.20211215.001

Zhang, T. T., Wang, H., Yue, Y., Huang, C. Y., and Zhang, L. W. (2009). Cenozoic subsidence features of Beitang Sag and relationship with tectonic evolution. *J. Earth Sci.* 20 (4), 746–754. doi:10.1007/s12583-009-0061-9

Zhang, Z. H., Wang, H. Y., Yang, X. B., Su, X. Y., Tian, Y. C., Wang, J., et al. (2023). Seismic interpretation and geological evaluation of hydrocarbon source rocks in volcanic-rich continental lacustrine rift basins: a case study of the Lower Cretaceous Yingcheng Formation from the Changling Fault Depression in the Songliao Basin, NE China. *Geoenergy Sci. Eng.* 221, 211397. doi:10.1016/j.geoen.2022.211397

Zhu, B. Y., Meng, J. H., Pan, R. F., Hu, H. Y., Song, C., Zhu, Z. P., et al. (2023). New insights into the evaluation criteria for high-quality deep marine shale gas reservoirs in the Longmaxi formation: evidence from organic matter pore development characteristics. *Front. Ecol. Evol.* 11, 1138991. doi:10.3389/fevo.2023.1138991

Zhu, G. Y., Yang, H. J., Zhang, B., Su, J., Zhang, C., Zhang, K., et al. (2013). Ultra-long distance migration of hydrocarbon. *Acta Petrol. Sin.* 29 (9), 3192–3212.

Zhu, Y. P., and Li, P. (2019). One improved burial history recovery method and computer model establishment. *J. Petrol. Explor. Prod. Te.* 9 (1), 75–86. doi:10.1007/s13202-018-0502-z

frontiers | Frontiers in Earth Science

TYPE Original Research
PUBLISHED 08 January 2024
DOI 10.3389/feart.2023.1334175

OPEN ACCESS

EDITED BY
Hu Li,
Southwest Petroleum University, China

REVIEWED BY
Xiaoping Zhou,
Chongqing University, China
Liuke Huang,
Southwest Petroleum University, China
Jun Lu,
Shenzhen University, China

*CORRESPONDENCE
Jingwei Zheng,
✉ zhengjingwei@cqu.edu.cn

RECEIVED 06 November 2023
ACCEPTED 18 December 2023
PUBLISHED 08 January 2024

CITATION
Wang Y, Wang M, Niu Z, Chen Z, Min R and Zheng J (2024), Fracture initiation pressure prediction of hydraulic fracturing for layered reservoirs considering borehole deformation.
Front. Earth Sci. 11:1334175.
doi: 10.3389/feart.2023.1334175

Fracture initiation pressure prediction of hydraulic fracturing for layered reservoirs considering borehole deformation

Yingwei Wang[1,2], Man Wang[1,2], Zehua Niu[1,2], Zhaofan Chen[1,2], Rui Min[1,2] and Jingwei Zheng[3]*

[1]Pingdingshan Tianan Coal Mining Co., Ltd., Pingdingshan, China, [2]State Key Laboratory of Coking Coal Exploitation and Comprehensive Utilization, Pingdingshan, China, [3]State Key Laboratory of Coal Mine Disaster Dynamics and Control, Chongqing University, Chongqing, China

Accurately predicting fracture initiation pressure is crucial for successfully applying hydraulic fracturing technology in layered reservoirs. However, existing models overlook the effects of rock anisotropy and borehole deformation. In this study, we simplified the layered reservoir to a transversely isotropic medium and developed a model to estimate borehole deformation precisely. Based on this estimated deformation, we created a model to predict fracture initiation pressure in hydraulic fracturing. By comparing previous models and experimental data, we validated the effectiveness of these proposed models. We examined the impacts of various factors on borehole deformation, fracture initiation pressure, and initiation angle. The results revealed that circular boreholes in layered reservoirs deform into elliptical boreholes under *in situ* stress, with the major axis not aligning with the principal stress direction, which highlights the significant impact of rock anisotropy on borehole deformation. Furthermore, the fracture initiation pressure of hydraulic fracturing either increases or decreases following borehole deformation, depending on specific geological parameters. The calculated initiation angle after borehole deformation is within 10°, closer to previous experimental results, underscoring the notable effect of borehole deformation on hydraulic fracturing. Our research indicates that the impact of borehole deformation on hydraulic fracturing is significant and should not be overlooked. This finding will offer fresh avenues for further study in the field of hydraulic fracturing.

KEYWORDS

borehole deformation, fracture initiation pressure, hydraulic fracturing, anisotropy, initiation angle

1 Introduction

Hydraulic fracturing technology is extensively utilized in layered reservoirs such as shale, tight sandstone, and coal (Abdulelah et al., 2018; Qu et al., 2022a; Lu et al., 2022). This method efficiently enhances reservoir permeability by creating artificial fractures, thereby significantly boosting the extraction of unconventional natural gas (Song et al., 2017; Zhao et al., 2020a; He et al., 2022a; He et al., 2022b; Li et al., 2022; Zhao et al., 2022; Liu et al., 2023). Accurately predicting and minimizing the fracture initiation pressure (FIP) near boreholes in rocks and comprehending fracture extension behavior is crucial (Wu et al., 2020; Huang et al., 2023a). The analysis of FIP through a mechanistic-based theoretical approach is widely acknowledged as an effective method (Shou and Zhou, 2021; Ren et al., 2022) and has been extensively researched by numerous scholars.

Hubbert and Willis. (1957) were the pioneers who proposed a theory to predict FIP. Subsequently, numerous scholars contributed significantly to the development of related theories (Eaton, 1969; Constant and Jr, 1988; Detournay and Cheng, 1988; Oriji and Ogbonna, 2012; Ma et al., 2017; Zhang et al., 2018.). While the accuracy of predicted values has improved over time and can generally meet basic engineering requirements, there are instances where a discrepancy exists between predicted and actual values (Ma et al., 2019). This discrepancy can be attributed to these models' assumption of uniform mechanical properties in all directions. At the same time, shale, tight sandstone, and coal exhibit significant anisotropic characteristics with varying mechanical properties on parallel and perpendicular bedding planes. As a result, these reservoirs typically be simplified as transverse isotropic mediums (Espinoza et al., 2013; Li and Zhang, 2019; Ma et al., 2021). Existing laboratory experiments on fracturing have shown that the FIP of hydraulic fracturing varies as the angle between the bedding plane and the borehole changes, highlighting the significant impact of rock anisotropy, a factor acknowledged by numerous scholars (Qu et al., 2022a; Liu et al., 2022; Zhang et al., 2023). Numerous researchers have conducted theoretical examinations on the influence of rock anisotropy. Aadnoy and Chenvert. (1987) were the first to propose a stability model for boreholes using anisotropic body theory. Since then, numerous researchers have adopted similar approaches to investigate the FIP for boreholes in transversely isotropic formation (Ong and Roegiers, 1995; Gupta and Zaman, 1999; Prioul et al., 2011; Zhu et al., 2014.). Do et al. (2017) developed a model incorporating hydraulic and mechanical anisotropy to predict the FIP of boreholes with permeable and impermeable boundaries. Sesetti and Ghassemi. (2018) also developed a model that considers elasticity and fracture anisotropy to predict FIP for boreholes in transversely isotropic formations. Ma et al. (2022) developed a model that considers the anisotropy of rock strength to predict FIP for both vertical and inclined boreholes. In addition, the heterogeneity of the reservoir influences the propagation of fractures (Wu et al., 2023), resulting in the creation of intricate fractures (Zhou et al., 2020; Huang et al., 2023b), which also significantly impact the extraction of reservoir gas (Zhao and Zhou, 2020b; Song et al., 2020). Therefore, it is crucial to consider the effect of reservoir anisotropy on the efficiency of hydraulic fracturing.

Several scholars have developed models to predict FIP for transversely isotropic reservoirs in hydraulic fracturing. However, these models are specifically designed for the circular borehole. Field logging data shows that circular boreholes can deform due to stress and mechanical anisotropy (Figure 1) (Zoback et al., 2003; Pierdominici et al., 2020; Han et al., 2021). Various studies have investigated the effects of borehole deformation. For instance, Haimson and Lee. (2004) discovered that circular boreholes in sandstone deform significantly and assume an elliptical shape under uneven loading. Zhai et al. (2015) observed that a circular borehole in an on-site coal seam became elliptical after redistributing *in situ* stresses. Gao and Ren. (2022) found that circular boreholes deform into elliptical boreholes due to stress exertion in hydraulic fracturing. Several researchers have studied the stress distribution around elliptical boreholes and concluded that changes in borehole shape affect the distribution of the stress field, which in turn affects the destructive behavior of the rock (Qi et al., 2018; Chen et al., 2020; Zhong et al., 2021). Scholars have established models based on theoretical mechanics to compute the deformation of circular boreholes and estimate their precise dimensions (Zou et al., 2018; Fang et al., 2022; Han et al., 2023). However, these models primarily consider the impact of stress anisotropy while disregarding the influence of mechanical anisotropy. Consequently, these models are not suitable for anisotropic formations. Moreover, current fracturing models have failed to establish a correlation between borehole deformation and FIP.

In this study, we developed a model to estimate borehole deformation in the layered reservoir. Subsequently, we formulated a mechanical model to predict the FIP in hydraulic fracturing, considering the shape and magnitude of the estimated borehole deformation. Our proposed model was verified by comparing them with previous models. Moreover, we conducted a thorough analysis to evaluate the influence of different factors on the extent of borehole deformation, FIP, and initiation angle.

2 FIP model after borehole deformation

2.1 Analysis of circular borehole deformation

This study defines compressive stress as positive and tensile stress as negative stress. The layered reservoir is assumed to be a homogeneous, continuous, linear transverse isotropic medium that undergoes small deformations. Due to the length of the boreholes being significantly more significant than their diameter, the generalized plan strain condition is applicable. In addition, this study ignores the effects of temperature, chemical environment, and seepage.

Assuming the bedding plane exhibits symmetry along the z-axis (Figure 2A), only stresses in the x_1oy_1 plane impact the borehole deformation and FIP, which allows for simplifying the analysis to a planar problem (Heng et al., 2021) (Figure 2B). In Figure 2B, we established the *in situ* stress coordinate system (x_1oy_1) is established along the direction of the *in situ* stress. The x_1 and y_1 axes align with the direction of the *in situ* stresses σ_H and σ_h, respectively. Additionally, we defined a bedding plane coordinate system (x_2oy_2) along the direction of the bedding plane. The x_2 and y_2 axes are parallel and perpendicular to the bedding plane (Figure 2C). We denoted the angle between the x_1 and x_2 axes as α. By employing the coordinate transformation formula (1), we can obtain the stress components in the bedding plane coordinate system.

$$\begin{cases} \sigma_\mathrm{x1} = \sigma_\mathrm{H}\cos^2\alpha + \sigma_\mathrm{h}\sin^2\alpha \\ \sigma_\mathrm{y1} = \sigma_\mathrm{H}\sin^2\alpha + \sigma_\mathrm{h}\cos^2\alpha \\ \tau_\mathrm{xy1} = (\sigma_\mathrm{h} - \sigma_\mathrm{H})\sin\alpha\cos\alpha \end{cases} \tag{1}$$

Where σ_h and σ_H are the minimum and maximum horizontal principal stresses, respectively, MPa; α is the inclination angle of the bedding plane, °.

The borehole deformation under generalized plane strain conditions is illustrated below (Please refer to Appendix A for detailed derivation):

$$\begin{cases} u = \left(\beta_{11}\left(1 + \sqrt{p+2q}\right)\sigma_\mathrm{x1} - q\beta_{11}\sigma_\mathrm{y1}\right)R\cos\theta \\ \quad + \left(\sqrt{p+2q}\,\beta_{11} + q\beta_{11} + \beta_{12}\right)\tau_\mathrm{xy1}R\sin\theta \\ v = \left(\dfrac{\sqrt{p+2q} + q}{q}\sigma_\mathrm{y1} - \dfrac{\sigma_\mathrm{x1}}{q}\right)\beta_{22}R\sin\theta \\ \quad + \left(\beta_{12} + \dfrac{\sqrt{p+2q} + 1}{q}\beta_{22}\right)\tau_\mathrm{xy1}R\cos\theta \end{cases} \tag{2}$$

Where u and v are the displacement in the directions of x_1 and y_1 axes, m.

The new coordinates points of the borehole wall, resulting from the borehole deformation under the influence of *in situ* stress, are as follows:

$$\begin{cases} x_1 = R\cos\theta - u \\ y_1 = R\sin\theta - v \end{cases} \tag{3}$$

2.2 Determination of shape after circular borehole deformation

The coordinates points of the borehole wall after the borehole deformation in Equation 3 satisfy the following equation:

$$Ax_1^2 + Bx_1y_1 + Cy_1^2 = 1 \tag{4}$$

where:

$$\begin{cases} A = \dfrac{e^2 + f^2}{(ce - df)^2}; B = \dfrac{-2cf - 2de}{(ce - df)^2}; C = \dfrac{c^2 + d^2}{(ce - df)^2} \\ c = R - \left(1 + \sqrt{p + 2q}\right)\beta_{11}R\sigma_{x1} - q\beta_{11}R\sigma_{y1} \\ d = -\left(\sqrt{p + 2q}\,\beta_{11} + q\beta_{11} + \beta_{12}\right)R\tau_{xy1} \\ e = R - \left(\dfrac{\sqrt{p + 2q}}{q} + 1\right)\beta_{22}R\sigma_{y1} + \dfrac{\beta_{22}}{q}R\sigma_{x1} \\ f = -\left(\beta_{12} + \dfrac{1 + \sqrt{p + 2q}}{q}\beta_{22}\right)R\tau_{xy1} \end{cases}$$

Equation 4 is the general equation of the ellipse, indicating that circular boreholes in anisotropic reservoirs will deform into elliptical boreholes under the effect of the *in situ* stress. This observation aligns with the logging data (Zoback et al., 2003; Han et al., 2021), indicating that the proposed model is consistent with the actual situation.

The major axis (a), minor axis (b), and angle β between the major axis of the ellipse and the coordinate axis x_1 can be determined using Equation 4 and relevant mathematical knowledge (β is defined as the deflection angle, the calculation procedure is provided in Appendix B).

$$\begin{cases} a = \sqrt{\dfrac{2}{A + C - \sqrt{(A - C)^2 + B^2}}} \\ b = \sqrt{\dfrac{2}{A + C + \sqrt{(A - C)^2 + B^2}}} \\ \beta = \dfrac{1}{2}\arctan\left(\dfrac{B}{A - C}\right) \end{cases} \tag{5}$$

When μ_1=μ_2=i, β=0, E_1=E_2, ν_{12}=ν_{13}, we can simplify the model to evaluate the deformation of a borehole in an isotropic stratum under positive stress; at this time, the major axis, minor axis, and deflection angle in Equation 5 are as follows:

$$a = R\left(1 - \frac{1 - \nu^2}{E}(3\sigma_H - \sigma_h)\right), b = R\left(1 - \frac{1 - \nu^2}{E}(3\sigma_h - \sigma_H)\right),$$
$$\beta = 0 \tag{6}$$

Equation 6 is consistent with the borehole deformation model in isotropic reservoirs, as Zou et al. (2018) established, indicating the proposed model's precision.

2.3 Stress distribution around the circular borehole after deformation

We analyzed the stress distribution around the elliptical borehole in hydraulic fracturing, considering the relevant parameters of the circular borehole after deformation, established a new coordinate system (x_3oy_3) (Figure 3), in which the x_3 and y_3 axes are parallel to the major and minor axes of the elliptical borehole, respectively. By applying the coordinate transformation formula (7), we obtained the stress components of the *in situ* stress in this coordinate system:

$$\begin{cases} \sigma_{x2} = \sigma_H\cos^2(\alpha + \beta) + \sigma_h\sin^2(\alpha + \beta) \\ \sigma_{y2} = \sigma_H\sin^2(\alpha + \beta) + \sigma_h\cos^2(\alpha + \beta) \\ \tau_{xy2} = (\sigma_h - \sigma_H)\sin(\alpha + \beta)\cos(\alpha + \beta) \end{cases} \tag{7}$$

We obtained the stress distribution around the elliptical borehole in anisotropic media using the stress analysis method for the planar orifice problem (Please refer to Appendix C for detailed derivation).

$$\begin{cases} \sigma_x = \sigma_{x2} + 2\mathrm{Re}\left[\mu_{11}^2\varphi_{11}'(z_1) + \mu_{22}^2\varphi_{22}'(z_2)\right] \\ \sigma_y = \sigma_{y2} + 2\mathrm{Re}\left[\varphi_{11}'(z_1) + \varphi_{22}'(z_2)\right] \\ \tau_{xy} = \tau_{xy1} - 2\mathrm{Re}\left[\mu_{11}\varphi_{11}'(z_1) + \mu_{22}\varphi_{22}'(z_2)\right] \end{cases} \tag{8}$$

Where

$$\begin{cases} \varphi_{11}'(z_1) = \dfrac{\mu_{22}\left(\sigma_{y2}a - \mathrm{i}\tau_{xy2}b - p_wa\right) + \tau_{xy2}a + \mathrm{i}p_wb - \mathrm{i}\sigma_{x2}b}{2\xi_1(\mu_{22} - \mu_{11})\sqrt{z_1^2 - a^2 - \mu_{11}^2b^2}} \\ \varphi_{22}'(z_2) = -\dfrac{\mu_{11}\left(\sigma_{y2}a - \mathrm{i}\tau_{xy2}b - p_wa\right) + \tau_{xy2}a + \mathrm{i}p_wb - \mathrm{i}\sigma_{x2}b}{2\xi 2(\mu_{22} - \mu_{11})\sqrt{z_2^2 - a^2 - \mu_{22}^2b^2}} \end{cases} \tag{9}$$

Thus on the borehole wall:

$$\xi_k = \cos\theta + \mathrm{i}\sin\theta, z_k = a\cos\theta + \mathrm{i}b\sin\theta \tag{10}$$

We can obtain the stress distribution around an elliptical borehole in a Cartesian coordinate system by substituting Equation 10, Equation 9 into Equation 8.

2.4 Prediction model of FIP for the elliptical borehole

If the tangential stress exerted on the borehole wall exceeds the tensile strength of the reservoir, the borehole will failure. Therefore, it is essential first to assess the tangential stress of the borehole. By utilizing the coordinate transformation formula (11), we can determine tangential stress distribution at any point along the borehole wall.

$$\begin{cases} \sigma_\theta = \sigma_x\sin^2\varphi + \sigma_y\cos^2\varphi - 2\tau_{xy}\sin\varphi\cos\varphi \\ \sin\varphi = \pm a\sin\theta/\sqrt{a^2\sin^2\theta + b^2\cos^2\theta} \\ \cos\varphi = \mp b\cos\theta/\sqrt{a^2\sin^2\theta + b^2\cos^2\theta} \end{cases} \tag{11}$$

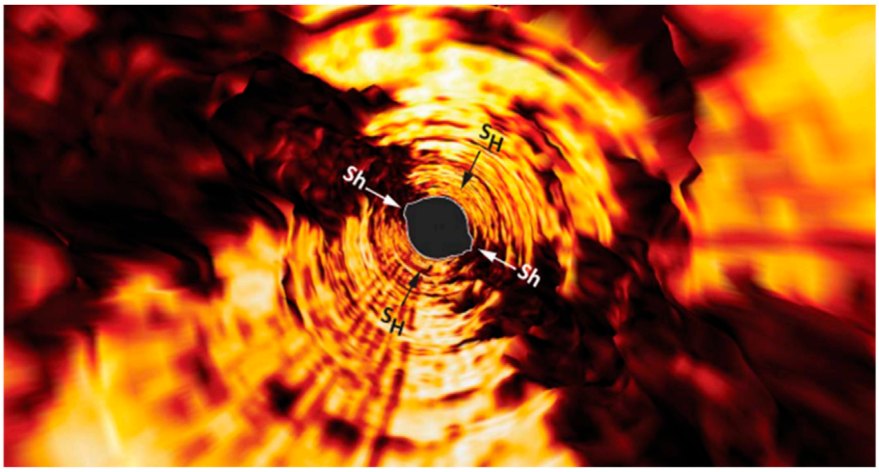

FIGURE 1
Three-dimensional borehole breakout view from ABI image of the PTA2 borehole wall. S_h and S_H are the orientations of the minimum and maximum horizontal principal stresses, respectively (Pierdominici et al., 2020).

Previous research indicated that anisotropic rocks have different tensile strengths in different directions (Ma et al., 2017). Furthermore, the N-E criterion can be used to accurately assess the tensile strength of anisotropic rocks in any direction as follows (Nova and Zaninetti, 1990):

$$T(\theta) = \frac{T_1 T_2}{T_1 \sin^2(\theta - \beta) + T_2 \cos^2(\theta - \beta)} \tag{12}$$

Where T_1 and T_2 are the tensile strength perpendicular and parallel to the bedding plane, respectively, MPa.

Suppose the tangential stress exceeds the rock's tensile strength. In that case, the rock enters the failure stage (Equation 13). At this moment, the pressure at which the fracturing fluid is injected, known as p_w, represents the FIP.

$$\sigma_\theta = -\sigma_t \tag{13}$$

Where σ_t is the tensile strength of the rock, MPa.

The initiation angle of the fracture can be determined using the following equation (Liang et al., 2022), where θ is the initiation angle.

$$\frac{\partial \sigma_\theta}{\partial \theta} = 0, \frac{\partial^2 \sigma_\theta}{\partial \theta^2} > 0 \tag{14}$$

3 Model validation

3.1 Model validation by different model comparisons

We have successfully validated the proposed borehole deformation model in Section 2.2. Furthermore, it is necessary to validate the proposed FIP model for the elliptical borehole in the anisotropic medium, and we can achieve it by degrading this model to an isotropic model and comparing it with existing models. The existing models that can be used for comparison are the elliptical model in the isotropic medium proposed by Aadnoy and Angell-olsen. (1995) (Eq. 15) and Ge et al. (2019) (Eq. 16), respectively. The specific forms of these models are as follows:

$$\begin{aligned}\sigma_\theta = {}& \frac{\sigma_{x2}\left(\left(c^2+2c\right)\sin^2\theta - \cos^2\theta\right) + \sigma_{y2}\left(\left(1+2c\right)\cos^2\theta - c^2\sin^2\theta\right)}{c^2\sin^2\theta + \cos^2\theta} \\ & -p_w\left(\frac{\begin{matrix} c^3\left(2c^2-3c+4\right)\sin^4\theta\cos^2\theta + c\left(4c^2-3c+2\right)\sin^2\theta\cos^4\theta \\ +c^5\left(2-c\right)\sin^6\theta + \left(2c-1\right)\cos^6\theta \end{matrix}}{\left(c^2\sin^2\theta+\cos^2\theta\right)\left(\begin{matrix} c^2\left(c^2+2\right)\sin^4\theta\cos^2\theta \\ +\left(2c^2+1\right)\sin^2\theta\cos^4\theta + \cos^6\theta + c^4\sin^6\theta \end{matrix}\right)}\right)\end{aligned} \tag{15}$$

$$\begin{aligned}\sigma_\theta = {}& \sigma_{x2}\frac{1-m^2+2m-2\cos 2\theta}{1-2m\cos 2\theta+m^2} + \sigma_{y2}\frac{1-m^2-2m+2\cos 2\theta}{1-2m\cos 2\theta+m^2} \\ & + p_w\frac{3m^2-2m\cos 2\theta-1}{1-2m\cos 2\theta+m^2}\end{aligned} \tag{16}$$

When calculating the tangential stress on the wall of the elliptical borehole, we utilize the following values: the borehole radius is 0.12 m, c is 1.2, m is 0.6, σ_{x2} is 50MPa, σ_{y2} is 30 MPa, τ_{xy2} is 0, and the fracturing fluid injection pressure is 20 MPa. We determine the tangential stresses on the borehole wall using Aadnoy's, Ge et al.'s, and our proposed model. We presented the results in Table 1. The table demonstrates that the proposed model yields similar results to Aadnoy's and Ge et al.'s models when μ_{11}=1.001i and μ_{22}=0.999i, which indicates the accuracy of our proposed model and its applicability in studying the stress distribution around the elliptical borehole in the anisotropic medium.

3.2 Model validation by experimental data

To validate the dependability of the proposed model, we substituted the experimental conditions and mechanical parameters from the literature (Liu et al., 2022) into our proposed model and Ma et al.'s model. (Ma et al., 2022). We presented the experiment and calculation results in Figure 4. The FIP decreases as the bedding inclination angle increases, and the calculation results align with the experimental findings. The concave

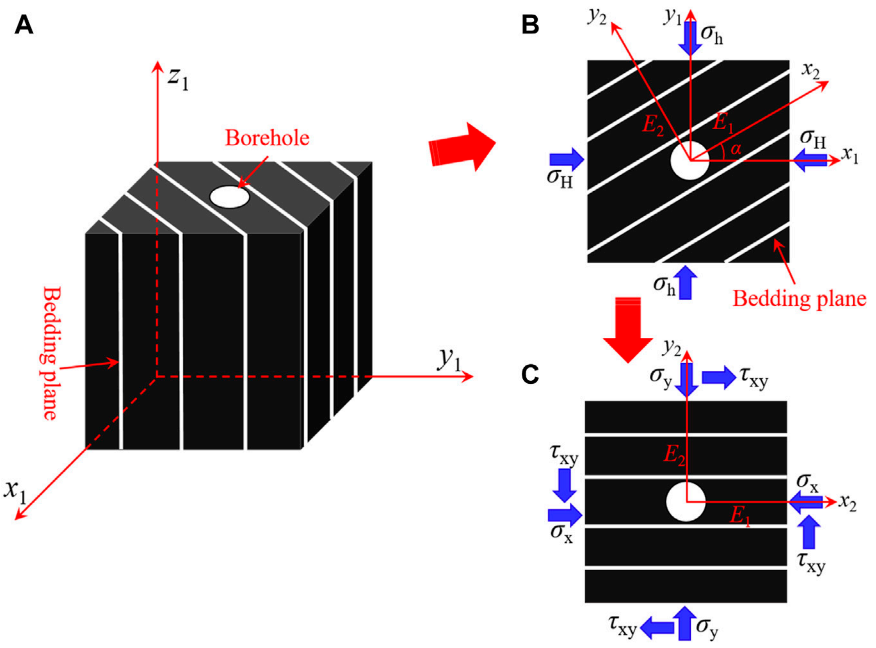

FIGURE 2
(A) A vertical borehole in the layered reservoir. **(B)** The stress distribution around the vertical borehole, with the bedding plane at an angle α to the axis of the maximum principle stress axis. **(C)**. The equivalent stress around the borehole after a rotation of angle α.

shape of the curve derived from the experimental data aligns with the results of our proposed model, whereas the curve model from Ma et al. exhibits a convex shape. Additionally, our model's calculation results closely match the experimental data, leading to a maximum 47.6% (23°) improvement in accuracy compared to Ma et al.'s model, which indicates the superiority of our model in predicting the FIP of reservoirs with a significant angle between the bedding plane and stress direction, highlighting its advanced predictive nature.

4 Analysis of factors impacting borehole deformation and FIP

We calculated the FIP and initiation angle of the initial circular borehole by substituting the radius (R) into Equations 13, 14 to replace the major axis (a) and minor axis (b) of the elliptical borehole, then calculated the size of the borehole deformation and the deflection angle (β) under various factors using Matlab software, and compared the FIP and the initiation angle of the initial circular borehole and the elliptical borehole. Table 2 presents the related parameters.

4.1 Effect of the *in situ* stress

The *in situ* stress significantly influences the deformation and FIP of the borehole. This study set various values of horizontal stress differences to investigate the borehole deformation and distribution of FIP (Figures 5, 6). Figure 5A shows that the length of the major and minor axes and the deflection angle of the deformed elliptical borehole decrease with increasing σ_{h}. Further analysis shows that the difference between the length of the major and minor axes first increases and then decreases as increasing σ_{h}, reaching a maximum value at 43 MPa. Notably, the deflection angle of the elliptical borehole is invariably greater than zero, indicating that the direction of the major axes of the deformed elliptical borehole is not consistent with the direction of the *in situ* stress in anisotropic reservoirs. Figure 5B shows that the FIP and initiation angle of both elliptical and circular boreholes increase with increasing σ_{h}; when σ_{h} is larger than 43.9MPa, the FIP of elliptical boreholes is slightly larger than that of circular boreholes. However, when σ_{h} is less than 43.9 MPa, the FIP of elliptical boreholes is smaller than that of circular boreholes, which suggests that borehole deformation arising under *in situ* stress can either increase or decrease borehole stability, depending on specific geological parameters. The initiation angle of the elliptical borehole is smaller than that of the circular borehole. The difference gradually decreases with increasing σ_{h}, which implies that considering the deformation of the boreholes in the calculations yields fracture initiation directions that are closer to the direction of the maximum principal stresses, which is more consistent with the existing experimental results (Heng et al., 2019; Liu et al., 2022).

According to the observations in Figure 6A, the length of both major and minor axes of the elliptical borehole decreases with increasing σ_{H}. Furthermore, the difference between the major and minor axes' lengths and the deflection angle increases with increasing σ_{H}. Figure 6B shows that the FIP and initiation angle of both elliptical and circular boreholes increase with increasing σ_{H}. When σ_{H} is less than 43.3 MPa, the FIP of elliptical boreholes is marginally more extensive than that of circular boreholes. However, when σ_{H} exceeds 43.3 MPa, the FIP of elliptical boreholes becomes smaller than that of circular boreholes. The initiation angle of

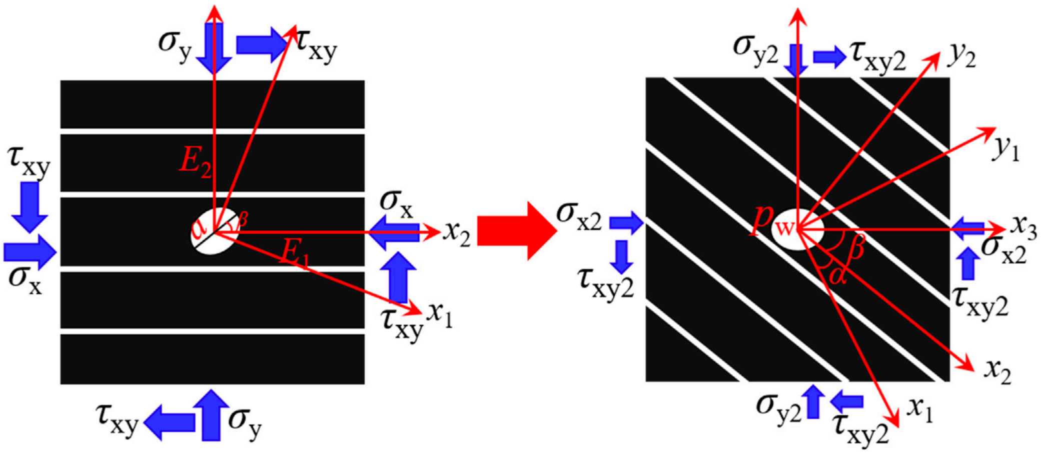

FIGURE 3
The stress distribution around the elliptical borehole.

elliptical boreholes is always smaller than that of circular boreholes, and the difference between the two gradually increases with increasing σ_H. A comparison between Figures 5, 6 indicates that an increase in the horizontal stress difference results in an increase in the deflection angle and the initiation angle, as well as a decrease in the FIP, which suggests that the study of the effect of *in situ* stress on borehole deformation and FIP can be simplified to study the impact of horizontal stress differences. However, it is essential to note that it is impossible to establish a direct relationship between the horizontal stress difference and the size of borehole deformation.

4.2 Effect of the bedding inclination angle

The bedding inclination angle (α), defined in this study as the angle between the directions of the bedding plane and the maximum principal stress, was investigated for its effects on borehole deformation and FIP. Figure 7A illustrates that as the α increases, the major axis of the deformed elliptical borehole lengthens. In contrast, the minor axis shortens, and the deflection angle increases and then decreases, reaching a maximum value of 44.33° at 22°. Significantly, there is a distinct alteration of the deflection angle at α when it comes to 22°, signifying a complete exchange of the major and minor axes of the deformation elliptical boreholes. These modifications demonstrate the bedding inclination angle's significant impact on borehole deformation.

It can be seen from Figure 7B that for both elliptical and circular boreholes, the FIPs decrease with increasing α. The difference in FIPs between them first increases and then falls with increasing α, reaching a maximum value of 9.99 MPa at 26°. Based on this observation, we advised choosing formations for field hydraulic fracturing that significantly differ between the directions of the bedding plane and the principal stress to reduce the FIP effectively. Furthermore, the initiation angle for circular boreholes first increases and then decreases as α increases, always resulting in negative values. The maximum initiation angle is approximately 12.4°. However, the initiation angle for elliptical boreholes follows a wavy distribution. It first increases and then decreases as α increases when α is less than 36°, resulting in positive values. The maximum initiation angle is around 10.44°. When α is greater than 36°, the initiation angle first increases and then decreases, but in this case, it results in negative values. Further analysis reveals that the maximum difference between the initiation angles of circular and elliptical boreholes is approximately 17.25°, which indicates that without considering borehole deformation, there may be a significant error in calculating the initiation angle. Therefore, evaluating the effect of borehole deformation when determining the initiation fracture location in hydraulic fracturing is crucial.

4.3 Effect of the elastic anisotropy

Previous research has shown that alterations in the elastic anisotropy ratio (E_1/E_2) surrounding the borehole result in modifications in the stress distribution around the borehole (Ding et al., 2018). Furthermore, variations in the parameters E1, E2, v12, and v12 in anisotropic materials result in changes in the shear modulus G_2. The St. Venant relationship elucidates the connection among these parameters above (Espada and Lamas, 2017; Dambly et al., 2019):

$$\frac{1}{G_{12}} = \frac{1}{E_1} + \frac{1}{E_2} + \frac{2\nu_{12}}{E_2} \tag{17}$$

The influence of elastic anisotropy ratio on borehole deformation and FIP was studied using the Saint-Venant relationship, as shown in Figures 8, 9. In Figure 8, we set E_2 as constant; an increase in E_1/E_2 results in an increase in the major axis length of the deformed elliptical borehole. Additionally, the minor axis length first increases and then decreases, while the difference between the two axes decreases and then increases, reaching its minimum value at E_1/E_2=1.4. The deflection angle follows a similar pattern, first increasing and decreasing, with the maximum deflection angle occurring at E_1/E_2=1.15. At this ratio, the deflection angle changed to 90°,

TABLE 1 Comparison of tangential stress on the wall of the elliptical borehole.

θ(°)	σ_θ (MPa)			
	Aadnoy's model	Ge's model	Our proposed model	
			μ_{11}=1.01i, μ_{22}=0.99i	μ_{11}=1.001i, μ_{22}=0.999i
0	24	24	23.9994	24.0000
5	24.7195	24.7195	24.7191	24.7195
10	26.8283	26.8283	26.8282	26.8283
15	30.1842	30.1842	30.1845	30.1842
20	34.5734	34.5734	34.5740	34.5734
25	39.7379	39.7379	39.7387	39.7379
30	45.4054	45.4054	45.4060	45.4054
35	51.3134	51.3134	51.3137	51.3134
40	57.2276	57.2276	57.2273	57.2276
45	62.9508	62.9508	62.9502	62.9508
50	68.3265	68.3265	68.3257	68.3265
55	73.2361	73.2361	73.2352	73.2361
60	77.5940	77.5940	77.5932	77.5940
65	81.3413	81.3413	81.3408	81.3413
70	84.4398	84.4398	84.4397	84.4398
75	86.8656	86.8656	86.8659	86.8656
80	88.6051	88.6051	88.6058	88.6051
85	89.6510	89.6510	89.6519	89.6510
90	90.0000	90.0000	90.0010	90.0000

indicating a complete exchange of positions between the elliptical major and minor axes. These changes mean the significant influence of the elastic anisotropy ratio on the borehole deformation. The FIP of elliptical and circular boreholes decreases with increasing E_1/E_2. However, the variation in FIP for elliptical boreholes is significantly higher, at 44.29%, compared to only 15.18% for circular boreholes, which suggests that the influence of E_1/E_2 on deformed elliptical boreholes is more significant and deserves more attention. Furthermore, the difference between FIP for elliptical and circular boreholes initially decreases and then increases with increasing E_1/E_2. When $E_1/E_2<1.1$, the FIP for elliptical boreholes is higher than that for circular boreholes, indicating that a lower elastic anisotropy ratio promotes more excellent stability for circular boreholes after deformation. The initiation angle for circular boreholes increases with increasing E_1/E_2, reaching a maximum value of approximately 16.99°, which indicates that the fracture initiation directions largely coincide with the direction of the maximum principal stresses. In the case of elliptical boreholes, however, the initiation angle initially increases and then decreases as the E_1/E_2 increases. It is worth noting that for $E_1/E_2<1.2$, the initiation angle is about 100°, suggesting that when elastic anisotropy is low, the fracture initiation direction of deformed elliptical boreholes is closer to the direction of minimum principal stress.

In Figure 9, we set E_1 as constant. As E_1/E_2 increase, the length of the major and minor axes of the elliptical borehole increase and decrease, respectively, and the difference between them constantly increases. Furthermore, the deflection angle increases and then decreases, reaching a maximum value of 19.69° at E_1/E_2=1.45. However, the total change in the deflection angle is about 6%. Comparing this with Figure 8A, it is clear that there are different distribution patterns in terms of the size of the borehole deformation and the deflection angle. Therefore, we considered that the specific values of E_1 and E_2 are the main factors affecting the borehole deformation, not just the E_1/E_2. By comparing and analyzing Figure 8B and Figure 9B, we found that the FIP values in both figures are identical when E_1/E_2 is the same, which indicates that when calculating the FIP, only the elastic anisotropy ratio needs to be considered, without specifying the actual values. However, the distribution pattern of the initiation angle differs between the two figures. In Figure 9B, the initiation angle for circular boreholes decreases with increasing E_1/E_2. In contrast, the initiation angle for elliptical boreholes first increases and then falls, which suggests that the specific values of E_1 and E_2 are essential factors affecting the initiation angle.

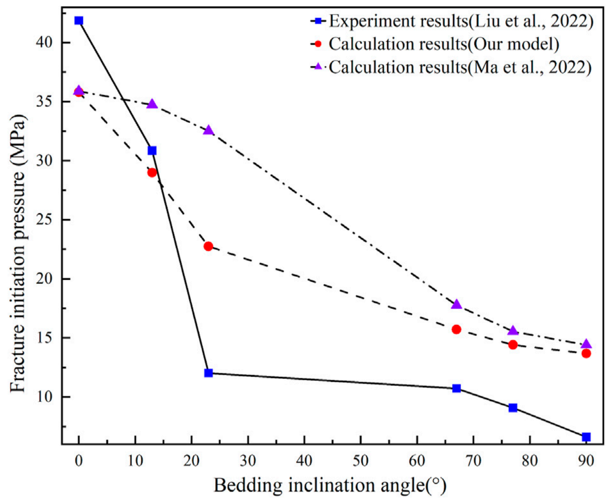

FIGURE 4
Comparison of calculated results in the present study with experimental results in the previous literature.

4.4 Effect of Poisson's ratio anisotropy

This section investigated the influence of Poisson's ratio anisotropy on borehole deformation and FIP. In Figure 10, we set ν_{13} as constant; as ν_{12}/ν_{13} increases, the major axis length of the borehole increases, while the minor axis length first increases and then decreases, reaching its maximum value at ν_{12}/ν_{13}=2.45. Furthermore, the deflection angle decreases continuously, with a maximum change of up to 59%. The maximum difference in deformation of the major and minor axes of the elliptical borehole is 0.28 mm. These results indicate that Poisson's ratio anisotropy has minimal influence on the borehole deformation but significantly influences the deflection angle. As shown in Figure 10B, the FIP decreases with increasing ν_{12}/ν_{13} for both the elliptical and circular boreholes. Furthermore, the difference between them first increases and then decreases, reaching a maximum value of 7.59 MPa at ν_{12}/ν_{13}=2.7. This observation indicates that high Poisson's ratio anisotropy can reduce the FIP after borehole deformation. Therefore, when conducting hydraulic fracturing in the field, reservoirs with high Poisson's ratio anisotropy could be selected to arrange the boreholes to minimize the FIP effectively. Moreover, the initiation angles of both elliptical and circular boreholes decrease with increasing ν_{12}/ν_{13}, and the initiation angle of elliptical boreholes is consistently smaller than that of circular boreholes. This finding suggests that borehole deformation brings the direction of fracture initiation closer to the direction of the maximum principal stress, consistent with existing experimental results (Heng et al., 2019; Liu et al., 2022).

In Figure 11, we set ν_{12} as a fixed value and observed that as ν_{12}/ν_{13} increases, the length of the major and minor axes of the elliptical borehole increases and decreases, respectively. The maximum change in size is about 0.06 mm. Additionally, the deflection angle continues to decline. Compared to Figure 10A, it is clear that Poisson's ratio anisotropy ratio has no significant influence on the length of the major and minor axes of the elliptical borehole. However, it does have a notable effect on the deflection angle. Nevertheless, we cannot predict the trend of the deflection angle solely based on Poisson's ratio anisotropy ratio trends. Furthermore, the analysis of Figure 10B reveals that as the ν_{12}/ν_{13} increases, the FIPs of elliptical and circular boreholes decrease. The difference between them initially decreases and then stabilizes. Moreover, the initiation angle of elliptical boreholes decreases while circular boreholes increase, albeit with a more minor change. We compared this to Figure 10B and could predict the FIP trend based on Poisson's anisotropy ratio. However, we could not predict the trend of the initiation angle.

TABLE 2 Basic parameters in MATLAB

Parameters/unit	Numerical value
In situ stress (σ_H/σ_h)/MPa	50/30
The tensile strength (T_m/T_b)/MPa	11.83/5.24
The elastic modulus (E_1/E_2)/MPa	7,200/3,600
The Poisson's ratio (ν_{12}/ν_{13})	0.25/0.2
The shear modulus (G_{12})/MPa	1800
the inclination angle of the bedding plane(α)/°	45
the radius of the borehole(R)/mm	108

4.5 Effect of strength anisotropy

Based on Equation 5, the strength anisotropy does not affect the borehole deformation but affects the FIP. To examine this effect, we kept the rock material's tensile strength constant while adjusting the bedding plane's tensile strength to achieve varying degrees of anisotropy. Figure 12 illustrates the relationship between the strength anisotropy ratio (T_m/T_b), FIP, and initiation angle for both elliptical and circular boreholes. As Tm/Tb increases, the FIP and angle decrease for both elliptical and circular boreholes. Additionally, the difference in FIPs between elliptical and circular boreholes decreases while the difference in initiation angles increases. Despite their lack of impact on borehole deformation, these findings highlight the significance of considering strength anisotropy in calculating FIPs and initiation angles for deformed elliptical boreholes.

5 Discussion

The analysis of logged data suggests that in layered reservoirs, circular boreholes can be transformed into elliptical boreholes under *in situ* stress (Zoback et al., 2003; Pierdominici et al., 2020; Han et al., 2021). Various researchers have created models to forecast the extent of borehole deformation (Zou et al., 2018; Fang et al., 2022; Han et al., 2023), but these models do not account for the impact of elastic anisotropy in layered reservoirs, which could affect the accuracy of the forecasts (Ma et al., 2019). Our study factors in layered reservoirs' elastic and stress anisotropy (Abdulelah et al., 2018; Qu et al., 2022b; Lu et al., 2022), and develops a model to anticipate the extent of deformation in vertical or horizontal boreholes. By substituting the reservoir parameters into the model, we discover that circular boreholes in layered reservoirs

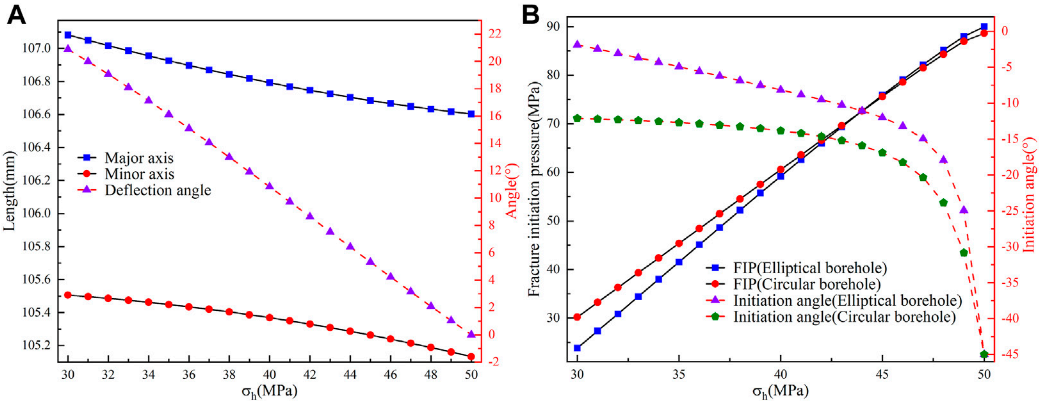

FIGURE 5
(A) Variation of the lengths of the major and minor axes and deflection angle for the elliptical borehole with σ_h. **(B)** Variation of the FIP and initiation angle for circular and elliptical boreholes with σ_h.

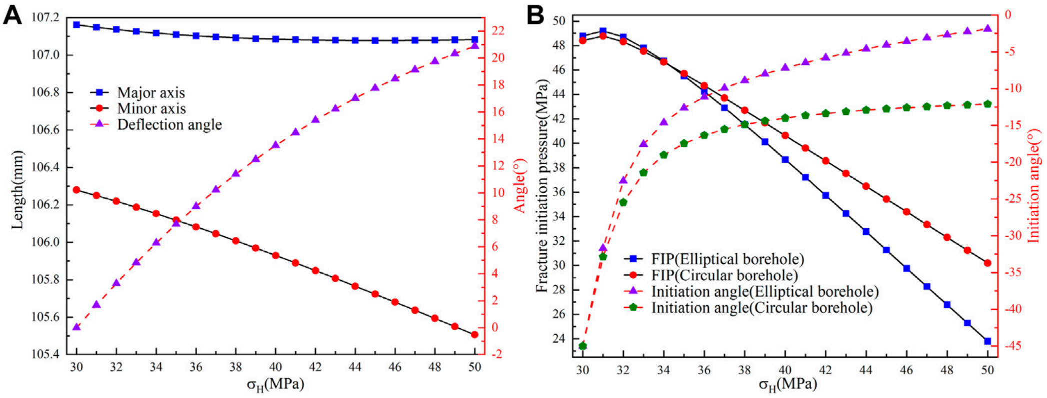

FIGURE 6
(A) Variation of the lengths of the major and minor axes and deflection angle for the elliptical borehole with σ_H. **(B)** Variation of the FIP and initiation angle for circular and elliptical boreholes with σ_H.

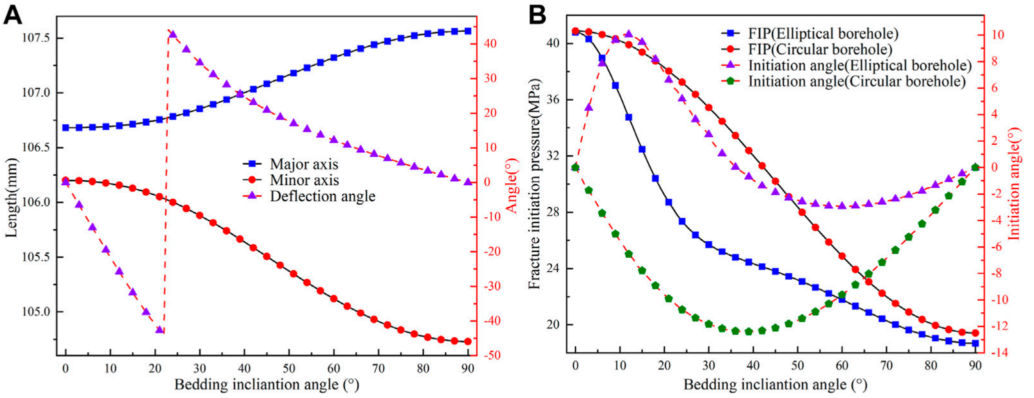

FIGURE 7
(A) Variation of the lengths of the major and minor axes and deflection angle for the elliptical borehole with bedding inclination angle. **(B)** Variation of the FIP and initiation angle for circular and elliptical boreholes with bedding inclination angle.

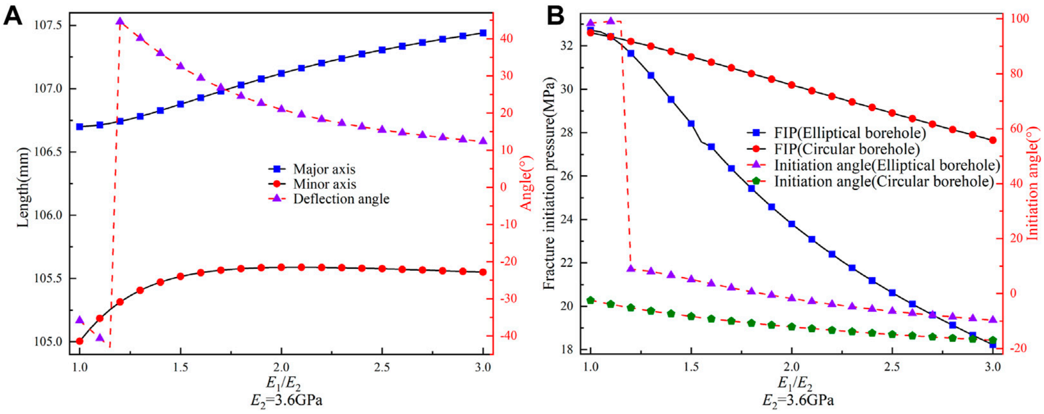

FIGURE 8
(A) Variation of the lengths of the major and minor axes and deflection angle for the elliptical borehole with E_1/E_2 (E_2=3.6 GPa). **(B)** Variation of the FIP and initiation angle for circular and elliptical boreholes with E_1/E_2.

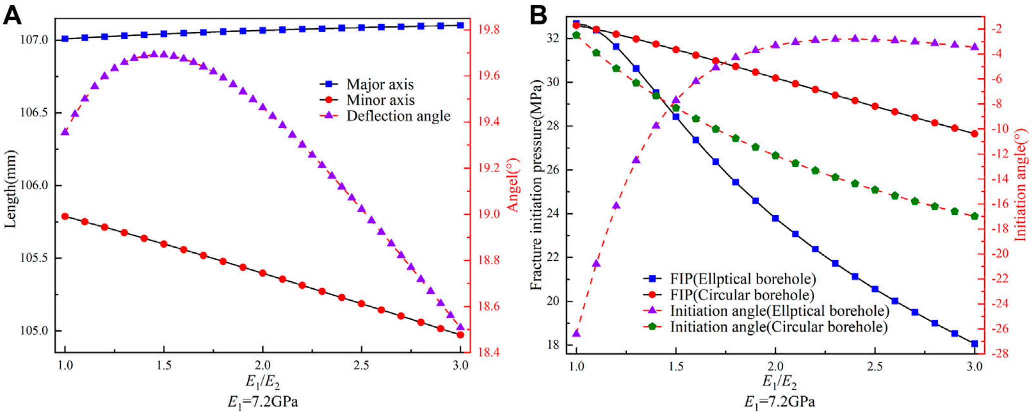

FIGURE 9
(A) Variation of the lengths of the major and minor axes and deflection angle for the elliptical borehole with E_1/E_2 (E_1=7.2 GPa). **(B)** Variation of the FIP and initiation angle for circular and elliptical boreholes with E_1/E_2.

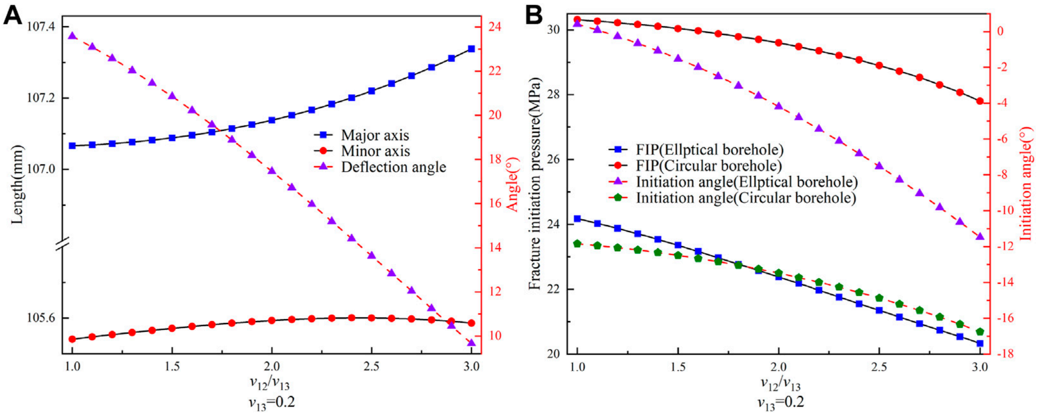

FIGURE 10
(A) Variation of the lengths of the major and minor axes and deflection angle for the elliptical borehole with v_{12}/v_{13} (v_{13}=0.2). **(B)** Variation of the FIP and initiation angle for circular and elliptical boreholes with v_{12}/v_{13}.

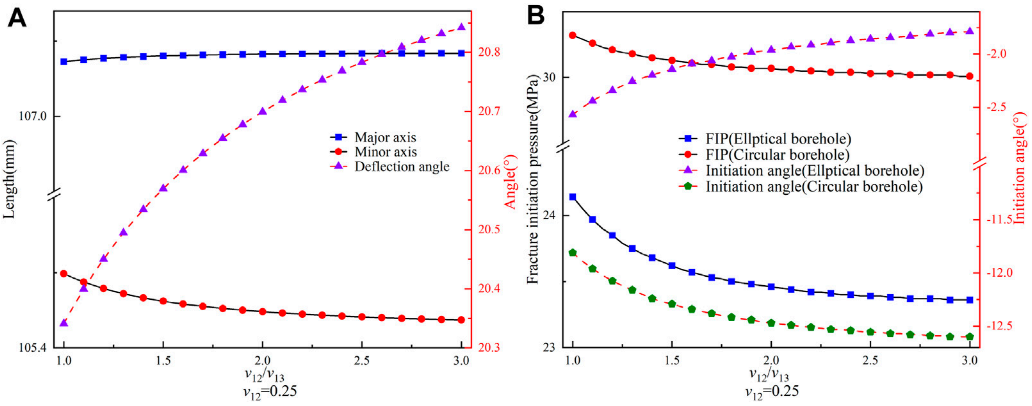

FIGURE 11
(A) Variation of the lengths of the major and minor axes and deflection angle for the elliptical borehole with v_{12}/v_{13} (v_{12}=0.25). **(B)** Variation of the FIP and i/nitiation angle for circular and elliptical boreholes with v_{12}/v_{13}.

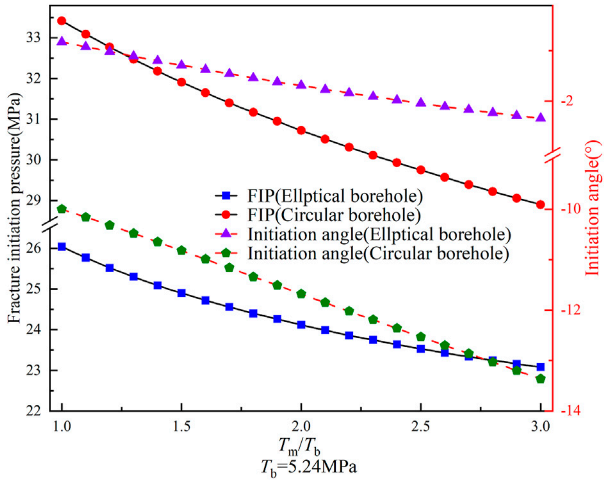

FIGURE 12
Variation of the FIP and initiation angle for circular and elliptical boreholes with T_m/T_b (T_b=5.24 MPa).

also transform into elliptical boreholes, which is consistent with previous findings (Zou et al., 2018; Fang et al., 2022; Han et al., 2023). Unexpectedly, our calculations indicate that the major axis direction of the deformed boreholes is incongruent with the direction of the *in situ* stress, differing from the previous model but aligning more closely with the logging data (Pierdominici et al., 2020), which highlights the superiority of our proposed model.

Using models and logging data, we have demonstrated that circular boreholes deform into elliptical boreholes under the influence of *in situ* stress and elastic anisotropy. Previous studies have indicated that the change in borehole shape impacts the FIP (Qi et al., 2018; Zheng et al., 2023). Several models have been developed to predict the FIP of elliptical boreholes (Chen et al., 2020; Zhong et al., 2021), but these models do not consider the effect of mechanical anisotropy in layered reservoirs. We have developed an improved FIP prediction model based on the forecasted borehole deformation and validated its accuracy by comparing it with the models of Aadnoy and Angell-olsen (1995) and Ge et al. (2019). Zang et al. (2023) observed, through digital image correlation during SC-CO_2 fracturing in the laboratory, that there is a strain concentration near the borehole before fracturing, which can cause borehole deformation, which suggests that our proposed model can also be used to predict the FIP of bedding shales for hydraulic fracturing in laboratory experiments (Liu et al., 2022). Based on the experimental findings by Liu et al. (2022), we have conducted a comparative analysis of our model and that of Ma et al. (2022). The results indicate a 47.6% enhancement in our model's accuracy, demonstrating our proposed model's advanced capability.

We compared the impacts of *in situ* stress, bedding inclination, and anisotropy parameters on FIP and initiation angle in circular and elliptical boreholes. Our findings indicate that elliptical boreholes may exhibit higher or lower initiation pressures than circular boreholes, depending on specific geologic parameters, which differs from previous models (Chen et al., 2020; Zhong et al., 2021; Zheng et al., 2023) due to the absence of a relationship between the amount of borehole deformation and FIP in the previous models. Furthermore, our proposed model predicts a deviation angle between the fracture initiation direction and the maximum principal stress direction of no more than 10°. In contrast, the deviation angle in the previous model is significantly larger (Heng et al., 2021; Ma et al., 2022). However, the experimental results demonstrate that the fracture initiation direction in anisotropic rocks aligns closely with the direction of maximum stress (Heng et al., 2019; Liu et al., 2022), highlighting the superior predictive performance of our model in determining the initiation angle.

The model proposed in this study is a two-dimensional model suitable only for horizontal or vertical boreholes. In contrast, inclined boreholes are more commonly encountered in on-site hydraulic fracturing operations (Ma et al., 2022; Zheng et al., 2023). Furthermore, the proposed model solely focuses on the tensile failure mode of the rock matrix. Previous experiments have demonstrated that layered rocks in hydraulic fracturing can exhibit various failure modes, including tensile and shear failure modes of the rock matrix and tensile and shear failure modes of the bedding plane (Li et al., 2018; Heng et al., 2021). Therefore, future research should optimize the proposed model by considering these two aspects to enhance its universality.

6 Conclusion

We formulated a model for predicting the vertical borehole deformation in layered reservoirs and developed a novel model for forecasting fracture initiation pressure (FIP) in hydraulic fracturing based on the expected deformation. We validated the proposed model's accuracy against previous models and experimental data. Furthermore, we examined the impact of *in situ* stress, bedding inclination, and reservoir anisotropic parameters on borehole deformation. We compared FIP and initiation angle changes in undeformed and deformed boreholes under varying conditions. The key findings of our study are summarized as follows.

1. The circular vertical boreholes in layered reservoirs change to elliptical due to *in situ* stress, and the major axis of elliptical boreholes deviates from the direction of the maximum principal stress.
2. Depending on the specific geological conditions, the borehole deformation can increase or decrease the FIP in hydraulic fracturing. Additionally, alterations in factors such as *in situ* stress, bedding inclination angle, and elastic modulus can result in more pronounced variations in FIP in elliptical boreholes than circular ones.
3. The initiation angles of elliptical boreholes are within 10°, which are notably lower when compared to that of circular boreholes, and the alteration in the *in situ* stress, bedding inclination angle, and elastic modulus result in minor modifications in the initiation angles of elliptical boreholes in comparison to those of circular boreholes. The borehole deformations can better explain the fracture propagation in hydraulic fracturing.

Data availability statement

The raw data supporting the conclusion of this article will be made available by the authors, without undue reservation.

Author contributions

YW: Methodology, Writing–original draft. MW: Investigation, Writing–original draft. ZN: Software, Writing–original draft. ZC: Data curation, Writing–original draft. RM: Formal Analysis, Writing–original draft. JZ: Writing–original draft, Writing–review and editing, Conceptualization, Validation.

Funding

The author(s) declare financial support was received for the research, authorship, and/or publication of this article. This study was financially supported by the Graduate Research and Innovation Foundation of Chongqing, China (No. CYB21024).

Conflict of interest

Authors YW, MW, ZN, ZC, and RM were employed by Pingdingshan Tianan Coal Mining Co., Ltd.

The remaining author declares that the research was conducted in the absence of any commercial or financial relationships that could be construed as a potential conflict of interest.

The reviewer XZ declared a shared affiliation with the author JZ to the handling editor at time of review.

Publisher's note

References

Aadnoy, B. S., and Angell-Olsen, F. (1995). Some effects of ellipticity on the fracturing and collapse behavior of a borehole. *Int. J. rock Mech. Min. Sci. Geomech. Abstr.* 32, 621–627. doi:10.1016/0148-9062(95)00016-A

Aadnoy, B. S., and Chenevert, M. E. (1987). Stability of highly inclined boreholes. *SPE Drill. Eng.* 2 (4), 364–374. doi:10.2118/16052-PA

Abdulelah, H., Mahmood, S., Al-Hajri, S., Hakimi, M., and Padmanabhan, E. (2018). Retention of hydraulic fracturing water in shale: the influence of anionic surfactant. *Energies* 11, 3342. doi:10.3390/en11123342

Chen, Y. L., Liu, Z., Zhang, X., He, S. M., Ma, D. X., and Zhou, J. (2020). Research on the collapse pressure of an elliptical wellbore considering the effect of weak planes. *Energ Source Part A* 42, 2103–2119. doi:10.1080/15567036.2019.1607929

Constant, W. D., and Jr, A. T. B. (1988). Fracture-gradient prediction for offshore wells. *SPE Drill. Eng.* 3 (02), 136–140. doi:10.2118/15105-PA

Dambly, M. L. T., Nejati, M., Vogler, D., and Saar, M. O. (2019). On the direct measurement of shear moduli in transversely isotropic rocks using the uniaxial compression test. *Int. J. Rock Mech. Min. Sci.* 113, 220–240. doi:10.1016/j.ijrmms.2018.10.025

Detournay, E., and Cheng, A. H.-D. (1988). Poroelastic response of a borehole in a non-hydrostatic stress field. *Int. J. rock Mech. Min. Sci. Geomech. Abstr.* 25 (3), 171–182. doi:10.1016/0148-9062(88)92299-1

Ding, Y., Luo, P. Y., Liu, X. J., and Liang, L. X. (2018). Wellbore stability model for horizontal wells in shale formations with multiple planes of weakness. *J. Nat. Gas. Sci. Eng.* 52, 334–347. doi:10.1016/j.jngse.2018.01.029

Do, D.-P., Tran, N.-H., Hoxha, D., and Dang, H.-L. (2017). Assessment of the influence of hydraulic and mechanical anisotropy on the fracture initiation pressure in permeable rocks using a complex potential approach. *Int. J. Rock Mech. Min. Sci.* 100, 108–123. doi:10.1016/j.ijrmms.2017.10.020

Eaton, B. A. (1969). Fracture gradient prediction and its application in oilfield operations. *J. Pet. Technol.* 21, 1353–1360. doi:10.2118/2163-PA

Espada, M., and Lamas, L. (2017). Back analysis procedure for identification of anisotropic elastic parameters of overcored rock specimens. *Rock Mech. Rock Eng.* 50 (3), 513–527. doi:10.1007/s00603-016-1129-3

Espinoza, D. N., Vandamme, M., Dangla, P., Pereira, J.-M., and Vidal-Gilbert, S. (2013). A transverse isotropic model for microporous solids: application to coal matrix adsorption and swelling. *J. Geophys. Res. Solid Earth* 118, 6113–6123. doi:10.1002/2013JB010337

Fang, X. X., Zhang, J. B., Liu, T., Zhang, Z., and Li, F. L. (2022). New prediction method of horizontal principal stress of deep tight reservoirs. *Sci. Rep.* 12, 12908. doi:10.1038/s41598-022-16954-1

Gao, Y. B., and Ren, J. (2022). Study on the effect of borehole size on gas extraction borehole strength and failure mode. *ACS Omega* 7, 25635–25643. doi:10.1021/acsomega.2c02834

Ge, Z. L., Zhong, J. Y., Lu, Y. Y., Cheng, L., Zheng, J. W., Zhou, Z., et al. (2019). Directional distance prediction model of slotting–directional hydraulic fracturing (SDHF) for coalbed methane (CBM) extraction. *J. Pet. Sci. Eng.* 183, 106429. doi:10.1016/j.petrol.2019.106429

Gupta, D., and Zaman, M. (1999). Stability of boreholes in a geologic medium including the effects of anisotropy. *Appl. Math. Mech.* 20, 837–866. doi:10.1007/BF02452483

Haimson, B., and Lee, H. (2004). Borehole breakouts and compaction bands in two high-porosity sandstones. *Int. J. Rock Mech. Min. Sci.* 41, 287–301. doi:10.1016/j.ijrmms.2003.09.001

Han, H. X., Yin, S. D., Chen, Z. H., and Dusseault, M. B. (2021). Estimate of *in situ* stress and geomechanical parameters for Duvernay Formation based on borehole deformation data. *J. Pet. Sci. Eng.* 196, 107994. doi:10.1016/j.petrol.2020.107994

Han, Z. Q., Li, M. H., Wang, C., Wang, J. C., and Huang, X. H. (2023). Application and discussion of the borehole radial deformation method in deep borehole geostress measurement. *Front. Earth Sci.* 11, 1102276. doi:10.3389/feart.2023.1102276

He, S., Qin, Q. R., Li, H., and Wang, S. L. (2022b). Deformation differences in complex structural areas in the southern sichuan basin and its influence on shale gas preservation: a case study of changning and luzhou areas. *Front. Earth Sci.* 9, 818155. doi:10.3389/feart.2021.818534

He, S., Qin, Q. R., Li, H., and Zhao, S. X. (2022a). Geological characteristics of deep shale gas in the silurian longmaxi formation in the southern sichuan basin, China. *Front. Earth Sci.* 9, 818543. doi:10.3389/feart.2021.818155

Heng, S., Liu, X., Li, X. Z., Zhang, X. D., and Yang, C. H. (2019). Experimental and numerical study on the non-planar propagation of hydraulic fractures in shale. *J. Pet. Sci. Eng.* 179, 410–426. doi:10.1016/j.petrol.2019.04.054

Heng, S., Zhao, R. T., Li, X. Z., and Guo, Y. Y. (2021). Shear mechanism of fracture initiation from a horizontal well in layered shale. *J. Nat. Gas. Sci. Eng.* 88, 103843. doi:10.1016/j.jngse.2021.103843

Huang, B. X., Li, H., Zhao, X. L., and Ying, Y. K. (2023a). Fracturing criterion of rock hydrofracturing considering pore pressure effect. *Front. Earth Sci.* 11, 111206. doi:10.3389/feart.2023.1111206

Huang, L. K., Tan, J., Fu, H. F., Liu, J. J., Chen, X. Y., Lao, X. C., et al. (2023b). The non-plane initiation and propagation mechanism of multiple hydraulic fractures in tight reservoirs considering stress shadow effects. *Eng. Fract. Mech.* 292, 109570. doi:10.1016/j.engfracmech.2023.109570

Hubbert, M. K., and Willis, D. G. (1957). Mechanics of hydraulic fracturing. *AIME Pet. Trans.* 210, 153–168. doi:10.2118/686-G

Li, C. F., and Zhang, Z. N. (2019). Modeling shale with consideration of bedding planes by cohesive finite element method. *Theor. App. Mech. Lett.* 9, 397–402. doi:10.1016/j.taml.2019.06.003

Li, H., Zhou, J. L., Mou, X. Y., Guo, H. X., Wang, X. X., An, H. Y., et al. (2022). Pore structure and fractal characteristics of the marine shale of the longmaxi formation in the changning area, southern sichuan basin, China. *Front. Earth Sci.* 10, 1018274. doi:10.3389/feart.2022.1018274

Li, N., Zhang, S. C., Zou, Y. S., Ma, X. F., Zhang, Z. P., Li, S. H., et al. (2018). Acoustic emission response of laboratory hydraulic fracturing in layered shale. *Rock Mech. Rock Eng.* 51, 3395–3406. doi:10.1007/s00603-018-1547-5

Liang, X., Hou, P., Xue, Y., Gao, Y. N., Gao, F., Liu, J., et al. (2022). Role of fractal effect in predicting crack initiation angle and its application in hydraulic fracturing. *Rock Mech. Rock Eng.* 55, 5491–5512. doi:10.1007/s00603-022-02940-6

Liu, Q., Li, J. L., Liang, B., Liu, J. J., Sun, W. J., He, J., et al. (2023). Complex wettability behavior triggering mechanism on imbibition: a model construction and comparative study based on analysis at multiple scales. *Energy* 275, 127434. doi:10.1016/j.energy.2023.127434

Liu, Q., Liang, B., Sun, W. J., Zhao, H., Hao, J. F., and Hou, M. R. (2022). Experimental study on hydraulic fracturing of bedding shale considering anisotropy effects. *ACS Omega* 7, 22698–22713. doi:10.1021/acsomega.2c02157

Lu, Y. Y., Zheng, J. W., Ge, Z. L., Zhou, Z., Wang, H. M., and Zhang, L. (2022). A study of variation in the initiation pressure and fracture distribution patterns of raw coal in SC-CO_2 fracturing under the true tri-axial system. *Rock Mech. Rock Eng.* 55, 3425–3438. doi:10.1007/s00603-022-02800-3

Ma, T. S., Gui, J. C., and Chen, P. (2021). Logging evaluation on mechanical-damage characteristics of the vicinity of the wellbore in tight reservoirs. *J. Pet. Explor Prod. Technol.* 11, 3213–3224. doi:10.1007/s13202-021-01200-7

Ma, T. S., Liu, Y., Chen, P., Wu, B. S., Fu, J. H., and Guo, Z. X. (2019). Fracture-initiation pressure prediction for transversely isotropic formations. *J. Pet. Sci. Eng.* 176, 821–835. doi:10.1016/j.petrol.2019.01.090

Ma, T. S., Wang, H. N., Liu, Y., Shi, Y. F., and Ranjith, P. G. (2022). Fracture-initiation pressure model of inclined wells in transversely isotropic formation with anisotropic tensile strength. *Int. J. Rock Mech. Min. Sci.* 159, 105235. doi:10.1016/j.ijrmms.2022.105235

Ma, T. S., Wu, B. S., Fu, J. H., Zhang, Q. G., and Chen, P. (2017). Fracture pressure prediction for layered formations with anisotropic rock strengths. *J. Nat. Gas. Sci. Eng.* 38, 485–503. doi:10.1016/j.jngse.2017.01.002

Nova, R., and Zaninetti, A. (1990). An investigation into the tensile behaviour of a schistose rock. *Int. J. rock Mech. Min. Sci. Geomech. Abstr.* 27, 231–242. doi:10.1016/0148-9062(90)90526-8

Ong, S. H., and Roegiers, J. C. (1995). “Fracture initiation from inclined wellbores in anisotropic formations,” in *International meeting on Petroleum engineering* (Beijing, China: IEEE), 14-17. (SPE 29993).

Oriji, A. B., and Ogbonna, J. (2012). “A new fracture gradient prediction technique that shows good results in gulf of Guinea,” in *All days (*abu dhabi, UAE: spe*), SPE-161209-MS* (UAE: SPE). doi:10.2118/161209-MS

Pierdominici, S., Millett, J., Kuck, J., Thomas, D., Jerram, D., Planke, S., et al. (2020). Stress field interactions between overlapping shield volcanoes: borehole breakout evidence from the island of Hawaii, USA. *J. Geophys. Res. Solid Earth* 125, e2020JB019768. doi:10.1029/2020JB019768

Prioul, R., Karpfinger, F., Deenadayalu, C., and Suarez-Rivera, R. (2011). “Improving fracture initiation predictions on arbitrarily oriented wells in anisotropic shales,” in *All days (calgary, alberta, Canada: spe), SPE-147462-MS* (Canada: SPE). doi:10.2118/147462-MS

Qi, D. X., Li, L. J., and Jiao, Y. S. (2018). The stress state around an elliptical borehole in anisotropy medium. *J. Pet. Sci. Eng.* 166, 313–323. doi:10.1016/j.petrol.2018.03.013

Qu, G. Z., Su, J., Zhao, M., Bai, X. J., Yao, C. J., and Peng, J. (2022b). Optimizing composition of fracturing fluids for energy storage hydraulic fracturing operations in tight oil reservoirs. *Energies* 15, 4292. doi:10.3390/en15124292

Qu, H., Tang, S. M., Liu, Y., Huang, P. P., Wu, X. G., Liu, Z. H., et al. (2022a). Characteristics of complex fractures by liquid nitrogen fracturing in brittle shales. *Rock Mech. Rock Eng.* 55 (4), 1807–1822. doi:10.1007/s00603-021-02767-7

Ren, L., Jiang, H., Zhao, J. Z., Lin, R., Wang, Z. H., and Xu, Y. (2022). Theoretical study on fracture initiation in deep perforated wells with considering wellbore deformation. *J. Pet. Sci. Eng.* 211, 110141. doi:10.1016/j.petrol.2022.110141

Sesetty, V., and Ghassemi, A. (2018). Effect of rock anisotropy on wellbore stresses and hydraulic fracture propagation. *Int. J. Rock Mech. Min. Sci.* 112, 369–384. doi:10.1016/j.ijrmms.2018.09.005

Shou, Y. D., and Zhou, X. P. (2021). A coupled hydro-mechanical non-ordinary state-based peridynamics for the fissured porous rocks. *Eng. Anal. Bound Elem.* 123, 133–146. doi:10.1016/j.enganabound.2020.12.001

Song, R., Liu, J. J., and Cui, M. M. (2017). A new method to reconstruct structured mesh model from micro-computed tomography images of porous media and its application. *Int. J. Heat. Mass Tran* 109, 705–715. doi:10.1016/j.ijheatmasstransfer.2017.02.053

Song, R., Wang, Y., Ishutov, S., Zambrano-Narvaez, G., Hodder, J. K., Chalaturnyk, R. J., et al. (2020). A comprehensive experimental study on mechanical behavior, microstructure and transport properties of 3D-printed rock analogs. *Rock Mech. Rock Eng.* 53 (12), 5745–5765. doi:10.1007/s00603-020-02239-4

Wu, F. P., Li, D., Fan, X. Z., Liu, J., and Li, X. J. (2020). Analytical interpretation of hydraulic fracturing initiation pressure and breakdown pressure. *J. Nat. Gas. Sci. Eng.* 76, 103185. doi:10.1016/j.jngse.2020.103185

Wu, M. Y., Jiang, C. B., Song, R., Liu, J. J., Li, M. H., Liu, B., et al. (2023). Comparative study on hydraulic fracturing using different discrete fracture network modeling: insight from homogeneous to heterogeneity reservoirs. *Eng. Fract. Mech.* 284, 109274. doi:10.1016/j.engfracmech.2023.109274

Zang, Y. X., Wang, Q., Wang, H. Z., Wang, B., Tian, K. J., Wang, T. Y., et al. (2023). Laboratory visualization of supercritical CO_2 fracturing in tight sandstone using digital image correlation method. *Geoenergy Sci. Eng.* 225, 211556. doi:10.1016/j.geoen.2023.211556

Zhai, C., Xu, Y. M., Xiang, X. W., Yu, X., Zou, Q. N., and Zhong, C. (2015). A novel active prevention technology for borehole instability under the influence of mining activities. *J. Nat. Gas. Sci. Eng.* 27, 1585–1596. doi:10.1016/j.jngse.2015.10.024

Zhang, Y. F., Long, A. F., Zhao, Y., Wang, C. L., Wu, S. F., and Huang, H. S. (2023). Impacts of wellbore orientation with respect to bedding inclination and injection rate on laboratory hydraulic fracturing characteristics of Lushan shale. *Fuel* 353 (1), 129220. doi:10.1016/j.fuel.2023.129220

Zhang, Y. S., Zhang, J. C., Yuan, B., and Yin, S. X. (2018). *In situ* stresses controlling hydraulic fracture propagation and fracture breakdown pressure. *J. Pet. Sci. Eng.* 164, 164–173. doi:10.1016/j.petrol.2018.01.050

Zhao, H., Li, W., Wang, L., Fu, J., Xue, Y. L., Zhu, J. J., et al. (2022). The influence of the distribution characteristics of complex natural fracture on the hydraulic fracture propagation morphology. *Front. Earth Sci.* 9, 784951. doi:10.3389/feart.2021.784931

Zhao, Z., Zhou, X. P., and Qian, Q. H. (2020a). Fracture characterization and permeability prediction by pore scale variables extracted from X-ray CT images of porous geomaterials. *Sci. China Technol. Sci.* 63 (5), 755–767. doi:10.1007/s11431-019-1449-4

Zhao, Z., and Zhou, Z. P. (2020b). Digital voxel-based fracture extraction: insights to characterization of single fracture flow and anisotropy permeability. *J.* Nat. Gas. Sci. Eng. 84, 103635. doi:10.1016/j.jngse.2020.103635

Zheng, J. W., Ge, Z. L., Lu, Y. Y., Zhou, Z., Zhou, J., and Fu, W. Y. (2023). Prediction of fracture initiation pressure for slotting-directional hydraulic fracturing based on the anisotropy of coal. *J. Energy Resour. Technol.* 145. doi:10.1115/1.4062960

Zhong, J. Y., Ge, Z. L., Lu, Y. Y., Zhou, Z., and Zheng, J. W. (2021). Prediction of fracture initiation pressure in multiple failure hydraulic fracturing modes: three-dimensional stress model considering borehole deformation. *J. Pet. Sci. Eng.* 199, 108264. doi:10.1016/j.petrol.2020.108264

Zhou, X. P., Zhao, Z., and Li, Z. (2020). Cracking behaviors and hydraulic properties evaluation based on fractural microstructure models in geomaterials. *Int. J. Rock Mech. Min. Sci.* 130, 104304. doi:10.1016/j.ijrmms.2020.104304

Zhu, H. Y., Guo, J. C., Zhao, X. C., Lu, Q. L., Luo, B., and Feng, Y. C. (2014). Hydraulic fracture initiation pressure of anisotropic shale gas reservoirs. *ge?ome?Chem. Eng.* 7, 403–430. doi:10.12989/GAE.2014.7.4.403

Zoback, M. D., Barton, C. A., Brudy, M., Castillo, D. A., Finkbeiner, T., Grollimund, B. R., et al. (2003). Determination of stress orientation and magnitude in deep wells. *Int. J. Rock Mech. Min. Sci.* 40, 1049–1076. doi:10.1016/j.ijrmms.2003.07.001

Zou, X. J., Wang, C. Y., and Han, Z. Q. (2018). A proposed method for estimating *in situ* stress direction using panoramic stereo-pair imaging and stressed borehole geometric shapes. *Int. J. Rock Mech. Min. Sci.* 104, 94–99. doi:10.1016/j.ijrmms.2018.02.010

Appendix A

The intrinsic equation, stress equilibrium equation, and strain compatibility equation in the bedding plane coordinate system under generalized plane strain are as follows (Qi et al., 2018).

$$\begin{pmatrix} \varepsilon_{\mathrm{x}} \\ \varepsilon_{\mathrm{y}} \\ \gamma_{\mathrm{xy}} \end{pmatrix} = \begin{pmatrix} \beta_{11} & \beta_{12} & 0 \\ \beta_{12} & \beta_{22} & 0 \\ 0 & 0 & \beta_{33} \end{pmatrix} \begin{pmatrix} \sigma_{\mathrm{x}} \\ \sigma_{\mathrm{y}} \\ \tau_{\mathrm{xy}} \end{pmatrix} \tag{A1}$$

Where $\beta_{11} = \frac{1}{E_1} - \frac{\nu_{12}^2}{E_2}$; $\beta_{12} = -\frac{\nu_{12}(1+\nu_{32})}{E_2}$; $\beta_{22} = \frac{1}{E_2} - \frac{\nu_{32}^2}{E_2}$; $\beta_{22} = \frac{1}{G_{12}}$

$$\frac{\partial \sigma_{\mathrm{x}}}{\partial x} + \frac{\partial \tau_{\mathrm{xy}}}{\partial y} = 0; \; \frac{\partial \tau_{\mathrm{xy}}}{\partial x} + \frac{\partial \sigma_{\mathrm{y}}}{\partial y} = 0 \tag{A2}$$

$$\frac{\partial^2 \varepsilon_{\mathrm{x}}}{\partial y^2} + \frac{\partial^2 \varepsilon_{\mathrm{y}}}{\partial x^2} = \frac{\partial^2 \gamma_{\mathrm{xy}}}{\partial x \partial y} \tag{A3}$$

Where E_1 and E_2 are the elastic modulus in the directions of x_1-axis, and y_1-axis, respectively, GPa; G_{12} is the elastic modulus in x_1oy_1 coordinate system, GPa; ν_{12} and ν_{32} are the Poisson's ratio in the directions of x_1-axis, and y_1-axis, respectively.

The stress function F (x, y) was introduced based on Equation (A2) and by substituting it into Equations (A1) and A3 yields (Aadnoy and Chenevert, 1987).

$$\beta_{22}\frac{\partial^4 F}{\partial x^4} + (2\beta_{12} + \beta_{33})\frac{\partial^4 F}{\partial x^2 \partial y^2} + \beta_{11}\frac{\partial^4 F}{\partial y^4} = 0 \tag{A4}$$

By introducing linear differential operators $D_k = \partial/\partial y - \mu_k \partial/\partial x \, (k = 1, 2, 3, 4)$, the fourth-order partial differential equation can be derived, which is entirely equivalent to Equation (A4). Hence, these are the roots of the Eigen equation.

$$\beta_{11}\mu^4 + (2\beta_{12} + \beta_{33})\mu^2 + \beta_{22} = 0 \tag{A5}$$

Equation (A5) has two pairs of conjugate complex roots:

$$z_k = x + \mu_k y, \bar{z}_k = x + \bar{\mu}_k y, \; (k = 1, 2) \tag{A6}$$

We expressed the stress function F (x, y) as follows:

$$F = 2\mathrm{Re}[F_1(z_1) + F_2(z_2)] \tag{A7}$$

where Re is the real part of the complex number, and F_1 (z_1) and F_2 (z_2) are arbitrary analytic functions of the complex variables z_1 and z_2. To simplify calculations, we introduced the following functions can be:

$$\varphi_1(z_1) = F_1'(z_1), \varphi_2(z_2) = F_2'(z_2) \tag{A8}$$

Substituting Equation (A8) into Equation (A7) and subsequently taking the derivative yields:

$$\begin{cases} \dfrac{\partial F}{\partial y} = 2\mathrm{Re}[\mu_1\varphi_1(z_1) + \mu_2\varphi_2(z_2)] \\ \dfrac{\partial F}{\partial x} = 2\mathrm{Re}[\varphi_1(z_1) + \varphi_2(z_2)] \end{cases} \tag{A9}$$

Based on Equation (A9), the stress component in the anisotropic medium can be represented by the analytical function as:

$$\begin{cases} \sigma_{\mathrm{x}} = \sigma_{\mathrm{x}1} + 2\mathrm{Re}\left[\mu_1^2\varphi_1'(z_1) + \mu_2^2\varphi_2'(z_2)\right] \\ \sigma_{\mathrm{y}} = \sigma_{\mathrm{y}1} + 2\mathrm{Re}\left[\varphi_1'(z_1) + \varphi_2'(z_2)\right] \\ \tau_{\mathrm{xy}} = \tau_{\mathrm{xy}1} + 2\mathrm{Re}\left[\mu_1\varphi_1'(z_1) + \mu_2\varphi_2'(z_2)\right] \end{cases} \tag{A10}$$

Where $\sigma_{\mathrm{x}1}$ and $\sigma_{\mathrm{y}1}$ are the normal stress in the directions of x_1-axis and y_1-axis, respectively, MPa.

The stress boundary condition can be determined by the external force p_{x} and p_{y} applied as:

$$\begin{cases} 2\mathrm{Re}[\mu_1\varphi_1(z_1) + \mu_2\varphi_2(z_2)] = -\displaystyle\int p_{\mathrm{x}} ds \\ 2\mathrm{Re}[\varphi_1(z_1) + \varphi_2(z_2)] = \displaystyle\int p_{\mathrm{y}} ds \end{cases} \tag{A11}$$

The equations to express the external forces p_{x} and p_{y} can be derived based on the boundary conditions shown in Figure 1 as follows:

$$\begin{cases} p_{\mathrm{x}} = \sigma_{\mathrm{x}1} R\cos\theta \dfrac{d\theta}{ds} + \tau_{\mathrm{xy}1} R\sin\theta \dfrac{d\theta}{ds} \\ p_{\mathrm{y}} = \tau_{\mathrm{xy}1} R\cos\theta \dfrac{d\theta}{ds} + \sigma_{\mathrm{y}1} R\sin\theta \dfrac{d\theta}{ds} \end{cases} \tag{A12}$$

Where R is the radius of the borehole and the slotting depth, m.

Substituting Equation (A12) into Equation (A11) and subsequently making the arc integral yields:

$$\begin{cases} 2\mathrm{Re}[\mu_1\varphi_1(z_1) + \mu_2\varphi_2(z_2)] = -\sigma_{\mathrm{x}1} R\sin\theta + \tau_{\mathrm{xy}1} R\cos\theta \\ 2\mathrm{Re}[\varphi_1(z_1) + \varphi_2(z_2)] = \tau_{\mathrm{xy}1} R\sin\theta - \sigma_{\mathrm{y}1} R\cos\theta \end{cases} \tag{A13}$$

Equation (A13) can be expanded into a Fourier series focusing on θ as follows:

$$\begin{cases} 2\mathrm{Re}[\mu_1\varphi_1(z_1) + \mu_2\varphi_2(z_2)] = \displaystyle\sum_{m=1}^{\infty}\left(a_{\mathrm{m}}e^{\mathrm{i}\theta\mathrm{m}} + \bar{a}_{\mathrm{m}}e^{-\mathrm{i}\theta\mathrm{m}}\right) = 2\mathrm{Re}\sum_{m=1}^{\infty}\left(\bar{a}_{\mathrm{m}}e^{-\mathrm{i}\theta\mathrm{m}}\right) \\ 2\mathrm{Re}[\varphi_1(z_1) + \varphi_2(z_2)] = \displaystyle\sum_{m=1}^{\infty}\left(b_{\mathrm{m}}e^{\mathrm{i}\theta\mathrm{m}} + \bar{b}_{\mathrm{m}}e^{-\mathrm{i}\theta\mathrm{m}}\right) = 2\mathrm{Re}\sum_{m=1}^{\infty}\left(\bar{b}_{\mathrm{m}}e^{-\mathrm{i}\theta\mathrm{m}}\right) \end{cases} \tag{A14}$$

where **i** and e are the imaginary unit and natural number, respectively. By comparing Equations (A13) and (A14) one obtains:

$$\begin{cases} \bar{a}_1 = \dfrac{\left(\tau_{\mathrm{xy}1} - \mathrm{i}\sigma_{\mathrm{x}1}\right)R}{2}, \bar{b}_1 = \dfrac{\left(\mathrm{i}\tau_{\mathrm{xy}1} - \sigma_{\mathrm{y}1}\right)R}{2} \\ \bar{a}_{\mathrm{m}} = \bar{b}_{\mathrm{m}} = 0, m \geq 2 \end{cases} \tag{A15}$$

To ascertain the analytical function φ_{k} (z_{k}) (k=1, 2) based on the stress boundary conditions, it is essential to map the circular domain on the complex plane z_{k} (i.e., the x_2oy_2 plane) to the outer region of the unit circle on the ξ_{k} plane, with the corresponding mapping function is:

$$\begin{aligned} z_k &= \frac{R(1 - \mathrm{i}\mu_k)}{2}\xi_k + \frac{R(1 + \mathrm{i}\mu_k)}{2}\frac{1}{\xi_k}, \\ \xi_k &= \frac{z_k + \sqrt{z_k^2 - R^2(1 + \mu_k^2)}}{R(1 - \mathrm{i}\mu_k)}, \; (k = 1, 2) \end{aligned} \tag{A16}$$

Thus, on the borehole wall:

$$z_k = R(\cos\theta + \mu_k\sin\theta), \xi_k = e^{\mathrm{i}\theta}, \; (k = 1, 2) \tag{A17}$$

As the distance is augmented, the pressure induced by the surface forces that act on the well wall gradually decreases, the intricate analytical function can be posited as follows:

$$\varphi_k(z_k) = \sum_{m=1}^{\infty} A_{km}\xi_k^{-m} = \sum_{m=1}^{\infty} A_{km}e^{-\mathrm{i}m\theta}, \; (k = 1, 2) \tag{A18}$$

The specific form of the analytic function can be derived by comparing Equations (A18) and (A16) as:

$$\begin{cases} \varphi_1(z_1) = \dfrac{R\left(\mu_2\sigma_{y1} - \mathrm{i}\mu_2\tau_{xy1} + \tau_{xy1} - \mathrm{i}\sigma_{x1}\right)}{2(\mu_1 - \mu_2)\xi_1} \\ \varphi_2(z_2) = \dfrac{R\left(\mu_1\sigma_{y1} - \mathrm{i}\mu_1\tau_{xy1} + \tau_{xy1} - \mathrm{i}\sigma_{x1}\right)}{2(\mu_2 - \mu_1)\xi_2} \end{cases} \tag{A19}$$

The deformation of the borehole caused by *in situ* stress can be determined using the intrinsic equation:

$$\begin{cases} u = \beta_{11}\sigma_{x1}x + \beta_{12}\sigma_{y1}x + 2\mathrm{Re}\left[p_1\varphi_1(z_1) + p_2\varphi_2(z_2)\right] \\ v = \beta_{12}\sigma_{x1}y + \beta_{22}\sigma_{y1}y + 2\mathrm{Re}\left[q_1\varphi_1(z_1) + q_2\varphi_2(z_2)\right] \end{cases} \tag{A20}$$

where $p_i = \beta_{11}\mu_i^2 + \beta_{12}$, $p_i = (\beta_{12}\mu_i^2 + \beta_{22})/\mu_i$, ($i$=1,2).

By comparing Equations (A17) and (A19) into Equation (A20) and subsequently simplifying, a specific formula for the displacement yields:

$$\begin{cases} u = \mathrm{Re}\left[\begin{pmatrix} (\beta_{11}(\mu_1 + \mu_2 - \mathrm{i}\mu_1\mu_2) + \mathrm{i}\beta_{12})\tau_{xy1} \\ +(\beta_{11}\mu_1\mu_2 - \beta_{12})\sigma_{y1} - \mathrm{i}\beta_{11}(\mu_1 + \mu_2)\sigma_{x1} \end{pmatrix} R(\cos\theta - \mathrm{i}\sin\theta)\right] \\ \quad + \beta_{11}\sigma_{x1}R\cos\theta + \beta_{12}\sigma_{y1}R\cos\theta \\ v = \mathrm{Re}\left[\begin{pmatrix} \left(\dfrac{\beta_{22}(\mathrm{i}\mu_1 + \mathrm{i}\mu_2 + 1)}{\mu_1\mu_2} - \beta_{12}\right)\tau_{xy1} \\ + \dfrac{\beta_{22}(\mu_1 + \mu_2)}{\mu_1\mu_2}\sigma_{y1} + \mathrm{i}\left(\dfrac{\beta_{22}}{\mu_1\mu_2} - \beta_{12}\right)\sigma_{x1} \end{pmatrix} R(\cos\theta - \mathrm{i}\sin\theta)\right] \\ \quad + \beta_{12}\sigma_{x1}R\sin\theta + \beta_{22}\sigma_{y1}R\sin\theta \end{cases} \tag{A21}$$

The relationship satisfied by the two roots of Equation (A5) is as follows:

$$\mu_1^2 + \mu_2^2 = -\frac{2\beta_{12} + \beta_{33}}{\beta_{11}}, \mu_1^2\mu_2^2 = \frac{\beta_{22}}{\beta_{11}} \tag{A22}$$

To eliminate the **Re** sign in Eq. 22, one may assume that $\mu_1\mu_2 = -q$, $\mu_1 + \mu_2 = i\sqrt{p + 2q}$, and that p and q are natural numbers (Heng et al., 2021). As a result, Equation (A21) can be simplified to Eq. 2.

Appendix B

The equation for an ellipse is typically represented in the following standard form:

$$\frac{X^2}{a^2} + \frac{Y^2}{b^2} = 1 \tag{B1}$$

By rotating the coordinate axes of the standard equation by β, the general equation of the ellipse (Eq. 4) can be obtained. The relationship between the corresponding coordinates can be expressed as follows:

$$\begin{cases} X = x_1\cos\beta + y_1\sin\beta \\ Y = y_1\cos\beta - x_1\sin\beta \end{cases} \tag{B2}$$

Substituting Eq. (B2) into Eq. (B1) and simplifying yields:

$$\left(\frac{\cos^2\beta}{a^2} + \frac{\sin^2\beta}{b^2}\right)x_1^2 + \left(\frac{\sin 2\beta}{a^2} - \frac{\sin 2\beta}{b^2}\right)x_1y_1 + \left(\frac{\sin^2\beta}{a^2} + \frac{\cos^2\beta}{b^2}\right)y_1^2 = 1 \tag{B3}$$

We compared Equations (B3) and (4) yields:

$$\begin{cases} \dfrac{\cos^2\beta}{a^2} + \dfrac{\sin^2\beta}{b^2} = A \\ \dfrac{\sin 2\beta}{a^2} - \dfrac{\sin 2\beta}{b^2} = B \\ \dfrac{\sin^2\beta}{a^2} + \dfrac{\cos^2\beta}{b^2} = C \end{cases} \tag{B4}$$

The solution to Eq. (B4) provides the values for the major axis a, the minor axis b, and the angle β between the directions of the major axis and the x_2 axes of the elliptical borehole. These values are illustrated in Equation 5.

Appendix C

To acquire the flexibility matrix of the medium in the x_3oy_3 coordinate system, we transform on the flexibility matrix in the x_2oy_2 coordinate system as follows (Ma et al., 2022):

$$[C'] = [M_\sigma]^T[C][M_\sigma] \tag{C1}$$

where $[C]$ is the flexibility matrix in the x_2oy_2 coordinate system, $[C']$ is the flexibility matrix in the x_3oy_3 coordinate system, and $[M_\sigma]$ is the bond matrix with the following form:

$$[C'] = \begin{pmatrix} c_{11} & c_{12} & c_{13} \\ c_{21} & c_{22} & c_{23} \\ c_{31} & c_{32} & c_{33} \end{pmatrix} \tag{C2}$$

$$[M_\sigma] = \begin{pmatrix} m^2 & n^2 & 2mn \\ n^2 & m^2 & -2mn \\ -mn & mn & m^2 - n^2 \end{pmatrix} \tag{C3}$$

where $m = \cos\beta$, and $n = \sin\beta$.

Equation (A5) can be modified in the following form:

$$c_{11}\mu^4 - 2c_{13}\mu^3 + (2c_{12} + c_{33})\mu^2 - 2c_{23}\mu + c_{22} = 0 \tag{C4}$$

It is typical for the Eigen Equation (C4) to exhibit two pairs of conjugate complex roots denoted as and $\bar{\mu}_{kk}$ (where k=1, 2).

The stress equations are derived using the method described in Appendix A, but the stress boundary conditions are changed. We can modify Equation 12 by considering the effects of fracturing fluid injection pressure and *in situ* stress (Zheng et al., 2023).

$$\begin{cases} p_x = (\sigma_{x2} - p_w)b\cos\theta\dfrac{d\theta}{ds} + \tau_{xy2}a\sin\theta\dfrac{d\theta}{ds} \\ p_y = \tau_{xy2}b\cos\theta\dfrac{d\theta}{ds} + \left(\sigma_{y2} - p_w\right)a\sin\theta\dfrac{d\theta}{ds} \end{cases} \tag{C5}$$

Where p_w is the injection pressure of fracturing fluid, MPa.

The final analytical functions obtained from Equation (C5) based on the calculation process in Appendix A are as follows:

$$\begin{cases} \varphi_1(z_1) = \dfrac{\mu_{22}\left(\mathrm{i}p_wa - \mathrm{i}\sigma_{y2}a - \tau_{xy2}b\right) + p_wb - \sigma_{x2}b - \mathrm{i}\tau_{xy2}a}{2(\mu_2 - \mu_1)\xi_1} \\ \varphi_2(z_2) = \dfrac{\mu_{11}\left(\mathrm{i}p_wa - \mathrm{i}\sigma_{y2}a - \tau_{xy2}b\right) + p_wb - \sigma_{x2}b - \mathrm{i}\tau_{xy2}a}{2(\mu_1 - \mu_2)\xi_2} \end{cases} \tag{C6}$$

Equation 9 can be obtained by taking the derivatives of φ_1 (z_1) and φ_2 (z_2) in Equation (C6) for z_1 and z_2, respectively.

frontiers | Frontiers in Earth Science

TYPE Original Research
PUBLISHED 18 January 2024
DOI 10.3389/feart.2023.1326861

OPEN ACCESS

EDITED BY
Hu Li,
Southwest Petroleum University, China

REVIEWED BY
Yumao Pang,
Shandong University of Science and Technology, China
Qiang Guo,
China University of Mining and Technology, China
Tianshou Ma,
Southwest Petroleum University, China

*CORRESPONDENCE
Dai Yunjie,
daiyunjie@cnpc.com.cn

RECEIVED 24 October 2023
ACCEPTED 31 December 2023
PUBLISHED 18 January 2024

CITATION
Fang Z, Yunjie D, Dongyan Z, Yu L, Jixiang H, Xuechun Z and Yaoli S (2024), A seismic prediction method of reservoir brittleness based on mineral composition and pore structure.
Front. Earth Sci. 11:1326861.
doi: 10.3389/feart.2023.1326861

A seismic prediction method of reservoir brittleness based on mineral composition and pore structure

Zhang Fang[1], Dai Yunjie[2]*, Zhou Dongyan[2], Lin Yu[2], He Jixiang[1], Zhang Xuechun[2] and Shi Yaoli[1]

[1]PetroChina Xinjiang Oilfield Company, Karamay, Xinjiang, China, [2]PetroChina Oriental Geophysical Company, Urumqi, Xinjiang, China

The Lucaogou Formation, a typical fine-grained mixed formation in the Jimusaer Sag of the Junggar Basin, exhibits considerable potential for hydrocarbon exploration. Accurate brittle prediction is a crucial factor in determining hydraulic fracturing effectiveness. However, the area features complex lithological characteristics, including carbonate rocks, clastic rocks, volcanic rocks, and gypsum interbeds, along with thin layering and sporadic sweet spots. Traditional prediction methods offer limited resolution and there is an urgent need for a seismic brittle prediction method tailored to this complex geological environment. This paper presents a multi-mineral composition equivalent model for complex lithologies that enables the accurate calculation of Vp and Vs These ratios serve as the foundation for pre-stack elastic parameter predictions, which include Poisson's ratio and Young's modulus. By comparing the predicted parameters with well-logging measurements, the prediction accuracy is improved to 82%, with particularly high conformity in intervals characterized by high organic matter and clay content. Additionally, a three-dimensional brittle modeling approach reveals that the brittleness of the reservoir exceeds that of the surrounding rock, showing a gradual improvement in brittleness with increasing burial depth from southeast to northwest. The central area exhibits relatively good brittleness, with a stable, blocky distribution pattern.

KEYWORDS

Jimusaer sag, fine-grained mixed reservoirs, complex mineralogy, rock physics modeling, brittleness

1 Introduction

The Lucaogou Formation in the Jimusaer Sag of the Junggar Basin hosts significant potential for hydrocarbon exploration, with estimated recoverable resources of approximately 238 million tons (Cao et al., 2016; Liu et al., 2017; Zhi et al., 2018; Cai, 2020; Yin et al., 2021; Yin et al., 2022). This formation represents one of the oldest terrestrial mixed clastic rock sequences in China, deposited in a saline lake basin. It features complex characteristics, such as the intermixing of carbonate rocks, clastic rocks, volcanic rocks, gypsum interbeds, source-reservoir integration, thin layering, and sporadic sweet spots (Zhang et al., 2019; Duan et al., 2020; Li et al., 2020; Wang and Wang, 2021; Wei et al., 2022). Rock physics and brittleness modeling are crucial components of comprehensive oil and gas seismic-geological-engineering research in this area. The modeling results not only impact pre-drilling sweet spot predictions but also influence the optimization of reservoir hydrofracturing processes (Wang et al., 2013; Yu et al., 2016; Wu et al., 2017; Feng et al., 2020; Gui et al., 2020; Jahed et al., 2020; Shan et al., 2021).

Prediction methods for rock physics and brittleness can generally be categorized into three types: 1) brittleness prediction based on rock mineral composition, which calculates the brittleness index profile for the entire well section using the mineral composition, achieving a high level of accuracy (Mukerji et al., 1995; Zhi and Zan, 2015; Li et al., 2019; Ma et al., 2019; Ba et al., 2021; Meng et al., 2021); 2) brittleness evaluation based on rock mechanical elastic parameters, relying on vertical and horizontal well logging wave data and pre-stack inversion. It employs the Rickman formula to compute the correlation between Young's modulus, Poisson's ratio, and the brittleness index (Meng et al., 2015; Li et al., 2017; Gui et al., 2023); 3) utilization of uniaxial and triaxial stress-strain tests on core samples to obtain correlations between rock physical parameters, mineral composition, bedding characteristics, hydrocarbon content, and other parameters (Wang et al., 2017; Chen et al., 2019; Tao et al., 2020; Liu et al., 2021). However, as rock physics and brittleness parameters are fundamentally a result of the comprehensive response of rock material composition, structure, porosity, and fluid under specific temperature and pressure conditions, predictions based solely on mineral composition or rock mechanical parameters have inherent limitations (Li, 2022; Li, 2023).

Regarding research methods, rock physics models can be broadly classified into three categories: 1) effective medium models that use volume-averaged mineral properties, such as Voigt–Reuss–Hill models (Chung and Buessem, 1967), Hashin-Shtrikman models (Neumann and Bohlke, 2016), Wood equations, Wyllie equations (Saleh and Castagna, 2004), and Raymer equations (Raymer et al., 1980), etc.,; 2) adaptive and scattering theory models that study the influence of internal pore structure and fluids on rock properties, such as the Differential Effective Medium (DEM) model, Kuster-Toksöz model (Hu and Weng, 2000), self-consistent approximation (SCA) model (Ignatchenko and Polukhin, 2016), and Gassmann equation.; 3) contact theory models based on particle interactions, such as the Hertz contact model (Muthukumar &DesRoches, 2006). These models can reflect the brittleness characteristics of reservoirs to some extent. However, the complex interplay between mixed clastic rock's intricate pore structure and mineral composition has made it challenging to establish a clear relationship between rock mechanical properties and geological parameters in the Lucaogou Formation of the Jimusaer Sag. Moreover, the reservoir in the study area consists of thin interbeds with multiple minerals, with each layer having a thickness of 1–4 m, making identification and prediction based solely on seismic data difficult.

In light of these challenges, this paper focuses on the Lucaogou Formation in the Jimusaer Sag, considering factors such as mineral composition and pore structure in combination to evaluate their impact on rock seismic elastic parameters. Appropriate rock physics equivalent theory models are chosen for the study area to obtain rock elastic parameters, and a brittleness index theoretical template is established to determine the spatial distribution model of reservoir brittleness. This research holds significant guidance for sweet spot predictions and fracturing process optimization.

2 Research data and methods

2.1 Research area

Jimusaer Sag is located in the southeast edge of the Junggar Basin, surrounded by Qitai uplift, Santai fault, Xidi fault and Jimusaer fault, which is in the form of a dustpan high in the east and low in the west. The Lucaogou Formation has developed throughout the entire depression, with an average thickness of about 200–350 m (Figure 1) (Yin et al., 2022; Yin et al., 2023a; Yin et al., 2023b). It belongs to the sedimentary system of saline lake basins, characterized by mixed carbonate clastic volcanic gypsum rocks, integrated source and reservoir, thin layer stacking, and dispersed desserts. The Lucaogou Formation has developed two "dessert bodies," upper and lower. The upper dessert body is located in the second section of the Lucaogou Formation, and the lithology is mainly composed of lithic sandstone, sandy dolomite, and feldspar lithic sandstone, interbedded with mudstone and dolomite mudstone; The porosity ranges from 1.1% to 2.4%, with an average of 9.88%; Permeability at $0.01 \times 10^{-3}\ \mu m^2 \sim 36.3 \times 10^{-3}\ \mu m^2$, with an average of $0.07 \times 10^{-3}\ \mu m^2$. The lower dessert body is located in the first section of the Lucaogou Formation, mainly composed of fine sandstone and cloudy sandstone, interbedded with muddy sandstone and mudstone. The porosity ranges from 2.1% to 26.5%, with an average of 8.75%; Permeability at $0.01 \times 10^{-3}\ \mu m^2$–$52.6 \times 10^{-3}\ \mu m^2$, with an average of $0.05 \times 10^{-3}\ \mu m^2$. This Formation is divided into two members, Lu1 and Lu2, and four sand groups, $P_1l_1^1$, $P_1l_1^2$, $P_2l_2^1$ and $P_2l_2^2$ from bottom to top. The major reservoirs are two sweet spot layers, the lower one ($P_2l_1^2$)is mainly dolomitic siltstone; the upper one ($P_2l_2^2$)is primarily composed of felsic siltstone, dolomitic siltstone and silty dolomite (Figure 1B).

2.2 Research data

For this research, over 100 thin-section photomicrographs were used to investigate the mineral composition and pore structure in the studied region. In terms of seismic data quality, a significant improvement was achieved by conducting a comprehensive and integrated interpretation based on the high-density 3D seismic data collected in the Ji25 area, which covered an area of 25 km^2 and included 484 coverage passes with a density of 774,400 traces. The seismic data has a dominant frequency of approximately 25 Hz, an effective bandwidth of 10–60 Hz, a signal-to-noise ratio greater than 15 dB, and a vertical resolution of approximately $\lambda/8$, as calculated by seismic inversion theory, allowing for the recognition of sand body thicknesses of around 20 m in areas with high signal-to-noise ratios. This quality largely satisfies the precision requirements for lithology and brittleness index prediction.

Utilizing data from core thin-section photomicrographs, scanning electron microscopy, and X-ray diffraction analysis, the research first identifies the microstructure and mineral composition of the rocks. Subsequently, considering the impact of factors such as mineral composition and pore structure on rock seismic elastic parameters, suitable rock physics equivalent theory models applicable to the study area are selected to obtain rock elastic parameters. A theoretical template for brittleness index is then

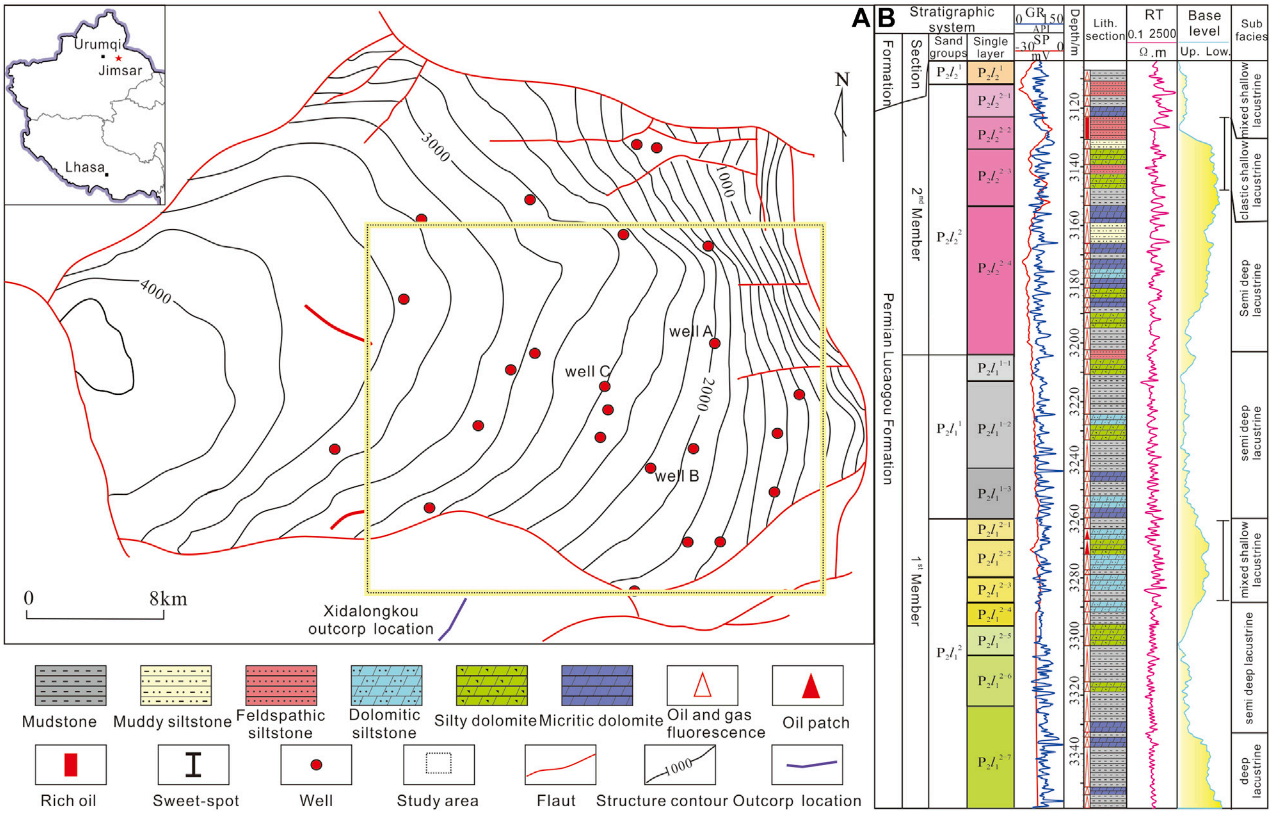

FIGURE 1
Location and composite stratigraphic column of the study area **(A)** Location and structures of the work area; **(B)** Composite stratigraphic column of the Lucaogou Formation.

established. Finally, integrating well-logging, seismic, and core data, a spatial distribution model for reservoir brittleness is developed.

2.3 Research methods

The research builds upon the Xu-White model (Keys and Xu, 2002) and refines the process of complex multi-mineral rock physics modeling to create a complex multi-mineral seismic rock physics model. The proposed model accounts for the layering and mineral composition characteristics of mixed clastic rocks, optimizing the process of mixing the matrix minerals. To address the complexity of pore structures in mixed clastic rocks, variable values are determined for layered and brittle mineral-related porosities, replacing previously used empirical constants to enhance pore description accuracy. The fluid mixture section is modified using the Beri model (Kőrösi et al., 2021) for fluid mixture equivalency, and the Boris model (Oran and Boris, 1981) is employed for fluid replacement. This results in the establishment of a saturated mixed clastic rock equivalent model. The specific workflow is depicted in Figure 2.

2.3.1 Equivalent model for brittle minerals

Among the four brittle minerals distributed in the studied area, quartz, feldspar, and calcite have similar abundancy, while dolomite content is relatively lower. Therefore, based on the characteristics of the content of these four brittle minerals, the following equivalent methods were employed.

1) Quartz, feldspar, and calcite were mixed using a self-consistent approximation (SCA) model that can simultaneously account for multiple mineral phases. Specifically, Berryman proposed a calculation of the equivalent volume and shear modulus for rock containing elliptical inclusions based on elastic wave scattering theory (Formula 1):

$$\sum_{i=1}^{N} f_i (K_i - K) P^i = 0 \tag{1}$$

In the equation, f_i represents the volume modulus of the ith inclusion, K is the equivalent volume/shear modulus for mineral grains, i is the mineral medium index, P^i is a parameter related to the composition and pore shape.

2) Using the mixture obtained in the previous step as the background medium and dolomite, as the filler, both are mixed using the Differential Effective Medium (DEM) model to obtain the equivalent modulus for brittle minerals (Formulas 2, 3):

$$(1-\varphi)\frac{d}{d\varphi}\left[K^*(\varphi)\right] = (K_2 - K^*)P^i(\varphi) \tag{2}$$

$$K^*(0) = K_{gr} \tag{3}$$

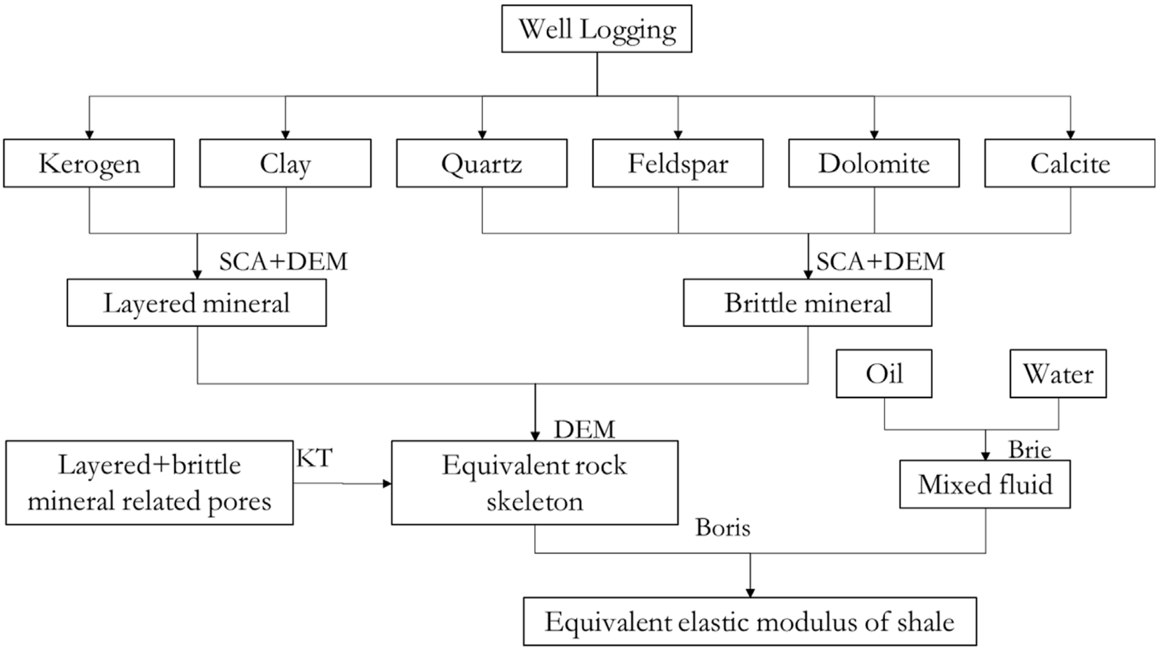

FIGURE 2
Complex multi-mineral mixed rock seismic rock physics model.

In the equation, K^* represents the elastic modulus of the rock matrix as inclusions are gradually added; K_2 represents the elastic modulus of the inclusions that are gradually added.

2.3.2 Layered minerals and equivalent models

Mixed clastic rocks often exhibit good clay layering, with a variety of clay mineral types. Additionally, different clay minerals have varying elastic properties. The heterogeneity of organic matter, such as kerogen, at different maturities also affects the heterogeneity of mixed clastic rocks. Considering the distribution and interactions of clay and organic matter in mixed clastic rocks, a self-consistent differential effective medium (SCA-DEM) model is used to mix layered minerals (organic matter and clay), resulting in an equivalent modulus with interconnected properties for organic matter-clay:

1) An equal amount of clay is taken in combination with kerogen, and both are mixed using a self-consistent model.
2) With the remaining clay as the background medium and the mixture obtained in step 1 as the filler, both are mixed using the differential effective medium (DEM) model (Cundall and Strack, 1979), resulting in an equivalent modulus with interconnected properties for kerogen-clay plastic minerals.
3) Using the plastic equivalent material composed of clay-kerogen as the background medium and brittle equivalent materials such as quartz and calcite as the filler, both are mixed using the DEM model to obtain the equivalent modulus of the rock framework.

2.3.3 Dry rock equivalent model

Using the rock framework as the background medium, pores are added to the background medium using the differential effective medium (DEM) model, resulting in the equivalent modulus for dry rock. A porosity anisotropy parameter is introduced in this context.

2.3.4 Saturated rock equivalent model

1) Fluid properties are calculated using the Batzle & Wang model (Han and Batzle, 2020) based on known temperature, pressure, oil density, formation water salinity, and gas-oil ratio. Fluid mixing is performed using Brie's exponent method (Kőrösi et al., 2021).
2) Since mixed clastic rock layers under oil saturation conditions exhibit significant velocity dispersion, the full-band Boris fluid replacement model is used to introduce mixed fluids into dry rock, thereby establishing a mixed clastic rock equivalent model that closely resembles real conditions. Boris fluid replacement model is shown below (Formula 4):

$$\frac{1}{K_{mf}(P,\omega)}=\frac{1}{K_h}+\frac{1}{\frac{1}{\frac{1}{K_{dry}(P)}-\frac{1}{K_h}}+\frac{3i\omega\eta}{8\varphi_c(P)a^2}} \tag{4}$$

The mineral composition of the mixed clastic rocks in the target area is primarily quartz, feldspar, carbonate minerals, clay, etc. When modeling, the mechanical parameters of each mineral component are set based on Mavko et al.'s work (Mavko and Nur, 1979). For example, the volume modulus of quartz is set to 37 GPa, the shear modulus to 44 GPa, and the density to 2.65 g/cm^3.

3 Mineral and pore structure characteristics

The study area in the Jimsar sag of the Junggar Basin hosts the Lucaogou Formation, which is a sedimentary sequence in a saline lake

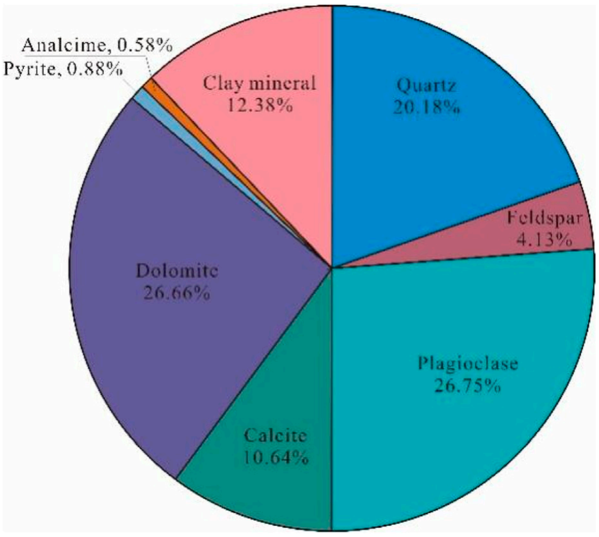

FIGURE 3
Mineral composition in the Jimusaer Lucaogou Formation.

basin. The rock samples exhibit a wide variety of mineral components, including quartz, potassium feldspar, plagioclase feldspar, calcite, dolomite, ankerite, pyrite, pyrrhotite, siderite, natrolite, thomsonite, and various clay minerals. XRD mineral content analysis was conducted on 142 core samples from the target interval in the study area. The results revealed that there are as many as 12 different minerals in the overall composition. Among these, calcite and plagioclase feldspar are the predominant minerals, each accounting for over 20% of the composition. Quartz and siderite follow, with a content range of 10%–15%. There are at least six minerals with an absolute content greater than 4%, indicating a complex mixed composition of multiple mineral components forming the mixed clastic rock's intricate rock framework. Specifically, in the upper sweet spots, the content of felsic minerals (feldspar and quartz) is relatively high, exceeding 40%, while in the lower sweet spots, mafic minerals are predominant, with a content exceeding 45%. The absolute content of clay minerals is generally low (less than 10%) and is primarily composed of illite and smectite, with small amounts of montmorillonite and kaolinite. The difference in clay mineral composition between the upper and lower sweet spots is not significant (Figure 3).

The complex mineral composition and content combinations in this region differ significantly from fine-grained sedimentary rocks and shale oil reservoirs in other basins. This reflects a mixed sedimentary rock type transitioning from clastic sedimentation to chemical sedimentation, or from volcanic clastic rocks to normal sedimentary rocks. The relative mineral content varies considerably in different depth intervals, and there are frequent changes in the relative mineral content along the vertical profile. This complexity indicates that the rock types and their combinations are highly intricate.

Pore structure is a crucial factor that influences fluid presence and changes in rock physical properties. Based on core and thin-section analysis data, the primary pore types in the Lucaogou Formation include intergranular dissolution pores (Figure 3A), intragranular dissolution pores, intercrystalline pores, microfractures, and a small number of oomoldic intergranular dissolution pores and biogenic framework pores, among others. In general, the relative content of intergranular pores in terrigenous clastic rock reservoirs is higher compared to other types of rock reservoirs, while in carbonate rock reservoirs, intergranular dissolution pores have a relatively higher content than in other rock types. Various types of fractures, including structural fractures, dissolution fractures, bedding fractures, and pressure solution fractures, have developed. The degree of fracture development is closely related to lithology, with carbonate rock fractures typically more well-developed than sandstone fractures. Overall, carbonate rock exhibits a stronger brittleness compared to sandstone (Figure 4).

4 Analysis of brittleness prediction effect

4.1 Prediction of mineral content and pore aspect ratio

The Lucaogou Formation exhibits a diverse range of mineral components, making it challenging to provide detailed characterizations for each mineral's content. However, by analyzing the petrophysical parameters of minerals and optimizing the consolidation of multiple mineral components, effective prediction of mineral content can be achieved. Initially, considering that minerals such as pyrite and siderite have minimal content, constituting less than 4% and having a negligible impact on the modeling results, they were excluded from the analysis. For both orthoclase and plagioclase feldspar, with densities of 2.59 and 2.61 g/cm^3, and compressional wave velocities of 5,590 and 5,749 m/s, respectively, their petrophysical properties are similar. As a result, they were combined and simplified into a single category, referred to as "feldspar." Using this approach, the complex mineral components were ultimately reduced to six categories: quartz, feldspar, calcite, dolomite, clay minerals, and kerogen. Through optimized well log interpretations, it became possible to predict the content of quartz, feldspar, calcite, dolomite, and clay minerals. However, the precise prediction of kerogen content (total organic carbon) is relatively complex (Formulas 5, 6). Therefore, this study applied the Passey formula to predict the kerogen content (Figure 5).

$$\Delta \log R = \log\left(\frac{R}{R^*}\right) + K \times (\Delta t\text{-}\Delta t^*) \tag{5}$$

$$TOC = 10^{2.297-0.1688\times R_O} \times \Delta \log R + B \tag{6}$$

Where, TOC represents the kerogen content, %; R stands for resistivity, ohm·m; K is the corresponding calibration factor, which is set at 0.02 in this area; Δt represents the sonic transit time, ohm·m; Δt* denotes the baseline for the sonic transit time, ohm·m; and B represents the TOC value for non-source rock intervals. There are usually four methods for calculating the content of cheese roots, namely, the Passey formula method, multivariate fitting method, density method, and natural gamma spectroscopy method. The calculation of kerogen was carried out using the four calculation methods mentioned above, and comparative verification showed that the content of kerogen obtained by the Passey formula method was in good agreement with the measured values in the well (Figure 5).

The fixed constant of pore aspect ratio cannot accurately describe the complex porosity types of the Lucaogou formation. In this study, mineral content is introduced, and a weighted method

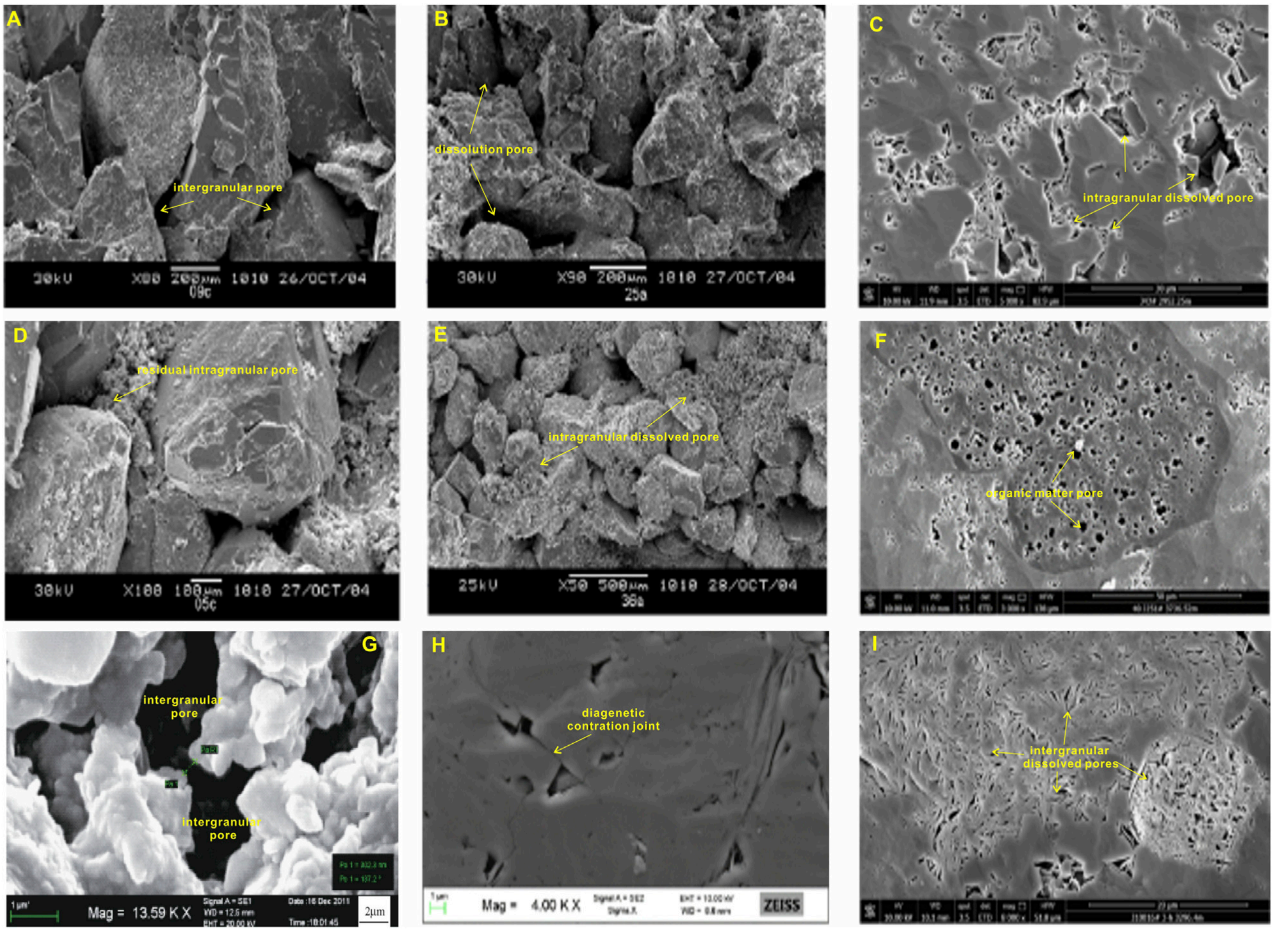

FIGURE 4
Microscopic Structure of Pore Types in the Jimusaer Lucaogou Formation **(A)** Primary intergranular pore **(B)** Intragranular and intergranular dissolution pores **(C)** intragranular dissolved pore **(D)** Residual intergranular pores **(E)** Intragranular and intergranular dissolution pores **(F)** Organic matter pore **(G)** Intergranular pore **(H)** Diagenetic contraction joint **(I)** Intragranular dissolved pores.

is used to calculate the porosity aspect ratio curve. The specific formula is as follows (Formula 7):

$$A = \Sigma\left(\left(\acute{V}/VT\right)^{*}\acute{A}\right) \qquad (7)$$

Where, A represents the porosity aspect ratio curve, Σ denotes the summation formula, V' stands for the content of a specific mineral, VT is the total mineral content, and A' represents the theoretical aspect ratio of a certain mineral. Table 1 contains the theoretical values of aspect ratios for different minerals. By applying the formula with the mineral content at various depth points and their respective theoretical aspect ratios, accurate determination of rock porosity aspect ratios can be achieved (Figure 6).

4.2 Comparison of rock physical template and logging data

The above method was used to complete the rock physics modeling of 72 vertical wells in the area. Taking a C well with shear wave logging data as an example, the predicted results were compared with the measured results. The prediction accuracy was improved especially in the layers with higher organic matter and clay content, where the consistency was higher (Figure 7). An overall analysis was conducted on 11 wells in the entire region with measured shear wave data. After using the Xu-White and Mixed rock Physics methods, and the point-to-point parameters are compared with the predicted longitudinal wave velocity (Vp), density and shear wave velocity (Vs), the measured data from 3,152–3,208 m in well C. The correlation coefficient between predicted and measured values was as high as 0.82, indicating that this method is highly accurate and reliable (Figure 8).

4.3 Analysis of brittleness prediction effect

1) Establishment of Brittleness Index Based on Elastic Parameter Method

The method for assessing brittleness based on elastic parameters primarily considers that higher Young's modulus (E) and lower Poisson's ratio (ν) indicate better rock brittleness. Rickman, using statistical methods, studied the relationship

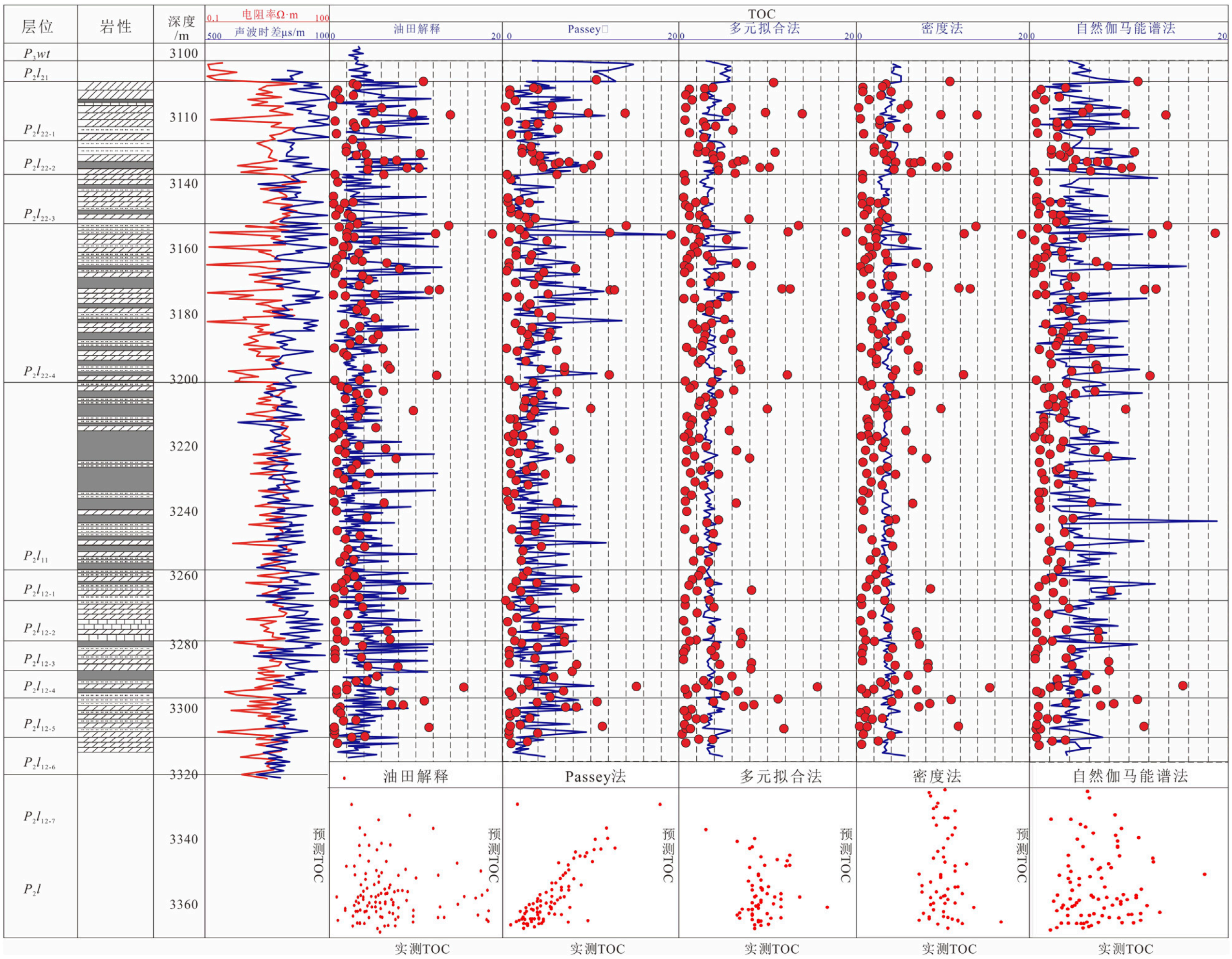

FIGURE 5
Comparison of results obtained by different methods for obtaining kerogen.

TABLE 1 Theoretical pore aspect ratio values for different pore types.

Pore type	Theory aspect ratio	Pore type	Theory aspect ratio
Intergranular pores (micropores)	0.12	Corrosion pores	0.8
Intragranular pores	0.12	microfractures	0.01
Clay pores	0.05	Clay particles	0.05
Casting hole	0.8	crystal particle	1

between rock brittleness and Young's modulus (E) and Poisson's ratio (ν). While, Young's modulus can be regarded as an index to measure the difficulty of rock elastic deformation. The greater the value, the greater the stress of the rock elastic deformation occurs to a certain extent, that is, the greater the rock stiffness, and the smaller the elastic deformation occurs under the action of a certain stress. Poisson's ratio refers to the ratio of the absolute value of the lateral positive strain to the axial positive strain when the rock is pulled or pressed, which is the elastic constant reflecting the lateral deformation of the rock. Rock brittleness is an inherent property of rock when ruptured by force. The fragility index characterizes the speed or difficulty of transient changes before rock rupture, rMeflecting the complexity of cracks formation after reservoir fracturing. Usually, rocks with a higher brittle index are harder and more brittle.

Young proposed that the ability of rocks to fail under loading can be quantified by Poisson's ratio, while Young's modulus reflects the rock's ability to maintain internal fractures after failure. He suggested that rock brittleness is positively correlated with Young's modulus and negatively correlated with Poisson's ratio. He established a brittleness index, which has been widely applied in oil fields in South America.

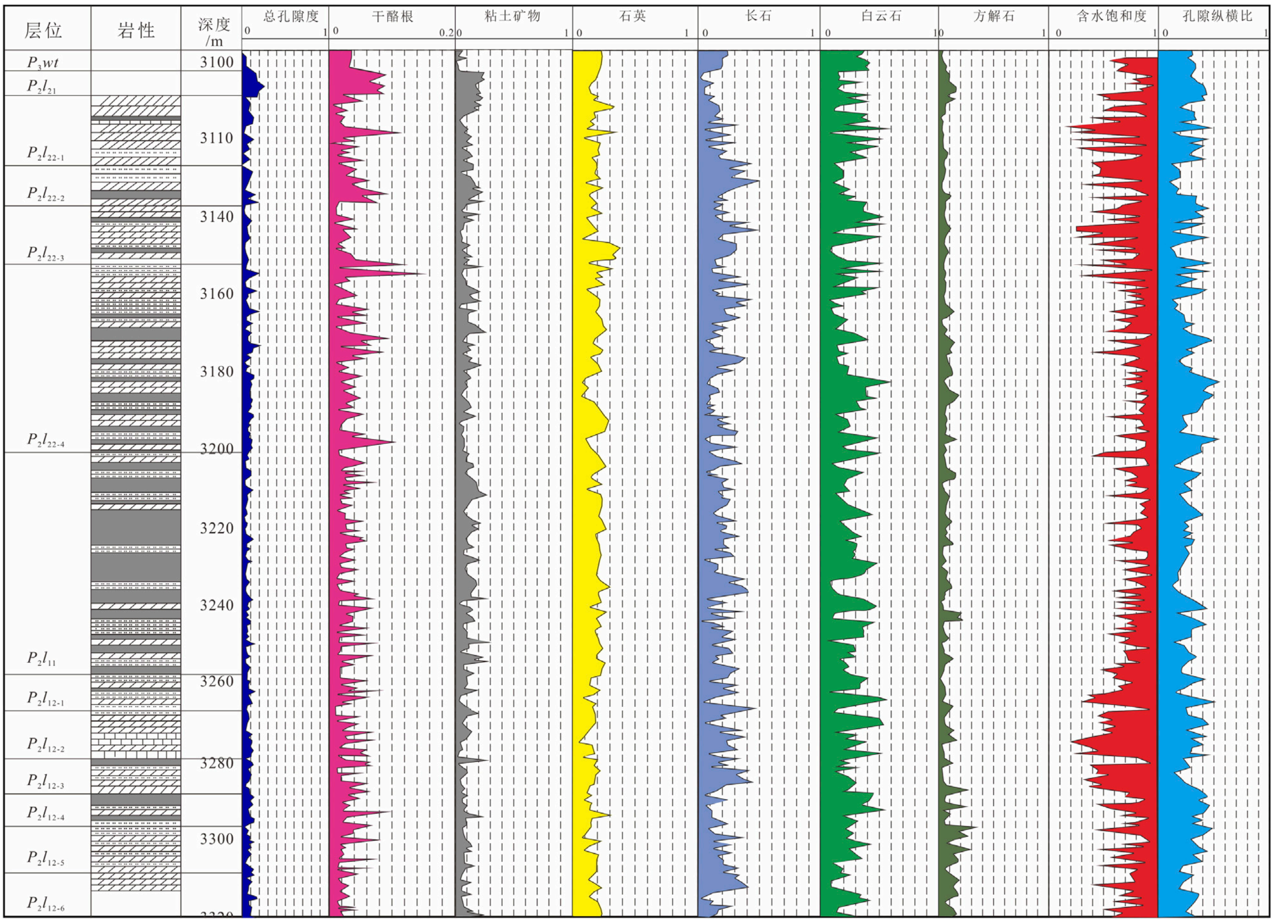

FIGURE 6
Prediction curve of pore width to length ratio in well C.

Obtain relevant elastic parameter data through the triaxial stress test of Jimusaer Lucaogou Formation, and conduct intersection analysis between elastic parameters and brittleness. It can be seen that the Young's modulus and Poisson's ratio are more sensitive to rock brittleness, and the Young's modulus is positively correlated with brittleness. The better the brittleness, the greater the Young's modulus; The Poisson's ratio is negatively correlated with brittleness. The better the brittleness, the smaller the Poisson's ratio, and a single Young's modulus or Poisson's ratio cannot better characterize the degree of brittleness of the rock. Based on the above understanding, the final optimal formula BI_{10} is selected to evaluate the reservoir brittleness index.

$$BI_{10} = E_{BRIT}/\upsilon_{BRIT} \tag{8}$$

Where, E_{BRIT} is normalized Young's modulus, GPa; υ_{BRIT} is normalized Poisson's ratio.

The above method considers not only the influence of mineralogy but also the impact of pore shape and pore fluids. It effectively characterizes the interaction of stress and strain in rocks and provides a reliable reflection of rock brittleness. It establishes a well-defined relationship between brittleness index and elastic parameters, serving as a valuable bridge for brittleness characterization based on seismic data. As a result, it finds wide application in unconventional reservoir brittleness assessment.

3) Brittleness Sensitivity Analysis

Through triaxial stress tests on the Lucaogou Formation in the Junggar Basin, relevant elastic parameter data were obtained, and a cross-plot analysis of elastic parameters and brittleness was conducted. The results show that Young's modulus and Poisson's ratio are sensitive indicators of rock brittleness. Young's modulus is positively correlated with brittleness, meaning that higher brittleness corresponds to larger Young's modulus. By contrast, Poisson's ratio is negatively correlated with brittleness, meaning that better brittleness corresponds to a smaller Poisson's ratio. It was observed that a single parameter, either Young's modulus or Poisson's ratio, cannot effectively represent the brittleness of the rock. The analysis confirms the validity of the previously mentioned formula (Figure 9).

3) Seismic Brittle Index Prediction

Leveraging the complex lithology and multiple mineral components of the mixed sedimentary rocks, high-precision

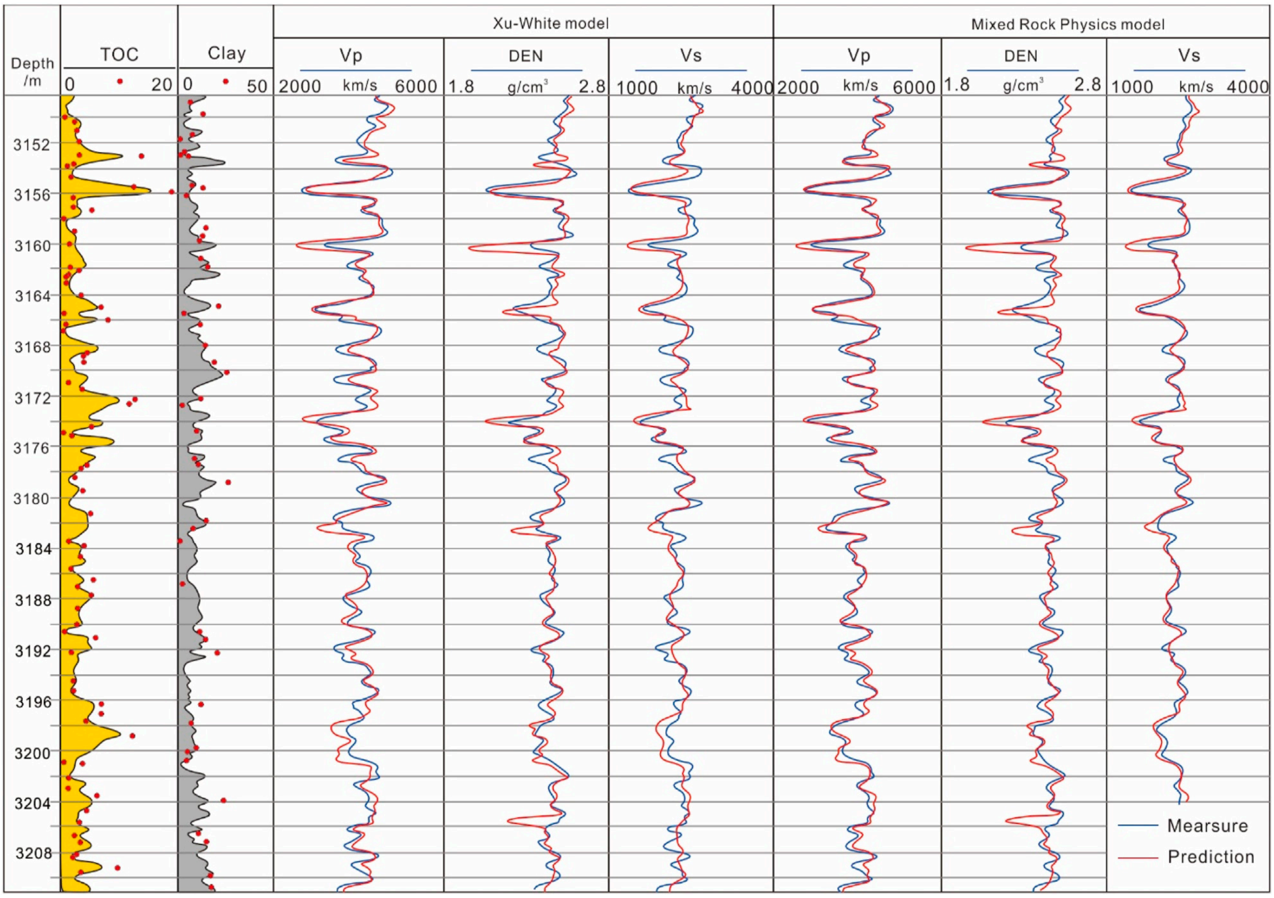

FIGURE 7
Comparison between Xu-White model and joint equivalent model in Well C.

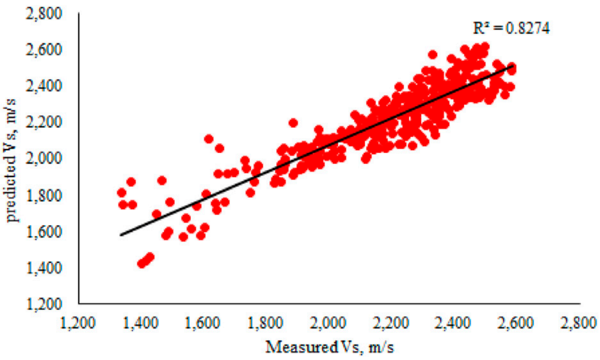

FIGURE 8
Correlation between rock physical prediction and actual measurement in well C.

Vp/Vs ratios can be obtained as the basis for pre-stack elastic parameter prediction. This allows for the calculation of sensitive rock mechanics parameters such as Poisson's ratio and Young's modulus (Figure 10), enabling quantitative predictions of brittleness and geomechanical sweet spots.

Building upon the pre-stack inversion, data on Young's modulus and Poisson's ratio are obtained, normalized, and entered into the brittleness index calculation formula to achieve quantitative brittleness characterization. From the prediction results, the upper and lower sweet spots exhibit better brittleness compared to the surrounding rocks, consistent with drilling observations. Additionally, to validate the reliability of the results, two wells (C and B) with similar sweet spot quality and hydraulic fracturing parameters were selected. The prediction results show that the sweet spot in well C has better brittleness, forming a complex fracture network with excellent reservoir space and high oil richness. By contrast, the sweet spot in well B exhibits lower brittleness and relatively lower oil richness. When considering the actual oil production results, well C averages 7.76 tons of daily oil production, while well B averages 0.71 tons of daily oil production. The prediction results align well with the actual situation, demonstrating the reliability of the prediction method. This also reflects that brittleness is one of the key controlling factors for high oil production in this mixed sedimentary rock region (Figure 11).

From the brittleness index contour map, it is observed that the brittleness in the study area gradually improves as the depth increases from southeast to northwest. Simultaneously, there is a clear east-west zonation feature. The central part of the area exhibits relatively good brittleness, showing stable block-like distribution.

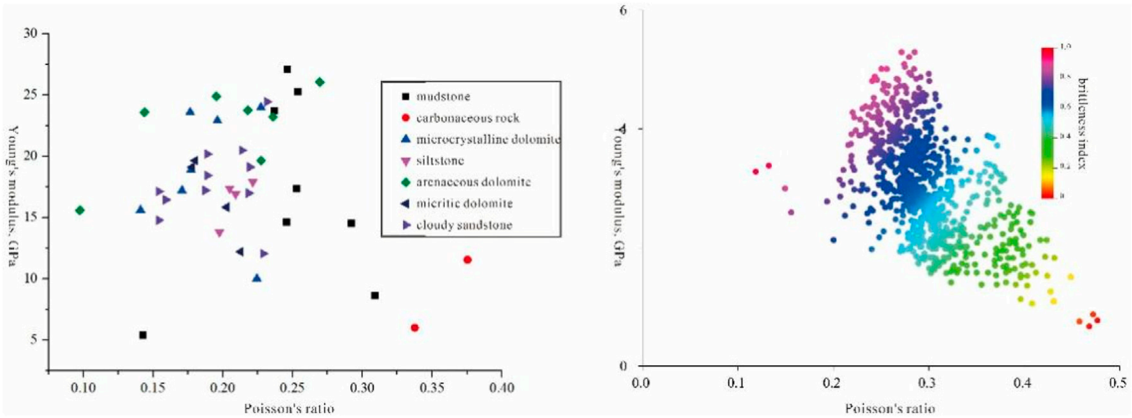

FIGURE 9
Intersection of Young's modulus and Poisson's ratio in the Permian Lucaogou Formation of Well C **(A)** Crossplot of data from different lithologies; **(B)** Crossplot of different brittle data.

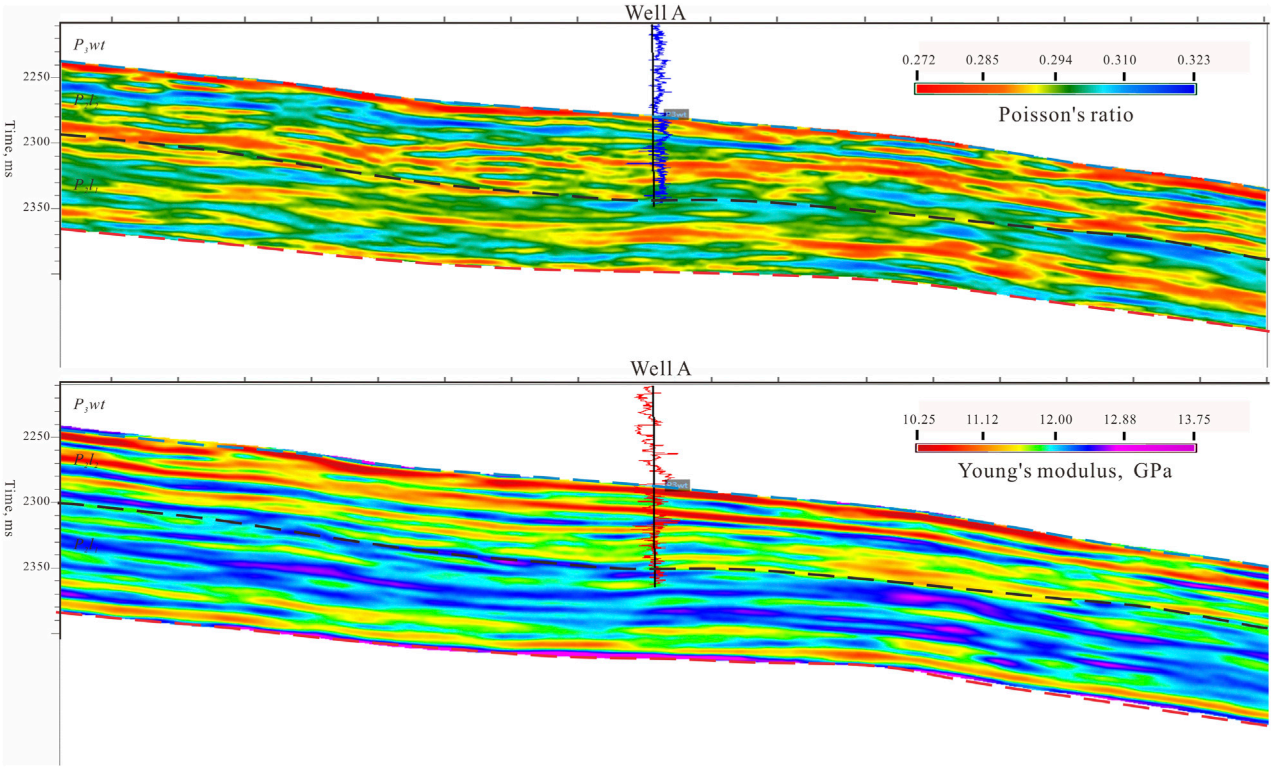

FIGURE 10
(A) Prediction Profile of Poisson's Ratio through Well A; **(B)** Yang's modulus prediction profile.

This central region is a favorable area for the subsequent deployment of horizontal wells (Figure 12).

5 Conclusion

1) In response to the complex lithology and pore structure of the Lucaogou Formation in the Jimusaer Sag, by utilizing a complex lithology multi-mineral component mixed rock equivalent model, high-precision brittleness index are obtained. These ratios serve as the basis for predicting elastic parameters in pre-stack analysis, including Poisson's ratio and Young's modulus, which are sensitive rock mechanics parameters. This enables the quantitative prediction of brittleness, stress conditions, and other engineering parameters.

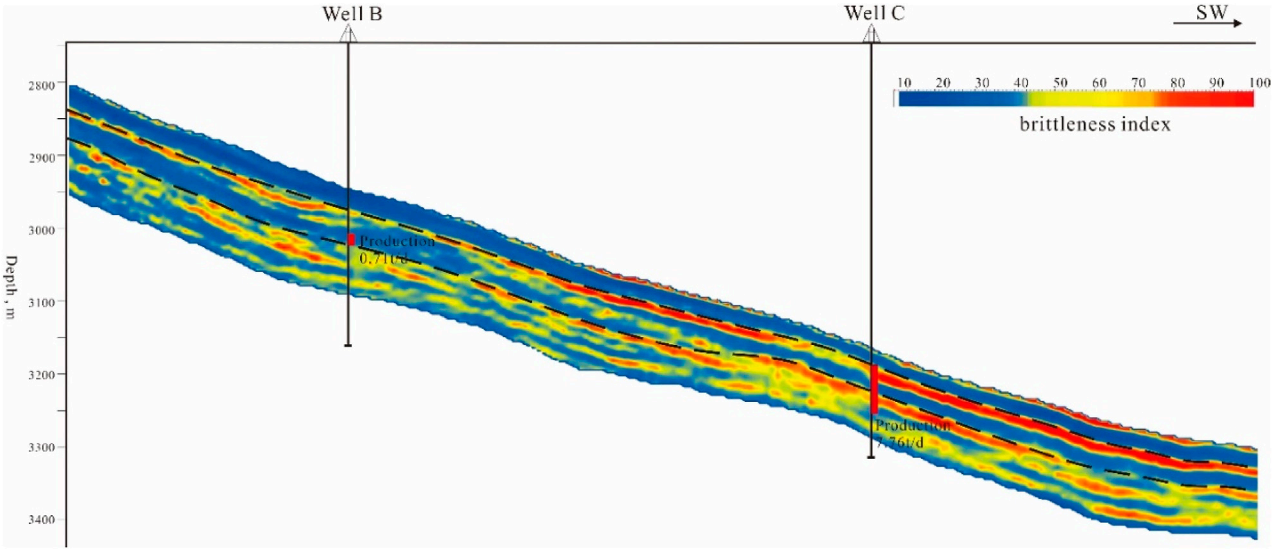

FIGURE 11
Brittle parameter profile of well B-C.

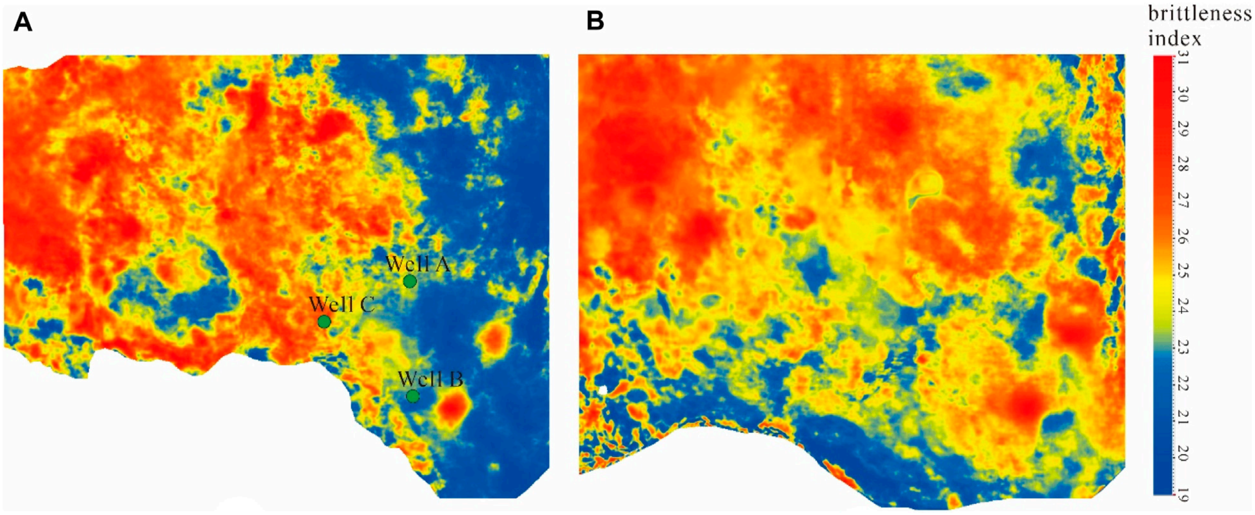

FIGURE 12
Brittleness Index Plan (?) of the Permian Lucaogou Formation in Well Block A **(A)** Top dessert body; **(B)** Lower dessert body.

2) The rock physics model developed in this study shows good alignment with well-logging interpretation results. The prediction accuracy has improved, especially in the intervals with high organic content and clay content, where the alignment is even better. This indicates that the method is highly accurate and reliable.
3) Examining the prediction results reveals that the brittleness of the upper and lower sweet spots is better than that of the surrounding rock, consistent with drilling observations. Analyzing the spatial distribution of brittleness indices, it can be observed that the brittleness in the study area gradually improves as depth increases from the southeast to the northwest. Furthermore, there is a distinct zonal pattern in the east-west direction, with the central area exhibiting relatively higher brittleness. This area demonstrates stable, block-like distribution and is considered a favorable region for future horizontal well deployment.

Data availability statement

The original contributions presented in the study are included in the article/supplementary material, further inquiries can be directed to the corresponding author.

Author contributions

ZF: Writing–original draft, Writing–review and editing. DY: Conceptualization, Data curation, Software, Writing–review and editing. ZD: Data curation, Methodology, Writing–review and editing. LY: Supervision, Writing–review and editing. HJ: Validation, Writing–review and editing. ZX: Project administration, Validation, Writing–review and editing. SY: Supervision, Writing–review and editing.

Funding

The author(s) declare that no financial support was received for the research, authorship, and/or publication of this article.

Conflict of interest

Authors ZF, HJ, and SY were employed by PetroChina Xinjiang Oilfield Company. Authors DY, ZD, LY, and, ZX were employed by PetroChina Oriental Geophysical Company.

Publisher's note

References

Ba, J., Hu, P., Tan, W., Müller, T. M., and Fu, L. Y. (2021). Brittle mineral prediction based on rock-physics modelling for tight oil reservoir rocks. *J. Geophys. Eng.* 18 (6), 970–983. doi:10.1093/jge/gxab062

Cai, M. F. (2020). Key theories and technologies for surrounding rock stability and ground control in deep mining. *J. Min. Strata Control Eng.* 2 (3), 033037. doi:10.13532/j.jmsce.cn10-1638/td.20200506.001

Cao, Z., Liu, G., Kong, Y., Wang, C., Niu, Z., Zhang, J., et al. (2016). Lacustrine tight oil accumulation characteristics: permian lucaogou formation in Jimusaer sag, junggar basin. *Int. J. Coal Geol.* 153, 37–51. doi:10.1016/j.coal.2015.11.004

Chen, G., Jiang, W., Sun, X., Zhao, C., and Qin, C. (2019). Quantitative evaluation of rock brittleness based on crack initiation stress and complete stress–strain curves. *Bull. Eng. Geol. Environ.* 78, 5919–5936. doi:10.1007/s10064-019-01486-2

Chung, D. H., and Buessem, W. R. (1967). The voigt-reuss-hill approximation and elastic moduli of polycrystalline MgO, CaF2, β-ZnS, ZnSe, and CdTe. *J. Appl. Phys.* 38 (6), 2535–2540. doi:10.1063/1.1709944

Cundall, P. A., and Strack, O. D. L. (1979). The development of constitutive laws for soil using the distinct element method. *Numer. methods geomechanics* 1, 289–317. doi:10.1680/geot.1979.29.1.47

Duan, Y., Xie, J., Li, B., Wang, M., Zhang, T., and Zhou, Y. (2020). Lithology identification and reservoir characteristics of the mixed siliciclastic-carbonate rocks of the lower third member of the Shahejie Formation in the south of the Laizhouwan Sag, Bohai Bay Basin, China. *Carbonates Evaporites* 35, 55–19. doi:10.1007/s13146-020-00583-8

Feng, R., Zhang, Y., Rezagholilou, A., Roshan, H., and Sarmadivaleh, M. (2020). Brittleness Index: from conventional to hydraulic fracturing energy model. *Rock Mech. Rock Eng.* 53, 739–753. doi:10.1007/s00603-019-01942-1

Gui, J., Guo, J., Sang, Y., Chen, Y., Ma, T., and Ranjith, P. (2023). Evaluation on the anisotropic brittleness index of shale rock using geophysical logging. *Petroleum* 9 (4), 545–557. doi:10.1016/j.petlm.2022.06.001

Gui, J. C., Mat, S., and Chen, P. (2020). Rock physics modeling of transversely isotropic shale: an example of the Longmaxi Formation in the Sichuan basin. *Chin. J. Geophys.* 63 (11), 4188–4204. doi:10.6038/cjg2020N0294

Han, D., and Batzle, M. (2020). *Velocity, density and modulus of hydrocarbon fluids–empirical modeling[C]//SEG international exposition and annual meeting*. China: SEG, 2000–1867.

Hu, G. K., and Weng, G. J. (2000). The connections between the double-inclusion model and the ponte castaneda–willis, mori–tanaka, and kuster–toksoz models. *Mech. Mater.* 32 (8), 495–503. doi:10.1016/s0167-6636(00)00015-6

Ignatchenko, V. A., and Polukhin, D. S. (2016). Development of a self-consistent approximation. *J. Phys. A Math. Theor.* 49 (9), 095004. doi:10.1088/1751-8113/49/9/095004

Jahed, A. D., Asteris, P. G., Askarian, B., Hasanipanah, M., Tarinejad, R., and Huynh, V. V. (2020). Examining hybrid and single SVM models with different kernels to predict rock brittleness. *Sustainability* 12 (6), 2229. doi:10.3390/su12062229

Keys, R. G., and Xu, S. (2002). An approximation for the Xu-White velocity model. *Geophysics* 67 (5), 1406–1414. doi:10.1190/1.1512786

Kőrösi, M., Béri, J., Arany, D., Varga, C., and Székely, E. (2021). Experimental investigation of chiral melting phase diagrams in high-pressure CO2 containing organic modifiers. *J. Supercrit. Fluids* 178, 105352. doi:10.1016/j.supflu.2021.105352

Li, H. (2022). Research progress on evaluation methods and factors influencing shale brittleness: a review. *Energy Rep.* 8, 4344–4358. doi:10.1016/j.egyr.2022.03.120

Li, H. (2023). Coordinated development of shale gas benefit exploitation and ecological environmental conservation in China: a mini review. *Front. Ecol.* 11, 1232395. doi:10.3389/fevo.2023.1232395

Li, H., Tang, H. M., Qin, Q. R., Zhou, H., Qin, Z., Fan, C., et al. (2019). Characteristics, formation periods and genetic mechanisms of tectonic fractures in the tight gas sandstones reservoir: a case study of Xujiahe Formation in YB area, Sichuan Basin, China. *J. Petroleum Sci. Eng.* 178, 723–735. doi:10.1016/j.petrol.2019.04.007

Li, T., Huang, Z., Feng, Y., Chen, X., Ma, Q., Liu, B., et al. (2020). Reservoir characteristics and evaluation of fluid mobility in organic-rich mixed siliciclastic-carbonate sediments: a case study of the lacustrine Qiketai Formation in Shengbei Sag, Turpan-Hami Basin, Northwest China. *J. Petroleum Sci. Eng.* 185, 106667. doi:10.1016/j.petrol.2019.106667

Li, Y., Jia, D., Rui, Z., Peng, J., Fu, C., and Zhang, J. (2017). Evaluation method of rock brittleness based on statistical constitutive relations for rock damage. *J. Petroleum Sci. Eng.* 153, 123–132. doi:10.1016/j.petrol.2017.03.041

Liu, B., Bechtel, A., Sachsenhofer, R. F., Gross, D., Gratzer, R., and Chen, X. (2017). Depositional environment of oil shale within the second member of permian lucaogou Formation in the santanghu basin, northwest China. *Int. J. Coal Geol.* 175, 10–25. doi:10.1016/j.coal.2017.03.011

Liu, X., Zhang, Z., Ge, Z., Zhong, C., and Liu, L. (2021). Brittleness evaluation of saturated coal based on energy method from stress–strain curves of uniaxial compression. *Rock Mech. Rock Eng.* 54, 3193–3207. doi:10.1007/s00603-021-02462-7

Ma, T., Peng, N., Chen, P., et al. (2019). *Experimental investigation of anisotropic brittleness under confining pressure for gas shale rocks[C]//ARMA US Rock Mechanics/Geomechanics Symposium*. USA: ARMA, 2019–0136.

Mavko, G. M., and Nur, A. (1979). Wave attenuation in partially saturated rocks. *Geophysics* 44 (2), 161–178. doi:10.1190/1.1440958

Meng, F., Wong, L. N., and Zhou, H. (2021). Rock brittleness indices and their applications to different fields of rock engineering: a review. *J. rock Mech. geotechnical Eng.* 13 (1), 221–247. doi:10.1016/j.jrmge.2020.06.008

Meng, F., Zhou, H., Zhang, C., Xu, R., and Lu, J. (2015). Evaluation methodology of brittleness of rock based on post-peak stress–strain curves. *Rock Mech. Rock Eng.* 48, 1787–1805. doi:10.1007/s00603-014-0694-6

Mukerji, T., Berryman, J., Mavko, G., and Berge, P. (1995). Differential effective medium modeling of rock elastic moduli with critical porosity constraints. *Geophys. Res. Lett.* 22 (5), 555–558. doi:10.1029/95gl00164

Muthukumar, S., and DesRoches, R. (2006). A Hertz contact model with non-linear damping for pounding simulation. *Earthq. Eng. Struct. Dyn.* 35 (7), 811–828. doi:10.1002/eqe.557

Neumann, R., and Böhlke, T. (2016). Hashin–Shtrikman type mean field model for the two-scale simulation of the thermomechanical processing of steel. *Int. J. Plasticity* 77, 1–29. doi:10.1016/j.ijplas.2015.09.003

Oran, E. S., and Boris, J. P. (1981). Detailed modelling of combustion systems. *Prog. Energy Combust. Sci.* 7 (1), 1–72. doi:10.1016/0360-1285(81)90014-9

Raymer, L. L., Hunt, E. R., and Gardner, J. S. (1980). *An improved sonic transit time-to-porosity transform[C]//SPWLA Annual Logging Symposium*. London: SPWLA, 1980.

Saleh, A. A., and Castagna, J. P. (2004). Revisiting the Wyllie time average equation in the case of near-spherical pores. *Geophysics* 69 (1), 45–55. doi:10.1190/1.1649374

Shan, S. C., Wu, Y. Z., Fu, Y. K., and Zhou, P. H. (2021). Shear mechanical properties of anchored rock mass under impact load. *J. Min. Strata Control Eng.* 3 (4), 043034. doi:10.13532/j.jmsce.cn10-1638/td.20211014.001

Tao, W., Tang, H., Wang, Y., and Ma, J. (2020). Evaluation of methods for determining rock brittleness under compression. *J. Nat. Gas Sci. Eng.* 78, 103321. doi:10.1016/j.jngse.2020.103321

Wang, J., Deng, Q., Wang, Z., Qiu, Y. s., Duan, T. z., Jiang, X. s., et al. (2013). New evidences for sedimentary attributes and timing of the "Macaoyuan conglomerates" on the northern margin of the Yangtze block in southern China. *Precambrian Res.* 235, 58–70. doi:10.1016/j.precamres.2013.06.003

Wang, J., and Wang, X. L. (2021). Seepage characteristic and fracture development of protected seam caused by mining protecting strata. *J. Min. Strata Control Eng.* 3 (3), 033511. doi:10.13532/j.jmsce.cn10-1638/td.20201215.001

Wang, Y., Li, C. H., Hu, Y. Z., and Zhou, X. L. (2017). A new method to evaluate the brittleness for brittle rock using crack initiation stress level from uniaxial stress–strain curves. *Environ. earth Sci.* 76, 799–818. doi:10.1007/s12665-017-7117-4

Wei, W., Azmy, K., and Zhu, X. (2022). Impact of diagenesis on reservoir quality of the lacustrine mixed carbonate-siliciclastic-volcaniclastic rocks in China. *J. Asian Earth Sci.* 233, 105265. doi:10.1016/j.jseaes.2022.105265

Wu, C., Li, B., Liu, Y., and Liang, S. Y. (2017). Surface roughness modeling for grinding of silicon carbide ceramics considering co-existence of brittleness and ductility. *Int. J. Mech. Sci.* 133, 167–177. doi:10.1016/j.ijmecsci.2017.07.061

Yin, S., Chen, G., Xu, C., and etal, (2022). Lithofacies architecture of lacustrine fine-grained mixed reservoirs and its controller sweet spot: a case study of Permian Lucaogou Formation shale oil reservoir in the Jimsar Sag, Juggar Basin. *Oil Gas Geol.* 43 (5), 1180–1193. doi:10.11743/ogg20220514

Yin, S., Chen, X., Yang, Y., et al. (2023a). Origin and sweet spots of typical low-resistivity oil reservoirs of fine-grained sedimentary rocks. *Oil Gas Geol.* 44 (8), 946–961.

Yin, S., Zhu, B., Guo, H., Xu, Z., Li, X., Wu, X., et al. (2023b). Architectural model of a dryland gravel braided river, based on 3D UAV oblique photogrammetric data: a case study of west dalongkou river in Eastern Xinjiang, China. *Acta Geol. Sin. Engl. Ed.* 97 (1), 269–285. doi:10.1111/1755-6724.14967

Yin, S., Zhu, B., Wu, Y., and Xu, F. (2021). Lithofacies architecture and distribution patterns of lacustrine mixed fine-grained rocks —a case study of permian lucaogou Formation in jimsar sag, NW China. *Front. Earth Sci.* 9, 782208. doi:10.3389/feart.2021.782208

Yu, W., Algeo, T. J., Du, Y., Zhang, Q., and Liang, Y. (2016). Mixed volcanogenic–lithogenic sources for Permian bauxite deposits in southwestern Youjiang Basin, South China, and their metallogenic significance. *Sediment. Geol.* 341, 276–288. doi:10.1016/j.sedgeo.2016.04.016

Zhang, J., Liu, G., Cao, Z., Tao, S., Felix, M., Kong, Y., et al. (2019). Characteristics and formation mechanism of multi-source mixed sedimentary rocks in a saline lake, a case study of the Permian Lucaogou Formation in the Jimusaer Sag, northwest China. *Mar. Petroleum Geol.* 102, 704–724. doi:10.1016/j.marpetgeo.2019.01.016

Zhi, S., and Zan, D. (2015). New brittleness indexes and their application in shale/clay gas reservoir prediction. *Petroleum Explor. Dev.* 42 (1), 129–137. doi:10.1016/s1876-3804(15)60016-7

Zhi, Y., Lian, H., Lin, S., et al. (2018). Geologic characteristics and exploration potential of tight oil and shale oil in Lucaogou Formation in Jimsar sag. *China Pet. Explor.* 23 (4), 76.

frontiers | Frontiers in Earth Science

TYPE Original Research
PUBLISHED 10 April 2024
DOI 10.3389/feart.2024.1368326

Microscopic pore structure characteristics and controlling factors of marine shale: a case study of Lower Cambrian shales in the Southeastern Guizhou, Upper Yangtze Platform, South China

Ruyue Wang[1,2,3,4,5]*, Yuejiao Liu[4]*, Zhi Li[1,2,3], Dahai Wang[1,2,3], Guanping Wang[1,2,3], Fuqiang Lai[4], Zhihao Li[1,2,3] and Jianhua He[5]

[1]State Key Laboratory of Shale Oil and Gas Enrichment Mechanisms and Efficient Development, Beijing, China, [2]Sinopec Key Laboratory of Shale Oil/Gas Exploration and Production Technology, Beijing, China, [3]Sinopec Petroleum Exploration and Production Research Institute, Beijing, China, [4]Chongqing Key Laboratory of Complex Oilfield Exploration and Development, Chongqing University of Science and Technology, Chongqing, China, [5]College of Energy, Chengdu University of Technology, Chengdu, China

OPEN ACCESS

EDITED BY
Hu Li,
Southwest Petroleum University, China

REVIEWED BY
Denglin Han,
Yangtze University, China
Jinbu Li,
Chinese Academy of Sciences (CAS), China
Tao Luo,
The University of Queensland, Australia

*CORRESPONDENCE
Ruyue Wang,
✉ wry1990@vip.qq.com
Yuejiao Liu,
✉ lyj523029007@qq.com

RECEIVED 10 January 2024
ACCEPTED 26 March 2024
PUBLISHED 10 April 2024

CITATION
Wang R, Liu Y, Li Z, Wang D, Wang G, Lai F, Li Z and He J (2024), Microscopic pore structure characteristics and controlling factors of marine shale: a case study of Lower Cambrian shales in the Southeastern Guizhou, Upper Yangtze Platform, South China.
Front. Earth Sci. 12:1368326.
doi: 10.3389/feart.2024.1368326

A systematic study of the pore structure characteristics of Lower Cambrian shales in the southeastern Upper Yangtze Platform, was conducted using organic geochemistry, mineralogy, nitrogen adsorption, physical property analysis, and scanning electron microscopy. The results indicate that: 1) The Total organic carbon (TOC) content shows a strong correlation with quartz and clay minerals. Shales with low TOC content and rich in clay minerals primarily exhibit slit-shaped and narrow slit-like inter-clay particle pores with pore size distribution is dominated by mesopores and macropores. Shales with high TOC content predominantly feature narrow slit-like and ink bottle-shaped pores with pore size distribution dominated by micropores and mesopores. 2) Shale pore structures vary significantly under different gas content and preservation conditions. Shales under favorable preservation conditions exhibit a relatively “high porosity, low permeability, and high gas content” pattern, with well-developed organic pores and a strong pore-permeability correlation. In contrast, shales under unfavorable preservation conditions appear dense, with excessively developed fractures increasing both average pore size and local permeability. The pore-permeability correlation is weak, presenting a relatively “low porosity, high permeability, and low gas content” pattern. 3) TOC content plays a crucial role in controlling pore structure, showing overall positive correlations with pore volume, specific surface area, and porosity, and negative correlations with pore size. High TOC content enhances shale plasticity, resulting in lower pore diameters. Factors such as compaction and unfavorable preservation conditions lead to the shrinkage, collapse, and closure of some narrow pore throats, negatively impacting pore volume, specific surface area, brittleness, and fractal dimension, exhibiting a negative correlation with TOC content. 4) The pore structure of Lower Cambrian shales is complex, with fractal dimensions D_1 and D_2 exhibiting negative correlations with average pore size and positive correlations with TOC, specific surface area, and total pore volume. A high D_1 value indicates well-preserved nanoscale pore surface structures with low complexity, suggesting minimal alteration by external fluids and better shale gas preservation. D_1 serves as an indicator for shale gas content and preservation conditions. D_2 shows better correlations with various pore structure parameters, making it suitable for characterizing pore structures.

KEYWORDS

pore structure, fractal dimension, preservation condition, Niutitang Formation, Bianmachong Formation, Lower Cambrian, South China

1 Introduction

Shale oil and gas, as an important supplement and replacement for conventional oil and gas resources, have become a global exploration and development hotspot. Shale gas is generated and stored in organic-rich mud shale formations, constituting a natural gas accumulation system with adsorption and free gas as its main occurrence modes (Hu et al., 2021; Wang et al., 2022). The discovery of the Fuling Shale Gas Field marks a significant breakthrough in China's shale gas exploration and development, playing a crucial role in leading and demonstrating unconventional oil and gas development and optimizing the energy structure in China. In recent years, with technological advancements and the rise of nanogeoscience (Wang et al., 2021a), research on the micro-pore structure of shale reservoirs has become a key focus in both domestic and international shale oil and gas exploration and development. As research deepens and new technologies emerge, there has been substantial progress in understanding shale micro-pore structures (Bernard et al., 2012; Wang et al., 2017; Zhu et al., 2019; Hackley et al., 2020; Xu et al., 2021; Sun M. et al., 2022; Sun Y. et al., 2022; Li et al., 2022).

Studies by Yang et al. (2016) and Wang et al. (2018) on the Longmaxi Formation in the Sichuan Basin revealed a positive correlation between organic matter abundance and shale pore volume and specific surface area. Liu et al. (2016), in their research on the micro-pore structure of Longmaxi Formation shale in southern Sichuan during the Lower Silurian period, found that approximately 80% of the shale reservoir space consists of micro- to mesopores. Poorly organic-rich shales are dominated by slit-shaped pores with a fractal dimension generally less than 2.75, and the storage space is mainly inorganic mineral pores. Conversely, richly organic shales primarily feature “ink bottle” shaped pores with a fractal dimension generally greater than 2.85, and the storage space is mainly organic pores. Zhang et al. (2020), in their study of Longmaxi Formation shale in Weiyuan area, suggested that the fractal dimension is mainly related to the degree of micro-pore development. Specifically, Total Organic Carbon (TOC) and quartz content control micro-pore development and show a positive correlation with the fractal dimension, while the volume fractions of carbonate rocks and clay minerals are negatively correlated with the fractal dimension.

The characteristics of shale reservoirs are collectively controlled by organic matter (OM), inorganic mineral composition, their evolution, and diagenetic processes. The pore characteristics of shale reservoirs vary significantly under different geological conditions, exhibiting strong heterogeneity (Aplin et al., 2006; Bernard et al., 2012; Wang et al., 2018; Dowey and Taylor, 2020; Liu Y. et al., 2021; Wang et al., 2021a; Liu D. et al., 2021; Sun M. et al., 2022; Lai et al., 2022; Wang et al., 2023a; Wang et al., 2023b; Dong et al., 2023; Shi et al., 2023). Additionally, influenced by the unique geological conditions in China, shale gas in southern marine shale formations is significantly constrained by preservation conditions (Wang et al., 2016; Liu D. et al., 2021; Guo et al., 2022; Wu et al., 2022). The development characteristics and controlling factors of shale pores in different thermal evolution stages and under the influence of tectonic preservation conditions are still not clear enough, and research on the response and constraints of shale pore structures to gas content and preservation conditions in southern China is still an area that requires further exploration (Wang et al., 2021a; 2022). This study focuses on the Lower Cambrian Niutitang Formation and Bianmachong Formation shales in the southeast part of the Yangtze region, aiming to provide insights for the exploration and development of Paleozoic ancient shale gas in complex tectonic regions in southern China and similar areas worldwide.

2 Geological setting

The study area is located at the southeastern margin of the Upper Yangtze Block. In the Early Cambrian, it experienced passive continental margin deep-water shelf sedimentation, with water depth gradually decreasing from southeast to northwest (Wang et al., 2017; Wei et al., 2022). The majority of the block comprises Cambrian sedimentary strata, with a total thickness ranging from 2,000 to 2,700 m. Organic-rich shales are mainly developed in the Lower Cambrian Niutitang Formation, Jiumenchong Formation, and Bianmachong Formation (Chen et al., 2020). In the study area, the Niutitang Formation shale exhibits significant thickness (50–70 m) and a widespread distribution in the Cengong block, predominantly consisting of black/gray-black siliceous shale. The Bianmachong Formation represents a suite of continental margin, relatively close to offshore, and shallow-water restricted marine-land source clastic sediments (Chen et al., 2020). It displays characteristics of both marine shale (sedimentary environment) and transitional shale (lithological composition), with predominant interbedding of gray-black shales and shale with thin interlayers of fine sand-siltstone. The maximum thickness of a single shale layer in the formation is 35.5 m.

3 Samples and methods

A total of 52 shale samples were collected from the Niutitang Formation and Bianmachong Formation in the study area, including TXA well, CYA well, and TMA well (Figure 1). In this study, a series of tests, analyses, and calculations were conducted on these 52 black shale samples, including Total Organic Carbon (TOC) content, maturity, mineral composition, organic geochemistry, Field Emission Scanning Electron Microscopy (FE-SEM), petrophysical properties, pore structure, methane isotherm adsorption, and fractal dimension analysis. All sample analyses were performed by SGS North America Inc. (Beijing) using unconventional oil and gas technology. The TOC content of the 52 samples was measured using a LECO CS-230 carbon-sulfur analyzer, following the guidelines of "GB/T 19,145-2003 Determination of Total Organic Carbon in Sedimentary Rocks." The asphaltene reflectance (R_b) of 9 samples was determined using an MPV-III microscope photometer, based on the method outlined in "SY/T 5124-1995 Method for Determination of Vitrinite Group Reflectance in Sedimentary Rocks." The equivalent vitrinite reflectance (R_o) was calculated using the formula $Ro = 0.3195 + 0.679R_b$ (Feng and Chen, 1988). Mineral composition analysis of 22 samples was conducted using a SmartLab9 X-ray diffractometer, following the guidelines of "SY/T 5163-2010 X-ray Diffraction Analysis of Clay Minerals and Common Non-Clay Minerals in Sedimentary Rocks." The pore volume and permeability of 52 samples were measured using an HKC-2 helium porosity tester, according to "SY/T 5336-2006." Nitrogen adsorption experiments and pore structure parameter analysis of 22 samples were performed using a Quadrasorb SI specific surface area and pore size analyzer, following the method outlined in "SY/T 6154-1995 Static Nitrogen Adsorption Capacity Method for Determining Rock Specific Surface Area and Pore Size Distribution." Scanning electron microscopy observations of 22 samples were conducted using a Quanta 200F FE-SEM at a temperature of 24°C and a humidity level of 35%. Shale gas content testing was conducted using the WX-1 integrated intelligent shale on-site desorption instrument developed by Wuxi Research Institute of Petroleum Geology, Sinopec Petroleum Exploration and Production Research Institute. The gas loss recovery method was based on the USBM method (Yang et al., 2022). In addition, this paper provides a comprehensive and systematic observation and description of shale fractures, including the measurement of the following metrics: 1) fracture type; 2) fracture inclination angle; and 3) fracture linear density (frequency of fracture occurrence per unit length).

Characterization by fractal dimension has been widely used to quantitatively describe pore surface roughness and the pore structure of heterogeneous porous media, and the FHH model presently is the most effective fractal model for studying pore structure of porous materials (Avnir and Jaroniec, 1989). Thus, the FHH model is used to describe the fractal characteristics of pore structure of shales in the study area. There are two distinct linear segments at a relative pressure (P/P_0) of 0–0.5 and 0.5–1, indicating that the pore spaces in shale have fractal characteristics in these two regions. Accordingly, the fractal dimension D_1 (P/P_0: 0–0.5) and D_2 (P/P_0: 0.5–1.0) are used to characterize the roughness of the pore surface and the complexity of the pore structure, respectively.

4 Results

4.1 Geochemical and mineral composition characteristics

The Total Organic Carbon (TOC) content of black shale samples from the Lower Cambrian in the study area ranges from 0.5% to 8.5%, with the equivalent vitrinite reflectance (R_o) ranging between 2.2% and 2.9%, indicating an over-mature stage. Specifically, the TOC content of the Bianmachong Formation shale mainly falls within the range of 0.5%–1.7%, while the Niutitang Formation shale exhibits TOC content ranging from 1.1% to 8.5%, with the majority exceeding 4% (Table 1). Regarding mineral composition, both the Bianmachong Formation and Niutitang Formation black shale are dominated by quartz and clay minerals (Table 1). The Bianmachong Formation shale has a quartz content ranging from 33.1% to 38.4%, with an average of 36.2%, and a relatively high clay mineral content ranging from 44.4% to 54.9%. In comparison, the Niutitang Formation shale has a higher quartz content ranging from 27.5% to 68.3%, with an average of 47.7%, and a clay mineral content ranging from 8.7% to 42.5%, with an average of 21.8%. The averages for feldspar, pyrite, and carbonate minerals are 11.5%, 10.1%, and 8.9%, respectively. There is a strong positive correlation between TOC content and the presence of quartz and clay minerals (Figure 2), indicating a close relationship between TOC and quartz. Shale intervals rich in TOC show elevated biogenic quartz content (Wang et al., 2017).

4.2 Physical properties and gas content

The statistical results of shale physical parameters (Table 2) indicate that the physical properties and gas content of Niutitang and Bianmachong shale formations are generally comparable. However, significant differences in pore volume are observed under different gas content and preservation conditions. Taking Niutitang Formation as an example, the average gas content in TXA well is 1.6 m^3/t, with methane accounting for over 80%. In CYA well, the average gas content is 1.0 m^3/t, with methane exceeding 95%. TMA well generally exhibits gas content below 0.3 m^3/t, with nitrogen accounting for over 95% (Wang et al., 2016). The gas content and preservation conditions in TXA, CYA, and TMA wells of the Niutitang Formation gradually deteriorate, and the porosity decreases accordingly (Table 2; Figure 3). In terms of permeability, the permeability of the Bianmachong and Niutitang shale in TX-1 well, which has better preservation and gas content, is generally below 2×10^{-3} mD, showing a good positive correlation between pore and permeability (Figure 3). On the other hand, the permeability of Niutitang shale in CYA and TMA wells is higher, with a weaker correlation between pore and permeability. Compared to TXA well, TMA well's Niutitang shale exhibits a smaller median radius, higher median pressure, denser reservoir, and generally demonstrates a "low porosity, high permeability, low gas content" characteristic. In contrast, the shale properties of TXA well, characterized by better preservation and gas content, generally show a "high porosity, low permeability, high gas content" pattern (Table 2; Figure 3).

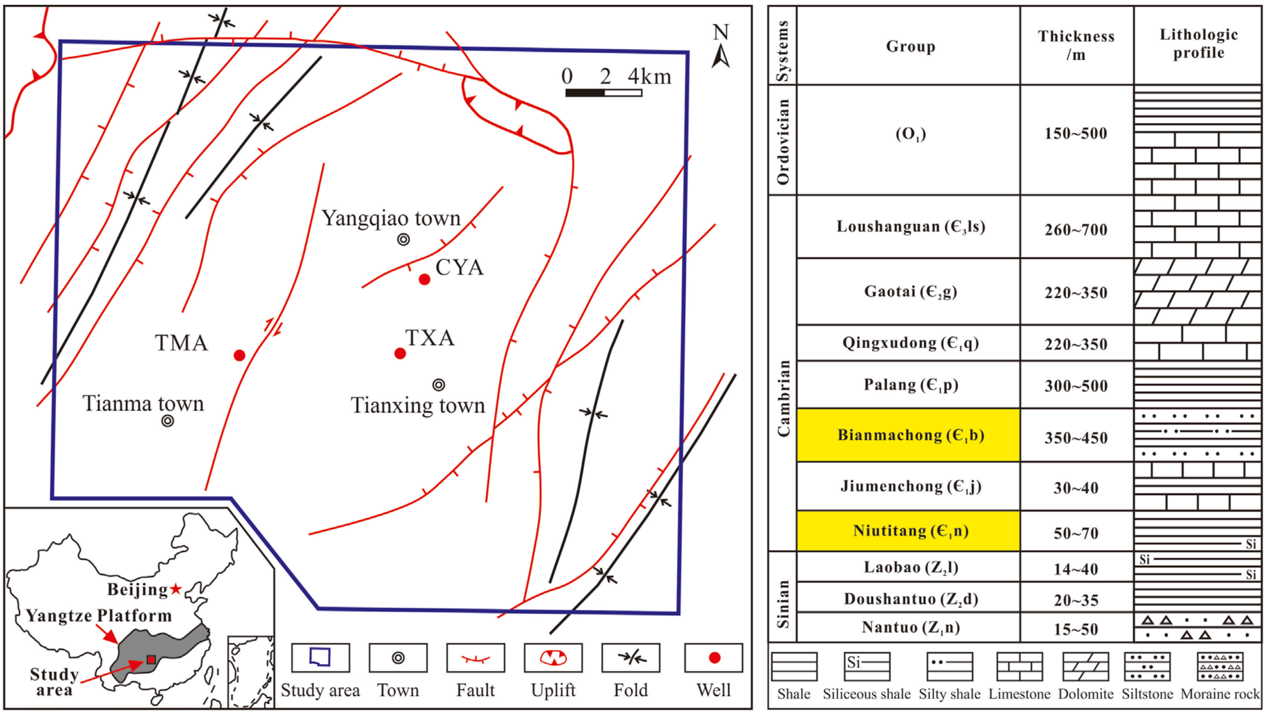

FIGURE 1
Location and stratigraphic characteristics of the study area.

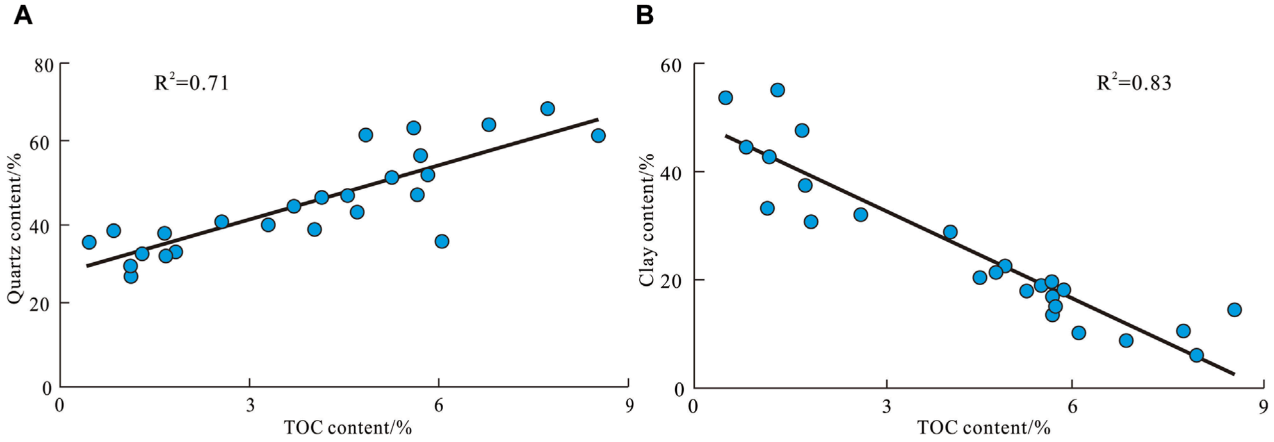

FIGURE 2
Correlations between TOC and mineral contents in Lower Cambrian shale. **(A)** Correlations between TOC and quartz content. **(B)** Correlations between TOC and clay mineral content.

4.3 Pore structure characteristics

4.3.1 Pore types

According to the classification by the International Union of Pure and Applied Chemistry (IUPAC) (Sing, 1985), nitrogen adsorption isotherms of 22 shale samples exhibit three types of curves: H2, H3, and H4 (Figures 4A–C), corresponding to ink bottle-shaped, slit-shaped, and narrow slit-like pores, respectively. The adsorption curves and corresponding pore types and parameter statistics are shown in Table 3. Clay-rich, organic-poor shales are dominated by slit-shaped pores, with a larger average pore diameter and lower pore volume and specific surface area. Organic-rich shales, on the other hand, are characterized by ink bottle-shaped and narrow slit-like pores, with a smaller average pore diameter and higher pore volume and specific surface area.

In comparison with the Lower Silurian Longmaxi Formation shale in southern China, the Lower Cambrian shale exhibits a lower degree of organic pore development and smaller pore sizes (Wang et al., 2017; 2018; Zhang et al., 2022). The average pore diameter is generally less than 4–5 nm (Table 3), and the nitrogen

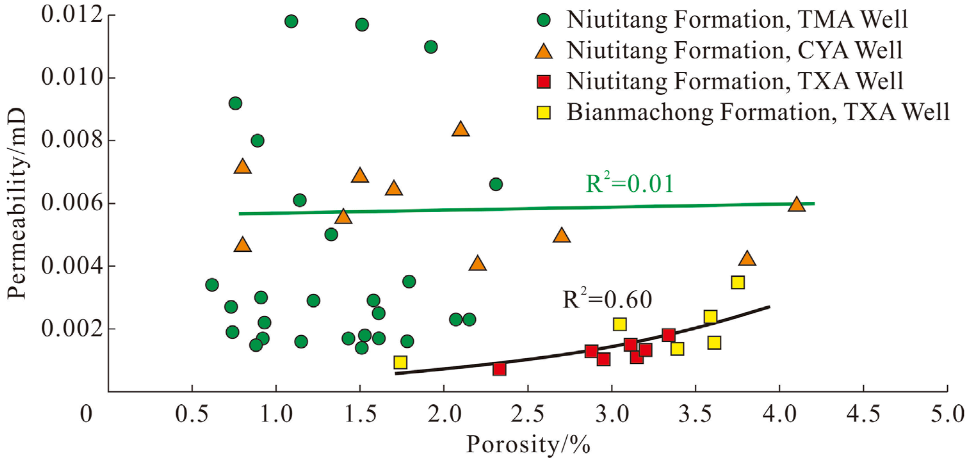

FIGURE 3
Characteristics of shale physical properties under different gas contents and preservation conditions.

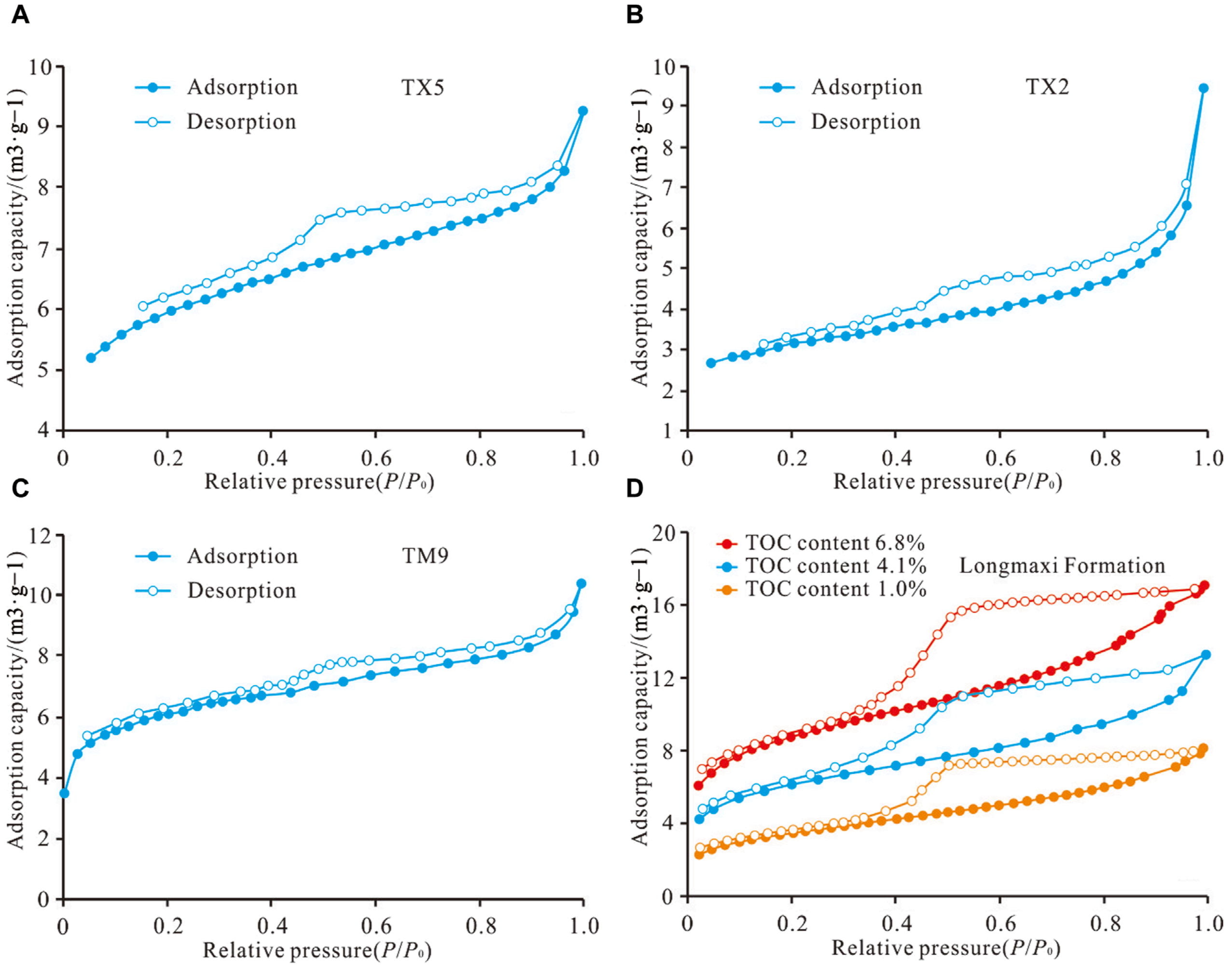

FIGURE 4
Shale Nitrogen Adsorption Isotherm Characteristics. **(A–C)** Liquid nitrogen adsorption and desorption isotherms of Cambrian shale samples. **(D)** Liquid nitrogen adsorption and desorption isotherms of Silurian Longmaxi shale samples (Yang et al., 2016).

TABLE 1 Statistical summary of TOC, maturity, and mineral composition parameters for Lower Cambrian shale.

Sample number	Depth/m	Formation	TOC content/%	Equivalent R_o/%	Quartz/%	Clay/%	Feldspar/%	Pyrite/%	Carbonate/%	Fractal dimension D_1	Fractal dimension D_2
TX1	1,451.9	Bianmachong	0.81	2.3	38.4	44.4	10.6	1.9	1.7	2.716	2.836
TX2	1,512.4		1.66	2.6	37.6	47.1	8.4	4.4	2.6	2.768	2.801
TX3	1,591.0		1.30	2.5	33.1	54.9	6.5	5.5	/	2.715	2.716
TX4	1,709.4		0.45	2.2	35.5	53.5	5.7	5.4	/	2.627	2.593
TX5	1,783.3	Niutitang	5.80	2.8	52.7	17.9	9.5	12.1	7.8	2.821	2.935
TX6	1,791.2		6.77	2.9	64.0	8.7	8.1	10.7	8.5	2.828	2.941
TX7	1,800.2		6.04	2.5	35.9	10.2	27.2	12.9	13.8	2.840	2.949
TM1	1,453.7		7.68	/	68.3	10.3	8.6	6.8	6.2	2.755	2.952
TM2	1,461.8		5.63	/	47.6	13.8	14.6	12.4	11.7	2.738	2.940
TM3	1,406.1		1.10	/	27.5	33.0	8.5	8.9	22.1	2.603	2.776
TM4	1,409.6		1.12		30.0	42.5	8.0	10.1	9.4	2.564	2.757
TM5	1,417.6		1.70	/	32.5	37.5	11.4	15.0	3.6	2.634	2.792
TM6	1,421.4		1.77	2.3	33.0	30.5	12.7	12.7	11.1	2.684	2.855
TM7	1,423.4		2.56	/	40.5	31.4	13.1	10.8	4.0	2.651	2.842
TM8	1,428.8		4.00	/	39.0	28.9	10.5	8.9	12.7	2.726	2.920
TM9	1,441.6		5.61	/	64.0	16.7	4.6	5.1	10.0	2.728	2.910
TM10	1,451.3		8.50	/	62.0	14.2	10.8	6.7	7.0	2.753	2.934
TM11	1,457.3		5.23	/	51.6	17.7	13.5	8.7	8.5	2.742	2.919
TM12	1,466.8		4.52	/	47.5	20.5	14.0	13.5	4.5	2.715	2.919
TM13	1,470.1		4.68	2.4	43.3	21.3	11.8	14.0	9.6	2.736	2.929
TM14	1,480.8		4.80	/	61.8	21.9	9.7	6.6	/	2.769	2.921
TM15	1,482.8		5.68	/	57.0	15.1	9.6	6.7	9.6	2.783	2.930

TABLE 2 Statistics of shale reservoir physical parameters in the study area.

Well name	Formation	Porosity/%	Permeability/ 10^{-3} mD	Gas content/ (m^3/t)	Median radius/μm	Median pressure/ MPa	Maximum pore throat radius/μm
TXA	$Є_1b$	(1.7–3.8)/3.3 (6)	(1.4–4.3)/2.3 (6)	(0.3–1.3)/1.0 (6)	(0.12–0.19)/0.14 (12)	(3.9–6.3)/5.3 (12)	(0.47–0.94)/0.67 (12)
	$Є_1n$	(2.3–3.3)/3.0 (7)	(0.7–1.8)/1.3 (7)	(0.9–2.8)/1.6 (14)	(0.15–0.20)/0.17 (7)	(3.6–5.1)/4.5 (7)	(0.62–0.94)/0.73 (7)
CYA	$Є_1n$	(0.8–4.1)/1.8 (10)	(4.1–8.4)/5.9 (10)	(0.2–4.5)/1.0 (12)	/	/	/
TMA	$Є_1n$	(0.6–2.3)/1.3 (29)	(1.4–13.7)/4.8 (29)	(0.1–0.3)/0.2 (33)	(0.02–0.12)/0.05 (15)	(6.2–38.6)/23.2 (15)	(0.35–1.03)/0.73 (15)

Note: (Min ~ Max)/Mean (Number of Samples).

TABLE 3 Pore types and parameter statistics of shale pores.

Curve type	Pore type	Sample number	Average TOC/%	Average pore diameter/nm	Average pore volume/ (10^{-3} cm^3/g)	Average specific surface area/(m^2/g)	Ration (%)
H2	Ink bottle	TM1, TM6, TX5, TX6, TX7	5.6	3.0	14.1	19.6	22.7
H3	Slit-shaped	TM3, TM4, TM5, TX1, TX2, TX4	1.1	5.7	11.0	8.9	27.3
H4	Narrow slit-like	TM2, TM7, TM8, TM9, TM10, TM11, TM12, TM13, TM14, TM15, TX3	4.7	3.5	13.9	18.8	50.0

adsorption quantity and hysteresis loop area are significantly smaller than those of the Longmaxi Formation (Figure 4D), indicating that the Longmaxi Formation has larger pore volume and more ink bottle-shaped organic pores (Liu et al., 2016).

4.3.2 Microscopic characteristics of pores

Microscopic features of shale under scanning electron microscopy reveal that the clay-rich shale of the Bianmachong Formation has a low TOC content, with well-developed interlayer pores between slit-shaped clay minerals (Figure 5A), corresponding to the morphology of adsorption isotherms, which are predominantly slit-shaped and narrow slit-like (Table 3). In comparison with the Bianmachong Formation, the Niutitang Formation shale has a higher TOC content, and the development of organic matter (OM) pores has increased, but the pore size of OM pores is generally less than 50 nm (Figures 5A–C). In contrast to the TXA well, the Niutitang Formation shale in the TMA well, which has poor preservation conditions, is denser, with smaller organic pore sizes (Figures 5B, C). The shale exhibits high levels of compression and deformation, with densely developed fractures, and noticeable phenomena of particle and aggregate compression and fragmentation, resulting in incomplete and irregular shapes (Figures 5D, E). Additionally, in the Niutitang Formation shale from the TMA well, narrow fissures between OM and mineral particles, formed either by OM shrinkage or mineral fracture, are commonly observed (Figure 5F). This is consistent with the predominant narrow slit-like morphology of pores corresponding to the N_2 adsorption isotherms of shale samples from the TMA well (Table 3).

4.3.3 Fractal dimensions

Fractal characteristics of shale pores (Table 1) show that the fractal dimension D_1 of Lower Cambrian shale ranges from 2.564 to 2.840, with a mean value of 2.723. The D_2 dimension ranges from 2.593 to 2.952, with a mean value of 2.867. D_2 is generally greater than D_1, indicating that the internal structure of the shale is significantly more complex than its surface structure. Both D_1 and D_2 are markedly greater than those of Longmaxi Formation shale in the Sichuan Basin and its surrounding areas, suggesting a higher complexity in the pore structure of the Lower Cambrian shale.

As shown in Figure 6, there is a negative correlation between clay mineral content and fractal dimensions (Figures 6A, D). The positive correlation of TOC with quartz content in marine shale makes the relationships between quartz, TOC, and fractal dimensions similar

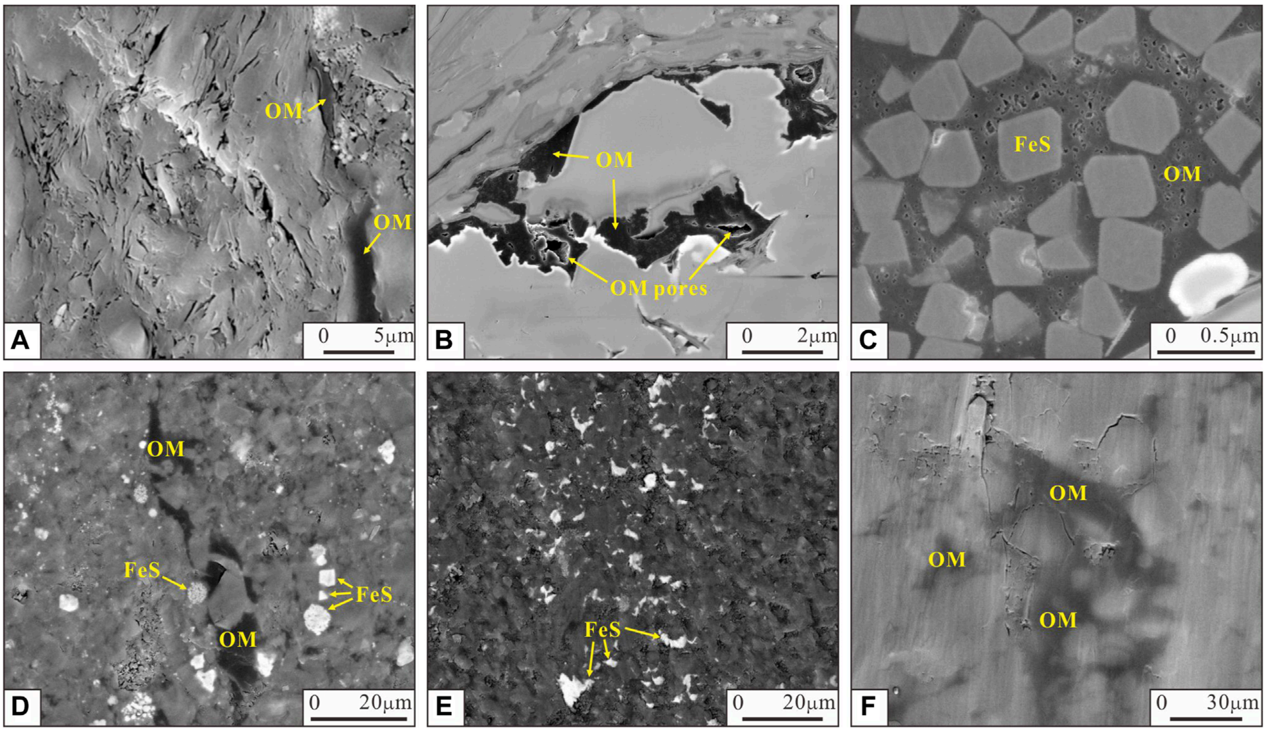

FIGURE 5
FE-SEM images of Lower Cambrian shale in the study area. **(A)** Well-developed interlayer pores between slit-shaped clay minerals are more prominent than OM pores, Bianmachong Formation, TXA well, 1,718.4 m. **(B)** Lower development of OM pores, Niutitang Formation, TXA well, 1,800.2 m. **(C)** OM pore sizes generally smaller than 20–50 nm, Niutitang Formation, TMA well, 1,450.5 m. **(D)** Microscopic features show well-preserved particle and aggregate shapes, particularly regular forms of pyrite (FeS) particles, Niutitang Formation, TXA well, 1,779.3 m. **(E)** Microscopic features reveal dense reservoir, with noticeable compression and fragmentation of pyrite (FeS) particles and aggregates, Niutitang Formation, TMA well, 1,445.3 m. **(F)** Low development of OM pores, narrow fissures developed at the edges of OM and minerals, Niutitang Formation, TMA well, 1,439.3 m.

to those of reservoir parameters (Figures 6B, C, E, F). Overall, the correlations between TOC, quartz content, clay minerals, and D_2 are better than those with D_1. It is noteworthy that with increasing TOC content, especially when TOC content exceeds 4%, the increase in fractal dimensions D_1 and D_2 is limited and tends to stabilize. Additionally, when TOC content exceeds 6%, a slight decrease in fractal dimensions D_1 and D_2 is observed with the increasing TOC content (Figures 6C, F).

The relationship between D_1 and D_2 and pore structure parameters reveals a negative correlation with average pore diameter and a positive correlation with specific surface area and total pore volume (Figure 7). Elevated values of D_1 and D_2 indicate the development of nanoscale pores, suggesting increased surface roughness and internal structural complexity. Generally, D_2 demonstrates stronger correlations with various pore structure parameters (Figures 7D–F). As D_2 increases, shale pore diameter gradually decreases, while pore volume and specific surface area increase. When D_2 surpasses 2.9, its variation with pore volume and specific surface area becomes limited, indicating stabilization in pore structure and complexity. Additionally, samples from TXA well with better gas content and preservation conditions exhibit significantly larger D_1 than samples from TMA well under the same conditions (Figures 6A–C, 7A–C), implying that shale pore surfaces in TXA well are notably rougher than those in TMA well.

5 Discussion

5.1 Impact of TOC content and mineral composition on pore structure

Interrelationships among shale pore structure parameters reveal a strong positive correlation between total pore volume and specific surface area, both of which are negatively correlated with average pore diameter (Figures 8J–L). Compared to the Bianmachong Formation shale, the Niutitang Formation shale has a smaller average pore diameter but larger specific surface area and pore volume (Figures 8A–C). In terms of the relationships between TOC, quartz, clay mineral content, and specific surface area, pore volume, and average pore diameter, the variations in reservoir pore structure parameters are primarily controlled by the positive correlation of TOC and quartz content. Specifically, average pore diameter is negatively correlated with TOC and quartz content but positively correlated with clay mineral content (Figures 8G–I). Specific surface area and total pore volume generally exhibit positive correlations with TOC and quartz content but negative correlations with clay mineral content (Figures 8D–F). Shales with low organic content (TOC content less than 2%) typically have a specific surface area less than 10 m^2/g, while shales with high organic content (TOC content greater than 2%) generally exhibit an

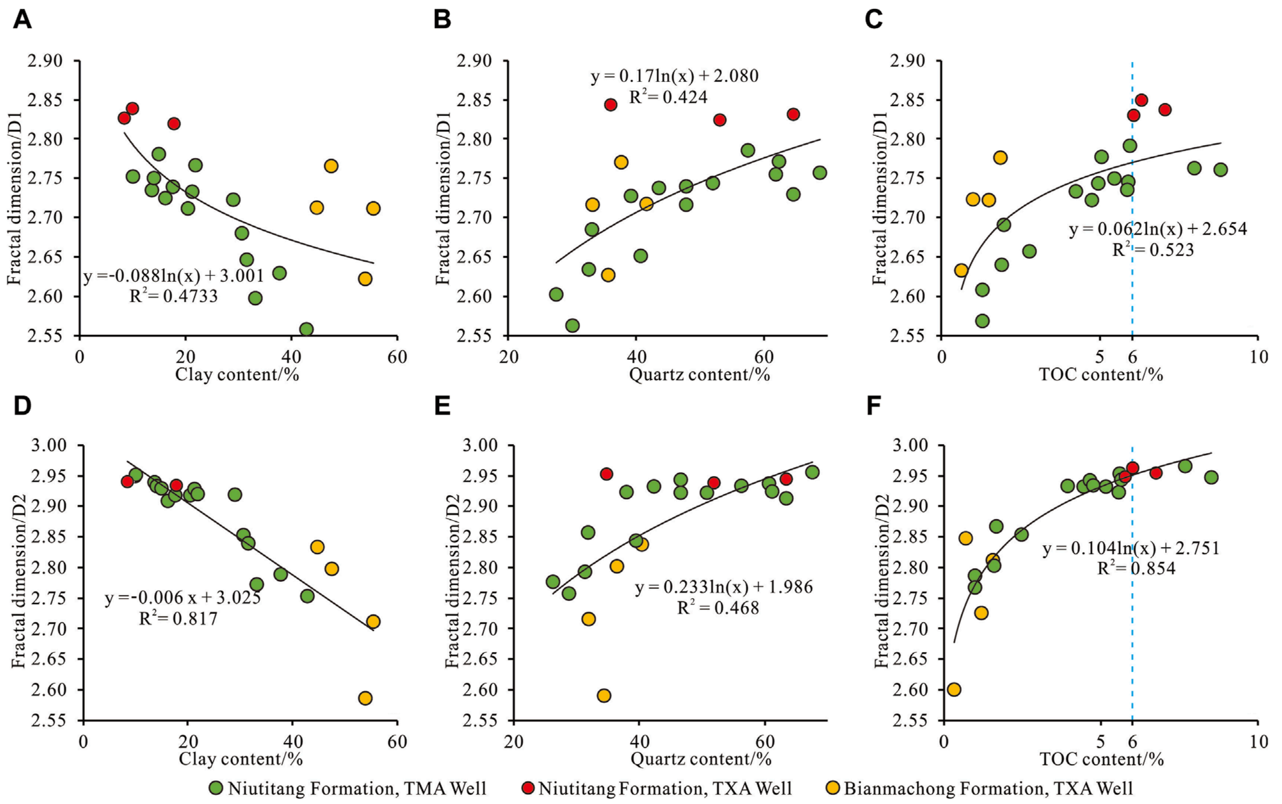

FIGURE 6
Correlations between fractal dimensions and reservoir parameters of shale. **(A)** Correlation between clay mineral content and fractal dimension D1. **(B)** Correlation between quartz content and fractal dimension D1. **(C)** Correlation between TOC content and fractal dimension D1. **(D)** Correlation between clay mineral content and fractal dimension D2. **(E)** Correlation between quartz content and fractal dimension D2. **(F)** Correlation between TOC content and fractal dimension D2.

average pore diameter less than 3–4 nm and a specific surface area greater than 20 m^2/g (Figures 8D, G). This indicates the abundant development of organic pores smaller than 5 nm within organic matter (Kuila et al., 2014; Wang et al., 2017), leading to a reduction in average pore diameter and an increase in specific surface area and pore volume, facilitating the adsorption of gases (Mosher et al., 2013). An anomalous decrease in specific surface area and total pore volume occurs when TOC and quartz content are excessively high (Figures 8A, B, D, E).

When the TOC content reaches 4%, the fractal dimensions D_1 and D_2 generally exceed 2.7 and 2.9, respectively, with a limited increase and a tendency to stabilize (Figures 6C, F). The pore structures exhibit similarity and convergence, indicating a stabilization of the pore structure. Studies by Vernik and Landis (1996) have shown that when the TOC content in shale exceeds 5%, organic matter between clay and detrital particles can form a continuous network structure, isolating clay and detrital particles from each other and stabilizing the shale pore structure. Therefore, when the TOC content is above 4%, the uniformity of shale pore development is high, dominated by organic pores and a small number of pores between clay mineral particles.

In the Niutitang Formation shale of the study area, the relationship between TOC content and porosity, as well as rock mechanical parameters, also exhibits a segmented pattern. When the TOC content is around 6.0% or higher, the relationship between TOC content and porosity, as well as elastic modulus, changes from positive correlation to negative correlation (Figure 9). This indicates that excessively high TOC content enhances shale plasticity (Milliken et al., 2013; Wang et al., 2017), leading to shrinkage and closure of some pores under compaction (Wang et al., 2017). The aforementioned relationships highlight the significant control of TOC and quartz content on shale reservoir pore structure. The coupling relationship between TOC, quartz content, and shale porosity, pore volume, specific surface area, fractal dimensions, and brittleness suggests a geological and engineering sweet spot in high-TOC and high-quartz content shale intervals that have not yet reached the TOC inflection point. For shale intervals with excessively high TOC content, such as the Niutitang Formation shale with TOC content exceeding 6%, the negative correlation between TOC content and average pore diameter, increased plasticity, and changes in pore structure parameters indicate a decreasing trend in porosity, pore volume, specific surface area, fractal dimensions, and brittleness (Figures 6C, F, 8A). This trend is unfavorable for the accumulation of shale gas and reservoir fracturing enhancements. Therefore, identifying the key parameters and their critical values controlling shale reservoir pore structure is of great significance for shale gas exploration and development.

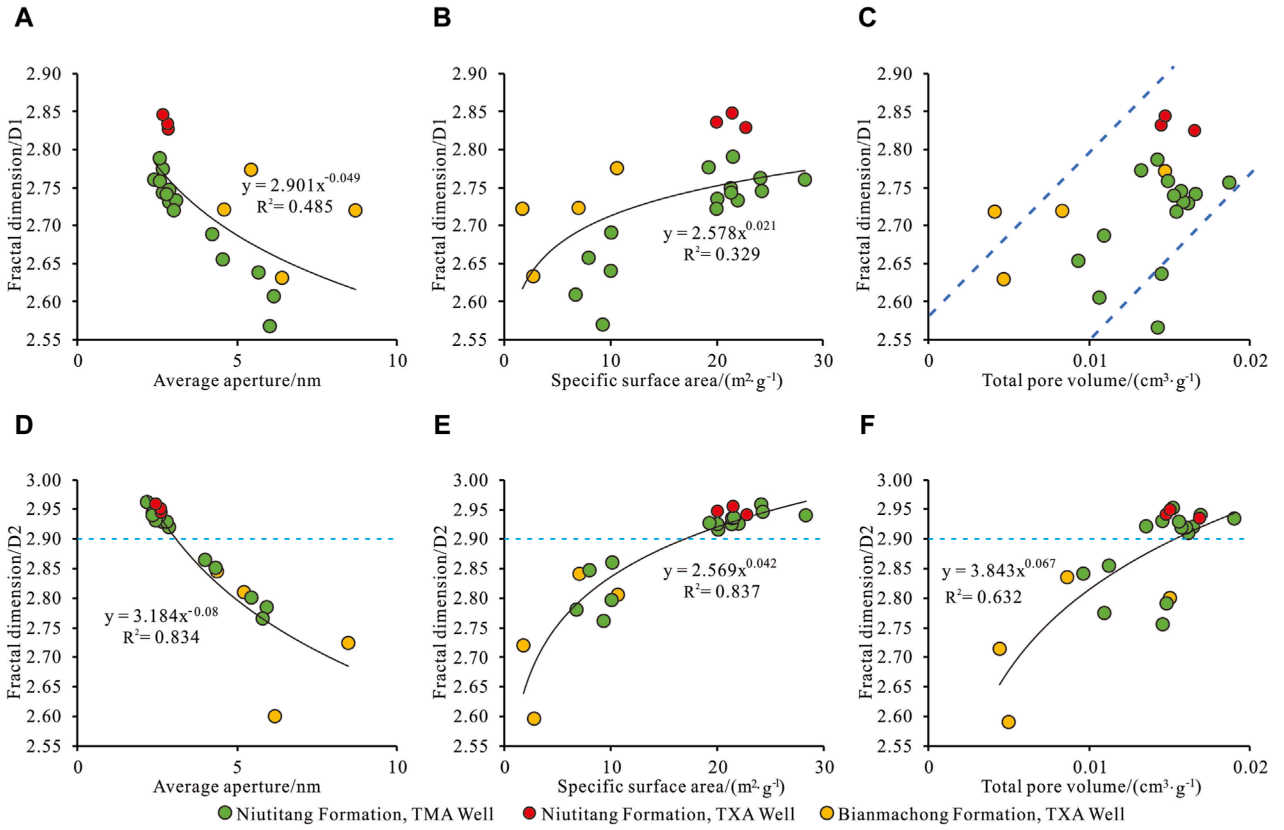

FIGURE 7
Correlations between fractal dimensions and pore structure parameters. **(A)** Correlation between pore size and fractal dimension D1. **(B)** Correlation between specific surface area and fractal dimension D1. **(C)** Correlation between total pore volume and fractal dimension D1. **(D)** Correlation between pore size and fractal dimension D2. **(E)** Correlation between specific surface area and fractal dimension D2. **(F)** Correlation between total pore volume and fractal dimension D2.

5.2 Impact of tectonic preservation conditions on pore structure and gas content

The tectonic preservation conditions are significant factors influencing shale gas enrichment and are closely related to the development of faults and fractures. Practical exploration and development of shale gas in southern China indicate that, influenced by multiple tectonic movements, shale fractures vary in degrees of development across different regions and stratigraphic units, exerting a crucial influence on the accumulation and preservation of shale gas (Wang et al., 2016; 2021b; Fan et al., 2020; 2024). The development scale of high-angle fractures often reflects the preservation conditions of shale gas, showing a strong correlation with shale brittleness. This fracture type is predominant in marine shale formations in southern China (Wang et al., 2021b).

There are noticeable differences in porosity and gas content under different preservation conditions in the Niutitang Formation. The drilling results of three wells in the study area (Figure 10) reveal that the TXA well is located in a structurally stable area, distant from faults, and the drilling operation proceeded smoothly. The shale gas content of the Niutitang Formation shale ranges from 1.1 to 2.9 m^3/t, with a maximum of 7.1 m^3/t. The CYA well is situated near a fault, experiencing four instances of lost circulation during the drilling of the shallow 500 m carbonate rock. The gas content ranges from 0.3 to 1.8 m^3/t. The TMA well is located in a strike-slip fault zone with highly developed highcarbonate rock. The gas content-angle faults and fractures. Numerous and large-scale high-angle fractures are encountered, and gas anomalies appear shortly after drilling into shallow layers. The on-site desorption gas content is only 0.1–0.3 m^3/t, with nitrogen (N_2) constituting over 95% of the gas composition, indicating that the shale gas preservation conditions of the TMA well have been significantly compromised (Wang et al., 2016). The relationship between fracture density and gas content in three wells in the study area is illustrated in Figure 10. The moderately developed fractures in the TXA well contribute to an increase in shale content. As the scale of fracture development increases, preservation conditions gradually deteriorate, leading to a decrease in gas content in CYA and TMA wells. Therefore, excessive fracture development disrupts shale gas preservation conditions, introducing external fluids. Under the influence of fractures and foreign fluids, the local permeability of shale increases, resulting in a weaker pore-permeability correlation overall, characterized by "low porosity, high permeability, low gas content" (Table 2; Figure 3).

The characteristics of N_2 adsorption-desorption isotherms also reflect differences in pore structure under different preservation conditions. Under the same geological conditions, the area of N_2 adsorption-desorption hysteresis loop corresponds well to

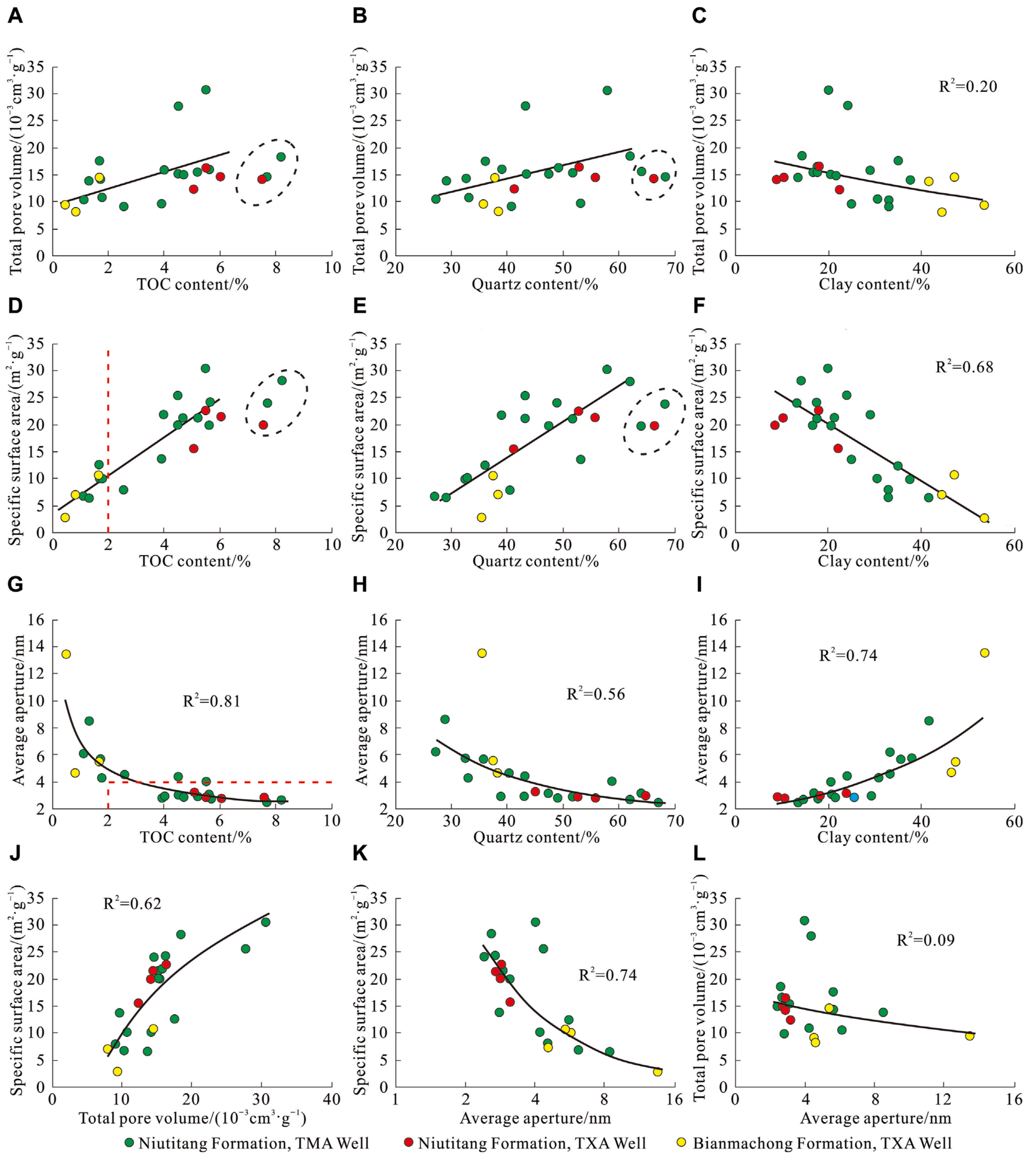

FIGURE 8
Correlations among TOC, mineral content and pore structure parameters. **(A)** Correlation between total pore volume and TOC content. **(B)** Correlation between total pore volume and quartz content. **(C)** Correlation between total pore volume and clay mineral content. **(D)** Correlation between specific surface area and TOC content. **(E)** Correlation between specific surface area and quartz content. **(F)** Correlation between specific surface area and clay mineral content. **(G)** Correlation between pore size and TOC content. **(H)** Correlation between pore size and quartz content. **(I)** Correlation between pore size and clay mineral content. **(J)** Correlation between total pore volume and specific surface area. **(K)** Correlation between pore size and specific surface area. **(L)** Correlation between pore size and total pore volume.

TOC content, representing the development of organic pores. In shale from TXA well with good gas content and preservation conditions, the area of N_2 adsorption-desorption hysteresis loop is significantly larger than in TMA well. The dominant pore type in TXA well is ink bottle-shaped organic pores, while TMA well exhibits predominantly narrow slit-like pores (Table 3). This phenomenon reflects that marine organic-rich shale reservoir spaces are primarily dominated by ink bottle-shaped organic pores. With

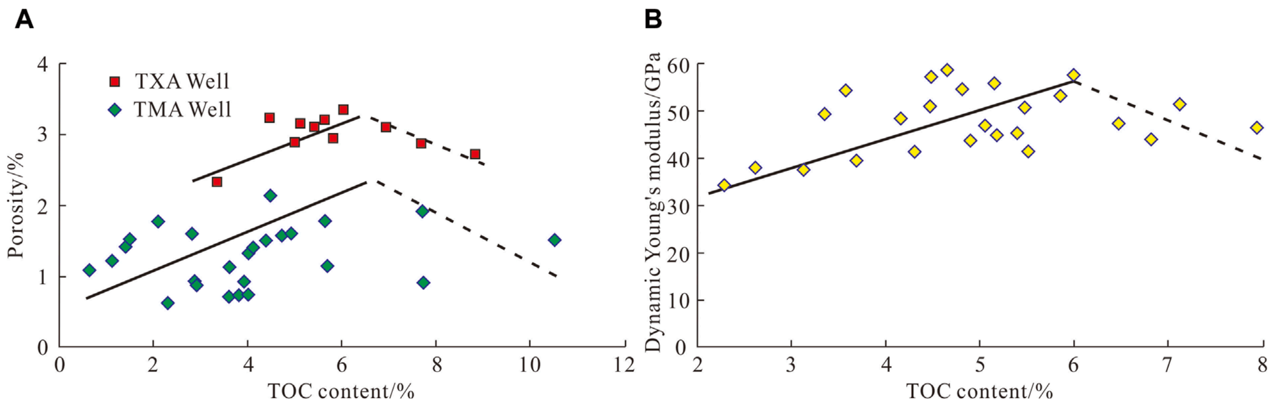

FIGURE 9
(A) Correlation between TOC content and porosity in the Niutitang shale. **(B)** Correlation between TOC content and dynamic Young's modulus in the Niutitang shale of well TX1.

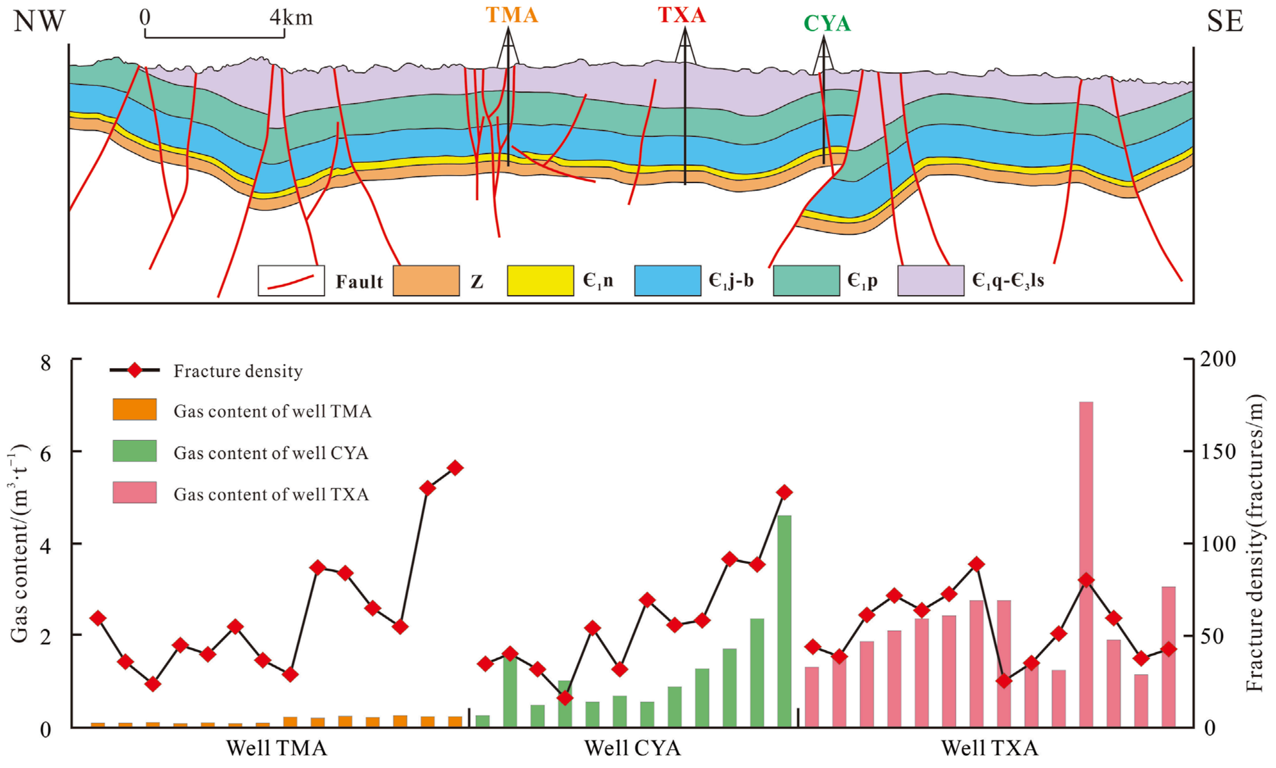

FIGURE 10
Structural position, fracture density, and gas content distribution of key wells in the Niutitang shale of the study area.

the deterioration of preservation conditions, decrease in formation pressure, and the escape of shale gas, organic pores gradually contract and close, and the proportion of slit-shaped pores between clay mineral particles in the storage space increases.

The relationship between fractal dimensions D_1 and D_2 and pore structure parameters indicates that both D_1 and D_2 play a certain indicative role in the development of nanoscale pores. High values of D_1 and D_2 suggest that the pore surface roughness and internal structure are complex, and the pores have not undergone external fluid alteration. Excessive fracture development and unfavorable preservation conditions in the TMA well result in varying degrees of alteration in shale pore structure, especially in pore surface structure. This alteration leads to a reduction in pore surface roughness, consequently causing a significant decrease in the fractal dimension D_1 compared to the TXA well samples (Figures 6A–C, 7A–C). Therefore, fractal dimension D_2 is suitable for characterizing the pore structure of shale, while fractal dimension D_1 reflects the degree of alteration of the pore structure. Both dimensions are crucial indicators of gas content and preservation conditions in shale, especially in structurally complex areas.

6 Conclusion

(1) In the Lower Cambrian shale of the southeastern Guizhou, there is a strong correlation between TOC content and quartz and clay minerals. Low-TOC, clay-rich shale primarily exhibits platy and slit-shaped interlayer pores dominated by mesopores and macropores, with pore sizes generally larger than 5 nm. Organic-rich shale, on the other hand, features mainly slit-shaped and ink bottle-shaped pores, with a pore size distribution primarily in the micropore and mesopore range, generally smaller than 4 nm. The specific surface area of organic-rich shale is 2–3 times that of clay-rich shale. Total pore volume and specific surface area are positively correlated, and clay content is positively correlated with average pore size. However, the correlations between total pore volume/specific surface area and clay mineral content/average pore size are negative.

(2) Significant differences in pore structure are observed in shale reservoirs under different gas contents and preservation conditions. Shale under favorable preservation conditions exhibits a relatively "high porosity, low permeability, and high gas content" feature, with higher pore volume and peak pore size and a well-developed organic pore network, leading to strong pore-permeability correlation. In contrast, shale reservoirs under unfavorable preservation conditions appear denser, with lower pore volume and peak pore size. Shrinkage and compaction of organic matter induce the development of contraction fractures, and excessive fracture development increases average pore size and local permeability. The pore-permeability correlation is weak, resulting in a "low porosity, high permeability, and low gas content" characteristic.

(3) TOC content plays a crucial role in controlling pore structure and shale brittleness. It is generally positively correlated with pore volume, specific surface area, and pore density, and negatively correlated with average pore size. Shale sections with excessively high TOC content exhibit enhanced plasticity, lower pore sizes, and factors such as compaction or unfavorable preservation conditions cause some narrow pores to shrink, collapse, and close. This results in negative correlations between TOC content and pore volume, pore density, specific surface area, brittleness, and fractal dimensions. Therefore, identifying key parameters and their critical values that control shale reservoir pore structure is essential for shale gas exploration and development.

(4) The pore structure of Lower Cambrian shale is complex, with fractal dimensions D_1 and D_2 negatively correlated with average pore size and positively correlated with TOC, specific surface area, and total pore volume. D_2 exhibits better correlations with various pore structure parameters and is suitable for characterizing shale pore structure. D_1 serves as an indicator of gas content and preservation conditions, with high D_1 values indicating well-maintained nanoscale pore surface structure and complexity, less affected by external fluid alteration, and conducive to shale gas preservation.

Data availability statement

The original contributions presented in the study are included in the article/Supplementary material, further inquiries can be directed to the corresponding authors.

Author contributions

RW: Conceptualization, Data curation, Formal Analysis, Funding acquisition, Investigation, Methodology, Project administration, Resources, Software, Supervision, Validation, Visualization, Writing–original draft, Writing–review and editing. YL: Writing–original draft, Writing–review and editing. ZhL: Writing–original draft, Writing–review and editing. DW: Writing–original draft, Writing–review and editing. GW: Writing–original draft, Writing–review and editing. FL: Writing–original draft, Writing–review and editing. ZaL: Writing–original draft, Writing–review and editing. JH: Writing–original draft, Writing–review and editing.

Funding

The author(s) declare that financial support was received for the research, authorship, and/or publication of this article. This research was funded by the Sinopec Ministry of Science and Technology Project (No. 21042-3).

Conflict of interest

The authors declare that the research was conducted in the absence of any commercial or financial relationships that could be construed as a potential conflict of interest.

Publisher's note

References

Aplin, A. C., Matenaar, I. F., McCarty, D. K., and van der Pluijm, B. A. (2006). Influence of mechanical compaction and clay mineral diagenesis on the microfabric and pore-scale properties of deep-water Gulf of Mexico mudstones. *Clays Clay Min.* 54, 500–514. doi:10.1346/CCMN.2006.0540411

Avnir, D., and Jaroniec, M. (1989). An isotherm equation for adsorption on fractal surfaces of heterogeneous porous materials. *Langmuir* 5 (6), 1431–1433. doi:10.1021/la00090a032

Bernard, S., Wirth, R., Schreiber, A., Schulz, H.-M., and Horsfield, B. (2012). Formation of nanoporous pyrobitumen residues during maturation of the barnett shale (fort worth basin). *Int. J. Coal Geol.* 103, 3–11. doi:10.1016/j.coal.2012.04.010

Chen, P., Lin, W., Gong, D., Shang, F., and Liu, X. (2020). Sedimentary geochemical characteristics and its sedimentary environment significance of the black shale of the Lower Cambrian Bianmachong Formation in the Cen'gong block, Guizhou Province. *Chin. J. Geol.* 55 (4), 1025–1043. doi:10.12017/dzkx.2020.063

Dong, T., Kang, L., Zhang, Y., and Gao, Y. (2023). Pore fractal characteristics of lacustrine shale of upper cretaceous nenjiang formation from the songliao basin, NE China. *Appl. Sci.* 13 (7), 13074295. doi:10.3390/app13074295

Dowey, P. J., and Taylor, K. G. (2020). Diagenetic mineral development within the upper jurassic haynesville-bossier shale, USA. *Sedimentology* 67, 47–77. doi:10.1111/sed.12624

Fan, C., Li, H., Qin, Q., He, S., and Zhang, C. (2020). Geological conditions and exploration potential of shale gas reservoir in Wufeng and Longmaxi Formation of southeastern Sichuan Basin, China. *J. Petroleum Sci. Eng.* 191, 107138. doi:10.1016/j.petrol.2020.107138

Fan, C., Nie, S., Radwan, A. E., Pan, Q., Shi, X., Li, J., et al. (2024). Quantitative prediction and spatial analysis of structural fractures in deep shale gas reservoirs within complex structural zones: a case study of the Longmaxi Formation in the Luzhou area, southern Sichuan Basin, China. *Asian Earth Sci.* 263, 106025. doi:10.1016/j.jseaes.2024.106025

Feng, G., and Chen, S. (1988). Relationship between the reflectance of bitumen and vitrinite in rock. *Nat. Gas. Ind.* 8 (3), 20–25.

Guo, X., Liu, R., Xu, S., Feng, P., Wen, T., and Zhang, T. (2022). Structural deformation of shale pores in the fold-thrust belt: the wufeng-longmaxi shale in the anchang syncline of central Yangtze block. *Adv. Geo-Energy Res.* 6 (6), 515–530. doi:10.46690/ager.2022.06.08

Hackley, P. C., Zhang, T., Jubb, A. M., Valentine, B. J., Dulong, F. T., and Hatcherian, J. J. (2020). Organic petrography of Leonardian (Wolfcamp A) mudrocks and carbonates, Midland Basin, Texas: the fate of oil-prone sedimentary organic matter in the oil window. *Mar. Pet. Geol.* 112, 104086. doi:10.1016/j.marpetgeo.2019.104086

Hu, Z., Wang, R., Liu, Z., Liu, G., Feng, D., Yang, Z., et al. (2021). Source-reservoir characteristics and coupling evaluations for the Lower Jurassic lacustrine shale gas reservoir in the Sichuan Basin. *Earth Sci. Front.* 28 (1), 261–272. doi:10.13745/j.esf.sf.2020.5.24

Kuila, U., McCarty, D. K., Derkowski, A., Fischer, T. B., Topor, T., and Prasad, M. (2014). Nano-scale texture and porosity of organic matter and clay minerals in organic-rich mudrocks. *Fuel* 135, 359–373. doi:10.1016/j.fuel.2014.06.036

Lai, F., Liu, Y., Zhang, H., Wang, H., Mao, H., and Zhang, G. T. (2022). Fracturing properties model of deep shale gas reservoir based on digital core simulation. *J. China Univ. Petroleum Ed. Nat. Sci.* 46 (05), 1–11. doi:10.3969/j.issn.1673-5005.2022.05.001

Li, H., Zhou, J., Mou, X., Guo, H., Wang, X., An, H., et al. (2022). Pore structure and fractal characteristics of the marine shale of the Longmaxi Formation in the changning area, southern Sichuan Basin, China. *Front. Earth Sci.* 10, 1018274. doi:10.3389/feart.2022.1018274

Liu, D., Guo, J., Pan, Z., Du, W., Zhao, F., Chen, Y., et al. (2021b). Overpressure evolution process in shale gas reservoir: evidence from the fluid inclusions in the fractures of Wufeng Formation-Longmaxi Formation in the southern Sichuan Basin. *Nat. Gas. Ind.* 41 (09), 12–22. doi:10.3787/j.issn.1000-0976.2021.09.002

Liu, W., Yu, L., Zhang, W., Fan, M., and Bao, F. (2016). Micro-pore structure of Longmaxi shale from southeast Sichuan Basin. *Mar. Geol. Quat. Geol.* 36 (3), 127–134. doi:10.16562/j.cnki.0256-1492.2016.03.012

Liu, Y., Lai, F., Zhang, H., Tan, Z., Wang, Y., Zhao, X., et al. (2021a). A novel mineral composition inversion method of deep shale gas reservoir in Western Chongqing. *J. Petroleum Sci. Eng.* 202, 108528. doi:10.1016/j.petrol.2021.108528

Milliken, K. L., Rudnicki, M., Awwiller, D. N., and Zhang, T. (2013). Organic matter-hosted pore system, Marcellus formation (Devonian), Pennsylvania. *AAPG Bull.* 97, 177–200. doi:10.1306/07231212048

Mosher, K., He, J., Liu, Y., Rupp, R., and Wilcox, J. (2013). Molecular simulation of methane adsorption in micro- and mesoporous carbons with applications to coal and gas shale systems. *Int. J. Coal Geol.* 109-110, 36–44. doi:10.1016/j.coal.2013.01.001

Shi, Z., Wang, H., Zhao, S., Zhou, T., Zhao, Q., and Qi, N. (2023). Rapid transgressive shale characteristics and organic matter distribution of the upper ordovician-lower silurian wufeng-longmaxi formations in southern Sichuan Basin, China. *J. Palaeogeogr. Chin. Ed.* 25 (04), 788–805. doi:10.7605/gdlxb.2023.04.065

Sing, K. S. W. (1985). Reporting physisorption data for gas/solid systems with special reference to the determination of surface area and porosity (Recommendations 1984). *Pure Appl. Chem.* 57 (4), 603–619. doi:10.1351/pac198557040603

Sun, M., Wen, J., Pan, Z., Liu, B., Blach, T. P., Ji, Y. P., et al. (2022a). Pore accessibility by wettable fluids in overmature marine shales of China: investigations from contrast-matching small-angle neutron scattering (CM-SANS). *Int. J. Coal Geol.* 255, 103987. doi:10.1016/j.coal.2022.103987

Sun, Y., Ju, Y., Zhou, W., Qiao, P., Tao, L., and Xiao, L. (2022b). Nanoscale pore and crack evolution in shear thin layers of shales and the shale gas reservoir effect. *Adv. Geo-Energy Res.* 6 (3), 221–229. doi:10.46690/ager.2022.03.05

Vernik, L., and Landis, C. (1996). Elastic anisotropy of source rocks: implications for hydrocarbon generation and primary migration. *AAPG Bull.* 80 (4), 531–544. doi:10.1306/64ED8836-1724-11D7-8645000102C1865D

Wang, R., Ding, W., Gong, D., Leng, J., Wang, X., Yin, S., et al. (2016). Gas preservation conditions of marine shale in northern Guizhou area: a case study of the Lower Cambrian Niutitang Formation in the Cen'gong block, Guizhou Province. *Oil Gas Geol.* 37 (1), 45–55. doi:10.11743/ogg20160107

Wang, R., Gong, D., Leng, J., Cong, S., Ding, W., Fu, F., et al. (2017). Developmental characteristics of the Lower Cambrian Niutitang shale reservoir in Northern Guizhou area: a case study in the Cengong block. *Earth Sci. Front.* 24 (06), 286–299. doi:10.13745/j.esf.yx.2017-10-4

Wang, R., Hu, Z., Dong, L., Gao, B., Sun, C., Yang, T., et al. (2021a). Advancement and trends of shale gas reservoir characterization and evaluation. *Oil Gas Geol.* 42 (1), 54–65. doi:10.11743/ogg20210105

Wang, R., Hu, Z., Lai, F., Liu, Y., Wu, Z., He, J., et al. (2023a). Resolution of secondary hyperparathyroidism after kidney transplantation and the effect on graft survival. *Oil Gas Geol.* 44 (02), 366–375. doi:10.1097/SLA.0000000000005946

Wang, R., Hu, Z., Long, S., Du, W., Wu, J., Wu, Z., et al. (2022). Comparison of risk scoring systems for upper gastrointestinal bleeding in patients after renal transplantation: a retrospective observational study in Hunan, China. *Oil Gas Geol.* 43 (2), 353–364. doi:10.1186/s12876-022-02426-3

Wang, R., Hu, Z., Sun, C., Liu, Z., Zhang, C., Gao, B., et al. (2018). Comparative analysis of shale reservoir characteristics in the Wufeng-Longmaxi (O_3w-S_1l) and Niutitang ($Є_1n$) Formations: a case study of wells JY1 and TX1 in the southeastern Sichuan Basin and its neighboring areas, southwestern China. *Interpretation* 6 (4), 31–45. doi:10.1190/INT-2018-0024.1

Wang, R., Hu, Z., Zhou, T., Bao, H., Wu, J., Du, W., et al. (2021b). Characteristics of fractures and their significance for reservoirs in Wufeng Longmaxi shale, Sichuan Basin and its periphery. *Oil Gas Geol.* 42 (6), 1295–1306. doi:10.11743/ogg20210605

Wang, R., Wang, G., Zhao, G., Qian, M., Liu, Y., He, W., et al. (2023b). Geological characteristics and resources potential of shale oil in chang 7 member of upper triassic yanchang Formation in fuxian area, southern ordos basin, western China. *Unconv. Resour.* 3 (1), 237–247. doi:10.1016/j.uncres.2023.06.001

Wei, H., Feng, Q., Yu, J., and Shan, C. (2022). Characteristics and sources of organic matter from the early cambrian Niutitang formtion and its preservation environment in Guizhou. *J. Earth Sci.* 33 (4), 933–944. doi:10.1007/s12583-020-1371-1

Wu, Z., Wang, S., Chen, J., Song, H., Wang, W., Wang, R., et al. (2022). Fracture propagation modes of lower cambrian shale filled with different quartz contents under seepage-stress coupling. *Geofluids* 2022, 1–18. doi:10.1155/2022/1051284

Xu, H., Zhou, W., Hu, Q., Yi, T., Ke, J., Zhao, A., et al. (2021). Quartz types, silica sources and their implications for porosity evolution and rock mechanics in the Paleozoic Longmaxi Formation shale, Sichuan Basin. *Mar. Petroleum Geol.* 128, 105036. doi:10.1016/j.marpetgeo.2021.105036

Yang, R., He, S., Hu, Q., Hu, D., Zhang, S., and Yi, J. (2016). Pore characterization and methane sorption capacity of over-mature organic-rich Wufeng and Longmaxi shales in the southeast Sichuan Basin, China. *Mar. Petroleum Geol.* 77 (11), 247–261. doi:10.1016/j.marpetgeo.2016.06.001

Yang, Z., Fan, M., Tao, C., Lu, L., and Qiang, M. (2022). Carbon isotope fractionation characteristics and significance of black shale desorded gas from Longmaxi Formation in Jiaoshiba area, Sichuan Basin. *Nat. Gas. Geosci.* 33 (8), 1295–1303. doi:10.11764/j.issn.1672-1926.2022.03.006

Zhang, K., Song, Y., Jia, C., Jiang, Z., Han, F., Wang, P., et al. (2022). Formation mechanism of the sealing capacity of the roof and floor strata of marine organic-rich shale and shale itself, and its influence on the characteristics of shale gas and organic matter pore development. *Mar. Petroleum Geol.* 140, 105647. doi:10.1016/j.marpetgeo.2022.105647

Zhang, Q., Liang, F., Liang, P., Zhou, S., Guo, W., Guo, W., et al. (2020). Investigation of fractal characteristics and its main controlling factors of shale reservoir: a case study of the Longmaxi shale in Weiyuan shale gas field. *J. China Univ. Min. Technol.* 49 (1), 110–122. doi:10.13247/j.cnki.jcumt.001068

Zhu, H., Ju, Y., Huang, C., Qi, Y., Ju, L., Yu, K., et al. (2019). Petrophysical properties of the major marine shales in the Upper Yangtze Block, south China: a function of structural deformation. *Mar. Petroleum Geol.* 110, 768–786. doi:10.1016/j.marpetgeo.2019.08.003

frontiers | Frontiers in Earth Science

TYPE Original Research
PUBLISHED 22 April 2024
DOI 10.3389/feart.2024.1365516

OPEN ACCESS

EDITED BY
Hu Li,
Southwest Petroleum University, China

REVIEWED BY
Yumao Pang,
Shandong University of Science and Technology, China
Shun He,
Southwest Petroleum University, China
Hamzeh Ghorbani,
Islamic Azad University, Iran

*CORRESPONDENCE
Yue Zhao,
✉ zhaoyue118000@163.com

RECEIVED 04 January 2024
ACCEPTED 08 April 2024
PUBLISHED 22 April 2024

CITATION
An Z, Zhao Y and Zhang Y (2024), Pore heterogeneity analysis and control mechanisms in Cambrian shale of the Shuijingtuo Formation, Yichang area, China. *Front. Earth Sci.* 12:1365516.
doi: 10.3389/feart.2024.1365516

Pore heterogeneity analysis and control mechanisms in Cambrian shale of the Shuijingtuo Formation, Yichang area, China

Zhengzhen An[1], Yue Zhao[1,2]* and Yanfei Zhang[3]

[1]Mining College of Liaoning Technical University, Fuxin, China, [2]College of Innovation and Practice Liaoning Technical University, Fuxin, China, [3]Shenyang Geological Survey Center, China Geological Survey, Shenyang, Liaoning, China

This study focuses on understanding the fractal characteristics and controlling factors of micropore structures within organic-rich shale of the Cambrian Shuijingtuo Formation in the Yichang area of Hubei Province. Mineralogy, petrology, and organogeochemical characteristics were confirmed through comprehensive testing methods, including whole-rock X-ray diffraction and organic geochemical analyses. Additional experiments included low-temperature carbon dioxide adsorption, low-temperature nitrogen adsorption, and high-pressure mercury injection. Fractal dimensions of micropores, mesopores, and macropores were calculated using the V-S, FHH, and MENGER sponge models, respectively. Results indicate that the Cambrian Shuijingtuo Formation represents a typical deposit from an alkaline water body, resulting in high-calcareous shale. Fractal dimensions were as follows: micropores (D1) ranged from 2.1138 to 2.3475 (average 2.2342), mesopores (D2) ranged from 2.5327 to 2.7162 (average 2.6171), and macropores (D3) ranged from 2.7361 to 2.9316 (average 2.82905). Correlations were observed between total organic carbon (TOC) content and Ro with D1 and D2 (positive) and D3 (negative). Shale pore volume and specific surface area exhibited positive correlations with D1 and D2 but negative correlations with D3. High bio-deposited silica positively influenced micropore and mesopore development, while clay mineral compaction and dehydration transformations favored macropore development. Carbonate minerals primarily contributed to regular macropores, with complex correlations involving fractal dimensions D1, D2, and D3. The research results provide theoretical support for analyzing pore fractal characteristics of shallow old Marine shale reservoirs and the prediction and development plan of high-quality reservoirs of the Shuijingtuo Formation in the Yichang area.

KEYWORDS

Yichang area, Shuijingtuo Formation, low-temperature gas adsorption, high-pressure mercury injection, fractal dimension, controlling factor

1 Introduction

As an unconventional reservoir, shale typically exhibits low porosity and permeability (Li, 2023). A large number of nanoscale pores and micro-fractures (faults) develop in shale, interweaving with each other to form a complex fissure-pore network. The occurrence states of gas in shale include the free state, adsorption state, and a small amount in the dissolved state (He et al., 2022a; 2022b). The proportion of gas content in different states is directly related to the pore structure, an important aspect of shale reservoir evaluation (Li et al., 2019a; Li B. et al., 2019). Gas in micropores and small-aperture mesoporous pores is mostly adsorbed on the inner wall of pores, while gas in large-aperture mesoporous pores and macropores is mostly in the free state (Gao et al., 2020; Zhao et al., 2022). The adsorbed gas content in shale gas is about 80% (Liu and Ostadhassan, 2019; Li, 2021), and characterization of pore complexity has become an important aspect of studying shale reservoir performance.

Due to the characteristics of small pore size and strong heterogeneity, the application of conventional reservoir pore characterization methods in shale reservoirs is extremely limited, which brings challenges to the characterization of shale pore structure (Dou et al., 2020). Shale pore types and morphologies can be observed using argon ion-polished scanning electron microscopy (Cheng et al., 2018). High-pressure mercury intrusion and low-temperature gas adsorption methods are employed for pore structure parameter testing. Low-temperature gas adsorption is more precise for micro-to-mesopore characterization (Jiang et al., 2016; Zeng et al., 2021; Abraham et al., 2022; Xia et al., 2022). Due to its larger kinetic diameter, nitrogen analysis introduces greater errors in characterizing micropore structures during low-temperature nitrogen gas adsorption. Carbon dioxide gas, with its smaller kinetic diameter, offers more accurate characterization of micro-pore structures. During high-pressure mercury intrusion experiments, changes occur in the small pore structures under high pressure, making this method mainly suitable for characterizing macropore structures. Scanning electron microscopy and gas adsorption are currently the most commonly used and effective methods for characterizing shale micro-pore structures (Ma et al., 2021).

Shale pore distribution exhibits significant heterogeneity, influenced by the presence and distribution of organic matter and inorganic minerals. This complexity poses challenges in quantitatively assessing shale pore structures. With the application of fractal theory in characterizing pore structures within unconventional reservoirs, numerous scholars have quantitatively characterized the fractal dimension of pores using different theoretical models (Fan et al., 2020a; Zhang et al., 2020). Zhang et al. (2020) calculated the fractal dimension of pores in different small layers in the Weiyuan area using the FHH model and obtained the most favorable reservoir development section at the bottom of small layer 1. Zhao et al. (2022) quantitatively characterized the shale surface's fractal and structural dimensions by conducting low-temperature nitrogen adsorption experiments. Their findings suggest that the content of organic matter and quartz is the main reason for the complexity of the pore structure. Sun et al. (2021) used low-temperature nitrogen adsorption and high-pressure mercury injection experiments to compare and analyze the complexity of shale pores in Qianjiang Sag and pointed out that the existence of oil film would reduce the complexity of pores, while the development of salt minerals would reduce the connectivity of pores. Xie et al. (2022) pointed out in their study of multi-scale fractal characteristics of shale pores using different gas adsorption experiments and high-pressure mercury intrusion experiments that different experimental methods have specific pore size adaptation ranges in characterizing pore complexity. Finding suitable gases as adsorption media and combining high-pressure mercury intrusion experiments can better characterize the complexity of pore sizes at different scales.

Therefore, understanding the pore structure heterogeneity and its controlling factors in shale formations is crucial for predicting and optimizing hydrocarbon production. This study delves into the intricate pore structure of shale formations, focusing specifically on the Longmaxi Formation in Western Hubei, China. We recognized the importance of shale petrology and geochemical characteristics in determining reservoir behavior, so we conducted a series of advanced laboratory experiments. These included low-temperature carbon dioxide and nitrogen adsorption and high-pressure mercury intrusion experiments. These methods allowed us to meticulously quantify the fractal dimensions of micro, meso, and macropores, providing insights into the hierarchical pore structure of the Longmaxi Formation.

Furthermore, we conducted a correlation analysis to elucidate the interplay between major mineral content, pore structure parameters, and fractal dimensions. By exploring their impact on pore complexity, we aim to unravel the underlying mechanisms shaping the heterogeneity of shale pore networks. This research aims to provide valuable theoretical support for upcoming shale oil and gas exploration endeavors, particularly in the Shuijingtuo Formation.

2 Geological setting

Regarding regional geological characteristics, the Huangling area is located in the northern part of the Yangtze Plate, within the complex tectonic zone known as the folded fault belt of Western Hunan and Hubei (Zhang et al., 2019). It lies in the southwestern sector of the Yichang Slope, bounded by the Huangling Anticline to the north and the Yichang Slope to the east (Figure 1A). To the southwest, it interfaces with the Yidu-Hefeng Anticline through the Jiunianxi Fault and Tianyangping Fault (Xu et al., 2022). The region's surface geological environment is complex, featuring numerous thrust faults and well-exposed stratigraphic sequences spanning the Precambrian to the Cenozoic. The Shuijingtuo Formation was deposited within the stable Yangtze Craton basin during the Jinning period. It was confined by the peripheral ancient landmass and shaped by marine transgressions, resulting in a restricted aquatic environment characterized by deep-water continental shelf facies, shallow-water mixed continental shelf facies, and submarine uplifts. Based on lithological and depositional environment differences, the Shuijingtuo Formation can be divided into three members from bottom to top. The lower part of the Shuijingtuo Formation (1st Member) predominantly comprises mudstone and limestone. The middle part of the Shuijingtuo Formation (2nd Member) consists mainly of black organic-rich shale deposited in a deep-water continental shelf environment (Luo et al., 2019a). This interval hosts abundant fossils such as graptolites and benthic algae and serves as the primary gas-bearing interval within the Shuijingtuo Formation. It is laterally parallel but unconformably overlies the underlying Baiyun Limestone Member of the Yimajiahe Formation (Figure 1B). The uppermost segment, the 3rd Member of the Yimajiahe Formation, represents the sedimentary product of a shallow-water mixed continental shelf environment, primarily composed of

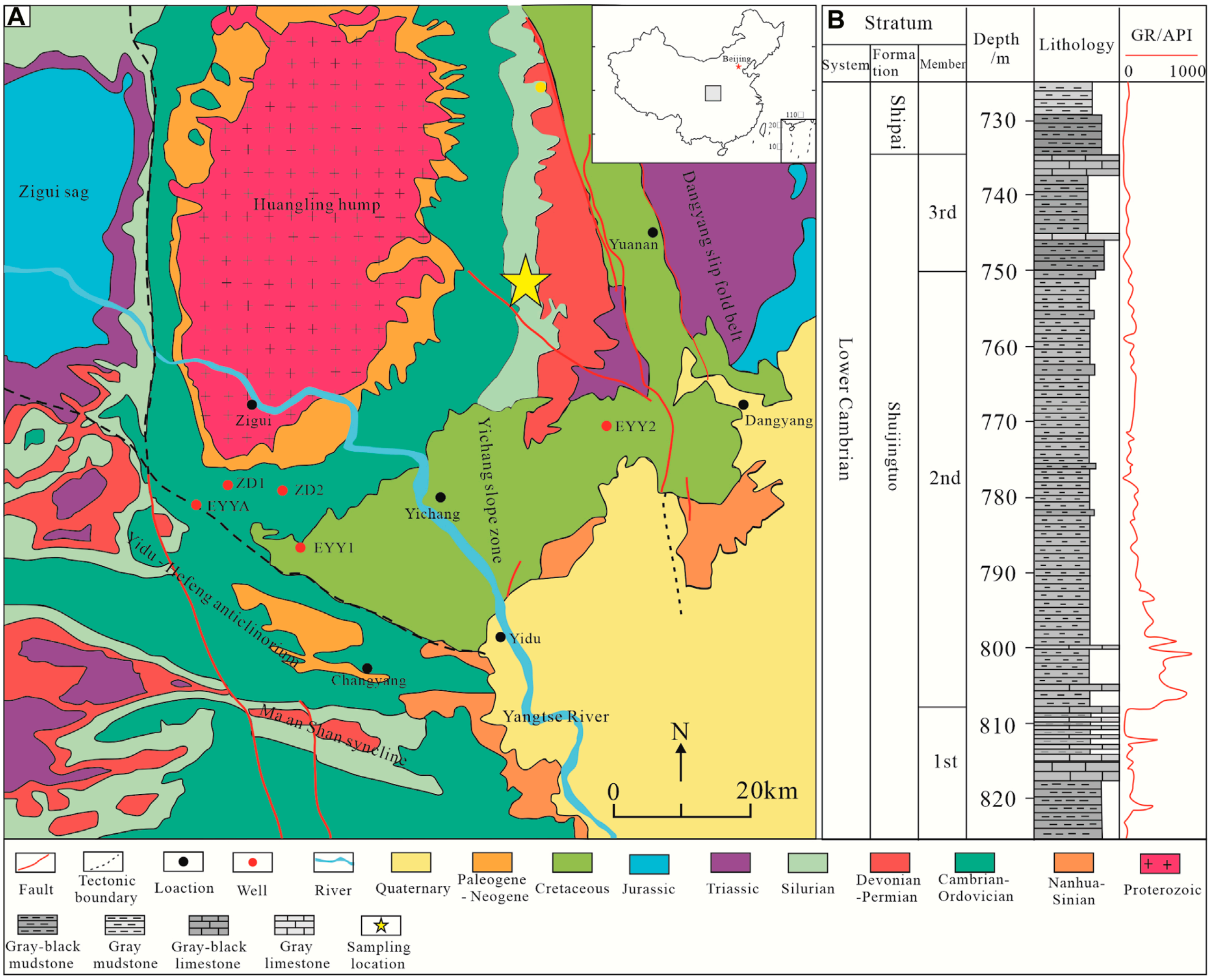

FIGURE 1
Regional structure position **(A)** and comprehensive stratigraphic column chart **(B)** in the study area.

interbedded limestone and clastic rocks. It is conformably overlain by the deep gray mudstone and siltstone of the Shipai Formation (Luo et al., 2019b).

The mudstone shale of the Shuijingtuo Formation has an early formation time and is characterized by a wide lateral distribution, substantial vertical effective thickness, high TOC content, and a high degree of thermal evolution (Zhang et al., 2023). The vertical distribution of TOC content gradually decreases based on typical well analyses. Continuous thicknesses with TOC content greater than 2% extend over 35 m from the base to the top, and thicknesses with TOC content greater than 1% extend over 65 m. The organic matter comprises Type I kerogen, with a minor presence of Type II_1 kerogen. In contrast to the Shuijingtuo Formation shale in the Chongqing and Guizhou regions, it is classified as high-calcium shale, with illite being the predominant clay mineral. The formation is generally buried at depths exceeding 2,000 m, classifying it as mid-shallow shale. Exploration practices have revealed significant variations in gas content and well productivity among different individual wells.

3 Samples and methods

The shale samples analyzed in this study were sourced from outcrop sections around the Huangling Uplift. Before sampling, surface vegetation was cleared, and the upper weathered or weakly weathered layers were removed from the shale outcrops using an excavator. We selected intact and fresh large blocks of shale samples during the sampling process, which were sealed in bags to preserve their integrity. The samples primarily consisted of unweathered, black, organic-rich shale.

3.1 Total organic carbon (TOC) content and maturity testing

We utilized an infrared carbon-sulfur analyzer (LECO CS844) manufactured by the American company LECO to determine the organic carbon content in the black shale samples from the Shuijingtuo Formation. Before experimental testing, fresh black shale samples were ground in agate mortars until they reached a particle size finer than 80 mesh. The powdered samples were then acid-washed using excess dilute hydrochloric acid for approximately 3 h. After acid washing, the powdered samples were rinsed with distilled water until they reached a neutral PH. Subsequently, the neutral powdered samples were dried at 65°C. The entire testing procedure followed the GB/T 19145-2003 standard, and solid-state infrared absorption was employed to measure the organic carbon content.

We conducted maturity testing using a polarizing microscope (Leica DM4500P) and a microphotometer (CRAIC QDI 302) manufactured by Leica and CRAIC, respectively. Before the experiments, the samples were mechanically crushed and polished. Subsequently, the polished samples were subjected to low-temperature drying at 45°C for 3.5 h in an oven. The experimental procedures followed GB/T 6948-1998 standards and SY/T 5124-2010.

3.2 Whole-rock X-ray diffraction (XRD) analysis

We conducted mineral composition and content analysis of shale using a multifunctional X-ray diffractometer, the Bruker D8ADVANCE, manufactured by Bruker in Germany. The X-ray source employed in the instrument was Cu-target. Before experimentation, shale samples were subjected to low-temperature drying and then finely ground to a particle size exceeding 200 mesh using an agate mortar, ensuring that the sample weight exceeded 0.5 g. The entire testing procedure was conducted at room temperature. During the experiments, the instrument was set to a voltage and current of 40 kV and 5 mA, respectively, and continuous scanning was performed at a minimum diffraction angle of 2°, following the SY/T5163-2010 standard.

3.3 Low-temperature gas adsorption

We conducted low-temperature nitrogen adsorption experiments using an ASAP2420 fully automated surface area and pore size distribution analyzer manufactured by Micromeritics Instrument, United States. Before the experiments, the samples underwent degassing to remove surface impurities. The samples were dried at low temperatures and then ground to a particle size of approximately 40 mesh using an agate mortar. Subsequently, the finely ground powder samples underwent 14 h of vacuum drying at 120°C, with the vacuum pressure below 1 Pa. High-purity liquid nitrogen with a purity exceeding 99.9% was used as the adsorption medium. Under constant temperature conditions at 77 K using liquid nitrogen, the sample's specific surface area, pore size, and pore volume were calculated using the BJH and BET principles (Wang et al., 2018).

We used a pore analyzer produced by Quantachrome Instruments with the model Quadrasorb SI for low-temperature carbon dioxide adsorption experiments. Before testing, the samples were subjected to vacuum treatment at 65°C to eliminate surface moisture. After drying, the samples were placed in liquid carbon dioxide for experimentation.

3.4 High-pressure mercury injection experiment

In this study, we utilized the AutoPore 9510, an automated mercury porosimeter manufactured by Micromeritics Instrument Corporation in the United States. During the testing phase, this instrument allowed for mercury injection pressures of up to 414 MPa, corresponding to a lower limit of approximately 3 nm in test pore size. Before the tests, we shaped the samples into cubes measuring 1 cm × 1 cm × 1 cm.

To minimize the influence of surface roughness on the mercury injection experiment, we employed the instrument to segment the samples, ensuring a flat surface. Before testing, the cubic samples underwent a 60°C drying process lasting 48 h. This step was crucial for eliminating internal impurities and guaranteeing that the original pore structure of the samples remained intact throughout the drying process.

The instrument's internal vacuum was maintained throughout the testing procedure, and the instrument automatically recorded data for mercury intrusion and extrusion processes (Zhu et al., 2019; Zuo et al., 2019).

3.5 Calculation of fractal dimension

The calculation of fractal dimensions involves various models, and the suitability and accuracy of different models vary depending on the pore sizes in question. The calculation methods for fractal dimensions of pores within different size ranges also differ (An et al., 2023). This study employed different calculation models for the fractal dimensions of micropores, mesopores, and macropores to accurately characterize.

In the low-temperature gas adsorption experiment, the kinetic diameter of CO_2 is 0.33 nm, which can be used to characterize the micropores of 0.33–1.4 nm (Shi et al., 2023). The low-temperature carbon dioxide adsorption experiment is well-suited for characterizing micropore complexity (Zhao et al., 2015). The micropore fractal dimension was calculated using the V-S model, with the specific calculation formula presented as follows:

$$LnV1 = \frac{3}{D1}LnS + \mathrm{k} \tag{1}$$

In the equation: "k" represents a dimensionless constant; "V_1" denotes the cumulative pore volume, measured in mL/g; "S" stands for the cumulative specific surface area, measured in m^2/g; "D1" represents the micropore fractal dimension, which is dimensionless.

Due to the activation and diffusion effect of nitrogen in micropores and the capillary condensation phenomenon in macropores, the application effect in mesoporous pores is better, so Low-temperature nitrogen adsorption experiments are well-suited for characterizing mesopores (Liu et al., 2023). The fractal dimension of mesopores in shale, as calculated using the FHH model, is determined by the following specific formula:

$$LnV = \mathrm{k} + (D2 - 3)Ln\left[\mathrm{Ln}\left(P_0/P\right)\right] \tag{2}$$

In the equation: "k" is a dimensionless constant; "V" represents the cumulative pore volume of a specific stage (e.g., mesopores), measured in mL/g; "P_0" is the vapor pressure of the gas at saturation, measured in MPa; "P" stands for the system's equilibrium pressure, measured in MPa; "D2" is the fractal dimension of mesopores and is dimensionless.

In the process of using high-pressure mercury injection to characterize pore structure, excessive pressure will destroy shale pores, affecting the experimental results, and it is suitable for macro pore characterization (>50 nm) (Wang et al., 2015). Therefore, High-pressure mercury injection experiments have a natural advantage in characterizing shale macropores (Kong et al., 2020). The fractal dimension of macropore porosity is calculated using the MENGER sponge model, with the specific formula provided as follows:

$$D3 = 4 + Ln\left(\mathrm{d}V_{\mathrm{p}}/d_{p}\right)/LnP \tag{3}$$

Where: "D3" is the macropore fractal dimension (dimensionless); "V_p" is the incremental pore volume (mL/g); "P" is the experimental pressure (MPa).

4 Results

4.1 Organic geochemical and petrological characteristics

The results of organic matter content and maturity testing show significant variations in the organic matter content of the Shuijingtuo Formation shale in the Yichang area. The overall content ranges from 0.88% to 4.62%, with an average of 2.56%. The equivalent vitrinite reflectance (Ro) values of organic matter range from 2.05% to 2.74%, with an average of 2.41%.

The whole-rock X-ray diffraction results reveal the complex mineral composition of the Shuijingtuo Formation shale (Table 1). The primary mineral types include feldspar, quartz, calcite, dolomite, and clay, among other major rock-forming minerals. Additionally, pyrite and siderite are notable occurrences. Among these, siliceous and clay minerals are the predominant rock-forming minerals, constituting over 70% of the total mineral content. Quartz content varies between 46% and 64%, with an average of 55.33%, while feldspar content ranges from 3% to 11%, averaging 6%. Clay mineral content falls between 14% and 35%, averaging 23.92%. Carbonate minerals account for 7%–19% of the composition, averaging 11.17%. Calcite content varies from 3% to 14%, averaging 6.8%, while dolomite content ranges from 2% to 7%, averaging 4.3%. Pyrite content is between 1% and 5%, with an average of 2.75%.

4.2 Shale porosity characteristics

Based on DFT, BJH models, and Washburn equations, low-temperature CO_2, N_2 adsorption data, and high-pressure mercury experiment data are processed to obtain the pore volume and specific surface area of micropores, mesoporous, and macropores. The experimental results revealed a total pore volume ranging from 12.63×10^{-3} to 28.71×10^{-3} mL/g, with an average pore volume of 19.50×10^{-3} mL/g (Table 2). Among these values, micropore volume varied between 1.56×10^{-3} and 7.64×10^{-3} mL/g, averaging at 4.228×10^{-3} mL/g, constituting an average of 21.26% of the total. Mesopore volume ranged from 3.77×10^{-3} to 15.58×10^{-3} mL/g, averaging at 7.925×10^{-3} mL/g, representing an average of 39.76%. Macropore volume fell between 4.85×10^{-3} and 11.4×10^{-3} mL/g, with an average of 7.35×10^{-3} mL/g, making up 38.98% of the total.

The shale's total specific surface area spanned from 9.54 to 17.54 m^2/g, with an average specific surface area of 13.55 m^2/g. Within this range, micropore specific surface area fluctuated between 6.84 and 13.42 m^2/g, averaging at 9.91 m^2/g, representing an average of 72.52%. Mesopore specific surface area ranged from 2.52 to 4.14 m^2/g, averaging at 3.19 m^2/g, averaging 24.11%. Macropore specific surface area ranged from 0.18 to 0.84 m^2/g, with an average specific surface area of 0.45 m^2/g, constituting an average of 3.35%.

4.3 Fractal dimension characteristics of pore structure

We determined the micropore fractal dimension, calculated using the V-S model, as D1; we denoted the mesopore fractal dimension, calculated using Eq. (1) the FHH model, as D2; and we assigned the macropore fractal dimension, calculated using Eq. (2) the MENGER sponge model, as D3 Eq. (3). According to the results obtained from these different models, there are significant variations in the micropore, mesopore, and macropore fractal dimensions. Specifically, D1 values for the samples range from 2.1138 to 2.3475, with an average of 2.2342. D2 values range from 2.5327 to 2.7162, with an average of 2.6171. D3 values range from 2.7361 to 2.9316, with an average of 2.82905 (Table 3).

The fractal dimension of pore structures in shale samples falls within the range of 2–3. A higher fractal value indicates a more complex pore system within the shale. The calculation results reveal a clear relationship of $D1 < D2 < D3$ (Figure 2). Notably, D1 is relatively close to the lower limit of the fractal theory, suggesting that micro-pores in the Shuijingtuo Formation shale have smoother surfaces and lower roughness, indicating a relatively simple pore structure. On the other hand, the maximum fractal dimension of macropores exceeds 2.9, approaching the theoretical upper limit, indicating that macropore structures in the Shuijingtuo samples are more complex with rougher pore surfaces.

5 Discussion

5.1 Shale pore heterogeneity influencing factors

The strong heterogeneity of pores in shale directly affects the gas occurrence state and flow mode. Pore heterogeneity is influenced by multiple factors, among which diagenetic minerals and organic matter are the two decisive factors affecting pore development (Li et al., 2019c; Fan et al., 2020b). Organic matter pyrolysis determines the morphology and development degree of organic pores (Borjigin et al., 2021), while diagenetic minerals affect the type and distribution of inorganic pores (Hao et al., 2022; Yin et al., 2022). Therefore, this study mainly explores

TABLE 1 Organic geochemistry and mineral composition characteristics of shale samples.

Sample number	TOC (%)	Ro (%)	Quartz (%)	Feldspar (%)	Calcite (%)	Dolomite (%)	Pyrite (%)	Sphalerite (%)	Clay minerals (%)
SJT-1	3.61	2.05	52	2	11	8	1	1	25
SJT-2	4.27	2.74	63	10	4	3	4	2	14
SJT-3	2.35	2.33	55	4	14	3	3	0	21
SJT-4	1.72	2.42	61	9	3	5	2	0	20
SJT-5	0.88	2.13	46	11	3	4	1	0	35
SJT-6	2.64	2.53	59	8	11	2	3	1	16
SJT-7	1.27	2.42	49	7	4	6	2	1	31
SJT-8	1.09	2.21	47	10	5	3	4	2	29
SJT-9	1.82	2.34	51	6	10	8	2	1	22
SJT-10	2.83	2.55	52	5	7	7	3	1	25
SJT-11	3.66	2.64	52	2	3	4	3	2	34
SJT-12	4.62	2.55	64	3	4	6	5	1	17

TABLE 2 Pore structure parameters of shale samples.

Sample number	Pore volume (×10^{-3} mL/g)				Specific surface area (m^2/g)			
	Total	Micropore	Mesopore	Macropore	Total	Micropore	Mesopore	Macropore
SJT-1	20.37	4.24	7.53	8.6	12.45	8.12	4.14	0.19
SJT-2	28.71	7.64	15.58	5.49	15.87	11.86	3.57	0.44
SJT-3	20.92	5.09	8.03	7.8	16.08	12.55	3.06	0.47
SJT-4	21.46	3.42	9.47	8.57	12.63	9.54	2.88	0.21
SJT-5	12.63	1.56	3.77	7.3	9.54	6.84	2.52	0.18
SJT-6	19.27	4.43	8.52	6.32	13.57	10.34	3.02	0.21
SJT-7	17.59	3.68	5.73	8.18	12.04	8.84	2.84	0.36
SJT-8	13.42	2.25	5.16	6.01	11.53	7.54	3.15	0.84
SJT-9	18.35	5.25	7.01	6.09	11.72	7.57	3.53	0.62
SJT-10	20.54	4.18	8.78	7.58	13.44	9.03	3.51	0.9
SJT-11	22.53	3.58	7.55	11.4	16.21	13.42	2.55	0.24
SJT-12	18.19	5.37	7.97	4.85	17.54	13.27	3.54	0.73

the controlling factors of shale pore heterogeneity from the relationship between organic matter content, maturity, inorganic mineral content, pore volume, specific surface area, and different fractal dimensions.

5.1.1 Influence of shale organic geochemical characteristics on heterogeneity

Organic pores are the most important pore type in mature organic-rich shale. The irregular and scattered distribution of

10.3389/feart.2024.1365516

TABLE 3 Distribution table of fractal dimension of shale samples.

Sample number	Micropore fractal dimension (D1)	Mesopore fractal dimension (D2)	Macropore fractal dimension (D3)
SJT-1	2.2328	2.6848	2.7984
SJT-2	2.3059	2.6837	2.8654
SJT-3	2.2108	2.5948	2.8316
SJT-4	2.1852	2.6126	2.9068
SJT-5	2.1138	2.5547	2.9316
SJT-6	2.2758	2.6038	2.7938
SJT-7	2.1347	2.6474	2.8453
SJT-8	2.1909	2.5327	2.9136
SJT-9	2.2743	2.5384	2.7754
SJT-10	2.2039	2.5779	2.8125
SJT-11	2.3343	2.6587	2.7361
SJT-12	2.3475	2.7162	2.7381

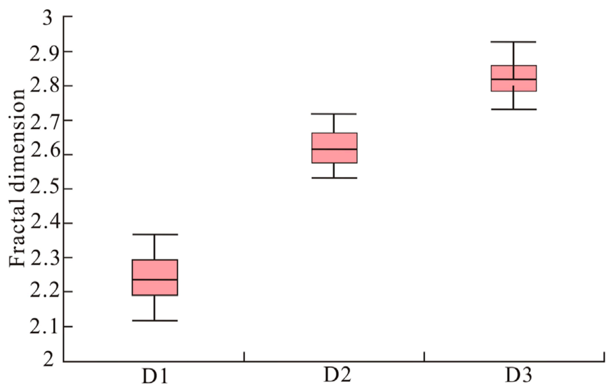

FIGURE 2
Box diagram of fractal dimension of different shale pores in the Shuijingtuo Formation.

organic matter in shale is one of the important reasons for the uneven distribution of organic pores. Organic matter is the basis for developing hydrocarbon-generating pores, and a certain degree of maturity is necessary for the thermal decomposition of organic matter to form pores. The two jointly control the development of organic matter (Cao et al., 2016; Li et al., 2022; Fan et al., 2024).

To further analyze the impact of organic matter content and maturity on pore heterogeneity, we conducted statistical and regression analyses to assess the relationships between organic matter content, maturity, and the fractal dimensions of micro, meso, and macro-pores. The results demonstrated a strong positive correlation between shale organic matter content and D1, with a correlation coefficient of 0.6797. Similarly, a significant positive correlation was observed between organic matter content and D2, with a coefficient of 0.5167. However, there was a moderate negative correlation between organic matter content and D3, with a correlation coefficient of 0.448 (Figure 3A).

The development of hydrocarbon-producing pores is directly linked to the thermal maturity of organic matter. Before reaching the late over-maturity stage, the number of hydrocarbon-producing pores increases with growing maturity, leading to irregular changes in pores of different sizes. According to the correlation analysis between shale sample fractal dimensions and maturity, during the early stages of high-over-maturity, there is a positive correlation between organic matter maturity and both D1 (correlation coefficient of 0.4344) and D2 (correlation coefficient of 0.4851). However, there is an overall decreasing trend in the relationship between maturity and D3, although the correlation coefficients are relatively low (Figure 3B).

Based on the correlation analysis between organic matter content and pore volume, as well as surface area, we found that the correlation coefficients between organic matter content and micro-pore surface area and pore volume were 0.5248 and 0.4939, respectively. For mesopores, the correlation coefficients were 0.2643 for surface area and 0.4113 for pore volume (Figures 3C, D). However, there was no significant correlation between organic matter content and macro-pore volume and surface area. This suggests that organic matter primarily contributes to micro and meso-pores.

During the early stages of over-maturity, organic matter undergoes thermal decomposition and gas generation phases The substantial loss of organic matter reduces its “supporting capacity,” leading to the collapse of organic matter (Li et al., 2020; Wu and

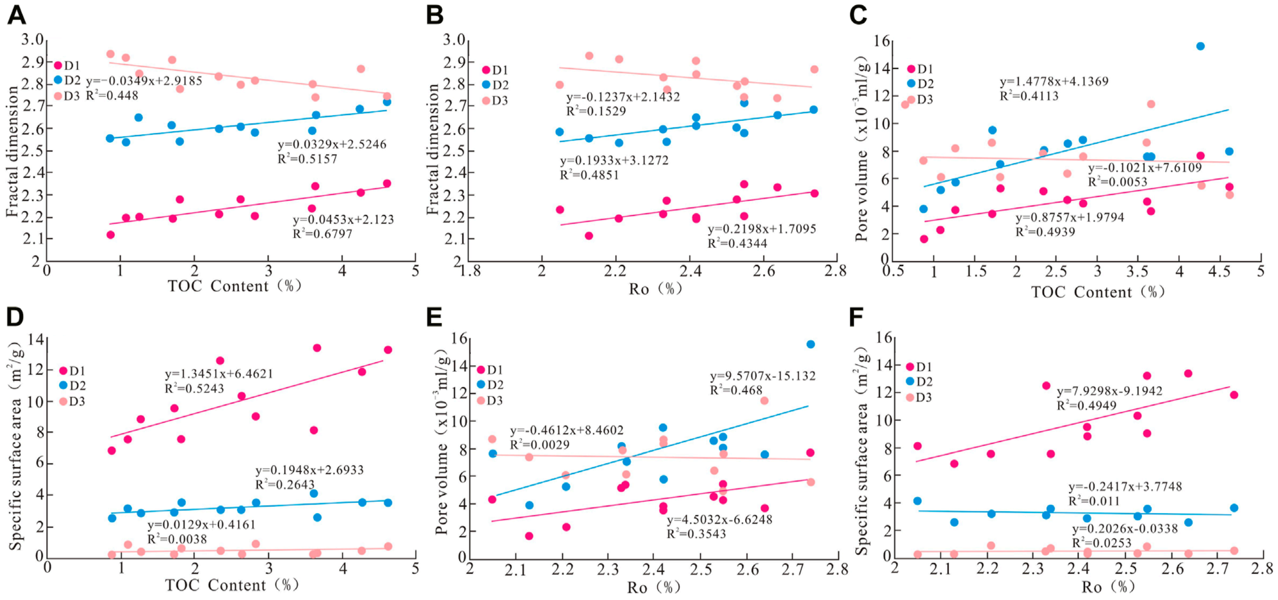

FIGURE 3
The relationship between the basal localization characteristics, the pore structure parameters, and the fractal dimension of shales in the Shuijingtuo Formation. **(A)** Fractal dimension and TOC; **(B)** Fractal dimension and Ro; **(C)** Pore volume and TOC; **(D)** Specific surface area and TOC; **(E)** Pore volume and Ro; **(F)** Specific surface area and Ro.

Lei, 2022). This phenomenon results in the extensive development of pores, and as hydrocarbon generation intensifies, the original pore sizes expand, increasing pore heterogeneity.

As organic matter content increases, various pore sizes receive some degree of stimulation, with the most substantial increase occurring in micro-pores, followed by meso-pores, while macro-pores show the least increase. Combining this with the earlier comparison of micro, meso, and macro-pore fractal dimensions, micro-pores exhibit the smallest fractal dimension, indicating simpler pore structures. With increasing organic matter content, both the quantity and heterogeneity of micro and mesopores increase, leading to higher values of D1 and D2.

As previously discussed, the organic matter in the study area is in a state of high-over maturity. The correlation coefficients between the thermal maturation level of shale samples and the fractal dimensions of micro and mesopores are moderate (Figures 3E, F).

On the one hand, as the thermal maturation level increases, organic matter undergoes more intense hydrocarbon generation, increasing the quantity of micro, meso, and macro-pores. During the over-maturity stage, as the thermal maturation level continues to rise, organic matter undergoes aromatization (Wu and Lei, 2022), which increases the roughness of pore walls and weakens the supporting capacity of pores for overlying strata. This results in irregular deformation of pores and an increase in the irregularity of pore shapes, leading to an increase in the fractal dimensions of micro and mesopores.

Regarding macropores, as the thermal maturation level increases, some mesopores continue to expand into macropores, increasing the total quantity of macro-pores. These macropores are often elliptical or circular, which, to some extent, reduces the fractal dimensions of macropores. This weakening effect on the complexity of macro-pores, along with the contribution of regularly shaped macropores by inorganic minerals, results in a lack of a strong correlation between the fractal dimensions of macropores and thermal maturity in the study area.

5.1.2 Relationship between shale pore structure parameters and fractal dimensions

Pore volume and specific surface area are characteristic parameters for evaluating shale gas storage capacity. The larger the pore volume, the larger the gas storage space; the larger the specific surface area, the stronger the gas adsorption capacity. The fractal dimension can quantify the complexity of pores and affect the ratio of adsorbed gas to free gas in shale. Therefore, a natural inherent relationship exists between pore volume, specific surface area, and fractal dimension.

According to the results of the correlation analysis between sample pore volume, specific surface area, and fractal dimensions, strong positive correlations were observed between micropore-specific surface area and D1, with correlation coefficients of 0.6202 (Figure 4A). In contrast, the correlation between micro-pore volume and D1 was weaker, with a coefficient of 0.3056 (Figure 4B). Mesopore specific surface area exhibited a significant positive correlation with D2, with a coefficient of 0.5946, while the correlation coefficient between mesopore volume and D2 was 0.31. In contrast, macro-pore volume and specific surface area showed an overall negative correlation with D3, but the correlation coefficients were smaller than D1 and D2.

Considering the contribution rates of micro, meso, and macro-pore specific surface areas and volumes, it can be observed that an increase in micro-pore fractal dimension is associated with an increase in pore volume and specific surface area. When pore

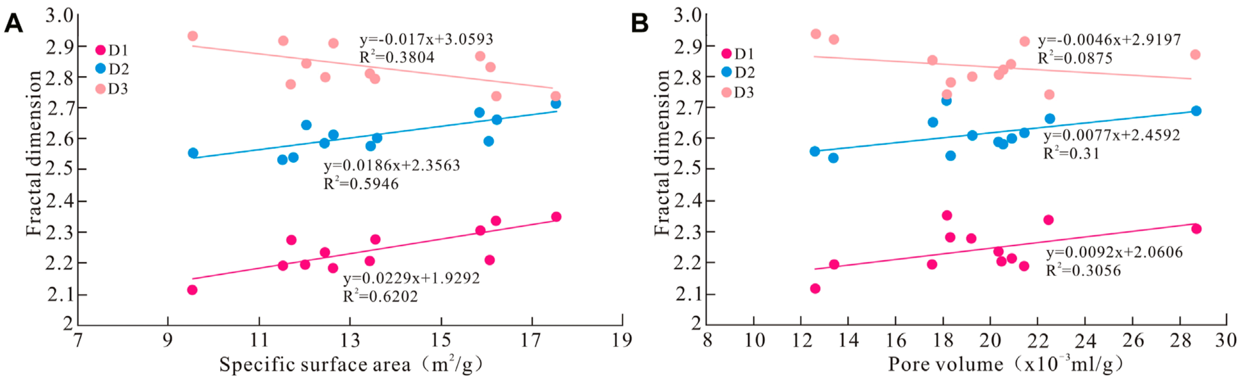

FIGURE 4
Correlation between specific surface area **(A)**, pore volume **(B)**, and fractal dimension of shales in the Shuijingtuo Formation.

volume and specific surface area increase, it indicates an increase in the number of micro-pores in shale, along with an increase in the uneven distribution of these micro-pores and their differences in pore size, leading to an increase in the fractal dimension. As mesopore sizes increase, the specific surface area provided by mesopores gradually decreases while pore volume increases. According to pore fractal theory, larger mesopore sizes correspond to larger fractal dimensions. The substantial difference in mesopore sizes results in a relatively weak overall correlation with D2. For macro-pores, an increase in specific surface area implies a decrease in the proportion of macro-pores in shale, leading to a certain degree of reduction in fractal dimension.

5.1.3 Impact of mineral composition on pore structure heterogeneity

Shale inorganic minerals can be divided into three categories: siliceous, clay, and carbonate. Different diagenetic minerals have significant differences in their resistance to compaction and dissolution (Huang et al., 2020), resulting in differences in pore types, contents, and pore sizes provided by different minerals during long-term burial diagenesis. The differences in mineral content and uneven distribution among different types of minerals in shale are important factors that increase the complexity of shale pores. In this study, we established correlations between the content of these three mineral categories and structural parameters, including pore volume, specific surface area, and fractal dimensions. The results indicate that the content of siliceous minerals exhibits a positive correlation with the micro- and mesopore volumes in shale, with correlation coefficients of 0.4941 and 0.5796, respectively (Figure 5A). However, it shows a negative correlation with the macropore volume, with a lower correlation coefficient. It exhibits a clear positive correlation with the specific surface area of micro-pores but does not show significant correlations with mesopores or macropores (Figure 5B). Considering the sedimentary environment and the source of siliceous minerals, the Wellsboro Formation was formed in an anoxic deep-water continental shelf (Zhang LL. et al., 2023). The warm water conditions were conducive to the proliferation of siliceous microorganisms, and the siliceous shells were preserved in anoxic water after their death. At the same time, biological soft tissue increased the organic matter content. A substantial portion is derived from organic matter and the correlation between siliceous minerals and organic matter content. Biological skeletons and the accumulation of organic matter typically exhibit significant zonation. According to the correlation curves between siliceous mineral content and the three types of pore fractal dimensions, siliceous minerals show a moderate positive correlation with D1 and D2, with correlation coefficients of 0.3258 and 0.3933, respectively, while exhibiting a weaker negative correlation with D3, with a correlation coefficient of 0.1191 (Figure 5C).

As one of the major diagenetic minerals, clay minerals play a crucial role as carriers for pore development in shale. The types and characteristics of pore development are influenced by the way minerals accumulate and their structure. The “layered stacking” of clay minerals and the “contact-embedded” distribution with other brittle minerals easily lead to numerous intergranular pores. Typically, such pores have irregular shapes and relatively large diameters.

In the case of the Shuijingtuo Formation, which formed early, montmorillonite undergoes dehydration and transformation due to compaction and temperature effects during the sediment compaction process. This increases the pore size within clay minerals as illite and illite-smectite interlayers become more abundant. Analyzing the correlation between clay mineral content and shale pore volume and specific surface area, it is observed that the volumes of micro and macropores and specific surface area in shale decrease as the content of clay minerals increases (Figures 5D, E). This phenomenon is primarily associated with clay minerals’ compaction and diagenetic transformation. There is, however, a certain positive correlation with macropore volume, mainly because clay minerals have larger pore diameters. An increase in clay mineral content significantly increases the number of these macropores, increasing macropore volume.

When comparing clay mineral content with different pore size fractal dimensions, a weak negative correlation is found between clay mineral content and D1 and D2, while a weak positive correlation is observed with D3 (Figure 5F). Although the correlation coefficients are relatively small, in conjunction with the source of macropores, it becomes evident that organic matter, siliceous minerals, and carbonate minerals in shale all contribute to

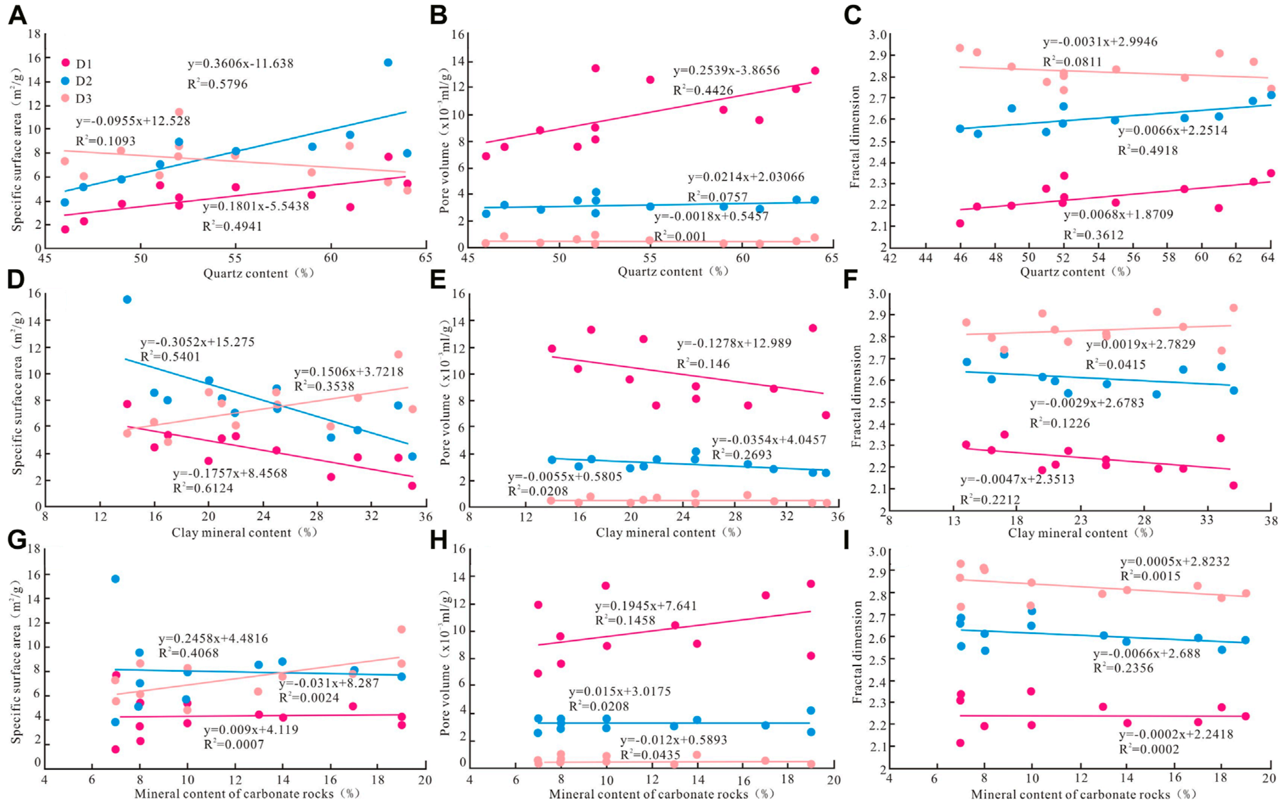

FIGURE 5
Correlation between inorganic minerals and pore structure parameters and fractal dimension. **(A–C)** Quartz content; **(D–F)** Clay mineral content; **(G–I)** Mineral content of carbonate rocks.

a certain amount of macropores. This leads to a less pronounced correlation between clay mineral content and D3. Clay minerals provide a variety of pore types with significant differences in pore size, primarily developing macropores. The varying contributions of clay minerals to the three categories of pore sizes interact with the contributions of other minerals, resulting in the complexity of fractal dimensions in pores of different sizes.

As one of the major diagenetic minerals, the shale in the Shuijingtuo Formation contains two carbonate minerals, calcite, and dolomite, with their content not exceeding 20%. Their distribution in the shale is highly heterogeneous. Being easily soluble minerals, they are prone to dissolution by groundwater under burial conditions, forming dissolution pores. Meanwhile, carbonate minerals located near organic-rich zones are susceptible to dissolution by organic acids produced during the thermal maturation of organic matter, resulting in a limited number of dissolution pores.

Through the analysis of the correlation between the content of carbonate minerals and structural parameters such as micropore, mesopore, and specific surface area in shale, it was found that there was no significant correlation between the content of carbonate minerals and micro-pore or mesopore pore volume or specific surface area. However, a certain positive correlation was observed between the content of carbonate minerals and macro-pore pore volume, with a correlation coefficient of 0.4068 (Figures 5G, H).

Taking into account the correlation between the content of carbonate minerals and the fractal dimensions of pores of different sizes, it was found that there was a weak negative correlation between the content of carbonate minerals and both D1 and D2, while a promoting effect was observed with D3 (Figure 5I). This suggests that carbonate minerals in the shale primarily contribute to macropores' development. The increase in the content of carbonate minerals, combined with their uneven distribution, effectively enhances the complexity and heterogeneity of macropore development.

Combined with the correlation between inorganic minerals, TOC, and different pore fractal dimensions, inorganic minerals and TOC content have different control effects on the pore fractal dimension (Figure 6). Siliceous minerals and organic matter promote the complexity of pores, while clay minerals and carbonate minerals have a weak negative correlation or no obvious correlation with the complexity of pores. This phenomenon is related to the pore types and existing forms provided by different minerals. Organic matter in shale shows a diffuse distribution and many irregular pores are formed by stacking organic matter and hydrocarbon pyrolysis. There are obvious differences in pore size, which greatly increases the complexity of pores. While a large amount of organic matter comes from the burial and accumulation of microorganisms, whose siliceous shells and skeletons form biosilicon, and siliceous minerals increase the supporting capacity between minerals. In compaction, the pores can maintain their original state and weaken the "uniformity" of pore morphology caused by compaction. Therefore, organic matter and siliceous minerals contribute the

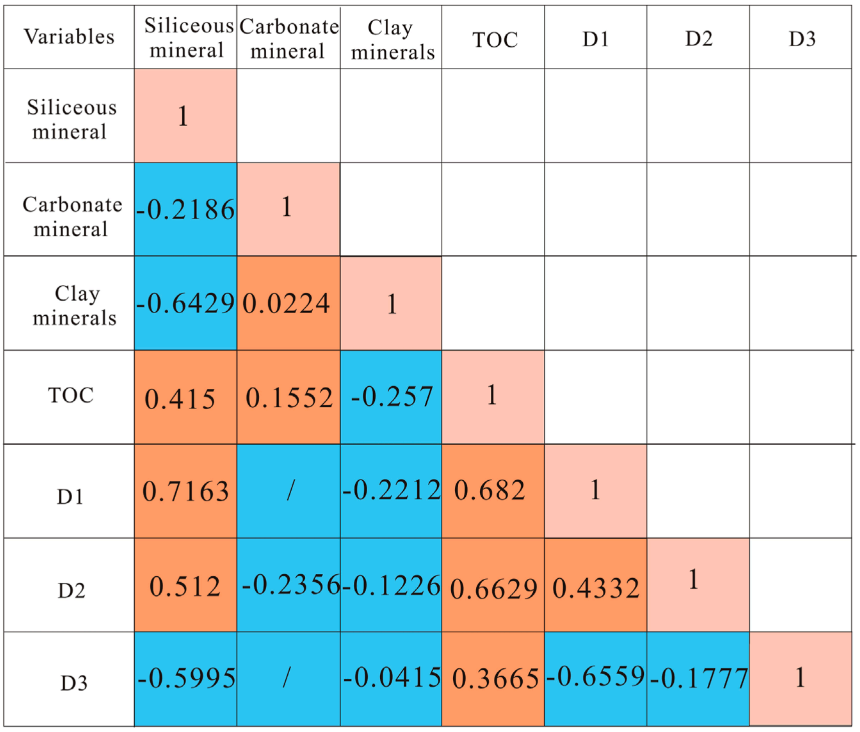

Variables	Siliceous mineral	Carbonate mineral	Clay minerals	TOC	D1	D2	D3
Siliceous mineral	1						
Carbonate mineral	-0.2186	1					
Clay minerals	-0.6429	0.0224	1				
TOC	0.415	0.1552	-0.257	1			
D1	0.7163	/	-0.2212	0.682	1		
D2	0.512	-0.2356	-0.1226	0.6629	0.4332	1	
D3	-0.5995	/	-0.0415	0.3665	-0.6559	-0.1777	1

FIGURE 6
Influencing factors of shale pore complexity.

most to pore complexity. However, carbonate minerals and clay minerals mainly provide large pore mesoporous and macro pores. According to fractal theory, increasing macro pore will reduce pore complexity.

5.2 Geological significance of fractal dimensions of shale pores

The pore structure of shale determines the occurrence state and flow mode of hydrocarbon molecules within the layer (Tian et al., 2016). The heterogeneity of pores also controls the storage performance of shale and the micro permeability of shale gas. Generally speaking, the more complex the pore structure, the more difficult the gas migration within the layer (Xiong et al., 2017), and the macroscopic manifestation is the decrease in the permeability of the storage mechanism. For different gas contents in different states, the stronger the heterogeneity of pores, the higher the proportion of adsorbed gas content. Therefore, the larger the fractal dimension, the more complex the shale pore structure, the stronger the heterogeneity, and the more unfavorable it is for shale gas development.

Combining the statistical analysis of fractal dimensions for different pore sizes in the Shuijingtuo Formation, it is evident that the fractal dimension for macro-pores is larger, while those for meso and micro-pores are smaller. This suggests that macro-pores exhibit stronger adsorption capabilities. When comparing the contribution rates of pore volume and specific surface area for the three pore categories, micro-meso pores, with smaller diameters, have a higher proportion than macro-pores. Specifically, micro-meso pores account for over 60% on average, with micropores specific surface area making up over 70%. These micro-pores offer more surface adsorption sites, resulting in a greater "adsorption potential" on the pore walls and weaker gas molecule "flowability."

In contrast, macro-pores have larger diameters. Although their rough and complex pore walls enhance gas molecule adsorption, numerous hydrocarbon molecules diffuse freely within these pores. The presence of these hydrocarbon molecules increases the shale's permeability. Consequently, a higher macropore content for shale reservoirs leads to greater matrix permeability.

Regarding gas occurrence within the strata, In terms of the gas occurrence state in the shale, the adsorption gas occupies a large space in the shale micropores (Figure 7A). The gas is mostly in the form of adsorbed gas; the content of adsorbed gas is small, and the gas fluidity is weak. The area occupied by adsorbed gas in the mesoporous pores increases (Figure 7B), and the proportion of adsorbed gas content decreases. With the further increase of the pore size, the proportion of adsorbed gas content in the macropores decreases (Figure 7C), the free gas content increases in the middle of the pores, and the gas fluidity increases.

Larger fractal dimensions for micro and mesopores indicate stronger pore structure and heterogeneity. This results in weaker gas adsorption capabilities, leading to a higher proportion of adsorbed gas content in shale, with over 57% being the maximum observed in the Shuijingtuo Formation. On the other hand, macro-pores,

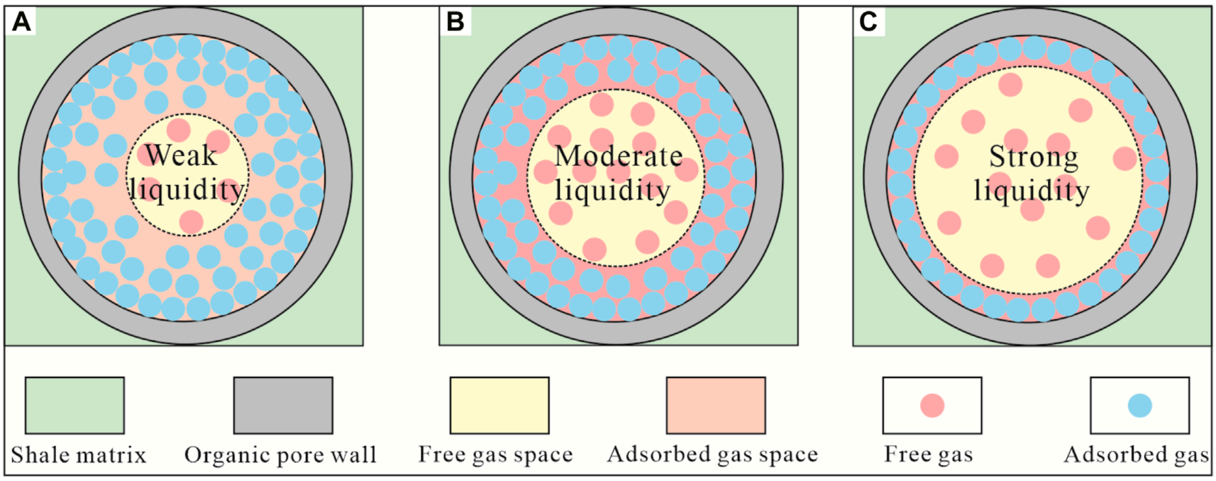

FIGURE 7
Differences in shale gas occurrence with different shale pore sizes. **(A)** Shale micropores; **(B)** Shale mesopores; **(C)** Shale macropores.

with their larger diameters, predominantly host gas molecules in a free state.

6 Conclusion

1. In the Huangling area, the Shuijingtuo Formation exhibits an organic matter content ranging from 0.88% to 4.26%, with Ro values falling between 2.05% and 2.74%, averaging at 2.409%. This indicates a state of high to over-maturity. The shale comprises approximately 54%–73% silica minerals, averaging 60.67%. Calcium minerals account for 7%–19%, averaging 11.17%, while clay minerals have an average content of 24%. These characteristics point to the formation of calcareous shale in an alkaline aquatic environment.
2. Utilizing low-temperature nitrogen and carbon dioxide adsorption and high-pressure mercury intrusion experiments, micropore, mesopore, and macropore fractal dimensions were computed using the V-S, FHH, and MENGER Sponge models. The micropore (D1) ranged from 2.1138 to 2.3475, averaging 2.2342. The mesopore (D2) ranged from 2.5327 to 2.7162, averaging 2.6171. The macropore (D3) ranged from 2.7361 to 2.9316, averaging 2.82905.
3. Organic matter is the foundation for shale micromeso pores, while maturity promotes hydrocarbon generation through organic matter pyrolysis. The combined effect of these factors contributes to the development of the shale's primary micromeso pores, promoting the shale's specific surface area. This relationship is positively correlated with D1 and D2 but negatively correlated with D3. Silica minerals and organic matter development exhibit a synergistic relationship, positively correlating with D1 and D2. Clay minerals primarily contribute to macro-pores in the shale, showing a positive correlation with shale macro-pore volume and a weak positive correlation with D3. In contrast, carbonate rocks mainly contribute to dissolved macropores, displaying a positive correlation with macropore volume but no significant correlation with pore fractal dimensions.

Data availability statement

The original contributions presented in the study are included in the article/Supplementary material, further inquiries can be directed to the corresponding author.

Author contributions

ZA: Conceptualization, Data curation, Formal Analysis, Investigation, Methodology, Software, Writing–original draft, Writing–review and editing. YuZ: Conceptualization, Formal Analysis, Funding acquisition, Project administration, Supervision, Validation, Writing–original draft, Writing–review and editing. YaZ: Formal Analysis, Investigation, Resources, Validation, Writing–original draft.

Funding

The author(s) declare that no financial support was received for the research, authorship, and/or publication of this article.

Conflict of interest

The authors declare that the research was conducted in the absence of any commercial or financial relationships that could be construed as a potential conflict of interest.

Publisher's note

References

Abraham, R. M., Taioli, F., and Nzekwu, A. I. (2022). Physical properties of sandstone reservoirs: implication for fluid mobility. *Energy Geosci.* 3 (4), 349–359. doi:10.1016/j.engeos.2022.06.001

An, C., Liu, G. D., Sun, M. L., You, F. L., Wang, Z. X., and Cao, S. Y. (2023). Analysis of shale pore structure characteristics based on nitrogen adsorption experiment and fractal FHH model: a case study of 7th member of Triassic Yanchang Formation in Huachi area, Ordos Basin. *Petrol. Geol. Exp.* 45 (3), 576–586. doi:10.11781/sysydz202303576

Borjigin, T., Lu, L. F., Yu, L. J., Zhang, W. T., Pan, A. Y., Shen, B. J., et al. (2021). Formation, preservation and connectivity control of organic pores in shale. *Petrol. explor. Dev.* 48 (4), 798–812. doi:10.1016/S1876-3804(21)60067-8

Cao, T. T., Song, Z. G., Liu, G. X., Yin, Q., and Luo, H. Y. (2016). Characteristics of shale pores, fractal dimension and their controlling factors determined by nitrogen adsorption and mercury injection methods. *Petrol. Geol. Rec. Eff.* 23 (2), 1–8. doi:10.13673/j.cnki.cn37-1359/te.20151215.002

Cheng, Y., Liu, C., Wu, W., Wen, M. Y., Nie, Q., and Lu, P. (2018). The application of argon ion polishing-environmental scanning electron microscopy to the research on shale nanometer-sized pores-Taking Sha-1 member in JX area as an example. *J. Chin. Electron Microsc. Soc.* 37 (1), 52–58. doi:10.3969/j.issn.1000-6281.2018.01.008

Dou, J. N., Lin, Y. Q., Shao, F., and Dong, H. M. (2020). Advances in characterization techniques and experimental methods of shale gas reservoir pore structure. *J. Xi'an Univ. Sci. Tech.* 40 (6), 1019–1030. doi:10.13800/j.cnki.xakjdxxb.2020.0612

Fan, C. H., Li, H., Qin, Q. R., He, S., and Zhong, C. (2020a). Geological conditions and exploration potential of shale gas reservoir in Wufeng and Longmaxi Formation of southeastern Sichuan Basin, China. *J. Petrol. Sci. Eng.* 191, 107138. doi:10.1016/j.petrol.2020.107138

Fan, C. H., Li, H., Zhao, S. X., Qin, Q. R., Fan, Y., Wu, J. F., et al. (2020b). Formation stages and evolution patterns of structural fractures in marine shale: case study of the Lower Silurian Longmaxi Formation in the Changning area of the southern Sichuan Basin, China. *Energy Fuel* 34 (8), 9524–9539. doi:10.1021/acs.energyfuels.0c01748

Fan, C. H., Nie, S., Li, H., Radwan, A. E., Pan, Q. C., Shi, X. C., et al. (2024). Quantitative prediction and spatial analysis of structural fractures in deep shale gas reservoirs within complex structural zones: a case study of the Longmaxi Formation in the Luzhou area, southern Sichuan Basin, China. *J. Asian Earth Sci.* 263, 106025. doi:10.1016/j.jseaes.2024.106025

Gao, Z., Fan, Y., Xuan, Q., and Zheng, G. (2020). A review of shale pore structure evolution characteristics with increasing thermal maturities. *Adv. Geo-Energy Res.* 4 (3), 247–259. doi:10.46690/ager.2020.03.03

Hao, M. Z., Jiang, Z. X., Nie, Z., Xue, Z. X., Zhong, G. H., He, S. J., et al. (2022). Development characteristics of pore connectivity in deep shale reservoirs and its controlling factors:a case study of Longmaxi Formation in southern Sichuan Basin. *Fault-Block Oil Gas. Field* 29 (6), 761–768. doi:10.6056/dkyqt202206007

He, S., Qin, Q. R., Li, H., and Wang, S. L. (2022b). Deformation differences in complex structural areas in the southern sichuan basin and its influence on shale gas preservation: a case study of changning and luzhou areas. *Front. Earth Sci.* 9, 818534. doi:10.3389/feart.2021.818534

He, S., Qin, Q. R., Li, H., and Zhao, S. X. (2022a). Geological characteristics of deep shale gas in the silurian Longmaxi Formation in the southern sichuan basin, China. *Front. Earth Sci.* 9, 818543. doi:10.3389/feart.2021.818155

Huang, Y. Q., Zhang, P., Zhang, J. C., and Yang, J. W. (2020). The Effect on the fractal characteristics of shale pores by mineral compositions of marine and marine-continental transitional shales. *Bull. Mineral. Petrol. Geoch.* 39 (3), 548–557. doi:10.19658/j.issn.1007-2802.2020.39.026

Jiang, Z. X., Tang, X. L., Li, Z., Huang, H. X., Yang, P. P., Yang, X., et al. (2016). The whole-aperture pore structure characteristics and its effect on gas content of the Longmaxi Formation shale in the southeastern Sichuan basin. *Earth Sci. Front.* 23 (2), 126–134. doi:10.13745/j.esf.2016.02.013

Kong, X. X., Xiao, D. S., Jiang, S., Lu, S. F., Sun, B., and Wang, J. M. (2020). Application of the combination of high-pressure mercury injection and nuclear magnetic resonance to the classification and evaluation of tight sandstone reservoirs: a case study of the Linxing Block in the Ordos Basin. *Nat. Gas. Ind.* 40 (3), 38–47. doi:10.3787/j.issn.1000-0976.2020.03.005

Li, B., Chen, F. W., Xiao, D. S., Lu, S. F., Zhang, L. C., Zhang, Y. Y., et al. (2019b). Effect of particle size on the experiment of low temperature nitrogen adsorption: a case study of marine gas shale in Wufeng-Longmaxi formation. *J. China Univ. Min. Tech.* 48 (2), 395–404. doi:10.13247/j.cnki.jcumt.000931

Li, H. (2023). Coordinated development of shale gas benefit exploitation and ecological environmental conservation in China: a mini review. *Front. Ecol. Evol.* 11, 1232395. doi:10.3389/fevo.2023.1232395

Li, H., Tang, H. M., Qin, Q. R., Wang, Q., and Zhong, C. (2019c). Effectiveness evaluation of natural fractures in Xujiahe Formation of Yuanba area, Sichuan basin, China. *Arab. J. Geosci.* 12 (6), 194. doi:10.1007/s12517-019-4292-5

Li, H., Tang, H. M., and Zheng, M. J. (2019a). Micropore structural heterogeneity of siliceous shale reservoir of the Longmaxi Formation in the southern Sichuan Basin, China. *Minerals* 9, 548. doi:10.3390/min9090548

Li, J. J., Qin, Q. R., Li, H., and Wan, Y. F. (2022). Numerical simulation of the stress field and fault sealing of complex fault combinations in Changning area, Southern Sichuan Basin, China. *Energy Sci. Eng.* 10 (2), 278–291. doi:10.1002/ese3.1044

Li, K., Kong, S., Xia, P., and Wang, X. (2020). Microstructural characterisation of organic matter pores in coal-measure shale. *Adv. Geo-Energy Res.* 4 (4), 372–391. doi:10.46690/ager.2020.04.04

Li, Y. Z. (2021). Mechanics and fracturing techniques of deep shale from the Sichuan Basin, SW China. *Energy Geosci.* 2 (1), 1–9. doi:10.1016/j.engeos.2020.06.002

Liu, K., and Ostadhassan, M. (2019). The impact of pore size distribution data presentation format on pore structure interpretation of shales. *Adv. Geo-Energy Res.* 3 (2), 187–197. doi:10.26804/ager.2019.02.08

Liu, R. B., Wei, Z. H., Jia, A. Q., He, S., Hou, Y. G., He, Q., et al. (2023). Fractal Characteristics of pore structure in deep overpressured organic-rich shale in Wufeng-Longmaxi Formation in Southeast Sichuan and its geological significance. *Earth Sci.* 48 (4), 1496–1516. doi:10.3799/dqkx.2022.177

Luo, S. Y., Chen, X. H., Liu, A., Li, H., and Sun, C. (2019a). Characteristics and geological significance of canister desorption gas from the Lower Cambrian Shuijingtuo Formation shale in Yichang area, Middle Yangtze region. *Acta Pet. Sin.* 40 (8), 941–955. doi:10.7623/syxb201908005

Luo, S. Y., Chen, X. H., Liu, H., Liu, A., and Wang, S. C. (2019b). Shale gas accumulation conditions and target optimization of lower cambrian Shuijingtuo Formation in Yichang area, west Hubei. *Earth Sci.* 44 (11), 3598–3615. doi:10.3799/dqkx.2019.179

Ma, R. Y., Zhang, J., Wang, M., Ma, W. P., and Zhao, J. G. (2021). Micro-pore characteristics and gas-bearing properties of marine continental transitional shale reservoirs in the Qinshui basin. *J. Henan Polytech. Univ.* 40 (4), 66–77. doi:10.16186/j.cnki.1673-9787.2019120015

Shi, D. S., Xu, Q. C., Guo, R. L., Liu, E. R., Zhu, D. S., Wang, H., et al. (2023). Pore structure characteristics and main controlling factors of Permian organic-rich shale in Lower Yangtze Region. *Nat. Gas. Geosci.* 33 (12), 1911–1925. doi:10.11764/j.issn.1672-1926.2022.09.005

Sun, Z. L., Wang, F. R., Han, Y. J., Hou, Y. G., He, S., Zheng, Y. H., et al. (2021). Characterization and evaluation of fractal dimension of intersalt shale oil reservoirs in Qianjiang Depression. *Bull Geol. Sci. Tech.* 41 (4), 125–137. doi:10.19509/j.cnki.dzkq.2021.0063

Tian, H., Zhang, S. C., Liu, S. B., Wang, M. Z., Zhang, H., Hao, J. Q., et al. (2016). The dual influence of shale composition and pore size on adsorption gas storage mechanism of organic-rich shale. *Nat. Gas. Geosci.* 27 (3), 494–502. doi:10.11764/j.issn.1672-1926.2016.03.0494

Wang, K. L., Li, K. Q., Wang, L. K., Gao, H. L., Wang, K. W., and Hu, P. Q. (2018). Mineral composition and gas-bearing characteristics of Wufeng-Longmaxi shale in Shizhu area, eastern Sichuan Basin. *J. Lanzhou Univ.* 54 (3), 285–291. doi:10.13885/j.issn.0455-2059.2018.03.001

Wang, X., Qi, M., Hu, Y. L., and Qiu, Y. S. (2015). Analysis of the shale pore structures by the combination of high-pressure mercury injection and fractal theory. *Petrol. Geol. Oilfield Dev. Daqing* 34 (2), 165–169. doi:10.3969./J.ISSN.1000-3754.2015.02.033

Wu, Y. H., and Lei, T. Z. (2022). Influence of hydrogenation at different temperatures on hydrocarbongeneration of source rocks. *J. Chongqing Univ.* 45 (5), 43–51. doi:10.11835/j.issn.1000-582x.2022.05.005

Xia, D. L., Wu, Y., Zou, M., Xia, D. D., and Pang, W. (2022). Quality characterization of tight sandstone reservoirs in the yanchang formation of the honghe oilfield, ordos basin, central China. *Energy Geosci.* 3 (4), 444–452. doi:10.1016/j.engeos.2021.07.001

Xie, W. D., Wang, M., Wang, H., and Duan, Q. Y. (2022). Multi-scale fractal characteristics of pores in transitional shale gas reservoir. *Nat. Gas. Geosci.* 33 (3), 451–460. doi:10.11764/j.issn.1672-1926.2021.06.006

Xiong, J., Liu, X. J., Liang, L. X., and Zeng, Q. (2017). Adsorption of methane in organic-rich shale nanopores: an experimental and molecular simulation study. *Fuel* 200, 299–315. doi:10.1016/j.fuel.2017.03.083

Xu, L. L., Wen, Y. R., Zhou, X. H., Ju, Z. L., Chen, H., Yang, J., et al. (2022). Paleoenvironment of the first member of Niutitang Formation on the southern margin of Huangling anticline, western Hubei province:a case study of well ZD-1. *Petroleum Geol. Exp.* 44 (3), 456–465. doi:10.11781/sysydz202203456

Yin, S. L., Xie, J. Y., Cheng, L. L., Wu, Y. X., Zhu, B. Y., Chen, G. Y., et al. (2022). Advances in continental shale oil research and problems of reservoir geology. *Acta Sedimentol. Sin.* 40 (4), 979–995. doi:10.14027/j.issn.1000-0550.2021.109

Zeng, H. B., Wang, F. R., Luo, J., Tao, T., and Wu, S. Q. (2021). Characteristics of pore structure of intersalt shale oil reservoir by low temperature nitrogen adsorption and high pressure mercury pressure methods in Qianjiang Sag. *Bull. Geol. Sci. Tech.* 40 (5), 242–252. doi:10.19509/j.cnki.dzkq.2021.0022

Zhang, J. Z., Zhu, D., Ci, X. H., Niu, Q., Zhang, H. X., Tang, Y. C., et al. (2019). Characteristics of carbon isotope while drilling and exploration significance of shale gas in Niutitang and Doushantuo formations in Well Eyangye-2,Yichang, Hubei, China. Acta Petrol. *Sin.* 40 (11), 1346–1357. doi:10.7623/syxb201911005

Zhang, L. L., Chen, G. X., Le, X. F., Zhang, Y., Shao, D. Y., Yan, J. P., et al. (2023a). Significance of water absorption characteristics and difference of pore structures in the Cambrian shale intervals, Yichang area for shale reservoir evaluation. *Earth Sci. Front.* 30 (3), 138–150. doi:10.13745/j.esf.sf.2022.5.38

Zhang, Q., Liang, F., Liang, P. P., Zhou, S. W., Guo, W., Guo, W., et al. (2020). Investigation of fractal charactrtistics and its main controlling factors of shale reservoir: a case study of the Longmaxi shale in Weiyuan shale gas field. *J. China Univ. Min. Techn.* 49 (1), 110–122. doi:10.13247/j.cnki.jcumt.001068

Zhang, Y., Huang, D., Zhang, L. L., Wan, C. H., Luo, H., Shao, D. Y., et al. (2023b). Biogenic silica of the lower cambrian Shuijingtuo Formation in Yichang,western Hubei province-features and influence on shale gas accumulation. *Earth Sci. Front.* 30 (3), 83–100. doi:10.13745/j.esf.sf.2022.5.40

Zhao, J. L., Tang, D. Z., Xu, H., and Xu, H. (2015). Fine characterization of the shale micropore structures based on the carbon dinxide adsorption experiment. Petrol. *Geol. Oilfield Dev. Daqing.* 34 (5), 156–161. doi:10.3969/J.ISSN.1000-3754.2015.05.030

Zhao, Y., Li, L., Si, Y. H., and Wang, H. M. (2022). Fractal characteristics and controlling factors of pores in shallow shale gas reservoirs: a case study of Longmaxi Formation in Zhaotong area, Yunnan Province. *J. Jilin Univ.* 52 (6), 1813–1829. doi:10.13278/j.cnki.jjuese.20220148

Zhu, W. C., Niu, L. L., and Li, S. H. (2019). Creep-impact test of rock: Status-of-the-art and prospect. *J. Min Strata Control Eng.* 1 (1), 013003. doi:10.13532/j.jmsce.cn10-1638/td.2019.02.007

Zuo, J. P., Yu, M. L., and Hu, S. Y. (2019). Experimental investigation on fracture mode of different thick rock strata. *J. Min Strata Control Eng.* 1 (1), 013007. doi:10.13532/j.jmsce.cn10-1638/td.2019.02.008

frontiers | Frontiers in Earth Science

TYPE Original Research
PUBLISHED 25 April 2024
DOI 10.3389/feart.2024.1375241

OPEN ACCESS

EDITED BY
Hu Li,
Southwest Petroleum University, China

REVIEWED BY
Hui Han,
Southwest Petroleum University, China
Shuangbiao Han,
China University of Mining and Technology, Beijing, China
Agnieszka Furmann,
Indiana University, United States

*CORRESPONDENCE
Shasha Sun,
✉ sunss69@petrochina.com.cn
Zhensheng Shi,
✉ shizs69@petrochina.com.cn

RECEIVED 23 January 2024
ACCEPTED 02 April 2024
PUBLISHED 25 April 2024

CITATION
Sun S, Shi Z, Dong D, Bai W, Wei L, Yin J and Qu J (2024), Formation and evolution of shale overpressure in deep Wufeng-Longmaxi Formation in southern Sichuan basin and its influence on reservoir pore characteristics.
Front. Earth Sci. 12:1375241.
doi: 10.3389/feart.2024.1375241

Formation and evolution of shale overpressure in deep Wufeng-Longmaxi Formation in southern Sichuan basin and its influence on reservoir pore characteristics

Shasha Sun[1]*, Zhensheng Shi[1]*, Dazhong Dong[1], Wenhua Bai[1], Lin Wei[2,3], Jia Yin[2,3] and Jiajun Qu[2,3]

[1]Research Institute of Petroleum Exploration and Development, PetroChina, Beijing, China, [2]School of Energy Resources, China University of Geosciences, Beijing, China, [3]Key Laboratory of Marine Reservoir Evolution and Hydrocarbon Enrichment Mechanism, Ministry of Education, Beijing, China

In the deep Longmaxi Formation shale gas reservoirs of the southern Sichuan Basin, strong overpressure is universally developed to varying degrees. However, there is currently a lack of in-depth research on the formation mechanisms, evolutionary patterns, and the controlling effects on reservoir pore characteristics of strong overpressure. This limitation significantly restricts the evaluation of deep shale gas reservoirs. This study selected typical overpressured shale gas wells in Yongchuan, Luzhou, and Dazu areas as research subjects. Through comprehensive methods such as log analysis, fluid inclusion analysis, and numerical simulation, the dominant mechanisms of strong overpressure formation were determined, and the pressure evolution from early burial to late strong uplift was characterized. Additionally, the impact of varying degrees of overpressure on reservoir pore characteristics was studied using techniques such as scanning electron microscopy, gas adsorption-mercury intrusion, and helium porosity testing. The research findings indicate that hydrocarbon generation expansion is the primary mechanism for strong overpressure formation. The pressure evolution in the early burial phase is controlled by the processes of kerogen oil generation and residual oil cracking into gas. The reservoir experienced three stages: normal pressure (Ordovician to Early Triassic), overpressure (Early Triassic to Early Jurassic), and strong overpressure (Early Jurassic to Late Cretaceous), with pressure coefficients of approximately 1.08, 1.56, and 2.09, respectively. During the late strong uplift phase, the adjustment of early overpressure occurred due to temperature decrease and gas escape, leading to a decrease in formation pressure from 140.55 MPa to 81.63 MPa, while still maintaining a state of strong overpressure. Different degrees of strong overpressure exert a significant control on the physical properties of shale reservoirs and the composition of organic matter pores. Variations exist in the organic matter pore morphology, structure, and connectivity within the deep Wufeng-Longmaxi shale. Higher overpressure favors the preservation of organic large pores and reservoir porosity. Under conditions of strong overpressure development, deep siliceous shales and organically rich clay shales exhibit favorable reservoir properties. By determining the dominant mechanisms of strong overpressure in the Wufeng-Longmaxi Formation and studying pore characteristics, this research not only deepens the understanding of the geological features of deep shale gas reservoirs but also provides a new perspective for understanding the overpressure mechanisms and reservoir properties of deep shale gas reservoirs. Moreover, it is of significant importance for guiding the exploration and development of deep Longmaxi shale and provides valuable references for further research in related fields.

KEYWORDS

strong overpressure, formation mechanism, pressure evolution, reservoir property, pore structure

1 Introduction

The formation and evolution of overpressure are crucial indicators for the accumulation and dissipation of shale gas. The pressure coefficient is generally positively correlated with gas content and production rate, making it a key reference indicator for assessing shale gas preservation conditions and evaluating sweet spots. Researchers have widely recognized that the formation and evolution of overpressure are critical controlling factors for the pore development and preservation as well as the enrichment and productivity of gas reservoirs (Guo et al., 2017; Yi et al., 2019; Shan et al., 2021; Wang and Wang, 2021; Jin and Nie, 2022). In the deep (burial depth of 3,500–4,500 m) Wufeng Formation-Longmaxi Formation shale gas reservoirs in southern Sichuan Basin, overpressure (pressure coefficient: 1.3–1.8) or strong overpressure (pressure coefficient: >1.8) is commonly developed (Li, 2023b). However, significant variations exist in shale porosity, gas content, and gas production among different deep areas.

The identification of overpressure causes and their relationships with hydrocarbon accumulation have been a focal point in both conventional and unconventional oil and gas exploration. In recent years, empirical research methods, including velocity-density crossplot method (Bowers, 1995) and porosity comparison method (Tingay et al., 2013), have gradually replaced relatively simple theoretical analyses. And new understandings have been obtained on the identification and analysis of overpressure causes. The prevailing view has denied attributing overpressure to disequilibrium compaction or undercompaction, while the importance and prevalence of hydrocarbon generation for causing overpressure, especially gas generation during fluid expansion and oil-cracking gas, have been increasingly confirmed (Tingay et al., 2013; Zhao et al., 2017). As the geological-geophysical response characteristics are understood, it is revealed that tectonic compression and pressure transmission are the causes of overpressure. It has been discovered that the overpressure in many basins or areas may be the result of multiple causes.

The study of pressure evolution has also moved towards quantitative characterization. The characterization of pressure evolution from shale burial to uplift mainly employs the method of fluid inclusion analysis to reconstruct paleopressure. For example, Tang et al. (2023) carried out inclusion analysis to determine the reduction of the pressure coefficient of the Longmaxi Formation shale in Lintanchang area of southeastern Sichuan Basin from 2.05 in the early uplift period to 1.1 currently. Based on inclusion analysis, Liu et al. (2021) concluded that the pressure coefficient of the Longmaxi Formation shale in the southern Sichuan Basin varied from 2.10 to 2.50 in the hydrogenation generation period to 1.92–2.16 in the uplift period. However, the pressure evolution in the process of sedimentation-subsidence burial is less researched. Various studies have simulated the complete process of pressure evolution in Longmaxi Formation shale using basin modeling software. Li et al. (2016) carried out simulation calculation with consideration of temperature decline and concluded that the pressure of the Longmaxi Formation shale decreased in the process of uplift with pressure coefficient increasing from 1.8 to 2.5. Wu et al. (2022) carried out simulation calculation with consideration of gas escape and concluded that the pressure of the Longmaxi Formation shale decreased in the process of uplift with pressure coefficient fluctuating slightly around 2.2. Due to differences in geological factors, the conclusions regarding the pressure and pressure coefficient evolution curves vary significantly, and scholars have different understandings on the increase and decrease of pressure coefficient in the process of uplift. Furthermore, deep shale gas reservoirs undergo intense compaction during the burial process. Scholars generally agree that the development of overpressure has a protective effect on the pores in deep shale, whereas pressure relief often leads to pore collapse, compared with normal-pressure and low-pressure shale gas reservoirs (Liu et al., 2012; He et al., 2019; Sun et al., 2021). However, a detailed characterization of the impact of overpressure (different overpressure coefficients) on pore development characteristics is still lacking.

To address the gaps mentioned above, this study focused on three overpressured shale gas wells in southern Sichuan with pressure coefficients of 1.86 (Well Z202 in Dazu area), 2.04 (Well H202 in Yongchuan area), and 2.24 (Well L202 in Luzhou area). The study firstly conducted theoretical analyses and applied various geophysical logging methods to identify the dominant mechanisms of overpressure formation. Subsequently, it constructed geological models of typical wells by virtue of the basin modeling software, and restored the paleopressure by systematically analyzing fluid inclusion. Based on this, it employed a mathematical model to quantitatively characterize the entire process of pressure evolution. Based on the geological context, the study explored the reasons for the differential overpressure evolution. Finally, a comparative analysis of porosity and pore structure characteristics of reservoirs with different pressure coefficients was conducted to clarify the impact of overpressure on reservoir pore features.

2 Regional geological background and pressure distribution of shale gas reservoirs

The Sichuan Basin is located on the northwest margin of the Yangtze Platform, representing a superimposed basin controlled by multiple tectonic movements since the Sinian. It has sequentially deposited marine, transitional, and continental strata on the Epiproterozoic basement (Wang et al., 2015; Liu et al., 2022). During the Late Ordovician to Silurian, the deep-water continental shelf environment resulted the deposition of two sets of high-quality shale formations in the Sichuan Basin, i.e., the Wufeng Formation and the Longmaxi Formation, with a thickness ranging from 300 to 600 m (Fan et al., 2020; Wang et al., 2022c). The Wufeng Formation-Longmaxi Formation in the Sichuan Basin is a primary target for marine shale gas exploration and development in China (Li, 2023a). The Wufeng Formation is dominated by black siliceous carbonaceous shale, with the Guanyinqiao Member at the top conformable with the overlying Longmaxi Formation, featuring thin interbeds of shell limestone. The Longmaxi Formation's organic-rich shale is mainly found in the Long 1 and Long 2 Member. The Long 1 Member is divided into the first sub-member (Long 1^1) and the second sub-member (Long 1^2). The lower part is characterized by predominantly carbonaceous shale, transitioning upwards into calcareous silty mudstone. The Long 1^1 Sub-member can be further subdivided into four beds: Long $1^1{}_1$, Long $1^1{}_2$, Long $1^1{}_3$, and Long $1^1{}_4$. In comparison with Long 1 Member, Long 2 Member has coarser grain sizes, primarily consisting of calcareous siltstone and calcareous silty shale (Ma et al., 2020). The Luzhou, Dazu, and Yongchuan areas in southern Sichuan have developed high-quality deep shale reservoirs of the Wufeng Formation-Longmaxi Formation, representing significant development areas with greater reserves. The Luzhou area is situated in a low-steepness tectonic zone, serving as a sedimentary center in southern Sichuan (Fan et al., 2024). The Wufeng Formation thickness ranges from 6 to 11 m. The Longmaxi Formation, thickest in southern Sichuan, has a thickness between 350 and 620 m, increasing gradually from south to north (Deng et al., 2021). The burial depth of the Wufeng-Longmaxi Formation here is relatively shallow in high structural areas, ranging from 2,700 to 2,800 m, and deeper in low structural areas, exceeding 3,800 m. The Dazu area lies at the junction of the moderately sloping and low-steepness tectonic zones in central Sichuan. The Wufeng Formation thickness is between 6.5 and 8.8 m. The Longmaxi Formation ranges from 200 to 530 m, with thickness increasing from north to south and stabilizing with distance from the denudation line. The burial depth of the Wufeng-Longmaxi Formation in the Dazu area mainly falls between 3,500 and 4,500 m (Li et al., 2022). The Yongchuan area is located in the gently folded zone of southeastern Sichuan, characterized by a "two depressions with one uplift between them" structural pattern. The Wufeng Formation-Longmaxi Formation is widely distributed here, with a sedimentary thickness of approximately 360–470 m. The overall variation in strata thickness is small, with burial depth gradually decreasing from northwest to southeast, generally ranging from 3,000 to 4,200 m.

Significant breakthroughs have been achieved in deep exploration, leading to the establishment of one development area (Block Well L203), three trial production areas (Block Well Z202, H202, and Y101), and an increase in deep shale gas production to 3 billion cubic meters. The pressure coefficient, indicating the ratio of actual fluid pressure to hydrostatic pressure at the same depth, is widely used to measure the intensity of formation pressure. Generally, a pressure coefficient less than 0.9 indicates abnormally low pressure, a coefficient between 0.9 and 1.2 suggests normal compaction, a coefficient between 1.2 and 1.8 indicates overpressure, and a coefficient exceeding 1.8 suggests strong overpressure. It is currently believed that under actual geological conditions, there are no strata with a pressure coefficient greater than 2.5, as pressures beyond this threshold may cause rock fracturing, leading to fluid migration along newly created conduits and subsequent reduction of the pressure coefficient to below the threshold (Tang et al., 2022). This research based on oilfield and published relevant data, presented the present-day pressure coefficient contour map of the Longmaxi Formation shale in southern Sichuan Basin (Figure 1). From the map, it is evident that the pressure coefficients in deep shale gas reservoirs in southern Sichuan are generally higher than 1.2. Specifically, the Yongchuan and Dazu areas have pressure coefficients ranging from 1.2 to 2.0, indicating varying degrees of overpressure, while the Luzhou area has an overall pressure coefficient exceeding 2.0, indicating strong overpressure. This study is a continuing study following our previous research of (Yin et al., 2023), but focused more on pressure evolution differences within three studied wells, and also its influence on reservoir pore characteristics.

3 Methods

3.1 Fluid inclusions and micro laser raman spectroscopy analysis

Microscope equipped with transmission white light and incident ultraviolet light was used to observe fluid inclusions' type and morphology in calcite veins. When the gas-liquid two-phase brine inclusions are artificially heated to a specific temperature, the multiphase state of the inclusions reverts to the initial single-phase fluid state, this specific temperature is homogenization temperature of the inclusion (Nie et al., 2020). By establishing a correlation curve between the Raman shift of methane gas and the pressure inside the inclusion, and based on the principle of maintaining constant total volume and composition of the inclusion, an iterative calculation model can be constructed to accurately calculate the capture pressure of the inclusion. The microthermometry measurements of thickly-polished sections were conducted using TH-600 Linkam heating platform, enabling determination of homogeneity temperature (Th) for gas-liquid two-phase brine inclusions with a reproducibility precision within ±0.1. Raman spectroscopic measurements were performed using JY/Horiba LABRAM HR800 raman spectroscopy equipped with a 532 nm green laser and output power ranging from 200 to 500 mW.

3.2 FIB-SEM image analysis

The ultra-high image resolution of focused ion beam-field emission scanning electron microscopy (FIB-SEM) enables effective

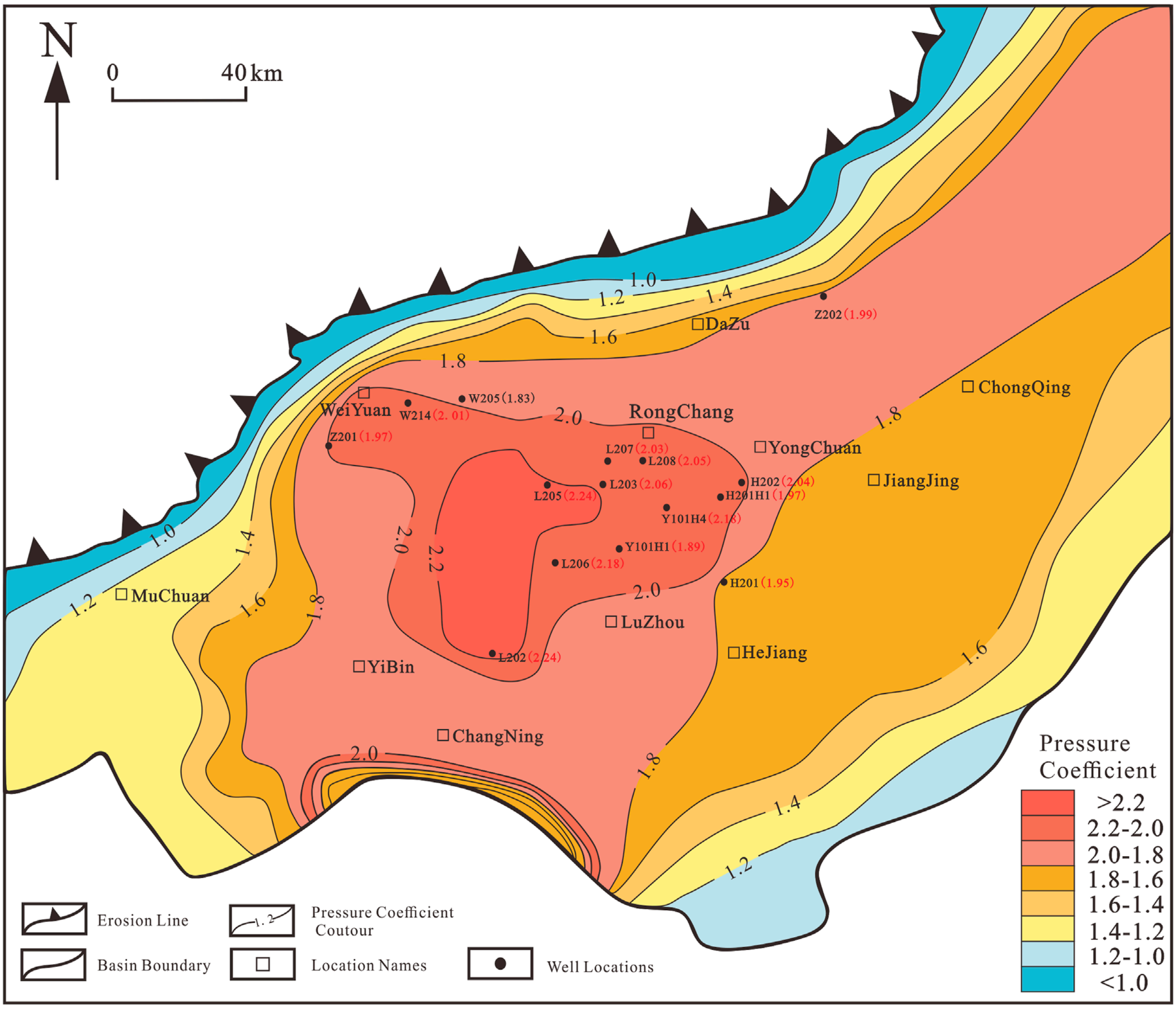

FIGURE 1
Planar distribution map of pressure coefficients in the Wufeng-Longmaxi formation shale gas reservoirs in the Southern and Southeastern Sichuan basin [adapted from Tang et al. (2022), with modifications].

observation of shale pore types and shapes. Prior to scanning, the shale sample is prepared into 1 cm^2 before further SEM analysis. To enhance surface conductivity and obtain superior image quality, a Sputter Coater argon ion grinding instrument is utilized to uniformly plate the sample surface with gold. Finally, the Quanta250FEG is employed for controlled temperature (24 °C) and humidity level (35%) scanning of shale samples.

3.3 Low temperature gas adsorption

Under isothermal conditions, the specific surface area and pore size distribution of porous materials are determined through physical adsorption processes on the sample surface using gases at pressures below their saturation vapor pressure. The characterization methods commonly employed for assessing shale pore structure include nitrogen and carbon dioxide adsorption. Nitrogen adsorption is particularly suitable for characterizing mesopores (pore size range: 2–50 nm) within a testing range of 1–300 nm, while carbon dioxide adsorption primarily focuses on micropores (pore size range: 0.4–2 nm). Previous studies have demonstrated that consistent characterization results can often be obtained in the overlapping pore size range between these two methods, thereby providing a foundation for achieving comprehensive characterization of "nanoscale" pores spanning from micropores to mesopores (Clarkson et al., 2013).

3.4 High pressure mercury injection

Mercury exhibits non-wettability towards typical solids, necessitating the application of additional pressure to facilitate its penetration into shale pores. The extent of pressure directly influences the pore radius accessible by mercury intrusion, with higher pressures enabling entry into smaller pores. By quantifying the amount of mercury infiltrating the pores at varying pressures, we can accurately determine the corresponding pore volume for a given size. In this experiment, we employed a Quantachrome Poremaster-60 mercury porosimeter pore analyzer within a test range spanning from 3.5 to 106 nm. The principle underlying the mercury intrusion method is encapsulated by Washburn's equation (Zheng et al., 2017),

$$P_C = \frac{2\sigma \cos \theta}{r}$$

where Pc is capillary pressure, MPa; σ is the air-mercury interfacial tension, 480 mN/m; θ is air-mercury contact angle, 140°; r is pore throat radius, μm.

3.5 Helium porosity test

Helium porosity measurements were carried out with Ultrapore-300 using helium expansion. The shale was made into cylindrical samples with a growth degree of 2.5 cm and a diameter of 2.5 cm. Subsequently, the sample was placed in a vacuum drying oven at 105 °C overnight. The volumetric density of the shale samples was measured by a caliper, while bone density calculations were performed based on multiple helium expansions conducted on dry samples. Finally, the porosity of the shale was determined by assessing the disparity between its volumetric density and skeletal density.

4 Analysis of overpressure formation mechanism in the Longmaxi formation

The formation mechanisms of overpressure in typical sedimentary basins mainly include disequilibrium compaction, clay mineral transformation, tectonic compression, and hydrocarbon generation expansion. The overpressure origins in different lithologies generally exhibit variations and the causes of overpressure in source rocks often differ from those in non-source rocks. In general, overpressure in shale (source rock) is closely related to hydrocarbon generation and diagenesis, while overpressure in non-source rocks is often associated with disequilibrium compaction, diagenesis, or pressure transmission (Zhao et al., 2017). In recent years, an increasing number of scholars believe that overpressure resulting from disequilibrium compaction occurs in mechanically compacted environments at shallow burial depths with low geothermal gradients (less than 70 °C). In contrast, the formation of the overpressure in deeper burial environments is primarily attributed to hydrocarbon generation expansion, clay mineral diagenesis, and other non-under compaction factors, or a combination of both mechanisms.

Recently, the Asia-Pacific region has become a hotspot for overpressure research, including basins such as Malay and Balama in Southeast Asia, and Bohai Bay, East China Sea, and Sichuan in China. Scholars have deepened their understanding of overpressure causes, and particularly have discovered and confirmed those related to non-under compaction, such as hydrocarbon generation, montmorillonite-illite transformation, and tectonic compression. Overpressure formed by fluid expansion includes hydrocarbon generation, hydrothermal expansion, and oil cracking gas, etc. Different scholars in China propose various overpressure causes for different shale gas reservoirs. For example, in the Yangtze region, mechanisms for pressure increase in gas-bearing shale intervals mainly include structural, hydrocarbon generation, and clay mineral dehydration-induced pressure increments (Li et al., 2016; Tang et al., 2022; Wang et al., 2022c) used log curve combinations to determine that the overpressure in the Wufeng-Longmaxi shale in the Chongqing and Fuling areas of the Sichuan Basin is attributed to hydrocarbon generation expansion. However, (Wu et al., 2022), suggested that the overpressure of the Haynesville and Barnett shales in the United States and the Jiaoshiba shale gas field in Chongqing are mainly caused by structural pressure due to the retention of natural gas caused by rapid short-term uplift. Hydrothermal pressure is the primary cause of early overpressure in shale gas reservoirs, while clay mineral dehydration occurs with increasing burial depth. For moderately to highly mature shale, the overpressure mechanism of oil cracking gas expansion is receiving increasing attention, though there are many challenges in the application of empirical methods. The traditionally belief that abnormal compaction trends in acoustic travel time/velocity deviation represent disequilibrium compaction has been increasingly challenged by scholars. Due to the complexity of overpressure causes and the diversity of factors affecting log results, log curve combination methods are widely applied (Wang Z.L. et al., 2003).

4.1 Comprehensive analysis of overpressure causes using multiple log methods

4.1.1 Log curve combination analysis

Overpressure related to hydrocarbon generation expansion manifests as abnormally high resistivity and acoustic transit time in logging responses, with density remaining constant or slightly decreasing. Clay mineral transformation alters and disrupts shale microstructure, leading to further densification and reduced porosity as well as abnormally high acoustic transit time and density. Tectonic compression essentially enhances the compaction effect of rocks; hence, generated overpressure does not cause significant anomalies in these three logging responses. In addition, some researchers believe that the synchronous occurrence of log curve inversions is crucial for the analysis of overpressure causes. (Bowers, 2002). suggested that if the inversions of sonic velocity, resistivity, and density logs are not synchronous, and the density inversion lags, it indicates strong overpressure. Meanwhile it reflects possible causes such as fluid expansion, montmorillonite-illite transformation, pressure transmission, or tectonic loading. Specifically, for overpressure caused by fluid expansion, the inversion of sonic velocity and resistivity is more significant than that of density.

From the log curves of Well L202 in the Luzhou area, it can be observed (Figure 2B) that the acoustic transit time and resistivity of the siliceous shale of the Wufeng Formation and the Long 1^1

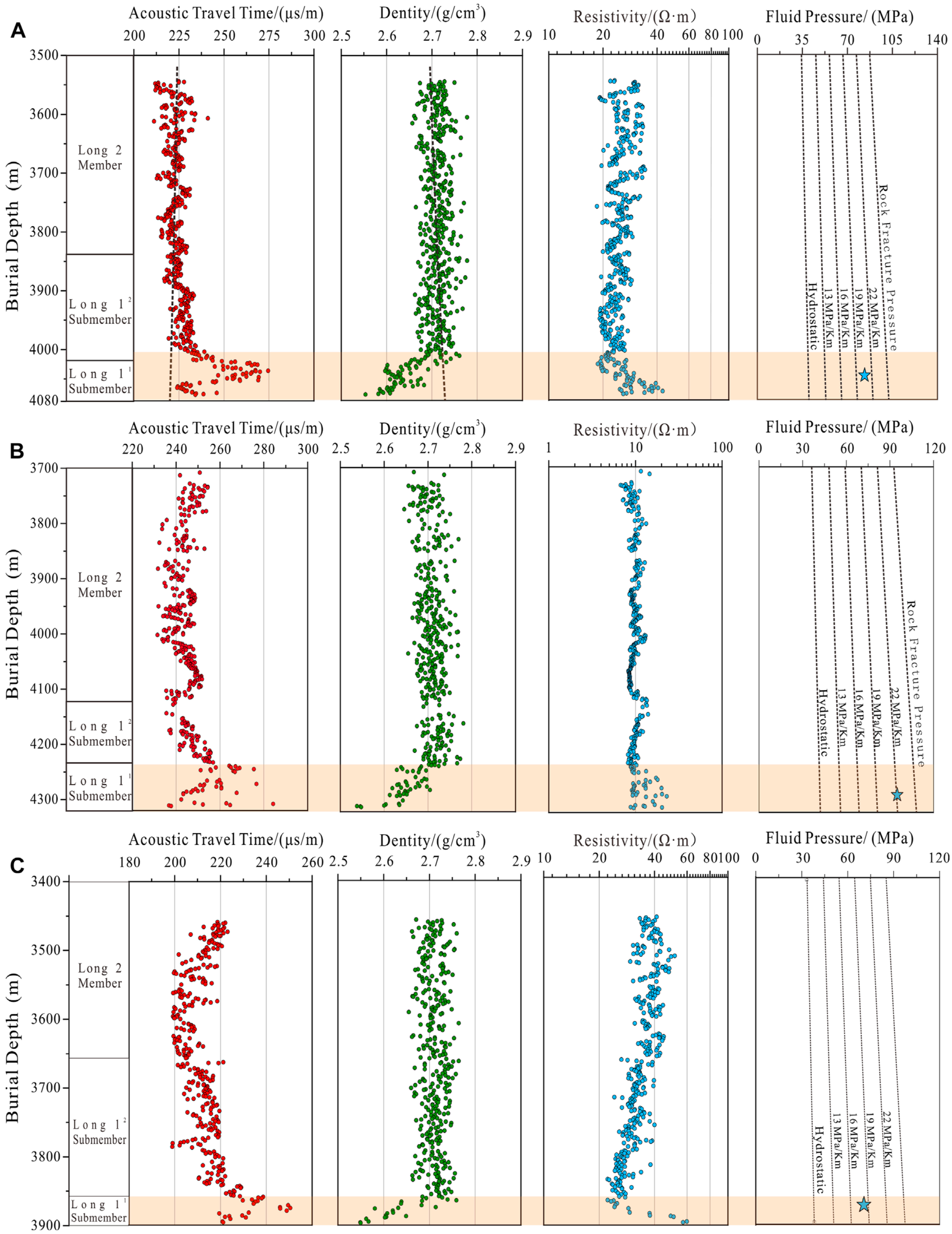

FIGURE 2
Overpressure distribution and causes identified from logging responses in the deep Longmaxi formation Shale of well H202 **(A)**, L202 **(B)**, and Z202 **(C)** in the southern Sichuan basin.

Sub-member (depth 4,230–4,320 m) show a noticeable increase compared with the overlying argillaceous shale of Long 1^2 Sub-member and Long 2 Member. But the density data exhibit a certain decrease. Logging responses of Well H202 and Z202 (Figures 2A–C) shows similar changing patterns indicating similar causes. These phenomena reveal the presence of significant overpressure, and the formation of overpressure is related to hydrocarbon generation expansion. This study also conducted research in other major shale gas production areas in China, and found similar examples include the Dazu area, Yongchuan area, and Jiaoshiba area. However, in the Luochang-Jianwu composite anticline of the northern Zhaotong area, the pressure values range between 1.75 and 1.98, and the inversion characteristics of log curve combination are different. The log curve of typical Well YS108 displays a decrease in sonic velocity, an increase in resistivity, and a decrease in density in the main producing beds of Long 1^1_1, Long 1^1_2, and Long 1^1_3 (Figure 3). The Zhaotong demonstration area is located on the southern margin of the Sichuan Basin, where structural reworking is relatively strong, and deformation zones are evident. The Jianwu composite anticline is located in a tectonic transition zone, and it is inferred that the overpressure may be caused by a composite origin of tectonic compression and hydrocarbon generation expansion. In addition to the Sichuan Basin, scholars have also studied the causes of overpressure in other areas in China by using the combination analysis of logging curves. Bozhong Sag shows the inversion of acoustic transit time and resistivity, and the density decreases slightly, which is considered to be the overpressure caused by hydrocarbon generation expansion (Yang et al., 2023). In Junggar Basin, the inversion depth of the density curve lags behind the acoustic time difference and the resistivity curve, which is considered to be the cause of fluid expansion or pressure conduction (Li et al., 2020).

4.1.2 Sonic velocity vs. density crossplot method

The classic application of the sonic velocity-density crossplot is illustrated in Figure 4A. Generally, overpressure and normal pressure formed by disequilibrium compaction falls on the loading curve. Overpressure formed by other mechanisms, on the other hand, tends to lie outside the loading curve (Conner et al., 2011; Tingay et al., 2013). Specifically, overpressure generated by fluid expansion mechanisms such as gas generation leads to a decrease in sonic velocity with increasing overpressure, while density remains unchanged or changes minimally. From the sonic velocity vs. density crossplot of three typical wells in the study area, it can be observed that data points from the normally pressured Long 2 Member and Long 1^2 Sub-member show an increase in sonic velocity with increasing density, forming the loading curve. In contrast, data points from the strongly overpressured Long 1^1 Sub-member deviate from the loading curve and do not follow the trend of the typical crossplot (Figures 4B–D). The overpressure data points in typical crossplot fall on or to the right of the loading curve. However, due to the slight reduction in density influenced by organic matter enrichment, the overpressure data points in the study area shift slightly to the left. Therefore, there could exist some controversy in using the sonic velocity vs. density crossplot to determine the dominant cause of overpressure.

In addition to the abovementioned methods, there are other techniques for identifying the causes of overpressure, such as the porosity comparison method and pressure retrograde calculating method. The identification of overpressure causes

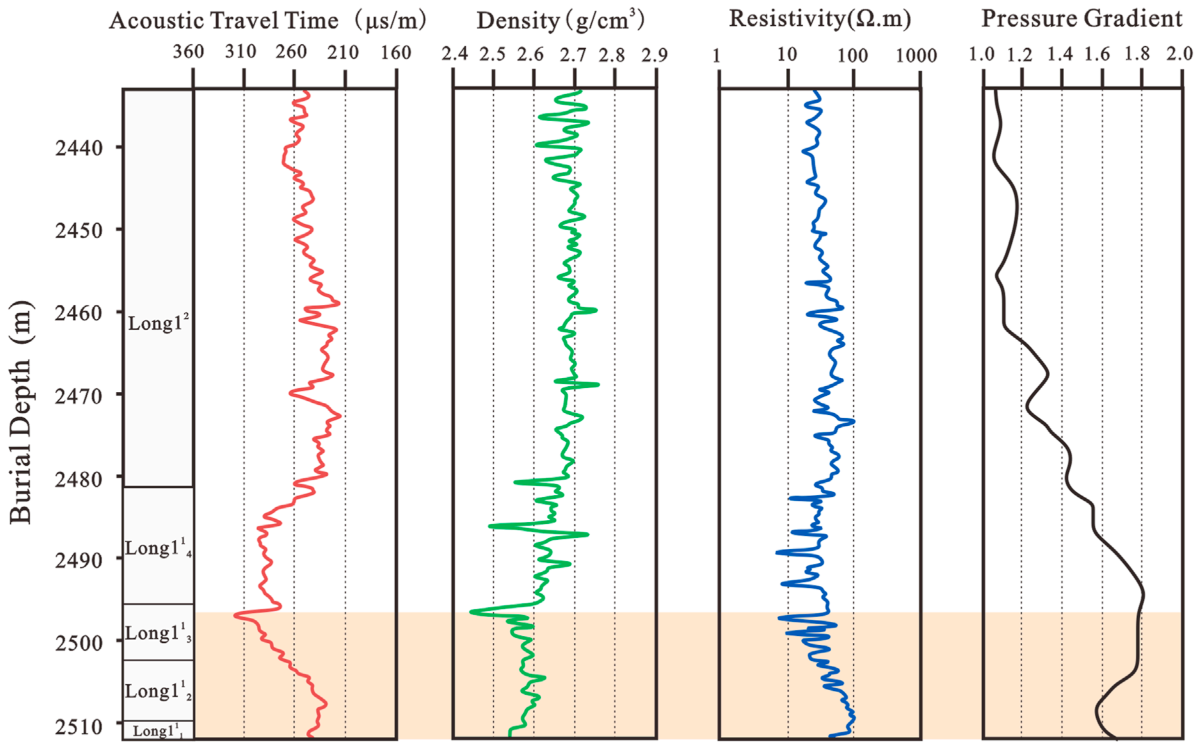

FIGURE 3
Overpressure distribution and causes identified from logging responses in the Longmaxi formation shale of well YS108, Zhaotong area, Southern Sichuan basin [modified from Chen et al. (2016); Rui et al. (2021)].

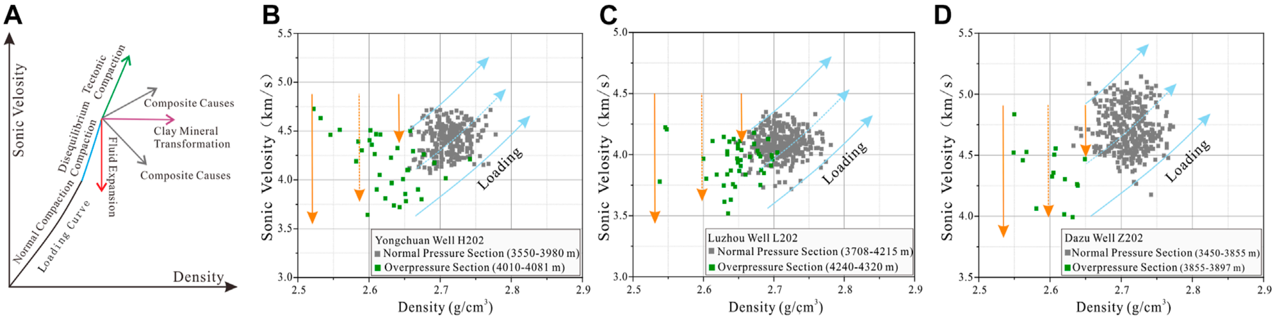

FIGURE 4
Typical plot for identifying shale overpressure using density vs. Sonic velocity crossplot (Zhao et al., 2017) **(A)**, Crossplots for density vs. Sonic velocity in the deep Longmaxi formation shale of Southern Sichuan Basin **(B–D)**.

requires a combination of various empirical methods, especially the comprehensive analysis of multiple factors (e.g., geological environments) affecting overpressure formation and distribution. Traditionally many scholars believed that in relatively young sedimentary environments with high sedimentation rates and low geothermal gradients, the primary formation mechanism of overpressure is disequilibrium compaction. However, it has been found that overpressure, whether in young basins with high sedimentation rate or pre-Cenozoic basins with lower sedimentation rate, is rarely dominated by disequilibrium compaction. On the contrary, overpressure is commonly associated with fluid expansion, diagenesis, tectonic compression, and pressure transmission (Zhao et al., 2017). Specifically, for the shale of the Wufeng Formation to the Longmaxi Formation in the Sichuan Basin, hydrocarbon generation, especially gas generation, is identified as the most important mechanism for overpressure during the shale burial stage.

4.2 The impact of tectonic uplift on overpressure

After undergoing burial processes, the shale of the Wufeng Formation to the Longmaxi Formation experienced a series of changes during the later stages of intense uplift, including a reduction in overlying load, temperature decrease, and cap rock denudation. Consequently, both pressure and pressure coefficients changed correspondingly. In comparison with the relatively consistent understanding of the mechanism for hydrocarbon generation-related overpressure, there is substantial difference between scholars regarding the impact of tectonic uplift movements on pressure. Qiu et al. (2020) argued that after strata uplift, the reduction in overlying pressure leads to the expansion of pore volume and fluid volume. Due to the higher fluid compressibility compared with rock, the expansion of fluid volume is slightly greater than that of pore volume, resulting in an increase in fluid pressure since confined fluids cannot be expelled. Gao et al. (2008); Yuan et al. (2020), on the other hand, proposed that during the uplift and denudation process, the reduction in overlying load leads to rebound in pore volume, while the contraction of pore fluid causes an increase in pore volume, fundamentally leading to the abnormal low pressure. Katahara and Corrigan, (2004) suggested that as the tectonic uplift process continues, the decrease in formation temperature causes both rock pore volume and fluid volume to contract. As the thermal expansion coefficient of fluid is greater than that of rock, the contraction of fluid volume is greater than that of pore volume, resulting in a decrease in formation pressure. Some scholars believe that the reduction in load leads to the expansion of pore and fluid, and the expansion of pore causes a decrease in formation pressure. During the later stages of uplift and unloading, pore rebound and temperature decrease lead to a decrease in formation pressure. However, since the hydrostatic pressure also significantly decreases, the formation pressure coefficient depends on the relative decrease (Ma et al., 2011). Additionally, uplift denudation causes brittle failure and overpressure rupture in rock layers, thus the generated overpressure fractures could result in shale gas loss and pressure release, resulting in a decrease in formation fluid pressure coefficient (Li., 2022). However, different wells may have different pressure coefficients, possibly related to the degree of fracture overpressure closure influenced by the shale over-consolidation ratio (OCR). When overpressure decreases to a certain level, fractures undergo overpressure closure, and OCR affects the way of shale damage and the degree of fracture closure, thereby controlling the extent of shale gas loss damage and the current formation pressure (Yuan et al., 2020). In general, during the uplift process, the formation water content in organic pores is low in the Silurian shale gas reservoir, and the effect of formation water contraction due to temperature decrease on the reservoir space can be ignored. Therefore, the changes in fluid pressure and pressure coefficients during the uplift process depend on the overall effects of pore rebound, temperature decrease, and overlying strata unloading.

5 Pressure evolution process and differential analysis

5.1 Research methods for pressure evolution

Basin simulation, numerical simulation, and paleo-pressure reconstruction are the three most commonly used methods for studying the pressure evolution process in geological formations.

Basin simulation involves setting key parameters to consider the influence of various geological factors and then simulating the evolution curve of formation pressure through software algorithms. The advantage of this method lies in its ability to quantitatively characterize the pressure characteristics of the entire evolution process. However, its accuracy is influenced by the software algorithm, the key parameter setting, and relevant geological factors. Numerical simulation applies appropriate computational models, combining with the main controlling factors of pressure evolution, to quantitatively calculate the entire process of pressure evolution. The accuracy of the results is influenced by the considered controlling factors and input parameters. Paleo-pressure reconstruction involves calculating ancient pressure and pressure coefficients using various methods based on burial history and thermal history. It provides a relatively quantitative description of the changes in formation pressure and pressure coefficients during geological periods. The advantage is the accuracy of the reconstruction results. But its limitation lies in only being able to clearly describe the pressure characteristics and changes at one or several moments, but unable to quantitatively characterize pressure features at any given moment or describe the entire pressure change process. Various scholars have conducted pressure evolution history reconstructions of the Longmaxi Formation shale in the Sichuan Basin using multiple methods (Li et al., 2016; Yuan et al., 2020; Liu et al., 2021; Wu et al., 2022). However, the shortcomings of the research methods introduce some uncertainty into the evolution results. In recent years, a new method combining basin simulation, numerical simulation, and paleo-pressure recovery has been proposed for studying the pressure evolution of geological formations (Qiu et al., 2020). This method has been successfully applied in the evaluation of pressure evolution in the Longmaxi Formation shale on the southeast margin and basin margin of the Sichuan Basin, the Ordovician strata in North Tarim uplift of the Tarim Basin, and the Permian strata in the Sulige Gas Field of the Ordos Basin (Qiu et al., 2020; Tang et al., 2022). This method first constructs a geological model (burial history-thermal history) using basin simulation software, then uses the corresponding mathematical model to quantitatively calculate the contributions of various factors after determining the dominated controlling factors of pressure evolution, and finally achieves a quantitative characterization of the entire pressure evolution process under the constraints of paleo-pressure recovery values and current pressure measurements. Thus, it can provide relatively accurate results and visually display pressure characteristics at different historical periods. Therefore, this study will apply this new method to recover the pressure evolution history of the deep Longmaxi Formation shale in the southern Sichuan in the entire process of sedimentary subsidence to structural uplift.

5.2 Pressure evolution of the deep layers of the Longmaxi formation shale in Southern Sichuan

5.2.1 Recovery of the burial history-thermal history-maturity history of typical shale reservoir

Using basin simulation software to build a geological model and achieve the quantitative characterization and dynamic analysis of the petroleum geological characteristics of petroliferous basins is of significant theoretical importance for studying the mechanisms of oil and gas generation, accumulation, and migration. In this study, the Petromod software's one-dimensional basin simulation technology was first employed. This study set various input parameters, such as the geological age, thickness, lithology, measured formation temperature, and vitrinite reflectance of each stratum. Subsequently, a geological model (burial history-thermal history-maturity history, Figure 5) of the deep Longmaxi Formation shale in Well H202 of the Yongchuan area was constructed, laying the foundation for the recovery of the pressure evolution history. The simulation results show that the evolution of the target layer can be divided into two stages. 1) A long-term subsidence stage (444–65 Ma), during which the shale underwent two rapid subsidence events, two slow subsidence events, and three weak uplift events. By 65 Ma, the maximum burial depth of the shale reached 6,700 m. The formation temperature increased from 25°C to 210°C, and the organic matter maturity increased from 0.2% to 2.7%. 2) A late strong uplift stage (650 Ma), during which the shale continued to experience strong uplift, with the current burial depth being approximately 4,100 m. The formation temperature decreased from 210°C to 129°C, while the organic matter maturity remained stable. Finally, the evolution curve of maturity over time obtained through simulation matched well with the measured equivalent vitrinite reflectance, validating the reliability of the geological model.

5.2.2 Numerical simulation of pressure enhancement by hydrocarbon generation

The mechanisms behind the formation of overpressure in sedimentary basins are diverse. Previous researchers, based on theoretical analyses of the geological background for overpressure formation and qualitative assessments of well log anomalies, have clarified that hydrocarbon generation expansion mechanisms (oil generation from kerogen, retained oil cracking into gas) are the dominant mechanisms for the formation of overpressure in the Longmaxi Formation shale in southern and southeastern Sichuan while the contributions from mechanisms such as disequilibrium compaction, clay mineral diagenesis, and tectonic compression are relatively insignificant (Gao et al., 2019; Tang et al., 2022). The above understanding indicates that during the long-term subsidence stage, the primary controlling factor for pressure evolution in the Longmaxi Formation shale is hydrocarbon generation. Therefore, this study utilizes a mathematical model of pressure enhancement by hydrocarbon generation (Guo et al., 2011) to quantitatively calculate the pressure and pressure coefficients of the Longmaxi Formation shale at different times.

Previous studies, through thermal simulation experiments and the proportions calculation of retained oil cracking gas using a mixture of methane and ethane end-members in the shale gas production areas of the Sichuan Basin, have shown that the proportion of retained oil cracking gas in natural gas ranges between 60% and 80%, while the proportion of kerogen cracking gas is relatively low (Zhang et al., 2018; Guo et al., 2020). For the Longmaxi Formation shale, the pressure enhancement model by hydrocarbon generation mainly considers two processes: kerogen thermal cracking to generate oil (Ro: 0.5%–1.3%) and crude oil cracking to generate gas (Ro: >1.3%). The detailed numerical simulation model assumption and calculation equations could be

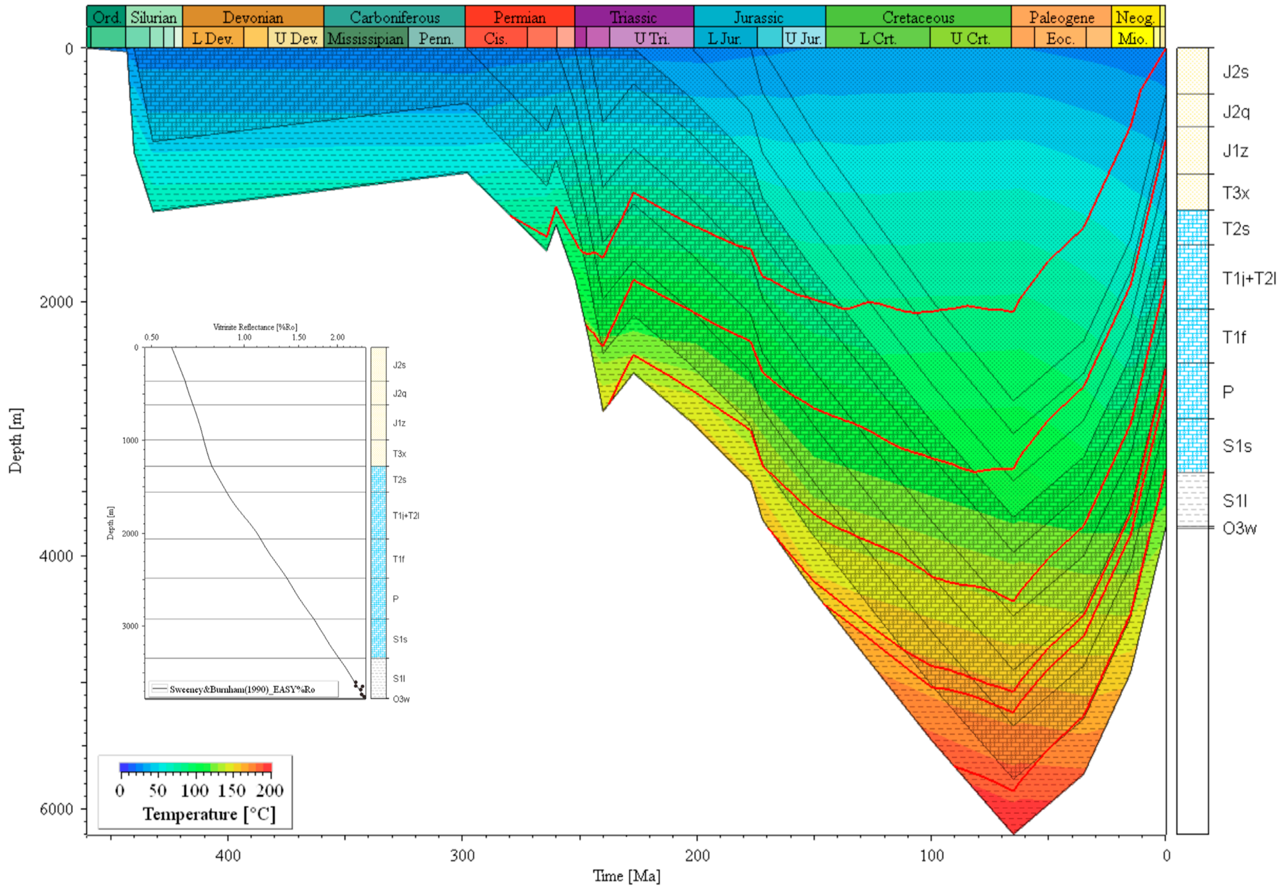

FIGURE 5
Burial history, thermal history, maturity evolution history, and geological model calibration results of Well H202 in Yongchuan area.

found in Yin et al. (2003). Table 1 shows the calculation result of pressure and pressure coefficients for the Longmaxi Formation shale gas reservoir in Well H202 from Yongchuan area. The final reservoir pressure reached 140.55 MPa with pressure coefficient being 2.09.

5.2.3 Recovery of typical shale hydrocarbon generation pressure

Taking well H202 in the Yongchuan area as an example, the depth, temperature, conversion rate, and cracking rate corresponding to the key time points in the geological model (such as the start of oil generation, peak oil generation, and crude oil cracking into gas) are introduced into the pressure enhancement model by hydrocarbon generation. Thus the pressure evolution curve of the shale during the subsidence stage is drawn (Table 1; Figures 7A, D). The pressure evolution of the Longmaxi Formation shale in the Yongchuan area can be divided into three stages based on the reservoir pressure state: 1) Normal pressure stage (Silurian to Early Triassic, 443–242 Ma): The shale experienced rapid and large-scale subsidence in the Silurian, and from the Ordovician to the Permian, it continued to experience slight uplift. Until the Early Triassic, it remained in a shallow burial state, and the organic matter was still in the immature to low-mature stage, with relatively limited hydrocarbon generation. Therefore, during this period, the pore fluid pressure in the shale was roughly equal to the hydrostatic pressure, indicating normal pressure conditions. The pore fluid pressure in the shale reached approximately 23.14 MPa by the Early Triassic, corresponding to a pressure coefficient of about 1.08; 2) Overpressure stage (Early Triassic to Early Jurassic, 242–195 Ma): The shale underwent slight uplift in the Middle to Late Triassic, followed by continued subsidence, increased formation temperature, and an increase in thermal maturity from 0.7% to about 1.3%. During this process, hydrocarbons continuously generated by the thermal cracking of kerogen accumulated in the shale, gradually forming overpressure (Wei et al., 2022). By the Early Jurassic, the cumulative pressure increase in the shale due to oil generation was approximately 17.66 MPa, and the pore fluid pressure reached about 49.05 MPa, corresponding to a pressure coefficient of about 1.56; 3) Super-strong overpressure stage (Early Jurassic to Late Cretaceous, 195–65 Ma): The shale experienced substantial subsidence during this period, with organic matter maturity increasing from 1.30% to 2.70%. The crude oil retained in the shale cracked to generate a large amount of natural gas, significantly increasing fluid pressure and forming strong overpressure. At the maximum burial depth, the cumulative pressure increase in the shale due to oil generation was approximately 55.73 MPa, and the pore fluid pressure reached about 140.55 MPa, corresponding to a pressure coefficient of about 2.09.

TABLE 1 Calculation results of pressure and pressure coefficient for the Longmaxi Formation shale gas reservoir in Well H202, Yongchuan area.

Time (Ma)	Depth (m)	Temperature (°C)	Ro (%)	Hydrostatic pressure (MPa)	Pressure increase (MPa)	Pressure (MPa)	Pressure coefficient
443	0	25	0.20	0.00	0.00	0.00	1.00
432	1,292	60	0.39	12.66	0.00	12.66	1.00
361	1,141	64	0.42	11.18	0.03	11.21	1.00
298	993	51	0.47	9.73	0.03	9.76	1.00
282	1,291	74	0.50	12.65	0.11	12.76	1.01
275	1,421	80	0.51	13.93	0.20	14.13	1.01
260	1,415	85	0.54	13.87	0.36	14.23	1.03
248	2,185	120	0.69	21.41	1.72	23.14	1.08
242	2,682	140	0.86	26.28	5.67	31.95	1.22
231	2,700	131	0.93	26.46	9.04	35.50	1.34
223	2,684	140	1.13	26.30	10.87	37.18	1.41
195	3,203	157	1.30	31.39	17.66	49.05	1.56
175	3,760	160	1.44	36.85	21.99	58.84	1.60
166	4,212	163	1.50	41.28	25.19	66.46	1.61
149	4,734	165	1.60	46.39	29.68	76.08	1.64
124	5,409	180	1.90	53.01	53.37	106.38	2.01
107	5,879	190	2.11	57.61	63.21	120.83	2.10
89	6,309	200	2.34	61.83	69.92	131.75	2.13
80	6,533	205	2.50	64.02	71.44	135.46	2.12
65	6,853	211	2.70	67.16	73.39	140.55	2.09

5.3 Pressure evolution during the uplift and denudation stage of the deep Longmaxi formation shale

5.3.1 Paleopressure recovery of vein fluid inclusions

Fibrous calcite veins developed in shale fractures are considered products of overpressure fluid activity (Meng et al., 2017; Wu et al., 2021). Fluid inclusion types, compositions, temperatures, and salinities within these veins are analyzed using techniques such as lithofacies observation, laser Raman spectroscopy, and micro-thermometry, which provides insights into fluid activity periods, allowing for the reconstruction of paleo-geothermal and paleo-pressure conditions. Taking the deep Yongchuan area in southern Sichuan as an example, the Longmaxi Formation shale exhibits a variety of fracture forms, dominantly characterized by extensional-shear fractures. Fibrous calcite veins are widely developed within the layers, often appearing in high-angle or nearly vertical orientations (Figure 6A). Lithofacies observations of the inclusions reveal that the fibrous calcite veins mainly contain single-phase methane inclusions and gas-liquid two-phase brine inclusions (Figure 6B). Among them, discretely dispersed single-phase methane inclusions exhibit characteristics of low transparency, with bright centers surrounded by a darker rim, primarily in the form of quadrilaterals and sub-rounded shapes. Gas-liquid two-phase brine inclusions are observed as colorless, transparent entities with small gas bubbles, predominantly in sub-rounded, irregular elliptical, and elongated forms, commonly coexisting with methane inclusions.

Laser Raman spectroscopy analysis of single-phase methane inclusions shows strong characteristic peaks only for the host mineral calcite (at wavenumbers approximately 156 cm^{-1}, 283 cm^{-1}, 713 cm^{-1}, and 1,086 cm^{-1}) and methane fluid (at wavenumber approximately 2,911.28 cm^{-1}), without other prominent Raman

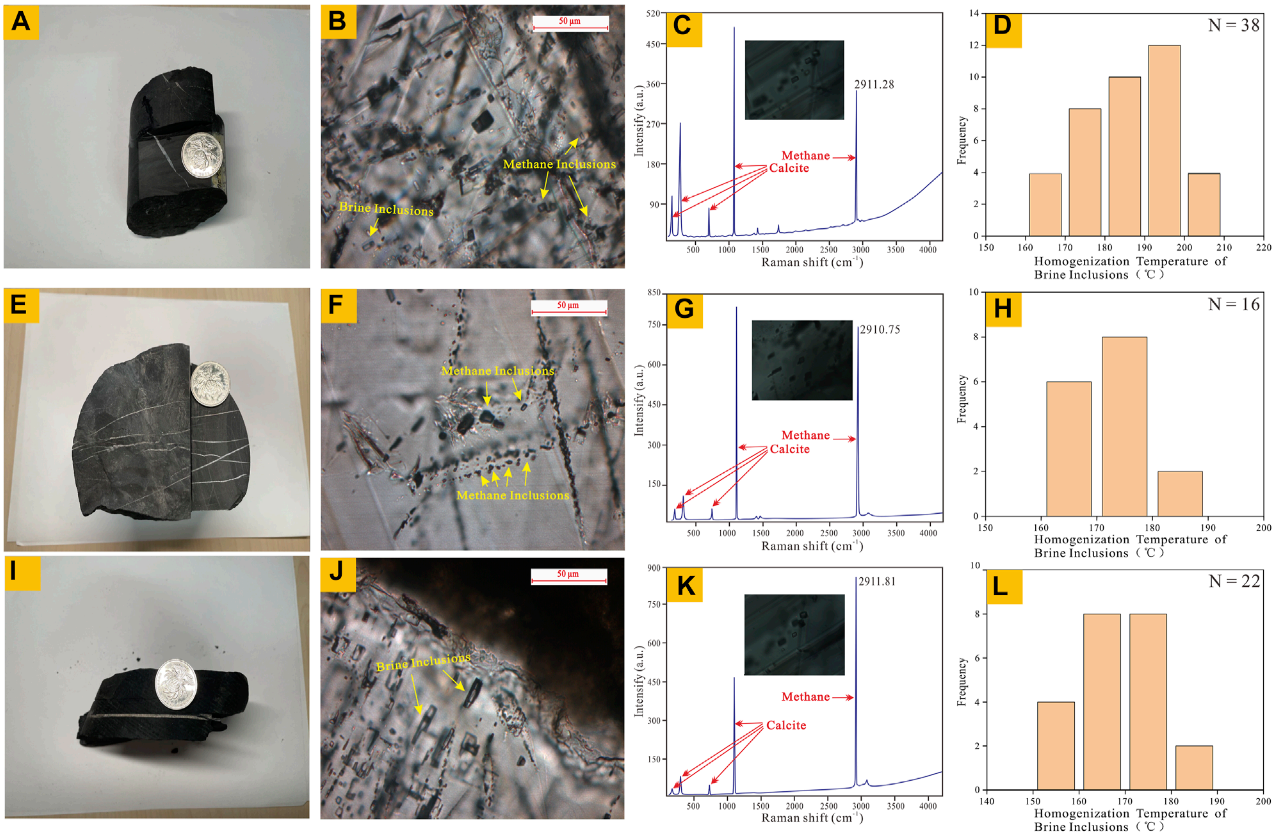

FIGURE 6
Characteristics of fibrous calcite veins in the Longmaxi formation shale of well H202 in the Yongchuan area **(A)**, Petrographic features of methane and brine inclusions within the veins **(B)**, Laser Raman spectrum of methane inclusions **(C)**, Homogenization temperatures of gas-liquid two-phase brine inclusions, N represents the number of inclusions analyzed **(D)**, Analysis results of vein and inclusions of well L202 in the Luzhou area **(E–H)** and well Z202 in the Dazu area **(I–L)**.

characteristic peaks observed (Figure 6C). This indicates that methane inclusions developed in calcite veins exhibit high methane purity. The wavenumber (V_d) of the characteristic peaks of methane fluid is a key parameter for calculating the density of individual methane inclusions. By introducing the measured peak wavenumbers of methane inclusions into an empirical formula based on a large amount of experimental data (Zhang et al., 2016), the density value of methane inclusions is calculated to be 0.261 g/cm^3, which exceeds 0.130 g/cm^3, so it is classified as a supercritical high-density methane inclusion. It provides favorable conditions for the accurate calculation of capture pressures.

From 150°C to 180°C, and 180°C–204°C. Those main maximum temperature data in L202 shows a unimodal distribution from 160°C to 180°C.

Micro-thermometry results of gas-liquid two-phase brine inclusions in well H202 and Z202 indicate a double peaks distribution of homogenization temperature (Figures 6D, L), ranging the geological model, the latest formation time of the veins is estimated to be approximately 15 Ma. Finally, the calculated density of methane inclusions and the measured minimum homogenization temperature of brine inclusions are input into the state equation of the supercritical methane system established by Duan et al. (1992). This yields the paleo-pressure of the Longmaxi Formation shale, and in conjunction with the geological model, the paleo-pressure coefficient is calculated. In the Yongchuan area, the Longmaxi Formation shale at 15 Ma, with a burial depth of 5,450 m in Well H202 exhibits a formation temperature of 165°C and a formation pressure of 95.21 MPa, corresponding to a pressure coefficient of 1.78. The differences between H202, Z202 with L202 indicate a greater uplifting process occurred in Yongchuan area compared to Dazu and Luzhou, which coincide with evolutionary models of pressure and pressure coefficient in those wells (Figure 8).

The extremely high pressures in fluid inclusions pose significant challenges for traditional microthermometry and pressure calculations. Wang et al. (2022a) used hydrothermal diamond-anvil cell (HDAC) to study fluid inclusions in fracture calcite and quartz veins from the Silurian Longmaxi Formation black shale in the eastern Sichuan Basin, ensuring the isochoricity of the fluid system and obtaining effective homogeneous temperatures; Raman spectroscopy quantitative analysis was applied to determine the composition of the inclusions, and the trapping pressure of single-phase gas phase inclusions coexist with brine inclusions

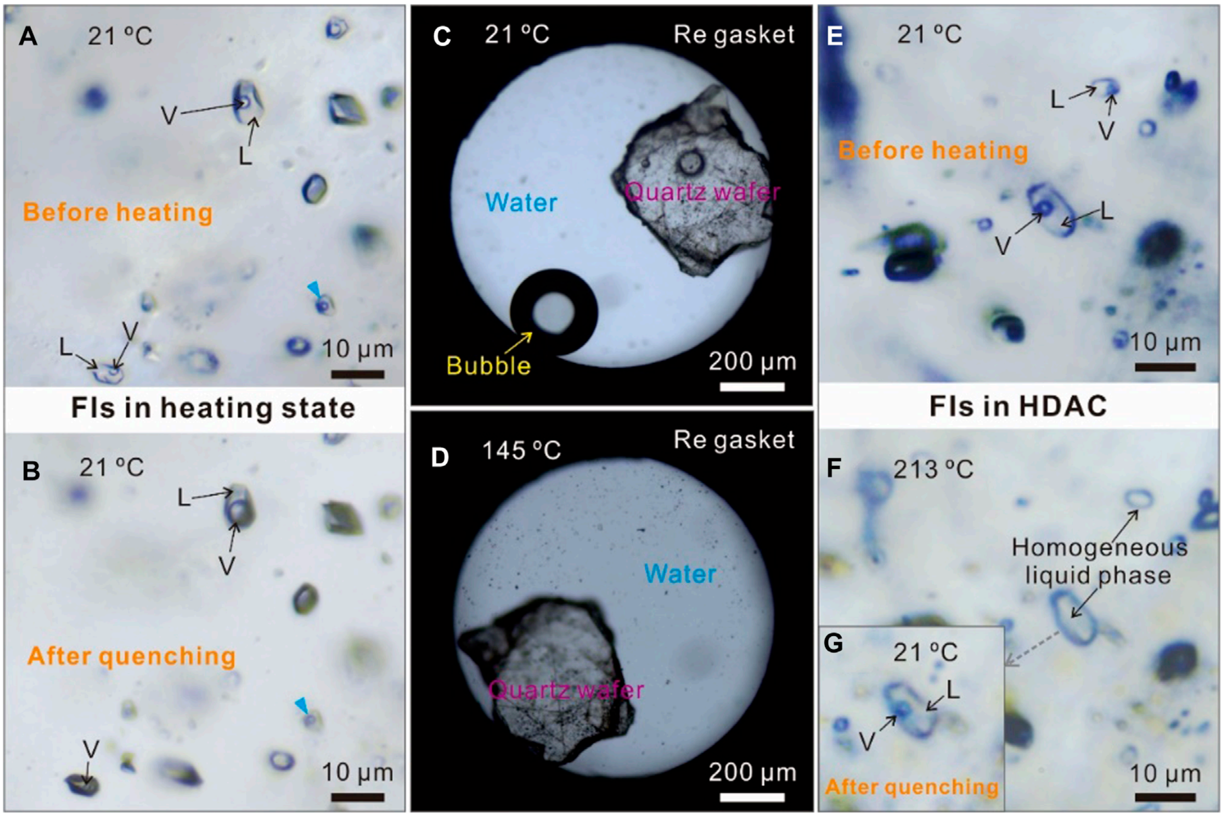

FIGURE 7
Comparison of temperature measurement results of inclusions (FI) in traditional heating stage **(A,B)** and HDPC **(C–G)** [adopted from Wang et al. 2022b].

was determined based on the state equation of the CH_4-CO_2 system, so as to overcome the problem of homogeneous pressure in gas-liquid two-phase inclusions exceeding the pressure range exceeding lithostatic pressure according to burial history curves. This provides direct geological evidence for generating extremely high-pressure fluids during hydrocarbon of the existing NaCl-H_2O-CH_4 system state equation. The results showed that the pressure of methane-rich ancient fluids can reach 2,310 bar, significantly generation processes. Figure 7 compared the result of temperature measurement in traditional heating stage and HDPC. When the inclusions are heated and quenched in the HDAC with a suitable external pressure, it can be found that the inclusions return to their pre-heating form.

5.3.2 Pressure evolution during the strong uplift of shale

Shales remained strong overpressured at present suggesting closed fluid systems and little gas loss. During the uplift and denudation stage, the hydrocarbon generation process of shale tends to stagnate. The main controlling factors of the pressure evolution change. Effects such as gas escape, temperature reduction, and pore rebound gradually alter fluid pressures during the uplift process (Xu et al., 2010; Wu et al., 2022). Tang et al. (2022) argued that the porosity and permeability of shale undergo rapid decline during burial, and cannot be restored to their initial state during uplift, resulting in a hysteresis rebound phenomenon. Consequently, it is imperative to consider this factor in calculations. Therefore, the subsequent equation was employed for computation,

$$\Delta P_T = -\frac{1}{3} \times \frac{1+\vartheta}{1-\vartheta} \times \frac{C_r}{C_r + C_w} \rho_r g \Delta h$$

Where, ΔP_T represents pressure (MPa), ϑ represents rock's Poisson ratio (0.25); C_r and C_w represent the coefficient of compressibility of rock and water; ρ_r represents the average density of the denudated formation (2.65×10^3 kg/m^3); g represents the acceleration of gravity (9.8 m/s^2); Δh indicates the denudation thickness of the formation(m).

However, Li et al. (2016) and Gao et al. (2019) proposed that Longmaxi Formation shale predominantly develops micro- and nano-scale pores, and the rebound degree does not significantly change with increasing denudation thickness. Hence its impact on pressure evolution is negligible.

In the uplift stage of Longmaxi Formation shale, a temperature decrease of approximately 80 °C inevitably led to changes in formation pressure. We employed two methods for pressure evolution during tectonic uplift. The first commonly used Soave-Redlich-Kwong (SRK) state equation is employed to quantitatively calculate the influence of temperature changes on fluid pressure in the gas reservoir during the uplift process. The calculation formula is as follows:

$$P = \frac{RT}{V-b} - \frac{a(T)}{V(V+b)}$$

$$\alpha(T) = \frac{0.4748\beta(T)R^2T_c^2}{P_c}$$

$$b = \frac{0.08664RT_c}{P_c}$$

$$[\beta(T)]^{0.5} = 1 + \left(0.48 + 1.576\omega - 0.176\omega^2\right)\left(1 - \left(\frac{T}{T_c}\right)^{0.5}\right)$$

Where, P represents pressure (MPa); T is temperature (K); V is molar volume of the gas (cm^3/mol); R is the gas constant (8.314 J/mol/K); a(T) denotes inter-molecular attraction; b is the volume of gas molecules; ω is the acentric factor of the gas; Tc and Pc are the critical temperature and pressure of the gas (190 K, 4.599 MPa); Tr is the relative temperature of the gas, i.e., the ratio of the actual absolute temperature to its critical temperature.

The second method is the equation of state (EOS) for supercritical CH_4 system by Duan et al. (1992). The main factors affecting pressure changes in shales are temperatures and gas escape, which has a linear relationship with gas density. The gas volume or gas density can be evaluated by the equation of state for supercritical CH_4 system (Duan et al., 1992).

$$Z = \frac{PV}{RT} = \frac{PrVr}{Tr} = 1 + \frac{B}{Vr} + \frac{C}{V_r^2} + \frac{D}{V_r^4} + \frac{E}{V_r^5} + \frac{F}{V_r^2}\left(\beta + \frac{\gamma}{V_r^2}\right)\exp\left(-\frac{\gamma}{V_r^2}\right)$$

$$B = \alpha 1 + \frac{\alpha 2}{T_r^2} + \frac{\alpha 3}{T_r^3}; C = \alpha 4 + \frac{\alpha 5}{T_r^2} + \frac{\alpha 6}{T_r^3}; D = \alpha 7 + \frac{\alpha 8}{T_r^2} + \frac{\alpha 9}{T_r^3}; E = \alpha 10 + \frac{\alpha 11}{T_r^2} + \frac{\alpha 12}{T_r^3};$$

$$F = \frac{\alpha}{T_r^3}; PrVr = \frac{P}{P_c} + \frac{V}{V_c}; V_c = \frac{RT_c}{P_c};$$

Empirical parameters $\alpha 1 - \alpha 12, \alpha, \beta, \gamma, T_c, and\, P_c$ in EOS for CH_4 are compiled by Duan et al. (1992). T_c is the critical temperature above which a gas cannot be liquefied by an increase of pressure. P_c is the pressure at given temperature to liquefy a gas. Tr and Pr can be calculated at given temperature and pressure condition in a specific basin.

For Well H202 in the Yongchuan area, the temperature data during the uplift stage is substituted into the above equation to calculate the pressure drop due to temperature decrease, which is equal to 27.99 MPa. The pressure drop caused by gas escape can be calculated by balancing the currently measured pressure values with the theoretical pressure values at the maximum burial depth. According to the first sets of calculation. The initial fluid pressure of the shale in Well H202 during the early uplift stage is 140.55 MPa, and the currently measured formation pressure is 81.63 MPa, resulting in a total pressure drop of 58.93 MPa. The pressure drop due to temperature decrease is 27.99 MPa, and the pressure drop due to gas escape is 30.94 MPa. Following method 2, the gas density in studied over-pressured shales is ~0.206 g/cm^3, and the gas density was ~0.255 g/cm^3 at maximum burial depths. Comparing the initial pressure before tectonic uplift and the present-day pressure coefficient, the loss of shale gas is ~15.5% of the initial total gas content. If pore rebound is taken into account, the pressure drop is calculated to be 27 MPa. Combining those above calculated values, restored paleo-pressure values, and currently measured pressures, the pressure evolution curve during the uplift stage of the shale in Well H202 is plotted (Figures 8A, D). It can be observed that fluid pressure shows a decreasing trend during the uplift stage, but the evolution of the pressure coefficient has a turning point, exhibiting a trend of initially decreasing and then increasing. This phenomenon arises because the early fluid pressure drop is greater than the overlying strata pressure drop, while the late-stage fluid pressure drop is less than the overlying strata pressure drop. The homogenization temperature test results of inclusions provide the essential reasons for this phenomenon. The homogenization temperature of inclusions in Well H202 ranges from 165°C to 204°C, corresponding to capture time from 65 to 15 Ma. This indicates that during this period, fractures opened to allow extensive gas escape, thus fluid pressure drop was significant. No inclusions below 165°C were found, suggesting that from 15 to 0 Ma, fractures closed to limit gas escape, and the fluid pressure drop was smaller. Therefore, based on the differences in controlling factors, the pressure evolution during the uplift process of the Longmaxi Formation shale in Well 202 can be divided into two stages: 1) Early Paleogene to Middle Neogene (65–15 Ma), the shale fluid pressure dropped from 140.55 MPa to 95.21 MPa. The pressure drop due to temperature decrease is 15.74 MPa, and the pressure drop due to gas escape is 29.60 MPa. During this period, strata denudation caused a decrease in overlying strata pressure by 13.63 MPa, which is less than the fluid pressure drop, resulting in a decrease in the pressure coefficient from 2.09 to 1.78; 2) Middle Neogene to Present (15–0 Ma), the shale fluid pressure dropped from 95.21 MPa to 81.63 MPa. The pressure drop due to temperature decrease is 12.25 MPa, and the pressure drop due to gas escape is 1.33 MPa. During this period, strata denudation causes a decrease in overlying strata pressure by 13.61 MPa, slightly higher than the fluid pressure drop, resulting in an increase in the pressure coefficient from 1.78 to 2.04. Throughout the entire uplift process, fluid pressure has not reached the fracture limit of the rock, and gas pressure release mainly occurs through diffusion or structural fracture. Uplifting caused gas escape in Luzhou area is not as heavy as in Dazu and Yongchuan (Figures 8B–F).

5.4 Analysis of differential pressure evolution of deep Longmaxi formation shale

Pressure evolution histories of the deep Longmaxi Formation shale were individually established for Well L202 in Luzhou area, and Well Z202 in Dazu area (Figures 8B,C,E,F). A comparative analysis reveals similarities in pressure evolution during the sedimentation–subsidence stage. Both shales exhibit intense overpressure due to hydrocarbon generation, reaching a formation pressure of approximately 140 MPa and a pressure coefficient of about 2.10 at the maximum burial depth of approximately 6,700 m. However, differences emerged during the uplift–denudation process. The Luzhou area experienced the smallest decrease in formation pressure (pressure drop due to temperature decrease and gas escape are 24.50 MPa and 21.63 MPa, respectively). Consequently, the current formation pressure and pressure coefficient are the highest, equal to 94.86 MPa and 2.24, respectively. Conversely, the Dazu area witnessed the largest decrease in formation pressure (pressure drop due to temperature decrease and

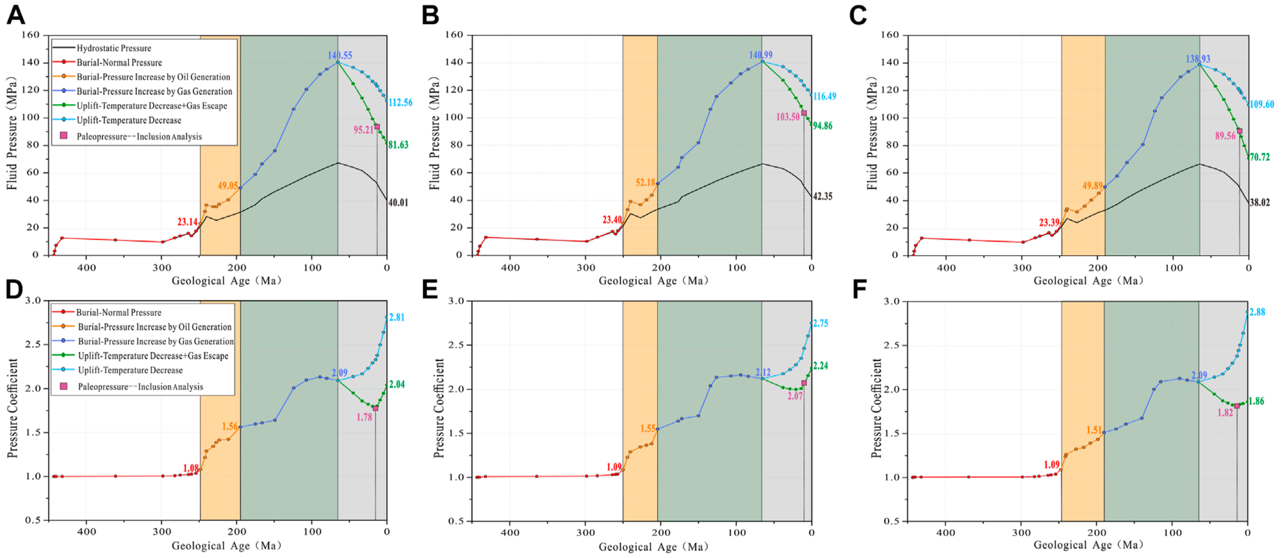

FIGURE 8
Evolutionary models of pressure and pressure coefficient in the deep Longmaxi formation shale gas reservoirs in the Yongchuan Area **(A,D)**, Luzhou area **(B,E)**, and Dazu area **(C,F)**.

gas escape are 29.33 MPa and 38.88 MPa, respectively). Thus, the current formation pressure and pressure coefficient are the lowest, equal to 70.72 MPa and 1.86, respectively. This discrepancy reflects variations in gas reservoir preservation conditions. The Luzhou area, situated within the internal part of the gently inclined tectonic zone in southern Sichuan, is featured by limited large faults and primarily small faults. The extent of shale gas escape and the pressure drop are relatively low, resulting in current gas reservoir pressure coefficients generally ranging from 2.0 to 2.4. Conversely, the Dazu area, located at the boundary of the southern and central Sichuan tectonic zones, hosts several large faults trending northeast to southwest. This may contribute to relatively higher shale gas escape and pressure drop, resulting in overall pressure coefficients ranging from 1.8 to 2.0.

6 Impact of varying degrees of overpressure on pore characteristics of deep shale gas reservoirs

6.1 Scanning electron microscopy (SEM) features of deep shale pores

Observations using high-resolution scanning electron microscopy revealed diverse spatial types of organic-rich shale reservoirs under overpressure conditions in the Long 1^1 Sub-member. Four types of pores are commonly observed, including organic matter pores, intragranular dissolution pores in brittle minerals, intergranular (interlayer) pores in clay minerals, and microfractures, with the first two being predominant (Figures 9A–I). Organic matter pores exhibit great advantages in bearing adsorbed and free methane. Consequently, the development of organic matter pores plays a crucial role in the enrichment of shale gas in the Longmaxi Formation. The organic matter pores in the samples are primarily irregular subcircular or ellipsoidal, appearing honeycomb-shaped or bead-like within the organic matter, with pore diameters ranging from 50 to 450 nm (Figures 9A, B). Their formation is associated with the extensive hydrocarbon generation and expulsion during the thermal maturation of organic matter. Additionally, a few organic matter pores are in the form of fissures distributed at the interface between organic matter and inorganic minerals, with a width of up to approximately 200 nm (Figure 9C). The origin is attributed to specific organic maceral and its shrinkage effects during thermal evolution (Wang et al., 2023a). Intragranular dissolution pores in brittle minerals generally exhibit a polygonal shape, with pore diameters ranging from 300 to 1,200 nm and poor connectivity (Figures 9D–F). Intergranular (interlayer) pores in clay minerals typically appear as fissures with directional distribution, with pore diameters ranging from 300 to 700 nm and good local connectivity (Figure 9G). Scholars have classified microfractures into three types based on their origins: structural fractures, diagenetic shrinkage fractures, and bedding slip fractures (Zeng et al., 2016). In the study area, diagenetic shrinkage fractures are well-developed (Figures 9H, I), often extending along the interface of minerals or organic matter, with lengths ranging from 8 to 20 μm. They are featured by limited opening and mostly unfilled. These fractures serve as one of the main spaces for the occurrence and migration of shale gas. In addition, a small number of primary intergranular pores in brittle minerals were observed, appearing as fissure-like, wedge-shaped, or cylindrical structures (Figure 9F).

6.2 Pore structure characteristics

The pore structure characteristics of shale reservoirs, including morphology, pore size distribution, pore volume, and specific surface area, are not only crucial parameters for evaluating reservoir performance but also significantly impact the distribution of shale

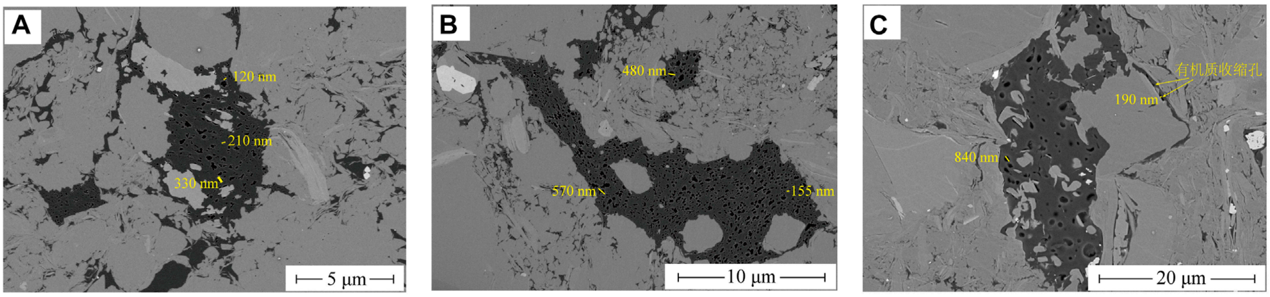

Well Z202 Long 1^1 Sub-member 3884m
Organic Matter Pores

Well H202 Long 1^1 Sub-member 4044m
Organic Matter Pores

Well L202 Long 1^1 Sub-member 4289m
Organic Matter Pores

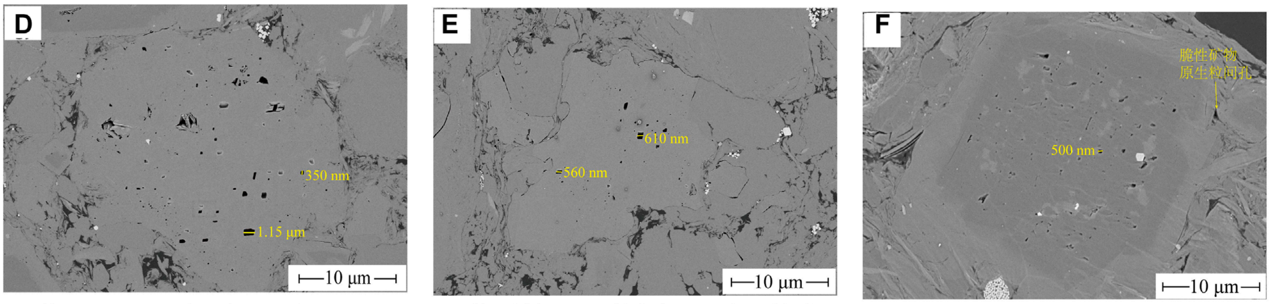

Well Z202 Long 1^1 Sub-member 3878m
Intragranular Dissolution Pores

Well H202 Long 1^1 Sub-member 4073m
Intragranular Dissolution Pores

Well L202 Long 1^1 Sub-member 4265m
Intragranular Dissolution Pores

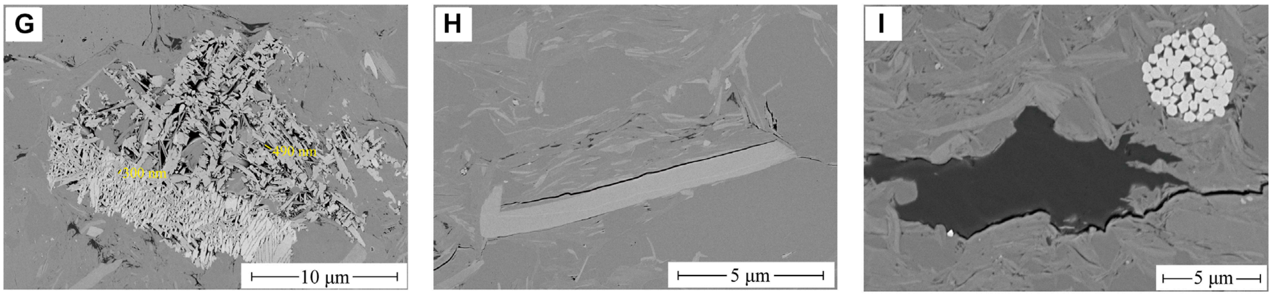

Well H202 Long 1^1 Sub-member 4044m
Inetergranular Pores

Well Z202 Long 1^1 Sub-member 3852m
Diagenetic Shrinkage Fractures

Well L202 Long 1^1 Sub-member 4240m
Diagenetic Shrinkage Fractures

FIGURE 9
Scanning electron microscope images of pore types in organic-rich Shale of the deep long 1^1 sub-member, including organic matter pores **(A–C)**, intragranular dissolution pores **(E–G)**, and diagenetic shrinkage fractures **(H–I)**.

oil and gas content in different occurrence states (Wei et al., 2021). Scholars have combined gas adsorption and high-pressure mercury injection experiments to characterize the pore structure of the deep Longmaxi Formation shale in southern Sichuan, and analyzed the influence of factors such as burial depth, total organic carbon (TOC) content, inorganic mineral composition, and water content on pore structure characteristics (Pan et al., 2015; Yang et al., 2016; Zhao et al., 2018). The research results indicate that the total pore volume of the shale ranges from 17.26 to 33.65 mm^3/g, with an average of 28.74 mm^3/g. The predominant pores are mesopores (2–50 nm) and micropores (<2 nm), with macropores (>50 nm) contributing a smaller proportion, averaging 23%, 73%, and 4%, respectively. In addition, the volume of pores with diameters less than 10 nm accounts for an average of 59%. In comparison with shallow shale at depths less than 3,000 m, deep shale at depths exceeding 3,500 m exhibits a significant increase in total pore volume (rising from 22.85 mm^3/g to 29.86 mm^3/g). The volume proportion of micropores within the total pore volume also significantly increases (from 15.34% to 21.85%), while the proportions of mesopores and macropores decrease (from 72.54% to 66.71% and from 12.12% to 11.44%, respectively). The TOC content correlates positively with the volumes of micropores and mesopores, with correlation coefficients reaching 0.81 and 0.42, while its correlation with macropore volume is only 0.21. The reservoir's water absorption rate increases from 1.84% to 2.84%, while the reduction rate in total pore volume rises from 10.7% to 21.8%. The decrease in specific surface area increases from 15.5% to 29.7% (Shi et al., 2023). Additionally, some scholars have employed scanning electron microscopy and image processing to analyze the structural characteristics of organic matter pores. They have explored the controlling effects of organic maceral, formation pressure (overpressure and normal pressure), and mineral composition. Studies show pores developed in bitumen generally have diameters larger than 25 nm, while those in bacterial aggregates and algal fragments have diameters ranging from 10 to 30 nm (Xie et al., 2021). Organic matter pores, protected under overpressure conditions, exhibit characteristics such as nearly circular shapes and diameters ranging from hundreds of nanometers to micrometers. In contrast, under normal pressure conditions, these pores undergo modification and exhibit irregular shapes with diameters ranging from tens to hundreds of nanometers (Liu et al., 2020). An increase in pyrite content promotes the development of organic matter pores, with the diameters of organic matter pores in the periphery ranging from 20 to 70 nm. They often appear as approximately elliptical and irregular shapes with some interconnected with each other.

To explore the impact of varying degrees of overpressure on pore structure characteristics of shale reservoirs, this study employed low-temperature carbon dioxide adsorption, nitrogen adsorption, and high-pressure mercury injection experiments to quantitatively characterize micropores, mesopores, and macropores in organic-rich shale samples from the Long 1^1 Sub-member, in Luzhou, Yongchuan, and Dazu areas. The results show that their total pore volume ranges from 23.80 to 43.70 mm^3/g, with an average of 32.45 mm^3/g, mainly contributed by mesopores. Contributions from micropores and macropores are comparatively lower (Figure 10). The average total pore volume of micropores is 1.98 mm^3/g, accounting for a proportion of 1.67%–9.88%, with an average of 6.24%. The average value of mesopores is 29.50 mm^3/g, accounting for a proportion of 84.03%–93.82%, with an average of 90.57%. The average value of macropores is 0.97 mm^3/g, accounting for a proportion of 1.60%–6.72%, with an average of 3.18%. The total specific surface area ranges from 23.05 to 47.05 m^2/g, with an average of 33.61 m^2/g, mainly contributed by mesopores and micropores, while macropores contribute less. The average total surface area of micropores is 6.79 mm^3/g, accounting for a proportion of 14.65%–28.27%, with an average of 20.15%. The average value of mesopores is 26.80 mm^3/g, accounting for a proportion of 71.70%–85.32%, with an average of 79.80%. The average value of macropores is 0.01 mm^3/g, accounting for a proportion of 0.02%–0.13%, with an average of 0.04% (Figure 10). However, with increasing pressure coefficients (Dazu < Yongchuan < Luzhou), there is no consistent pattern in the variation of total pore volume, total specific surface area, and their proportions in micropores, mesopores, and macropores. This suggests that the influence of increased overpressure (1.86–2.24) on shale pore volume and specific surface area is relatively limited.

On the basis of gas adsorption characteristics, this study utilized Ar-ion polishing SEM technique to systematically observe and continuously capture images of organic pores in samples from the Long 1^1 Sub-member in the study area (Figure 11). The pore size distribution and morphological features of organic pores were statistically analyzed by employing image processing software (Avizo 2019) for statistical analysis of the. SEM images provide better resolution and statistical significance for pores above 10 nm. The study documented a total of 8,767 organic pores, revealing a pore size range of 10–1,200 nm. The pore size distribution exhibits significant variations in different areas, with 10–50 nm pores accounting for 30.11%–65.79% of the total, 50–100 nm pores accounting for 23.71%–49.40%, and >100 nm pores accounting for 10.50%–45.92% (Figure 12A). The morphological features of the pores can be defined using the shape factor, and calculated through Eq. 1:

$$F = 4\pi S/C^2 \tag{1}$$

Where, S is pore cross-sectional area. C is pore cross-sectional perimeter Within the range of 0–1.0, the values closer to 1.0 indicate a more circular pore shape, and the values closer to 0 suggest increasingly irregular pore shapes. The statistical results indicate that organic pores with a shape factor greater than 0.7 constitute over 65% of the total, while those with a shape factor lower than 0.4 account for less than 9% (Figure 12B). This implies that the organic pores in the target layer of the study area are predominantly circular or subcircular, with fewer irregular and extremely irregular flattened angular pores.

The study further conducted a comparative analysis on the distribution characteristics of the organic pore sizes in samples from different overpressured zones. The results indicate that with an increase in the pressure coefficient, there is an overall trend of enlargement in the organic pores of shale (Figure 12A). In the Dazu area, which has the lowest shale pressure coefficient (1.86), the pore size distribution is concentrated in the 10–25 nm, 25–50 nm, and 50–75 nm intervals, with proportions reaching 19.32%, 46.47%, and 16.94%, respectively. In the Yongchuan area, with an intermediate shale pressure coefficient (2.04), the pores slightly enlarge, concentrating in the 25–50 nm, 50–75 nm, and 75–100 nm intervals, with proportions of 37.11%, 34.99%, and 14.41%, respectively. In the Luzhou area, with the highest shale pressure coefficient (2.24), there is a significant enlargement of pores. The proportions of pores in the 10–50 nm and 50–100 nm intervals decrease to 30.11% and 23.97%, respectively, while the proportion of pores exceeding 100 nm significantly increases to 45.92%. These features suggest that in deep shale formations with widespread strong overpressure, higher degrees of overpressure make greater contribute to the development of organic pores larger than 100 nm. Conversely, decreasing overpressure results in the compression of organic pores, leading to an overall reduction in pore size to less than 100 nm, particularly in the 10–50 nm range. Many scholars agree that overpressure has a protective effect on the preservation of shale organic pores (Liu, 2015; Wang et al., 2019; Wang et al., 2023b), but there are few studies on the effect of overpressure on organic macropores in Longmaxi Formation.

6.3 Porosity characteristics

In the research related to the middle and shallow Longmaxi Formation shale reservoirs in the southern and southeastern Sichuan Basin, the helium porosity is commonly observed to range between 2% and 8%. The variations in porosity are jointly controlled by the formation pressure coefficient and the lithofacies (Nguyen et al., 2013; Li et al., 2017; Nabawy et al., 2022). On one hand, as the pressure conditions transit from normal pressure to overpressure, the compaction effect from overlying strata gradually diminishes, maintaining the porosity of shale reservoir at relatively high levels. On the other hand, the compressive strength of siliceous shale, clayey shale, and silty shale decreases

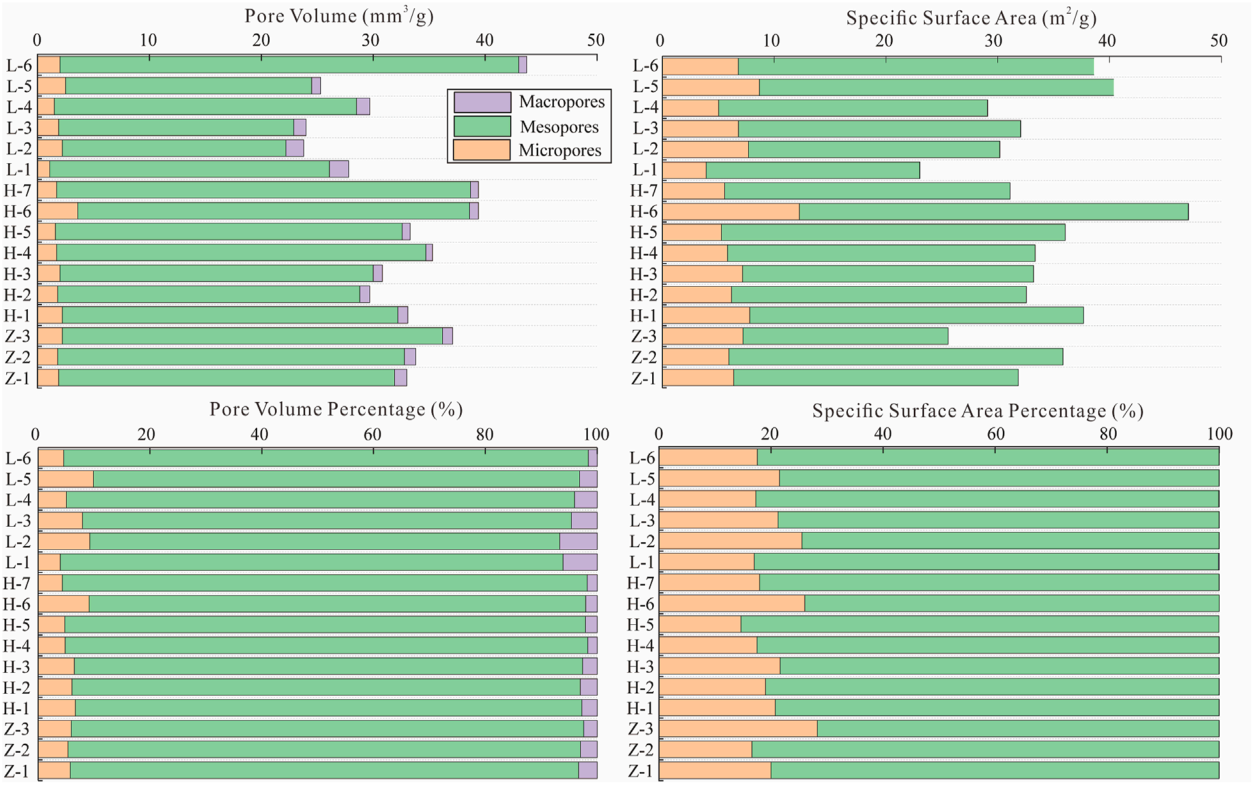

FIGURE 10
Pore structure characteristics of organic-rich shale in the deep long 1^1 sub-member (Z-1 to Z-3: samples from well Z202 in Dazu area, pressure coefficient 1.86; H-1 to H-7: samples from well H202 in Yongchuan area, pressure coefficient 2.04; L-1 to L-6: samples from well L202 in Luzhou Area, pressure coefficient 2.24).

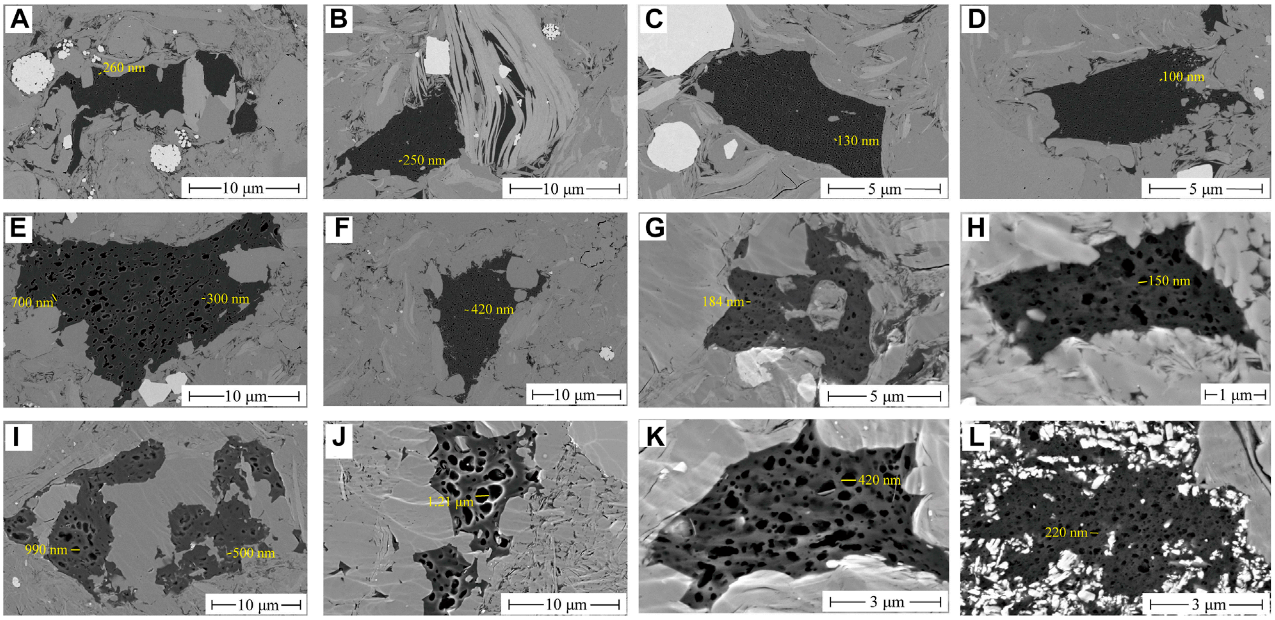

FIGURE 11
Morphological characteristics of organic pores in organic-rich shale of the deep long 1^1 sub-member in Southern Sichuan **(A–D)** Dazu area; **(E–H)** Yongchuan area; **(I–L)** Luzhou area.

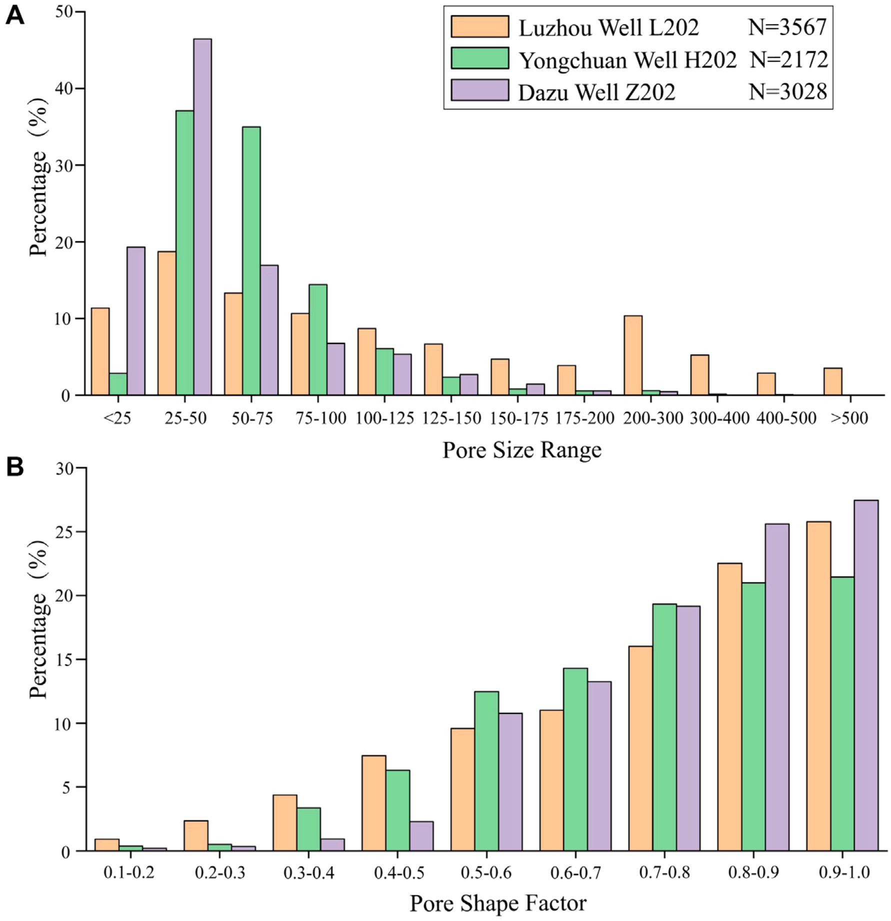

FIGURE 12
Comparative analysis of organic pore size range **(A)** and shape factor **(B)** in the deep long 1^1 sub-member, Southern Sichuan Area. 'N' represents the total number of statistically analyzed organic pores.

in sequence. Under the same normal pressure conditions, siliceous shale exhibits lower compaction, thereby retaining higher porosity and better reservoir capacity. In contrast, clayey shale and silty shale undergo significant compaction and alteration, leading to a substantial reduction in porosity and reservoir capacity, and they ultimately transform into cap rocks. When normal pressure shifts to overpressure, the compaction intensity of clayey shale significantly decreases, resulting in a notable increase in porosity, sometimes even surpassing that of siliceous shale. Consequently, clayey shale may also exhibit favorable reservoir capacity under overpressure conditions.

The analysis of helium porosity in the deep Long 1^1 Sub-member shale of the southern Sichuan region, encompassing 188 core samples from three areas, reveals a distribution range similar to that of the middle and shallow layers, ranging from 1% to 8%. The variation in porosity also exhibits a strong correlation with the formation pressure coefficient and the lithofacies. With increasing pressure coefficient, the distribution range and average of the shale porosity gradually increase (see Figure 13A). In the Dazu area, where the pressure coefficient is the lowest (1.86), the porosity ranges from 1.17% to 5.57%, with an average porosity of only 3.18%. In the Yongchuan area, with a moderate pressure coefficient (2.04), the porosity varies from 2.58% to 7.78%, and the average porosity is 4.28%. The Luzhou area, with the highest pressure coefficient (2.24), exhibits porosity distribution ranging from 3.21% to 7.73%, and an impressive average porosity of 5.03%. Evaluation standards for middle and shallow Longmaxi Formation shale reservoirs often categorize those with porosity exceeding 5.0 as Class I reservoirs (Zhao et al., 2016). When this criterion is applied to assess the deep shale porosity, only 4.35% of the Dazu area samples meet Class I reservoir standards, while the Yongchuan area reaches 23.21%, and the Luzhou area attains the highest, at 45.35%. These results show that, in deep shale formations characterized by prevalent strong overpressure, enhanced overpressure helps counteract the compaction effect, improving porosity and enhancing reservoir quality. Additionally, both siliceous shale and clayey shale are developed in the Long 1^1 Sub-member in Well H202 of the Yongchuan area. Analysis indicates that siliceous shale has a porosity distribution ranging from 2.58% to 5.42%, with an average value of 3.86%, and only 6.06% exceeding 5.0. In contrast, clayey shale exhibits relatively superior porosity characteristics, with a distribution between 2.76% and 7.78%, an average value of 4.90%, and an impressive 47.83% exceeding 5.0 (see Figure 13B). This observation indicates that the development of overpressure significantly improves the porosity and quality of clayey shale.

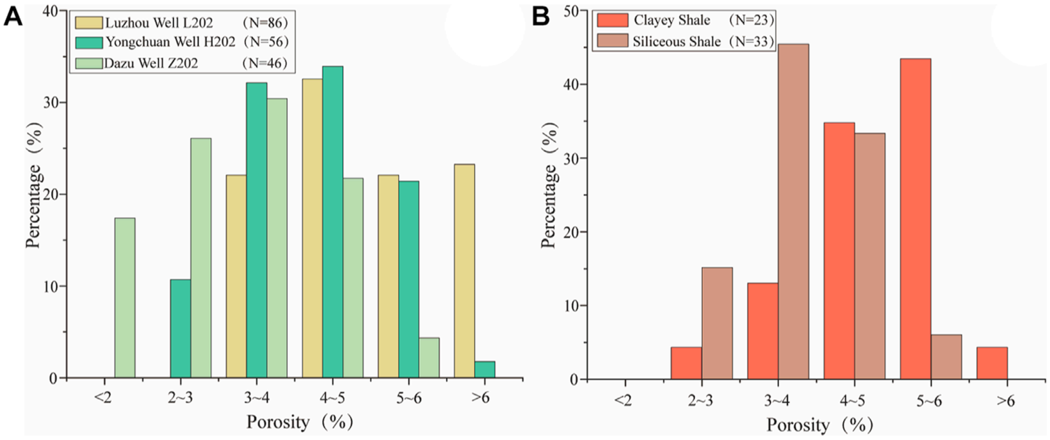

FIGURE 13
Comparison of pore volume in the long 1^1 sub-member shale reservoir under different pressure coefficients **(A)**, and comparison of pore volume in the Clayey and Siliceous shales in the Yongchuan area under overpressure conditions **(B)**.

7 Conclusion

A detailed study on the formation mechanisms, evolutionary patterns, and the controlling effects on reservoir pore characteristics of strong overpressure have been made and the following conclusions can be reached.

The well log curve combination method and the sonic velocity-density crossplot method, sediment burial and hydrocarbon generation history, fluid inclusion paleo-pressure recovery together confirm that hydrocarbon generation expansion is the dominant mechanism for the formation of strong overpressure in the deep Longmaxi Formation shale gas reservoir. Overpressured intervals exhibit the log characteristics of significantly increase of acoustic travel time and high resistivity, and significantly decrease of density.

In the long-term subsidence process, the deep Longmaxi Formation shale gas reservoir has been influenced by the effects of kerogen oil generation and retained oil cracking into gas. It experienced three stages: normal pressure (Silurian to Early Triassic), overpressure (Early Triassic to Early Jurassic), and strong overpressure (Early Jurassic to Late Cretaceous), with corresponding pressure coefficients of 1.08–1.09, 1.51–1.56, and 2.09–2.12, respectively. During the late strong uplift process, the initially formed overpressure underwent some adjustment due to temperature reduction and gas escape. Fluid pressure gradually decreased from 138.93–140.99 MPa to 70.72–94.86 MPa. The pressure coefficient showed a change trend of decreasing first and then increasing, and currently strong overpressure is still maintained.

Different degrees of strong overpressure have a significant control on the porosity and pore structure of the shale gas reservoir. Higher pressure coefficients contribute to maintaining high porosity and organic macropores. Deep Wufeng-Longmaxi Formation shale exhibits differences in morphological characteristics, structure and connectivity of organic matter pores. This study provides valuable insights for the further understanding and evaluation of deep shale gas reservoirs.

Data availability statement

The original contributions presented in the study are included in the article/supplementary material, further inquiries can be directed to the corresponding authors.

Author contributions

SS: Project administration, Funding acquisition, Writing–review and editing, Writing–original draft, Investigation, Data curation, Conceptualization. ZS: Supervision, Writing–review and editing, Writing–original draft, Funding acquisition, Formal Analysis, Data curation, Conceptualization. DD: Methodology, Investigation, Funding acquisition, Writing–original draft. WB: Writing–original draft, Resources, Project administration, Data curation, Conceptualization. LW: Writing–original draft, Visualization, Methodology, Formal Analysis, Conceptualization. JY: Writing–review and editing, Validation, Supervision, Investigation, Data curation. JQ: Writing–review and editing, Visualization, Supervision, Methodology.

Funding

The author(s) declare that financial support was received for the research, authorship, and/or publication of this article. This research was supported by Science and Technology Management Department of PetroChina “Research on Stress Change, Tectonic Activation and Possible Induced Earthquake Mechanism in Shale Gas Development Zones of South Sichuan” (No. 2022DJ8004).

Conflict of interest

Authors SS, ZS, DD, and WB were employed by PetroChina.

The remaining authors declare that the research was conducted in the absence of any commercial or financial relationships that could be construed as a potential conflict of interest.

Publisher's note

References

Bowers, G. L. (1995). Pore pressure estimation from velocity data: accounting for overpressure mechanisms besides undercompaction. *SPE Drill. Complet.* 10, 89–95. doi:10.2118/27488-pa

Bowers, G. L. (2002). Detecting high overpressure. *Lead. Edge* 21, 174–177. doi:10.1190/1.1452608

Chen, Z. P., Liang, X., Zhang, J. H., Wang, G. C., Liu, C., Li, Z. F., et al. (2016). Genesis analysis of shale reservoir overpressure of Longmaxi Formation in Zhaotong demonstration area, dianqianbei depression. *Nat. Gas. Geosci.* 27 (3), 442–448. (In Chinese with English abstract). doi:10.11764/j.issn.1672-1926.2016.03.0442

Clarkson, C. R., Solano, N., Bustin, R. M., Bustin, A. M. M., Chalmers, G. R. L., He, L., et al. (2013). Pore structure characterization of North American shale gas reservoirs using USANS/SANS, gas adsorption, and mercury intrusion. *FUEL* 103, 606–616. doi:10.1016/j.fuel.2012.06.119

Conner, O. S., Swarbrick, R. E., and Lahann, R. (2011). Geologically driven pore fluid pressure models and their implications for petroleum exploration. Introduction to thematic set. *Geofluids* 11, 343–348. doi:10.1111/j.1468-8123.2011.00354.x

Deng, J. X., Wang, C. Y., Zhao, Q., Guo, W., Tang, G. Y., and Zhao, J. G. (2021). Depositional and diagenetic controls on macroscopic acoustic and geomechanical behaviors in Wufeng-Longmaxi Formation shale. *Front. Earth Sci.* 9, 617831. doi:10.3389/feart.2021.617831

Duan, Z., Moller, N., and Weare, J. H. (1992). An equation of state for the CH4-CO2-H2O system: I. Pure systems from 0 to 1000°C and 0 to 8000 bar. *Geochimica Cosmochimica Acta* 56, 2605–2617. doi:10.1016/0016-7037(92)90347-l

Fan, C. H., Li, H., Qin, Q. R., He, S., and Zhong, C. (2020). Geological conditions and exploration potential of shale gas reservoir in Wufeng and Longmaxi Formation of southeastern Sichuan Basin, China. *J. Petroleum Sci. Eng.* 191, 107138. doi:10.1016/j.petrol.2020.107138

Fan, C. H., Nie, S., Li, H., Radwan, A. E., Pan, Q. C., Shi, X. C., et al. (2024). Quantitative prediction and spatial analysis of structural fractures in deep shale gas reservoirs within complex structural zones: a case study of the Longmaxi Formation in the Luzhou area. southern Sichuan Basin, China. *J. Asian Earth Sci.* 263, 106025. doi:10.1016/j.jseaes.2024.106025

Gao, G., Gang, W. Z., Fan, H. C., Sang, T. Y., and Nie, C. Q. (2008). Research advances for the genesis of abnormally low formation pressure in petroliferous basins. *Nat. Gas. Geosci.* 19 (3), 311–315. (In Chinese with English abstract).

Gao, J., Zhang, J. K., He, S., Zhao, J. X., He, Z. L., Wo, Y. J., et al. (2019). Overpressure generation and evolution in Lower Paleozoic gas shales of the Jiaoshiba region, China: implications for shale gas accumulation. *Mar. Petroleum Geol.* 102, 844–859. doi:10.1016/j.marpetgeo.2019.01.032

Guo, X. S., Hu, D. F., Li, Y. P., Wei, Z. H., Wei, X. F., and Liu, Z. J. (2017). Geological factors controlling shale gas enrichment and high production in Fuling shale gas field. *Petroleum Explor. Dev.* 44 (4), 513–523. doi:10.1016/s1876-3804(17)30060-5

Guo, X. S., Li, Y. P., Borjigen, T., Wang, Q., Yuan, T., Shen, B. J., et al. (2020). Hydrocarbon generation and storage mechanisms of deep-water shelf shales of ordovician Wufeng Formation–silurian Longmaxi Formation in Sichuan Basin, China. *Petroleum Explor. Dev.* 47 (1), 204–213. doi:10.1016/s1876-3804(20)60019-2

Guo, X. W., He, S., Zheng, L. J., and Wu, Z. Z. (2011). A quantitative model for the overpressure caused by oil generation and its influence factors. *Acta Pet. Sin.* 32 (4), 637–644. (In Chinese with English abstract). doi:10.7623/syxb201104011

He, X. P., He, G. S., Gao, Y. Q., Zhang, P. X., Lu, S. F., and Wan, J. Y. (2019). Geological characteristics and enrichment laws of normal-pressure shale gas in the basin-margin transition zone of SE Chongqing. *Nat. Gas. Ind. B* 6 (4), 333–346. doi:10.1016/j.ngib.2018.12.003

Jin, Z. J., and Nie, H. K. (2022). Evolution history of overpressured and normally pressured shale gas reservoirs in Wufeng Formation–Longmaxi Formation, Sichuan Basin, China: an analysis from the perspective of source and seal coupling mechanism. *Energy and Fuels* 36, 10870–10885. doi:10.1021/acs.energyfuels.2c01925

Katahara, K. W., and Corrigan, J. D. (2004). Effect of gas on poroelastic response to burial or erosion. *AAPG Mem.* 76, 73–78.

Li, H. (2023a). Coordinated development of shale gas benefit exploitation and ecological environmental conservation in China: a mini review. *Front. Ecol. Evol.* 11, 1232395. doi:10.3389/fevo.2023.1232395

Li, H. (2023b). Deciphering the formation period and geological implications of shale tectonic fractures: a mini review and forward-looking perspectives. *Front. Energy Res.* 11, 1320366. doi:10.3389/fenrg.2023.1320366

Li, J., Li, H., Yang, C., Wu, Y. J., Gao, Z., and Jiang, S. L. (2022). Geological characteristics and controlling factors of deep shale gas enrichment of the Wufeng-Longmaxi Formation in the southern Sichuan Basin, China. *Lithosphere* 12, 4737801. doi:10.2113/2022/4737801

Li, J., Tang, Y., Wu, T., Zhao, J. Z., Wu, H. Y., Wu, W. T., et al. (2020). Overpressure origin and its effects on petroleum accumulation in the conglomerate oil province in Mahu Sag, Junggar Basin, NW China. *Petroleum Explor. Dev.* 47 (4), 726–739. doi:10.1016/s1876-3804(20)60088-x

Li, S. J., Yuan, Y. S., Sun, W., Sun, D. S., and Jin, Z. J. (2016). The formation and destroyment mechanism of shale gas overpressure and its main controlling factors in Silurian of Sichuan Basin. *Nat. Gas. Geosci.* 27 (5), 924–931. (In Chinese with English abstract). doi:10.11764/j.issn.1672-1926.2016.05.0924

Li, Z., Wu, S. H., Xia, D. L., Zhang, X. F., and Huang, M. (2017). Diagenetic alterations and reservoir heterogeneity within the depositional facies: a case study from distributary-channel belt sandstone of Upper Triassic Yanchang Formation reservoirs (Ordos Basin, China). *Mar. Petroleum Geol.* 86, 950–971. doi:10.1016/j.marpetgeo.2017.07.002

Liu, B., Lue, Y. F., Zhao, R., Tu, X. X., Guo, X. B., and Shen, Y. (2012). Formation overpressure and shale oil enrichment in the shale system of lucaogou Formation, mahu sag, sangtanghu basin, NW China. *Petroleum Explor. Dev.* 39 (6), 699–705. doi:10.1016/S1876-3804(12)60099-8

Liu, D. D., Guo, J., Pan, Z. K., Zhao, W., Du, F. P., Chen, Y., et al. (2021). Overpressure evolution process in shale gas reservoir: evidence from the fluid inclusions in the fractures of Wufeng Formation-Longmaxi Formation in the southern Sichuan Basin. *Nat. Gas. Ind.* 41 (9), 12–22. (In Chinese with English abstract).

Liu, H. L., Zhang, J. H., and Ji, Y. B. (2022). The controlling effect of kerogen type of shale on asphaltene nanopore and its exploration significance. *Unconv. Oil gas* 9 (3), 1–10. (In Chinese with English abstract). doi:10.19901/j.fcgyq.2022.03.01

Liu, R. B. (2015). Analyses of influences on shale reservoirs of Wufeng-Longmaxi Formation by overpressure in the south-eastern part of Sichuan Basin. *Acta Sedimentol. Sin.* 33 (4), 817–827. doi:10.14027/j.cnki.cjxb.2015.04.020

Liu, S. G., Ye, Y. H., Ran, B., Jiang, L., Li, Z. W., Li, J. X., et al. (2020). Evolution and implications of shale pore structure characteristics under different preservation conditions. *Reserv. Eval. Dev.* 10 (5), 1–11. (In Chinese with English abstract).

Ma, D. W., Qiu, N. S., and Xu, W. (2011). Analysis on mechanism of abnormal low pressure in Sulige gas field, Ordos Basin. *Chin. J. Geol.* 46 (4), 1055–1067.

Ma, X. H., Xie, J., Yong, R., and Zhu, Y. Q. (2020). Geological characteristics and high production control factors of shale gas reservoirs in Silurian Longmaxi Formation, southern Sichuan Basin, SW China. *Petroleum Explor. Dev.* 47, 901–915. doi:10.1016/s1876-3804(20)60105-7

Meng, Q. F., Hooker, J., and Cartwright, J. (2017). Early overpressuring in organic-rich shales during burial: evidence from fibrous calcite veins in the Lower Jurassic Shales-with-BEEF Member in the Wessex Basin, UK. *J. Geol. Soc.* 174, 869–882. doi:10.1144/jgs2016-146

Nabawy, B. S., Lashin, A. A., and Barakat, M. K. (2022). Implementation of lithofacies and microfacies types on reservoir quality and heterogeneity of the late cretaceous upper bahariya member in the shurouk field, shoushan basin, north western desert, Egypt. *J. Asian Earth Sci.* 224, 105014. doi:10.1016/j.jseaes.2021.105014

Nguyen, B. T. T., Jones, S. J., Goulty, N. R., Middleton, A. J., Grant, N., Ferguson, A., et al. (2013). The role of fluid pressure and diagenetic cements for porosity preservation in Triassic fluvial reservoirs of the Central Graben, North Sea. *AAPG Bull.* 97 (8), 1273–1302. doi:10.1306/01151311163

Nie, H. K., He, Z. L., Wang, R. Y., Zhang, G. R., Chen, Q., Li, D. H., et al. (2020). Temperature and origin of fluid inclusions in shale veins of Wufeng–Longmaxi Formations, Sichuan Basin, South China: implications for shale gas preservation and enrichment. *J. Petroleum Sci. Eng.* 193, 107329. doi:10.1016/j.petrol.2020.107329

Pan, L., Xiao, X. M., Tian, H., Zhou, Q., Chen, J., Li, T. F., et al. (2015). A preliminary study on the characterization and controlling factors of porosity and pore structure of the Permian shales in Lower Yangtze region, Eastern China. *Int. J. Coal Geol.* 146, 68–78. doi:10.1016/j.coal.2015.05.005

Qiu, N. S., Liu, Y. F., Liu, W., and Jia, J. K. (2020). Quantitative reconstruction of formation paleo-pressure in sedimentary basins and case studies. *Sci. China Earth Sci.* 50 (6), 793–806. doi:10.1007/s11430-019-9556-8

Rui, Y., Wang, C. J., Zhang, F. S., Yao, Y. B., Guo, N., and Zheng, R. (2021). Characterization of micro-pore throats in the shale gas reservoirs of Zhaotong national shale gas demonstration area. *Nat. Gas. Ind.* 41 (1), 78–85. (In Chinese with English abstract).

Shan, S. C., Wu, Y. Z., Fu, Y. K., and Zhou, P. H. (2021). Shear mechanical properties of anchored rock mass under impact load. *J. Min. Strata Control Eng.* 3 (4), 22–24. doi:10.13532/j.jmsce.cn10-1638/td.20211014.001

Shi, X. W., Wu, W., Hu, H. Y., Liu, L. H., Zhu, Y. Q., Pan, R. F., et al. (2023). The whole apertures of deeply buried Wufeng-Longmaxi Formation shale and their controlling factors in Luzhou district, Sichuan Basin. *Earth Sci.* 48 (1), 158–172. (In Chinese with English abstract).

Sun, C. X., Nie, H. K., Dang, W., Chen, Q., Zhang, G. R., Li, W. P., et al. (2021). Shale gas exploration and development in China: current status, geological challenges, and future directions. *Energy and Fuels* 35 (8), 6359–6379. doi:10.1021/acs.energyfuels.0c04131

Tang, J. M., He, J. H., Wei, L. M., Li, Y., Deng, H. C., Li, R. X., et al. (2023). Pressure evolution of deep shale gas reservoirs in Wufeng-Longmaxi formation, Lintanchang area, southeast Sichuan Basin and its geological significance. *Petroleum Geol. Exp.* 45 (4), 739–750. (In Chinese with English abstract).

Tang, L., Song, Y., Zhao, Z. G., Jiang, Z. X., Jiang, S., Chen, X. Z., et al. (2022). Origin and evolution of overpressure in shale gas reservoirs of the upper ordovician Wufeng Formation–lower silurian Longmaxi Formation in the Sichuan Basin. *Nat. Gas. Ind.* 42 (10), 37–53. (In Chinese with English abstract).

Tingay, M. R. P., Morley, C. K., Laird, A., Limpornpipat, O., Krisadasima, K., Pabchanda, S., et al. (2013). Evidence for overpressure generation by kerogen-to-gas maturation in the northern Malay Basin. *AAPG Bull.* 97, 639–672. doi:10.1306/09041212032

Wang, Z. L., Sun, M. L., Geng, P., Song, Y., and Li, Y. H. (2003). The development features and formation mechanisms of abnormal high formation pressure in southern Junggar region. *Petroleum Explor. Dev.* 30(1), 32–34. doi:10.3321/j.issn:1000-0747.2003.01.008

Wang, Y. M., Dong, D. Z., Li, X. J., Huang, J. L., Wang, S. F., and Wu, W. (2015). Stratigraphic sequence and sedimentary characteristics of lower silurian Longmaxi Formation in Sichuan Basin and its peripheral areas. *Nat. Gas. Ind. B* 2(2), 222–232. doi:10.1016/j.ngib.2015.07.014

Wang, Q., Wei, X. F., Wei, F. B., Yan, J. H., and Wan, L. (2019). Overpressure in shale gas reservoirs of Wufeng-Longmaxi formations, Fuling area, southeastern Sichuan Basin. *Petroleum Geol. Exp.* 41(3), 333–340.

Wang, J., Wang, X. L., Yang, P., Wu, Z. Y., Li, G., McGoogan, J. M., et al. (2021). Coronavirus disease 2019 outbreak in Beijing's Xinfadi Market, China: a modeling study to inform future resurgence response. *J. Min. Strata Control Eng.* 3 (3), 62–70. doi:10.1186/s40249-021-00843-2

Wang, L., Liu, B., Bai, L. H., Ostadhassan, M., Gentzis, T., Wang, B. Y., et al. (2023a). Maceral evolution of lacustrine shale and its effects on the development of organic pores during low mature to high mature stage: a case study from the Qingshankou Formation in northern Songliao Basin, northeast China. *Petroleum Sci.* 20 (5), 2709–2725. doi:10.1016/j.petsci.2023.08.025

Wang, Z. H., Gao, P., Feng, Y., Liu, R. B., and Yuan, T. (2023b). Pore structure characteristics and main controlling factors of the ultra-deep shales of the Wufeng-Longmaxi Formation in Eastern Sichuan Basin. *J. Northeast Petroleum Univ.* 479(1), 57–69.

Wang, Y. M., Wang, H. Y., Qiu, Z., Shen, J. J., Zhang, Q., Zhang, L. F., et al. (2022a). Basic characteristics of key interfaces in upper ordovician Wufeng Formation – lower silurian Longmaxi Formation in Sichuan Basin and its periphery, SW China. *Petroleum Explor. Dev.* 49(1), 37–51. doi:10.1016/s1876-3804(22)60003-x

Wang, X. L., Hu, W. X., Qiu, Y., Liu, Y. F., Jia, D., Cao, J., et al. (2022b). Fluid inclusion evidence for extreme overpressure induced by gas generation in sedimentary basins. *Geology* 50(7), 765–770. doi:10.1130/g49848.1

Wang, P. W., Chen, X., Liu, Z. B., Du, W., Li, D. H., Jin, W. J., et al. (2022c). Reservoir pressure prediction for marine organic-rich shale: a case study of the Upper Ordovician Wufeng-Lower Silurian Longmaxi shale in Fuling shale gas field, NE Sichuan Basin. *Oil Gas Geol.* 43 (2), 467–476. (In Chinese with English abstract).

Wei, L., Sun, S. S., Dong, D. Z., Shi, Z. S., Yin, J., Zhang, S. D., et al. (2021). Petrographic characterization and maceral controls on porosity in overmature marine shales: examples from ordovician-silurian shales in China and the U.S. *Geofluids* 2021, 1–31. doi:10.1155/2021/5582262

Wei, L., Yin, J., Li, J. S., Zhang, K., Li, C. Z., and Cheng, X. (2022). Mechanism and controlling factors on methane yields catalytically generated from low-mature source rocks at low temperatures (60–140°C) in laboratory and sedimentary basins. *Front. Earth Sci.* 10, 889302. doi:10.3389/feart.2022.889302

Wu, A. B., Cao, J., and Zhang, J. K. (2021). Bedding-parallel calcite veins indicate hydrocarbon–water–rock interactions in the over-mature Longmaxi shales, Sichuan Basin. *Mar. Petroleum Geol.* 133, 105303. doi:10.1016/j.marpetgeo.2021.105303

Wu, J., Chen, X. Z., Liu, W. P., Wu, W., Gao, Y., Luo, C., et al. (2022). Fluid activity and pressure evolution process of wufeng-longmaxi shales, southern Sichuan Basin. *Earth Sci.* 47 (2), 518–531. (In Chinese with English abstract).

Xie, G. L., Liu, S. G., Jiao, K., Deng, B., Ye, Y. H., Sun, W., et al. (2021). Organic pores in deep shale controlled by macerals: classification and pore characteristics of organic matter components in Wufeng Formation-Longmaxi Formation of the Sichuan Basin. *Nat. Gas. Ind.* 41 (9), 23–34. (In Chinese with English abstract). doi:10.3787/j.issn.1000-0976.2021.09.003

Xu, H., Zhang, J. F., Jia, C. Z., Tang, D. Z., and Yin, W. (2010). Influence of tectonic uplift-erosion on formation pressure. *Petroleum Sci.* 7, 477–484. doi:10.1007/s12182-010-0094-9

Yang, F., Ning, Z. F., Wang, Q., Zhang, R., and Krooss, B. M. (2016). Pore structure characteristics of lower Silurian shales in the southern Sichuan Basin, China: insights to pore development and gas storage mechanism. *Int. J. Coal Geol.* 156, 12–24. doi:10.1016/j.coal.2015.12.015

Yang, Y., Guo, D. M., Cheng, L. L., Yuan, S. B., Cheng, G. Y., and Yin, S. L. (2023). Organic carbon content correction and overpressure genesis analysis for overpressure strata of Dongying Formation in Bozhong Sag. *Mud Logging Eng.* 34 (2), 103–108.

Yi, J. Z., Bao, H. Y., Zheng, A. W., Zhang, B. Q., Shu, Z. G., Li, J. Q., et al. (2019). Main factors controlling marine shale gas enrichment and high-yield wells in South China: a case study of the Fuling shale gas field. *Mar. Petroleum Geol.* 103, 114–125. doi:10.1016/j.marpetgeo.2019.01.024

Yin, J., Wei, L., Sun, S. S., Shi, Z. S., Dong, D. Z., and Gao, Z. Y. (2003). Overpressure generation and evolution in deep Longmaxi Formation Shale reservoir in southern Sichuan Basin: influences on pore development. *Energies* 16, 2533. doi:10.3390/en16062533

Yuan, Y. S., Fang, Z. X., He, X. P., Li, S. J., Peng, Y. M., and Long, S. X. (2020). Normal pressure formation mechanism of Longmaxi shale gas in Pengshui and its adjacent areas. *Reserv. Eval. Dev.* 10 (1), 9–16. (In Chinese with English abstract). doi:10.13809/j.cnki.cn32-1825/te.2020.01.002

Zeng, L. B., Lyu, W. Y., Li, J., Zhu, L. F., Weng, J. Q., Yue, F., et al. (2016). Natural fractures and their influence on shale gas enrichment in Sichuan Basin, China. *J. Nat. Gas Sci. Eng.* 30, 1–9. doi:10.1016/j.jngse.2015.11.048

Zhang, J. L., Qiao, S. H., Lu, W. J., Hu, Q. C., Chen, S. G., and Liu, Y. (2016). An equation for determining methane densities in fluid inclusions with Raman shifts. *J. Geochem. Explor.* 171, 20–28. doi:10.1016/j.gexplo.2015.12.003

Zhang, S. C., He, K., Hu, G. Y., Mi, J. K., Ma, Q. S., Liu, K. Y., et al. (2018). Unique chemical and isotopic characteristics and origins of natural gases in the Paleozoic marine formations in the Sichuan Basin, SW China: isotope fractionation of deep and high mature carbonate reservoir gases. *Mar. Petroleum Geol.* 89, 68–82. doi:10.1016/j.marpetgeo.2017.02.010

Zhao, J. H., Jin, Z. J., Hu, Q. H., Liu, K. Y., Jin, Z. K., Hu, Z. Q., et al. (2018). Mineral composition and seal condition implicated in pore structure development of organic-rich Longmaxi shales, Sichuan Basin, China. *Mar. Petroleum Geol.* 98, 507–522. doi:10.1016/j.marpetgeo.2018.09.009

Zhao, J. Z., Li, J., and Xu, Z. Y. (2017). Advances in the origin of overpressures in sedimentary basins. *Acta Pet. Sin.* 38 (9), 973–998. (In Chinese with English abstract).

Zhao, S. X., Yang, Y. M., Zhang, J., Wang, L. S., Wang, X. Z., Luo, C., et al. (2016). Micro-layers division and fine reservoirs contrast of lower silurian Longmaxi Formation shale, Sichuan Basin, SW China. *Nat. Gas. Geosci.* 27 (3), 470–487.

Zheng, J., Liu, H. B., Wang, K. K., and You, Z. J. (2017). A new capillary pressure model for fractal porous media using percolation theory. *J. Nat. Gas Sci. Eng.* 41, 7–16. doi:10.1016/j.jngse.2017.02.033

frontiers | Frontiers in Environmental Science

TYPE Original Research
PUBLISHED 06 May 2024
DOI 10.3389/fenvs.2024.1391445

OPEN ACCESS

EDITED BY
Hu Li,
Southwest Petroleum University, China

REVIEWED BY
Yifan Gu,
Southwest Petroleum University, China
Lei Gong,
Northeast Petroleum University, China

*CORRESPONDENCE
Dongxi Liu,
✉ llddxx@163.com

RECEIVED 25 February 2024
ACCEPTED 22 April 2024
PUBLISHED 06 May 2024

CITATION
Yang X, Yin H, Yang L, Xu L, Chen J, Liu D, Jiang C and Jiang Z (2024), Evolution of black shale sedimentary environment and its impact on organic matter content and mineral composition: a case study from Wufeng-Longmaxi Formation in Southern and Eastern Sichuan Basin.
Front. Environ. Sci. 12:1391445.
doi: 10.3389/fenvs.2024.1391445

Evolution of black shale sedimentary environment and its impact on organic matter content and mineral composition: a case study from Wufeng-Longmaxi Formation in Southern and Eastern Sichuan Basin

Xinrui Yang[1,2], Hongchuan Yin[1,2], Licheng Yang[1,2], Liangjun Xu[1,2], Junyu Chen[1,2], Dongxi Liu[1,2]*, Chan Jiang[3] and Zengzheng Jiang[4]

[1]Chongqing Gas Field, PetroChina Southwest Oil and Gas Field Company, Chongqing, China, [2]Collaborative Innovation Center of Shale Gas Resources and Environment, Chengdu, China, [3]Exploration Division, PetroChina Southwest Oil and Gas Field Company, Chengdu, China, [4]Sichuan Geotech Science and Technology Ltd., Chengdu, China

Due to global geological events and differences in regional sedimentary environments, marine shale reservoirs of Wufeng-Longmaxi Formation in Eastern and Southern Sichuan Basin exhibit significant heterogeneity in organic matter content and mineral composition. In order to reveal the influence of paleoenvironment evolution on reservoir heterogeneity, key geochemical indicators of elements were used to reconstruct the sedimentary environment of marine shale in Eastern and Southern Sichuan Basin. The influence mechanism of paleoenvironment on organic matter content and mineral components was also explored. The results indicate that the Wufeng-Longmaxi Formation in the Southern and Eastern Sichuan Basin can be divided into two third-order sequences (Sq 1 and Sq 2). Each third-order sequence is divided into a transgressive system tract (TST) and a highstand system tract (HST). The average TOC content in the Eastern Sichuan Basin is the highest during the TST1 period with reaching 4.2%, while reached its maximum at 3.9% during the TST2 period in the Southern Sichuan Basin. Due to the influence of high paleo-productivity, the organic matter accumulation and quartz content in the eastern Sichuan region were higher than those in the southern Sichuan region from the TST1 to the middle TST2 period. However, the organic matter accumulation and quartz content in the late TST2 period were lower than those in the southern Sichuan region due to the dilution of terrestrial debris. During the HST2 period, due to the influence of higher paleo-productivity, clay adsorption and preservation condition, the TOC content in the eastern Sichuan region slightly increased in the early stage. At the same time, the marine shale in the southern Sichuan region has a high content of quartz minerals and a low content of clay minerals due to strong weathering intensity and input of coarse-grained debris (silt-size quartz).

KEYWORDS

sedimentary environment, paleoenvironmental condition, ordovician-silurian, organic matter, black shale, Sichuan Basin

Introduction

The Ordovician-Silurian black shale in the Sichuan Basin is a key contributor to China's breakthrough in shale gas production (Chen et al., 2017a; Jiang et al., 2022). At present, a gas field with an annual production capacity of 20 billion cubic meters has been built in the Ordovician-Silurian black shale with a burial depth of less than 3500 m in the Changning, Weiyuan, and Zhaotong areas in the Southern Sichuan Basin (Chen et al., 2017b; Cai et al., 2023; Fan et al., 2024). However, the Ordovician-Silurian black shale with a burial depth of less than 3500 m only accounts for 16% of the shale gas geological resources (Fu et al., 2019; Dong D. et al., 2022; Li, 2023a), and deep (burial depth>3500 m) marine shale gas is clearly the main driver of future production growth (Fu et al., 2021a; Fu et al., 2021b; Li, 2023b). Due to the influence of regional tectonic environment, there are significant differences in the sedimentary thickness and paleoenvironment of the Ordovician-Silurian shale in the Eastern and Southern Sichuan Basin (Guo et al., 2019; Jin et al., 2020; Huang et al., 2023). The degree of organic matter enrichment and mineral composition in the shale will also vary. Therefore, restoring the paleo-sedimentary evolution process of shale and clarifying its impact on the distribution of organic-rich intervals and mineral components is of great significance for promoting efficient shale gas exploration in the Eastern and Southern Sichuan Basin (Jiang et al., 2018; Wei et al., 2021).

The Ordovician-Silurian black shale was formed during a turbulent geological history transition period (Katian to Aeronian), influenced by global and regional geological events such as volcanic eruptions, orogeny, glaciation, biotic extinction, and global sea-level changes (Wu et al., 2018; Dong T. et al., 2022; Li et al., 2022). In order to analyze the evolutionary characteristics of the black shale sedimentary environment, logging curve cycles and distribution of biogenic graptolite zones were used to establish a sequence stratigraphic framework (Wang et al., 2019), which is helpful for the comparative study of subsequent paleoenvironmental evolution. The sedimentary paleoenvironment mainly affects the enrichment of organic matter by controlling the accumulation process of organic matter (primary productivity, redox conditions, terrestrial input, sedimentation rate), and has produced three commonly used models: the "preservation model", the "productivity model", and the most common "multi-factor control model" (Armstrong et al., 2009; Berry, 2010; Zhao et al., 2019). In addition, the indirect impact of global or regional geological events on shale sedimentation and organic matter enrichment should not be ignored (Song et al., 2023; Xie et al., 2023). The control effect of sedimentary paleoenvironment on shale mineral composition can be summarized in three aspects: firstly, it affects the development of biogenic siliceous quartz or biogenic calcareous carbonate (Cai et al., 2022; Chen et al., 2023); secondly, it directly affects the type and content of mineral components in sedimentary areas through input from source and terrestrial sources (Wu et al., 2022); The third is the enrichment of minerals such as authigenic carbonates and pyrite (Liu et al., 2019; Chen et al., 2023).

Compared with the abundant achievements of previous studies, sedimentary and elemental geochemistry methods have been applied in this study, and multiple paleo-environmental factors such as paleo-redox, paleo-productivity, terrestrial debris input, and paleo-climate have been discussed. Under the isochronous stratigraphic framework, the evolutionary characteristics of paleoenvironment in the Eastern and Southern Sichuan Basin have been identified, and the shale sedimentation process has been restored. Meanwhile, the impact of sedimentation on the distribution and mineral composition of organic-rich shale has been discussed. The research results provide a reference basis for predicting and optimizing the "sweet spot area" of shale gas in the Sichuan Basin.

Geological setting

The Ordovician-Silurian black shale was formed during the extinction of the South China Basin and the formation of the South China Orogenic Belt. After the Middle Ordovician, the Huaxia block collided with the Yangtze block. As the main part of the Upper Yangtze Plate, the Sichuan Basin and its periphery have entered the stage of foreland basin evolution (Zhang et al., 2020; Wang et al., 2022). During the Late Ordovician to Early Silurian, with the strengthening of compression from southeast to northwest, the paleo-uplift in the Central Sichuan Basin and the paleo-uplift in the Central Guizhou-Xuefeng outside the basin alternately uplifted (Jiang et al., 2019; Jiang et al., 2020), resulting in the distribution of the foreland depression belt in the "three uplifts sandwiched with one depression" (Zhang et al., 2022), and the sedimentary facies and provenance regions were controlled by the peripheral uplifts. Between the paleo-uplifts, there are semi-closed stagnant basins, forming two depression centers in Southern and Eastern Sichuan (Figure 1). The northern part of southern Sichuan is located at the southern edge of the Leshan-Longnvsi paleo-uplift, while the southern part is blocked by the Central Guizhou paleo-uplift and the Xuefeng paleo-land, forming a semi-enclosed basin with strong water limitations. Due to its proximity to the Central Guizhou paleo-uplift, terrigenous debris material may mainly come from the foreland uplift zone, including the Central Guizhou paleo-uplift, as well as the Xuefeng paleo-uplift, with limited supply from the Central Sichuan paleo-uplift. The western part of the Eastern Sichuan Basin is closer to the paleo-uplift in Central Sichuan, and the northern edge is

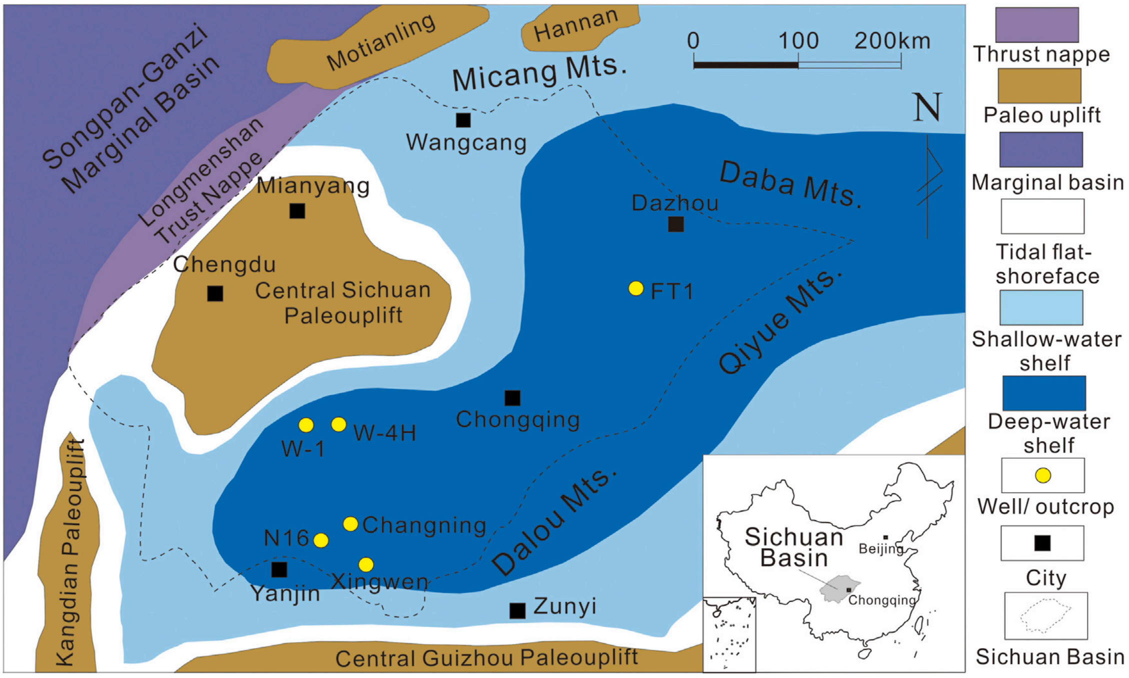

FIGURE 1
Geological background and location of studied wells during the sedimentary period of the Wufeng Formation-Longmaxi Formation in the Sichuan Basin and its surrounding areas.

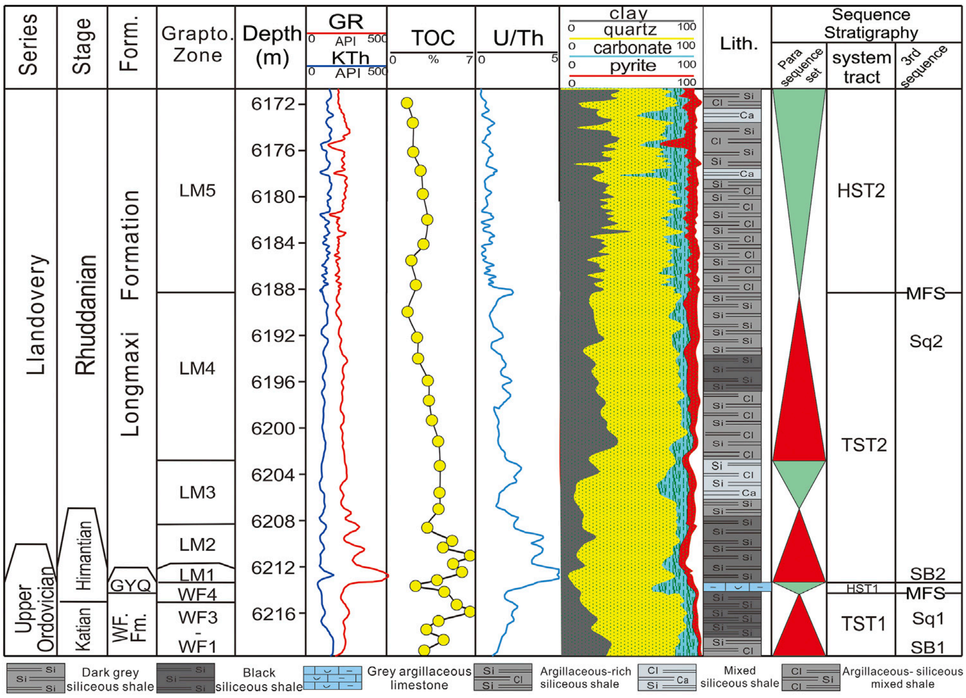

FIGURE 2
Sequence division of shale interval in Well FT-16. TST, Transgressive system tract; HST, Highstand system tract; SB, Sequence boundary, MFS, Maximum flooding surface).

closer to the Qinling Ocean, which is connected to external water bodies. The limitations of its water bodies are weak, and its provenance may mainly come from the paleo-uplift in Central Sichuan Basin.

The black shale of the Ordovician Wufeng Formation-Silurian Longmaxi Formation is widely developed in southern China, and belongs to the Katian Stage-Aeronian Stage in terms of geological age (Brenchley et al., 2003). Except for the top 1–2 m of the Ordovician Wufeng Formation, which is composed of shell limestone or carbonate-bearing mudstone rich in Hirnantian fauna fossils, all other intervals are shale rich in graptolite fossils.

The shale intervals studied in this article are Katian Stage, Hirnantian Stage, and Rhuddanian Stage, which correspond to the WF1-WF3, WF4-LM1, and LM2-LM5 of the graptolite biozone, respectively (Chen X. et al., 2017; Huang et al., 2023). By combining lithology, logging response, and graptolite biozone, and referring to previous classification schemes (Figure 2), the shale interval can be divided into two third-order sequences (Sq 1 and Sq 2) and four individual tracts (TST1, HST1, TST2, and HST2). The Wufeng Formation and GYQ Member form the first third-order sequence (Sq 1), with black siliceous shale and argillaceous-rich siliceous shale (TST1) from the Wufeng Formation at the bottom and argillaceous limestone (HST1) from the GYQ Member above. The lower part of the Longmaxi Formation is the second third-order sequence (Sq 2), with the bottom boundary in contact with the overlying siliceous shale through transgression. The black siliceous shale in the lower part of the Longmaxi Formation is divided into TST2, and the second maximum flood surface (MFS) has been identified, representing the transition from deep water to shallow water and the beginning of HST2.

Samples and methods

Sample collection and measurement

34 shale samples from the Well FT-1 in the Eastern Sichuan Basin. When selecting samples, non matrix parts such as calcite veins were avoided. All samples were measured for TOC value, mineral composition, and bulk element content. Previous studies have obtained detailed elemental geochemical data for marine shale intervals in the southern Sichuan region (Huang et al., 2023), laying the foundation for comparing paleoclimate, terrestrial debris input, paleoproductivity, and bottom water redox conditions with the Eastern Sichuan Basin. In addition, to clarify the provenance and tectonic background of the Southern Sichuan Basin, this study cited 59 sets of data obtained from the Changning and Xingwen Outcrop of the Southern Sichuan Basin (Li, 2017). The XRD experiment was completed at the China Petroleum Exploration and Development Research Institute and measured using a Japanese Nikkei X-ray diffractometer. The determination of element content was completed within Kehui Testing (Tianjin) Technology Co., Ltd. Trace and rare earth elements were determined using ICP-MS (Jena PQ MS) high-resolution plasma spectrometer, and the main elements were determined using XRF-1800 wavelength dispersive X-ray fluorescence spectrometer. The TOC test was conducted using the CS744-MHPC carbon and sulfur analyzer at the unconventional experimental center of CNOOC Energy Development.

Indicator calculation and calibration

The enrichment factor (X_{EF}) can eliminate the influence of terrestrial debris and distinguish the degree of element enrichment in sediments. The calculation formula is: $X_{EF}=(X/Al)_{sample}/(X/Al)_{standard.}$

X and Al represent the element content and Al content in the sediments, respectively, and “standard” refers to the standardized background values. PAAS (Taylor and McLennan, 1985) and UCC (McLennan, 2001) are frequently used for normalization in previous studies, and we select the PAAS in this study. Al is not easily affected by weathering or post-depositional alteration, so the ratio of element content to Al is used to remove the influence of terrestrial debris.

The calculation method for trace element content in sediments of non detrital origin (biogenic or authigene enrichment) is as follows: $E_{org}/E_{bio} = E_{sample}\text{-}Al_{sample}\times(E/Al)_{detr}$

E_{bio} represents the organic or biological portion of an element that exceeds a specific terrestrial input standard. The portion exceeding the average shale is calculated by subtracting the estimated fragment source from the total element content in the sample. E_{sample} and Al_{sample} represent the abundance of a certain element and Al element in the shale sample, respectively, and (E/Al) detr is the ratio of the average abundance of E and Al under specific standards (McLennan, 2001). In practical research, PAAS is often used to estimate terrestrial inputs, with commonly used $(Si/Al)_{detrs}$ and $(Ba/Al)_{detrs}$ of 3.11 and 0.0075, respectively (Taylor, 1964; Wedepohl, 1971; Dymond et al., 1992). The Chemical Weathering Index (CIA) is commonly used to determine the degree of paleoweathering. In order to exclude the influence of oxides from non terrestrial debris sources, it is necessary to calibrate the CaO content to obtain the CaO content (CaO*) in silicates.

$$CIA_{corr} = \left[Al_2O_3/\left(Al_2O_3 + CaO^{*} + Na_2O + K_2O_{corr}\right)\right] \times 100\%$$

$$CaO_{(adjust)} = CaO\text{-}\left(P_2O_5 \times 10/3\right)$$

In the formula, if $CaO_{(adjust)} > Na_2O$, then $CaO^{*} = Na_2O$; If $CaO_{(adjust)} < Na_2O$, then $CaO^{*} = CaO_{(adjust)}$. The above units are all in mol

Results

Shale lithofacies and mineral compositions

Using the ternary diagram of mineral composition, shale lithofacies types were classified (Figure 3A). The results indicate that in the Southern Sichuan Basin, the main types are argillaceous-rich siliceous shale, mixed siliceous shale, and siliceous-argillaceous mixed shale. The Eastern Sichuan Basin is mainly composed of siliceous shale, argillaceous-rich siliceous shale, and mixed siliceous shale. The mineral components of different system tracts in the Eastern and Southern Sichuan Basin are shown in Table 1. The carbonate mineral content of marine shale in Southern Sichuan is generally higher than that in Eastern Sichuan, while the feldspar content is generally lower than that in Eastern Sichuan. The content of clay minerals and pyrite in marine shale in the Southern Sichuan Basin is higher in TST1, and lower in other periods than in the Eastern Sichuan Basin. However, the content of quartz is only higher

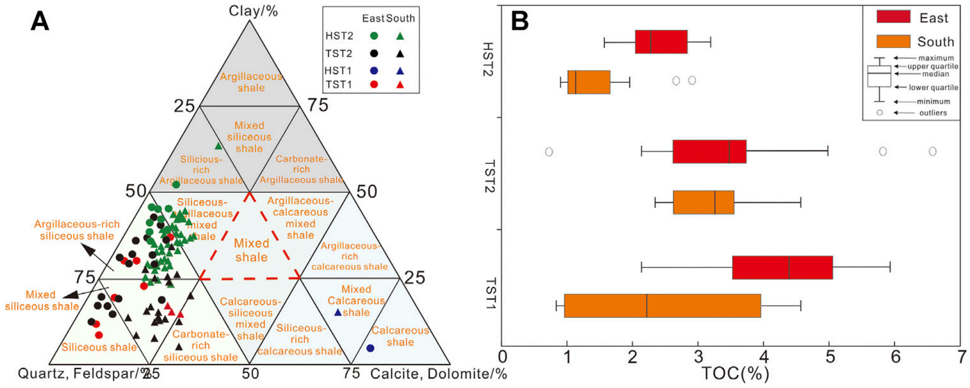

FIGURE 3
Mineral composition in different system tracts **(A)** and box-plots of TOC range **(B)** in Eastern and Southern Sichuan Basin. Total organic carbon (TOC) content range.

TABLE 1 Mineral composition characteristics and TOC content of shales in different area and system tracts (Well N16, W1, W4-H in southern Sichuan from Huang et al., 2023).

Well	N16, W1, W4-H				FT-1			
Systems tract	TST1	HST1	TST2	HST2	TST1	HST1	TST2	HST2
Sample number	17	2	30	81	7	1	17	9
Quartz (%)	38.7	10.3	51.9	37.1	59.2	12.9	53.5	32.4
K-feldspar (%)	1.8	0.0	0.7	1.7	0.7	0.0	0.7	0.1
Plagioclase (%)	3.4	0.7	5.0	7.1	7.3	0.4	8.4	11.2
Calcite (%)	15.8	78.6	12.9	10.3	6.5	68.1	4.4	6.7
Dolomite (%)	7.7	2.1	5.8	3.9	2.3	4.6	2.5	5.3
Clay (%)	29.3	8.0	20.3	37.4	20.8	8.9	25.1	40.7
Pyrite (%)	3.5	0.5	3.5	2.4	3.1	5.1	4.6	3.3
TOC (%)	2.2	0.7	3.9	1.5	4.2	2.3	4.0	2.4
Carbonate minerals (%)	23.5	80.6	18.7	14.2	8.8	72.7	6.9	12.0

in HST2 period, and lower in other periods than in the Eastern Sichuan Basin.

From the characteristics of changes in different system tracts, from TST1 to HST2, the clay content in the Eastern Sichuan Basin continued to increase while the quartz content continued to decrease. However, the quartz content in the Southern Sichuan Basin shows a trend of first increasing and then decreasing, while the change in clay content is opposite. In addition, the TST1 and TST2 sedimentary samples in the Eastern Sichuan are more dispersed, indicating that the mineral composition during this period is complex and varied. It is possible that the study area is close to the provenance region, and the water is relatively shallow, making it more susceptible to the influence of sea-level changes and terrestrial inputs.

The TOC content of marine shale in the eastern Sichuan region is generally higher than that in the southern Sichuan region (Figure 3B), with the highest average TOC value during the TST1 period, reaching 4.2%. The average TOC value of marine shale in the southern Sichuan region reached its maximum during the TST2 period, at 3.9%. From TST1 to HST2 period, the average TOC in Southern Sichuan showed a trend of first increasing and then decreasing, while the average TOC in Eastern Sichuan continued to decrease. The maximum variation in TOC during the TST1 period in Eastern and Southern Sichuan may be related to rapid changes in the paleoenvironment or frequent geological events during this period.

Paleo-environmental conditions and differences

Paleo-redox condition

The redox level is a key factor in the preservation of organic matter. Redox-sensitive elements Mo, U, V, Cr, Ni, and Co are commonly used for the reconstruction of bottom water redox environments (Tribovillard et al., 2006). These elements are

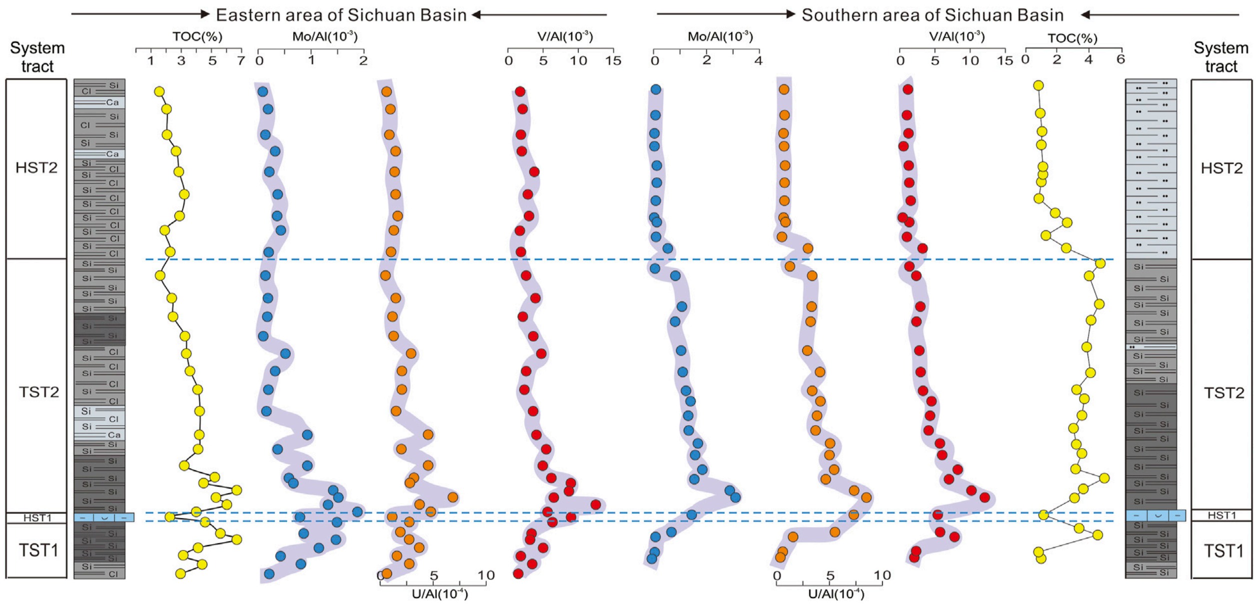

FIGURE 4
Comparison of common paleo-redox indicators in different system tracts in Eastern and Southern Sichuan Basin.

prone to precipitate in sediment under reducing conditions, while they are prone to dissolve in water under oxidizing conditions (Tribovillard et al., 2012). In order to weaken the dilution effect of terrestrial debris, the ratio of element content to Al content was used as an indicator in this study. Figure 4 shows that the reducibility of bottom water in both Eastern and Southern Sichuan increases rapidly during the TST1 period, and reaches its maximum in the early TST2 period before slowly decreasing.

In order to quantify redox levels in different system tracts and areas, the cross-plots of Th/U-Ni/Co, V/Cr-V/(V + Ni), and Mo$_{EF}$-U$_{EF}$ were applied (Figures 5A–C). In the Southern Sichuan Basin, the data points of TST1 reflect a gradual transition from suboxic to anoxic, sample distribution area and data points exhibit stronger reduction of anoxic bottom water in the early TST2 with some intervals even reaching the euxinic condition, while gradually decrease to weak anoxic or suboxic conditions during the late TST2 and HST2 period. The TST1 period in the Eastern Sichuan Basin is mainly in a anoxic environment, and the bottom water reduction in the TST2 period is also reach its maximum, manifested by some data points being close to the euxinic zone. In addition, a small number of data points in the late TST2 period near the suboxic zone may be related to a decrease in the degree of late reduction. The reducing conditions in HST2 continued slowly decreasing after a slight increase, and it remained mainly in a weak anoxic environment in the early period.

Mo/TOC can be used to determine the degree of limitation of water bodies (Algeo and Lyons, 2006; Algeo and Tribovillard, 2009). The data points of TST1 in the Southern Sichuan Basin are relatively scattered (Figure 5D), suggesting an unstable degree of water limitation. Considering the continuous uplift of the surrounding paleo-uplift and the anoxic bottom water environment, the Mo/TOC ratio is mostly less than 4.5, suggesting that the water is strongly restricted in the middle and later periods of TST1. The Mo/TOC enclosed area in the TST2 period is widely distributed, but mainly in a moderately enclosed environment. Its changing characteristics also indicate that as the degree of transgression increases, the degree of restriction gradually strengthens. During the HST2 period, the reducibility of water decreased, but the degree of restriction was significantly reduced in the early suboxic-anoxic environment. The TST1 data points in the Eastern Sichuan are relatively scattered, with Mo/TOC values mostly greater than 4.5, indicating moderate restriction. The limitations of TST2 period have changed significantly, with some data points having Mo/TOC ratios less than 4.5, indicating a significant increase in restriction during certain intervals, but still in a moderately restricted environment. The degree of restriction in HST2 period decreases with the decrease of sea-level.

Paleo-productivity condition

The content of Ba, Cu, Ni, and Zn is closely related to the life activities of marine organisms, Ba$_{bio}$ and (Cu + Ni + Zn)/Al can serve as reliable indicators for evaluating productivity. The Ba$_{bio}$ in Figure 6 reflects that the paleo-productivity of the Eastern Sichuan showed an overall increasing trend during the TST1-HST2 period, while showed an increasing trend during the TST1-TST2 period and a decreasing trend in HST2 in Southern Sichuan. The (Cu + Ni + Zn)/Al indicates that the paleo-productivity of these two regions all showed a unimodal distribution, increasing during the TST1 period and reaching its peak in the early TST2 period before slowly decreasing.

The Si$_{excess}$ in the black shale of the Wufeng-Longmaxi Formation is related to biogenic origin, so this study also used Si$_{excess}$ to evaluate paleo-productivity (Cai et al., 2022). There is a negative correlation between Si$_{excess}$ and Al (Figure 5E), ruling out the possibility of terrestrial input and clay mineral transformation to form Si$_{excess}$. The positive correlation between K$_2$O-Rb (Figure 5F)

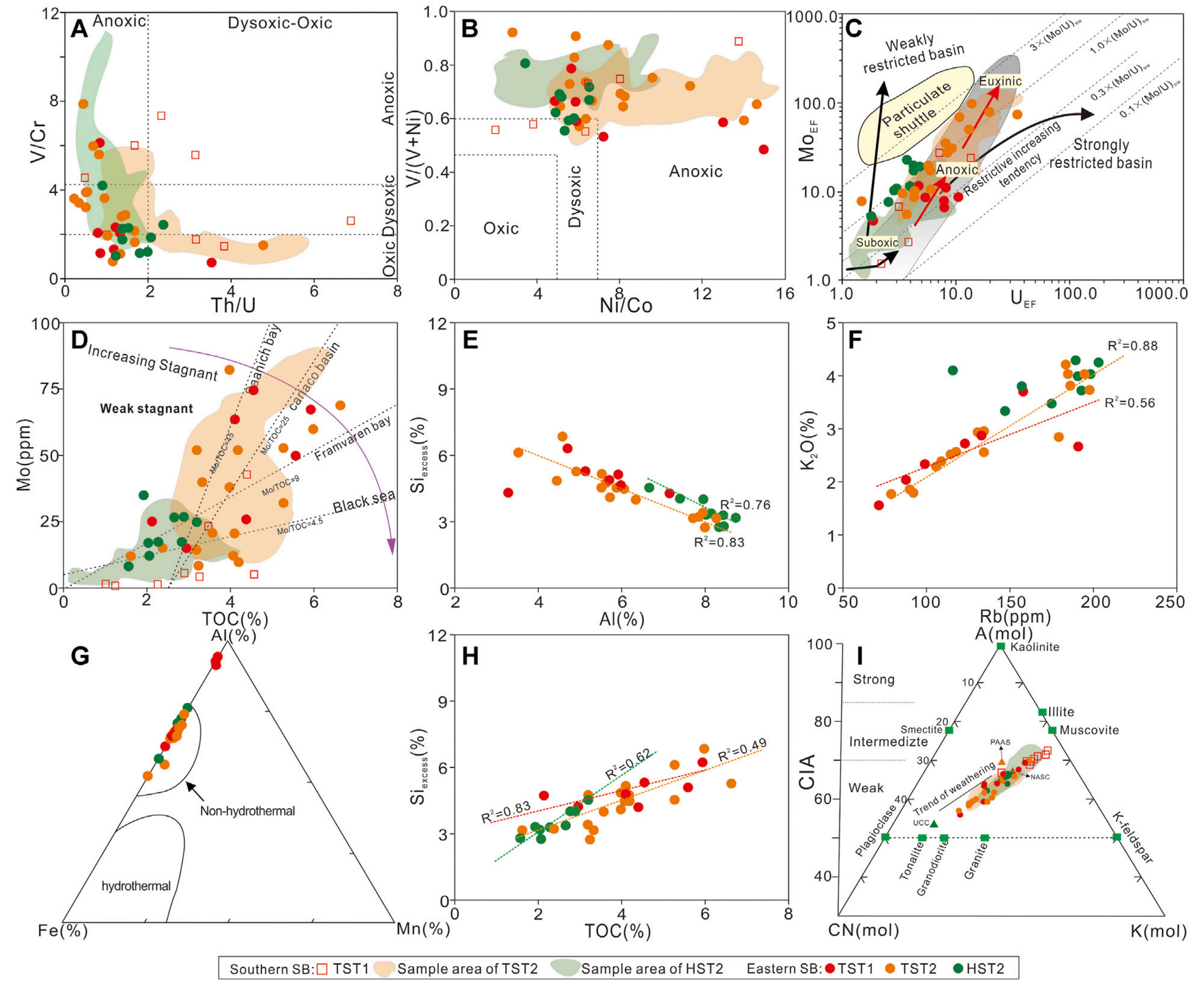

FIGURE 5
Correlation diagrams of geochemical elements. **(A–D)** Paleo-redox conditions discrimination diagrams. **(E–H)** Silicon source discrimination diagrams. **(I)**)A-CN-K diagrams, reflecting weathering intensity and provenance.

indicates that the source of Si_{excess} is not related to magmatic activity or provenances (Floyd and Leveridge, 1987; Huang et al., 2023). The Al-Fe-Mn data (Figure 5G) points all fall into the non hydrothermal zone, indicating that the formation of Si_{excess} is independent of hydrothermal activity (Xie et al., 2021). The positive correlation between Si_{excess} and TOC (Figure 5H) confirms its correlation with biological sources. The Si_{excess} in the Eastern Sichuan generally maintains a trend of first increasing and then decreasing from TST1 to HST2, with the highest paleo-productivity values distributed in the early period of TST2. The peak of the total amount of Si_{excess} in Southern Sichuan also appeared in the early period of TST2 and gradually decreased thereafter.

Due to the fact that Ba_{bio} is not suitable for oxygen-deficient environment, while the mass fraction of Cu, Zn and Ni is closely related to the sedimentation amount of organic matter, and suitable for reducing environment. As a result, there is no consistency in these indicators, and the reasons for this can be fully explained. As for Ba_{bio}, sulfate reduction reactions are common on the surface and/or bottom of sediments in anoxic and euxinic environments during TST1 and HST2, barium sulfate is a latent source of sulfate, and partial dissolve when sulfate supply is insufficient, resulting in a lower content of barium and estimated productivity. On account of the eastern and southern Sichuan are mainly in a relatively reducing environment, (Cu + Ni + Zn)/Al is basically consistent with the change trend of Si_{excess}, and that also verified the accuracy of the our results. In conclusion, the paleo-productivity during the depositional process of TST1 and TST2 in Eastern and Southern Sichuan is stronger than that of HST2. In addition, the Si_{excess} and (Cu + Ni + Zn)/Al in Eastern Sichuan is generally higher than that in Southern Sichuan, reflecting the strong paleo-productivity of the former.

Terrestrial input condition

Al and Zr elements are not easily migrated during transportation and can be used as effective indicators to characterize the intensity of terrestrial inputs. Al is mainly came from fine-grained aluminosilicate clay minerals, while Zr existed in clay minerals and coarse-grained minerals (quartz, zircon, etc.). Therefore, Zr/Al ratio is considered an

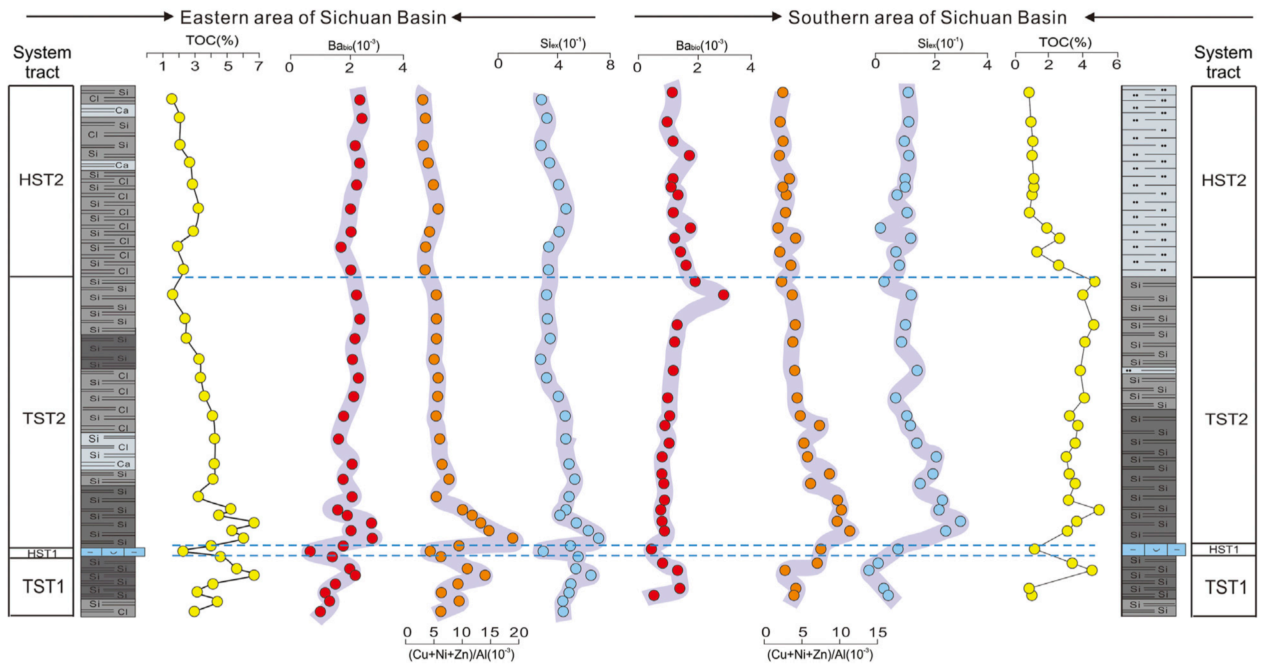

FIGURE 6
Comparison of common paleo-productivity indicators in different system tracts in Eastern and Southern Sichuan Basin.

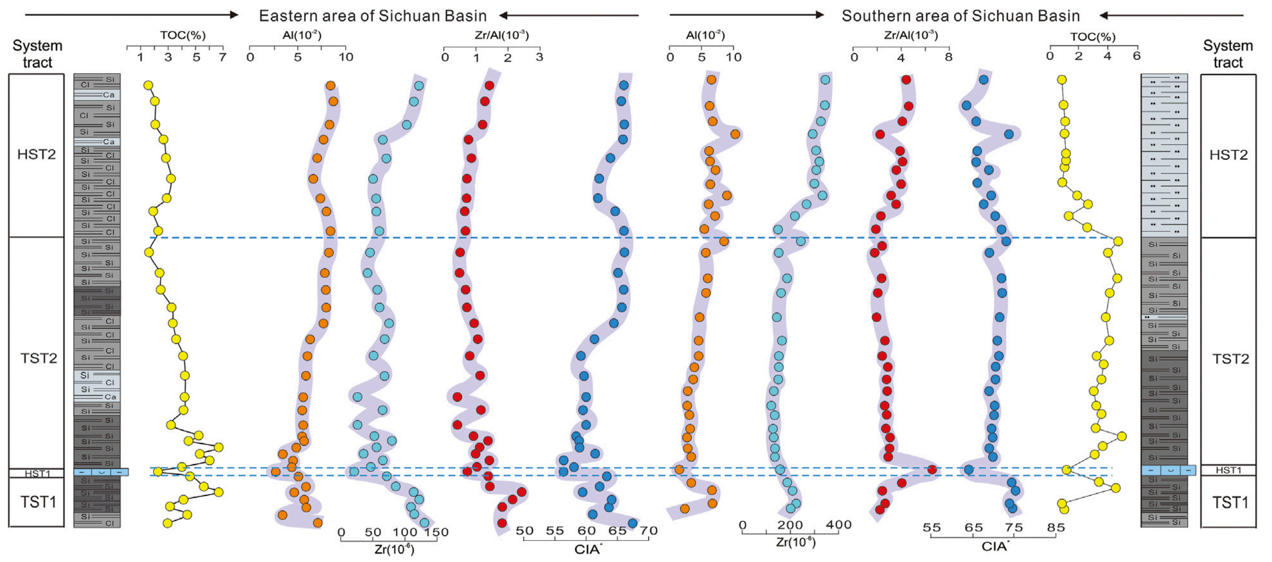

FIGURE 7
Comparison of common terrigenous clastic input and paleo weathering indicators in different system tracts in Eastern and Southern Sichuan Basin.

effective indicator for quantifying the content of coarse-grained debris in terrestrial inputs. Figure 7 indicates that the changes of Zr and Al curves in the Eastern and Southern Sichuan is basically consistent, showing a gradually decreasing trend during the TST1 and HST1 periods, as well as a fluctuating trend during the TST2 period and a gradually increasing trend during the HST2 period. The variation of Al contents suggest that the total terrestrial input amount of fine-grained clay minerals are similar in this two areas. However, the overall Zr content in the Eastern Sichuan Basin is lower than that in the Southern Sichuan Basin, especially during the TST1 period with rapid drop. This indicates that the difference in terrestrial input during the TST1-HST2 sedimentary period between the Eastern and the Southern Sichuan is relatively small, but the input of coarse-grained debris is lower during the TST1-HST2 period in the eastern Sichuan.

Zr/Al in the Eastern Sichuan showed a slow decreasing trend during TST1-TST2, suggesting a significant slowdown in the input rate of coarse-grained debris, while a slow increase during HST2 indicates a faster input of coarse-grained debris. However, the input of coarse-grained debris in the Southern Sichuan Basin remained relatively stable during the TST1-TST2 period, while it also increased during the HST2 period. In addition, the Zr/Al values in the Southern Sichuan were higher than those in the Eastern Sichuan at all periods. This indicates that the input rate of coarse-grained debris in the sediment composition of the Eastern Sichuan Basin is generally lower than that of the Southern Sichuan, especially during the HST2 deposition period. During this period, the development of more mixed shale in the Southern Sichuan can be confirmed. In the late period of TST2, the Al content gradually increased, but the Zr/Al and Zr contents showed a slow decreasing trend in fluctuation. It is speculated that the rapid increase of fine-grained clay minerals diluted coarse-grained minerals, resulting in an opposite trend of Al, Zr, and Zr/Al.

Paleoclimate and weathering intensity

The Chemical Index of Alteration (CIA) is often used to indicate the climate and physical and chemical weathering intensity of provenance region. CIA values of 50–65, 65–80, and 80–100 indicate weak, moderate, and strong weathering degrees, respectively, and correspond to cold-dry, warm-humid, and hot-humid conditions, respectively. In the actual application process, in order to exclude the influence of CaO content that is bound to non-silicates, the corrected CIA (CIA *) was calculated in this study (Figure 5I; Figure 7). The lowest values of CIA * in both the Eastern and Southern Sichuan appear at HST1, indicating a global temperature drop during the Hirantanian glaciation. The CIA * value in the Southern Sichuan ranges from 60 to 75. During the TST1-HST2 period, the CIA * gradually decreases and undergoes an evolutionary process from a hot warm climate to a cold dry climate. The cooling event caused by the Hirnantian glaciation is still accompanied by the early deposition of TST2. The CIA * value in the Eastern Sichuan ranges from 55 to 70 during the TST1 to early TST2 period and a CIA * value below 65, indicating a cold-dry environment. In the late period of TST2, the CIA * was greater than 65, and the climate gradually became mild. However, in the early period of HST2, it experienced a short-term cold-dry climate, and in the late period, it eventually transformed into a warm-humid climate. Compared with the input indicators of terrestrial debris, it is found that the low degree of chemical weathering in the cold climate during the TST tract is an important reason for the low input of terrestrial debris.

Provenance condition and tectonic setting

The differences in provenances not only affect the mineral compositions, but also control the types of terrestrial nutrient inputs. The Al_2O_3/TiO_2 ratio of fine-grained sediments can effectively identify the type of source rocks. Due to the low solubility of Al and Ti oxides at low temperatures, their proportion in sedimentary rocks is very close to that of the source rock. The distribution of Al_2O_3/TiO_2 ratio in<8, 8–21, and>21 indicates basic, neutral, and acidic igneous rocks, respectively. The provenance in the southern Sichuan region is mainly a mixture of neutral and acidic igneous rocks (Figure 8A). The provenance in the Eastern Sichuan is a mixture of neutral and acidic igneous rocks in TST1, while in TST2 and HST2 are neutral igneous rocks. The weathering trend of the A-CN-K diagram (Figure 5I) further confirm that the provenance in Southern Sichuan during TST1-TST2 tends to be neutral igneous rocks, and HST2 tends to be acidic igneous rocks. While in the Eastern Sichuan during the TST1-HST2 tends to have neutral granodiorite sources.

Due to the higher content of compatible element Sc and lower content of incompatible elements Zr and Th in basic rocks compared to acidic rocks, and the relatively constant abundance of Sc, Zr, and Th during weathering, the Zr/Sc-Th/Sc ratio can be used for source rock type analysis. Figure 8B shows that the distribution plots in the Southern Sichuan is more towards the upper right than that in the Eastern Sichuan, also suggesting that there are more acidic igneous components in provenance. In addition, in the provenance composition of the Eastern Sichuan, TST1 period is more acidic and HST2 period is more neutral.

Roser and Korsch (1986) proposed that the $K_2O/Na_2O\text{-}SiO_2$ cross-plot can be effectively used to distinguish the tectonic environment of fine-grained sedimentary rocks. The results indicate that the Eastern Sichuan is in an active continental margin environment during the early Wufeng period. The data points of the Longmaxi period in the Southern Sichuan are close to the active continental margin, but the data points of the Wufeng period are closer to the passive continental margin environment (Figure 8C). Stable rare earth and trace element combinations (such as La, Th, Sc, Zr, etc.) can also be used to analyze and determine tectonic backgrounds. The Th-Sc-Zr/10 and Th-Co-Zr/10 diagrams established by Bhatia and Crook (1986) were applied for background analysis (Figures 8D, E). The analysis reveals that the majority of data points fall within or proximate to the active continental margin zone, while a minimal proportion is dispersed in the continental island arc zone. Compared to Eastern Sichuan, the Southern Sichuan exhibits a stronger correlation to the active continental margin region. The sedimentary tectonic context in both regions remains steady from Late Ordovician to Early Silurian, characterized predominantly by an active continental margin setting.

Impact of paleo-environmental condition on OM accumulation and mineral composition

The formation of black shale from the Ordovician Wufeng Formation to the Silurian Longmaxi Formation in the Sichuan Basin is the result of geological events and various paleo-environmental conditions. Under this influence, there are significant differences in TOC and mineral composition between different system tracts in the Eastern and Southern Sichuan (Figure 9).

TST 1 period

Under the influence of the Caledonian Movement, the Xuefeng paleo-uplift and the Central Sichuan underwater uplift rapidly uplifted. In the Kaitian stage, relative sea-level rise led to a transformation of the sedimentary environment from an early open platform to a restricted basin, initiating the deposition of black shale in the Wufeng Formation.

In the early TST 1 period, intense tectonic uplift enhanced the intensity of detrital input. The separation effect of paleo-uplift and relative sea-level rise leads to an increasing reduction and restriction

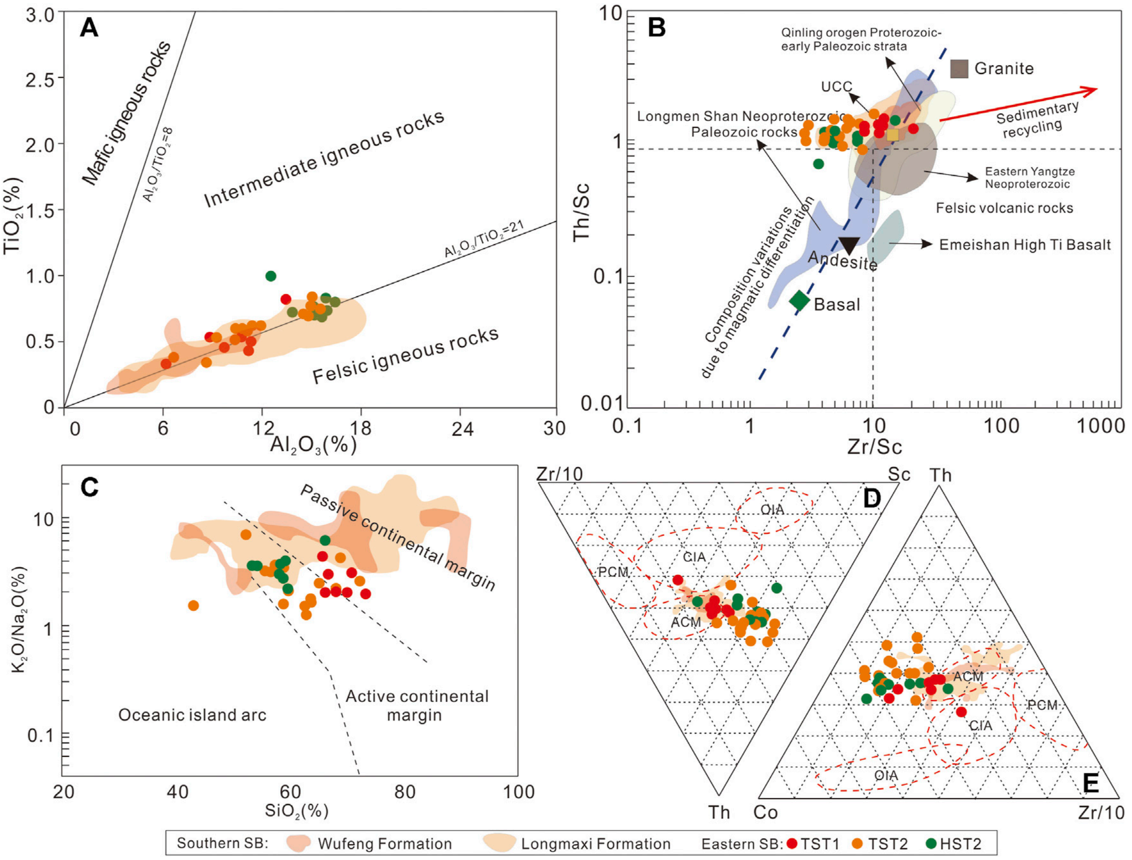

FIGURE 8
Correlation diagrams of geochemical elements. **(A, B)** Provenance discrimination diagrams; **(C–E)** Tectonic setting discrimination diagrams. According to Roser and Korsch (1986); OIA. Oceanic Island Arc; CIA. Continental island arc; ACM. Active continental margin; PM. Passive continental margin.

of bottom water, but also accompanied by intermittent relative oxic conditions. Active tectonic activity also promotes volcanic eruptions, and the volcanic ash formed by it is transported and deposited in the ocean, providing rich nutrients for surface seawater. Under this setting, plankton such as graptolites have proliferated on a large scale, and the productivity level of the water surface is constantly improving. These plankton can be preserved as organic matter under anoxic conditions after death. In the late TST 1 period, tectonic activity tended to stabilize, but the early large-scale volcanic activity had led to a gradual cooling of the global climate and changes in graptolite biodiversity, triggering the Late Ordovician extinction. In cold climates, the weathering intensity is weak, and the amount of terrestrial input is significantly reduced. A large number of aquatic organisms die, providing organic matter supply and enhancing the reducibility of bottom water through degradation of organic matter. During this period, organic-rich siliceous shale is mainly formed.

During TST 1 period, the trend of TOC variation in the Eastern Sichuan and Southern Sichuan is consistent, but the average value of the former is significantly higher than that of the latter. It is speculated that this phenomenon is related to the high paleo-productivity in the Eastern Sichuan. The high excess Si and a large amount of siliceous organisms confirm the enrichment of organic matter, manifested by a higher quartz content in Eastern Sichuan than in Southern Sichuan (Table 1). The detrital input in the Eastern and Southern Sichuan is basically the same, and both provenances tend to be acidic magmatic rocks. The high content of feldspar in the Eastern Sichuan is related to the relatively cold-arid climate background, where feldspar is weakly affected by weathering during transportation. Due to being closer to the Central Guizhou-Xuefeng paleo-uplift, there is more input of coarse-grained carbonate debris in the Southern Sichuan Basin, which is characterized by high carbonate mineral content, especially in the late TST 1 period. This has also been confirmed by the Zr/Al ratio.

HST 1 period

In the mid to late Hirnantian stage, the formation of glaciers on the Gondwana continent led to a significant decrease in global sea-level (Bertrand et al., 1996), resulting in sharp shallowness of water mass and unfavorable organic matter preservation under the oxic bottom water condition. A thin layer of carbonate-rich argillaceous limestone was deposited in a shallow water environment.

TST 2 period

The Hirnantian glaciation has ended, and global temperatures are rapidly rising. Glacial melting has caused widespread transgression. Volcanic activity and tectonic movements tend to stabilize. In the early TST 2 period, the separation of paleo-uplift and sea-level rise kept the bottom water in a restricted and anoxic

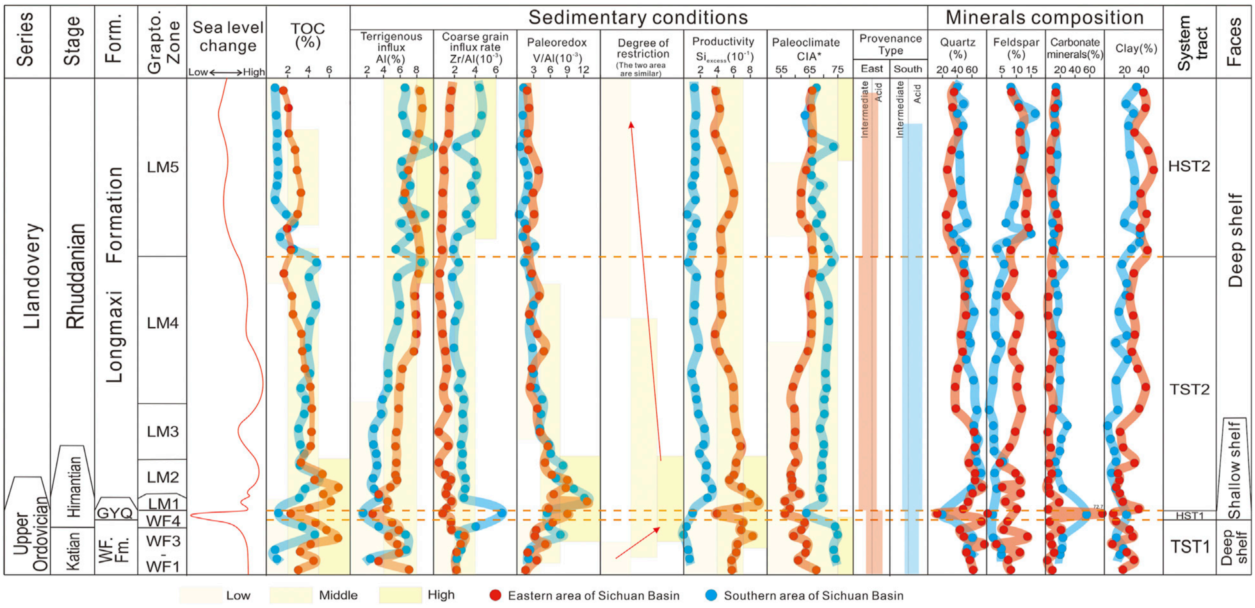

FIGURE 9
The Paleoenvironment, TOC and minerals composition evolution process in the Southern and Eastern area of Sichuan basin during the Late Ordovician-Early Silurian.

condition. Climate warming has led to an increase in weathering intensity and enhanced detrital influx. The glacial melting results in a large amount of cold fresh water flowing into the ocean, which not only brings nutrients but also causes stratification of fresh and saline water, exacerbating anoxic conditions. Planktonic organisms, including radiolarians and graptolites, have once again flourished on a large scale, increasing productivity levels. The continuously sinking biological remains continue to consume dissolved oxygen in the bottom water, maintaining anoxic environments, even euxinic environments. During early TST 2 period, less detrital influx helps to weaken the dilution effect and form organic-rich siliceous shale. During middle TST 2 period, the sea-level continues to rise, increasing the circulation between the restricted basin and the ocean, and reducing the restriction degree of bottom water. However, under moderate to strong paleo-productivity, the consumption of oxygen by the remains of organisms still ensures that the bottom water is in an suboxic-anoxic environment. In the late TST 2 period, the fluctuating sea-level drop results in limited surface water productivity. The increase in dissolved oxygen in bottom water is not conducive to organic matter preservation. The humid climate leads to an increase in the intensity of paleo-weathering, while the increase in terrestrial input disrupts the enrichment of organic matter. Compared to the middle TST 2 period, the organic carbon content is significantly reduced, and the shale lithology is argillaceous-rich siliceous shale or mixed siliceous shale.

During early-middle TST 2 period, the high productivity level in the Eastern Sichuan leads to a higher average TOC content than in the Southern Sichuan. In the late TST 2 period, the paleo-productivity in the Eastern Sichuan is still at a high level, but the rapidly increasing weathering intensity has led to a significantly higher detrital influx than in the Southern Sichuan. The dilution effect of terrestrial debris reduces the accumulation of organic matter in the Eastern Sichuan. The mineral composition indicates that the quartz content in the Eastern Sichuan was higher in the early TST 2 period (Figure 9), which is related to the deposition of a large amount of biogenic quartz, while the late TST 2 period was lower than that in the Southern Sichuan (Table 1). The clay content in the Eastern Sichuan is higher than that in the Southern Sichuan, while the carbonate content is lower than that in the Southern Sichuan. This is related to the large amount of terrestrial debris input and the high proportion of clay minerals. From the perspective of provenance differences, the Eastern Sichuan Basin is mainly composed of neutral igneous rocks, while the Southern Sichuan Basin is mainly composed of acidic igneous rocks. The former has a higher proportion of plagioclase feldspar in sediment supply, while the latter has a higher proportion of potassium feldspar. However, potassium feldspar is prone to kaolinization during transportation, so the mineral composition in eastern Sichuan has a significantly higher content of feldspar, mainly plagioclase feldspar.

HST 2 period

The climate in the late Rhuddanian stage continued to warm, with a slow decrease in sea-level, but there was short-term transgression. The tectonic uplift intensifies the weathering process in the provenance region, and the amount of terrestrial input continues to increase. The productivity level has undergone significant changes (significantly higher in Eastern Sichuan than in Southern Sichuan), but the bottom water conditions are not conducive to the preservation of organic matter. Diluted by terrestrial debris, organic matter is dispersed in sediments. More and more terrestrial quartz and clay minerals have replaced biogenic quartz as the main component of minerals, and the shale lithofacies are gradually transitioning to argillaceous-siliceous mixed shale.

The low productivity, low preservation conditions, and high terrestrial input in the Southern Sichuan Basin are reflected in a rapid decrease in TOC. The TOC in the Eastern Sichuan increased in the early stages and gradually decreased in the later stages, which is speculated to be related to higher paleoproductivity and a high proportion of clay in terrestrial debris. The high productivity in the Eastern Sichuan not only brings organic matter input, but also consumes the oxygen content of the bottom water during deposition, which to some extent increases the reducibility of the bottom water. In addition, high clay content is conducive to the adsorption and rapid settling of organic matter, reducing consumption during the sinking process, and facilitating the aggregation and preservation of organic matter.

The difference in the detrital influx between the Eastern and Southern Sichuan is small, but the quartz mineral content in Southern Sichuan is higher than that in Eastern Sichuan (Table 1), while the clay content is lower than that in Eastern Sichuan. This is related to the slightly stronger weathering intensity and coarse-grained debris input (silt-size quartz) in Southern Sichuan. The provenance sources in the Eastern Sichuan tend to be neutral magmatic rocks, while those in the Southern Sichuan tend to be acidic magmatic rocks. Moreover, the climate in the Eastern Sichuan Basin is cold-dry, with low weathering intensity. Therefore, the mineral composition of plagioclase in the Eastern Sichuan Basin is relatively high, while the content of quartz and potassium feldspar in the Southern Sichuan is higher (Table 1). The content of carbonate rocks in Southern Sichuan is higher than that in Eastern Sichuan, especially in calcite, which is related to the high input of coarse-grained carbonate debris. The average value of pyrite in the Eastern Sichuan is 37.5% higher than that in the Southern Sichuan, which indirectly confirms that the oxygen content in the bottom water of the Eastern Sichuan is lower, which is conducive to the formation of pyrite.

Conclusion

1) The lower part of the Longmaxi Formation-Wufeng Formation in the Southern and Eastern Sichuan Basin can be divided into two third-order sequences (Sq 1 and Sq 2). Sq 1 is composed of the Wufeng Formation and GYQ Member, while Sq 2 is composed of the lower part of the Longmaxi Formation. Each third-order sequence consists of a set of transgressive system tracts (TSTs) and a set of high-level system tracts (HSTs).
2) The TOC content in Eastern Sichuan is higher than that in Southern Sichuan. During the TST1 period, the average TOC content in Eastern Sichuan was the highest, reaching 4.2%. The average TOC content in Southern Sichuan reached its maximum at 3.9% during the TST2 period. From TST1 to HST2, the clay content in eastern Sichuan continued to increase while the quartz content continued to decrease. However, the quartz content in southern Sichuan shows a trend of first increasing and then decreasing, while the change in clay content is opposite.
3) During the TST1 period, the TOC range in Eastern Sichuan is significantly higher than that in Southern Sichuan, which is related to its high paleoproductivity. In the early to middle TST2 period, the high paleoproductivity in Eastern Sichuan resulted in a higher TOC content than in Southern Sichuan. In the late TST2 period, the accumulation of organic matter in Eastern Sichuan was lower than that in Southern Sichuan due to the dilution effect of terrestrial debris. During the HST2 period, the TOC in Southern Sichuan showed a rapid decrease trend. The TOC in Eastern Sichuan slightly increased in the early HST2 period, which is related to higher paleoproductivity and the adsorption and preservation of clay.
4) During the TST1 period, the quartz content in Eastern Sichuan was higher than that in Southern Sichuan, which is related to the abundant accumulation of biogenic silica. During the TST2 period, due to the high input of terrestrial debris and the high proportion of clay minerals, the quartz content in Eastern Sichuan was higher than that in Southern Sichuan in the early period, but the opposite was true in the late period. The mineral content of clay in Eastern Sichuan has always been higher than that in Southern Sichuan. During the HST2 period, compared with Eastern Sichuan, the stronger weathering intensity and coarse-grained debris input (mainly composed of silt-size quartz) in Southern Sichuan resulted in higher quartz mineral content and lower clay mineral content.

Data availability statement

The raw data supporting the conclusion of this article will be made available by the authors, without undue reservation.

Author contributions

XY: Conceptualization, Methodology, Writing–original draft. HY: Formal Analysis, Investigation, Supervision, Writing–review and editing. LY: Conceptualization, Investigation, Project administration, Writing–review and editing. LX: Conceptualization, Investigation, Project administration, Writing–review and editing. JC: Investigation, Methodology, Writing–original draft. DL: Conceptualization, Investigation, Methodology, Writing–original draft. CJ: Methodology, Project administration, Supervision, Writing–review and editing. ZJ: Investigation, Project administration, Software, Validation, Writing–review and editing.

Funding

The author(s) declare that financial support was received for the research, authorship, and/or publication of this article. The research was supported by the National Natural Science Foundation of China (Grant No. 42272171) and Science and Technology Cooperation Program of CNPC–SWPU Innovation Alliance (Grant No. 2020CX020104).

Conflict of interest

Authors XY, HY, LY, LX, JC, and DL were employed by PetroChina Southwest Oil and Gas Field Company. Author CJ was employed by PetroChina Southwest Oil and Gas Field Company. Author ZJ was employed by Sichuan Geotech Science and Technology Ltd. Company.

Publisher's note

References

Algeo, T. J., and Lyons, T. W. (2006). Mo-total organic carbon covariation in modern anoxic marine environments: implications for analysis of paleoredox and paleohydrographic conditions. *Paleoceanography* 21, 16–23. doi:10.1029/2004PA001112

Algeo, T. J., and Tribovillard, N. (2009). Environmental analysis of paleoceanographic systems based on molybdenum-uranium covariation. *Chem. Geol.* 268, 211–225. doi:10.1016/j.chemgeo.2009.09.001

Armstrong, H. A., Abbott, G. D., Turner, B. R., Makhlouf, I. M., Muhammad, A. B., Pedentchouk, N., et al. (2009). Black shale deposition in an Upper Ordovician–Silurian permanently stratified, peri-glacial basin, southern Jordan. *Palaeogeogr. Palaeoclimatol. Palaeoecol.* 273, 368–377. doi:10.1016/j.palaeo.2008.05.005

Berry, W. B. N. (2010). Black shales: an Ordovician perspective. *Geol. Soc. Am. Special Pap.* 466, 141–147. doi:10.1130/2010.2466(09)

Bertrand, P., Shimmield, G., Martinez, P., Grousset, F., Jorissen, F., Paterne, M., et al. (1996). The glacial ocean productivity hypothesis: the importance of regional temporal and spatial studies. *Mar. Geol.* 130, 1–9. doi:10.1016/0025-3227(95)00166-2

Bhatia, M. R., and Crook, K. A. W. (1986). Trace element characteristics of graywackes and tectonic setting discrimination of sedimentary basins. *Contrib. Mineral. Petrol.* 92 (2), 181–193. doi:10.1007/BF00375292

Brenchley, P. J., Carden, G. A., Hints, L., Kaljo, D., Marshall, J. D., Martma, T., et al. (2003). High-resolution stable isotope stratigraphy of Upper Ordovician sequences: constraints on the timing of bioevents and environmental changes associated with mass extinction and glaciation. *Geol. Soc. Am. Bull.* 115, 89–104. doi:10.1130/0016-7606(2003)115<0089:HRSISO>2.0.CO;2

Cai, G., Gu, Y., Jiang, Y., and Wang, Z. (2023). Pore structure and fluid evaluation of deep organic-rich marine shale: a case study from Wufeng–Longmaxi Formation of Southern Sichuan Basin. *Appl. Sci.* 13, 7827. doi:10.3390/app13137827

Cai, S. Q., Hu, Y. M., Zhao, B. M., Ngia, N., Liu, A., Liao, R. Q., et al. (2022). Source of silica and its implications for organic matter enrichment in the Upper Ordovician-Lower Silurian black shale in western Hubei Province, China: insights from geochemical and petrological analysis. *Petroleum Sci.* 19 (1), 74–90. doi:10.1016/j.petsci.2021.10.012

Chen, L., Jiang, Z., Liu, K., Tan, J., Gao, F., and Wang, P. (2017a). Pore structure characterization for organic-rich Lower Silurian shale in the Upper Yangtze Platform, South China: a possible mechanism for pore development. *J. Nat. Gas Sci. Eng.* 46 (2017), 1–15. doi:10.1016/j.jngse.2017.07.009

Chen, L., Jiang, Z., Liu, K., Wang, P., Liu, Y., Bi, H., et al. (2017b). Relationship between pore characteristics and occurrence state of shale gas: a case study of Lower Silurian Longmaxi shale in the Upper Yangtze Platform, South China. *Interpretation* 5 (3), T437–T449. doi:10.1190/INT-2016-0191.1

Chen, X., Fan, J., Wang, W., Wang, H., Nie, H., Shi, X., et al. (2017c). Stage-progressive distribution pattern of the Lungmachi black graptolitic shales from Guizhou to Chongqing,central China. *Sci. China Earth Sci.* 60, 1133–1146. doi:10.1007/s11430-016-9031-9

Chen, Y., Zhao, J. H., Hu, Q. H., Liu, K. Y., Wu, W., Luo, C., et al. (2023). Origin of carbonate minerals and impacts on reservoir quality of the Wufeng and Longmaxi shale, Sichuan Basin. *Petroleum Sci.* 20 (6), 3311–3336. doi:10.1016/j.petsci.2023.08.012

Dong, D., Liang, F., Guan, Q., Jiang, Y., Zhou, S., Yu, R., et al. (2022a). Development model and identification evaluation technology of Wufeng-Longmaxi Formation quality shale gas reservoirs in the Sichuan Basin. *Nat. Gas. Ind.* 42 (8), 96–111. doi:10.3787/j.issn.1000-0976.2022.08.008

Dong, T., Wang, C., Liang, X., Wang, G., and Jiang, S. (2022b). Paleodepositional conditions and organic matter accumulation mechanisms in the upper ordovician-lower silurian wufeng-longmaxi shales, middle Yangtze region, South China. *Mar. Petroleum Geol.* 143 (2022), 105823. doi:10.1016/j.marpetgeo.2022.105823

Dymond, J., Suess, E., and Lyle, M. (1992). Barium in deep-sea sediment: a geochemical proxy for paleoproductivity. *Paleoceanography* 7 (2), 163–181. doi:10.1029/92PA00181

Fan, C. H., Nie, S., Li, H., Radwan, A. E., Pan, Q. C., Shi, X. C., et al. (2024). Quantitative prediction and spatial analysis of structural fractures in deep shale gas reservoirs within complex structural zones: a case study of the Longmaxi Formation in the Luzhou area, southern Sichuan Basin, China. *J. Asian Earth Sci.* 263 (2024), 106025. doi:10.1016/j.jseaes.2024.106025

Floyd, P. A., and Leveridge, B. E. (1987). Tectonic environment of the Devonian Gramscatho basin, south Cornwall: framework mode and geochemical evidence from turbiditic sandstones. *J. Geol. Soc.* 144 (4), 531–542. doi:10.1144/gsjgs.144.4.0531

Fu, Y., Jiang, Y., Dong, D., Hu, Q., Lei, Z., Peng, H., et al. (2021b). Microscopic pore-fracture configuration and gas-filled mechanism of shale reservoirsin the western Chongqing area,Sichuan Basin,China. *Petroleum Explor. Dev.* 48 (5), 1063–1076. doi:10.1016/s1876-3804(21)60091-5

Fu, Y., Jiang, Y., Hu, Q., Luo, T., Li, Y., Lei, Z., et al. (2021a). Fracturing flowback fluids from shale gas wells in western chongqing: geochemical analyses and relevance for exploration and development. *J. Nat. Gas Sci. Eng.* 88 (2021), 103821. doi:10.1016/j.jngse.2021.103821

Fu, Y., Jiang, Y., Wang, Z., Hu, Q., Xie, J., Ni, G., et al. (2019). Non-connected pores of the Longmaxi shale in southern Sichuan Basin of China. *Mar. Petroleum Geol.* 110 (2019), 420–433. doi:10.1016/j.marpetgeo.2019.07.014

Guo, X., Qin, Z., Yang, R., Dong, T., He, S., Hao, F., et al. (2019). Comparison of pore systems of clay-rich and silica-rich gas shales in the lower Silurian Longmaxi formation from the Jiaoshiba area in the eastern Sichuan Basin, China. *Mar. Petroleum Geol.* 101 (2019), 265–280. doi:10.1016/j.marpetgeo.2018.11.038

Huang, Z., Li, Z., Shi, W., Yang, X., Wang, X., and Young, S. (2023). Differential sedimentary mechanisms of upper ordovician-lower silurian shale in southern Sichuan Basin, China. *Mar. Petroleum Geol.* 148 (2023), 106040. doi:10.1016/j.marpetgeo.2022.106040

Jiang, C., Zhang, H., Zhou, Y., Gan, H., Pu, J., Jiang, Y., et al. (2022). Paleogeomorphic characteristics of Wufeng-Longmaxi formation andits influence on development of high-quality shale in Dazu area,Western Chongqing. *J. Central South Univ. Sci. Technol.* 53 (9), 3628–3640. doi:10.11817/j.issn.1672-7207.2022.09.026

Jiang, Y., Chen, L., Qi, L., Luo, M., Chen, X., Tao, Y., et al. (2018). Characterization of the lower silurian Longmaxi marine shale in changning area in the South Sichuan Basin, China. *Geol. J.* 53, 1656–1664. doi:10.1002/gj.2983

Jiang, Y., Fu, Y., Lei, Z., Gu, Y., Qin, L., and Cao, Z. (2019). Experimental NMR analysis of oil and water imbibition during fracturingin Longmaxi shale,SE Sichuan Basin. *J. Jpn. Petroleum Inst.* 62 (1), 1–10. doi:10.1627/jpi.62.1

Jiang, Z., Song, Y., Tang, X., Li, Z., Wang, X., Wang, G., et al. (2020). Controlling factors of marine shale gas differential enrichment in southern China. *Petroleum Explor. Dev.* 47 (3), 661–673. doi:10.1016/S1876-3804(20)60083-0

Jin, C., Liao, Z., and Tang, Y. (2020). Sea-level changes control organic matter accumulation in the Longmaxi shales of southeastern Chongqing, China. *China. Mar. Petrol. Geol.* 119, 104478. doi:10.1016/j.marpetgeo.2020.104478

Li, H. (2023a). Coordinated development of shale gas benefit exploitation and ecological environmental conservation in China: a mini review. *Front. Ecol. Evol.* 11, 1232395. doi:10.3389/fevo.2023.1232395

Li, H. (2023b). Deciphering the formation period and geological implications of shale tectonic fractures: a mini review and forward-looking perspectives. *Front. Energy Res.* 11, 1320366. doi:10.3389/fenrg.2023.1320366

Li, Y., Zhou, A., Xie, W., Qiu, X., Dai, Y., Hu, X., et al. (2022). Lithofacies division and main controlling factors of reservoir development in Wufeng Formation-Long$_1$ sub-member shale in the Luzhou region, South Sichuan Basin. *Nat. Gas. Ind.* 42 (8), 112–123. doi:10.3787/j.issn.1000-0976.2022.08.009

Li, Y. F. (2017). "Geochemical characteristics and organic matter accumulation of Late Ordovician-Early Silurian shale in the Upper Yangtze Platform, and implications for paleoenvironment," (Gansu, China: Lanzhou University). Master dissertation.

Liu, Z. Y., Chen, D. X., Zhang, J. C., Lü, X. X., Wang, Z. Y., Liao, W. H., et al. (2019). Pyrite morphology as an indicator of paleoredox conditions and shale gas content of the Longmaxi and Wufeng shales in the middle Yangtze area, South China. *Minerals* 9 (7), 428. doi:10.3390/min9070428

McLennan, S. M. (2001). Relationships between the trace element composition of sedimentary rocks and upper continental crust: trace element composition and upper continental crust. *Geochem. Geophys. Geosystems* 2, 2000GC000109. doi:10.1029/2000gc000109

Roser, B. P., and Korsch, R. J. (1986). Determination of tectonic setting of sandstone-mudstone suites using SiO_2 content and K_2O/Na_2O ratio. *J. Geol.* 94, 635–650. doi:10.1086/629071

Song, L. C., Chen, Q., Li, H. J., and Deng, C. Z. (2023). Roller-coaster atmospheric-terrestrial-oceanic-climatic system during Ordovician-Silurian transition: consequences of large igneous provinces. *Geosci. Front.* 14 (3), 101537. doi:10.1016/j.gsf.2023.101537

Taylor, S. R. (1964). Abundance of chemical elements in the continental crust: a new table. *Geochem. Cosmochim. Acta* 28 (8), 1273–1285. doi:10.1016/0016-7037(64)90129-2

Taylor, S. R., and McLennan, S. M. (1985). The continental crust: its composition and evolution. *Blackwell* 312.

Tribovillard, N., Algeo, T. J., Baudin, F., and Riboulleau, A. (2012). Analysis of marine environmental conditions based on molybdenum-uranium covariation-Applications to Mesozoic paleoceanography. *Chem. Geol.* 324-325, 46–58. doi:10.1016/j.chemgeo.2011.09.009

Tribovillard, N., Algeo, T. J., Lyons, T., and Riboulleau, A. (2006). Trace metals as paleoredox and paleoproductivity proxies: an update. *Chem. Geol.* 232 (1/2), 12–32. doi:10.1016/j.chemgeo.2006.02.012

Wang, Y., Li, X., Wang, H., Jiang, S., Chen, B., Ma, J., et al. (2019). Developmental characteristics and geological significance of the bentonite in the upper ordovician wufeng-lower silurian Longmaxi formationin eastern Sichuan Basin, SW China. *Petroleum Explor. Dev.* 46 (4), 687–700. doi:10.1016/s1876-3804(19)60226-0

Wang, Z., Jiang, Y., Fu, Y., Lei, Z., Xu, C., Yuan, J., et al. (2022). 基于核磁共振表征渝西地区五峰组-龙一₁亚段页岩储层孔隙结构及非均质性. *Earth Sci.* 47 (2), 490–504. doi:10.3799/dqkx.2021.076

Wedepohl, K. H. (1971). Environmental influences on the chemical composition of shales and clays. *Phys. Chem. Earth* 8, 307–333. doi:10.1016/0079-1946(71)90020-6

Wei, C., Dong, T., He, Z., He, S., He, Q., Yang, R., et al. (2021). Major, trace-elemental and sedimentological characterization of the upper Ordovician Wufeng-lower Silurian Longmaxi formations, Sichuan Basin, south China: insights into the effect of relative sea-level fluctuations on organic matter accumulation in shales. *Mar. Petroleum Geol.* 126, 104905. doi:10.1016/j.marpetgeo.2021.104905

Wu, J., Liang, C., Yang, R. C., Hu, Z. Q., Li, W. J., and Xie, J. (2022). The genetic relationship between paleoenvironment, mineral compositions and lithofacies in the Ordovician–Silurian Wufeng–Longmaxi sedimentary succession in the Sichuan Basin, SW China. *J. Asian Earth Sci.* 236, 105334. doi:10.1016/j.jseaes.2022.105334

Wu, L. Y., Lu, Y. C., Jiang, S., Liu, X., and He, G. (2018). Effects of volcanic activities in ordovician wufeng-silurian Longmaxi period on organic-rich shale in the upper Yangtze area,South China. *Petroleum Explor. Dev.* 45 (5), 862–872. doi:10.1016/s1876-3804(18)30089-2

Xie, H. R., Liang, C., Wu, J., Cao, Y. C., Han, Y., Liu, Y. D., et al. (2023). Multiple geological events controlling rock types development: a case study of Wufeng-Longmaxi formation in southern Sichuan Basin, China. *Geoenergy Sci. Eng.* 227, 211826. doi:10.1016/j.geoen.2023.211826

Xie, X. M., Zhu, G. Y., and Wang, Y. (2021). The influence of syngenetic hydrothermal silica fluid on organic matter preservation in lower Cambrian Niutitang Formation, South China. *Mar. Petroleum Geol.* 129, 105098. doi:10.1016/j.marpetgeo.2021.105098

Zhang, K., Peng, J., Liu, W., Li, B., Xia, Q., Cheng, S., et al. (2020). The role of deep geofluids in the enrichment of sedimentary organic matter: a case study of the late ordovician-early silurian in the upper Yangtze region and early cambrian in the lower Yangtze region, South China. *Geofluids* 2020, 1–12. doi:10.1155/2020/8868638

Zhang, K., Song, Y., Jia, C., Jiang, Z., Han, F., Wang, P., et al. (2022). Formation mechanism of the sealing capacity of the roof and floor strata of marine organic-rich shale and shale itself, and its influence on the characteristics of shale gas and organic matter pore development. *Mar. Petroleum Geol.* 140 (2022), 105647. doi:10.1016/j.marpetgeo.2022.105647

Zhao, J., Jin, Z., Hu, Q., Liu, K., Liu, G., Gao, B., et al. (2019). Geological controls on the accumulation of shale gas: a case study of the early Cambrian shale in the Upper Yangtze area. *Mar. Petroleum Geol.* 107 (2019), 423–437. doi:10.1016/j.marpetgeo.2019.05.014

frontiers | Frontiers in Earth Science

TYPE Original Research
PUBLISHED 25 July 2024
DOI 10.3389/feart.2024.1403575

OPEN ACCESS

EDITED BY
Hu Li,
Sichuan University of Science and Engineering, China

REVIEWED BY
Yifan Gu,
Southwest Petroleum University, China
Qingguang Li,
Guizhou University, China

*CORRESPONDENCE
Junfeng Cao,
✉ cjinyan006@126.com

RECEIVED 19 March 2024
ACCEPTED 28 June 2024
PUBLISHED 25 July 2024

CITATION
Zhang H, Cao J, Lan B, Chen Y, Zhang Q, Men Y, Feng X and Yu Q (2024), Organic matter enrichment model of Permian Capitanian-Changhsingian black shale in the intra-platform basin of Nanpanjiang basin. *Front. Earth Sci.* 12:1403575. doi: 10.3389/feart.2024.1403575

Organic matter enrichment model of Permian Capitanian-Changhsingian black shale in the intra-platform basin of Nanpanjiang basin

Haiquan Zhang[1,2], Junfeng Cao[1,2]*, Baofeng Lan[3], Yi Chen[4], Qian Zhang[1,2], Yupeng Men[1,2], Xintao Feng[1,2] and Qian Yu[1,2]

[1]Chengdu Center of China Geological Survey, Geosciences Innovation Center of Southwest China, Chengdu, China, [2]Key Laboratory of Sedimentary Basin and Oil and Gas Resources, Ministry of Natural Resources, Chengdu, China, [3]Guizhou Energy Industry Research Institute Co., Ltd., Guiyang, China, [4]Guizhou Research Institute of Petroleum Exploration and Development, Guiyang, China

The Permian Capitanian-Changhsingian black shale formed in intra-platform basins are the major source rocks in Southwest China. However, the depositional conditions and organic matter accumulation of these black shales are not well understood. In this study, geochemical characteristics comprise TOC, major, trace and REEs from sixty-two samples from the studied outcrop in Northern Nanpanjiang Basin, Southwest China are systematically investigated to determine silicon source, paleo-ocean productivity, and paleo-redox conditions to reveal their influence on organic matter enrichment under 3rd-order sequence. The Capitanian-Changhsingian black shale in the study area is the result of the combined effects of active extensional activity, high paleo-productivity maintained by volcanic activity, and dysoxic and anoxic conditions represented by biological extinction events. There are differences in the factors controlling organic matter accumulation in black shale at different stages. The controlling factors for the organic enrichment during Capitanian (SQ2) are the rapidly deepening water mass of extensional rifts and the high productivity induced by volcanic ash in the igneous provinces, as well as the global anoxic event represented by "negative carbon isotope shift." The controlling factors during Changhsingian are the deepening of water mass under the reactivation of extensional rifts, resulting in a dysoxic environment, and the high productivity maintained by volcanic activity in South China. The Wuchiapingian black shale was formed under dysoxic conditions under the stagnation of extensional activity, and intermittent volcanic activity in South China maintained the high paleo-productivity level of the Wuchiapingian stage.

KEYWORDS

Permian Capitanian, organic matter, enrichment model, black shale, intra-platform basin, Nanpanjiang basin

Introduction

With the development of advanced geochemical indices of elements (Algeo and Maynard, 2004; Zhao et al., 2016; Wei et al., 2022), the paleoenvironmental conditions and organic matter enrichment mechanism of black organic-rich shale have become a research hotspot in recent years (Qiu and Zou, 2020; Gu et al., 2022; Liu et al., 2022). Shale deposited under different formation environments show significant differences in mineral composition, organic matter types, and sweet spot distribution (Li, 2023; Fan et al., 2024; Liu et al., 2024), which in turn affect the various performance characteristics of shale reservoirs (Loucks et al., 2009; Ross and Marc Bustin, 2009; Labani et al., 2013). Affected by the successful exploration of shale oil and gas in North America (Jiang et al., 2016; Jiang et al., 2018; Zou et al., 2019; Cai et al., 2023a), the Chinese Ministry of Land and Resources has conducted a survey and evaluation of the potential shale gas resources throughout China (Bai et al., 2023; Cai et al., 2023b; Fang et al., 2023; Wang et al., 2023). In recent years, the Permian black shale of transitional, and lacustrine in China have achieved industrial production capacity and are expected to form large-scale production capacity, becoming a new field for shale gas production on a large scale (Dong et al., 2021; Lin et al., 2021; Jiao et al., 2023). However, influenced by the complexity of the geological background (Mei et al., 2007; Shen et al., 2019), research on the Permian marine shale is rare.

Organic matter accumulation is a complex physical-chemical process that involves many factors, such as redox condition of bottom seawater, sedimentation rate, productivity of surface water, and geological event (Hu et al., 2018; Gu et al., 2022; Tan et al., 2024). The main controlling factors for organic matter enrichment in modern and paleo marine sediments have been extensively discussed over the past 30 years (Pedersen et al., 1990; Arthur and Sageman, 1994; Wei et al., 2012; Ding et al., 2018). Currently, the controlling factors for organic matter enrichment can be summarized as primary productivity and favorable preservation conditions. The productivity school believes that organic matter accumulation is mainly controlled by the biological productivity of the ocean surface, and the impact of water redox properties is limited. The typical representative is the rising ocean currents on the continental margin. The oxidation-reduction school believes that low marine surface productivity can also form organic rich sediments in hypoxic environments, especially in sulfide environments, with modern anoxic basins such as the Black Sea and Cretaceous marine anoxic events as typical representatives. Moreover, few scholars believe that an appropriate sedimentation rate is the key factor causing organic matter enrichment, and either too high or too low sedimentation rates are not conducive to organic matter enrichment.

At present, organic matter content plays a crucial role in shale hydrocarbon enrichment (Han et al., 2021; Zhang et al., 2022). Therefore, in the early stage of shale resource exploration, it is necessary to identify the mechanism of organic matter enrichment. The type and abundance of organic matter are the results of sedimentary processes, which are controlled by environmental conditions (Tribovillard et al., 2012; Zhang et al., 2018). Based on the geochemical analysis of the Permian marine shale in the Nanpanjiang Basin, this study elaborates on the environmental sensitivity indicators of black shale formed in the intra-platform basin, analyzes the impact of geological events on the shale sedimentary environment, and establishes an organic matter enrichment model for black shale in the intra-platform basin.

Geological setting

The studied outcrop is located in the southern Ziyun area (Figure 1A), Nanpanjiang Basin. During the Permian period, the outcrop belonged to the Nanpanjiang sedimentary division of the South China platform basin sedimentary system (Peng et al., 2006). Under the background of late Paleozoic extensional subsidence, the Nanpanjiang Basin formed a passive continental margin rift type basin, forming a special sedimentary pattern of connected continental platforms, shallow water isolated platforms, and intra platform basins within the basin (Peng et al., 2006; Yin et al., 2014). The studied outcrop is located in a basin within the carbonate platform, representing a deep-water sedimentary sequence (Wang et al., 2022). In the late Middle Permian to early Late Permian, the area where this outcrop was located was strongly affected by the rapid uplift of the crust dome caused by the impact of the Emeishan mantle plume on the bottom of the lithosphere. In the transitional zone between the relatively uplifted and relatively subsidence areas (Zhai et al., 2020), crustal activity was outcrop, and a large amount of volcanic material was deposited in the deep-water sediments of this section, manifested as frequent interbeddings of bentonite in black marine shale (Lai et al., 2008; Gu et al., 2022). Based on lithological combinations and biological zoning, the Guadalupian-Lopingian of the studied outcrop can be divided into four stages (Figure 1B), corresponding to four third-order sequences (Mei et al., 2007). The Wordian stage comprises medium-bedded bioclastic limestone. The Capitanian stage comprises siliceous and clayey black shale abundant with fossils of radiolarians and foraminifera (Figure 2). The Wuchiapingian strata is composed of silty mudstone, siltstone and shale intercalated with thin-bedded limestone. The lower strata of Changhsingian stage comprises limestone, bioclastic limestone and organic-poor mudstone. The upper Changhsingian stage comprise black shale intercalated with thin-bedded limestone.

Samples and methods

Sample collection

This study conducted a careful field investigation on the studied profiles and sampled them layer by layer, totaling 62 shale samples. During the collection process, avoid areas with severe weathering effects to ensure that all samples come from fresh surfaces. Make all samples into thin sections to observe microscopic characteristics. Using an agate mortar, the remaining portion of the shale sample was ground into a 200 mesh powder for elemental geochemical testing and total organic carbon (TOC) testing.

TOC measurement

The total organic carbon content is not only an important part of improving organic carbon isotope stratigraphy, but also plays an important role in evaluating source rock quality. The samples pre-treated with the aforementioned organic carbon isotopes were subjected to sufficient combustion in an environment of high temperature and pure oxygen flow. Subsequently, strong oxidants were used to react in acidic solutions, and the collected CO_2 gas

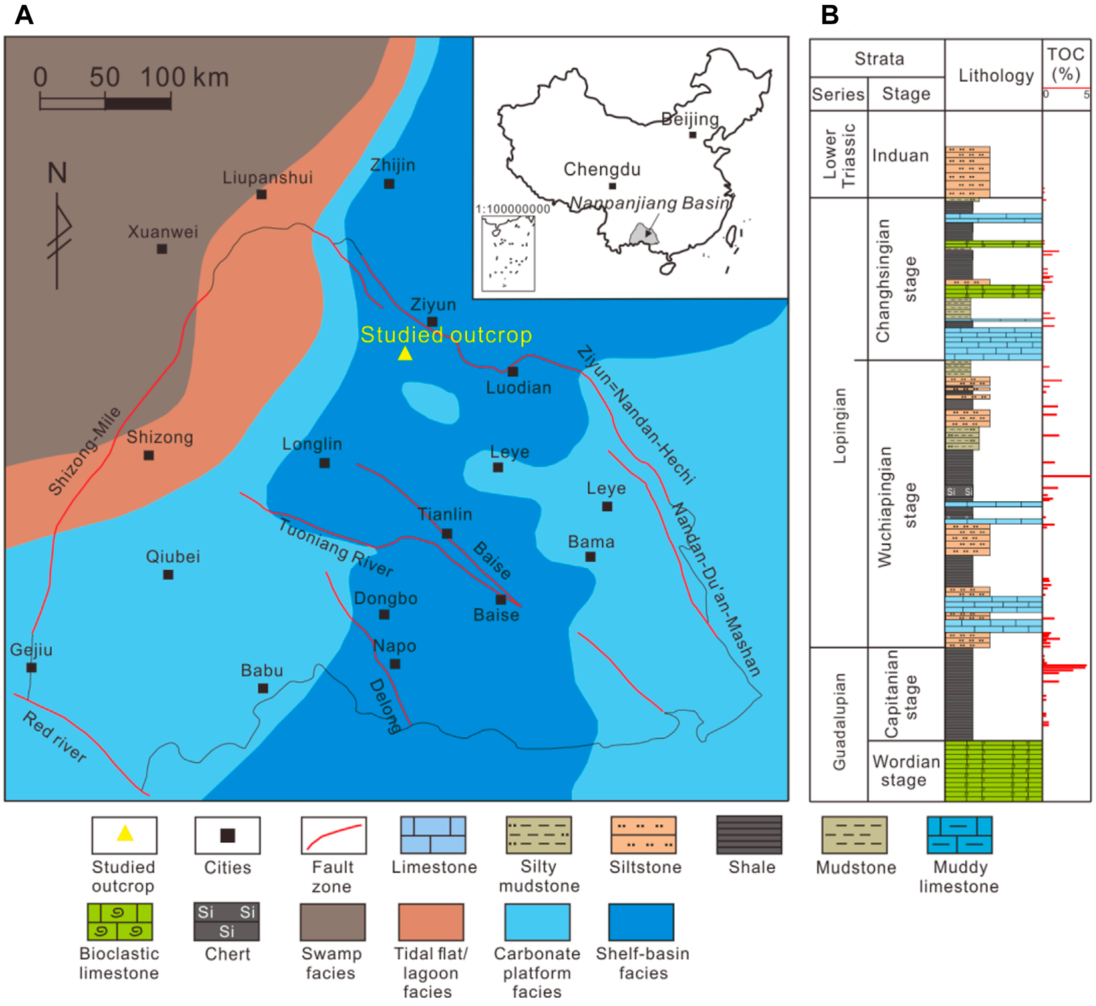

FIGURE 1
(A) Sedimentary environment of Nanpanjiang Basin during Permian Capitanian-Changhsingian (modified from Gu et al., 2022). **(B)** Generalized stratigraphy of Guadalupian-Lower Triassic strata of the studied outcrop.

was purified in a vacuum system to remove interfering substances. Although the instrument calculated the content of organic carbon by measuring the content of CO_2. The TOC measurement was carried out using the Elemental VarioMACRO CHNS elemental analyzer in the Key Laboratory of Unconventional Oil and Gas of PetroChina at Southwest Petroleum University.

Bulk element concentration

The major elements were measured by using the PE ELAN DRC-E type ICP-MS (Inductively Coupled Plasma Mass Spectrometry) made in the United States, and the $Li_2B_4O_7$ and $LiBO_2$ (67:33) mixed flux was used to melt samples with the high-temperature automatic gas sample machine of Glaisse in Canada. The test conditions are: X-ray working voltage 40 kV current 60 rnA, analysis accuracy better than 5%.

Trace Elements and Rare Earth Elements (REE): Dry a 200 mesh sample in an oven at 105°C. After drying, weigh 25 mg of the sample and place it in a high-pressure dissolution tank called Teflon. Add 0.5 mL of concentrated HF, heat and evaporate to dryness at 120°C. After removing some of the sample for 1 day, add 1 mL of concentrated HF and 0.5 mL of concentrated HNO_3. Place the PTFE inner tank in a steel sleeve, tighten it, and heat it in a 190°C oven for 2,448 h. Dissolve the sample and evaporate it to dryness at 120°C until it becomes a wet salt, Add 1 mL of HNO_3 and evaporate to a wet salt state at 140°C to remove excess HF from the sample. Finally, add 5 mL of 30% (v/v) HNO_3, seal and heat at 140°C for 4 h. After cooling, add 1 mL of 500 ng/mL Rh internal standard solution and dilute to 50 mL. The instrument used in the experiment is the Finnigan Element 2 mass spectrometer, and the Millipore water purification system Milli-Q is used to prepare 18 M Ω. Ultra pure water, sample treatment is carried out in a Class 100 ultra clean laboratory. The error is less than 10%. The determination of trace elements and rare earth elements was carried out using ICP-MS with an error of less than 5%.

X-ray diffraction

Extract <2 from each shale sample using sedimentation method μ M clay particles are made into directional sheets. First, rinse

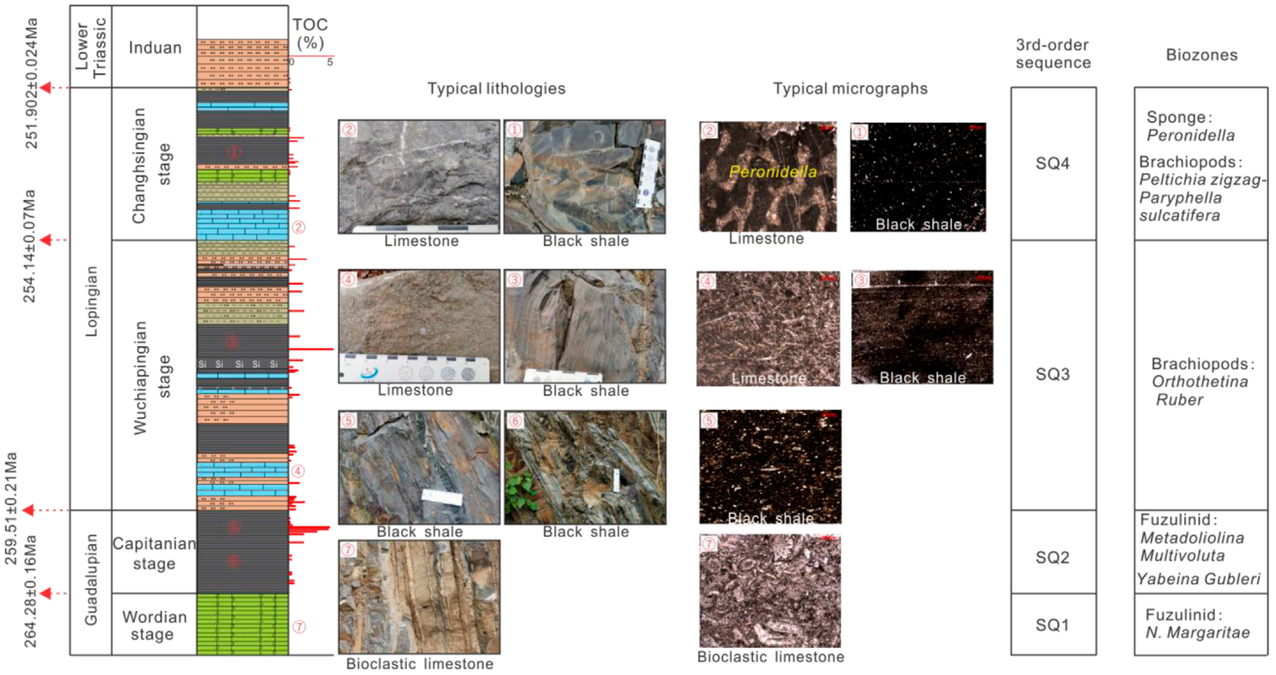

FIGURE 2
Comprehensive stratigraphic column for the Guadalupian-Lower Triassic in the studied outcrop. Sequence column is from Mei et al. (2007). Biozones are from National Commission on Stratigraphy of China (Wang et al., 2014).

repeatedly with distilled water, then place it in a 2000 mL quartz beaker, add 1,500 mL of distilled water and mix thoroughly. After 20 h at 25°C, the upper part of the solution should be <2 μ The suspension is sucked into a centrifuge tube and centrifuged at 2,500 rpm for 10 minutes. The sediment at the bottom of the centrifuge tube is <2 μ Sample of m particles. Add 2 mL of distilled water and apply the emulsified mud like sample onto two 20 –30 cm flat glass plates to make directional plates, which are then dried naturally and treated with ethylene glycol. When treating the sample with ethylene glycol, steam method is used at a temperature of 600 and heated for about 12 h. The instrument used is the Broker D8 Advance X-ray powder diffractometer, Cu target, instrument voltage 4.0 kV, tube current 40 mA, scanning speed 250/min, scanning step width 0.0167°, scanning range 3°–25° (2 θ).

Results

Major elements

The chemical composition of the Capitanian black shale in the studied outcrop is mainly SiO_2, with a content of 37.0%–65.0%, an average of 52.9%, followed by Al_2O_3 and TFe_2O_3, with an average content of 15.2% and 9.6%, respectively. The remaining oxides include MgO, CaO, Na_2O, K_2O, TiO_2, and MnO, with average contents of 2.5%, 3.5%, 1.1%, 2.3%, 2.6%, and 0.2%, respectively. The SiO_2 content of black shale in the Wuchiapingian-Changhsingian stage ranges from 37.9% to 55.3%, with an average value of 45.2%, which is significantly lower than that of the Capitanian shale. The average content of Al_2O_3 and TFe_2O_3 is 13.4% and 11.6%, respectively. The other oxides include MgO, CaO, Na_2O, K_2O, TiO_2, and MnO, with an average content of 3.1%, 7.8%, 2.1%, 1.9%, 2.6%, and 0.2%, respectively. The SiO_2 content of the Ordovician-Silurian black shale in South China ranges from 28.3% to 81.7%, with an average value of 60.0%. The average contents of Al_2O_3 and TFe_2O_3 are 12.7% and 4.9%, respectively. The other oxides include MgO, CaO, Na_2O, K_2O, TiO_2, and MnO, with average contents of 2.4%, 3.7%, 1.1%, 3.5%, 0.6%, and 0.03%, respectively. In contrast, in terms of SiO_2 content, the Ordovician-Silurian black shale is higher than the Capitanian shale, and the Wuchiapingian-Changhsingian shale are the lowest. In terms of TiO_2 and MnO content in shale, the Capitanian, Wuchiapingian-Changhsingian shale are significantly higher than the Ordovician-Silurian shale (Table 1).

The Capitanian black shale sample has a high loss on ignition (average 12.8%), and the Wuchiapingian-Changhsingian black shale also has a high loss on ignition (average 12.1%). The $SiO_2/(K_2O + Na_2O)$ values of Capitanian black shale range from 10.6 to 55.2, with an average of 19.7. The value distribution of SiO_2/Al_2O_3 ranges from 2.2 to 5.3, with an average value of 3.7. The value of $(K_2O + Na_2O)/Al_2O_3$ ranges from 0.1 to 0.3, with an average value of 0.2. The value distribution of MnO/TiO_2 ranges from 0.02 to 0.2, with an average value of 0.1. The $SiO_2/(K_2O + Na_2O)$ values of the Wuchiapingian-Changhsingian black shale range from 9.4 to 18.3, with an average of 12.4. The value distribution of SiO_2/Al_2O_3 ranges from 2.8 to 6.1, with an average value of 4.0. The value of $(K_2O + Na_2O)/Al_2O_3$ ranges from 0.3 to 0.4, with an average value of 0.3. The value distribution of MnO/TiO_2 ranges from below 0.1 to 0.2, with an average value of 0.1.

TABLE 1 Comparison of major elements average (%) in black shales among different Formation.

Strata/Stage	SiO_2	Al_2O_3	TFe_2O_3	MgO	CaO	Na_2O	K_2O	TiO_2	MnO
Wuchiapingian-Changhsingian	52.91	15.22	9.56	2.47	3.49	1.07	2.26	2.55	0.15
Capitanian	45.24	13.39	11.58	3.05	7.83	2.12	1.88	2.55	0.19
Ordovician-Silurian	59.98	12.71	4.91	2.35	3.69	1.09	3.51	0.63	0.03

Trace and rare earth elements

The Capitanian black shale sample has a V content between 77.8×10^{-6}–344.0×10^{-6}, with an average of 188.27×10^{-6}. In the black shale of Changhsingian, the average V content increases to 229.0×10^{-6}. The Mo content in the black shale of Capitanian is between 0.6×10^{-6}–5.0×10^{-6}, with an average of 2.02×10^{-6}. The Mo value of black shale in the Changhsingian stage increased to 9.71×10^{-6}. The Cr distribution of Capitanian black shale ranges from 14.9×10^{-6} to 136.6×10^{-6}, with an average of 76.1×10^{-6}. The Cr value of Changhsingian black shale is significantly higher, distributed between 76.0×10^{-6} and 287.0×10^{-6}, with an average of 160.8×10^{-6}. The Ba content of the Capitanian black shale is distributed between 88.85×10^{-6}–623.96×10^{-6}, with an average of 354.31×10^{-6}. The Ba content of the black shale belonging to Changhsingian stage is distributed between 239.0×10^{-6}–$2{,}289.0 \times 10^{-6}$, with an average of 723.4×10^{-6}.

The distribution range of ∑REE in the black shale sample of Capitanian is 46.32×10^{-6}–941.85×10^{-6}, with an average value of 357.27×10^{-6}. The ∑REE distribution range of the Changhsingian black shale sample is 143.94×10^{-6}–416.86×10^{-6}, with an average value of 284.53×10^{-6}.

Discussions

The distribution characteristics of organic matter and silicon components can intuitively reflect the close relationship between the lithological changes and organic matter content of organic-rich shale. In addition, it also indicates that in order to reveal the synchronous coupling mechanism between organic matter enrichment and silicon enrichment in the formation, it is necessary to first clarify the source and origin of silicon components in shale, and then identify the symbiotic coupling mechanism that determines the synchronous enrichment of organic matter and silicon. The measurement results suggest that the major elemental composition of Capitanian shale, Wuchiapingian shale, and Changhsingian shale is similar to the characteristics of siliceous rocks formed by volcanic biochemical processes (Table 2). High values of loss on ignition are related to the rich organic matter in the shale samples. There is a significant difference in the background values of the parameters and hydrothermal genesis of the Capitanian, Wuchiapingian - Changhsingian black shale (Table 2).

Yamamoto (1987) proposed that hot water activity can lead to the enrichment of Fe and Mn elements. After analyzing 42 Cretaceous rock samples from the North Pacific, Adachi et al. (1986) proposed that the enrichment of TFe_2O_3 is an important feature of hydrothermal silica. The TFe_2O_3 content in the black shale is not high, and the Capitanian black shale is distributed between 1.3% and 12.8%, with an average of only 9.8%. The MnO content is extremely low, with an average of only 0.2%. The TFe_2O_3 content in the Wuchiapingian-Changhsingian black shale is also not high, ranging from 4.9% to 14.8%, with an average value of only 11.3% and an average MnO content of only 0.2%, both of which do not have typical hydrothermal genesis characteristics.

The Al/(Al+Fe+Mn) value in marine sediments is a marker for measuring the content of hydrothermal components in sediments (Adachi et al., 1986). This ratio increases with the distance away from the expansion center, thereby distinguishing the contribution of hydrothermal components to sediments. The Al/(Al + Fe + Mn) values of hydrothermal sediments located in the eastern Pacific Ocean are mostly between 0.01 and 0.2, and their ratio is less than 0.35 due to the influence of hot water. The average ratio of hydrothermal silica collected from the North Pacific is 0.12, while the ratio of semi oceanic silica from the Kamiaso biogenic Triassic in central Japan is 0.60. The Al/(Al + Fe + Mn) values of black shale in the studied outcrop range from 0.43% to 0.59%, with an average of 0.52. The Al/(Al + Fe + Mn) value of Wuchiapingian-Changhsingian black shale ranges from 0.4% to 0.6%, with an average of 0.5, which is close to the value of pure biogenic silicon. On the Al Fe Mn triangulation, the majority of the samples from the Capitanian stage are located within the biogenic zone, with a few samples adjacent to the Wuchiapingian-Changhsingian stage (Figure 3). The silicon in the black shale of Capitanian, Wuchiapingian-Changhsingian in the studied outcrop is of non-hydrothermal origin, and the vast majority of Capitanian shale is biogenic silicon.

Mn in siliceous rocks is often considered as a marker element from the deep ocean (Sugisaki), and the MnO/TiO_2 ratio can be used as a marker to determine the distance of siliceous sediments from the ocean basin (Halamić et al., 2005). The ratio of siliceous rocks deposited on continental slopes and marginal seas closer to the continent should be less than 0.5, and siliceous sediments on open ocean bottoms can reach 0.5–3.5. The MnO/TiO_2 values in the Capitanian black shale in the studied outcrop are 0.02–0.2, with an average of 0.09. The MnO/TiO_2 values in the Wuchiapingian-Changhsingian black shale are 0.04–0.2, with an average of 0.09, suggesting that the siliceous rocks in the study area were formed in the sedimentary environment of the continental slope and marginal seas closer to the continent.

V and Mo are bioactive elements, and their high enrichment indicates that the formation of silicon in shale is related to biological activity. The Capitanian black shale sample shows a higher V content than the abundance of sedimentary rocks, which is 1.55 times higher. In the black shale of Changhsingian, the V value increases to 229 ×

TABLE 2 Comparison of major elements in typical biogenic, hydrothermal, and volcanic mudstone/shale.

Major element proxy	Biogenic mudstone/shale		Hydrothermal mudstone/shale		Volcanic mudstone/shale	Volcanic-biogenic mudstone/shale
Al/(Al + Fe + Mn)	0.5	0.22	0.22	0.28	0.57	0.29
$SiO_2/(K_2O + Na_2O)$	872.36	258.94	159.7	111.8	35.75	82.44
SiO_2/Al_2O_3	135.15	104.81	65.7	45.63	13.66	23.05
$(K_2O + Na_2O)/Al_2O_3$	0.15	0.4	0.41	0.42	0.38	0.28
MnO/TiO_2	0.67	18.75	8.89	9.75	0.25	0.8

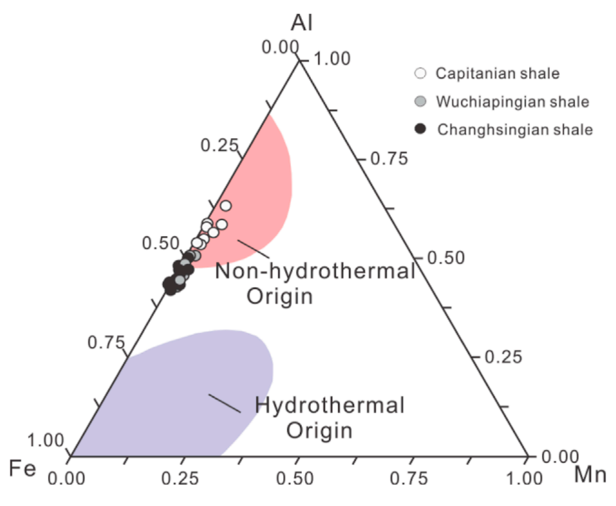

FIGURE 3
Al-Fe-Mn column Triangle diagram of black shale in the studied outcrop. Hydrothermal and non-hydrothermal fields are cited from Adachi et al. (1986).

10^{-6}. The Mo content in the black shale of Capitanian is slightly lower than that of sedimentary rocks. The Mo value of black shale in the Changhsingian stage increased to 9.71 × 10^{-6}. This could imply that the formation of black shale in this area exhibits strong biological effects, and the biological activity has significantly increased from the Capitanian stage to the Changhsingian stage.

Cr is a mantle friendly element with an average content of 76.3. The Cr distribution of Capitanian black shale is slightly higher than the abundance of sedimentary rocks at 63.0. And the Cr value of Changhsingian black shale is much higher than the abundance of sedimentary rocks of 63.0. This phenomenon can be attributed to the extensional movement of the Changhsingian stage, which led to the development of rising ocean currents near the fault zone, bringing in a large amount of Cr elements.

Siliceous sediments of hydrothermal origin are usually positively correlated with Ba and SiO_2. In generally, siliceous rocks of pure biogenic origin contain higher Ba content (Li et al., 2014). There is a weak negative correlation between Ba and SiO_2 in the black shale, with a correlation coefficient of −0.17 (Figure 4). The Ba content of the Capitanian black shale is slightly lower than the abundance of Ba in sedimentary rocks. The Ba content of the black shale belonging to Changhsingian stage is 1.57 times the abundance of Ba in sedimentary rocks. Therefore, it reflects a relatively strong biological activity, and the biological activity intensity of the Changhsingian black shale is significantly higher than that of the Capitanian black shale.

The overall ΣREE of siliceous sediments related to hydrothermal activity is relatively low, while siliceous rocks affected by terrestrial debris have relatively high ΣREE. The ΣREE distribution range of the Changhsingian black shale sample is generally higher than the standard shale (204.1 × 10^{-6}). REE is an important chemical tracer for restoring paleo-marine environments, distinguishing redox conditions, and distinguishing between hydrothermal or non-hydrothermal sediments. In general, hydrothermal sedimentary siliceous rocks have low ΣREE, significant loss of Ce, and

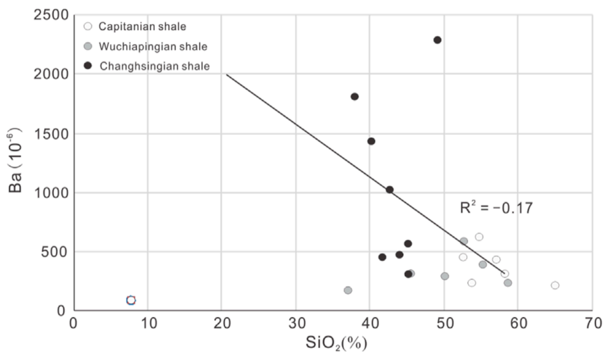

FIGURE 4
Correlation between Ba and SiO_2 of black shale in the studied outcrop.

insignificant loss of Eu, even exhibiting Eu positive anomalies. However, the rare earth elements in non hydrothermal sedimentary siliceous rocks are similar to shale, relatively enriched in light rare earth elements The characteristics of LREE enrichment, ∑HREE non-enrichment, ∑LREE/∑HREE average value of 10.22, negative Ce anomaly, and weak positive Eu anomaly once again confirm that black shale does not belong to hydrothermal sedimentation.

Previous studies have shown that La enrichment exists in metal-rich sediments and high-temperature hydrothermal fluids, leading to the occurrence of negative Ce anomalies (Bao et al., 2008). Use Pr/Pr∗ values to test for the occurrence of negative Ce anomalies caused by La enrichment. When $Ce/Ce* < 1$ and $Pr/Pr* \approx 1$, it indicates the occurrence of positive La anomalies (Figure 5, Zone d). According to the Ce/Ce∗ - Pr/Pr∗ plot of black shale, the data points are all located in the d and e zones, with Pr/Pr∗ values greater than 1, indicating that the negative anomaly of Ce is not affected by the enrichment of La. Weak influence of high-temperature hydrothermal solution.

Therefore, the black shale in the studied outcrop is mainly biogenic, and the relative content of biogenic silicon and terrestrial detrital silicon can be quantitatively calculated and judged by the biogenic silicon content in various lithofacies. Previous studies suggested that the Post Archean Australia Shale (PAAS) represented the average chemical composition of the upper crust, and its source was typical terrestrial debris (Ma et al., 2017). Therefore, the value of $Al_2O_3 \times (SiO_2/Al_2O_3)_{PAAS}$ can be used to represent the silicon content of terrestrial debris in the study area, and the calculation formula is as follows:

$$\mathrm{Bio\,SiO_2(\%)} = \mathrm{SiO_2} - \mathrm{Al_2O_3} \times (\mathrm{SiO_2}/\mathrm{Al_2O_3})_{\mathrm{PAAS}}$$

Bio SiO_2 represents the content of biogenic silicon, SiO_2 and Al_2O_3 represent the content of silica and alumina respectively, and $(SiO_2/Al_2O_3)_{PAAS}$ represents the ratio of silica and alumina in the Post Archean Australia Shale (PAAS). The results indicate that the content of biogenic silicon in black shale of study area accounts for 23.13%–80.90% of the total silicon. The average value of biogenic silicon is over 50% in terms of the total silicon.

Many researchers have conducted extensive research on the sources of silicon in shale and investigated the effects of terrestrial detrital silicon and biogenic silicon on TOC enrichment (Milliken et al., 2016; Milliken and Olson, 2017). As shown in Figure 6, there is a relationship between different types of silica and TOC: Devonian-Mississippian Muskwa and Besa River black shale, mainly composed of biogenic quartz (derived from siliceous radiolarians), have a sedimentary environment in the deep-water area outside the slope, and biogenic quartz has a high degree of correlation with TOC, indicating that biogenic silica has a significant contribution to the enrichment of TOC (Figure 6A).

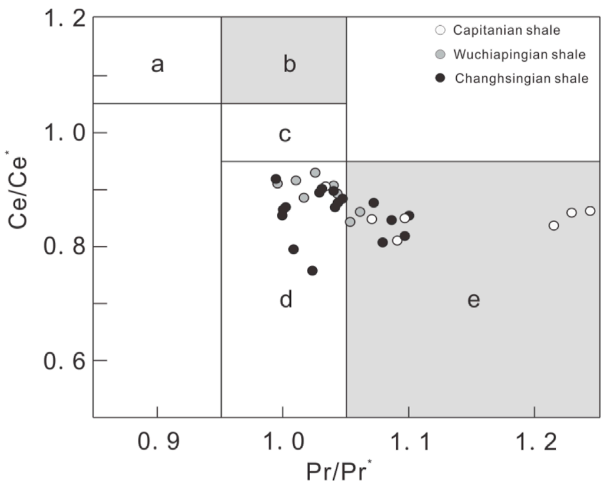

FIGURE 5
Cross-plot of Ce/Ce∗ and Pr/Pr∗ in the black shale. Zone a represents a positive anomaly in Ce. Zone b represents a negative La anomaly and no Ce anomaly. Zone c represents that both Ce and La are normal. Zone d represents a positive anomaly in La and no anomaly in Ce. Zone e represents negative Ce anomaly.

The Ordovician-Silurian black shale is rich in biogenic silicon, characterized by synchronous changes in biogenic silicon and organic matter, with a correlation coefficient of up to 0.80 (Figure 6B), indicating that the sinking fluxes of organisms with siliceous skeletons have a significant enrichment effect on TOC (Ge et al., 2021; Xiong et al., 2021).

In order to more accurately reflect the relationship between silicon content and TOC, as well as the vertical evolution characteristics, this study conducted a correlation analysis between SiO_2 and TOC in black shale (Figure 7), indicating that there was no significant correlation between SiO_2 and TOC in the Permian black shale in the studied outcrop. Based on the observation of thin-sections, a large number of radiolarian individuals and fragments were observed in the Capitanian black shale. Silicon is mainly biogenic, and biogenic silicon mainly comes from radiolarians. The siliceous components of the black shale in Wuchiapingian and Changhsingian are mainly volcanic quartz silicon and terrestrial detrital silicon.

Previous studies have used the chemical composition ratios of siliceous rocks in known sedimentary environments to map and delineate the projection areas of siliceous rocks on continental margins, distant oceans, and mid ocean ridges (Wang et al., 2016). As shown in Figure 8, almost all samples fall into the continental margin area or are distributed adjacent to the continental margin. In summary, the consistent geochemical characteristics of black shale indicate that it was formed in an anoxic environment on the continental margin.

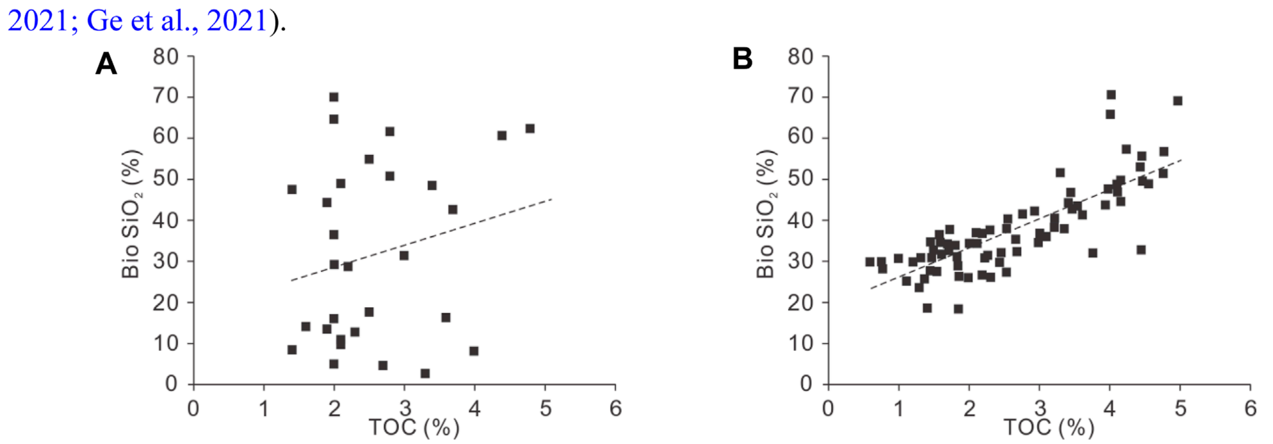

FIGURE 6
Cross-plot of TOC and Bio SiO_2 content in the Devonian-Mississippian black shale (Ross and Marc Bustin, 2009) **(A)** and Ordovician-Silurian black shale **(B)**.

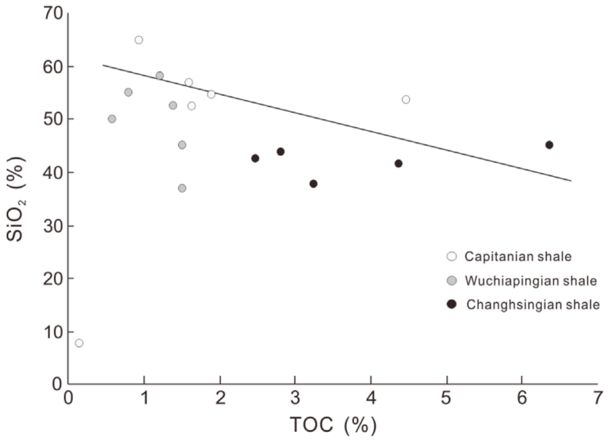

FIGURE 7
Correlation between TOC and SiO_2 content in black shale.

Paleo-ocean productivity

The productivity of marine surface organisms depends on the richness of nutrients in the surface water. The richer the nutrients, the more prosperous the organisms are, and the stronger the carbon production capacity of photosynthesis, resulting in greater productivity. The elements that can reflect the nutritional level of water include N, P, Fe, Cu, Ni, and Zn (Tribovillard et al., 2006). N and P are greatly affected by recycling and later diagenesis, while Fe are influenced by carbonate dissolution and recrystallization, etc., which make them unreal. Cu, Zn, and Ni as nutrient elements, combine with organic matter or form organic complexes for precipitation and burial, and high levels of Cu, Zn, and Ni reflected higher paleo-productivity (Tribovillard et al., 2006; Fathy et al., 2018). Therefore, Cu, Zn, and Ni can be used as indicators to reflect the level of ancient productivity. Another way to characterize the primary productivity of water surface is through the organic carbon flux of the water mass. High productivity enhances the organic carbon flux of the water mass. Organic carbon forms a local sulfate reduction microenvironment through complexation with trace metal elements or decomposition of organic matter, resulting in the precipitation of certain trace metal elements. The higher the organic carbon flux of the water mass, the greater the burial amount of certain trace metal elements.

In addition to hydrothermal activities, the main sources of these nutrients are biogenic and terrigenous, only biogenic elements can reflect the change of paleoproductivity. Before using these trace elements, the influence of terrestrial sources should be eliminated, and Ti or Al should be used to correct the above elements (Taylor and McLennan, 1985). The formula is:

$$X_{xs} = X_{total} - Ti_{total} \times (X/Ti)_{PAAS}$$

X_{xs} represents the excess value of X, which is obtained by Ti correction of the trace element content in the sample using the trace element content in PAAS. Xtotal is the total element content of the tested rock sample, and $(X/Ti)_{PAAS}$ represents the ratio of element content to Ti in PAAS. The (X/Ti) PAAS used is quoted from Taylor and McLennan (1985). If the calculation result is positive, it indicates that the element is relatively PAAS and exhibits marine autogenesis enrichment or volcanic hydrothermal enrichment. If the calculation result is negative, it indicates that the content of this element in the sample is mainly contributed by terrestrial materials.

The correlation between Ba and Mo and organic carbon flux in water mass is significant, which can reflect surface productivity. Dymond et al. (1992) established for the first time a calculation model for surface productivity using Ba as an indicator, using data obtained from sediment traps. The sources of Ba mainly include biogenic barium and terrestrial barium. Only the portion of Ba contributed by the source of students can reflect primary productivity. The calculation formula for biogenic Ba (Ba_{bio}) is consistent with the formula for excess trace elements. High marine productivity results in a large amount of organic carbon input, forming a large amount of hydrogen sulfide, which reacts with molybdate to form thiomolybdate, and is buried together with iron

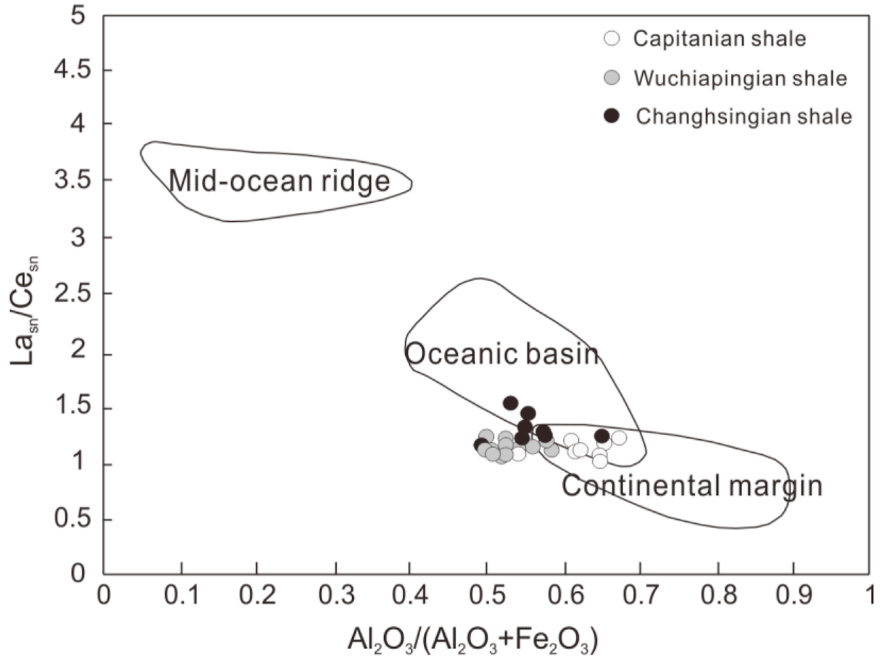

FIGURE 8
Correlation between $Al_2O_3/(Al_2O_3+Fe_2O_3)$ and La_{sn}/Ce_{sn} content in black shale (modiated from Wang et al., 2016).

sulfides and organic matter. The more organic carbon is input, the more Mo is deposited and buried. The advantage of Mo as an input parameter for organic carbon is that it is less affected by later changes, as the binding of iron sulfides to Mo is irreversible.

Cu_{bio}, Zn_{bio}, Ni_{bio}, and Ba_{bio} are used to reflect the paleo-productivity evolution of black shale (Shen et al., 2014). All elements are corrected by Ti, and negative excess element values are removed. The changes in paleo-marine productivity of the Capitanian-Changhsingian black shale obtained in the end are shown in Figure 9. The productivity of the ancient ocean corresponding to the Capitanian black shale is relatively high, while the productivity of the Wuchiapingian stage paleo ocean has decreased. In the early Changhsingian stage, the productivity of paleo-oceans significantly increased again. Overall, volcanic tuff has a significant promoting effect on the productivity of paleo-oceans. Further comparison between the evolution of paleo-productivity and the distribution characteristics of TOC reveals a consistent correspondence between high biological productivity and high organic matter accumulation. However, in the Wuchiapingian stage, the changes in productivity are not as significant as those in total organic carbon. The productivity has a controlling effect on organic carbon enrichment, but it is not the only controlling factor for organic carbon enrichment.

In recent years, many studies suggested that the efficient indicator for evaluating shale redox conditions is the U/Th ratio (Jones and Manning, 1994), and there is a significant correlation between TOC value and U/Th ratio. However, previous studies of the Permian Shanxi Formation transitional shale in North China suggested that the shale intervals heavily disturbed by terrestrial debris generally have lower U/Th ratios and poor correlation with TOC (Zhang et al., 2021). Taking this study as an example (Figure 10): The overall U/Th ratio is relatively low, and there is no trend of changes in redox conditions at different stages.

The results indicate that V/Cr is significantly better than U/Th and Ni/Co in reflecting the changes in redox conditions in the study area. Under the 3rd-order sequence framework, V/Cr well reflects the trend of change, with SQ2's V/Cr ranging from 1.40 to 3.77, with an average of 2.41 ($n = 13$), SQ3's V/Cr ranging from 1.09 to 2.89, with an average of 2.23 ($n = 10$), and SQ4's V/Cr ranging from 1.15 to 2.28, with an average of 1.64 ($n = 12$). Except for SQ2, the high value range of V/Cr is inconsistent with the development location of black shale, suggesting that the dysoxic and anoxic environment is not the only controlling factor for the development of black shale.

The Guadalupian-Lopingian boundary (G-LB) is a critical period in the development of Earth's history, during which the Earth's climate system experienced the disappearance of Late Paleozoic ice chambers and transitioned to Mesozoic greenhouses, accompanied by a series of major geological events such as the extinction of biological clusters (Stanley and Yang, 1994; Wignall and Bond, 2023), the eruption of Emeishan basalt (Sun et al., 2010), and a significant drop in sea-level to the lowest point of the Phanerozoic era (Haq and Schutter, 2008; Shen et al., 2019; Zhao et al., 2019). These events have more or less affected the global carbon cycle and are recorded in the inorganic carbon isotope changes of marine carbonate rocks (Wang et al., 2004; Shen et al., 2013). Therefore, carbon isotopes can also better reflect the global or regional changes in redox conditions of seawater during the Capitanian-Changhsingian stage. The results of intensive carbon isotope testing in the study area and other regions of South China (Figure 11) show that in the late Capitanian stage (SQ2), carbon isotopes showed a significant "negative shift". This phenomenon existed in multiple outcrops in the Upper Yangtze region, indicating

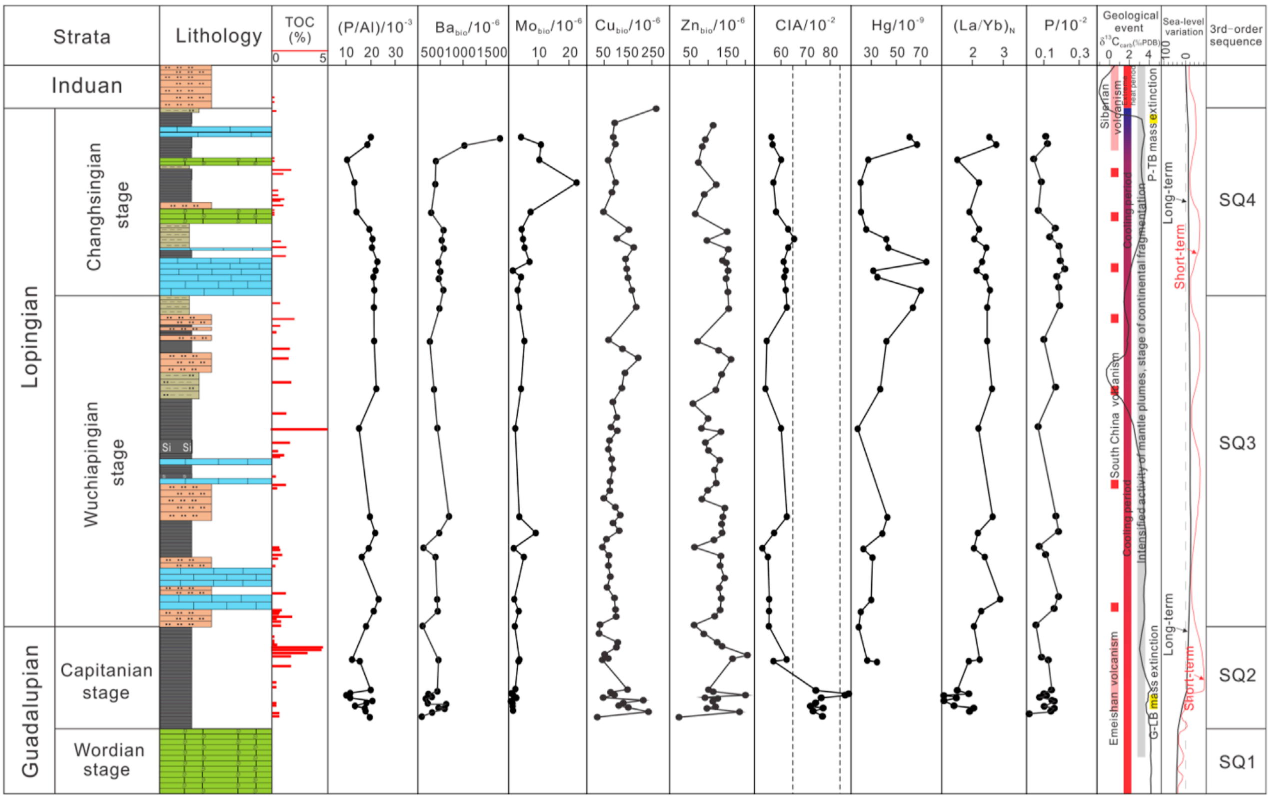

FIGURE 9
Comprehensive column for the paleo-productivity proxies during Guadalupian-Lower Triassic in the studied outcrop. Sea-level data are from Haq and Schutter (2008). Geological events are from Isozaki (2009), Wignall et al. (2009), Shen et al. (2013) and Chen et al. (2013). Paleo-redox condition under sequence framework.

the existence of regional anoxic events in seawater during this period, In the late SQ3-early SQ4 period, there was also a common phenomenon of negative carbon isotope shift in the Upper Yangtze region, indicating that seawater had regional anoxic characteristics during this period (Figure 12).

Organic matter accumulation is a complex physical-chemical process that involves many factors, such as redox condition of bottom seawater, sedimentation rate, productivity of surface water, and geological event. The main controlling factors for organic matter enrichment in modern and paleo marine sediments have been extensively discussed over the past 30 years (Pedersen et al., 1990; Arthur and Sageman, 1994; Wei et al., 2012; Ding et al., 2018). Three fundamental models have been identified for the accumulation of organic matter in organic-rich sediments: (1) enhanced organic productivity, (2) enhanced organic matter preservation, associated with reducing conditions and (3) low sedimentation rate (minimal detrital dilution). Sea-level fluctuations appear to exert a fundamental control on all three factors and therefore on organic matter accumulation. Currently, it is generally believed that organic matter enrichment is closely related to the preservation of large-scale biogenetic material, and the prerequisite for large-scale biogenetic material preservation is favorable sedimentary-burial conditions (such as anoxic and appropriate sedimentation rate). Consequently, the controlling factors for organic matter enrichment can be summarized as primary productivity and favorable preservation conditions in the marine surface. The productivity school, represented by Pedersen et al. (1990), Sageman et al. (2003), and Gallego-Torres et al. (2007), believes that organic matter accumulation is mainly controlled by the biological productivity of the ocean surface, and the impact of water redox properties is limited. The typical representative is the rising ocean currents on the continental margin. The oxidation-reduction school represented by Arthur and Sageman (1994) and Mort et al. (2007) believes that low marine surface productivity can also form organic rich sediments in hypoxic environments, especially in sulfide environments, with modern anoxic basins such as the Black Sea and Cretaceous marine anoxic events as typical representatives. Scholars such as Ibach (1982) and Morton et al. (2000) believe that an appropriate sedimentation rate is the key factor causing organic matter enrichment, and either too high or too low sedimentation rates are not conducive to organic matter enrichment.

From a global perspective, this area is located in the southwestern part of the South China during the Capitanian stage (Figure 13). Overall, SQ2-SQ4 has experienced one glacial event (Kamura glacial event), two biotic extinction events (G-LB and P-TB biotic extinction events), and two anoxic events (late Capitanian stage, late Wuchiapingian stage-early Changhsingian stage), Three major volcanic activities (Emeishan Igneous Province, South China Acidic Volcanic Activity, and Siberian Igneous

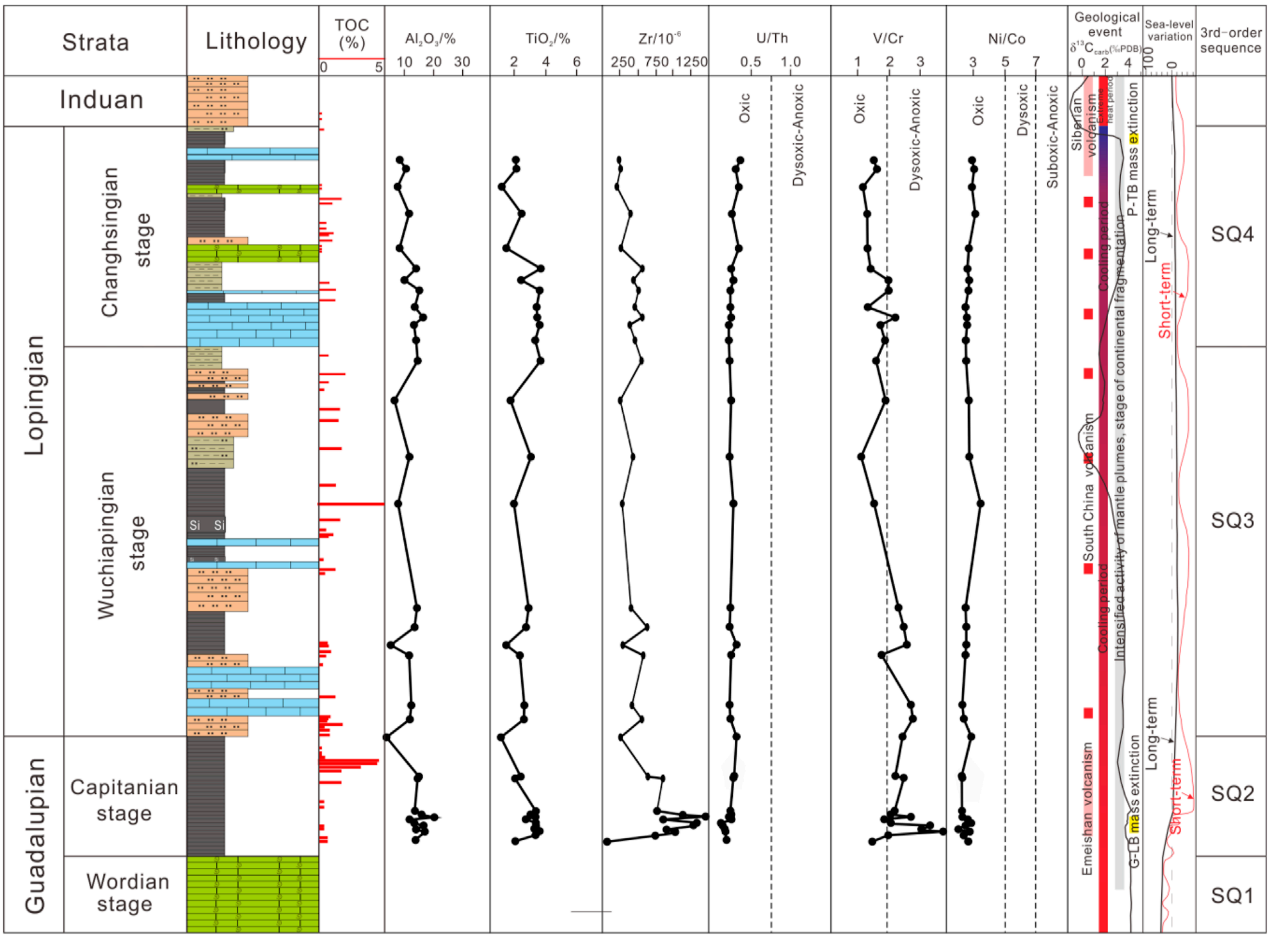

FIGURE 10
Comprehensive column for the terrestrial input and paleo-redox proxies during Guadalupian-Lower Triassic in the studied outcrop. Sea-level data are from Haq and Schutter (2008). Geological events are from Isozaki (2009), Wignall et al. (2009), Shen et al. (2013) and Chen et al. (2013).

Province). During this period, global sea levels experienced a period of "one regression and one transgression".

The Upper Yangtze region, where the study area is located, was dominated by shallow carbonate platform environment in the late Wordian stage before SQ2 sedimentation. The water in the entire area is in an oxic environment, characterized by moderate paleo-productivity and shallow water depth. Due to the seafloor expansion superimposed by the Kamura event (Figure 14), the global sea level of the Capitanian stage where SQ2 is located continuously decreased, reaching the lowest point in geological history by the end of the Capitanian stage (Haq and Schutter, 2008). Due to the volcanic ash formed by the eruption of the Emeishan Large Igneous Province, which is rich in nutrients such as Fe, P, N, Si, and Mn, it can promote the proliferation of algae and other organisms, and improve the primary productivity of surface seawater, During this period, due to the extensional rift activity induced by the Emeishan Large Igneous Province, the water in the rift area has rapidly deepened, resulting in a anoxic environment in intra-platform basin and shelf around extensional rift area. Meanwhile, the end of the glacial event is conducive to a significant rise in sea level, creating a hypoxic environment. The ocean is strongly retained, controlled by the upwelling of anoxic bottom seawater, and a large amount of organic carbon has been deposited and preserved due to the G-LB extinction event.

During SQ3, the extensional rift activity stagnated, and the differences in sedimentary landforms gradually disappeared due to the enhancement of terrestrial supply. The global sea-level further decreased, and the water conditions gradually changed from anoxic to dysoxic. In the later stage, they evolved into oxic conditions (Figure 14). Multiple periods of acidic volcanic activity in South China have maintained a high level of paleo-productivity in seawater. Under dysoxic conditions, organic matter can still be enriched in large quantities, forming the Wuchiapingian black shale. In the early stage of SQ4, the entire Changhsingian stage area was dominated by platform environment, with low sea-level and high paleo-productivity, all of which were in an oxic environment. However, at this time, it is a anoxic event of bottom water in deep sea, and the sedimentary paleo-geomorphology in the study area cannot cater to this period of anoxic event and does not have the conditions for organic matter enrichment. Accompanied by the Emeishan Rift Movement, the extensional subsidence activity resumed, and the water in the late SQ4 extensional subsidence area deepened sharply

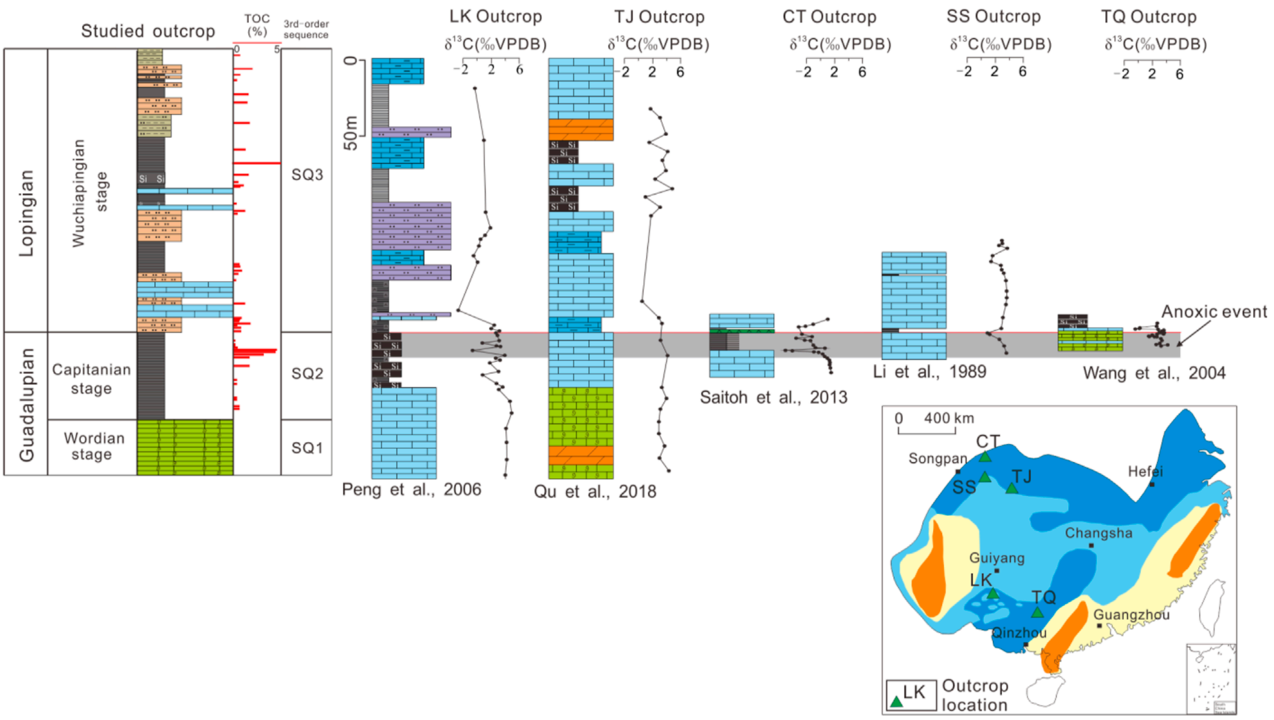

FIGURE 11
Comparison of carbon isotopes at the Guadalupian-Lopingian boundary (G-LB) between the studied outcrop and other typical outcrops in South China (Li et al., 1989; Wang et al., 2004; Peng et al., 2006; Saitoh et al., 2013; Qu et al., 2018).

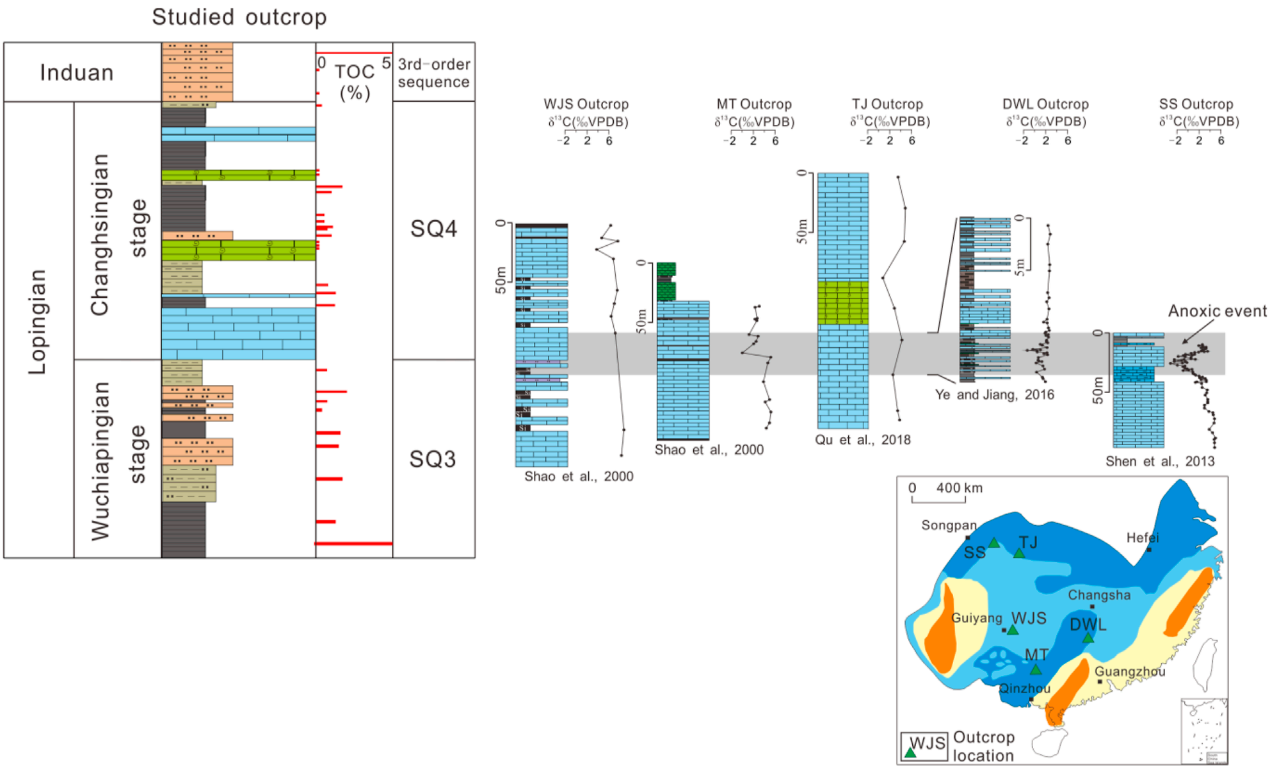

FIGURE 12
Comparison of carbon isotopes at the Wuchiapingian-Changhsingian boundary between the studied outcrop and other typical outcrops in South China. Organic matter enrichment and evolution model under sequence framework (Shao et al., 2000; Shen et al., 2013; Ye and Jiang, 2016; Qu et al., 2018).

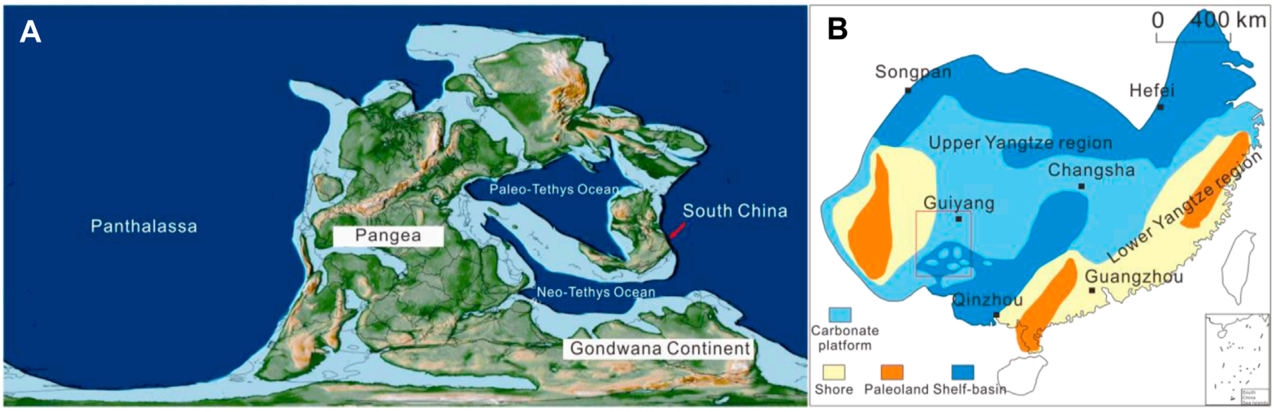

FIGURE 13
Paleogeographic characteristics during Guadalupian stage. **(A)** Global paleogeographic distribution (Scotese, 2016). **(B)** Paleogeographic characteristics of South China during Guadalupian stage (Qu et al., 2018).

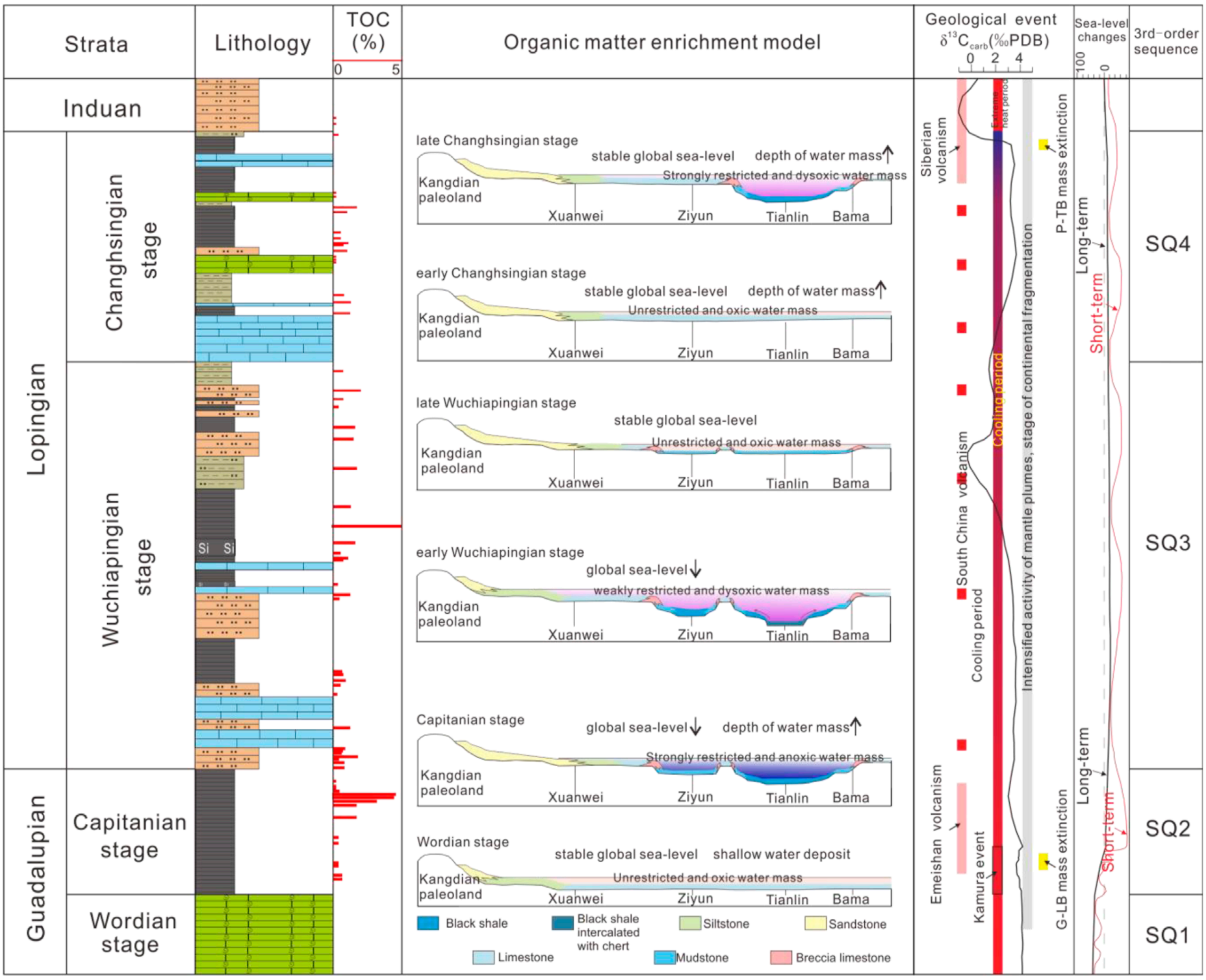

FIGURE 14
Organic matter enrichment models within the 3rd-order sequence framework during Guadalupian-Lower Triassic in the studied outcrop. Sea-level data are from Haq and Schutter (2008). Geological events are from Isozaki (2009), Wignall et al. (2009), Shen et al. (2013) and Chen et al. (2013).

again, with a sharp increase in ocean retention. The dysoxic water conditions resulted in the preservation of large-scale organic matter, forming the black shale during the Changhsingian stage (Figure 14).

Conclusion

1) The Permian Capitanian-Changhsingian black shale in the Northern Nanpanjiang Basin was formed in continental slope and marginal-sea sediments near the continent in the intra-platform basin. The SiO_2 content of the Capitanian-Changhsingian black shale is lower than that of the Ordovician-Silurian black marine shale and shows a gradually decreasing trend. The silicon in the black shale of the Capitanian stage, Wuchiapingian stage and Changhsingian stage in the study area is of non-hydrothermal origin, while the majority of the Capitanian stage is biogenic silicon. The TiO2 and MnO content of the Capitanian-Changhsingian black shale is significantly higher than that of the Ordovician-Silurian shale, and its major elemental composition is similar to that of siliceous rocks formed by volcanic biochemical processes.
2) The factors controlling the Capitanian black shale deposition are the rapidly deepening water mass of extensional rifts and the high productivity induced by volcanic ash in the major igneous provinces, as well as the global anoxic event represented by "negative carbon isotope shift". The factors controlling the Changhsingian black shale deposition are the deepening of water mass under the reactivation of extensional rifts, resulting in a dysoxic environment, and the high productivity maintained by volcanic activity in South China. The Wuchiapingian black shale was formed under dysoxic conditions under the stagnation of extensional activity, and intermittent volcanic activity in South China maintained the high paleo-productivity level of the Wuchiapingian stage.

Data availability statement

The original contributions presented in the study are included in the article/Supplementary Material, further inquiries can be directed to the corresponding author.

Author contributions

HZ: Conceptualization, Funding acquisition, Investigation, Visualization, Writing–original draft. JC: Investigation, Methodology, Project administration, Supervision, Writing–original draft. BL: Formal Analysis, Supervision, Validation, Writing–original draft. YC: Formal Analysis, Methodology, Writing–review and editing. QZ: Data curation, Resources, Software, Writing–review and editing. YM: Data curation, Investigation, Writing–review and editing. XF: Formal Analysis, Supervision, Writing–review and editing. QY: Supervision, Validation, Writing–review and editing.

Funding

The author(s) declare that financial support was received for the research, authorship, and/or publication of this article. The research was supported by the Guizhou Provincial Fund Project [Grant No. (2022)ZD005] and Guizhou Provincial Fund Project [Grant No. (2023)-344].

Conflict of interest

Author BL was employed by Ltd.

The remaining authors declare that the research was conducted in the absence of any commercial or financial relationships that could be construed as a potential conflict of interest.

Publisher's note

References

Algeo, T. J., and Maynard, J. B. (2004). Trace element behavior and redox facies in core shales of Upper Pennsylvanian Kansas-type cyclothems. *Chem. Geol.* 206, 289–318. doi:10.1016/j.chemgeo.2003.12.009

Arthur, M. A., and Sageman, B. B. (1994). Marine black shales: depositional mechanisms and environments of ancient deposits. *Annu. Rev. Earth Planet. Sci.* 22, 499–551. doi:10.1146/annurev.ea.22.050194.002435

Bai, L., Duan, L., Gao, Z., Ma, G., Yang, A., Liu, Z., et al. (2023). Controlling effect of shale pore connectivity on the adsorption state of shale gas: a case study of continental shale of Jurassic Ziliujing Formation, Sichuan Basin. *Energy fuels.* 37, 14891–14905. doi:10.1021/acs.energyfuels.3c02721

Bao, S. X., Zhou, H. Y., Peng, X. T., Ji, F. W., and Yao, H. Q. (2008). Geochemistry of REE and yttrium in hydrothermal fluids from the Endeavour segment, Juan de Fuca Ridge. *Geochem. Journey.* 42 (4), 359–370. doi:10.2343/geochemj.42.359

Cai, G., Gu, Y., Fu, Y., Jiang, Y., Wei, Z., Wang, Z., et al. (2023b). Pore system classification of Jurassic Da'anzhai Member lacustrine shale: insight from pore fluid distribution. *Energy Explor. Exploitation* 0 (0), 900–921. doi:10.1177/01445987231154613

Cai, G., Gu, Y., Jiang, Y., and Wang, Z. (2023a). Pore structure and fluid evaluation of deep organic-rich marine shale: a case study from Wufeng–Longmaxi Formation of Southern Sichuan Basin. *Appl. Sci.* 13, 7827. doi:10.3390/app13137827

Chen, B., Joachimski, M. M., Shen, S. Z., Lambert, L. L., Lai, X. L., Wang, X. D., et al. (2013). Permian ice volume and palaeoclimate history: oxygen isotope proxies revisited. *Gondwana Res.* 24 (2013), 77–89. doi:10.1016/j.gr.2012.07.007

Ding, J., Zhang, J., Tang, X., Huo, Z., Han, S., Lang, Y., et al. (2018). Elemental geochemical evidence for depositional conditions and organic matter enrichment of black rock series strata in an inter-platform basin: the lower carboniferous datang formation, Southern Guizhou, Southwest China. *Minerals* 8 (11), 480–509. doi:10.3390/MIN8110509

Dong, D., Qiu, Z., Zhang, L., Li, S., Zhang, Q., Li, X., et al. (2021). Progress on sedimentology of transitional facies shales and new discoveries of shale gas. *Acta Sedimentol. Sin.* 39 (1), 29–45. doi:10.14027/j.issn.1000-0550.2021.002

Dymond, J., Suess, E., and Lyle, M. (1992). Barium in deep-sea sediment: a geochemical proxy for paleoproductivity. *Paleoceanography* 7 (2), 163–181. doi:10.1029/92PA01080

Fan, C. H., Nie, S., Li, H., Radwan, A. E., Pan, Q. C., Shi, X. C., et al. (2024). Quantitative prediction and spatial analysis of structural fractures in deep shale gas reservoirs within complex structural zones: a case study of the Longmaxi Formation in the Luzhou area, southern Sichuan Basin, China. *J. Asian Earth Sci.* 263, 106025. doi:10.1016/j.jseaes.2024.106025

Fang, R., Jiang, Y., Sun, S., Luo, Y., Qi, L., Dong, D., et al. (2023). Controlling factors of organic matter accumulation and lacustrine shale distribution in Lianggaoshan Formation, Sichuan Basin, SW China. *Front. Earth Sci.* 11, 1218215. doi:10.3389/feart.2023.1218215

Fathy, D., Wagreich, M., Gier, S., Mohamed, R. S. A., Zaki, R., and El Nady, M. M. (2018). Maastrichtian oil shale deposition on the southern Tethys margin, Egypt: insights into greenhouse climate and paleoceanography. *Palaeogeogr. Palaeoclimatol. Palaeoecol.* 505, 18–32. doi:10.1016/j.palaeo.2018.05.017

Gallego-Torres, D., Martínez-Ruiz, F., Paytan, A., Jiménez-Espejo, F. J., and Ortega-Huertas, M. (2007). Pliocene-holocene evolution of depositional conditions in the eastern mediterranean: role of anoxia vs. productivity at time of sapropel deposition. *Palaeogeogr. Palaeoclimatol. Palaeoecol.* 246 (2–4), 424–439. doi:10.1016/j.palaeo.2006.10.008

Ge, X. Y., Mou, C. L., Yu, Q., Liu, W., Meng, X., He, J. L., et al. (2021). A study on the enrichment of organic materials in black shales of the wufeng to longmaxi formations in eastern Sichuan Basin. *Sediment. Geol. Tethyan Geol.* 41 (3), 418–435. doi:10.19826/j.cnki.1009-3850.2020.12001

Gu, Y., Hu, D., Wei, Z., Liu, R., Hao, J., Han, J., et al. (2022). Sedimentology and geochemistry of the upper permian linghao formation marine shale, central Nanpanjiang Basin, SW China. *Front. Earth Sci.* 10, 914426. doi:10.3389/feart.2022.914426

Halamić, J., Marching, V., and Goričan, Š. (2005). Jurassic radiolarian cherts in north-western Croatia: geochemistry, material provenance and depositional environment. *Geol. Carpathica* 56 (2), 123–136. doi:10.1111/j.1472-4669.2005.00045.x

Han, H., Dai, J., Guo, C., Zhong, N., Pang, P., Ding, Z., et al. (2021). Pore characteristics and factors controlling lacustrine shales from the Upper Cretaceous Qingshankou Formation of the Songliao Basin, Northeast China: a study combining SEM, low-temperature gas adsorption and MICP experiments. *Acta Geol. Sin. Engl. Ed.* 95 (2), 585–601. doi:10.1111/1755-6724.14419

Haq, B. U., and Schutter, S. R. (2008). A chronology of Paleozoic sea-level changes. *Science* 322, 64–68. doi:10.1126/science.1161648

Hu, T., Pang, X., Wang, Q., Jiang, S., Wang, X., Huang, C., et al. (2018). Geochemical and geological characteristics of permian lucaogou formation shale of the well ji174, jimusar sag, junggar basin, China: implications for shale oil exploration. *Geol. J.* 2017, 2371–2385. doi:10.1002/gj.3073

Ibach, L. E. J. (1982). Relationship between sedimentation rate and total organic carbon content in ancient marine sediments. *AAPG Bulletin.* 66 (2), 170–188. doi:10.1306/03B59A5D-16D1-11D7-8645000102C1865D

Isozaki, Y. (2009). Integrated "plume winter" scenario for the double-phased extinction during the Paleozoic–Mesozoic transition: the G-LB and P-TB events from a Panthalassan perspective. *J. Asian Earth Sci.* 36 (2009), 459–480. doi:10.1016/j.jseaes.2009.05.006

Jiang, Y., Chen, L., Qi, L., Luo, M., Chen, X., Tao, Y., et al. (2018). Characterization of the lower silurian longmaxi marine shale in changning area in the South sichuan basin, China. *Geol. J.* 53, 1656–1664. doi:10.1002/gj.2983

Jiang, Y., Song, Y., Qi, L., Chen, L., Tao, Y., Gan, H., et al. (2016). Fine lithofacies of China's marine shale and its logging prediction: a case study of the Lower Silurian Longmaxi marine shale in Weiyuan area, southern Sichuan Basin,China. *Earth Sci. Front.* 23 (1), 107–118. doi:10.13745/j.esf.2016.01.010

Jiao, F., Wen, S., Liu, X., Xiong, X., Li, S., Gu, Y., et al. (2023). Research progress in exploration theory and technology of transitional shale gas in the Ordos Basin. *Nat. Gas. Ind.* 43 (4), 11–23. doi:10.3787/j.issn.1000-0976.2023.04.002

Jones, B., and Manning, D. A. C. (1994). Comparison of geochemical indices used for the interpretation of palaeoredox conditions in ancient mudstones. *Chem. Geol.* 111 (1–4), 111–129. doi:10.1016/0009-2541(94)90085-X

Labani, M. M., Rezaee, R., Saeedi, A., and Al Hinai, A. (2013). Evaluation of pore size spectrum of gas shale reservoirs using low pressure nitrogen adsorption, gas expansion and mercury porosimetry: a case study from the Perth and Canning Basins, Western Australia. *J. Petroleum Sci. Eng.* 112, 7–16. doi:10.1016/j.petrol.2013.11.022

Lai, X., Wang, W., Wignall, P. B., Bond, D. P. G., Jiang, H., Ali, J. R., et al. (2008). Palaeoenvironmental change during the end-Guadalupian (Permian) mass extinction in sichuan, China. *Palaeogeogr. Palaeoclimatol. Palaeoecol.* 269 (1-2), 78–93. doi:10.1016/j.palaeo.2008.08.005

Li, H. (2023). Coordinated development of shale gas benefit exploitation and ecological environmental conservation in China: a mini review. *Front. Ecol. Evol.* 11, 1232395. doi:10.3389/fevo.2023.1232395

Li, H. Z., Zhai, M. G., Zhang, L. C., Gao, L., Yang, Z. J., Zhou, Y. Z., et al. (2014). Distribution, microfabric, and geochemical characteristics of siliceous rocks in central orogenic belt, China: implications for a hydrothermal sedimentation model. *Sci. World J.* 780910 (4), 1–25. doi:10.1155/2014/780910

Li, Z., Zhan, L., Dai, J., Jin, R., Zhu, X., Zhang, J., et al. (1989). *Research on the Permian Triassic biostratigraphy and event stratigraphy in northern Sichuan and southern Shaanxi.* Beijing: Beijing Geological Publishing House, 435.

Lin, M., Xi, K., Cao, Y., Liu, Q., Zhang, Z., and Li, K. (2021). Petrographic features and diagenetic alteration in the shale strata of the permian lucaogou formation, jimusar sag, junggar basin. *J. Petroleum Sci. Eng.* 203, 108684. doi:10.1016/j.petrol.2021.108684

Liu, W., Gao, P., Xiao, X., Zhao, Y., Xing, Y., and Li, J. (2024). Variable depositional environments and organic matter enrichment of Early Cambrian shales in the Middle Yangtze region, South China. *J. Asian Earth Sci.* 259 (2024), 105874. doi:10.1016/j.jseaes.2023.105874

Liu, Z., Yan, D., Yuan, D., Niu, X., and Fu, H. (2022). Multiple controls on the organic matter accumulation in early Cambrian marine black shales, middle Yangtze Block, South China. *J. Nat. Gas Sci. Eng.* 100 (2022), 104454. doi:10.1016/j.jngse.2022.104454

Loucks, R. G., Reed, R. M., Ruppel, S. C., and Jarvie, D. M. (2009). Morphology, genesis, and distribution of nanometer-scale pores in siliceous mudstones of the Mississippian Barnett Shale. *J. Sediment. Res.* 79 (12), 848–861. doi:10.2110/jsr.2009.092

Ma, K., Hu, S. Y., Wang, T. S., Zhang, B. M., Qin, S. F., Shi, S. Y., et al. (2017). Sedimentary environments and mechanisms of organic matter enrichment in the Mesoproterozoic Hongshuizhuang Formation of northern China. *Palaeogeogr. Palaeoclimatol. Palaeoecol.* 75, 176–187. doi:10.1016/j.palaeo.2017.02.038

Mei, M., Ma, Y., Deng, J., Chu, H., and Zheng, K. (2007). Sequence stratigraphy framework and paleogeographical setting of the Lo-ping of the Pemian of Dian-Qian-Gui Basin and its adjacent areas. *Sci. China Ser. D* 37 (5), 605–617. doi:10.3969/j.issn.1674-7240.2007.05.004

Milliken, K. L., Ergene, S. M., and Ozkan, A. (2016). Quartz types, authigenic and detrital, in the upper cretaceous eagle ford formation, South Texas, USA. *Sediment. Geol.* 339 (2016), 273–288. doi:10.1016/j.sedgeo.2016.03.012

Milliken, K. L., and Olson, T. (2017). Silica diagenesis, porosity evolution, and mechanical behavior in siliceous mudstones, Mowry Shale (Cretaceous), Rocky Mountains, U.S.A. *J. Sediment. Res.* 88, 366–387. doi:10.2110/jsr.2017.24

Mort, H. P., Adatte, T., Föllmi, K. B., Keller, G., Steinmann, P., Matera, V., et al. (2007). Phosphorus and the roles of productivity and nutrient recycling during oceanic anoxic event 2. *Geology.* 35 (6), 483–486. doi:10.1130/G23475A.1

Morton, R. A., Ward, G. H., and White, W. A. (2000). Rates of sediment supply and sea-level rise in a large coastal lagoon. *Marine Geology.* 167 (3–4), 261–284. doi:10.1016/S0025-3227(00)00030-X

Pedersen, T. F., and Calvert, S. E. (1990). Anoxia vs. Productivity: What Controls the Formation of Organic-Carbon-Rich Sediments and Sedimentary Rocks? *AAPG Bulletin.* 74 (1), 454–466. doi:10.1306/0C9B232B-1710-11D7-8645000102C1865D

Peng, B., Wang, Y., Fan, W., and Peng, T. (2006). Carbon isotope composition changes of Maokouian-Wuchiapingian and the environmental effect of Emeishan large igneous province at Lekang section, Guizhou Province. *Geochimica* 35 (2), 126–132. doi:10.19700/j.0379-1726.2006.02.002

Qiu, Z., and Zou, C. (2020). Unconventional Petroleum Sedimentology: Connotation and prospect. *Acta Sedimentol. Sin.* 38 (1), 1–29. doi:10.14027/j.issn.1000-0550.2019.116

Qu, H., Li, P., Luo, T., Guan, L., Fan, Y., and Wang, L. (2018). Carbon isotopic evolution characteristics and the geological significance of the Permian carbonate stratotype section in the Northern Upper-Yangtze Region, Southern China. *Acta Geol. Sin. Engl. Ed.* 92 (6), 2367–2381. doi:10.1111/1755-6724.13733

Ross, D. J. K., and Marc Bustin, R. (2009). The importance of shale composition and pore structure upon gas storage potential of shale gas reservoirs. *Mar. Petroleum Geol.* 26, 916–927. doi:10.1016/j.marpetgeo.2008.06.004

Sageman, B. B., Murphy, A. E., Werne, J. P., Straeten, C. A. V., and Lyons, T. W. (2003). A tale of shales: the relative roles of production, decomposition, and dilution in the accumulation of organic-rich strata, middle-upper devonian, Appalachian basin. *Chemical Geology.* 195 (1), 229–273. doi:10.1016/S0009-2541(02)00397-2

Saitoh, M., Isozaki, Y., Ueno, Y., Yoshida, N., Yao, J., and Ji, Z. (2013). Middle-Upper Permian carbon isotope stratigraphy at Chaotian, South China: Pre-extinction multiple upwelling of oxygen-depleted water onto continental shelf. *J. Asian Earth Sci.* 67–68, 51–62. doi:10.1016/j.jseaes.2013.02.009

Scotese, C. (2016). PALEOMAP PALEOATLAS FOR GPLATES AND THE PALEODATAPLOTTER PROGRAM. *50th Annu. GSA North-Central Sect. Meet.*, 275387. doi:10.1130/abs/2016NC-275387

Shao, L., Zhang, P., Dou, J., and Shen, S. (2000). Carbon isotope compositions of the Late Permian carbonate rocks in southern China: their variations between the Wujiaping and Changxing formations. *Palaeogeogr. Palaeoclimatol. Palaeoecol.* 161 (2000), 179–192. doi:10.1016/S0031-0182(00)00122-X

Shen, J., Zhou, L., Feng, Q., Zhang, M., Lei, Y., Zhang, N., et al. (2014). Paleo-productivity evolution across the Permian-Triassic boundary and quantitative calculation of primary productivity of black rock series from the Dalong Formation, South China. *Sci. China Earth Sci.* 57 (7), 1583–1594. doi:10.1007/s11430-013-4780-5

Shen, S., Cao, C., Zhang, H., Bowring, S. A., Henderson, C. M., Payne, J. L., et al. (2013). High-resolution $\delta^{13}C_{carb}$ chemostratigraphy from latest Guadalupian through earliest Triassic in South China and Iran. *Earth Planet. Sci. Lett.* 375 (2013), 156–165. doi:10.1016/j.epsl.2013.05.020

Shen, S., Zhang, H., Zhang, Y., Yuan, D., Chen, B., He, W., et al. (2019). Permian integrative stratigraphy and timescale of China. *Sci. China Earth Sci.* 62, 154–188. doi:10.1007/s11430-017-9228-4

Stanley, S. M., and Yang, X. (1994). A double mass extinction at the end of the Paleozoic Era. *Science* 266 (5189), 1340–1344. doi:10.1126/science.266.5189.1340

Sun, Y., Lai, X., Wignall, P. B., Widdowson, M., Ali, J. R., Jiang, H. S., et al. (2010). Dating the onset and nature of the Middle Permian Emeishan Large Igneous Province eruptions in SW China using conodont biostratigraphy and its bearing on mantle plume uplift models. *Lithos* 119 (1/2), 20–33. doi:10.1016/j.lithos.2010.05.012

Tan, J., Jiang, Y., Li, X., Ji, C., Gu, Y., and Wang, Z. (2024). Paleoenvironment of marine-continental transitional shales in the lower Permian Shanxi formation, southeastern Ordos Basin, China. *Energy Geosci.* 5 (2024), 100261. doi:10.1016/j.engeos.2023.100261

Taylor, S. R., and McLennan, S. M. (1985). *The continental crust: its composition and evolution*. Oxford: Blackwell Scientific Publications.

Tribovillard, N., Algeo, T. J., Baudin, F., and Riboulleau, A. (2012). Analysis of marine environmental conditions based on molybdenum-uranium covariation-Applications to Mesozoic paleoceanography. *Chem. Geol.* 324-325, 46–58. doi:10.1016/j.chemgeo.2011.09.009

Tribovillard, N., Algeo, T. J., Lyons, T., and Riboulleau, A. (2006). Trace metals as paleoredox and paleoproductivity proxies: An update. *Chem. Geol.* 232, 12–32. doi:10.1016/j.chemgeo.2006.02.012

Wang, E., Guo, T., Li, M., Xiong, L., Dong, X., Wang, T., et al. (2023). Reservoir characteristics and oil properties of a lacustrine shale system: Early Jurassic black shale from the Sichuan Basin, SW China. *J. Asian Earth Sci.* 242 (2023), 105491. doi:10.1016/j.jseaes.2022.105491

Wang, W., Cao, C., and Wang, Y. (2004). The carbon isotope excursion on GSSP candidate section of Lopingian-Guadalupian boundary. *Earth Planet. Sci. Lett.* 220 (2004), 57–67. doi:10.1016/S0012-821X(04)00033-0

Wang, X. D., Lv, X. B., Cao, X. F., Yuan, Q., Wang, Y. F., Liu, W., et al. (2016). Petrology and geochemistry of the banded iron formation of the Kuluketage Block, Xinjiang, NW China: Implication for BIF depositional setting. *Resour. Geol.* 66 (4), 313–334. CNKI:SUN:KCDZ.0.2014-S1-231. doi:10.1111/rge.12107

Wang, X. P., Wang, Q. Y., and An, X. Y. (2022). Characteristics of sedimentary environment and evolution of Permian in southern Sichuan Basin: An example from the profile of Gulin Bajiaocun in Sichuan Province. *Sediment. Geol. Tethyan Geol.* 42 (3), 398–412. doi:10.19826/j.cnki.1009-3850.2022.05009

Wang, Z., Huang, Z., Yao, J., and Ma, X. (2014). Characteristics and main progress of the stratigraphic chart of China and directions. *Acta Geosci. Sin.* 35 (3), 271–276. doi:10.3975/cagsb.2014.03.01

Wei, H., Chen, D., Wang, J., Yu, H., and Tucker, M. E. (2012). Organic accumulation in the lower Chihsia formation (Middle Permian) of South China: constraints from pyrite morphology and multiple geochemical proxies. *Palaeogeogr. Palaeoclimatol. Palaeoecol* 353–355 (2012), 73–86. doi:10.1016/j.palaeo.2012.07.005

Wei, W., Yu, W., Algeo, T. J., Herrmann, A. D., Zhou, L., Liu, J., et al. (2022). Boron proxies record paleosalinity variation in the North American Midcontinent Sea in response to Carboniferous glacio-eustasy. *Geology* 5, 537–541. doi:10.1130/G49521.1

Wignall, P. B., and Bond, D. P. G. (2023). The great catastrophe: causes of the Permo-Triassic marine mass extinction. *Natl. Sci. Rev.* 11 (1), nwad273. doi:10.1093/nsr/nwad273

Wignall, P. B., Sun, Y., Bond, D. P. G., Izon, G., Newton, R. J., Védrine, S., et al. (2009). Volcanism, mass extinction, and carbon isotope fluctuations in the Middle Permian of China. *Science* 324, 1179–1182. doi:10.1126/science.1171956

Xiong, G. Q., Liu, C. L., Dong, G. M., and Cui, W. (2021). A study of element geochemistry of mudstones of upper Ordovician Wufeng formation and lower Silurian Longmaxi formation in southern Daba Mountain. *Sediment. Geol. Tethyan Geol.* 41 (3), 399–417. doi:10.19826/j.cnki.1009-3850.2020.07001

Yamamoto, K. (1987). Geochemical characteristics and depositional environments of cherts and associated rocks in the Franciscan and Shimanto Terranes. *Sediment. Geol.* 52, 65–108. doi:10.1016/0037-0738(87)90017-0

Ye, Q., and Jiang, H. (2016). Conodont biostratigraphy and a negative excursion in carbonate carbon isotopes across the Wuchiapingian-Changhsingian boundary at the Dawoling Section, Hunan Province. *Earth Sci.* 41 (11), 1883–1892. doi:10.3799/dqkx.2016.130

Yin, H., Jiang, H., Xia, W., Feng, Q., Zhang, N., and Shen, J. (2014). The end-Permian regression in South China and its implication on mass extinction. *Earth-Science Rev.* 137 (2014), 19–33. doi:10.1016/j.earscirev.2013.06.003

Zhai, G., Wang, Y., Liu, G., Zhou, Z., Zhang, C., and Liu, X. (2020). Enrichment and accumulation characteristics and prospect analysis of the Permian marine continental multiphase shale gas in China. *Sediment. Geol. Tethyan Geol.* 40 (3), 102–117. doi:10.19826/j.cnki.1009-3850.2020.07003

Zhang, J., Li, X., Zhang, X., Zhang, M., Cong, G., Zhang, G., et al. (2018). Geochemical and geological characterization of marine-continental transitional shales from Longtan Formation in Yangtze area, South China. *Mar. Petroleum Geol.* 96, 1–15. doi:10.1016/j.marpetgeo.2018.05.020

Zhang, L. F., Dong, D. Z., Qiu, Z., Wu, C. J., Zhang, Q., Wang, Y. M., et al. (2021). Sedimentology and geochemistry of Carboniferous-Permian marine-continental transitional shales in the eastern Ordos Basin, North China. *Palaeogeogr. Palaeoclimatol. Palaeoecol.* 571, 110389. doi:10.1016/j.palaeo.2021.110389

Zhang, K., Song, Y., Jia, C., Jiang, Z., Han, F., Wang, P., et al. (2022). Formation mechanism of the sealing capacity of the roof and floor strata of marine organic-rich shale and shale itself, and its influence on the characteristics of shale gas and organic matter pore development. *Mar. Petroleum Geol.* 140, 105647. doi:10.1016/j.marpetgeo.2022.105647

Zhao, J., Jin, Z., Jin, Z., Geng, Y., Wen, X., and Yan, C. (2016). Applying sedimentary geochemical proxies for paleoenvironment interpretation of organic-rich shale deposition in the Sichuan Basin, China. *Int. J. Coal Geol.* 163, 52–71. doi:10.1016/j.coal.2016.06.015

Zhao, T. Y., Algeo, T. J., Feng, Q. L., Zi, J. W., and Xu, G. (2019). Tracing the provenanceof volcanic ash in Permian-Triassic boundary strata, South China: Constraints from inherited and syn-depositional magmatic zircons. *Palaeogeogr. Palaeoclimatol. Palaeoecol.* 516, 190–202. doi:10.1016/j.palaeo.2018.12.002

Zou, C., Zhu, R., Chen, Z., Ogg, J. G., Wu, S., Dong, D., et al. (2019). Organic-matter-rich shales of China. *Earth Sci. Rev.* 189, 51–78. doi:10.1016/j.earscirev.2018.12.002

Frontiers in Earth Science

Investigates the processes operating within the major spheres of our planet

Advances our understanding across the earth sciences, providing a theoretical background for better use of our planet's resources and equipping us to face major environmental challenges.

Discover the latest Research Topics

See more →

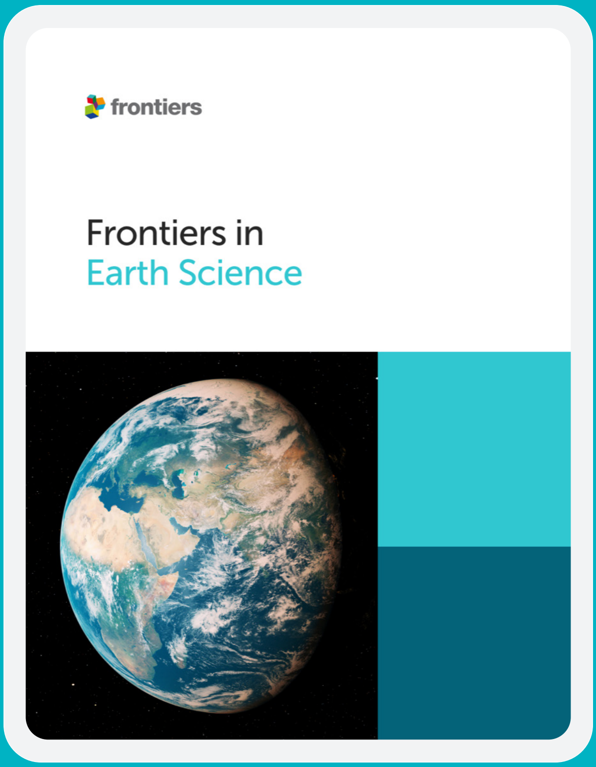

frontiers

Frontiers in
Earth Science

Frontiers

Avenue du Tribunal-Fédéral 34
1005 Lausanne, Switzerland
frontiersin.org

Contact us

+41 (0)21 510 17 00
frontiersin.org/about/contact

frontiers | Research Topics